Universität Hamburg
DER FORSCHUNG | DER LEHRE | DER BILDUNG

# Interfacially polymerized ion-selective membranes for water purification

## Dissertation

in conformity with the requirements for the degree of
*Doctor rerum naturalium* (Dr. rer. nat.)
submitted to the University of Hamburg

Faculty of Mathematics, Informatics and Natural Sciences

Department of Chemistry

Submitted by

Nicolás Cevallos-Cueva

Hamburg, 2026

| | |
|---|---|
| Supervisor: | Prof. Dr. Volker Abetz |
| Co-supervisor: | Dr. Md. Mushfequr Rahman |
| 1st Referee: | Prof. Dr. Volker Abetz |
| 2nd Referee: | Dr. Werner Pauer |
| 3rd Referee: | Prof. Dr. Katja Loos |
| Examination Committee: | Prof. Dr. Volker Abetz<br>Prof. Dr. Gerrit A. Luinstra<br>Priv. Doz. Dr. Christoph Wutz |
| Date of Disputation: | 28.08.2026 |
| Approval Date: | 29.09.2026 |

The dissertation was written under the supervision of Prof. Dr. Volker Abetz at the Institute of Membrane Research (Department of Materials Chemistry and Mass Transport) of the Helmholtz-Zentrum Hereon. The work was started in January 2021 and the dissertation was submitted in May 2026.

# Publications

This dissertation is based on the following peer-reviewed publications:

I. N. Cevallos-Cueva, M. M. Rahman, H. H. Kinfu, V. Abetz, *Chemical Engineering Journal* **2024**, *493*, DOI 10.1016/j.cej.2024.152775.

II. N. Cevallos-Cueva, M. M. Rahman, H. H. Kinfu, V. Abetz, *Journal of Membrane Science* **2025**, *721*, DOI 10.1016/j.memsci.2025.123808.

III. N. Cevallos-Cueva, M. M. Rahman, H. H. Kinfu, V. Abetz, *Journal of Membrane Science* **2025**, *736*, DOI 10.1016/j.memsci.2025.124642.

IV. N. Cevallos-Cueva, M. M. Rahman, H. H. Kinfu, V. Abetz, *Desalination* **2026**, *622*, DOI 10.1016/j.desal.2025.119765.

# Contents

**Publications** iii

**Nomenclature** vii

**Zusammenfassung** xi

**Abstract** xiii

**1 Introduction** 1
- 1.1 Membrane Separation Processes: An Overview . . . 1
  - 1.1.1 Membrane separation as a class of technologies . . . 1
  - 1.1.2 Non-pressure-driven processes . . . 1
  - 1.1.3 Pressure-driven processes . . . 3
  - 1.1.4 The Position and Functional Role of NF . . . 4
- 1.2 Technological and Societal Relevance . . . 7
  - 1.2.1 $Na^+/Mg^{2+}$ separation . . . 7
  - 1.2.2 Nitrate removal . . . 8
- 1.3 Fundamentals of NF Membranes . . . 9
  - 1.3.1 Thin-film composite architecture . . . 9
  - 1.3.2 Interfacial polymerization process . . . 10
  - 1.3.3 Influence of monomer chemistry and concentration . . . 12
  - 1.3.4 Morphological descriptors of the selective layer . . . 17
- 1.4 Mechanisms of Ion Transport and Separation . . . 22
  - 1.4.1 Steric hindrance (size exclusion) . . . 23
  - 1.4.2 Donnan exclusion and electrostatics . . . 24
  - 1.4.3 Dielectric exclusion and desolvation penalties . . . 25
  - 1.4.4 Coupled transport fluxes . . . 29
  - 1.4.5 Mechanistic models used in NF . . . 31
  - 1.4.6 Summary and role in the dissertation . . . 39
- 1.5 State of the Art and Knowledge Gaps . . . 39
  - 1.5.1 Established knowledge . . . 40
  - 1.5.2 Knowledge gaps . . . 41
  - 1.5.3 Synthesis and implications . . . 43

**2 Scientific Objectives of the Dissertation** 45

**3 Cumulative Part of the Dissertation** 47
- 3.1 Publication I . . . 47
- 3.2 Publication II . . . 64
- 3.3 Publication III . . . 79
- 3.4 Publication IV . . . 92

**4 Comprehensive Discussion** **109**
4.1 From IP Variables to Effective Descriptors . . . 109
4.2 When Mechanisms Control Selectivity . . . 110
4.2.1 $NO_3^-/SO_4^{2-}$: when dielectric exclusion controls separation . . . 111
4.2.2 $Na^+/Mg^{2+}$: preferential $Mg^{2+}$ diffusion suppression . . . 111
4.3 Electrolyte Identity Reshapes Effective Descriptors . . . 112
4.4 Robust Fitting and Interpretability Constraints . . . 113
4.5 Design Implications . . . 114
4.5.1 Nitrate removal design: manage coupled transport . . . 114
4.5.2 $Na^+/Mg^{2+}$ design: preferential $Mg^{2+}$ suppression . . . 115
4.5.3 Electrolyte-specific design rules . . . 115
4.6 Limitations and Outlook . . . 115
4.7 Outcome . . . 116

**References** **119**

**Appendix** **129**
List of hazardous substances used in the study according to GHS . . . 129
Online accessible Supporting Information . . . 131
Publication I . . . 131
Publication II . . . 144
Publication III . . . 160
Publication IV . . . 170

**Acknowledgement** **197**

**Declaration on oath / Affidavit** **199**

# Nomenclature

## Abbreviations

| Abbreviation | Definition |
|---|---|
| AFM | Atomic force microscopy |
| AEP | Aminoethylpiperazine (aqueous-phase monomer) |
| ATR-FTIR | Attenuated total reflectance Fourier-transform infrared spectroscopy |
| DAP | 1,4-bis(3-aminopropyl)piperazine |
| DE | Dielectric exclusion |
| DSPM | Donnan–Steric Pore Model |
| DSPM-DE | Donnan–Steric Pore Model with Dielectric Exclusion |
| ED | Electrodialysis |
| ENP | Extended Nernst–Planck (equation) |
| IEP | Isoelectric point |
| IP | Interfacial polymerization |
| MF | Microfiltration |
| MPD | *m*-Phenylenediamine |
| MWCO | Molecular weight cut-off |
| NF | Nanofiltration |
| PA | Polyamide |
| PALS | Positron annihilation lifetime spectroscopy |
| PEG | Polyethylene glycol |
| PIP | Piperazine |
| PS | Polysulfone |
| RBS | Rutherford backscattering spectroscopy |
| RMS | Root-mean-square (e.g. roughness metric) |
| RO | Reverse osmosis |
| SEM | Scanning electron microscopy |
| SEDE | Steric, electric and dielectric exclusion model |
| TEM | Transmission electron microscopy |
| TFC | Thin-film composite |
| TMC | Trimesoyl chloride |
| TMS | Teorell–Meyer–Sievers (model) |
| TST | Transition state theory |
| UF | Ultrafiltration |
| VOC | Volatile organic compounds |

# Variable Names

## Latin symbols

| Symbol | Definition | Unit |
|---|---|---|
| $A$ | Membrane area | [$m^2$] |
| $a_i$ | Activity of species $i$ | [–] |
| $C_0$ | Total monomer concentration (functionality-weighted sum of monomer concentrations; IP kinetics section) | [$mol\,m^{-3}$] |
| $c_{A0}$ | Initial concentration of reactant $A$ in the aqueous phase (IP kinetics section) | [$mol\,m^{-3}$] |
| $c_{B0}$ | Initial concentration of reactant $B$ in the organic phase (IP kinetics section) | [$mol\,m^{-3}$] |
| $c_i$ | Concentration of species $i$ (local; phase-dependent by context) | [$mol\,m^{-3}$] |
| $c_{i,f}$ | Bulk feed concentration of species $i$ | [$mol\,m^{-3}$] |
| $c_{i,m}$ | Feed-side membrane-surface concentration of species $i$ (concentration polarization) | [$mol\,m^{-3}$] |
| $c_{i,p}$ | Permeate concentration of species $i$ | [$mol\,m^{-3}$] |
| $c_X$ | Effective membrane fixed-charge density | [$mol\,m^{-3}$] |
| $d_{H_2O}$ | Thickness of near-wall oriented-water layer | [m] |
| $D$ | Electric displacement field (polarization displacement) | [$C\,m^{-2}$] |
| $D_{A,1}$ | Diffusion coefficient of reactant $A$ in phase 1 (aqueous) | [$m^2\,s^{-1}$] |
| $D_{A,2}$ | Diffusion coefficient of reactant $A$ in phase 2 (organic) | [$m^2\,s^{-1}$] |
| $D_i$ | Diffusion coefficient of species $i$ (context-dependent effective value) | [$m^2\,s^{-1}$] |
| $D_{i,\infty}$ | Bulk diffusion coefficient of species $i$ | [$m^2\,s^{-1}$] |
| $e$ | Elementary charge | [C] |
| $F$ | Faraday constant | [$C\,mol^{-1}$] |
| $I$ | Electric current density (set to $I = 0$ under zero-current closure) | [$A\,m^{-2}$] |
| $J_i$ | Molar flux of species $i$ | [$mol\,m^{-2}\,s^{-1}$] |
| $J_{i,\mathrm{adv}}$ | Advective (convective) contribution to $J_i$ | [$mol\,m^{-2}\,s^{-1}$] |
| $J_{i,\mathrm{elec}}$ | Electromigrative contribution to $J_i$ | [$mol\,m^{-2}\,s^{-1}$] |
| $J_{i,\mathrm{diff}}$ | Diffusive contribution to $J_i$ | [$mol\,m^{-2}\,s^{-1}$] |
| $J_v$ | Volumetric solvent flux | [$m\,s^{-1}$] |
| $k_{c,i}$ | Mass-transfer coefficient for species $i$ in the bulk | [$m\,s^{-1}$] |
| $k^{\bullet}_{c,i}$ | Corrected mass-transfer coefficient for species $i$ in the boundary layer (concentration-polarization model) | [$m\,s^{-1}$] |

| Symbol | Definition | Unit |
|---|---|---|
| $k_B$ | Boltzmann constant | [J K$^{-1}$] |
| $k'$ | Effective reaction-rate constant (IP kinetics section) | [s$^{-1}$] |
| $K_A$ | Partition coefficient of reactant $A$ into the organic phase (IP kinetics section) | [−] |
| $K_{i,a}$ | Hindrance factor for advection of species $i$ | [−] |
| $K_{i,d}$ | Hindrance factor for diffusion of species $i$ | [−] |
| $l_b$ | Bjerrum length in bulk water | [m] |
| $l_{\text{pore}}$ | Bjerrum length in pore water | [m] |
| $l_m$ | Bjerrum length in the membrane matrix | [m] |
| $P$ | Pressure | [Pa] |
| $P_i$ | Solute passage of species $i$ ($P_i = c_{i,p}/c_{i,f}$) | [−] |
| $r$ | radial coordinate in the pore cross-section | [m] |
| $r_i$ | (Hydrated/Stokes) radius of species $i$ | [m] |
| $r_{\text{pore}}$ | Effective pore radius | [m] |
| $R$ | Universal gas constant | [J mol$^{-1}$ K$^{-1}$] |
| $R_i$ | Solute rejection/retention of species $i$ ($R_i = 1 - c_{i,p}/c_{i,f}$) | [−] |
| $R_{i,obs}$ | Experimental/observed solute rejection/retention of species $i$ | [−] |
| $R_{i,real}$ | Solute rejection/retention of species $i$ at infinite stirring velocity (neglecting concentration-polarization) | [−] |
| $T$ | Temperature | [K] |
| $V$ | Polarized volume in dielectric self-energy expression | [m$^3$] |
| $V_i$ | Partial molar volume of species $i$ | [m$^3$ mol$^{-1}$] |
| $W$ | Self-energy (dielectric exclusion framework; context-dependent) | [J] |
| $W_B$ | Born self-energy of an ion in a dielectric continuum | [J] |
| $x$ | Spatial coordinate (transport direction) | [m] |
| $z_i$ | Valence of species $i$ | [−] |

## Greek symbols

| Symbol | Definition | Unit |
|---|---|---|
| $\Delta\Psi_D$ | Donnan potential difference (across a solution/membrane interface) | [V] |
| $\Delta W$ | Dielectric self-energy difference (membrane vs. solution) | [J] |
| $\Delta W_i$ | Dielectric-exclusion energy penalty for species $i$ | [J] |

| Symbol | Definition | Unit |
|---|---|---|
| $\Delta x_e$ | Effective thickness-to-porosity ratio (effective transport length) | [m] |
| $\varepsilon$ | Relative permittivity (dielectric constant; medium-dependent by context) | [−] |
| $\varepsilon_0$ | Vacuum permittivity | [F m$^{-1}$] |
| $\varepsilon_b$ | Relative permittivity of bulk water (bulk dielectric constant) | [−] |
| $\varepsilon_m$ | Relative permittivity of the polymer matrix | [−] |
| $\varepsilon^*$ | Relative permittivity of near-wall oriented-water layer (two-layer dielectric picture) | [−] |
| $\varepsilon_{\text{pore}}$ | Effective relative permittivity (dielectric constant) of pore water | [−] |
| $\Phi_{S,i}$ | Steric partition coefficient of species $i$ | [−] |
| $\Phi_{D,i}$ | Donnan partition coefficient of species $i$ | [−] |
| $\Phi_{DE,i}$ | Dielectric exclusion coefficient of species $i$ | [−] |
| $\Phi_{\text{Born},i}$ | Born-type dielectric exclusion coefficient of species $i$ | [−] |
| $\Phi_{\text{image},i}$ | Image-force dielectric exclusion coefficient of species $i$ | [−] |
| $\gamma_i$ | Activity coefficient of species $i$ | [−] |
| $\kappa$ | Inverse Debye length (screening parameter) | [m$^{-1}$] |
| $\kappa_{PD}$ | Partition–diffusion coefficient factor of reactant (IP kinetics) | [−] |
| $\lambda_i$ | Size ratio ($\lambda_i = r_i/r_{\text{pore}}$) | [−] |
| $\mu_i$ | Electrochemical potential of species $i$ | [J mol$^{-1}$] |
| $\mu_i^0$ | Reference electrochemical potential of species $i$ | [J mol$^{-1}$] |
| $\rho_e$ | Local electric charge density | [C m$^{-3}$] |
| $\sigma$ | Surface charge density | [C m$^{-2}$] |
| $v$ | Planar interfacial reaction rate (IP kinetics) | [mol m$^{-2}$ s$^{-1}$] |
| $\xi$ | Electrical potential gradient at the feed-solution/membrane interface | [V m$^{-1}$] |
| $\zeta$ | Dielectric-mismatch parameter in the screened polarization term | [−] |
| $\Psi$ | Electric potential | [V] |

# Zusammenfassung

Die Nanofiltration (NF) ist ein druckgetriebenes Membranverfahren, das zwischen Ultrafiltration und Umkehrosmose einzuordnen ist und breit eingesetzt wird, wenn nicht eine vollständige Entsalzung, sondern eine partielle Salzabtrennung erforderlich ist. In dieser Dissertation werden Dünnschicht-Kompositmembranen (TFC) für die Nanofiltration mit einer mittels Grenzflächenpolymerisation hergestellten selektiven Schicht für zwei Anwendungen entwickelt und untersucht: die Trennung von $Na^+/Mg^{2+}$ (Wasserenthärtung und Magnesiumrückgewinnung) sowie die Nitratentfernung aus Misch-Elektrolyt-Lösungen. Obwohl die Grenzflächenpolymerisation (interfacial polymerization, IP) ein etabliertes Verfahren zur Herstellung von NF-Membranen ist, fehlt im Feld bislang systematische, für die Membranauslegung relevante Evidenz, die IP-Bedingungen und Elektrolytidentität mit denjenigen Membraneigenschaften verknüpft, welche den selektiven Ionentransport letztlich bestimmen. Zur Schließung dieser Lücke werden in dieser Dissertation Polyamid-TFC-NF-Membranen mittels IP hergestellt und ihr Verhalten auf der Grundlage gekoppelter Ausschluss- und Transportmechanismen interpretiert. Die hier untersuchten Membranserien basieren auf der Chemie von Piperazin (PIP) und Trimesoylchlorid (TMC), wobei in der wässrigen Phase neben Piperazin auch Aminoethylpiperazin (AEP) und 1,4-Bis(3-aminopropyl)piperazin (DAP) als piperazinbasierte Monomere eingesetzt werden. Ihre Trennleistung wird mit dem Donnan–Steric Pore Model with Dielectric Exclusion (DSPM-DE) analysiert.

Anstatt die Membranstruktur als feste nominelle Größe zu behandeln, beschreibt diese Dissertation das Membranverhalten über einen kompakten Satz effektiver Deskriptoren: Porenradius $r_{\mathrm{pore}}$, Schichtdicken-zu-Porositäts-Verhältnis $\Delta x_\epsilon$, Festladungsdichte $c_X$ und Dielektrizitätskonstante im Porenraum $\varepsilon_{\mathrm{pore}}$. Diese Deskriptoren werden in allen vier Publikationskapiteln konsistent durch Anpassung an Neutralstoff- und Elektrolyt-Rückhaltedaten bestimmt; zudem werden die entsprechenden Stoffflussbeiträge in diffusions-, elektromigrations- und advektionsgetriebene Anteile zerlegt. Auf diese Weise verknüpft die Dissertation systematisch Variablen der Membranherstellung und Elektrolytidentität mit dem Ionentransportverhalten. Die Elektrolytidentität wird explizit über Vergleiche innerhalb von Elektrolytreihen mit gemeinsamem Anion ($Cl^-$ bzw. $SO_4^{2-}$) berücksichtigt, sodass direkt bewertet werden kann, wie die ionische Umgebung den für eine gegebene Membranchemie abgeleiteten effektiven Deskriptorsatz verändert.

Für die nitratselektive NF in der PIP/TMC-Reihe mit variierter Konzentration lässt sich die $NO_3^-/SO_4^{2-}$-Trennung am konsistentesten durch dielektrischen Ausschluss erklären. In praktischer Hinsicht bedeutet dies, dass bereits relativ kleine Änderungen von $r$pore die Ionenselektivität deutlich stärker beeinflussen können, wenn sie mit Änderungen der dielektrischen Umgebung im Porenraum einhergehen. Die Ergebnisse zeigen ferner, dass der Nitrattransport in Mischsalzsystemen stark mit dem Transport anderer Ionen gekoppelt ist. Unter bestimmten ternären Bedingungen kann diese Kopplung sogar zu einer negativen Nitratrückhaltung führen, das heißt, das Retentat wird zum nitratabgereicherten Produktstrom. Die Analyse identifiziert zugleich eine Grenze des vorliegenden Rahmens: Trends im System $Na^+/NO_3^-/Cl^-$ weisen auf ionenspezifische Effekte hin, die über die vorliegende

DSPM-DE-Implementierung hinausgehen, in der $NO_3^-$ und $Cl^-$ als vergleichbare einwertige Ionen behandelt werden.

Für die Trennung von $Na^+/Mg^{2+}$ nimmt die Selektivität zu, wenn der Transport von $Mg^{2+}$ stärker unterdrückt wird als der von $Na^+$. Im Rahmen des DSPM-DE ist dieses Verhalten mit Membranen verknüpft, die sowohl ladungsselektiver werden als auch den Ionentransport im Porenraum stärker einengen. In der PIP/TMC-Reihe erweisen sich $\Delta x_e$ und $c_X$ als die zentralen, synthesebezogenen Deskriptoren. Ersteres beeinflusst vor allem die Permeanz, während Letzteres die Ionenpartitionierung und die internen Ionenkonzentrationen stark prägt. Die Dissertation zeigt darüber hinaus, dass die $Na^+/Mg^{2+}$-Leistung nicht allein aus dem Verhalten der Kationen interpretiert werden kann, weil der Gegenionentransport das elektrische Feld in der Membran und damit die gesamte Flussbilanz beeinflusst.

Die Monomeridentität (AEP vs. DAP) verändert die Selektivität, indem sie den gekoppelten Deskriptorsatz verschiebt, anstatt nur einen einzelnen dominanten Parameter zu modifizieren. In der AEP/DAP-Reihe werden Unterschiede in der $NO_3^-/SO_4^{2-}$-Partitionierung primär durch $c_X$ über den Donnan-Ausschluss bestimmt. Gleichzeitig bleibt der dielektrische Ausschluss relevant, ist im untersuchten Konzentrationsbereich jedoch nicht mehr der dominierende Faktor. Schließlich ist die Elektrolytidentität nicht lediglich eine Betriebsbedingung, die auf eine feststehende Membran angewendet wird. Die Deskriptorwerte unterscheiden sich zwischen $Cl^-$- und $SO_4^{2-}$-Systemen erheblich, insbesondere für $\varepsilon$pore und $c_X$. Daraus folgt, dass Deskriptorwerte, die in einer Elektrolytumgebung abgeleitet wurden, nicht automatisch auf eine andere übertragen werden sollten.

Insgesamt stellt diese Dissertation systematische Zusammenhänge zwischen IP-Variablen, effektiven Membrandeskriptoren und selektivem Ionentransport in Polyamid-TFC-NF-Membranen her. Sie liefert eine physikalisch fundierte Grundlage für das Verständnis und die Auslegung von Membranen für magnesiumbezogene Trennaufgaben und die Nitratentfernung unter Misch-Elektrolyt-Bedingungen und zeigt zugleich, dass die angepassten Deskriptoren als effektive Größen zu interpretieren sind, deren Aussagekraft vor allem in relativen Vergleichen innerhalb kontrollierter Membranserien verlässlich ist.

# Abstract

Nanofiltration (NF) is a pressure-driven membrane process that lies between ultrafiltration and reverse osmosis, and it is widely used when partial salt separation is needed rather than complete desalination. In this dissertation, thin-film composite (TFC) NF membranes with an interfacially polymerized selective layer are developed and analyzed for two applications: $Na^+/Mg^{2+}$ separation (water softening and magnesium valorization) and nitrate removal from mixed-electrolyte solutions. Although interfacial polymerization (IP) is an established route for producing NF membranes, a central limitation in the field is the lack of systematic, design-relevant evidence linking IP conditions and electrolyte identity to the membrane properties that ultimately control selective ion transport. To address this gap, this dissertation develops polyamide TFC NF membranes formed by IP and interprets their behavior in terms of coupled exclusion and transport mechanisms. The membrane series investigated here are based on piperazine (PIP)/trimesoyl chloride (TMC) chemistry, with variation of the aqueous-phase piperazine-based monomer using aminoethylpiperazine (AEP) and 1,4-bis(3-aminopropyl)piperazine (DAP). Their separation performance is analyzed within the Donnan–Steric Pore Model with Dielectric Exclusion (DSPM-DE).

Rather than treating membrane structure as a fixed nominal quantity, this dissertation describes membrane behavior through a compact set of effective descriptors: pore radius $r_{\text{pore}}$, thickness-to-porosity ratio $\Delta x_e$, fixed-charge density $c_X$, and pore dielectric constant $\varepsilon_{\text{pore}}$. These descriptors are obtained consistently across all four publication chapters by fitting neutral-solute and mixed-electrolyte retention data, and the corresponding solute flux is decomposed into diffusion-, electromigration-, and advection-driven contributions. In this way, the dissertation systematically connects membrane fabrication variables and electrolyte identity to ion transport behavior. Electrolyte identity is treated through common-anion comparisons ($Cl^-$ vs. $SO_4^{2-}$), showing how the ionic environment reshapes the effective descriptor set inferred for a given membrane chemistry.

For nitrate-selective NF in the concentration-varied PIP/TMC series, $NO_3^-/SO_4^{2-}$ separation is most consistently explained by dielectric exclusion. In practical terms, relatively small changes in $r_{\text{pore}}$ can have a much stronger effect on ion selectivity when they are accompanied by changes in the dielectric environment inside the pores. The results also show that nitrate transport in mixed-salt systems is strongly coupled to the transport of other ions. Under some ternary conditions, this coupling can even lead to negative nitrate retention, meaning that the retentate becomes the nitrate-depleted product stream. The analysis also identifies a limit of the present framework: trends in the $Na^+/NO_3^-/Cl^-$ system indicate ion-specific effects beyond the present DSPM-DE implementation, in which $NO_3^-$ and $Cl^-$ are treated as comparable monovalent ions.

For $Na^+/Mg^{2+}$ separation, selectivity increases when $Mg^{2+}$ transport is suppressed more strongly than $Na^+$ transport. Within the DSPM-DE framework, this behavior is associated with membranes becoming more charge-selective and more confining. In the PIP/TMC series, $\Delta x_e$ and $c_X$ emerge as key synthesis-linked descriptors. The former mainly influences permeance, whereas the latter strongly affects ion partitioning and internal ion concentrations.

The dissertation further shows that $Na^+/Mg^{2+}$ performance cannot be interpreted from cation behavior alone, because counter-ion transport influences the electric field inside the membrane and therefore the overall flux.

Monomer identity (AEP vs. DAP) reshapes selectivity by shifting the coupled descriptor set rather than modifying a single dominant parameter. In the AEP/DAP series, $NO_3^-/SO_4^{2-}$ partitioning differences are governed primarily by $c_X$ through Donnan exclusion. At the same time, dielectric exclusion remains relevant but is no longer the main factor across the tested concentration range. Finally, electrolyte identity is not simply an operating condition applied to a fixed membrane. Descriptor values differ substantially between $Cl^-$ and $SO_4^{2-}$ systems, especially for $\varepsilon_{\text{pore}}$ and $c_X$. As a result, descriptor values inferred in one electrolyte environment should not automatically be transferred to another.

Taken together, this dissertation establishes systematic links between IP variables, effective membrane descriptors, and selective ion transport in polyamide TFC NF membranes. It provides a mechanistic basis for understanding and designing membranes for magnesium-related separations and nitrate removal under mixed-electrolyte conditions, while also showing that the fitted descriptors should be interpreted as effective quantities whose meaning is most reliable in relative comparisons within controlled membrane series.

# 1

# Introduction

## 1.1. Membrane Separation Processes: An Overview

### 1.1.1. Membrane separation as a class of technologies

Membrane separation is a technique for separating one or several components from a mixture by applying a driving force. The core of this technique is the membrane, which is a selective layer that permeates solutes at faster rates than the other components of the mixture based on their physicochemical properties such as size, charge, or solubility.

Selective transport of solutes refers to the different rates at which each solute permeates through the membrane. Depending on the driving force, i.e., the effective force pushing the solutes from the feed toward the permeate side, membrane processes can be categorized into non-pressure (e.g., electrical, concentration and gradient-driven operations) and pressure-driven processes (Figure 1.1). Among these, pressure-driven membranes dominate water treatment [1].

### 1.1.2. Non-pressure-driven processes

Electrodialysis (ED) is one of the most established non-pressure-driven membrane separation processes, whose driving force is an electrical potential gradient applied across a stack of alternating cation- and anion-exchange membranes. In an ED stack, the ion-exchange membranes are placed between an anode and a cathode. Under an applied electric field, cations migrate toward the cathode and anions toward the anode, selectively permeating through the corresponding ion-exchange membranes. This yields alternating diluate and concentrate streams. ED typically operates under low or atmospheric hydraulic pressure and is suitable for moderate-salinity feeds, where energy consumption scales with ion concentration rather than water volume. The process was industrially realized in the 1950s following the development of durable crosslinked ion-exchange polymers. Since then, ED has been used extensively for brackish-water desalination, food-industry demineralization, and waste-stream treatment. However, ED is inherently limited to charged species and becomes less competitive for high-salinity feeds due to increased electrical resistance and concentration polarization, which raise energy consumption and reduce process efficiency. Because many

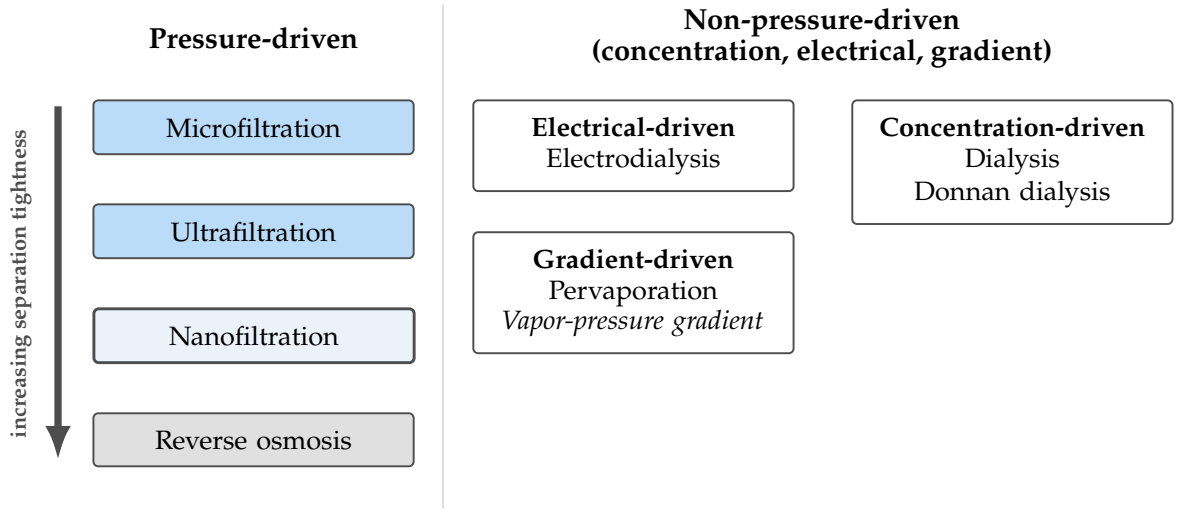



**Figure 1.1:** Classification of membrane separation processes by driving force. Pressure-driven processes are ordered by increasing separation tightness from microfiltration to reverse osmosis. Non-pressure-driven operations include electrical-, concentration-, and other gradient-driven processes.

aqueous separations require high throughput and retention of both ionic and neutral solutes, pressure-driven membrane processes are often preferred in water treatment [2].

Pervaporation is a membrane process that separates liquid mixtures through a vapor-pressure (chemical potential) gradient rather than hydraulic pressure. A liquid feed contacts one side of a dense selective membrane, with the permeate being withdrawn as a vapor on the opposite side, typically under vacuum or with a sweep gas followed by condensation. Separation stems from a solution–diffusion mechanism, where components with higher solubility and mobility in the membrane permeate preferentially as vapor. Pervaporation became commercially relevant in the early 1980s for dehydration of alcohols such as ethanol and isopropanol using crosslinked membranes. Later, it was extended to the removal of volatile organic compounds (VOC) from water and the separation of azeotropic mixtures in combination with distillation. Typical operating temperatures of approximately 50–120 °C provide the required vapor-pressure driving force, avoiding the high temperatures of distillation. However, relatively low fluxes and heating demands constrain pervaporation, limiting its application for large-scale separations. Accordingly, for applications dealing with high throughput and energy efficiency, pressure-driven membrane processes have become a preferred option [2].

Dialysis is among the earliest membrane processes and operates only by diffusion across a concentration gradient. It relies on unassisted solute diffusion through a membrane and is, therefore, intrinsically limited in throughput. Consequently, dialysis has been replaced by ultrafiltration or electrodialysis, where external driving forces and more selective membranes yield faster and better separations [2].

A variant, Donnan dialysis, utilizes ion-exchange membranes containing fixed charges that allow counter-ion diffusion and reject co-ions. Driven by concentration and/or pH gradients, ions of opposite charge can diffuse in opposite directions to maintain electroneutrality. Early applications included concentration or recovery of metal ions using cation-exchange membranes. Although it can achieve moderate performance, it generally lacks high selectivity

among ions of the same charge and remains of limited industrial significance due to slow transport rates and narrow applicability [2].

In general, dialysis-based processes are examples of passive, diffusion-driven transport, which are effective in certain low-energy or chemically demanding environments. However, their limitations in throughput and selectivity are fundamental, and in many practical separations these constraints are overcome by pressure-driven membrane processes [2].

### 1.1.3. Pressure-driven processes

Pressure-driven membrane processes can be classified considering the pore size of the membrane, characteristics of the retained particles (e.g., size, shape, and charge), and the applied transmembrane pressure. Accordingly, microfiltration (MF), ultrafiltration (UF), nanofiltration (NF), and reverse osmosis (RO) are the most prominent pressure-driven membrane processes [1].

MF membranes retain particles or solids larger than 0.1 µm based on a size-sieving mechanism [3]. The process utilizes porous membranes that work as selective barriers with typical pore sizes in the range of 0.1 to 10 µm. Operationally, constant-flux operation is often adopted to maintain a stable permeate rate, with transmembrane pressure increasing as fouling accumulates and is controlled by appropriate hydrodynamics and periodic cleaning. MF provides an economical option for polishing relatively clean streams, such as sterile filtration in pharmaceutical processing or final water purification for microelectronics. It is also applied to fouling-prone feeds in biotechnology, oily-water treatment, and municipal water and wastewater treatment [2]. Among pressure-driven processes, MF generally offers the highest water permeance and therefore achieves high throughputs at comparatively low pressures.

UF membranes filter particles whose size is between 2 nm and 0.1 µm, making them ideal to separate large dissolved molecules of natural organic material [3]. Particles larger than the pore size of the membranes are retained based on a size sieving mechanism, with selectivity commonly expressed by the molecular weight cut-off (MWCO) corresponding to the smallest molecule 90 % rejected by the membrane. Compared to MF, UF exhibits lower water permeance and typically operates at higher pressures, generally below about 10 bar [2]. Commercially, UF applications expanded rapidly from electrocoat paint recovery and whey protein concentration to juice clarification, oil–water emulsion treatment, and polymer recovery. The process's versatility stems from its ability to reject suspended or colloidal species while allowing complete passage of water and dissolved salts. However, UF performance can be limited by concentration polarization and membrane fouling, which cause the formation of gel or cake layers that reduce flux. Crossflow operation, module hydrodynamics, and chemical or hydraulic cleaning are control strategies to maintain operation. Consequently, energy consumption stems mainly from the need to circulate feed solutions at high velocities to mitigate fouling. UF is a well-established and mature pressure-driven process but it cannot discriminate effectively between small neutral solutes and dissolved salts, motivating the development of membranes capable of partial desalination and ion selectivity [1, 2].

RO is the most widely applied pressure-driven membrane process, enabling the separation of water from dissolved salts and low-molecular-weight solutes [1, 2]. RO has traditionally been described using a solution–diffusion framework through a dense selective layer. However,

more recent experimental and computational work suggests that transport in RO membranes can also involve pressure-driven flow through interconnected sub-nanometer free-volume pathways [4]. RO requires elevated pressures to overcome both hydraulic resistance and the osmotic pressure of saline feeds, which increases the specific energy demand, particularly at higher salinities. The technology evolved from early studies of osmotic phenomena in the 1850s and became practical when the Loeb–Sourirajan anisotropic cellulose acetate membrane (1962) considerably improved flux without sacrificing salt rejection. Notably, the interfacial polymerization of polyamide thin-film composites in the 1970s produced membranes that combined high (water) permeance with > 99 % salt rejection. This allowed the desalination of large-scale brackish and seawater and the production of ultrapure water for the electronics and pharmaceutical industries [2]. Commercial RO systems use spiral-wound or hollow-fiber modules operating at pressures of 5–120 bar [1], strongly depending on feed salinity. Despite its success, RO remains limited by fouling and scaling, necessitating pretreatment and periodic cleaning, and its high operating pressures motivate the use of lower-pressure, partially selective membranes in applications where complete desalination is unnecessary [5].

Among these pressure-driven processes, NF occupies the intermediate regime between ultrafiltration and reverse osmosis, combining moderate salt retention with higher permeance than RO. NF emerged from the development of low-pressure RO membranes with intentionally reduced salt rejection but greatly increased water flux [2]. In contrast to UF, NF can retain not only macromolecules and colloids but also a substantial fraction of dissolved organic micropollutants and multivalent ions. Many polymeric NF membranes bear ionizable groups, rendering the membrane surface charged when the membrane is in contact with the feed solution. The electrostatic interaction between ions and the surface charge of the NF membrane results in NF membranes being capable of removing ions smaller than their pore size. As a result, NF membranes typically reject multivalent ions much more strongly than monovalent ones (e.g., $MgSO_4 \gg NaCl$). This partial ion rejection gives NF its distinctive functionality for processes where complete desalination is unnecessary but selective ion separation and moderate operating pressures ($\sim$ 3 to 20 bar) provide substantial energy advantages, such as water softening, removal of organic micropollutants, and pretreatment of desalination feeds [2, 6].

Thus, NF bridges the gap between UF and RO by coupling moderate salt retention with high permeance.

### 1.1.4. The Position and Functional Role of Nanofiltration

The intermediate nature of NF is not only structural but also functional. Among pressure-driven membrane processes, NF integrates features of both porous membranes (MF and UF) and dense membranes (RO). Accordingly, transport through NF is commonly described by a mixed pore-transport nature in which advective flow through nanometer-scale free-volume pathways is coupled to diffusive and charge-related contributions, yielding permeate fluxes typically higher than RO but lower than UF [6]. This intermediate functionality is also reflected in separation behavior: MF and UF separation is dominated by steric (size-sieving) exclusion, whereas RO has traditionally been described by solution–diffusion through a dense selective layer [1, 5], although recent work also points to pore-flow-like, pressure-driven transport through transient free-volume pathways in RO membranes [4]. In contrast, NF combines steric hindrance with charge-related effects, which become particularly important

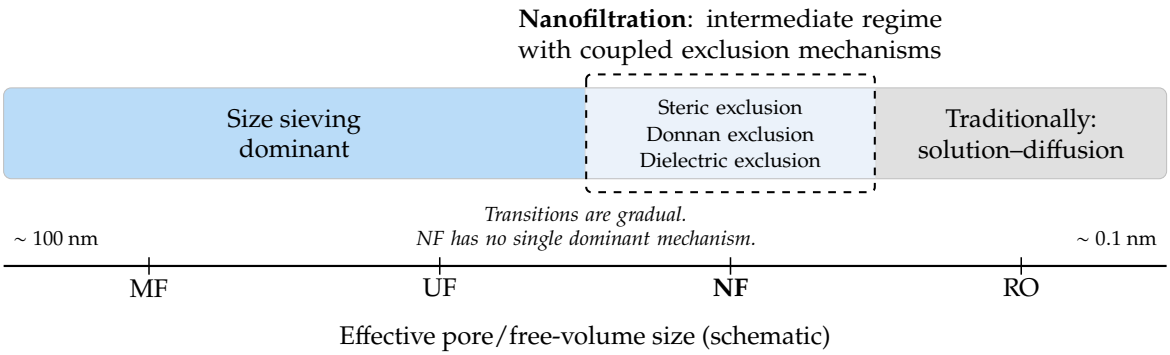



**Figure 1.2:** Pressure-driven membrane-process spectrum and dominant separation mechanisms across MF–UF–NF–RO. The horizontal axis is schematic (log-like) to emphasize gradual transitions in characteristic length scale. NF is highlighted as an intermediate regime where steric exclusion and charge-related effects (Donnan and dielectric exclusion) jointly govern ion partitioning and selectivity.

for ionic solutes. As shown in Figure 1.2, the dominant separation picture shifts from size sieving in MF/UF toward coupled steric, Donnan and dielectric exclusion in NF, with RO representing the tight end of the spectrum.

Upon quantitative comparison with adjacent processes, NF provides a compromise in performance. Performance in NF membranes is usually expressed in terms of flux, permeance, rejection and selectivity. Flux, $J$, is defined as the amount of a component (i.e., solute moles, solvent volume or mass) passing per unit time through a unit of membrane surface area normal to the membrane. Permeance is the flux of a component per unit transmembrane pressure. Solute $i$ retention or rejection, $R_i$, measures how much of a solute is retained or rejected by the membrane and is defined as $R_i = 1 - c_{i,p}/c_{i,f}$, where $c_{i,f}$ and $c_{i,p}$ are the solute concentrations in the feed and permeate, respectively. Selectivity quantifies the relative ability of a membrane to separate two solutes and is defined as the ratio of their solute passages, $P_i/P_j$, where $P_i = c_{i,p}/c_{i,f}$ [7].

Typical operating pressures of NF range between 3 and 20 bar, with water permeances ranging between 1.5–30 $\mathrm{L\,h^{-1}\,m^{-2}\,bar^{-1}}$ with typical NaCl retention ranging between 20–90 % [2, 6]. These values place NF between UF and RO in both permeance and salt retention. As illustrated in Figure 1.3, NF's combination of high flux and partial NaCl rejection yields an energy consumption lower than RO, enabling energy-efficient separations that neither UF nor RO can achieve.

At the molecular level, ion removal in NF arises from coupled interfacial partitioning/exclusion and in-pore transport [8]. Firstly, steric, Donnan, and dielectric exclusion mechanisms are responsible for the exclusion or partitioning of ions between the bulk-solution/membrane interfaces [7, 9–13]. Steric exclusion stems from the relative size of ions to the membrane pore openings, causing a higher retention of larger solutes. Charge-related effects contribute through Donnan and dielectric exclusion, which are distinct in origin. Donnan exclusion originates from the charged functional groups of the membrane. The equilibrium between the bulk solution and these charged groups results in an electric potential at the membrane interface, the Donnan potential, which attracts counterions and repels coions [12]. This electrostatic effect increases with the valence of the ion. Dielectric exclusion reflects the energetic penalty associated with transferring ions from bulk water into a lower-permittivity

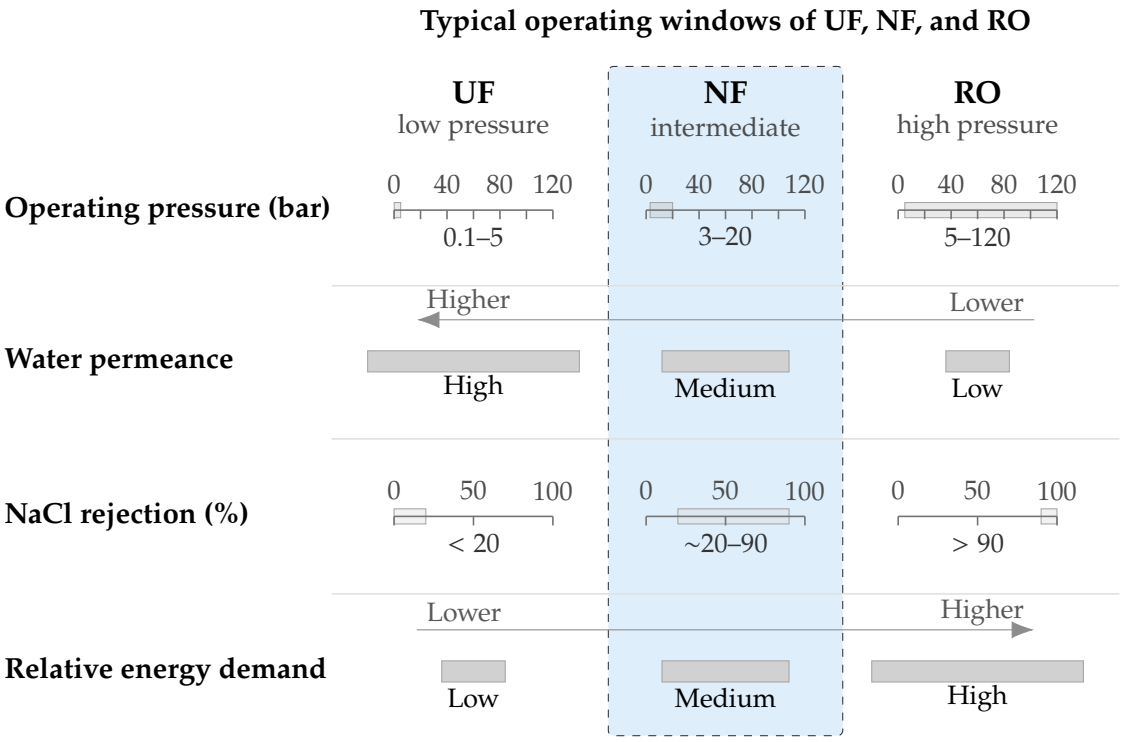



**Figure 1.3:** Graphical comparison of typical operating windows and qualitative performance trends for UF, NF, and RO. Operating pressure and NaCl rejection are shown as indicative ranges, while water permeance and relative energy demand are indicated qualitatively to emphasize functional trade-offs rather than benchmark specific membranes or operating conditions [1, 2]. The highlighted NF column illustrates its intermediate position between UF and RO in terms of pressure requirement, permeance, and partial NaCl rejection.

pore environment. For instance, the relative dielectric constant of polymeric materials and pure water (at 20 °C) is ~3–6 and 80, respectively [13]. This mismatch results in an exclusion of charged solutes. Contrary to Donnan exclusion mechanisms, dielectric exclusion depends on the valence but not on the sign of the ion [14]. Once the ions are either partitioned or excluded at the membrane interface, their transport through the membrane pores occurs by a combination of diffusive, advective, and electromigrative mechanisms [12, 15]. Specifically, advection results from the solvent flux, a concentration gradient drives diffusion, and electromigration arises due to an electrical potential gradient, making it specific to charged species. Consequently, NF exhibits a mixed transport nature responsible for the selective separation of ions based on their size, valence, and charge.

In summary, NF combines the high throughput of UF with the selective capabilities of RO. Its moderate operating pressure and partial ion retention make NF energetically advantageous. These attributes have made NF an attractive separation technology in water treatment and resource recovery, as discussed next.

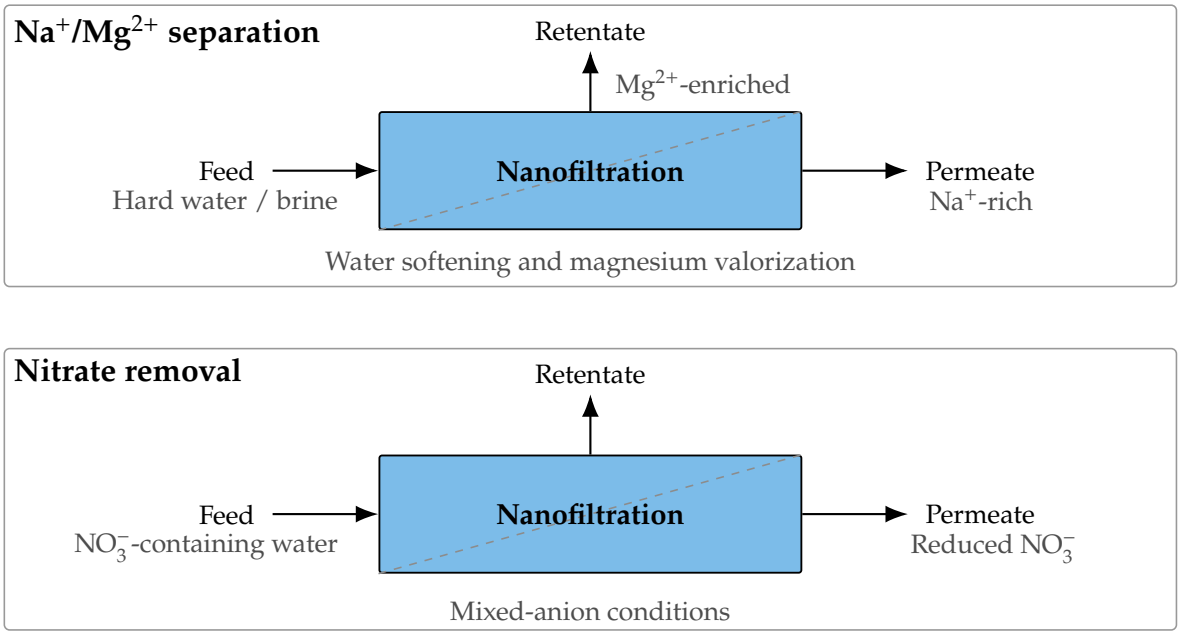



**Figure 1.4:** Application anchors used throughout this dissertation. The upper panel frames selective $Na^+/Mg^{2+}$ separation (water softening and magnesium valorization), while the lower panel frames nitrate removal under mixed-anion conditions. These two reference problems motivate the subsequent chapters and mechanistic analysis.

## 1.2. Technological and Societal Relevance

The functional balance between permeance and selectivity that characterizes NF also explains its increasing technological relevance in modern water treatment. The ability of NF to separate ions of different charge is particularly valuable in addressing current challenges in drinking-water production and resource management. NF is applied in diverse areas including drinking-water softening, removal of organic micropollutants, brine valorization, and contaminant control. Among these, two applications illustrate the societal and technological importance of this process and are examined here in greater detail: selective $Na^+/Mg^{2+}$ separation and nitrate removal. Figure 1.4 schematizes these two application anchors and the corresponding feed/permeate/retentate framing used throughout the dissertation.

### 1.2.1. $Na^+/Mg^{2+}$ separation

NF is commonly employed in drinking-water production, mainly for hardness removal and partial desalination. Water hardness stems from the presence of divalent cations (e.g., $Ca^{2+}$ and $Mg^{2+}$), so an effective softening method should ideally remove them selectively. Traditional processes such as lime softening and ion-exchange can achieve this but they are operationally and economically limited [10]. For instance, lime softening doses a calculated amount of calcium hydroxide to precipitate $CaCO_3$ and $Mg(OH)_2$, making it an expensive process that requires conditioning of the softened water to prevent corrosion. In turn, ion-exchange resins soften water by replacing $Ca^{2+}$ and $Mg^{2+}$ with $Na^+$ from the resins, which must be constantly recharged using sodium brines [10]. In contrast, NF membranes can soften

water continuously without relying on harsh chemicals. By selectively rejecting multivalent cations such as $Ca^{2+}$ and $Mg^{2+}$, NF achieves efficient hardness removal while allowing monovalent ions (e.g., $Na^{+}$) to pass through. The resulting permeate is of higher quality than lime-treated water because of the concurrent removal of color and turbidity [1]. This controlled ion selectivity also helps to avoid scaling in subsequent processes and reduces the need for chemical conditioning. Therefore, NF systems have become attractive technologies for the reliable production of drinking water [16].

Beyond water softening, NF is an emerging and promising technology for magnesium recovery, a strategic priority owing to magnesium's designation as a critical raw material by the European Commission [17]. Magnesium is an attractive choice for developing lightweight yet mechanically robust alloys due to its low density. Accordingly, magnesium alloys increasingly substitute aluminum in automotive and aerospace components, structural materials, biomedical implants, and energy-storage systems [18]. However, its sustainable supply largely relies on valorization of seawater and brines, which contain abundant yet dilute magnesium salts. In general, magnesium recovery from these sources is carried out through the separation of magnesium salts followed by electrolysis. Traditionally, magnesium was extracted from seawater by adding lime to precipitate it as magnesium hydroxide. The problem is that this hydroxide cannot be used directly to produce metallic magnesium. It must first be reconverted into magnesium chloride, either by acid treatment or by thermal treatment followed by acidification. Although once economically viable, rising energy costs after the 1990s rendered this route unprofitable [18]. Consequently, modern resource-recovery schemes now focus on circular-economy approaches that maximize recovery while minimizing waste generation [19].

Within such circular resource-recovery schemes, NF is commonly integrated to enable profitable and sustainable $Mg^{2+}$ extraction. NF is used as a preliminary step to separate seawater/brine into a permeate (rich in monovalent ions) and a retentate (rich in multivalent ions) (Figure 1.4). This reduces volumes and increases concentrations in the $Mg^{2+}$-rich stream, improving technical and economic efficiency while removing species that could hinder downstream recovery [20–22]. As $Na^{+}$ is the most abundant cation in seawater/brine, the ability of NF processes to separate $Mg^{2+}$ from $Na^{+}$ allows its selective concentration and further recovery.

Taken together, water softening by selective ion rejection and magnesium recovery through concentration and valorization demonstrate NF's role in coupling drinking-water production with resource recovery. These features make NF a key technology in circular-economy approaches that combine water purification with the sustainable supply of critical minerals.

### 1.2.2. Nitrate removal

In environmental remediation, NF is considered a strong alternative for water purification, capable of removing a wide range of pollutants from water bodies in one step [6]. Among these, nitrate is one of the most widespread contaminants in surface and groundwater globally. Over recent decades, nitrate contamination of groundwater has increasingly driven water quality decline, linked to anthropogenic inputs, such as fertilizer and pesticide use, agricultural runoff, and insufficient wastewater treatment [23].

As a result, nitrate concentrations in aquifers often exceed the World Health Organization's guideline of $50\,mg\,L^{-1}$, raising both health and environmental concerns [23]. Elevated

nitrate levels are associated with methemoglobinemia in infants and contribute to eutrophication [24, 25]. Therefore, its selective removal is a practical priority for water purification and environmental remediation.

While biological denitrification, active metal reduction, and RO technologies can reduce nitrate concentrations effectively, these methods necessitate periodic regeneration, generate residual brines, or demand high energy requirements [23]. NF offers a complementary pressure-driven method that can selectively remove nitrate without chemical additives.

Because nitrate is monovalent, it is often rejected less strongly than multivalent anions such as $SO_4^{2-}$. However, NF has proved effective in removing enough nitrate (retention between $\sim$ 40–80 %) and larger or more highly charged anions such as sulfate [26–32]. This performance allows compliance with water-quality standards while operating at significantly lower pressures than RO.

The two cases, i.e., $Na^+/Mg^{2+}$ separation and nitrate removal, together capture the range of NF selectivity. The former addresses exclusion of divalent cations, whereas the latter concerns control of a monovalent anion. Taken together, they span the mechanistic range of NF operation and show that NF modulates ionic composition rather than removing salts indiscriminately. Accordingly, NF is used not only for water softening and contaminant removal but also for selective ion management aligned with sustainable water-resource objectives.

To explain how NF achieves tunable selectivity and which material features set its performance, the next section examines the structural and chemical fundamentals of NF membranes and the interfacial polymerization process that defines their properties.

## 1.3. Fundamentals of Nanofiltration Membranes

The $Na^+/Mg^{2+}$ separation and the partial rejection of nitrate described above are typically achieved with thin-film composite (TFC) NF membranes, the gold standard architecture across both NF and RO [5, 9, 33]. Although alternative architectures (symmetric, asymmetric) and materials (inorganic, hybrid) have been explored, polymeric TFC membranes dominate owing to their high flux, scalable processing, reproducibility, and lower cost [2, 9, 34, 35]. Therefore, the next sections examine the structural and chemical characteristics of TFC membranes, with emphasis on how interfacial polymerization governs charge, morphology, and, ultimately, ion selectivity.

### 1.3.1. Thin-film composite architecture

TFC membranes comprise a bilayer structure, formed through a sequential two-step fabrication process. In the first step, a thick, porous, and non-selective support layer is produced (typically via phase inversion), which provides mechanical stability and low hydraulic resistance. In the second step, an ultra-thin selective layer is formed on top of the support. These two layers differ in their chemical composition and function, with the upper layer serving as the principal barrier to mass transport [34], as schematically illustrated in Figure 1.5.

Because permeance is inversely proportional to the thickness of the selective film, reducing its thickness enhances permeance. For example, a TFC membrane comprising a 10-nm thick polyamide (PA) selective layer exhibits a solvent permeance more than two orders of magnitude

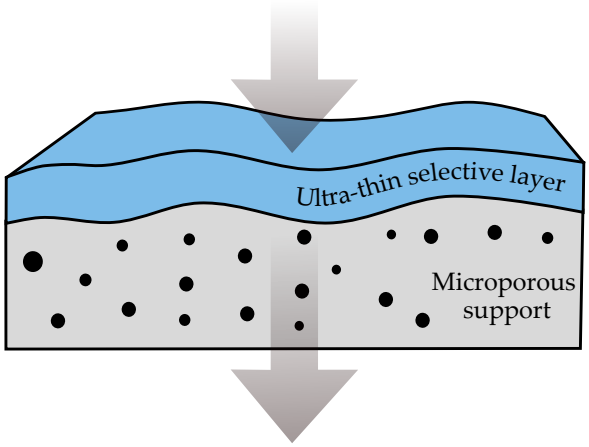



**Figure 1.5:** Thin-film composite membrane architecture. Schematic cross-section of a thin-film composite nanofiltration membrane comprising a microporous support and an ultra-thin selective layer. The selective layer provides the dominant resistance to mass transport, whereas the support ensures mechanical stability with low hydraulic resistance.

higher than that of a commercial TFC NF membrane, while maintaining a comparable acid fuchsin (585 Da) rejection of approximately 99 % [36]. Since the fabrication of the thin selective film and the porous support are decoupled, each can be individually optimized. Consequently, synthesis of the selective layer can be tailored for specific separation applications [33].

There are several techniques for forming thin polymeric films on top of porous supports, e.g., layer-by-layer assembly, dip coating, spray coating, spin coating, in-situ polymerization, plasma polymerization, and grafting [37, 38]. However, IP stands out as the dominant technology for both NF and RO for its scalability, simplicity, and inherent ability to produce defect-free, ultra-thin and crosslinked layers [39–41]. The prevalence of IP-based TFC membranes provides the foundation for the material systems examined in this dissertation.

### 1.3.2. Interfacial polymerization process

Interfacial polymerization (IP) is a localized reaction that takes place at the interface between two immiscible phases containing reactive monomers, producing an ultrathin polymeric film. Although most membrane applications rely on a liquid–liquid interface, IP can also be carried out at liquid–solid or liquid–gas boundaries [42]. In a typical system, the monomers are dissolved in the respective aqueous and organic phases. However, in some systems, the phase itself may participate in the reaction (e.g., water acting as a reactant) [43] or contain catalysts or initiators that promote film formation [44, 45].

The localized nature of IP strongly affects polymer growth. Because diffusion toward the interface is rate-limiting, monomers are more likely to react with a growing polymer chain than with unreacted monomers in bulk solution. At particular molecular-weight ranges, precipitation of the nascent polymer at the interface can occur, resulting in different molecular-weight distributions that differ from those formed in bulk conditions [46]. These characteristics of IP are responsible for the formation of ultrathin films with high molecular weights and cross-linked structures [39].

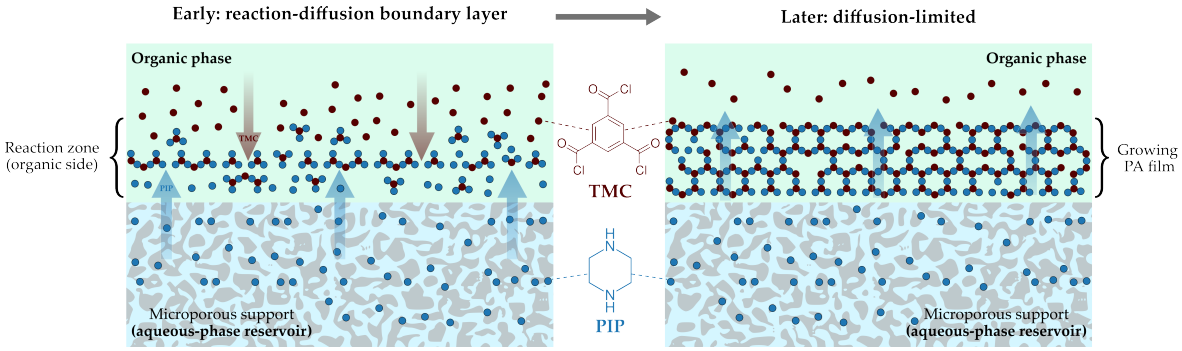



**Figure 1.6:** Interfacial polymerization (IP) at the aqueous/organic interface on a microporous support. The aqueous-phase reservoir within the microporous support supplies the amine monomer (illustrated as PIP), which diffuses upward into the organic-side reaction–diffusion boundary layer, while the acyl chloride (illustrated as TMC) diffuses within the organic phase toward the reaction zone. **Early:** an organic-side reaction–diffusion boundary layer forms at the interface. **Later:** a growing polyamide (PA) film restricts further monomer transport, leading to diffusion-limited, self-limiting film growth.

IP has been employed to prepare TFC membranes since the pioneering work of Morgan in the 1960s, who first proposed using interfacial polycondensation to produce a thin selective layer on top of a porous support for RO [46]. Cadotte subsequently optimized this process in the 1970s, leading to the TFC membrane architecture that is still implemented at industrial scale [47]. In particular, a thin-film polyamide (PA) layer was synthesized on top of a microporous polysulfone (PS) support through the reaction of *m*-phenylenediamine and trimesoyl chloride (TMC) at the interface between water and an organic solvent. This chemistry remains the benchmark for commercial RO and NF membranes.

For NF applications, a closely related Schotten–Baumann-type reaction is commonly used. Aqueous piperazine (PIP) acts as the amine monomer, while TMC dissolved in an organic solvent (e.g., hexane or isoparaffin) serves as the acyl chloride. The microporous support acts not only as the reservoir for the aqueous solution but also co-defines the water–organic interface [48]. Once the two phases come into contact, PIP diffuses into the organic phase and reacts with TMC, forming a cross-linked PA network at the interface. Because TMC is poorly soluble in water while PIP has high aqueous solubility, the reaction predominantly takes place in the organic phase [49, 50]. PIP diffusion into the organic phase is typically promoted by using an excess of amine in the aqueous phase.

The IP process is regarded as self-limiting. Figure 1.6 illustrates the transition from an early reaction–diffusion boundary layer at the interface to a later diffusion-limited growth regime as the nascent PA film develops. As the PA film forms, it progressively restricts further monomer diffusion, slowing polymer growth and confining the final film thickness to tens or hundreds of nanometers [49]. The resulting ultra-thin PA film is cross-linked and selectively permeable, which are key characteristics for NF.

Several factors control the formation and physico-chemical properties of the resulting PA layer, including monomer concentrations, monomer diffusivities, reaction time, solvent choice, and temperature [51]. As an illustration, shorter reaction times typically yield thinner, more permeable layers, whereas extended polymerization produces denser, less permeable films with higher solute rejections [52–54].

Importantly, the conditions of IP also determine the distribution of residual functional

groups, such as unreacted amines and hydrolyzed acyl chlorides, which render the surface charge of the resulting film [55]. These chemical features directly control the ion-specific selectivity discussed in Section 1.4. The following section focuses on how monomer chemistry and concentration shape the structure and composition of the PA network.

### 1.3.3. Influence of monomer chemistry and concentration

IP can generate a wide range of polymer chemistries, including polyesters, polyureas, polyurethanes, polyimides, and polyamides [39, 56]. From a structural point of view, three elements of the interfacially polymerized network can be distinguished: the *network former*, the *bridge molecule*, and the *anchor* [56]. The network former is typically an at least trifunctional electrophile (e.g., acyl halides, aromatic or aliphatic trihalides, sulfonyl halides, epoxides), which provides branching points and enables crosslinking. The bridge molecule is an at least difunctional nucleophile (e.g., diamines, alcohols, thiols) that links network-former units. Their reaction yields the anchor (e.g., amide, ester, imide), which largely determines the chemical stability of the network [39, 56–60]. For instance, polyester anchors can improve resistance to chlorine attack compared to PA, while imide bonds yield superior thermal stability [39, 57–60]. Nevertheless, in NF, the majority of commercial TFC membranes are based on aromatic PA formed by amine–acyl chloride reactions [9]. This is a consequence of their mature fabrication technology, favorable cost–performance balance, and their ability to provide highly crosslinked, mechanically robust, and chemically stable selective layers. Accordingly, the discussion below focuses on PA anchors and examines how the chemistry and concentration of the network former and bridge molecule govern the characteristics of the PA network and, ultimately, NF membrane performance.

The properties of the formed polymer depend strongly on the reactivity and *local* concentration of the monomers at the interface, the stability of the solvent interface, and the number of reactive groups on each monomer [39]. In addition to geometric characteristics such as thickness, area, and porosity, the permeance and, in particular, the selectivity of IP-based films are critically governed by their physicochemical characteristics, including polarity, fixed-charge content, degree of crosslinking, and water content (swelling) [51].

#### Monomer chemistry, network packing, and functional-group distribution

Within PA NF membranes, the chemistry of the diamine (bridge) and acyl chloride (network former) determines the fundamental architecture of the resulting network. Fully aromatic diamines such as *m*-phenylenediamine (MPD) form rigid, semi-planar structural units that can pack efficiently when reacted with TMC. Molecular modeling has shown that among a range of monomer combinations, MPD–TMC is unique in forming minimal-energy substructures that are essentially planar and can pack in a graphitic, sheet-like fashion, yielding a dense network with limited fractional free volume [61]. In contrast, alternative diamines generally form minimal-energy substructures with various degrees of bending and twisting, which hinder efficient packing and generate significant fractional free volume with relatively large cavities, thereby reducing selectivity [61].

Semi-aromatic poly(piperazine amide) networks derived from the aliphatic, non-planar PIP illustrate these effects. The chair conformation of PIP makes the crosslinked network more difficult to pack tightly, increasing the internal free volume of the active layer [51, 54, 62]. As a result, PIP-based PA layers exhibit higher hydrophilicity, higher water uptake

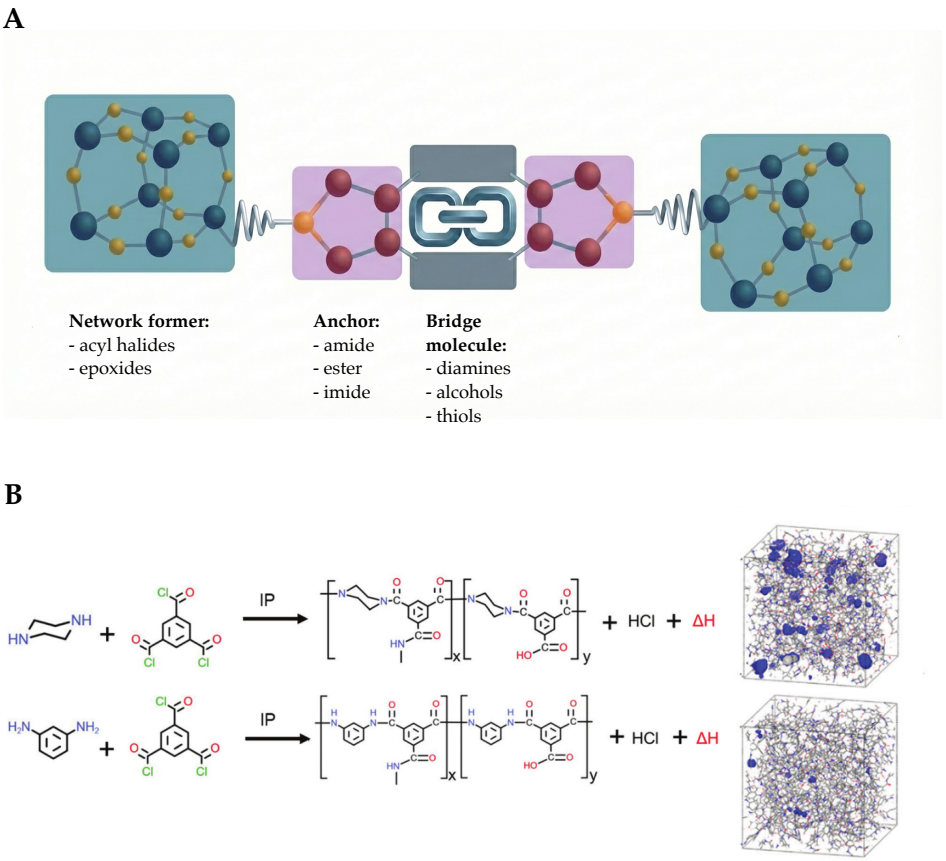



**Figure 1.7:** PA network formation and monomer-chemistry effects. **(A)** Interfacial polymerization network-building picture defining the *network former* (e.g., trifunctional acyl chloride), *bridge* (e.g., diamine), and *anchor* (e.g., amide link), adapted from [56]. **(B)** Conceptual MPD–TMC versus PIP–TMC packing contrast: planar/dense segments with smaller voids versus non-planar/open connectivity with larger cavities, motivating how amine structure can shift the effective microstructure of the polyamide selective layer, reproduced from [38].

and permeance, and lower surface roughness and selectivity compared with MPD-based membranes. Molecular simulations support this picture, indicating that the distorted PIP structure yields larger cavities with more free volume than fully aromatic MPD-based networks [63]. Interestingly, despite the nominally more hydrophobic character of PIP amide units, the larger free-volume cavities allow the PIP-based networks to absorb more water, which further differentiates their transport behavior from that of MPD–TMC films.

Figure 1.7 summarizes these network-building roles (Figure 1.7A) and illustrates how MPD–TMC versus PIP–TMC chemistry can translate into denser versus more open PA packing (Figure 1.7B).

At the molecular level, the type and position of functional groups, the stereochemistry and conformational flexibility, and the charge distribution of the monomers all strongly influence their reactivity and arrangement at the interface [64]. Electron-donating and -withdrawing substituents can modulate the nucleophilicity of amine or hydroxyl groups and the electrophilicity of acyl chlorides, thereby tuning the reaction rate [65]. Likewise, twisted or rigid monomer conformations modify diffusion rates and packing, which in turn affects the

thickness and internal free volume of the resulting film [64]. Such molecular design principles have been exploited to increase permeance by enlarging pore size, increasing microporosity, and reducing tortuosity, or to adjust surface hydrophilicity and charge [64].

In aqueous–organic IP systems, most electrophilic monomers (e.g., acyl chlorides) are susceptible to side reactions with water [39]. Hydrolysis of acyl chlorides generates carboxylic groups, so that even in the absence of complete reaction with the diamine, a fraction of acyl chloride functionalities is converted into –COOH groups. At the same time, amine-rich regions may contain unreacted $–NH_2$ functionalities. Thus, the resulting PA networks contain neutral amide linkages, residual carboxylic and amine groups, and their protonated/deprotonated forms [55]. These ionizable groups render the amphoteric charge behavior characteristic of PA NF membranes, with the actual charge distribution being closely coupled to the degree of crosslinking and water uptake [51].

Having established how monomer chemistry and side reactions give rise to ionizable groups within the network, it is useful to examine how the reactivity and partitioning of the monomers, together with their transport, control where and how rapidly the polyamide film forms during IP.

### Monomer reactivity, partitioning, and reaction kinetics

As outlined in Section 1.3.2, the formation of the PA selective layer by IP involves the reaction of amines in the aqueous phase and acyl chlorides in the organic phase. The polyamidation reactions underlying NF selective-layer formation are typically Schotten–Baumann-type nucleophilic acyl substitution reactions, in which amine or hydroxyl groups attack the carbonyl carbon of acyl chlorides [46]. Therefore, the overall polymerization rate is governed by the intrinsic reaction kinetics as well as by the transport of monomers to and across the interface.

The second-order rate constant for the reaction between the aqueous-phase reactant A (usually a diamine) and the organic-phase reactant B (typically an acyl chloride) depends strongly on monomer chemistry. Reactions between aliphatic or cycloaliphatic diamines, such as PIP, and aliphatic or aromatic acyl chlorides are extremely rapid, with reported rate constants above $10^3\ \mathrm{m^3\,kmol^{-1}\,s^{-1}}$ [66]. In contrast, aromatic diamines such as MPD react more slowly because the nitrogen lone electron pair is partially delocalized into the benzene $\pi$-system, which lowers its nucleophilicity and reduces the reaction rate. For aromatic diamines, reported rate constants typically lie between 10 and $10^3\ \mathrm{m^3\,kmol^{-1}\,s^{-1}}$ [66]. Thus, for otherwise similar conditions, PIP–TMC reactions can proceed significantly faster than MPD–TMC reactions.

Monomer chemistry also controls the equilibrium partitioning of the aqueous-phase monomer into the organic phase. The partition coefficient $K_A$ of reactant A (bridge molecule) from water (phase 1) into the organic solvent (phase 2) can vary by more than five orders of magnitude depending on the structure of the reactant and the solvent [67]. Since aromatic diamines are less hydrophilic, they typically exhibit larger octanol–water partition coefficients and higher $K_A$ values than aliphatic diamines, alcohols, polyamines or cyclodextrins [67]. For example, MPD shows mean estimated partition coefficients of $4.3 \times 10^{-3}$ and $5.7 \times 10^{-3}$ across several linear and branched alkanes, whereas PIP exhibits mean $K_A$ values roughly five times lower ($9.6 \times 10^{-4}$–$1.1 \times 10^{-3}$) [67]. Consequently, under otherwise identical bulk concentrations and solvents, the interfacial concentration of MPD in the organic phase is substantially higher than that of PIP, even though PIP is more reactive.

The overall planar reaction rate $v$ for the consumption of reactant A per unit interfacial area scales linearly with $K_A c_{A0}$ and with the square root of an effective rate–diffusion factor, $v \propto K_A c_{A0} \sqrt{k' D_{A2}}$, where $c_{A0}$ is the initial concentration of A in phase 1 (water), $D_{A2}$ is its diffusion coefficient in phase 2 (organic phase), and $k'$ is related to the intrinsic reaction rate constant [67]. The partition–diffusion coefficient factor $\kappa_{PD} = K_A \sqrt{D_{A2}/D_{A1}}$ controls the time at which diffusion resistance in phase 1 becomes important. In practice, $K_A$ is typically the most sensitive parameter, and small changes in monomer structure or in the choice of organic solvent can lead to orders-of-magnitude changes in the reaction-rate scale [67].

The support layer also influences the local concentration and supply of aqueous-phase reactant A (bridge molecule). In particular, its porosity and thickness determine the effective concentration of A in phase 1 (water) and the extent of diffusion resistance before reaching the interface [67]. In addition, like-dissolves-like strategies for solvent selection, or adding miscible co-solvents, can markedly increase the partitioning of the diamine into the organic phase, thereby accelerating interfacial synthesis and typically yielding denser and rougher selective layers [68].

From a kinetic perspective, IP is governed by coupled diffusion and reaction phenomena, with the growth of the PA layer proceeding through the reaction–diffusion stages described next.

**Monomer concentration, stoichiometry, and growth regimes**

The interplay between monomer chemistry and concentration gives rise to characteristic kinetic regimes during IP. Reaction–diffusion models and *in situ* experiments indicate that film growth can be divided into three stages [50, 69]. In the first stage, quasi-stationary concentration profiles are established, and a reaction–diffusion boundary layer develops in the organic phase. In the second stage, a nascent polymer film fills the reaction zone at an approximately constant rate, limited by the diffusion of aqueous phase monomer into this zone. In the third stage, once the nascent film becomes sufficiently dense, growth transitions to a diffusion-limited regime in which the monomer flux through the film controls the rate. Experimental studies have shown that roughly half of the final polyamide thickness can form within the first ~2 s of reaction, underscoring the importance of the early kinetic stages [69].

Monomer concentrations significantly affect these stages. On the one hand, increasing the initial concentrations of reactants generally accelerates the IP reaction and can lead to rougher and more heterogeneous selective-layer structures [36, 52, 53, 57, 70–77]. In particular, increasing the bulk concentration of the bridge molecule (diamine) in the water phase enhances the planar reaction rate linearly, while increasing the bulk concentration of the network former (acyl chloride) in the organic phase, $c_{B0}$ , enhances it with the square root of $c_{B0}$ [67]. On the other hand, reaction–diffusion modeling shows that the overall effect of increasing the total monomer concentration $C_0$ (the functionality-weighted sum of amine and acid concentrations in the organic phase) is more complex: higher $C_0$ both increases the monomer diffusion (which tends to thicken the resulting PA film) and accelerates the reaction (which tends to form a denser nascent barrier and thus limits further growth) [50]. As a result, the PA film thickness as a function of $C_0$ may exhibit a minimum at an optimal concentration, as observed experimentally for aromatic polyamide membranes prepared from MPD and TMC [51, 71].

Experimental observations further indicate that decreasing monomer concentrations can, under certain conditions, reduce the active-layer thickness and produce thinner, more uniform

films [69, 77–79]. Uniformly reducing both monomer concentrations slows diffusion and polymerization rates according to Fick's law, which diminishes the extent of self-accelerating growth and favors the formation of thin layers [69]. However, excessively low concentrations increase the relative importance of hydrolysis side reactions of acyl chlorides, potentially compromising crosslinking and selectivity [80]. This has motivated the development of anhydrous IP systems that allow synthesis of ultrathin, highly crosslinked polyamide nanofilms at reduced monomer concentrations [81].

For specific monomer pairs, the relationship between amine concentration and active-layer thickness can deviate from simple monotonic trends. For example, diffusion–limitation models suggest that lower amine concentration should yield thinner films. In contrast, Freger's self-limiting IP model predicts that high amine concentrations can also produce thin films by rapidly forming a dense nascent layer that restricts subsequent diffusion of aqueous monomer, thereby limiting further growth [50]. Consistent with this, thin active layers have been reported at both low and high amine concentrations, depending on the system and conditions [78, 79]. For PIP/TMC membranes, the relatively large internal free volume of the nascent active layer means that PIP diffusion into the organic phase is not effectively blocked, so lower PIP concentrations are more likely to yield thinner films [63]. These examples highlight that each monomer combination requires independent optimization of reactant concentrations.

Monomer functionality and stoichiometry provide additional tools to control network characteristics. IP typically involves di-, tri- or multi-functionalized monomers. The reaction of two difunctional monomers yields a predominantly linear polymer that may crystallize and form a dense film prone to swelling, whereas including trifunctional acyl chlorides such as TMC introduces branching and crosslinking [39]. Interestingly, full replacement of TMC by a diacid chloride is not necessary to dramatically alter film properties: mixing diacid chloride with TMC to obtain a fractional functionality already produces films with characteristics similar to fully crosslinked networks [51].

Owing to the stoichiometry of the polyamidation reaction, the fixed-charge content is stoichiometrically coupled to the degree of crosslinking [51]. This means that every reactive group of a monomer yields either a PA bond or a fixed-charge if it fails to react. In the early stages, the reaction zone where the incipient film forms contains an approximately stoichiometric ratio of amine and acyl chloride, so the initial film is expected to be relatively weakly charged [50]. During the subsequent diffusion-limited growth stage, amine molecules diffuse through the nascent film and react with a large excess of TMC in the organic phase. This reaction can increase the density of carboxylic groups (after hydrolysis) near the surface, thereby enhancing the surface charge [51]. The actual outcome depends on the local monomer concentrations and the balance between crosslinking and side reactions. As a result, monomer stoichiometry offers a way to control where fixed charges are generated within the PA film.

Maintaining a sufficiently low value of the ratio $K_A(c_{A0}/c_{B0})$ is essential to preserve a stoichiometric excess of reactant B [67]. If this condition is not met, the reaction zone may shift from acid-rich to amine-rich, fundamentally altering the balance between crosslinking and fixed-charge generation [77]. In practice, the optimal combination of monomer concentrations, functionalities, and stoichiometry is strongly system-dependent and must be determined empirically for each chemistry [39].

In summary, monomer chemistry and concentration act together to define the kinetic regime of IP, the resulting network architecture and functional-group distribution. These

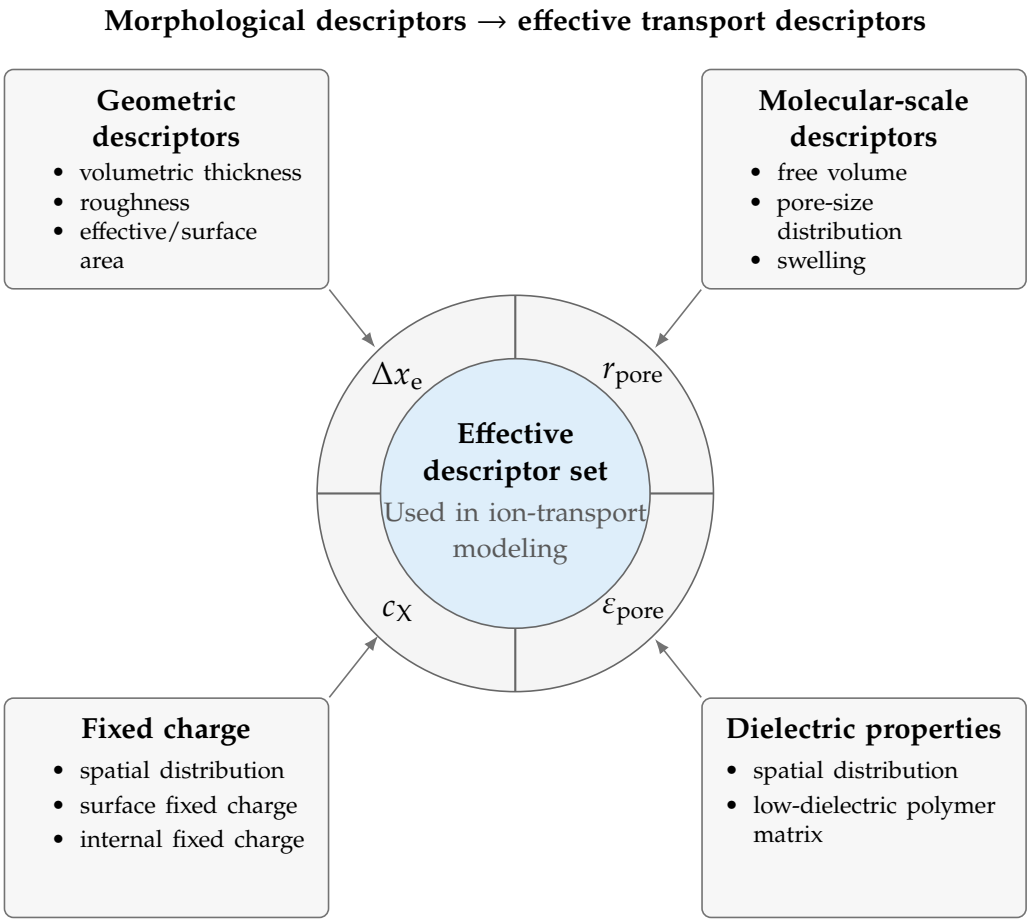



**Figure 1.8:** Mapping of morphological descriptors of the PA selective layer to the effective transport descriptor set used in ion-transport modeling. Morphological descriptors are grouped into geometric, molecular-scale, fixed-charge, and dielectric-property families and condensed into an effective descriptor set ($\Delta x_e$, $r_{pore}$, $c_X$, $\varepsilon_{pore}$).

aspects provide the microscopic basis for the morphological descriptors discussed in Section 1.3.4.

## 1.3.4. Morphological descriptors of the selective layer

As discussed in Section 1.3.3, the chemistry and concentrations of the monomers used in IP determine how the PA selective layer forms and evolves. The outcome of this process can be described in terms of a set of morphological descriptors that are directly linked to permeance and selectivity. Key descriptors include the effective thickness, pore-size distribution and free volume, surface roughness and effective area, water content and swelling, and the spatial distribution of fixed charge and dielectric properties [51]. In the following, these descriptors are defined and connected to NF performance, providing the structural basis for the transport mechanisms discussed in Section 1.4. Figure 1.8 summarizes the descriptor families and their mapping to the compact effective descriptor set used in ion-transport modeling.

### Geometric descriptors: thickness, roughness, and effective area

Among geometric descriptors, the thickness of the IP-based selective layer is particularly important because it contributes to transport resistance and is thus inversely related to permeance [2]. However, for nanoporous PA films thickness is not a single unambiguous quantity, since pores, voids, roughness, and lateral inhomogeneity reduce the hydraulic resistance relative to a dense film of the same overall thickness [82]. Therefore, it is useful to distinguish between a *superficial* (or volumetric) thickness, defined as the total volume of the PA layer divided by the membrane footprint area. The *effective* (or equivalent) thickness instead corresponds to the thickness of a hypothetical homogeneous, laterally smooth film that would provide the same overall transport resistance as the actual selective layer. In this sense, geometric descriptors are best understood as descriptors of a rough and heterogeneous selective layer rather than as single, uniformly defined structural values.

Several experimental techniques can be used to characterize PA-layer thickness, but they probe different aspects of the selective layer. Cross-sectional scanning electron microscopy (SEM) or transmission electron microscopy (TEM), as well as atomic force microscopy (AFM), profilometry, and ellipsometry where applicable, primarily provide volumetric thicknesses [36, 49, 70, 71, 83–90]. Mass-based approaches such as Rutherford backscattering spectroscopy (RBS) and Attenuated total reflectance Fourier-transform infrared (ATR-FTIR) instead quantify mass per unit area and are less sensitive to internal voids and to the poorly defined PA–support boundary [51, 88, 90–95]. Accordingly, no single measurement fully captures the transport-relevant thickness of rough and heterogeneous PA films. Complementary measurements are often required to relate observed morphology to transport behavior.

This distinction is especially important when comparing different PA morphologies. For fully aromatic RO-type membranes, the PA skin is often highly crumpled and internally inhomogeneous, so only part of the apparent volumetric thickness may dominate transport resistance [51]. For semi-aromatic PIP-based NF membranes, the active layer is commonly interpreted more successfully as a comparatively uniform film, for which a homogeneous-layer description is more reasonable [82, 87]. Thus, for NF membranes, a single effective thickness can often serve as a useful descriptor of the average resistance of the selective layer, even though the underlying morphology remains heterogeneous.

Top-surface morphology adds a second geometric aspect: the effective surface area available for transport. AFM roughness parameters such as root-mean-square (RMS) roughness are useful for describing surface topography, but they do not by themselves quantify the transport-active area [96–99]. Ridge–valley features, nodules, and bubble-like protuberances can increase the apparent area, yet their contribution to permeance depends on whether they are connected to the underlying water-filled network and to the permeate side [38, 51, 100]. Consequently, a rougher surface does not necessarily imply a larger effective filtration area or higher permeance.

These geometric features also influence fouling. Rough surfaces can promote foulant accumulation in valleys and crumpled regions, whereas appropriately designed protrusions may increase wall shear and mitigate fouling [101, 102]. Overall, geometric descriptors are useful not only for describing membrane morphology, but also for relating that morphology to the resistance and interfacial area relevant to transport.

### Free volume, pore-size distribution, and swelling

Beyond macroscopic thickness and roughness, NF performance is strongly governed by the molecular-scale free volume and pore-size distribution of the PA layer. Because the barrier-controlling pathways are sub-nanometer and structurally heterogeneous, pore size cannot usually be resolved directly and is therefore commonly inferred from transport behavior or from free-volume-sensitive techniques such as positron annihilation lifetime spectroscopy (PALS) [86, 103–110]. Accordingly, the PA active layer is better understood as containing a distribution of free-volume elements rather than a single, uniformly defined pore size. For PIP-based NF membranes, estimates based on water permeance and transport models typically yield effective pore radii on the order of 0.2 to 0.4 nm [106–108].

In practice, commercial TFC NF membranes are not isoporous but instead display a log-normal distribution of pore sizes over a given range [111]. For NF membranes prepared by IP, the PA active layer is heterogeneous both across its thickness and in the plane of the film, and does not exhibit a single, uniform pore size. These structural variations reflect the influence of the morphology and chemistry of the support, as well as the lack of control of the IP process [38]. Additives such as surfactants can promote a more even distribution of amine monomers at the aqueous–organic interface and enhance their diffusion into the organic phase. As a result, defect formation is suppressed and the active layer becomes more homogeneous, with a narrower pore-size distribution [112].

Water uptake and swelling provide an additional descriptor that is closely connected with free volume. The water content of PA membranes plays a role similar to porosity. Specifically, water-filled regions form the percolating pathways for both water and small solutes, and their fraction correlates with water permeability [113]. When appropriate measures of PA thickness are used, different PA films follow a general correlation between intrinsic permeability and swelling [87]. This trend suggests that the effect of swelling on water transport is primarily geometric. A lower water fraction appears to reduce the effective surface area and make the percolation pathways more tortuous. At the same time, the mobility of water remains close to its bulk value, even in the smallest pores and at moderate swelling [113].

The magnitude of swelling differs between RO and NF PA layers. For RO active layers, the water mass fraction is typically below 10 %, whereas NF active layers exhibit larger water fractions, often in the range of 15 to 50 % [87, 114]. Flory–Rehner analyses are consistent with NF materials having more repeat units between crosslinks than their RO counterparts, consistent with their higher swelling and larger free volume [114]. These differences in water content and free volume contribute to the higher water permeance and more moderate salt/water selectivity of NF membranes compared to RO. Also, they modulate the dielectric environment and the strength of electrostatic interactions, as discussed below.

### Spatial charge distribution and dielectric microenvironment

The PA selective layer contains a variety of ionizable groups stemming from incomplete reactions and side reactions during IP, including carboxylic groups formed by the hydrolysis of acyl chlorides and residual amine moieties [55]. Importantly, the local environment of these ionizable groups is highly heterogeneous. In smaller network pores, the reduced water content creates a weakly polarizable, low-dielectric medium, in which Coulomb interactions are strongly enhanced and charge separation is poorly stabilized [55]. Deprotonation in such regions is energetically costly and, therefore, associated with higher apparent $pK_a$ values. Groups at or near the membrane surface experience a more polar, water-rich

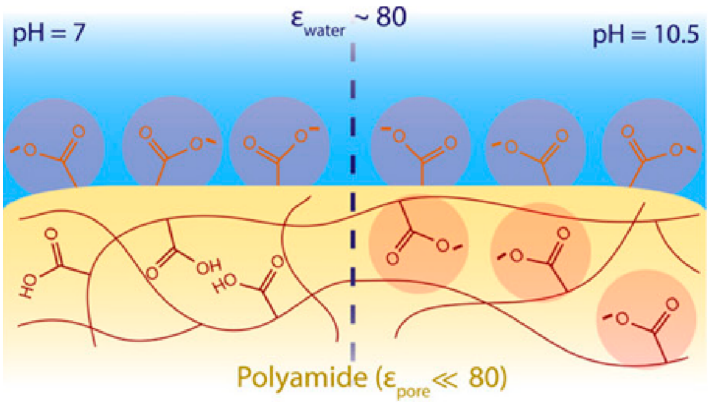



**Figure 1.9:** Dielectric-microenvironment control of carboxylic-group ionization in PA. In nanoconfined, weakly polarizable pore water within the low-permittivity polyamide matrix ($\varepsilon_{\text{pore}} \ll \varepsilon_{\text{water}}$), charge separation is poorly stabilized, suppressing R–COOH deprotonation at neutral pH (left) and thereby increasing the apparent $pK_a$. At higher pH (right), reduced proton activity enables stabilization of the excess charge and promotes R–$COO^-$ formation. Reproduced from [55].

environment that favors dissociation, whereas ionizable groups in the membrane pores remain largely uncharged under conditions where surface sites are already ionized [55]. This microenvironment- and pH-dependent ionization behavior is illustrated schematically in Figure 1.9. This spatial heterogeneity helps explain why effective charges inferred from transport or electrokinetic measurements can differ significantly from nominal fixed-charge densities calculated from chemical composition [115, 116].

Experimental comparisons of charge measurements corroborate this point. When nominal fixed-charge densities estimated from RBS or ATR-FTIR are converted to effective charge densities using standard models, discrepancies arise between the predicted and measured ion rejections [115]. This indicates that the effective charge governing ion transport is different from the nominal charge derived from chemical composition [51]. These discrepancies indicate that only a fraction of the nominal ionizable groups actually participates in Donnan exclusion. Therefore, ionization occurring in larger, more hydrated aggregate pores and in near-surface regions is expected to dominate the effective charge contributing to ion transport. On the other hand, groups confined within dense, low-dielectric network pores remain mostly uncharged and make only a minor contribution to the measured ion rejections.

Consequently, the dielectric microenvironment of the PA layer is a morphological descriptor in its own right. Regions with low water content and high polymer density have low polarity, thereby acting as a low-dielectric environment. In these regions, it is energetically unfavorable for ions to enter, so their partitioning into the membrane is reduced, and dielectric exclusion is enhanced. In contrast, water-rich domains behave more like bulk aqueous solution, with higher effective dielectric constants and smaller energetic penalty for ion entry to the membrane [14, 51]. Thus, maximizing dielectric exclusion requires a combination of low polymer polarity and very small pore sizes, while maintaining enough hydration to allow percolating transport pathways for water and ions [51]. Overall, these trends suggest that the most favorable barrier properties are expected for dense matrices with a high content of mildly hydrophilic groups capable of binding water, yet a rigid structure that prevents excessive swelling and the formation of large, highly hydrated clusters [51].

In NF membranes, fixed charges play a stronger role in ion transport than in RO [51].

Accordingly, the interplay between charge distribution, free volume and dielectric environment is critical because it governs the balance between Donnan and dielectric exclusion.

**Structure–property relationships in NF membranes**

The interplay between monomer chemistry and concentration ultimately determines the nanoscale architecture and charge characteristics of the PA selective layer and, through them, the morphological descriptors introduced above. As discussed in Section 1.3.3, fully aromatic MPD–TMC PA networks form dense, efficiently packed structures with small free-volume elements and relatively low polarity, whereas PIP-based networks are looser and more hydrated. Collectively, these features control water permeance and selective separation in NF membranes [64].

Fully aromatic MPD–TMC networks, with their rigid planar substructures and efficient packing, can form dense matrices with small free-volume elements and relatively low polarity. These features are favorable for strong dielectric exclusion and high salt/water selectivity in tight NF and RO applications [51]. In contrast, PIP-based membranes exhibit looser networks with larger free-volume cavities and higher water uptake, leading to higher water flux and more moderate salt/water selectivity at a given transmembrane pressure [51, 54, 62]. However, their larger free volume and the presence of ionizable amine sites make PIP-based membranes particularly attractive for NF, where size- and charge-based discrimination between ions is required [51, 64]. Building on this concept, PIP-derived monomers such as aminoethylpiperazine (AEP) and 1,4-bis(3-aminopropyl)piperazine (DAP) combine a secondary amine in the piperazine ring with additional primary amines on side alkyl chains. These structural differences alter the IP process, rendering PA selective layers with distinct thicknesses, pore sizes and charge densities [64, 74, 117–119]. In this way, the surface charge can often be shifted toward more positive values compared to conventional PIP-based NF membranes. As a result, AEP- and DAP-based NF membranes exhibit different morphologies and transport properties, which can be exploited to tailor monovalent/divalent ion selectivity for specific separations. In the context of this dissertation, such tunability is particularly relevant for $Na^+/Mg^{2+}$ separation and nitrate removal in drinking-water applications.

Consistent with the discussion above, the best barrier characteristics are obtained for dense, rigid matrices that are moderately hydrated and contain small, well-defined free-volume elements [51]. Adjusting monomer concentrations provides a relatively simple way to co-tune several of these characteristics. Higher planar reaction rates, achieved by increasing bulk concentrations of the aqueous-phase and organic-phase monomers or from stronger partitioning of the aqueous-phase monomer into the organic phase (higher $K_A$), generally promote rapid film formation, greater heterogeneity and increased surface roughness. For some monomer chemistries, however, higher planar reaction rates can also induce self-limiting behavior that reduces effective thickness for certain chemistries [36, 51, 67, 70–73, 78, 79, 120]. Conversely, lowering concentrations can enlarge free volume and enhance permeance, at the risk of hampering selectivity and increasing the prevalence of defects or hydrolysis-derived functionalities [63, 69, 81, 121–123]. Furthermore, charge density and sign are highly sensitive to monomer concentration and the local environment. Thus, even traditional NF systems such as PIP/TMC can be tuned to exhibit positively charged surfaces and achieve high monovalent/divalent cation selectivity [124].

For separations such as $Na^+/Mg^{2+}$, networks with controlled pore size and predominantly positive surface charge favor strong $Mg^{2+}$ exclusion while allowing $Na^+$ to pass [38, 125–127].

For anions such as nitrate, moderately tight, charge-tuned layers can provide partial $NO_3^-$ rejection at high water flux. In all cases, the permeance–selectivity trade-offs observed in NF can be interpreted in terms of the same underlying set of morphological descriptors developed in this section.

**Summary**

In summary, the PA selective layer of NF membranes is best described by a set of morphological descriptors. Geometric characteristics such as effective thickness, roughness and surface area quantify the macroscopic resistance and available interface for transport. Molecular-scale descriptors, including free volume, pore-size distribution and swelling, capture the internal connectivity of water-filled pathways and relate directly to water permeance and hydraulic selectivity. Finally, the spatial distribution of fixed charge and dielectric properties links morphology to electrostatic interactions. This distribution determines how ions and polar solutes experience Donnan and dielectric exclusion as they enter and go through the membrane.

These descriptors provide a unified framework for connecting synthesis conditions (Section 1.3.3) to NF performance. They also map naturally onto the three main exclusion mechanisms in NF, namely steric exclusion (pore size and free volume), Donnan exclusion (surface and internal fixed charge) and dielectric exclusion (low-dielectric polymer matrix). In Section 1.4, they are incorporated into ion-transport models to quantitatively interpret $Na^+/Mg^{2+}$ separation and nitrate removal. This enables a mechanistic decomposition of experimental separation data into steric, Donnan and dielectric contributions, as well as ion transport through the membrane.

## 1.4. Mechanisms of Ion Transport and Separation

Section 1.3.4 summarized the morphological descriptors of the PA selective layer that are most relevant for transport. In this section, these descriptors are used to describe how ions partition into, and move through, NF membranes. The aim is to develop a mechanistic framework that will be applied throughout this dissertation.

Ion separation in NF results from coupled partitioning and transport within the pores. At the membrane/solution interface, steric, Donnan (electrostatic), and dielectric interactions determine the local ion concentrations inside the pores, as summarized schematically in Figure 1.10. Along the pore length, ions are transported by coupled advection, diffusion, and electromigration. These contributions depend on concentration gradients and on the electric field established by charge separation.

Accordingly, Sections 1.4.1–1.4.3 introduce steric exclusion, Donnan and dielectric exclusion as general physical mechanisms. Then Section 1.4.4 introduces the governing flux expressions. These sections are formulated without yet imposing model-specific assumptions. Finally, Section 1.4.5 assembles these elements into the Donnan–Steric Pore Model with Dielectric Exclusion (DSPM-DE), which serves as a central modeling tool in this dissertation. The descriptors defined in Section 1.3.4 are used as effective parameters in the DSPM-DE framework.

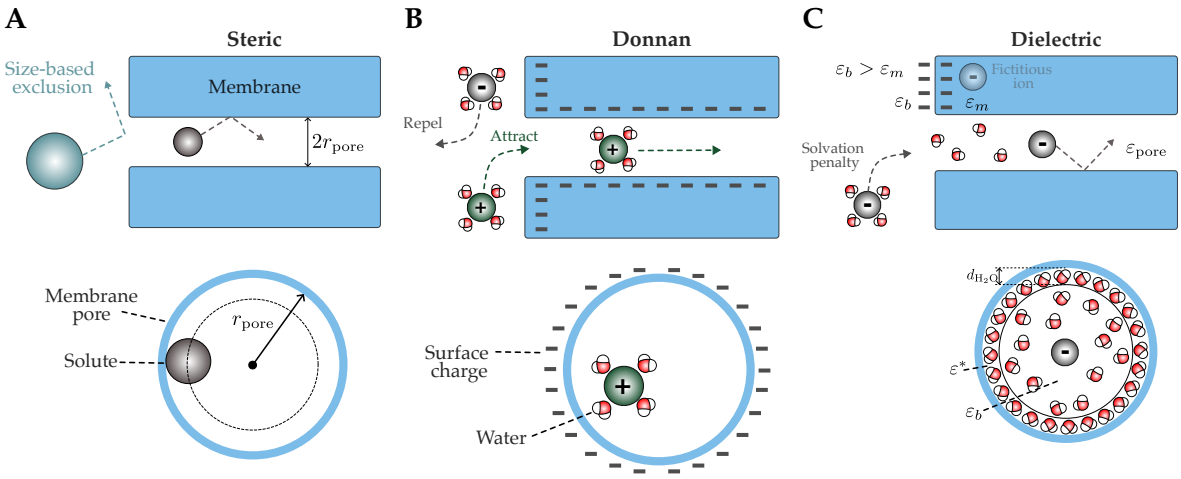



**Figure 1.10:** Schematic illustration of a membrane pore highlighting ion-partitioning mechanisms. At the pore entrance, pore-phase concentrations are governed by **(A)** *steric exclusion*, where only solute centres within the accessible cross-section can enter; **(B)** *Donnan exclusion*, where fixed membrane charge at the pore walls establishes an interfacial Donnan potential that yields co-ion depletion and counter-ion enrichment; and (C) *dielectric exclusion*, where dielectric contrast between bulk water ($\varepsilon_b$) and the low-permittivity pore environment defined by the polymer matrix ($\varepsilon_m$) introduces a self-energy entry penalty $\Delta W_i$, including solvation (Born-type) and polarization (image-charge) contributions. In confined pores, $\varepsilon_{pore}$ is treated as an effective property of pore water, often represented by a near-wall oriented-water layer ($d_{H_2O}$, $\varepsilon^*$).

### 1.4.1. Steric hindrance (size exclusion)

Steric exclusion arises because solutes have finite size and NF pores are narrow [7]. A solute can only enter a pore if its center fits within the accessible cross-section of the pore (Figure 1.10A) [12]. This geometric restriction becomes dominant for neutral solutes and uncharged membranes.

Classical steric hindrance models were originally developed for ultrafiltration of macromolecules, combining geometric exclusion of solute centers with hydrodynamic interactions near pore walls [12]. In NF, pore radii approach molecular dimensions, so continuum assumptions may be questionable [12]. Nevertheless, steric relations remain useful as effective descriptors of size-based partitioning.

For ions, the relevant size is typically the hydrated size rather than the bare ionic radius [7]. Hydration reflects ion–water affinity and can invert trends based on crystal radii. Stokes radii are often used as effective hydrated radii in mechanistic NF models, and they are inferred from limiting ionic equivalent conductance and reflect the mobility of the ion with its associated water [128]. For example, $r_{Mg^{2+}} = 3.47$ Å, $r_{Na^+} = 1.84$ Å, and $r_{Cl^-} = 1.21$ Å [10].

Steric exclusion is commonly expressed using the size ratio:

$$\lambda_i = \frac{r_i}{r_{pore}} \tag{1.1}$$

where $r_i$ is the (hydrated/Stokes) solute radius and $r_{pore}$ is the pore radius [12]. A simple steric partition coefficient follows from geometric exclusion of solute centres:

$$\Phi_{S,i} = (1 - \lambda_i)^2, \qquad \lambda_i < 1 \tag{1.2}$$

and $\Phi_{S,i} = 0$ for $\lambda_i \geq 1$ [12].

Physically, $\Phi_{S,i}$ describes the accessible cross-sectional area for solute centers divided by the total pore area [12]. Therefore, for neutral solutes, it represents the ratio between the average solute concentration inside the pore and the solute concentration outside the pore.

Nevertheless, steric exclusion is not the only size-related limitation. Even after entry, solute transport is reduced by hindered diffusion and hindered advection. Hindrance factors are often taken from macroscopic hydrodynamic calculations, whose direct applicability at nanopore dimensions is not guaranteed [12].

Section 1.3.4 showed that the PA selective layer contains a distribution of free-volume elements rather than a single geometric pore [38, 51]. In practice, pore-size non-uniformity is difficult to determine directly, with PALS being among the few feasible techniques for probing such non-uniformity [129]. In general, pore size and its distribution are inferred by fitting rejection data for neutral solutes. For commercial TFC NF membranes, log-normal distributions are frequently used for uncharged transport [130].

For mechanistic modeling, this complexity is often represented using a single effective pore radius $r_{\text{pore}}$ [12]. This effective radius is biased toward the barrier-controlling pathways that dominate rejection [51]. In this dissertation, $r_{\text{pore}}$ is obtained from polyethylene glycol (PEG) retention data, specifically using PEG 200, which means that the membrane active layer is represented using idealized cylindrical-pore relations. This geometry is simplified, but it enables consistent comparisons across membranes and conditions.

Steric effects can be isolated using neutral solutes such as PEG or dyes [7]. For ions, steric hindrance acts together with electrostatic and dielectric interactions. Small changes in $r_{\text{pore}}$ strongly affect selectivity in the sub-nanometer regime [51]. This sensitivity is important for separating $Mg^{2+}$ from $Na^{+}$, because their hydrated sizes differ substantially. Different radius definitions may also be required for partitioning and transport, which becomes relevant if dehydration contributes as an additional partitioning mechanism.

## 1.4.2. Donnan exclusion and electrostatics

Donnan exclusion arises from electrostatic interactions between ions and fixed charges in the membrane, which may result from ionised functional groups or from adsorbed ions [7, 12]. In PA NF membranes, carboxylic and amine functionalities yield an amphoteric charge [51]. Their ionisation is heterogeneous, as discussed in Section 1.3.4. As a result, transport is governed by an effective fixed charge density rather than a nominal chemical charge [51].

Fixed charges generate electrical double layers next to the pore walls [12]. The thickness of these layers is set by the Debye length and depends on electrolyte concentration inside the pores [12]. Electrostatic effects are critical in NF because pore sizes are often smaller than the Debye length [7]. As a result, electrical double layers overlap and strongly influence ion partitioning [7]. Accordingly, co-ions are repelled, while counter-ions are enriched (Figure 1.10B). This unequal partitioning builds a Donnan potential at the membrane/solution interface, which further influences exclusion or partitioning of both co-ions and counter-ions into the membrane [7].

At equilibrium, each ion satisfies equality of electrochemical potential across the interface, yielding a Boltzmann-type partition relation [13]:

$$\frac{c_{i(0)}}{c_{i,\text{f}}} = \Phi_{D,i} = \exp\left(\frac{-z_i F}{RT}\Delta\Psi_D\right) \tag{1.3}$$

where $z_i$ is the ion valence, $\Delta\Psi_D$ is the Donnan potential difference, $c_{i(0)}$ and $c_{i,f}$ are the concentrations of ion $i$ in the pore phase and in the adjacent bulk solution, respectively; $F$ is Faraday's constant, $R$ is the gas constant, and $T$ is the absolute temperature. In general, a Donnan potential exists at both the feed-side and permeate-side interfaces. Accordingly, distinct partition factors can be written for each interface.

Inside the pores, electroneutrality couples all ions to the fixed charge:

$$\sum_i z_i c_{i(0)} + c_X = 0 \tag{1.4}$$

where $c_X$ denotes the effective fixed charge density. In narrow NF pores, one can often approximate ion concentrations as laterally uniform, which supports an electroneutrality-based Donnan description in mechanistic models [12].

Because both feed and permeate solutions must remain electroneutral, ions are coupled in transport, implying that counter-ions cannot enter without an accompanying co-ion flux. This coupling contributes to co-ion and counter-ion competition effects in mixed electrolytes [7]. Donnan effects favor rejection of multivalent co-ions and influence monovalent/divalent separation [12].

The magnitude of Donnan exclusion depends on $c_X$, ion valence, and bulk concentration. It also depends on pH through charge regulation of carboxylic and amine groups [131]. Increasing ionic strength shortens the Debye length and screens electrostatic interactions [132, 133]. Solution ions can further modify effective charge through adsorption and specific interactions [134]. For example, highly polarizable chloride can adsorb to PA and increase its negative charge, while cations of different stickiness can neutralize charge to different extents. In particular, correlations between zeta potential and (water) permeance indicate a significant contribution of solution ions to Donnan exclusion [134].

In summary, Donnan exclusion links fixed charge to ion partitioning through an interfacial Donnan potential and an electroneutrality constraint in the pore phase. These relations couple co-ion exclusion and counter-ion enrichment via the effective fixed charge density $c_X$.

### 1.4.3. Dielectric exclusion and desolvation penalties

The transport pathways of PA NF membranes are confined within a polymer matrix whose permittivity ($\varepsilon_m$) is far below that of bulk water ($\varepsilon_b$) [14, 135]. In this setting, dielectric exclusion can be described as a change in electrostatic self-energy when an ion moves between media of different permittivity (Figure 1.10C). While the self-energy is positive, the transfer energy $\Delta W$ depends on the permittivities of the initial and final environments, and transfer from bulk water to a lower-dielectric membrane environment is expected to yield a positive $\Delta W$ (an entry penalty) [14]. This dielectric contrast is large for polymeric NF materials (typical dielectric constants ~3–6 ) relative to water (relative dielectric constant ~ 80 at 25 °C), and is used in PA contexts [135]. In this sense, dielectric exclusion provides a mechanism for ion exclusion that does not rely on fixed membrane charge, but on the energetic cost of placing charge in a low-permittivity environment [12, 136].

A convenient starting point is the Born self-energy, where dielectric exclusion is treated as an ion solvation/self-energy problem inside the membrane rather than primarily an ion–ion interaction problem [14]. In this context, the main factor is the solvation energy $W$ of an ion, interpreted as a self-energy arising from interaction with the surrounding medium. The

dielectric self-energy is defined through the dielectric energy density, and the Born formula follows for charging an ion (metallic sphere) in a uniform dielectric [14]:

$$W = \int_V \frac{1}{2\varepsilon_0 \varepsilon} D^2 dV \tag{1.5}$$

$$W_B(r_i, \varepsilon) = \frac{(z_i e)^2}{8\pi \varepsilon_0 \varepsilon r_i} \tag{1.6}$$

where $W$ is the dielectric self-energy, $D$ is the electric displacement field, $V$ is the polarized volume, $W_B$ is the Born self-energy, $\varepsilon_0$ is the vacuum permittivity, and $\varepsilon$ is the relative permittivity (dielectric constant) of the medium. Within this continuum picture, the membrane penalty is the difference in self-energy between membrane and solution, $\Delta W$, and the dependence on valence and ion size follows directly from the Born relation. Importantly, dielectric self-energy is not purely local. In particular, a significant fraction of the Born self-energy $W_B$ is accumulated over distances of several ion radii. As a result, water retained very close to the ion and more distant dielectric contributions may influence membrane transfer in different ways [14].

In confined pores, the permittivity relevant for dielectric exclusion is that of the pore solvent environment and does not necessarily coincide with the bulk-water value. Accordingly, $\varepsilon_{\text{pore}}$ is considered the dielectric constant of the pore solvent phase rather than the membrane matrix, and is modeled as an effective average reflecting structured/oriented water near the pore walls [137]. This distinction is made explicit in the "single oriented water layer" picture, which consists of a reduced-dielectric layer ($\varepsilon^*$) adjacent to the pore wall and an inner annulus exhibiting bulk-like properties (Figure 1.10C). It also highlights the lack of an independent direct measure of the pore dielectric constant [137]. Confinement promotes solvent structuring, which in turn reduces dielectric response, providing a mechanistic justification for $\varepsilon_{\text{pore}} < \varepsilon_b$ in narrow pores [13, 78].

Beyond the classical Born picture of charging an ion in a uniform dielectric, dielectric exclusion in membrane separations becomes membrane-specific. Indeed, additional dielectric interfaces are present (membrane–solution interfaces and pore–matrix interfaces), and computing $W$ in the presence of interfaces requires solving electrostatics with boundary conditions [14]. Near a planar water/low-$\varepsilon$ boundary, the excess self-energy can be viewed as a Coulomb interaction with a reflected fictitious "image" charge, and the image-charge magnitude is scaled by $(\varepsilon_{\text{b}} - \varepsilon_m)/(\varepsilon_b + \varepsilon_m)$ [14]. From the solution side, this yields a repulsive interaction when $\varepsilon_b > \varepsilon_m$, consistent with dielectric exclusion as an interfacial energetic barrier [14, 138]. Extending this picture to pores, ions tend to remain near the pore center, where the distance from interfaces is maximized, and $W$ is minimized.

These interface contributions are strongly geometry dependent. For a fixed nearest-interface distance, the strength of dielectric exclusion is reported to increase from planar interfaces to slits, cylinders, and finally spheres. This ordering implies that spherical pore models may overestimate dielectric exclusion in realistic pore geometries [14]. For a spherical pore center, the self-energy is written as a correction to the bulk Born value, depending on $r_i/r_{\text{pore}}$ and $\varepsilon_{\text{pore}}/\varepsilon_m$.

$$W = W_B(r_i, \varepsilon_{\text{pore}}) \left[ 1 + \frac{r_i}{r_{\text{pore}}} \left( \frac{\varepsilon_{\text{pore}}}{\varepsilon_m} - 1 \right) \right] \tag{1.7}$$

where $W_B(r_i, \varepsilon_{\text{pore}})$ is the Born self-energy in a uniform pore dielectric environment, $\varepsilon_m$ is the relative permittivity of the membrane matrix, and $r_i$ and $r_{\text{pore}}$ are the effective ion and pore radii.

A common simplification expresses the transfer penalty for spherical pores as the sum of an image-charge contribution and a Born term. However, it is noted that such additivity does not generally hold for non-spherical pore geometries [14]. The decomposition can be written as:

$$\frac{\Delta W}{k_B T} = \frac{z_i^2}{2}\left(\frac{l_m - l_{\text{pore}}}{r_{\text{pore}}} + \frac{l_{\text{pore}} - l_b}{r_i}\right) \tag{1.8}$$

where $l_b$, $l_{\text{pore}}$, and $l_m$ are the Bjerrum lengths in bulk water, in pore water, and in the membrane matrix, respectively; $k_B$ is the Boltzmann constant; $z_i$ is the ion valence; and $r_i$ and $r_{\text{pore}}$ are the effective ion and pore radii.

Within NF modeling practice, additional complications are also important to mention. Electrolyte screening and multiple-image effects can make the energetic barrier larger than the simplest single-plane estimate, with the magnitude depending on pore size and dielectric contrast [12, 137]. An explicit dielectric-exclusion energy expression used in NF modeling combines Debye–Hückel screening terms and an image charge contribution [137].

$$\frac{\Delta W}{k_B T} = \frac{W(0^+) - W(0^-)}{k_B T} = l_b\left\{\kappa(0^-) - \frac{\varepsilon_b}{\varepsilon_{\text{pore}}}\left[\kappa(0^+) + \frac{1}{r_{\text{pore}}}\ln\left(1 - \zeta\, e^{-2r_{\text{pore}}\kappa(0^+)}\right)\right]\right\} \tag{1.9}$$

where $\Delta W$ is the dielectric-exclusion (excess-solvation) energy difference across the interface, defined as the difference between the screened self-energies $W$ evaluated just inside and just outside the pore entrance, $W(0^+)$ and $W(0^-)$, respectively; $\varepsilon_{\text{pore}}$ and $\varepsilon_b$ are the relative permittivities of pore water and bulk water, and $r_{\text{pore}}$ is the effective pore radius; $\kappa(0^+)$ and $\kappa(0^-)$ are the inverse Debye lengths evaluated at the interface on the pore side and bulk-solution side, respectively; and $\zeta$ is the dielectric-mismatch parameter appearing in the screened polarization term (as defined in the original model) [137].

At sub-nanometer length scales, dielectric-continuum assumptions are further challenged by dielectric saturation near ions and interfaces, including anisotropic response, which motivates the use of effective parameters instead of bulk constants [12, 14]. At the same time, some studies caution that the existence and magnitude of image-force contributions in NF conditions can be uncertain and potentially screened at higher ion concentrations. This uncertainty motivates a more cautious use of such terms in modeling [11].

At the level of NF-relevant selectivity, dielectric exclusion is repeatedly linked to trends that steric size and Donnan exclusion alone cannot reproduce [13, 14, 137]. A key implication is that dielectric exclusion can provide a mechanism to exclude both divalent cations and divalent anions more strongly than monovalent ions in the same membrane. In contrast, Donnan exclusion alone rejects multivalent co-ions but favors multivalent counter-ions. This makes the role of ion valence clear: in limiting cases, the excess solvation energy scales with $(z^2)$ and appears in the exponent of the partition coefficient, implying that multivalent ions can be excluded strongly [12, 13]. In addition, dielectric exclusion and Donnan exclusion are described as coupled phenomena, leading to a non-trivial interaction. In fact, including dielectric exclusion lowers pore ion concentrations relative to a purely steric–Donnan contribution, thereby reducing charge screening and strengthening Donnan

exclusion. Conversely, fixed charge attracts counterions into the pore through the Donnan effect, increasing the ionic strength and thereby reducing dielectric contributions driven by polarization and interfacial interactions [13, 138].

Several experimental and theoretical results are used to motivate the practical relevance of dielectric penalties even when electrostatic Donnan exclusion is weak. Ion rejection at the isoelectric point is highlighted as sensitive to $\varepsilon_{\text{pore}}$, and ignoring dielectric exclusion (fixing $\varepsilon_{\text{pore}} = \varepsilon_b$) can underpredict NaCl rejection in model calculations [139]. In particular, dielectric exclusion is reported to yield finite rejection even when the surface charge is taken as zero ($\sigma = 0$), and this contribution is reported to be relevant for multivalent ions. For example, $CaSO_4$ can still exhibit significant rejection at the isoelectric point (IEP) [136]. In the same framework, a spatially varying near-wall permittivity is indicated to modify near-surface proton distributions. As a result, the pH at which the rejection minimum is observed (apparent IEP) can shift and the rejection–pH curve can be reshaped. In this broader solvation-energy view, dielectric effects also include pore-entry changes to the hydration environment that contribute to the same effective barrier. For similarly charged monovalent ions, ions are stabilized in bulk water by their hydration shells, which also increase their effective size [140]. Under nanoconfinement, this hydration environment can be partly rearranged or reduced during entry to the pore, introducing an additional energy barrier that depends on hydration strength [140]. In this way, monovalent–monovalent selectivity arises even when charge and steric effects are similar. In addition, the previous analysis attributes some ion-specific differences near the IEP to an entropic barrier term within a Transition State Theory (TST) framework, rather than to size or valence alone [139].

In the modeling framework adopted in this dissertation, dielectric exclusion is implemented as a partitioning penalty, expressed through a Boltzmann factor associated with a self-energy difference $\Delta W$ between membrane and solution $\exp(-\Delta W/k_B T)$. This is consistent with the capillary-model view that dielectric exclusion can be formulated through distribution coefficients linked to excess solvation energy via a Boltzmann factor of the form $\exp(-W)$ [138]. In mechanistic NF models, this dielectric partitioning is often implemented as multiplicative factors along with steric and Donnan terms, including a Donnan factor $\exp(-z_i\Delta\Psi)$ and separate Born and image-force factors $\exp(-\Delta W_{i,\text{Born}})$ and $\exp(-\Delta W_{i,\text{image}})$, respectively [13, 64]. At the same time, modeling choices differ across the literature. Some studies state that image-force partitioning is not treated and that dielectric exclusion is accounted for by ion solvation only [137]. On the other hand, others include image-charge self-energy terms [141], but report that image-force contributions can be small, e.g., when dielectric partitioning is decomposed as $\Phi_{DE,i} = \Phi_{\text{Born},i}\Phi_{\text{image},i}$ with $\Phi_{\text{image},i}$ typically in the range 0.9–1 [135]. A practical justification for preferring Born-based approaches is that resolving polarization for uncertain pore geometries can be too complex, so that omitted effects are often absorbed into effective parameters [12, 139]. Accordingly, fitted values of $\varepsilon_{\text{pore}}$ are interpreted in this dissertation as effective parameters that incorporate both intrinsic dielectric exclusion and additional neglected mechanisms, such as dehydration and specific ion–membrane interactions like image-charges [139]. Dielectric exclusion is then quantified through a Born-type expression for the self-energy difference between the pore and bulk solution:

$$\Phi_{DE,i} = exp\left(\frac{-\Delta W_i}{k_B T}\right), \quad \Delta W_i = \frac{z_i^2 e^2}{8\pi\varepsilon_0 r_i}\left(\frac{1}{\varepsilon_{\text{pore}}} - \frac{1}{\varepsilon_b}\right) \tag{1.10}$$

where $\Phi_{DE,i}$ is the dielectric exclusion coefficient of ion $i$, $\Delta W_i$ is the dielectric self-energy difference between pore and bulk solution, $z_i$ is the ion valence, $e$ is the elementary charge, $k_B$ is the Boltzmann constant, $\varepsilon_0$ is the vacuum permittivity, and $\varepsilon_{\text{pore}}$ and $\varepsilon_b$ are the relative permittivities (dielectric constants) of pore water and bulk water, respectively; $r_i$ is the effective ion radius (taken here as the Stokes radius).

In summary, dielectric exclusion is interpreted as a self-energy barrier incurred when an ion is transferred from bulk water into the low-permittivity environment defined by PA transport pathways. Although a continuum description allows this barrier to be written compactly, its physical origin is still polarization-driven and thus sensitive to the representation of the pore environment. This is why the pore dielectric constant is treated here as an effective quantity. It captures the local dielectric response of pore water, and, in mechanistic NF models, implicitly incorporates unresolved contributions such as interfacial polarization, image-force effects, and other non-Born effects. A closely related point for the next sections is that the reduction of water permittivity inside nanopores is not treated as a purely abstract parameter. Instead, it can be represented in terms of a simple structural picture, comprising a near-wall layer of water molecules with constrained orientation and reduced dielectric response that surrounds a more bulk-like pore interior. When framed in this way, $\varepsilon_{\text{pore}}$ remains mechanistically interpretable. At the same time, its effective character is shown, along with the limitations imposed by pore geometry, electrolyte screening, and uncertainty in the nanoscale effect of dielectric exclusion. These connections are important because they define how dielectric penalties are included in the partitioning step. They also clarify why the fitted $\varepsilon_{\text{pore}}$ introduced later should be interpreted as an effective descriptor of the transport environment, rather than as a direct measure of any single microscopic mechanism.

## 1.4.4. Coupled transport fluxes

Sections 1.4.1–1.4.3 described how ions enter the pore phase through steric, Donnan, and dielectric partitioning. Once inside, ions are transported through the selective layer by coupled advection, diffusion, and electromigration [7, 142]. This section introduces the general in-pore transport framework later used within the DSPM-DE model.

### Extended Nernst–Planck equation

A compact way to derive the transport form is to start from electrochemical potential [143, 144]. For species $i$:

$$\mu_i = \mu_i^0 + RT \ln a_i + V_i P + z_i F \Psi \tag{1.11}$$

where $a_i = c_i \gamma_i$ is the activity, $V_i$ is the partial molar volume, $P$ is pressure, and $\Psi$ is electrical potential. Here, $\mu_i^0$ denotes the reference (standard-state) electrochemical potential of species $i$. In one dimension across the membrane coordinate $x$, a constitutive relation writes the flux as [143, 144]:

$$J_i = -\frac{c_i D_i}{RT} \frac{d\mu_i}{dx} + c_i J_v \tag{1.12}$$

where $x$ is the coordinate normal to the membrane (from feed toward permeate side), $D_i$ is the (effective) diffusion coefficient of species $i$ in the pore phase, and $J_v$ is the volumetric solvent flux.

Substituting $\mu_i$ gives:

$$J_i = -\frac{c_i D_i}{RT}\left(RT\frac{d\ln c_i}{dx} + RT\frac{d\ln \gamma_i}{dx} + V_i\frac{dP}{dx} + z_i F\frac{d\Psi}{dx}\right) + c_i J_v \tag{1.13}$$

In NF, the barodiffusion contribution, $V_i dP/dx$, is typically small for dilute solutes and is commonly omitted in NF pore models because the dominant effect of hydrostatic pressure is already represented through the solvent flow term $c_i J_v$ [142]. For clarity, variations of $\gamma_i$ are also often neglected [143]. With these simplifications, one obtains the extended Nernst–Planck (ENP) equation:

$$J_i = -D_i\frac{dc_i}{dx} - \frac{z_i F}{RT}c_i D_i\frac{d\Psi}{dx} + c_i J_v \tag{1.14}$$

For transport in charged nanopores, confinement modifies both diffusion and advection, which is commonly represented using hindrance factors for diffusion and advection [145]. They depend on the size ratio $\lambda_i = r_i/r_{\text{pore}}$, where $r_i$ is the Stokes radius of the solute.

$$J_i = -K_{i,d}D_{i,\infty}\frac{dc_i}{dx} - \frac{z_i F}{RT}c_i K_{i,d}D_{i,\infty}\frac{d\Psi}{dx} + K_{i,a}c_i J_v \tag{1.15}$$

where $K_{i,d}$ and $K_{i,a}$ are the hindrance factors for diffusion and advection, respectively, and $D_{i,\infty}$ is the bulk (free-solution) diffusion coefficient of species $i$.

This form makes the flux decomposition explicit. Diffusion is driven by concentration gradients ($dc_i/dx$). Electromigration is driven by the electric field or by a potential gradient, $d\Psi/dx$. Advection represents solvent drag, where ions are carried by the solvent flux $J_v$.

The total flux can then be written as

$$J_i = J_{i,\text{diff}} + J_{i,\text{elec}} + J_{i,\text{adv}} \tag{1.16}$$

with:

$$\begin{aligned} J_{i,\text{diff}} &= -K_{i,d}D_{i,\infty}\frac{dc_i}{dx} \\ J_{i,\text{elec}} &= -\frac{z_i F}{RT}c_i K_{i,d}D_{i,\infty}\frac{d\Psi}{dx} \\ J_{i,\text{adv}} &= K_{i,a}c_i J_v \end{aligned} \tag{1.17}$$

However, ENP (Eq. 1.15) contains the internal potential gradient $d\Psi/dx$, which is not specified independently but must be determined through an additional electrostatic constraint [146].

### Closure for the electric potential

In charged nanopores, the three driving forces are not independent. Membrane charge and charge conservation impose constraints that couple ion concentrations and the electric field. As a result, the electrical potential gradient cannot be specified independently of the concentration fields. Therefore, ENP must be supplemented by a closure to determine $\Psi$ (or $d\Psi/dx$) [147]. Different modeling frameworks correspond to different closure choices, which differ in how they resolve space charge, and they correspond to different levels of detail in NF modeling.

A general continuum closure solves ENP together with Poisson's equation:

$$-\frac{d}{dx}\left(\varepsilon_0 \varepsilon \frac{d\Psi}{dx}\right) = \rho_e, \qquad \rho_e = F\left(\sum_i z_i c_i + c_X\right) \tag{1.18}$$

where $\varepsilon_0\varepsilon$ is the permittivity of the medium, with $\varepsilon_0$ the vacuum permittivity and $\varepsilon$ the relative permittivity, and $\rho_e$ is the local electric charge density. In principle, this approach resolves space charge and electrical double layers [148, 149].

A commonly used alternative is an electroneutrality closure in quasi-neutral regions [7, 150]. In the electroneutral approximation within the pore, the mobile-ion charge balances the fixed charge (Eq. 1.4) and determines the potential implicitly by enforcing this constraint together with transport. In membrane models, an important related concept is the Donnan potential, $\Delta\Psi_D$. At interfaces, $\Delta\Psi_D$ is obtained from Donnan equilibrium (Eq. 1.3) together with electroneutrality in the membrane phase, and provides the boundary concentrations for solving ENP across the selective layer [7].

A third common closure is the open-circuit, zero-current condition [151]. In pressure-driven membrane processes, there is no external electrical circuit [2, 146]. The electric field then develops such that the net current vanishes. Defining the current density as

$$I = F\sum_i z_i J_i \tag{1.19}$$

the closure reads $I = 0$. Combined with ENP, this provides an explicit condition for $d\Psi/dx$. Physically, the membrane potential gradient then emerges from the requirement that diffusion- and advection-driven charge transport is balanced by electromigration.

At the macroscopic level, the resulting transmembrane potential difference is often termed the filtration potential. It reflects both the applied pressure, which gives rise to a streaming potential through the active layer, and the concentration differences induced by selective ion transport, which in turn drive diffusive ion fluxes through the pores [152]. These coupled transport contributions and the corresponding one-dimensional transport domain are summarized in Figure 1.11.

**Boundary conditions**

In practice, ENP is solved across an effective thickness-to-porosity ratio $\Delta x_e$, with boundary concentrations at each interface set by the steric, Donnan, and dielectric partitioning relations introduced before. At steady state, the molar flux $J_i$ is constant across the membrane thickness. These boundary conditions connect interfacial partitioning to transmembrane transport. Together with the interfacial partitioning relations from Sections 1.4.1–1.4.3, these transport equations form the core of the DSPM-DE model introduced in Section 1.4.5.

## 1.4.5. Mechanistic models used in Nanofiltration

Several modeling approaches have been used to describe solute rejection in NF. They differ mainly in whether the membrane is treated as a phenomenological black box or represented through explicit partitioning and transport steps.

Early NF descriptions were frequently formulated within irreversible thermodynamics, where transport is expressed through phenomenological relations without a mechanistic

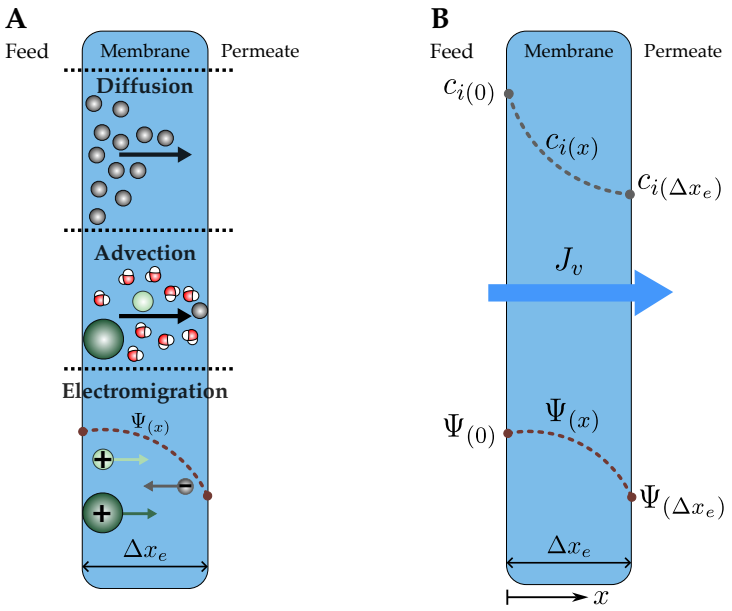



**Figure 1.11:** Schematic and mathematical representation of one-dimensional ionic transport across the effective thickness-to-porosity ratio ($\Delta x_e$). **(A)** Schematic depiction of the three contributions to the ionic flux in the extended Nernst–Planck (ENP) equation: *diffusion* driven by concentration gradients, *advection* with the permeating solvent, and *electromigration* driven by an electric potential gradient. **(B)** Corresponding one-dimensional transport domain used in the ENP formulation, showing the solvent flux $J_v$, the in-pore concentration field $c_{i(x)}$ with boundary values $c_{i(0)}$ and $c_{i(\Delta x_e)}$, and the electric potential $\Psi(x)$ with $\Psi_{(0)}$ and $\Psi_{(\Delta x_e)}$; $\Psi_{(x)}$ is determined through the electrostatic closure.

representation of how solutes enter and move through the selective layer [153]. While such approaches can capture overall separation performance, they do not directly connect fitted parameters to membrane structural or physicochemical characteristics [142].

Mechanistic NF models instead describe solute transport based on the ENP equation, combined with an electrostatic description of the membrane phase [7, 142]. In this framework, models based on the ENP equation have been coupled to fixed-charge concepts originally developed for ion-exchange membranes. These modeling approaches include the Teorell–Meyer–Sievers (TMS) description and related extensions that address assumptions such as uniform charge distributions [7, 142]. Within NF pore models, the selective layer is represented through idealized pores, and ion rejection is attributed to a combination of separation potentials that control pore entry and transmembrane transport [31].

In the framework used throughout this dissertation, these separation potentials correspond to steric, Donnan exclusion arising from fixed charge, and dielectric exclusion driven by the dielectric contrast between the pore environment and bulk water. Historically, the Donnan–steric partitioning pore model (DSPM) was introduced to combine steric and electrostatic partitioning [154]. However, extensions that include dielectric effects (e.g., SEDE-type formulations) were developed to improve the description of multivalent-ion rejection [13]. In this context, combining ENP transport with equilibrium partitioning or exclusion at the solution/membrane interfaces yields the Donnan–Steric Pore Model with Dielectric Exclusion (DSPM-DE) as a compact mechanistic description of selective transport in NF [150].

Accordingly, this dissertation adopts DSPM-DE as the central mechanistic NF model,

building on the partitioning and transport framework developed in Sections 1.4.1–1.4.4. Therefore, the following subsections state the assumptions used to implement these mechanisms in the DSPM-DE model, summarize the governing equations in the form used in this dissertation, and outline how the effective parameters are inferred from experimental data.

### Model assumptions and structure

As established in Section 1.3, the membrane's active layer is described through effective structural and physicochemical descriptors that support mechanistic interpretation without requiring a fully resolved microstructural representation. In line with this, the DSPM-DE framework adopted in this dissertation is formulated for TFC membranes under a pressure-driven transport direction from feed to permeate. In this representation, the hydraulic and diffusive resistances of the microporous support are assumed negligible compared to the selective layer, such that separation is attributed only to the active layer. The selective layer is modeled as a porous medium consisting of parallel cylindrical pores with a uniform characteristic pore size [7]. Accordingly, porosity and tortuosity are not treated as independently accessible quantities but are grouped into an effective thickness-to-porosity ratio ($\Delta x_e$), which is used as the macroscopic transport length scale of the selective layer [7]. Transport through the active layer is treated as one-dimensional and at steady state, neglecting lateral concentration gradients (e.g., along the crossflow direction).

Solutes are represented as hard spheres characterized by a hydrated size, and Stokes radii are commonly used as the corresponding input parameter in the DSPM-DE model. For the electrolyte conditions typically addressed with this model, the in-pore ENP formulation is commonly simplified by neglecting activity-coefficient gradients and treating solute–solute interaction effects implicitly. At the same time, activity coefficients can still be retained in the interfacial partitioning relations when boundary concentrations are evaluated. Dielectric exclusion is implemented using a Born-type description, with the dielectric constant of water inside pores ($\varepsilon_{\text{pore}}$) considered as spatially constant.

The membrane charge is represented by a volumetric fixed-charge density that is commonly taken as spatially uniform, while allowing that spatially varying charge descriptions can be introduced when needed. Electroneutrality is imposed in the membrane phase and in the adjacent feed- and permeate-side solutions. In this dissertation, this constraint is applied as introduced earlier in the electrostatic closure discussion (Section 1.4.4), and it is therefore not rederived here.

Structurally, the DSPM-DE describes NF as a sequence of coupled steps: (i) transport from the bulk feed toward the feed/membrane interface, (ii) interfacial partitioning between the aqueous phase and the pore phase, (iii) in-pore transport across $\Delta x_e$, and (iv) a second partitioning step between the membrane domain and the permeate-side solution [7]. Selective ion transport induces concentration polarization, leading to the accumulation or depletion of species adjacent to the feed-solution/membrane interface. Concentration polarization is represented by a concentration gradient across a boundary layer next to the membrane surface [155]. Within this framework, solute partitioning at the membrane interfaces is described by steric, Donnan, and dielectric contributions (Sections 1.4.1–1.4.3), while transport within the pore phase is governed by the ENP framework, accounting for hindered diffusion, electromigration, and advection (introduced in Section 1.4.4). Based on these assumptions and structural elements, the next subsection summarizes the coupled boundary conditions, transport equation, and electrostatic constraints that define the DSPM-DE model used in this

dissertation. An overview of the coupled DSPM-DE structure and its inputs and outputs is shown in Figure 1.12.

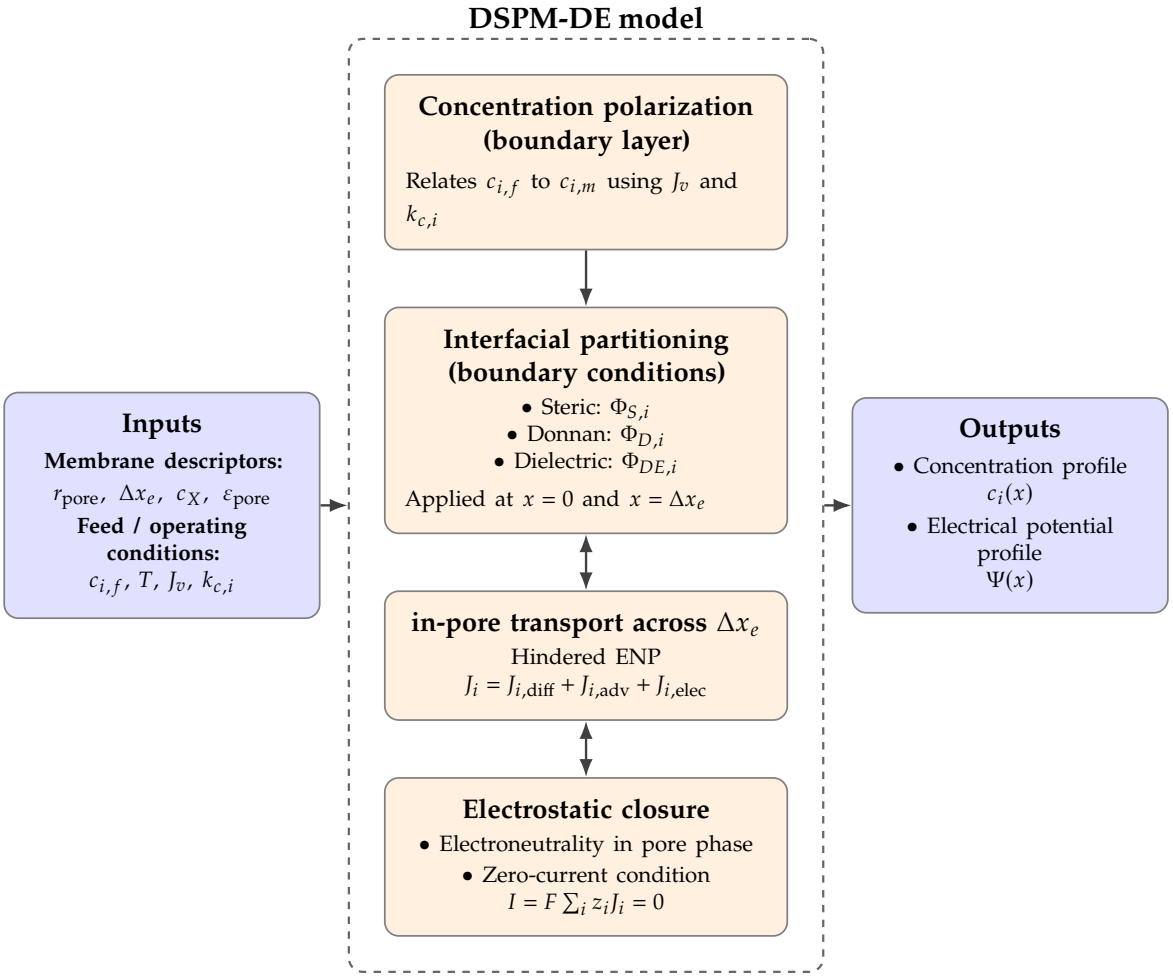



**Figure 1.12:** Schematic overview of the DSPM-DE framework used in this dissertation. Effective membrane descriptors and feed/operating conditions are provided as inputs to the DSPM-DE model (dashed box), which comprises concentration polarization (where $c_{i,m}$ is the concentration of ion i in the feed-solution/membrane interface), interfacial partitioning, hindered extended Nernst–Planck transport, and electrostatic closure. Double-headed arrows indicate that these components are solved as a coupled system. The model yields the in-pore concentration profile $c_i(x)$ and the electrical potential profile $\Psi(x)$.

## Governing equations

In DSPM-DE, the governing equations are written as a coupled boundary-condition problem that combines interfacial partitioning and in-pore transport as discussed above. Solving this coupled boundary-value problem across $\Delta x_e$ yields the steady-state in-pore concentration profiles $c_{i(x)}$ and the corresponding electrical potential $\Psi(x)$ consistent with the closure condition. Derivations are not repeated here. Instead, the final system is summarized in the form used throughout this dissertation, building on the partitioning relations introduced in Sections 1.4.1–1.4.3 and the transport and closure framework introduced in Section 1.4.4.

**In-pore transport (ENP with hindrance)** As introduced in Section 1.4.4, the transport of each ionic species is described by the hindered ENP equation (Eq. 1.15), in which hydrodynamic confinement enters through diffusion $K_{i,d}$ and advection $K_{i,a}$ hindrance factors that depend on the size ratio $\lambda_i$ (Eq. 1.1). The diffusion hindrance factor is determined from [7, 155].

$$K_{i,d} = \begin{cases} \dfrac{\left[\begin{array}{c} 1 + \frac{9}{8}\lambda_i \ln(\lambda_i) - 1.56034\lambda_i \\ +0.528155\lambda_i^2 + 1.91521\lambda_i^3 - 2.81903\lambda_i^4 \\ +0.270788\lambda_i^5 + 1.10115\lambda_i^6 - 0.435933\lambda_i^7 \end{array}\right]}{(1-\lambda_i)^2}, & \text{if } \lambda_i \le 0.95 \\ 0.984\left(\frac{1-\lambda_i}{\lambda_i}\right)^{2.5} & \text{if } \lambda_i > 0.95 \end{cases} \tag{1.20}$$
$$K_{i,a} = \frac{1 + 3.867\lambda_i - 1.907\lambda_i^2 - 0.834\lambda_i^3}{1 + 1.867\lambda_i - 0.741\lambda_i^2}$$

Here, the dependence of $K_{i,d}$ and $K_{i,a}$ on $\lambda_i$ makes the steric contribution controlled by $r_{\text{pore}}$, as defined earlier.

**Interfacial partitioning boundary conditions** Partitioning between the external solutions and the pore phase is implemented through boundary conditions that combine steric, Donnan, and dielectric partition factors, together with activity coefficients. At the feed/membrane interface ($x = 0$) and at the membrane/permeate interface ($x = \Delta x_e$), the boundary conditions are written as:

$$\begin{aligned} c_{i(0)}\gamma_{i(0)} &= c_{i,m}\gamma_{i,m}\Phi_{S,i}\Phi_{D,i}^{x=0}\Phi_{DE,i} \\ c_{i(\Delta x_e)}\gamma_{i(\Delta x_e)} &= c_{i,p}\gamma_{i,p}\Phi_{S,i}\Phi_{D,i}^{x=\Delta x_e}\Phi_{DE,i} \end{aligned} \tag{1.21}$$

where subscript $m$ denotes the feed solution at the interface; $c_{i,p}$ is the permeate concentration; $\gamma_i$ denotes the activity coefficients in the corresponding phases; and $\Phi_{S,i}$, $\Phi_{D,i}$, and $\Phi_{DE,i}$ are the steric, Donnan, and dielectric exclusion coefficients, respectively (evaluated at the corresponding interface). In this form, $\Phi_{S,i}$, $\Phi_{D,i}$, and $\Phi_{DE,i}$ correspond to the steric (Eq. 1.2), Donnan (Eq. 1.3), and dielectric exclusion (Eq. 1.10) or partitioning coefficients introduced earlier in Sections 1.4.1–1.4.3.

**Electrostatic constraints and closure** Following the closure discussion in Section 1.4.4, electroneutrality constraints are imposed in the external solutions adjacent to the membrane and within the membrane phase, and the zero-current condition (Eq. 1.19) is applied to determine the electrical potential. These relations were already introduced and are therefore not restated here.

**Concentration polarization at the feed-side interface** To evaluate the interfacial concentration ($c_{i,m}$) entering the partitioning condition, concentration polarization is accounted for by describing transport across the boundary layer next to the membrane surface. The boundary-layer flux relation is written as [156]:

$$J_i = -k_{c,i}^{\bullet}\left(c_{i,m} - c_{i,f}\right) + J_v c_{i,m} - z_i c_{i,m} D_{i,\infty}\frac{F}{RT}\xi \tag{1.22}$$

where $k^{\bullet}_{c,i}$ is a mass-transfer coefficient, $c_{i,f}$ denotes the bulk feed concentration, $D_{i,\infty}$ is the bulk diffusion coefficient of species $i$, and $\xi$ is the electrical potential gradient at the feed-solution/membrane interface.

**Permeate-side relation under dead-end conditions** For the case without sweep flow (dead-end filtration), the steady-state molar flux can be related to the permeate concentration $c_{i,p}$ through [146]:

$$J_i = J_v c_{i,p} \tag{1.23}$$

where $c_{i,p}$ is the permeate concentration of species $i$ under steady-state conditions.

Taken together, this framework links the model input parameters to the underlying mechanisms in the formulation used here: steric terms enter through $\lambda_i$ and thus through $r_{\text{pore}}$, Donnan terms are controlled by the fixed-charge descriptor $c_X$, and dielectric exclusion is controlled by the effective pore dielectric constant ($\varepsilon_{\text{pore}}$), as introduced earlier. Transport through the pore is then formulated over an effective thickness $\Delta x_e$, representing the characteristic thickness of the transport domain across which solutes are transported from the feed-solution/membrane interface to the membrane/permeate-solution interface. Therefore, the next subsection focuses on how these effective parameters are obtained in practice and how fitted descriptors are linked to experimentally determined rejections and operating conditions.

### Parameter estimation and link to experiments

With the partitioning and transport mechanisms introduced and assembled in the coupled system above, DSPM-DE requires four input membrane parameters: the membrane effective pore radius ($r_{\text{pore}}$), the effective thickness-to-porosity ratio ($\Delta x_e$), the pore dielectric constant ($\varepsilon_{\text{pore}}$), and the volumetric fixed-charge density ($c_X$). In most studies, these inputs are obtained by fitting NF performance data, rather than being determined independently.

**Determination of $r_{\text{pore}}$ and $\Delta x_e$** For uncharged solutes, Donnan and dielectric exclusion do not apply in DSPM-DE, such that steric exclusion is the only partitioning mechanism. Solving the model under this condition yields an analytical expression for rejection that can be used to determine $r_{\text{pore}}$ and $\Delta x_e$ from neutral-solute filtration data typically assessed over varying operating conditions such as pressure or flux [154].

$$R_{i,\text{real}} = 1 - \frac{K_{i,a}\Phi_{S,i}}{1 - (1 - K_{i,a}\Phi_{S,i})\exp\left(-\frac{K_{i,a}J_v\Delta x_e}{K_{i,d}D_{i,\infty}}\right)} \tag{1.24}$$

here, $\Phi_{S,i}$ is the steric partition coefficient introduced earlier (Eq. 1.2), and the hindrance factors $K_{i,a}$ and $K_{i,d}$ are those used in the hindered ENP formulation summarized above (Eq. 1.20); $c_{i,m}$ and $c_{i,p}$ are the feed-solution/membrane interface and permeate concentrations, respectively; $\Delta x_e$ is the effective thickness-to-porosity ratio; $J_v$ is the volumetric solvent flux; and $D_{i,\infty}$ is the bulk diffusion coefficient.

To connect this expression to experimentally observed rejections $R_{i,\text{obs}}$, concentration polarization must be considered when $c_{i,m} \neq c_{i,f}$. Concentration polarization is accounted for through a mass-transfer coefficient $k_{c,i}$ as [154]:

$$\ln\left(\frac{1-R_{i,\text{real}}}{R_{i,\text{real}}}\right) = \ln\left(\frac{1-R_{i,\text{obs}}}{R_{i,\text{obs}}}\right) - \frac{J_v}{k_{c,i}} \tag{1.25}$$

where $R_{i,\text{real}}$ is the solute retention at infinite stirring velocity, and $k_{c,i}$ is the feed-side mass-transfer coefficient. Accordingly, when $J_v$ is used as an input, $r_{\text{pore}}$ and $\Delta x_e$ can be estimated simultaneously by fitting the model to neutral-solute retention data [7].

**Determination of $\varepsilon_{\text{pore}}$ and $c_X$** For electrolytes, dielectric exclusion and Donnan exclusion both contribute to rejection in DSPM-DE, and $\varepsilon_{\text{pore}}$ and $c_X$ are typically determined by fitting salt retention data once $r_{\text{pore}}$ and $\Delta x_e$ are fixed [150]. Because dielectric exclusion and charge effects are interconnected in the model response, an isoelectric-point (IEP) based fitting strategy has been used. The IEP is determined from single-salt experiments and dielectric and charge parameters are then estimated sequentially [150]. This strategy implicitly assumes a homogeneous membrane charge and treats the fitted pore dielectric constant as an intrinsic membrane property independent of solution composition, which has been questioned in DSPM-DE studies [7].

More generally, several studies dealing with the DSPM-DE model report that both $c_X$ and $\varepsilon_{\text{pore}}$ vary with feed composition and concentration [157–162]. $c_X$ is obtained by fitting mixed-salt rejection data and is interpreted as an apparent effective charge that supports consistent comparisons across membranes and conditions. Ion-dependent variations in fitted $c_X$ have been reported and attributed to interfacial phenomena such as adsorption, electrostatic screening, and binding–association effects [31, 158–163]. These effects are not included in the model, so that fitted $c_X$ adjusts to reproduce observed retentions. Similarly, co-ion partitioning and transport [8], as well as ion-specific adsorption and screening, have been discussed as factors influencing $\varepsilon_{\text{pore}}$ and thus ion selectivity within the DSPM-DE model [131, 134, 136, 139, 162, 164].

A key practical consequence of this coupling is parameter identifiability. Fitting single-salt retention curves can lead to non-unique combinations of $\varepsilon_{\text{pore}}$ and $c_X$, whereas fitting mixed-salt retention allows an unambiguous determination [165]. Within this framework, the model parameters are understood as effective descriptors of membrane structure rather than direct physical measurements. This makes them suitable for systematic comparison among different membranes and filtration conditions.

In parallel to direct fitting, semi-empirical approaches have been used to estimate $\varepsilon_{\text{pore}}$ as an explicit function of $r_{\text{pore}}$ [150, 166]. In the pore-layer picture, the dielectric constant is treated as a volume-weighted average between a near-wall oriented water layer with dielectric constant $\varepsilon^*$ (determined by membrane material), thickness $d_{\text{H}_2\text{O}}$ and a bulk-like pore core dielectric constant $\varepsilon_{\text{b}}$ (Figure 1.10C), giving [150, 166]:

$$\begin{aligned}
\varepsilon_{\text{pore}} &= \frac{\int_0^{r_{\text{pore}}-d_{\text{H}_2\text{O}}} 2\pi r\,\varepsilon_b\,dr + \int_{r_{\text{pore}}-d_{\text{H}_2\text{O}}}^{r_{\text{pore}}} 2\pi r\,\varepsilon^*\,dr}{\pi r_{\text{pore}}^2} \\
\varepsilon_{\text{pore}} &= \varepsilon^* + (\varepsilon_b - \varepsilon^*)\left(1 - \frac{d_{\text{H}_2\text{O}}}{r_{\text{pore}}}\right)^2
\end{aligned} \tag{1.26}$$

where $r$ is the radial coordinate in the pore cross-section.

However, the parameter $\varepsilon^*$ cannot be determined experimentally, and its value is, therefore, not independently known. This simplification has been criticized for its limited consistency with NF model assumptions, motivating approaches that determine $\varepsilon_{\text{pore}}$ directly from filtration data.

Finally, determination of DSPM-DE input parameters is experimentally demanding, as it requires sequential fitting to neutral and then charged solutes, and relies on regression procedures that are sensitive to assumed parameter independence and auxiliary relations [7]. To mitigate these limitations, alternative strategies have been proposed in which global and local optimization schemes are used to regress all four membrane parameters directly from charged-species experiments [167]. These choices in parameter estimation directly affect both the interpretability of the fitted parameters and the practical limitations of the DSPM-DE framework, as summarized next.

### Strengths and limitations

The DSPM-DE model provides a comprehensive mass-transport description of selective species transport through NF membranes by using membrane morphological and physicochemical features as model inputs. These inputs provide a compact set of effective descriptors for interpreting membrane performance. A practical strength of DSPM-DE is that it combines interfacial exclusion at the bulk-solution/membrane interfaces with an ENP-based transport description inside pores. This supports mechanistic assessment of how membrane characteristics affect ion transport, using the flux framework introduced in Section 1.4.4.

These strengths come with recognized limitations that follow directly from the simplifying assumptions used in the standard DSPM-DE formulation [7]. The model often represents the pore structure through an averaged pore size, even though measured pore-size distributions are more representative of PA NF morphologies [51]. Similarly, the conventional implementation assumes uniform distributions of membrane properties, including a spatially constant volumetric charge density and a constant pore dielectric constant. However, both inputs have been reported to depend on electrolyte composition and concentration and, thus, to require calibration for each feed solution.

A related practical limitation is that the DSPM-DE input parameters are typically obtained by fitting rejection data, because it is challenging to determine these quantities independently under filtration conditions. As discussed in Section 1.4.5, fitted values of $c_X$ and $\varepsilon_{\text{pore}}$ are therefore interpreted as apparent effective descriptors that absorb interfacial phenomena not included in the model formulation.

Finally, dielectric exclusion in DSPM-DE is commonly implemented via a Born-type term (Section 1.4.3), a simplification that remains debated in the literature [7, 14, 135, 137]. In this context, the choice of ionic radius entering the Born-type description is recognized as an additional modeling sensitivity, and different radius definitions have been investigated across DSPM-DE studies [7, 166]. Although inclusion of image forces and other non-Born effects has been proposed, the resulting complexity has limited adoption, motivating the use of an effective $\varepsilon_{\text{pore}}$ [12, 135, 139].

Taken together, DSPM-DE provides a mechanistic framework that is detailed enough to rationalize selective ion transport through the effective membrane descriptors. However, the fitted parameters require careful interpretation under the underlying assumptions and solution-specific calibration discussed above. This balance between mechanistic insight and effective parameter interpretation motivates the use of DSPM-DE as a unifying analysis

framework across the dissertation chapters, as summarized below.

### 1.4.6. Summary and role in the dissertation

Sections 1.4.1–1.4.4 established the mechanistic building blocks that are assembled in the DSPM-DE model: interfacial partitioning between the external solutions and the pore phase, combined with ENP-based in-pore transport across an effective thickness $\Delta x_e$. Consistent with the flux decomposition introduced in Section 1.4.4, the DSPM-DE formulation used here also quantifies the relative contributions of diffusion, electromigration, and advection to the overall transmembrane solute flux. Within this description, the DSPM-DE framework provides a compact mechanistic model in which rejection is controlled by a small set of effective membrane descriptors and the associated electrostatic closure, rather than by purely phenomenological transport coefficients.

Across these building blocks, the three dominant exclusion mechanisms are included. Steric exclusion is governed by the effective pore size ($r_{\mathrm{pore}}$). Donnan exclusion is governed by the effective fixed-charge density ($c_X$) and depends on solution conditions such as pH and electrolyte composition/concentration, which are reflected in fitted effective charge descriptors in practical implementations. Dielectric exclusion is governed by the effective pore dielectric constant ($\varepsilon_{\mathrm{pore}}$) and the dielectric contrast between the pore environment and bulk water, which enters the model through the dielectric partitioning step introduced in Section 1.4.3.

In the cumulative part of this dissertation, this DSPM-DE framework is applied to interpret $Na^+/Mg^{2+}$ separation and nitrate removal in the membrane systems developed in this work. The focus is on how monomer chemistry and monomer concentration during interfacial polymerization influence the effective parameters ($r_{\mathrm{pore}}, \Delta x_e, \varepsilon_{\mathrm{pore}}, c_X$) and, through them, NF selectivity and permeance.

## 1.5. State of the Art and Knowledge Gaps

This section summarizes the state of knowledge required to frame selective ion separations by PA TFC NF membranes and then identifies the unresolved issues that still limit rational membrane design. As established in the preceding sections, mechanistic interpretation is formulated in terms of coupled interfacial partitioning and in-pore transport, expressed through effective membrane descriptors [7]. Accordingly, the focus here is not on restating that framework, but on identifying what it still cannot resolve without systematic mechanistic evidence.

The scope is restricted to PA TFC NF membranes relevant to selective $Na^+/Mg^{2+}$ separations and nitrate removal, including the influence of electrolyte environment and common-ion effects on selectivity [7, 157–162].

Figure 1.13 summarizes how the unresolved links discussed below arise between design variables, effective descriptors, and mechanistic interpretation for the two targeted separations.

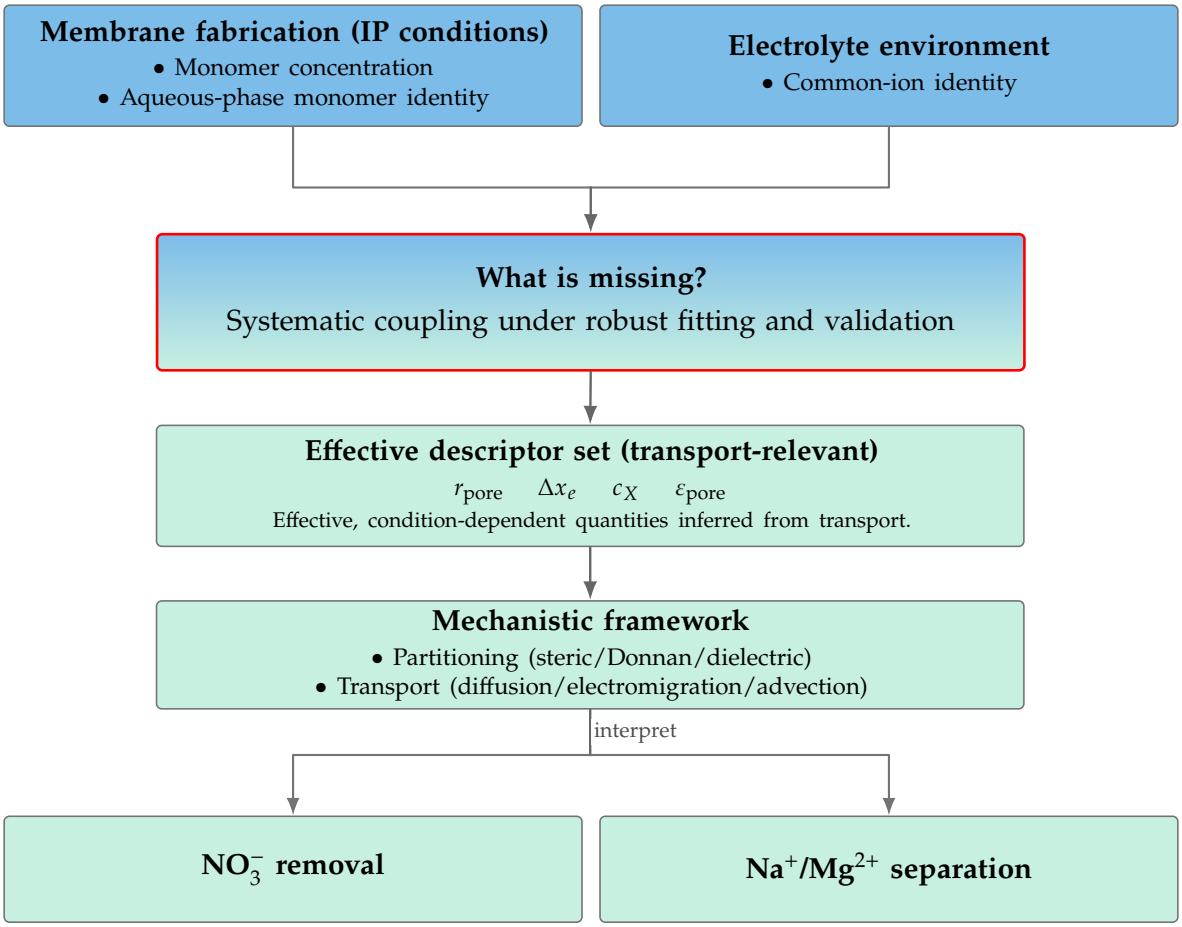



**Figure 1.13:** Mechanistic interpretation is formulated in terms of coupled interfacial partitioning/exclusion and in-pore transport expressed through an effective descriptor set. The key limitation is the lack of systematic evidence linking IP conditions and monomer chemistry to coupled descriptor shifts under mixed-electrolyte conditions and across common-ion identity. Because effective descriptors can be non-unique and not directly transferable between electrolyte environments, robust fitting and validation are required for a mechanistic interpretation of $NO_3^-$ removal and $Na^+/Mg^{2+}$ separation.

### 1.5.1. Established knowledge

NF typically exhibits stronger rejection of multivalent ions than monovalent ions, while monovalent selectivity is often partial and dependent on the operating conditions [2, 6, 9]. In practice, separation performance is, therefore, not captured by a single "best membrane" comparison. Rejection and selectivity depend on the target ion pair and on the solution composition that sets the relevant driving forces and strength of the exclusion phenomena [7, 131–134]. Consequently, performance outcomes are only meaningful when tied to a specific separation problem and its operating conditions.

A common trade-off is that gains in selectivity are often accompanied by permeance penalties [7, 51, 111, 168, 169]. This selectivity–permeance coupling is not a general law. However, it represents a recurring practical limitation for PA TFC NF membranes, particularly when selectivity relies on tuning electrostatic effects that also influence water and ion transport [51].

**Intrinsic complexity of $Na^+/Mg^{2+}$ separation and nitrate removal**

Selective $Na^+/Mg^{2+}$ separation is not explained by steric exclusion alone [38, 125–127]. Electrostatic and dielectric effects can become dominant and transport is governed by coupled contributions rather than a single controlling mechanism [7, 139, 170]. As a result, the same structural change can increase or decrease selectivity depending on how it reshapes Donnan and dielectric partitioning and the in-pore electrical potential gradient [147, 152]. This sensitivity motivates a mapping of the fabrication conditions with effective descriptors under controlled electrolyte environments, instead of inferring mechanisms solely from performance trends.

For $NO_3^-$, the challenge is different. As a monovalent anion, $NO_3^-$ commonly exhibits partial rejection that is sensitive to both membrane fixed charge and solution composition, including competitive effects in mixed electrolytes [6, 26, 158]. This places emphasis on understanding how membrane descriptors and electrolyte environment together shift the balance between exclusion at the interfaces and coupled transport within the active layer [7, 31, 169]. Accordingly, advancing understanding toward rational membrane design requires relating synthesis-driven changes in effective descriptors to nitrate selectivity across representative mixed-salt environments.

## 1.5.2. Knowledge gaps

Even within a mechanistic framework based on membrane descriptors, key interpretation steps remain challenging because these descriptors represent effective values [7, 51, 139]. They can incorporate heterogeneity in charge distribution, free-volume structure, pore size distribution, and dielectric microenvironment into single parameters, which depend on the conditions under which they are inferred [7, 51, 139]. Therefore, mechanistic interpretation requires systematic study designs that distinguish changes arising from fabrication from shifts associated with the solution environment in partitioning and transport.

**Fabrication-descriptor linkage**

A knowledge gap remains in systematically connecting IP conditions with the full set of effective descriptors used to interpret ion selectivity [7, 51, 67, 69]. Monomer concentrations are widely recognized as key parameters shaping PA TFC NF membrane properties [38, 64, 67, 69]. However, studies often do not establish how changes in fabrication conditions are reflected in a coupled manner across effective thickness, pore-size-related descriptors, fixed-charge, and dielectric descriptors [130, 169, 171]. As a result, mechanistic interpretation is frequently limited to identifying a dominant effect from performance outcomes, rather than mapping how fabrication conditions position a membrane within a descriptor set.

This knowledge gap is amplified by the common focus on operating-condition effects while the membrane itself is treated as fixed. Such studies can be mechanistically informative, but they do not directly resolve how IP fabrication conditions set the descriptors that govern partitioning and transport [157, 159, 162, 165, 172]. In contrast, mechanistic analyses coupled with fabrication conditions remain comparatively limited. When available, they often address only subsets of the model inputs, which limits how broadly the resulting insights can be generalized [130, 169, 171]. Addressing this knowledge gap requires study designs that systematically vary IP conditions and interpret the resulting membranes using a complete descriptor set under controlled electrolyte compositions.

**Nitrate: fabrication–descriptor gap** For nitrate removal, mechanistic understanding has been developed through operating-condition variations and through studies focused on commercially available membranes [6, 26, 158]. This has elucidated how combined exclusion mechanisms can sharpen differences between monovalent anions under particular conditions, but it leaves a knowledge gap relevant to membrane design [29]. In particular, membranes fabricated for nitrate separation with varying monomer concentrations during IP are not yet systematically linked to changes in membrane descriptors in a consistent framework. Consequently, it remains difficult to move from identifying which operating conditions improve nitrate rejection to establishing which IP fabrication changes produce the descriptor shift required for nitrate selectivity. The resulting knowledge gap is the lack of synthesis–descriptor–selectivity maps for $NO_3^-$ under mixed-electrolyte conditions and interpreted within a consistent mechanistic framework.

**$Na^+/Mg^{2+}$: fabrication–descriptor gap** For $Na^+/Mg^{2+}$ separation, modeling studies have extensively examined the influence of operating parameters such as pH, temperature, and feed concentration on selectivity [159, 161, 162, 165]. However, systematic fabrication-linked mechanistic mapping remains underexplored. This is particularly evident under conditions where Donnan effects become dominant and changes in effective membrane charge can qualitatively alter transport behavior [38, 125–127]. In this context, varying only one or two effective inputs at a time is insufficient to understand how monomer concentrations jointly tune the coupled descriptor set governing partitioning and transport contributions [130, 169, 171]. The resulting knowledge gap is the absence of fabrication-linked descriptor maps spanning transitions in effective membrane charge. Thus, how coupled transport contributions shift under Donnan-dominant conditions relevant to $Na^+/Mg^{2+}$ separation remains unresolved.

### Monomer-chemistry effects

A second knowledge gap concerns the effect of monomer identity. Changes in aqueous-phase monomer chemistry are widely reported to alter membrane formation, morphology, charge density, and ultimately selectivity [38, 64, 117]. However, many studies that vary monomer structure rely primarily on experimental performance trends. How these trends relate to changes in the underlying exclusion and transport contributions within a unified mechanistic framework often remains unresolved. As a result, monomer chemistry is often limited to an empirical role, rather than serving as a predictive design variable [38, 51, 64, 117]. Addressing this knowledge gap requires monomer-chemistry comparisons that quantify how ion transport shifts through the effective descriptor set, rather than treating selectivity changes as empirical outcomes.

This limitation is especially relevant when subtle differences in monomer structure lead to changes in selectivity [64, 74, 117–119]. Without a mechanistic interpretation of how steric, Donnan, and dielectric exclusion, together with in-pore transport contributions, shift across the effective descriptor set, interpretation remains ambiguous. In particular, it becomes difficult to determine whether improved selectivity reflects a specific change in a dominant mechanism or the simultaneous change of multiple membrane properties and transport contributions.

**Electrolyte and common-ion effects**

A third knowledge gap is the incomplete mechanistic integration of electrolyte identity and common-ion effects with membrane structure and charge. Both simulations and experiments indicate that $Na^+/Mg^{2+}$ selectivity can differ significantly between feed solutions containing sulfate and chloride, depending on the membrane fixed charge [7, 8, 31]. Yet a comprehensive treatment that integrates electrolyte identity and the coupled descriptor set remains underexplored.

Two unresolved aspects follow from this. First, co-ion partitioning and transport, together with ion-specific screening and adsorption effects, can modulate the effective dielectric environment [8, 131, 134]. As a result, selectivity can change in ways that are not captured by electrostatics alone. Second, the interplay between increasing positive charge density and anion identity has not been systematically established, despite its relevance for cation selectivity in realistic electrolyte conditions [38, 125–127]. Accordingly, electrolyte-specific selectivity shifts cannot be interpreted by transferring a descriptor set inferred under one common-ion identity to another without targeted mechanistic studies that vary both effective membrane charge and common-ion identity. This motivates study designs that vary common-ion identity alongside effective membrane charge, enabling a mechanistic separation of Donnan- and dielectric-dominated behavior under realistic electrolyte environments.

**Model interpretability**

Even when mechanistic models are used, their fitted inputs represent effective descriptors that absorb structural and chemical heterogeneity into a small parameter set [7, 51]. Consequently, parameter values may not be uniquely identifiable across different electrolyte environments. Similar fits can sometimes be obtained through compensating changes in multiple descriptors [7, 139, 161, 165]. This does not challenge the mechanistic framework but constrains interpretation. Therefore, mechanistic interpretation must be stated in terms of effective contributions under clearly defined assumptions and operating conditions.

In this context, a key unresolved issue is the establishment of robust fitting and validation strategies [165, 167]. These are needed to distinguish membrane-driven descriptor changes (set by fabrication and monomer chemistry) from solution-driven shifts in partitioning and coupled transport. Addressing this interpretability knowledge gap is essential for translating fitted model parameters into physically meaningful design rules for specific separations.

## 1.5.3. Synthesis and implications

Taken together, the central unresolved issues are not the absence of a mechanistic framework. Rather, they lie in the lack of systematic evidence that links fabrication conditions and monomer chemistry to coupled shifts in transport-relevant effective descriptors. This knowledge gap is particularly relevant across electrolyte environments that can qualitatively change the governing contributions. For $NO_3^-$, this appears as a knowledge gap between mechanistic insights obtained by varying operating conditions and the systematic mapping of descriptors as a function of synthesis conditions for nitrate-selective membranes. For $Na^+/Mg^{2+}$, this appears as limited understanding of how fabrication influences selectivity under conditions where Donnan exclusion becomes significant. In addition, common-ion effects are not yet treated in a unified manner across different effective membrane

charges. These knowledge gaps define what remains to be resolved to support a mechanistic interpretation of ion transport behavior in PA TFC NF membranes.

# 2

# Scientific Objectives of the Dissertation

Section 1.5 identified the unresolved issues that still limit rational design of PA TFC NF membranes for selective ion separations. The objectives below translate these open questions into four publication-linked research aims that structure the cumulative dissertation. Each objective corresponds to one publication-based section and responds directly to one knowledge gap or gap cluster identified in Section 1.5. The overarching objective of this dissertation is to relate IP design variables (monomer concentration and aqueous-phase monomer chemistry), together with electrolyte environment (common-ion effects), to selective ion transport for $Na^+/Mg^{2+}$ separation and nitrate removal. This relation is established through a mechanistically consistent interpretation in terms of coupled interfacial exclusion and in-pore transport, expressed by the effective descriptor set ($r_{pore}$, $\Delta x_e$, $c_X$, $\varepsilon_{pore}$).

In the Cumulative Part of the Dissertation (Chapter 3), Publication I addresses the fabrication-descriptor knowledge gap in the context of nitrate-selective NF. Its objective is to systematically vary IP monomer concentrations and determine how these fabrication changes translate into coupled shifts of the effective descriptor set and the corresponding balance between interfacial exclusion and in-pore transport contributions governing $NO_3^-$ rejection under representative mixed-electrolyte conditions. Publication II extends the same fabrication-linked logic to $Na^+/Mg^{2+}$ separation. Here, it is well established that increasing positive effective charge can improve $Na^+/Mg^{2+}$ selectivity, but how IP monomer concentrations co-tune the full descriptor set that governs this selectivity remains insufficiently resolved. Therefore, its objective is to resolve how IP monomer concentrations jointly tune the coupled descriptor set. It further clarifies how these coupled descriptor shifts redistribute both exclusion contributions and in-pore flux coupling in mixed-salt environments relevant to $Na^+/Mg^{2+}$ selectivity. Publication III addresses the monomer-chemistry knowledge gap, which remains when monomer identity is treated primarily through performance trends. Its objective is to isolate the mechanistic role of aqueous-phase monomer chemistry (AEP vs. DAP) for nitrate-selective NF. Selectivity shifts are attributed to coupled changes across the effective descriptor set, and then translated into changes in exclusion mechanisms together with in-pore transport contributions for $NO_3^-$ in mixed electrolytes. Publication IV targets the incomplete mechanistic integration of common-ion effects with membrane structure and charge. Its objective is to establish a unified interpretation of $Na^+/Mg^{2+}$ selectivity that connects monomer chemistry and monomer concentration to descriptor shifts and then to electrolyte-specific selectivity changes. This clarifies how common-anion identity (e.g., $Cl^-$ vs.

$SO_4^{2-}$) shifts the balance between Donnan and dielectric exclusion together with flux coupling under mixed-salt conditions.

Together, these objectives define the logic of the cumulative dissertation. The sequence is designed to be systematic. First, fabrication-driven descriptor mapping is established for $NO_3^-$. Then, it is extended to $Na^+/Mg^{2+}$ under charge-tuned conditions, then complemented by monomer-identity attribution for nitrate selectivity, and finally integrated with electrolyte identity and common-ion effects for $Na^+/Mg^{2+}$. This sequence turns the cumulative thesis into a single mechanistic argument: fabrication variables and electrolyte identity do not act on one isolated membrane property, but on a coupled descriptor combination that controls partitioning, transport, and selectivity.

At the chemistry level, the dissertation treats IP conditions and electrolyte identity as variables that set the morphological and physicochemical characteristics of the PA selective layer as expressed through effective descriptors rather than nominal structure. At the membrane-science level, it translates selective trends into condition-specific changes in descriptor values, interfacial partitioning, and transmembrane flux contributions.

Taken together, these objectives aim to strengthen the mechanistic link between IP design variables and selective ion transport in PA TFC NF membranes. This matters because $Na^+/Mg^{2+}$ separation and $NO_3^-$ rejection are both governed by coupled exclusion and in-pore transport under mixed-electrolyte conditions, where intuitive design rules often fail. A descriptor-based interpretation provides a common basis for comparing membranes prepared under different conditions and for distinguishing fabrication-driven shifts from solution-driven effects. In this way, this dissertation targets separation-relevant understanding needed to rationally position NF membranes for magnesium-focused separations, as well as for nitrate removal in drinking-water treatment. Accordingly, the Cumulative Part of the Dissertation is organized as four publications that progress from fabrication-driven descriptor shifts (Publications I–II), to monomer-chemistry-driven selectivity changes (Publication III), and finally to electrolyte-identity effects through common-anion comparison (Publication IV).

# 3

# Cumulative Part of the Dissertation

This chapter compiles the four first-author publications on which this cumulative dissertation is based. Each of the following sections begins with a brief synopsis, followed by the complete text of the corresponding publication.

## 3.1. Publication I: Mass transport mechanism of nitrate selective nanofiltration membranes on the basis of the Donnan steric pore model with dielectric exclusion (DSPM-DE)

This section establishes the dissertation's descriptor-based interpretation of nitrate-selective NF by using IP monomer concentration as a controlled fabrication variable and by interpreting single- and mixed-electrolyte behavior within the DSPM-DE interpretation framework. It sets the fabrication–descriptor–selectivity coupling that the next section extends to cation selectivity, while maintaining the same compact effective descriptor set and mechanistic framework.

Chemical Engineering Journal 493 (2024) 152775



Contents lists available at ScienceDirect

Chemical Engineering Journal

journal homepage: www.elsevier.com/locate/cej





# Mass transport mechanism of nitrate selective nanofiltration membranes on the basis of the Donnan steric pore model with dielectric exclusion (DSPM-DE)

Nicolás Cevallos-Cueva [a], Md. Mushfequr Rahman [a,*], Hluf Hailu Kinfu [a], Volker Abetz [a,b]

[a] Helmholtz-Zentrum Hereon, Institute of Membrane Research, Max-Planck-Straße 1, 21502 Geesthacht, Germany
[b] University of Hamburg, Institute of Physical Chemistry, Martin-Luther-King-Platz 6, 20146 Hamburg, Germany

ARTICLE INFO

*Keywords:*
Interfacial polymerization
Nanofiltration
Thin film composite membranes
Nitrate removal
Selective ion separation
DSPM-DE model

ABSTRACT

Nanofiltration (NF) membranes can play an important role to mitigate the nitrate pollution, emphasizing the necessity for understanding its mass transport mechanism to enhance water purification strategies. This study focuses on the nitrate separation capabilities of thin film composite NF membranes having a polyamide (PA) selective layer. The selective layer of the membranes was fabricated through interfacial polymerization, with varying piperazine (PIP) and trimesoyl chloride (TMC) monomer concentrations on porous polyacrylonitrile substrates. We studied their retention on aqueous solutions of PEG 200, single salts (NaCl, $NaNO_3$, $Na_2SO_4$), and mixed salts (NaCl + $NaNO_3$ and $NaNO_3$ + $Na_2SO_4$). Through a new fitting scheme, the Donnan Steric Pore Model with Dielectric Exclusion (DSPM-DE) was utilized to correlate the PIP and TMC concentrations with the ion transport and exclusion mechanisms responsible for the membranes' nitrate separation capabilities. The model could simulate the $Na^+/NO_3^-/SO_4^{2-}$ system but not $Na^+/NO_3^-/Cl^-$. Dielectric exclusion and diffusion were the dominant partitioning and transport mechanisms, respectively, explaining the high retentions of sulfate (96 to 99 %) and the negative retentions of nitrate (−24 to 11 %). This study sheds light on the potential of NF membranes having PA selective layers for efficient nitrate/sulfate separation, providing valuable insights into the underlying transport and exclusion mechanisms.

## 1. Introduction

Nitrate is touted as a major pollutant of increasing environmental concern since it has been associated with methemoglobinemia [1] and eutrophication of water bodies [2]. Its presence in surface and groundwater has increased due to the intensive application of fertilizers and pesticides [3], failing to comply with water quality standards. For instance, 27.1 % of measuring groundwater points in Germany have nitrate levels higher than the EU nitrate limit of 50 ppm [4]. Nitrate contamination of groundwater has been one of the major reasons for the reduction of drinking water quality during the last decades [5]. Therefore, the selective removal of nitrate is necessary for effective water remediation. Nanofiltration (NF) membranes are capable of selectively removing ions based on their size, charge, as well as diffusivity and solubility within the membrane [6]. Several studies have proven that there are commercial NF membranes which are successful in selectively removing nitrate [7–13]. The selective separation of nitrate from other ions in water is largely dictated by the physichochemical features of the NF membrane which are inherently dependent on the fabrication conditions [14]. Most commercial NF membranes are thin-film composite membranes (TFC) containing a polyamide (PA) based selective layer fabricated by interfacial polymerization (IP) on top of a microporous support layer [15]. Altering the IP reaction conditions can tailor the desired membrane characteristics, e.g. effective pore size [14]. Among these conditions, the monomer concentrations are key parameters determining the properties of the resulting TFC NF membranes [14,16–25]. However, there is a lack of comprehensive studies on the role of monomer concentrations in the preparation of TFC NF membranes for nitrate removal. It is crucial to understand how the concentrations of the monomers involved in the IP process correlate to the properties of the TFC NF membranes responsible for the selective nitrate separation capabilities. This would require a systematic study of mass transport modelling of a series of membranes prepared at varying monomer concentrations. A detailed understanding of the influence of membrane fabrication parameters on ion transport mechanisms reveals

* Corresponding author.
*E-mail address:* mushfequr.rahman@hereon.de (Md.M. Rahman).

https://doi.org/10.1016/j.cej.2024.152775
Received 12 April 2024; Received in revised form 21 May 2024; Accepted 1 June 2024
Available online 2 June 2024
1385-8947/© 2024 The Authors. Published by Elsevier B.V. This is an open access article under the CC BY license (http://creativecommons.org/licenses/by/4.0/).

**Nomenclature**

*Variable*

| | |
|---|---|
| $A$ | temperature dependent correction factor for the activity coefficient (−) |
| $A_{mb}$ | effective membrane area for filtration experiments ($m^2$) |
| $c_{i,1}$ | concentration of ion $i$ at the pore entrance on the feed side ($mol/m^3$) |
| $c_{i,f}$ | concentration of ion $i$ in the feed solution ($mol/m^3$) |
| $c_{i,N}$ | concentration of ion $i$ at the pore entrance on the permeate side ($mol/m^3$) |
| $c_{i,p}$ | concentration of ion $i$ in the permeate ($mol/m^3$) |
| $c_{i,m}$ | concentration of ion $i$ in the feed-solution/membrane interface ($mol/m^3$) |
| $c_{i,n}$ | concentration of ion $i$ in node $n$ ($mol/m^3$) |
| $c_{i,r}$ | concentration of ion $i$ in the retentate ($mol/m^3$) |
| $c_i$ | concentration of ion $i$ in the membrane active layer ($mol/m^3$) |
| $c_x$ | volumetric membrane charge density ($mol/m^3$) |
| $d_{H_2O}$ | thickness of a single layer of water molecules (m) |
| $D_{i,\infty}$ | diffusion coefficient of species $i$ in the bulk ($m^2/s$) |
| $e_0$ | electronic charge (1.602E-09 C/J) |
| $F$ | Faraday constant (96500 C/mol) |
| $J_{i,adv}$ | advective flux of species $i$ ($mol/m^2/s$) |
| $J_{i,diff}$ | diffusive flux of species $i$ ($mol/m^2/s$) |
| $J_{i,elect}$ | electromigrative flux of species $i$ ($mol/m^2/s$) |
| $J_i$ | molar flux of species $i$ ($mol/m^2/s$) |
| $J_v$ | solution flux (m/s) |
| $k_{c,i}$ | mass transfer coefficient of species $i$ in the bulk (m/s) |
| $k^{\bullet}_{c,i}$ | corrected mass transfer coefficient (m/s) |
| $K_{i,a}$ | hindrance factor of advection (−) |
| $K_{i,d}$ | hindrance factor of diffusion (−) |
| $k_B$ | Boltzmann constant (1.38066E-23 J/K) |
| $L$ | characteristic length of the stirrer (0.03 m) |
| $N_A$ | Avogadro number (6.023E23 $mol^{-1}$) |
| $N_c$ | number of ions in the system (−) |
| NF | nanofiltration (−) |
| PA | polyamide (−) |
| PAN | polyacrylonitrile (−) |
| $Pe_m$ | Peclet number (−) |
| PIP | piperazine (−) |
| $R$ | ideal gas constant (8.314 J/K/mol) |
| $R^{model}_{i,real}$ | theoretical retention of species $i$ at infinite stirring velocity (−) |
| $R^{exp}_{i,j}$ | experimental retention of ion $i$ (−) |
| $R^{mod}_{i,j}$ | modeled retention of ion $i$ (−) |
| $R_{i,obs}$ | observed or experimental retention of species $i$ (−) |
| $R_{i,real}$ | retention of species $i$ at infinite stirring velocity (−) |
| $r_{pore}$ | effective pore radius (m) |
| $r_i$ | stokes radius of species $i$ (m) |
| $Re$ | Reynolds number (−) |
| $S_{a/b}$ | selectivity (real) from mixed salt retention tests (−) |
| $S^*_{a/b}$ | selectivity (ideal) from single salt retention tests (−) |
| $Sc$ | Schmidt number (−) |
| $Sh$ | Sherwood number (−) |
| $T$ | temperature (K) |
| TFC | Thin film composite membrane (−) |
| TMC | trimesoyl chloride (−) |
| $x$ | direction across the membrane active layer from the feed towards the permeate side (m) |
| $z_i$ | valence of ion $i$ (−) |

*Greek*

| | |
|---|---|
| $\Delta\Psi_{D,f}$ | Donnan potential at the feed-solution/membrane interface (V) |
| $\Delta\Psi_{D,p}$ | Donnan potential at the permeate-solution/membrane interface (V) |
| $\Delta m$ | change of mass (g) |
| $\Delta t$ | ellapsed time (s) |
| $\Delta W_i$ | Born solvation energy barrier of ion $i$ (J) |
| $\Delta x_e$ | thickness-to-porosity ratio (effective membrane active layer thickness) (m) |
| $\delta x_n$ | distance between two consecutive nodes (m) |
| $\delta_{H_2O}$ | density of liquid water at room temperature ($g/m^3$) |
| $\gamma_{i,1}$ | activity coefficient of ion $i$ at the pore entrance on the feed side (−) |
| $\gamma_{i,m}$ | activity coefficient of ion $i$ in the feed-solution/membrane interface (−) |
| $\gamma_{i,N}$ | activity coefficient of ion $i$ at the pore entrance on the permeate side (−) |
| $\gamma_{i,p}$ | activity coefficient of ion $i$ in the permeate (−) |
| $\lambda_i$ | ratio of solute radius to pore radius (−) |
| $\omega$ | stirring speed ($s^{-1}$) |
| $\Phi^{x=0}_{D,i}$ | Donnan exclusion coefficient of ion $i$ at the pore entrance on the feed side (−) |
| $\Phi^{x=\Delta x_e}_{D,i}$ | Donnan exclusion coefficient of ion $i$ at the pore entrance on the permeate side (−) |
| $\Phi_{DE,i}$ | dielectric exclusion coefficients of ion $i$ (−) |
| $\Phi_{S,i}$ | steric exclusion coefficient of ion $i$ (−) |
| $\Psi$ | electrical potential inside the membrane active layer (V) |
| $\Psi_n$ | electrical potential in node $n$ (V) |
| $\Psi_f$ | electrical potential in feed solution (V) |
| $\Psi_p$ | electrical potential in permeate solution (V) |
| $\sigma^2_{i,j}$ | variance (−) |
| $\varepsilon_{bulk}$ | dielectric constant of water in the bulk (−) |
| $\varepsilon_{pore}$ | dielectric constant of water inside the pores (−) |
| $\varepsilon_0$ | permitivity of vacuum (8.854E-12 F/m) |
| $\varepsilon_r$ | dielectric constant of the medium (−) |
| $\varepsilon^*$ | dielectric constant of a single layer of water molecules next to the pore walls (−) |
| $\xi$ | electrical potential gradient at the feed-solution/membrane interface (V/m) |

the underlying features to enhance separation performance of the membranes.

The first attempt to describe solute transport through NF membranes was based on the thermodynamics of irreversible processes by considering the membrane as a black box [26]. Hence, the membrane's structural and electrical parameters could not be correlated to its filtration performance. Later, other models were derived based on the Extended Nernst Planck (ENP) equation [27,28]. Finally, Bowen and Welfoot [29] in 2002 combined the ENP equation with the equilibrium partitioning between the membrane and the adjacent solution, leading to the Donnan, Steric Pore Model with Dielectric Exclusion (DSPM-DE). The DSPM-DE model is a comprehensive mass transport model that describes the overall selective transport of species through a NF membrane by taking into account the structural parameters of the membrane as model input parameters. These parameters are the effective pore size, $r_{pore}$, thickness-to-porosity-ratio of the selective layer, $\Delta x_e$, the water dielectric constant inside the pore, $\varepsilon_{pore}$, and the membrane charge density, $c_x$. The determination of these parameters involves fitting experimental retention results. It is challenging to determine these

parameters by performing independent experiments [30]. For example, while streaming zeta potential measurement can be used to determine $c_x$, it does not represent the effective membrane charge density under the filtration conditions. Several studies dealing with the DSPM-DE model in NF membranes have reported a variation in the values of the membrane charge density and the dielectric constant inside the pore with the feed solution composition and concentration [31–36]. Generally, the PA layer in TFC NF membranes is negatively charged at neutral pH conditions because of the presence of carboxylic groups formed by hydrolysis of unreacted acid chloride groups from trimesoyl chloride (TMC) [23–25,37]. Notably, the interactions of these charged groups with the ions of the feed solution, such as ion adsorption and binding [31–33,36,38], and charge screening [34] have been held responsible for the membrane charge density difference. Regarding the dielectric constant, the degree of orientation of water molecules within the pores of the membrane explained the difference in $\varepsilon_{pore}$ values at different feed solution concentrations [33,34,38,39].

The selectivity of the NF membranes is determined by the rate at which different ions pass through them, which is described by the ion transport and the exclusion or partitioning mechanisms. In recent years considerable effort has been made to understand the underlying mechanism of selective nitrate transport by varying the operating conditions of nanofiltration. By varying the pH of the feed solution and using a charged (NF270) and an uncharged (CK) commercial NF membrane, Epsztein *et al.* [10] found that coupling Donnan with steric exclusion mechanisms enhances the difference in rejection between $Cl^-$ and $NO_3^-$. From the study of three commercial membranes (NF90, NF270, and XC-N) at different pH and temperature, Popova et al. [7] concluded that the selective permeation of $NO_3^-$ over $NO_2^-$ and $NH_4^+$ through stems from the energy barrier of diffusion and dehydration to enter the pores of the membrane. Santafé-Moros et al. [32] explored the applicability of DSPM-DE to model the nitrate selectivity of a commercial NF90 membrane using tertiary ion mixtures $Na^+/NO_3^-/SO_4^{2-}$ and $Na^+/NO_3^-/Cl^-$. Hence, so far the studies of ion transport mechanism have mostly been limited to commercially available membranes. They have focused on the operating parameters and modification of the commercial NF membranes to alter their nitrate separation performance. However, a gap exists in the literature regarding the impact of the monomer concentrations on the properties of membranes specifically designed for nitrate removal in the context of the DSPM-DE model. The DSPM-DE model describes the mechanism of– i) exclusion of the ions at the membrane surface owing to partitioning between the bulk solutions and the interface of the membrane and ii) transport of the ions through the pores of the membranes. To the authors' knowledge, there are no studies systematically correlating the intrinsic properties of the TFC NF membranes, attributed to the fabrication conditions, with the transport/exclusion mechanisms underlying nitrate removal. Not only nitrate but also the role of monomer concentration on the exclusion and transport mechanism of no other ionic system have been explored even for the most successfully used aqueous and organic phase monomer pairs to prepare TFC membranes for NF, *i.e.* piperazine (PIP) and trimesoyl chloride (TMC), respectively.

In this work, for the first time, the concentrations of PIP and TMC used for the preparation of the TFC membranes are correlated with the DSPM-DE model to provide valuable insights into their effects on the nitrate separation capabilities of the TFC membranes in terms of the exclusion or partitioning mechanisms and the ion transport. We fabricated ten NF membranes via IP with varying concentrations of PIP and TMC and characterized them to assess the influence of the monomer concentrations on the membranes' properties. We evaluated their performance with retention tests in aqueous solutions of PEG 200, single salts (NaCl, $NaNO_3$, $Na_2SO_4$), and mixed salts (NaCl + $NaNO_3$ and $NaNO_3$ + $Na_2SO_4$). Finally, we utilized the DSPM-DE model to explain the observed rejection results through the exclusion coefficients and the contributions to the transmembrane ionic molar fluxes. This sheds new light on the mechanisms of selective nitrate separation of the membranes as a function of the concentrations of PIP and TMC used in their synthesis. This approach enhances our understanding of the nitrate separation process and contributes to the development of more efficient NF membranes specifically tailored for nitrate separation.

## 2. Description of the DSPM-DE model

In NF membranes, the transmembrane pressure drives the transport of species from the feed side toward the permeate side. The DSPM-DE model assumes that the resistance against mass transport of the microporous support layer of a TFC membrane is negligible compared to that of the selective layer. The selective layer is solely responsible for the separation capabilities, and it is modeled as a porous structure with parallel cylindrical pores. Accordingly, the tortuosity and porosity of the selective layer cannot be separately computed; their values are grouped together in $\Delta x_e$. The transport of species through the membrane active layer is considered to take place only in one dimension at a steady state. The species are considered as hard spheres, characterized by their Stokes radius to measure their size. The membrane charge density is considered to be spatially constant. Electroneutrality condition is maintained inside the membrane and in the feed and permeate solution next to it [30]. First, there is an initial mass transport from the feed solution towards the feed solution/membrane interface; then, the species partition between the feed solution and the NF membrane, followed by the transport of species through the membrane active layer, and finally there is another partitioning of species between the membrane domain and the permeate side [29]. Due to the selectivity of the membrane, there is concentration polarization, *i.e.* an accumulation/depletion of species next to the feed solution/membrane interface. The concentration polarization is represented as a concentration gradient next to the interface across a boundary layer. The molar flux of each species $i$, $J_i$, in this boundary layer is given by [40]:

$$J_i = -k_{c,i}^{\bullet}\left(c_{i,m} - c_{i,f}\right) + J_v c_{i,m} - z_i c_{i,m} D_{i,\infty}\frac{F}{RT}\xi \tag{1}$$

where $c_{i,m}$ and $c_{i,f}$ are the concentration of ion $i$ in the feed-solution/membrane interface and concentration of ion $i$ in the feed solution, respectively; $z_i$ is the valence of ion $i$; $\xi$ is the electrical potential gradient at the feed-solution/membrane interface. Other constants or parameters are: the Faraday constant, $F$; the ideal gas constant, $R$; the temperature, $T$; the diffusion coefficient of species $i$ in the bulk, $D_{i,\infty}$. The corrected mass transport coefficient, $k_{c,i}^{\bullet}$, is computed by taking into account the solution flux, $J_v$, as follows:

$$k_{c,i}^{\bullet} = k_{c,i}\left(\frac{J_v}{k_{c,i}} + \left(1 + 0.26\left(\frac{J_v}{k_{c,i}}\right)^{1.4}\right)^{-1.7}\right) \tag{2}$$

The conventional mass transfer coefficient, $k_{c,i}$, is calculated through mass-transfer correlations:

$$Sh = 0.23Re^{0.567}Sc^{0.33} = \frac{k_{c,i}L}{D_{i,\infty}} \tag{3}$$

where $Sh$ is the Sherwood; $Re$ is the Reynolds, and $Sh$ is the Schmidt number. $L$ is the characteristic length of the stirrer.

The electroneutrality condition in the fluid phase next to the membrane phase is given by:

$$0 = \sum_{i=1}^{N_c} z_i c_{i,m} \tag{4}$$

The partitioning expression is [30]:

$$c_{i,1}\gamma_{i,1} = c_{i,m}\gamma_{i,m}\Phi_{S,i}\Phi_{D,i}^{x=0}\Phi_{DE,i} \tag{5}$$

where $c_{i,1}$ is the concentration of ion $i$ at the pore entrance on the feed

side; $\gamma_{i,1}$ and $\gamma_{i,m}$ are the activity coefficients of ion $i$ at the pore entrance on the feed side and in the feed-solution/membrane interface, respectively. For ion $i$, $\Phi_{S,i}$ is the steric exclusion coefficient, $\Phi_{DE,i}$ the dielectric exclusion coefficient, and $\Phi_{D,i}^{x=0}$ the Donnan exclusion coefficient at the pore entrance on the feed side.

Similarly, the equilibrium correlation at the interface between membrane active layer and the permeate side is given by:

$$c_{i,N}\gamma_{i,N} = c_{i,p}\gamma_{i,p}\Phi_{S,i}\Phi_{D,i}^{x=\Delta x_e}\Phi_{DE,i} \tag{6}$$

Activity coefficients of ion $i$, $\gamma_i$, account for the non-ideality of the solutions. They are calculated through Davies equation [41]:

$$\ln(\gamma_i) = -Az_i\left(\frac{\sqrt{I}}{1+\sqrt{I}} - 0.3I\right) \tag{7}$$

The ionic strength, $I$, and the temperature dependent correction factor for the activity coefficient, $A$, are given by:

$$I = 0.5\sum_{i=1}^{Nc} z_i^2 c_i \tag{8}$$

$$A = \frac{e_0^3\sqrt{N_A}}{\ln(10)4\pi\sqrt{2\varepsilon_0^3\varepsilon_r^3 k_B^3 T^3}} \tag{9}$$

where $e_0$ is the electronic charge, $N_A$ the Avogadro number, $\varepsilon_0$ the permittivity of vacuum, $\varepsilon_r$ dielectric constant of the medium, and $k_B$ the Boltzmann constant.

The steric partitioning coefficient accounts for the probability of an ion to enter the pore based on its size relative to the pore entrance (as shown in Fig. 1a):

$$\Phi_{S,i} = (1-\lambda_i)^2 \tag{10}$$

$$\lambda_i = \frac{r_i}{r_{pore}} \tag{11}$$

where $r_i$ is the Stokes radius of species $i$.

Donnan partitioning arises due to the electrostatic interactions between the solutes and the membrane fixed charges, which is displayed in Fig. 1. It depends on the Donnan potentials across the two solution-membrane interfaces, $\Delta\Psi_{D,f}$ and $\Delta\Psi_{D,p}$, which result from the difference in concentration of ions between membrane and the adjacent solutions. There are two Donnan partitions – i) at the feed solution-membrane interface and ii) the membrane-permeate solution interface.

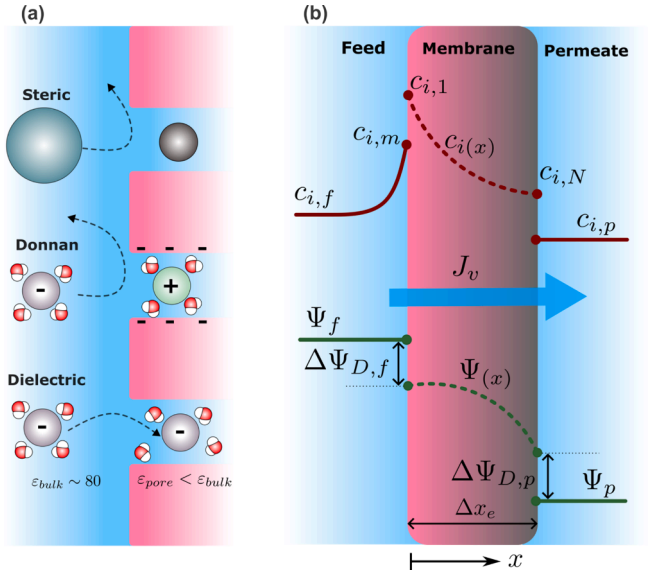



**Fig. 1.** Schematic representation of (a) exclusion mechanisms at pore openings of the membrane, *i.e.* steric (size-based separation), Donnan or electrostatic (charge-based separation), and dielectric (separation due to the energy barrier for the ion to shed its hydration shell and enter the pore). (b) Theoretical concentration and potential profile developed across the active layer of NF membranes giving rise to diffusive, electromigrative, and advective fluxes of species $i$.

$$\Phi_{D,i}^{x=0} = exp\left(\frac{-z_i F}{RT}\Delta\Psi_{D,f}\right) \tag{12}$$

$$\Phi_{D,i}^{x=\Delta x_e} = exp\left(\frac{-z_i F}{RT}\Delta\Psi_{D,p}\right) \tag{13}$$

The reduction of the dielectric constant of water inside nanopores results in an excess of solvation energy inside the pore (Fig. 1). This energy barrier, $\Delta W_i$, is computed through the Born formula with the values of the dielectric constant inside the pores, $\varepsilon_{pore}$, and in the bulk solution, $\varepsilon_{bulk}$:

$$\Delta W_i = \frac{z_i^2 e^2}{8\pi\varepsilon_0 r_i}\left(\frac{1}{\varepsilon_{pore}} - \frac{1}{\varepsilon_{bulk}}\right) \tag{14}$$

Based on the Born model, the dielectric exclusion coefficient is computed by:

$$\Phi_{D,i} = exp\left(\frac{-\Delta W_i}{k_B T}\right) \tag{15}$$

The transport of solutes through the pores of the selective layer is described by the Extended Nernst Plank (ENP) Equation:

$$J_i = -K_{i,d}D_{i,\infty}\frac{dc_i}{dx} - \frac{z_i F c_i K_{i,d} D_{i,\infty}}{RT}\frac{d\Psi}{dx} + K_{i,a}c_i J_v \tag{16}$$

where $K_{i,d}$ is the hindrance factor of diffusion; $c_i$ is the concentration of species $i$ in the membrane active layer; $x$ is the coordinate in the direction across the membrane active layer from the feed towards the permeate side; $\Psi$ is the electrical potential inside the membrane active layer; and $K_{i,a}$ is the hindrance factor of advection.

The total molar flux of each species $i$ is given by the sum of three contributions: diffusion (due to concentration gradient), electromigration (due to electrical potential gradient), and advection (solvent flow). Fig. 1b shows the transport of species through the active layer of the membrane along with the qualitative concentration and potential profiles.

In the absence of sweep flow, such as in a dead-end geometry, the total molar flux in steady state is also given by [42]:

$$J_i = J_v c_{i,p} \tag{17}$$

where $c_{i,p}$ is the concentration of ion $i$ in the permeate.

Due to the relative size of the solutes to the pore size, diffusive and advective hindrance factors are included in the ENP equation to account for the restricted or hindered transport of species through the membrane pores.

$$K_{i,a} = \frac{1 + 3.867\lambda_i - 1.907\lambda_i^2 - 0.834\lambda_i^3}{1 + 1.867\lambda_i - 0.741\lambda_i^2} \tag{18}$$

Calculation of the hindrance factor of diffusion, $K_{i,d}$, depends on the value of $\lambda_i$:

$$\lambda_i \le 0.95 : K_{i,d} = \frac{\left[\begin{array}{c} 1 + \frac{9}{8}\lambda_i\ln(\lambda_i) - 1.56034\lambda_i \\ +0.528155\lambda_i^2 + 1.91521\lambda_i^3 - 2.81903\lambda_i^4 \\ +0.270788\lambda_i^5 + 1.10115\lambda_i^6 - 0.435933\lambda_i^7 \end{array}\right]}{(1-\lambda_i)^2} \tag{19}$$

$$\lambda_i > 0.95 : K_{i,d} = 0.984\left(\frac{1-\lambda_i}{\lambda_i}\right)^{2.5} \quad (20)$$

Electroneutrality condition is maintained inside the membrane active layer between the fixed charges of the polymeric matrix and the ionic species:

$$-c_x = \sum_{i=1}^{N_c} z_i c_i \quad (21)$$

Likewise, on the permeate side electroneutrality is expressed by:

$$0 = \sum_{i=1}^{N_c} z_i c_{i,p} \quad (22)$$

The advective contribution to total molar flux is the transport of solutes caused by solvent flow due to the applied pressure gradient.

$$J_{i,adv} = K_{i,a} c_i J_v \quad (23)$$

The applied pressure gradient gives rise to a concentration gradient led by the selective properties of the membrane [43]. This concentration gradient of species in the membrane active layer is the driving force of diffusive flux, and is described by:

$$J_{i,diff} = -K_{i,d} D_{i,\infty} \frac{dc_i}{dx} \quad (24)$$

The electrical potential gradient generated in the membrane active layer due to the transport of charged species (under a simultaneous pressure and concentration gradient) through the charged polymeric matrix drives the electromigrative flux [44]:

$$J_{i,elec} = -\frac{z_i F c_i K_{i,d} D_{i,\infty}}{RT} \frac{d\Psi}{dx} \quad (25)$$

In order to solve the system of equations of the DSPM-DE model, the unknown physical characteristics of the membrane must be determined. This is explained in detail in the next sections.

## 3. Materials and methods

### 3.1. Materials

All chemicals were used without modification. Piperazine anhydrous (PIP) (>99 %), trimesoyl chloride (TMC) and *n*-heptane were purchased from Sigma-Aldrich Chemie GmbH (Germany). A microporous polyacrylonitrile (PAN) membrane prepared by nonsolvent induced phase separation at Helmholtz-Zentrum Hereon was used as support layer. Poly(ethylene glycol) (PEG) of average molecular weight 200 Da was purchased from VWR International GmbH (Germany). NaCl (>99.5 %), $Na_2SO_4$ (>99 %), $NaNO_3$ were purchased from Merck KGaA (Germany), Carl Roth Gmbh (Germany) and Honeywell Speciality Chemicals Seelze GmbH (Germany), respectively.

### 3.2. Fabrication of the polyamide NF membranes

IP was performed on a microporous polyacrylonitrile support for 90 s followed by a heat treatment in vacuum oven for at 60 °C for 30 min. Aqueous solutions containing five different concentrations of PIP (0.125, 0.25, 0.50, 0.75, 1.00 %w-w) and organic solutions two concentrations of TMC (0.15 and 0.30 %w-w) were used to prepare the PA layers of ten TFC membranes, respectively (details in supporting information). At least three membranes were fabricated under each IP reaction condition. The membranes are labeled PIPxTMCy, where x and y are %w-w concentration of PIP and TMC during the IP reaction.

### 3.3. Membrane morphology characterization

The membrane morphology analysis was conducted with scanning electron microscopy (SEM). SEM images were captured with a Merlin SEM (Zeiss, Jena, Germany) at accelerating voltages between 1.5 and 3 keV using an InLens secondary electron detector. Before imaging, the samples were dried under vacuum at 60° C for at least 72 h and coated with 1–1.5 nm platinum using a CCU-010 coating device (Safematic, Zizers, Switzerland). The cross-fractured specimens were prepared in liquid nitrogen.

The topography data of the membrane surfaces were obtained by an Atomic Force Microscopy MultiMode 8 instrument from Bruker, USA, in Tapping mode. Typical scan areas were 3 μm x 3 μm. RTESPA-150 probes (tip radius ≈ 8 nm, spring constant ≈ 5 N/m) were applied for these measurements. Roughness values Rq and Ra were calculated with the program NanoScope Analysis 1.9. Rq, also called RMS roughness, is the root mean square average of height deviations taken from the mean image data plane.

Further morphology analysis was carried out with Transmission Electron Microscopy (TEM). The membrane samples were prepared for TEM imaging by embedding them in an epoxy resin (EPO-TEK 301). The embedded samples were then cured at room temperature for 3 days. Thin sections of the membrane's cross-section, approximately 30 nm thick, were prepared using an Ultracut UCT ultramicrotome (Leica Microsystems GmbH) equipped with a diamond knive (Diatome Ltd). The TEM measurements were performed using a TecnaiTM G2 F20 (FEI Thermo Fisher Scientific) operating in bright field mode at an acceleration voltage of 120 kV. The microscope is equipped with a OneView camera (Gatan, Inc.) for imaging.

### 3.4. Membrane performance evaluation

Retention and pure water permeance determination experiments were carried out in a stirred cell (stirrer length of 3 cm) from Millipore (EMD Millipore XFUF07601) with a reduced effective membrane area of 1.77 $cm^2$ in a dead-end filtration mode (details provided in supporting information). All retention experiments were conducted at 300 rpm to minimize the effects of concentration polarization. Each measurement was repeated at least three times to ensure reproducibility. The retention of PEG 200 and ionic species, $R_{i,obs}$, was computed by considering the average concentration of feed solution and retentate solution with the formula:

$$R_{i,obs} = 1 - \frac{2c_{i,p}}{c_{i,f} + c_{i,r}} \quad (26)$$

The ideal selectivity, $S^*_{a/b}$, from single salt retention tests and the selectivity, $S_{a/b}$, from mixed salt retention test were computed with the following equation:

$$S^*_{a/b} \text{ or } S_{a/b} = \frac{1 - R_{a,obs}}{1 - R_{b,obs}} \quad (27)$$

### 3.5. Determination of the input parameters of the DSPM-DE model

The four membrane property parameters that needed to be determined to serve as input parameters to solve the DSPM-DE model are $r_{pore}$, $\Delta x_e$, $\varepsilon_{pore}$ and $c_x$ [30]. $r_{pore}$ and $\Delta x_e$ were obtained by fitting PEG 200 retention test results, while $\epsilon_{pore}$ and $c_x$ by fitting mixed salt retention results. The details of fitting is provided in the supporting information. The objective functions presented were minimized with a dual annealing algorithm in Python, from the SciPy library [45]. Dual annealing is a global optimization function with the option to set a gradient-free local search that simultaneously minimizes the considered input parameters. The convergence criterion is the tolerance, which was fixed to $10^{-6}$, and Nelder-Mead was used as local optimizer.

### 3.6. Determination of exclusion coefficients and molar fluxes of ions using the DSPM-DE model

Once these input parameters of the model were obtained, the system of equations was solved to simulate the mass transport through the membrane active layer. In this regard, Gerades et al. developed a computer program to simulate this phenomenon through charged NF membranes [41]. It is based on the discretization of the ENP equations (finite-difference scheme) and the linearized form not only of the discretized equations but also of the other equations of the model. The set of discretized and/or linear equations obtained to solve the system of differential equations is described in the supporting information. The set of linear equations was solved iteratively in Python via Linear Algebra Package (LAPACK) provided by NumPy library. In each iteration, the linear coefficients are updated and the system of linear equations is solved again until the residuals are smaller than $10^{-4}$. As a result, the concentration and potential profiles across the active layers of the membranes were determined. Consequently, this allowed the computation of different contributions to partitioning and overall molar fluxes according to the DSPM-DE model.

The steric, Donnan, and dielectric exclusion coefficients were computed with Eqs. (10), (12), (14) and (15). The overall exclusion coefficient was computed as the product of the three coefficients. It is worth mentioning that the Donnan exclusion coefficient has one value on the feed side and another on the permeate side as shown in Eqs. (12) and (13). Only the coefficient in the feed side is reported in this paper.

The contributions of advection, diffusion and electromigration to molar flux across the membrane active layer were determined with the discretized forms of Eq. (16) (supporting information). The concentration and potential profiles were considered linear for qualitative comparison and analysis. The flowchart presented in Fig. 2 summarizes the method used to obtain the exclusion coefficients and the transmembrane molar fluxes.

## 4. Results and discussion

### 4.1. Membrane morphology

SEM micrographs of the top surface and cross-section of the pristine PAN support and the fabricated TFC membranes are presented in Fig. 3. From the SEM micrographs and the FTIR spectra (provided in supporting information) of the TFC membranes, it is evident that interfacial polymerization of PIP and TMC at all concentration led to the formation of a thin polyamide (PA) layer on top of the pristine PAN support. The PA layers consist of nanoscale heterogenous granular features. Formation of such heterogenous surface features is common for membranes containing a PA layer prepared by interfacial polymerization of PIP and TMC on top of a microporous support [46]. The dry state thickness of the PA layers of the TFC membranes are determined from the cross-section SEM images. The average thickness of the polyamide layers varies between 20 – 60 nm. The inhomogeneities of the PA layers add uncertainty to the values of the average thickness observed via the SEM. The average thickness of the PA layers increased more than two-fold for an 8-fold increase of PIP concentration (*i.e.* from 0.125 %w-w to 1 %w-w) for the membranes prepared at both TMC concentrations 0.15 and 0.3 %w-w, respectively. Hence, in spite of the uncertainty involved in the determination of the thickness via SEM, it is obvious that the increase of PIP concentration led to an increase in the PA layer thickness. However, there is no significant increase in the thickness of the PA layers owing to the increase of TMC concentration from TMC concentration from TMC 0.15 %w-w to 0.3 %w-w.

The thickness and morphology of the PA layers are influenced by several factors related to the kinetics of polymerization. At the initial stage of polymerization, a discontinuous PA layer forms at the reaction zone. It is well established that owing to the limited solubility of acid chloride in the aqueous phase and better solubility of diamines in the organic phase the reaction zone of interfacial polymerization forms in the organic phase near the interphase [46,47]. The growth of the PA layer is often assumed to proceed via a two-step procedure. At the initial stage of the polymerization, discrete low molecular, highly branched polyamides form at the reaction zone. Owing to the limited solubility of the branched polyamide, it is assumed that the first few seconds of rapid polymerization lead to the formation of colloidal particles containing surface functional groups [48]. The second stage involves the cross-linking of these colloidal particles and a thus huge increase of the molecular weight of the PA. The scale of heterogeneity of the final PA layer is influenced by the size and structure of the aggregating colloidal particles [48]. As the diamine reacts at an extremely fast rate with acid chlorides, the growth of the polyamide layer is limited by the diffusion of the monomers. At the initial stage, the polymerization is largely influenced by the diffusion of the monomers from the bulk towards the reaction zone [48]. At this stage the diffusion of PIP and TMC towards the reaction zone increases with concentration. The growth kinetics slows down abruptly once the incipient PA layer forms at the reaction zone [47,49]. That is because the growth of the incipient PA layer hinders the diffusion of monomers towards the reaction zone. Most of the models of interfacial polymerization assume that the diffusion of TMC through the incipient layer stops at an earlier stage compared to that of PIP (schematically represented in Fig. 3l). Owing to the high polarity difference of acidic TMC with the PA layer, it is assumed that TMC does not diffuse through the layer [47,49]. At this stage, the diffusion of PIP through the PA layer becomes the limiting factor for the growth of the PA layer. As PIP diffuses through the PA layer, it immediately reacts with TMC. A major implication of this assumption is that the PA film thickness is dependent only on the concentration of PIP (as diffusion of PIP through the PA layer is dependent on its concentration) and is independent of the TMC concentration. Hence, the SEM images (Fig. 3a–k) of the prepared TFC membranes show the validity of this assumption. If the interfacial polymerization is allowed to proceed for sufficient time, eventually self-termination will occur due to a growing resistance of the PA layer against diffusion of diamines. It is worth mentioning that hydrolysis of TMC may also act as a competing reaction and influence the termination of the polymerization. Recently, Yang [50] studied the growth of a PA layer on a microporous polysulfone support owing to the reaction between PIP and TMC using *in situ* FTIR spectroscopy. It was found that on unmodified polysulfone support after the first 50 s the growth of PA layer slows down but proceeds at a slower rate at least up to 300 s (the maximum duration of the study). The theoretical studies of Freger *et al.*[47] suggested that the PA layer growth slows down abruptly after the first 30 s while diffusion limited growth of PA layer proceeds at least up to 200 s. As in our study the interfacial polymerization was stopped after 90 s by adding 150 ml of *n*-heptane (details of fabrication are provided in the supporting information), it is logical to state that the polymerization was terminated while the diffusion-limited growth of the PA layer was still going on. As the diffusion of PIP is proportional to its concentration, we see an increase in the PA layer thickness with the concentration of PIP.

The origin of these nanoscale granular features remains a topic of debate [14]. So far, there are two possible explanations. First, the heat rate of interfacial reaction leads to an increase of temperature locally. This results in convection of monomers leading to interfacial instabilities. Second, the granular features are related to formation of $CO_2$ during the interfacial reaction. The heat of reaction from the IP triggers the release of $CO_2$ and other gases with low solubility. These gases are confined between the microporous support and the incipient layer forming nanovoids or hollow protuberances. The release of a greater amount of $CO_2$ contributes to an increase in the size of the granular features of the resulting PA layer, thereby increasing its roughness [14]. From the present study, we cannot confirm either of these phenomena. But it is evident that a stronger driving force of monomer diffusion (due to higher monomer concentration) in the reaction zone not only increases the thickness (Fig. 3) but also the roughness (Fig. 4k) of the PA

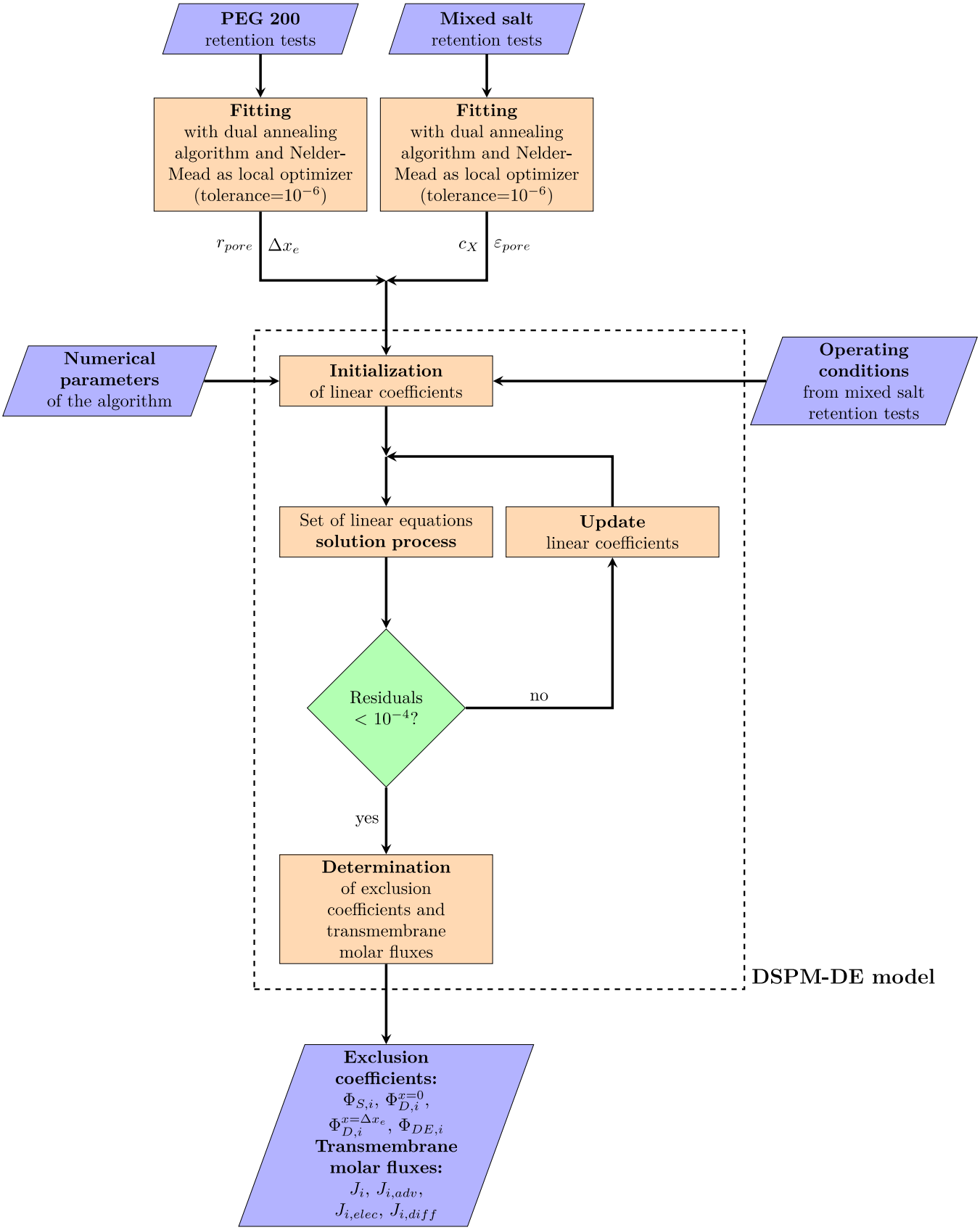



**Fig. 2.** Flowchart describing the application of the DSPM-DE model to simulate the mixed salt retention tests to elucidate the separation capabilities of the fabricated membranes in terms of the exclusion mechanisms and the transmembrane molar fluxes. The details of the fitting procedures and the set of linear and discretized equations of the model are provided in the supporting information.

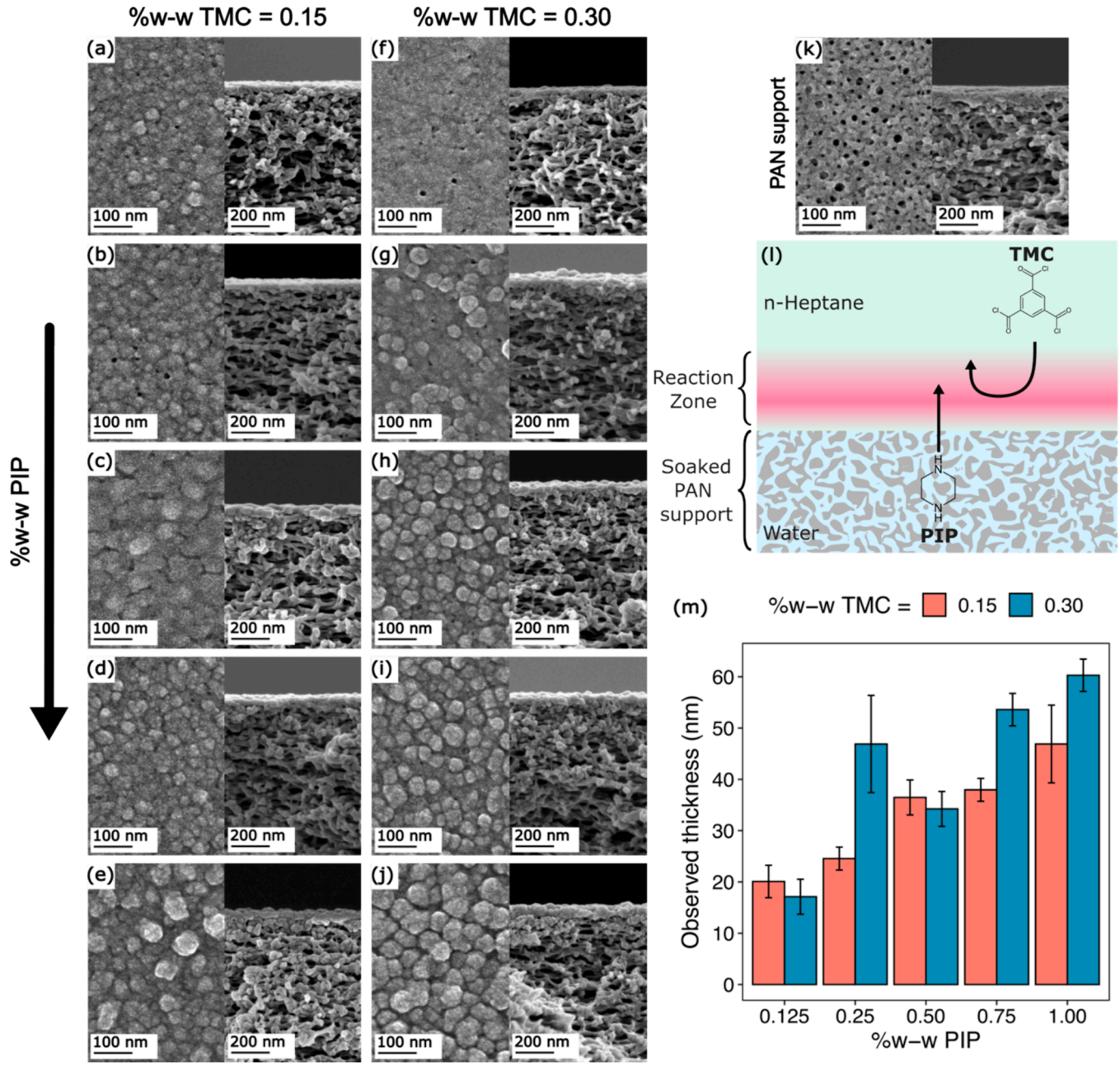



**Fig. 3.** Top-surface (left) and cross-sectional (right) SEM micrographs of the PAN support (k), and fabricated membranes at different PIP and TMC concentrations: % w-w PIP: 0.125 (a, f), 0.25 (b, g), 0.50 (c, h), 0.75(d, i) and 1.00 (e, j). (l) Schematic representation of the PIP and TMC diffusion towards the reaction zone in the organic phase; TMC is assumed to not diffuse through the PA incipient layer. (m) Observed thickness of the PA active layers of the fabricated membranes from cross-section SEM images; the error bars represent the standard deviation.

layer.

### 4.2. *Effective pore size and thickness-to-porosity ratio*

Compared to charged species, the permeation of neutral molecules is easier to correlate with the structural features of membranes as the latter is necessarily dictated only by size sieving. Fig. 5a shows the retentions of neutral molecule PEG 200 by the TFC membranes at transmembrane pressures in the range 0.5 – 4 bar. Fig. 5b and c depict the influence of PIP and TMC concentration on $r_{pore}$ and $\Delta x_e$ (obtained by fitting the PEG 200 retention data) of the fabricated membranes, respectively. Overall, for the 5 membranes prepared using a TMC concentration of 0.15 %w-w the values of $r_{pore}$ vary only in the range 0.65 – 0.7 nm. Comparatively, larger variation of $r_{pore}$ (between 0.6 – 0.7 nm) is observed for the membranes prepared at a TMC concentration of 0.30 %w-w. At a PIP concentration of 0.125 %w-w, no significant change of $r_{pore}$ and $\Delta x_e$ are observed between the membranes prepared using TMC concentrations of 0.15 % w-w and 0.3 % w-w. A distinct difference of $r_{pore}$ and $\Delta x_e$ is observed for the two TMC concentrations for higher PIP concentrations. Both $r_{pore}$ and $\Delta x_e$ values are lower for the membranes prepared using 0.3 % w-w TMC compared to those using 0.15 % w-w. $\Delta x_e$ can be termed as a measure of the resistance of the membrane against mass transport. The PIP0.5TMC0.3 membrane has the lowest $r_{pore}$ and $\Delta x_e$ among the 10 membranes. It means although PIP0.5TMC0.3 has the smallest pores, it has the lowest resistance against mass transport among the 10 membranes. While the SEM image shows no significant difference between the thickness of the PIP0.5TMC0.3 and PIP0.5TMC0.15, the obtained values of $\Delta x_e$ are significantly different for the two membranes. This

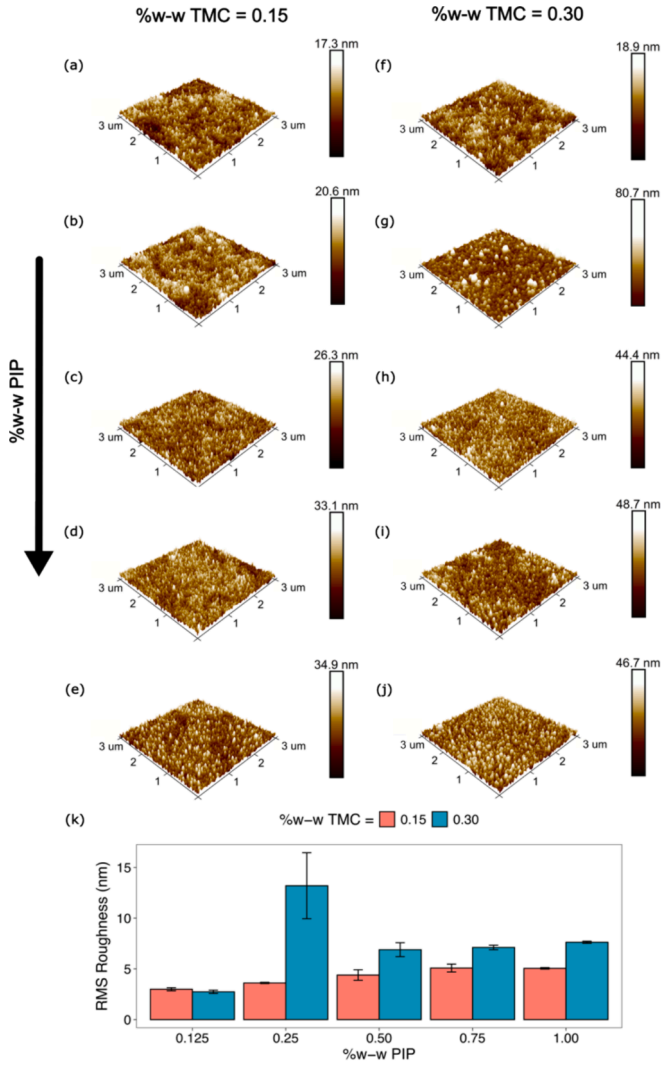



**Fig. 4.** AFM surface images of the PA layers of the fabricated membranes at different PIP and TMC concentrations: %w-w PIP: 0.125 (a, f), 0.25 (b, g), 0.50 (c, h), 0.75(d, i) and 1.00 (e, j). (k) RMS roughness obtained from AFM analysis for the fabricated membranes.

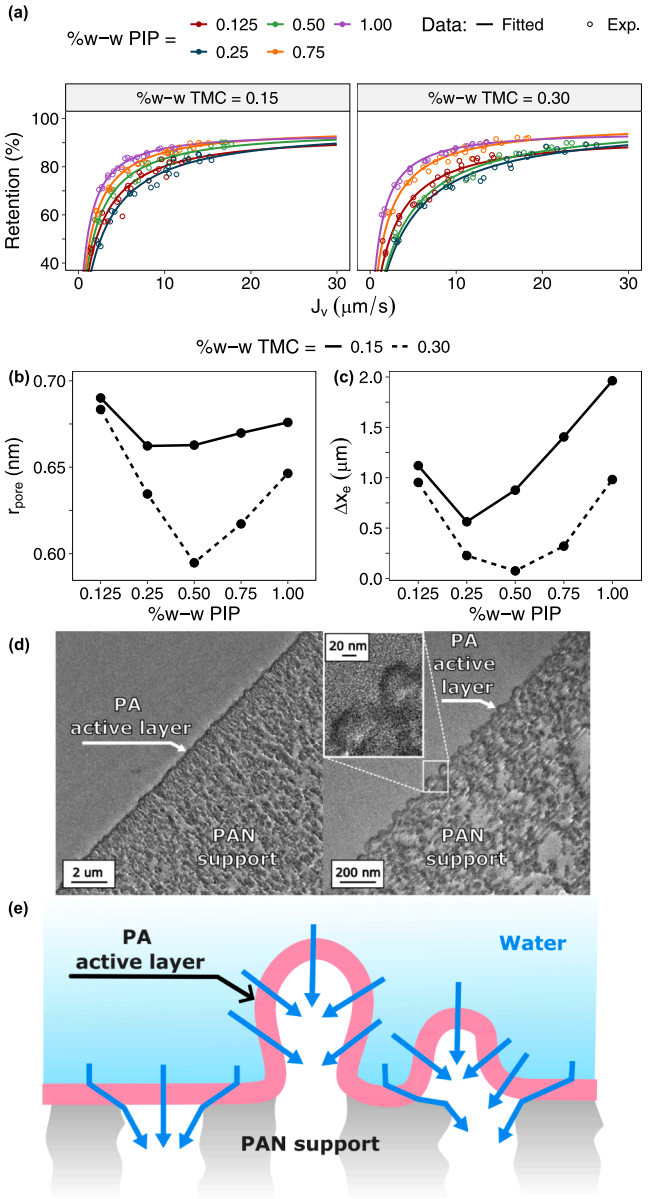



**Fig. 5.** (a) Retention tests fitted vs. experimental results for PEG 200, conducted with a 500 ppm feed solution concentration, to obtain (b) $r_{pore}$ and (c) $\Delta x_e$ for the fabricated membrane. (d) Cross-sectional TEM images of the PIP1TMC0.30 membrane, as a representative example highlighting the observed heterogeneity in the thickness of the PA active layers. (e) Schematic representation of the funnel effect, depicting the paths water molecules follow to enter the pores and permeate through them.

observation is not surprising as the values of $\Delta x_e$ are strongly influenced by the porosity and tortuosity which are not discernible in the cross-section SEM images of the PA layers. Owing to the extreme thinness of the PA layer, it is difficult to distinguish internal features of the PA layers containing nanoscale roughness via SEM. Fig. 5d shows the TEM images of the cross-section of the polyamide layer and the PAN support in its close vicinity. At lower magnification the PA layer appears rather as a rough top layer of the membrane. The TEM images of higher magnification prove the presence of nanoscale heterogeneities in the polyamide layer which is schematically represented in Fig. 5e. While the values obtained from SEM represent the apparent average thickness, it is obvious that locally the thickness of PA layers varies significantly owing to the heterogeneity which has an impact on the local mass transport. Moreover, the resistance of the TFC membranes against mass transport is influenced by a phenomenon called "funnel effect" (schematically represented in Fig. 5e). This phenomenon implies the permeating substances can reach the pores of the substrate easily through the parts of the PA layer just above the pores of the substrate while a much longer path length is required to permeate through the regions of the PA layer away from the substrate pores [51,52]. Underneath the surface of the heterogeneous PA layers, there are regions with nanovoids that reduce the influence of the "funnel effect" by facilitating easier passage of permeating substances to reach the pores of the substrate layer [46,51,52]. Therefore, the TFC membranes having PA layers consist of localized regions where permeance is significantly higher than the neighboring regions. Such uneven distribution of mass transport through the PA selective layer is averaged out in the value of $\Delta x_e$. Although the apparent thickness of the PA layer observed in the SEM images does not seem to be significantly different for the membranes prepared using 0.15 % w-w and 0.3 % w-w TMC, both the size sieving ability and the resistance of the PA layer against mass transport are significantly influenced by the TMC concentration. As explained earlier, the TMC concentration definitely has a strong influence on the kinetics of the diffusion-limited polymerization at the very early stage during the formation of the discontinuous PA layer, *i.e.* the colloidal particles. It is often hypothesized that the separation performance of the PA layer is

largely determined within the first few seconds of interfacial polymerization. This hypothesis is supported by the fact that for PIP concentrations of 0.25 – 1 % w-w, the membranes prepared using lower TMC concentration, *i.e.* 0.15 % w-w, consist of higher $r_{pore}$ and $\Delta x_e$ compared to those prepared using 0.3 % w-w.

### 4.3. Retention of single salts and the corresponding ideal nitrate selectivities

Single salt retention of NaCl, $NaNO_3$, and $Na_2SO_4$ by the membranes from their corresponding aqueous solutions were investigated, respectively (Fig. 6). In addition to $r_{pore}$ and $\Delta x_e$, the retention of ions are dictated by the charge of the membranes. Streaming zeta potential was performed to investigate the surface charge of the membrane. As expected, owing to the PA layer, the surface of the prepared membranes has a negative charge (supporting information). Due to the electrostatic repulsion, the membranes show significantly higher retention of divalent $SO_4^{2-}$ compared to the monovalent $NO_3^-$ and $Cl^-$, respectively. The permeate fluxes vary in accordance with the $\Delta x_e$ values (Fig. 5). More permeable membranes are associated with smaller $\Delta x_e$ values.

$Cl^-$ rejection is larger than that of $NO_3^-$ for all membranes tested, reaching the largest difference in PIP0.125 membranes for both TMC concentrations. As a result, $S^*_{NO_3^-/Cl^-}$ is larger than 1 for all the membranes (Fig. 6b). $Cl^-$ has a lower ionic volume than $NO_3^-$; therefore, it has a larger hydration energy than $NO_3^-$ (−340 vs. −300 kJ/mol [53]). Consequently, $Cl^-$ experiences a larger energy barrier of dehydration than $NO_3^-$ which contributes to its higher retention. In addition, the lower ionic volume of $Cl^-$ is associated with a larger ionic density, which makes it more electrostatically rejected by negatively charged membranes [10]. For both TMC concentrations, $Cl^-$ retention reaches a minimum for the PIP concentration 0.5 w-w%. Considering the trend of change of $r_{pore}$ for the prepared membranes, it appears that larger-pore-sized membranes achieve larger rejections, which is counterintuitive from an only steric exclusion point of view. Therefore, there is an interplay of other membrane characteristics, such as the thickness of the membrane active layer, the charge of the membrane, etc. Thicker membranes render less diffusive fluxes, decreasing the overall permeation of the species while increasing their retention. For example, the PIP0.5TMC0.3 membrane has the smallest $\Delta x_e$ (Fig. 5b) which is reflected in the largest value of permeate flux among all membranes tested. It presents the smallest retention and selectivity although it has the smallest $r_{pore}$. This means that $\Delta x_e$ plays an important role in elucidating the effect of the membrane's physical characteristics on $Cl^-/NO_3^-$ separation. The $S^*_{NO_3^-/Cl^-}$ values of the membranes are only slightly different from each other, *i.e.* in the range 1.0—1.2. As $SO_4^{2-}$ is almost completely rejected by the membranes, the $S^*_{NO_3^-/SO_4^{2-}}$ values are very large. A comparison of the $S^*_{NO_3^-/SO_4^{2-}}$ values and the corresponding fluxes suggests that the membranes do not completely follow the permeability selectivity trade-off relationship. For example, the $S^*_{NO_3^-/SO_4^{2-}}$ of PIP1.0TMC0.3 is more than twice that of PIP0.125TMC0.3, although the flux through PIP1.0TMC0.3 is significantly higher. The $\Delta x_e$ values of these two membranes are almost equal. Hence, it is evident that the $NO_3^-$ selectivities of the membranes are not dictated solely by $\Delta x_e$.

### 4.4. Retention of mixed salts and the corresponding real nitrate selectivities

Retention of ions from feed solutions containing two ternary ionic mixtures comprised of – i) $Na^+/NO_3^-/Cl^-$ (*i.e.* mixture of NaCl + $NaNO_3$) and ii) $Na^+/NO_3^-/SO_4^{2-}$ (*i.e.* mixture of $Na_2SO_4$ + $NaNO_3$) were investigated. The feed solutions contained mixtures of equimolar anions and the corresponding cations. For the ternary ionic mixtures $Na^+/NO_3^-/Cl^-$ the retention of $Na^+$ by the membranes are lower compared to those of $NO_3^-$ & $Cl^-$ (Fig. 7a). A different scenario is observed when the membranes contain the ternary ionic mixture $Na^+/NO_3^-/SO_4^{2-}$ (Fig. 7b). In this case, $NO_3^-$ has lowest retention among the three ions for

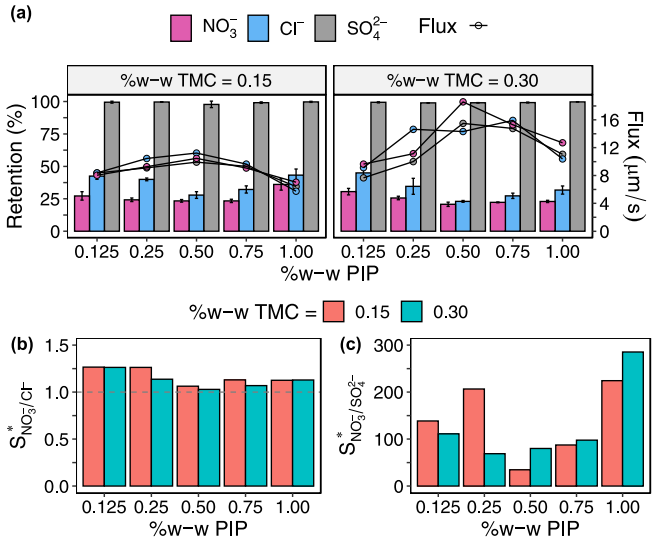



**Fig. 6.** (a) Single salt retention results (anion retention and permeate flux) as a function of the PIP and TMC monomer concentrations with feed solution concentration of 200 ppm. Owing to electroneutrality the cation retentions are similar like the anion retentions in case of single salts. Ideal selectivities of ion pairs – (b) $NO_3^-/Cl^-$ (c) $NO_3^-/SO_4^{2-}$.

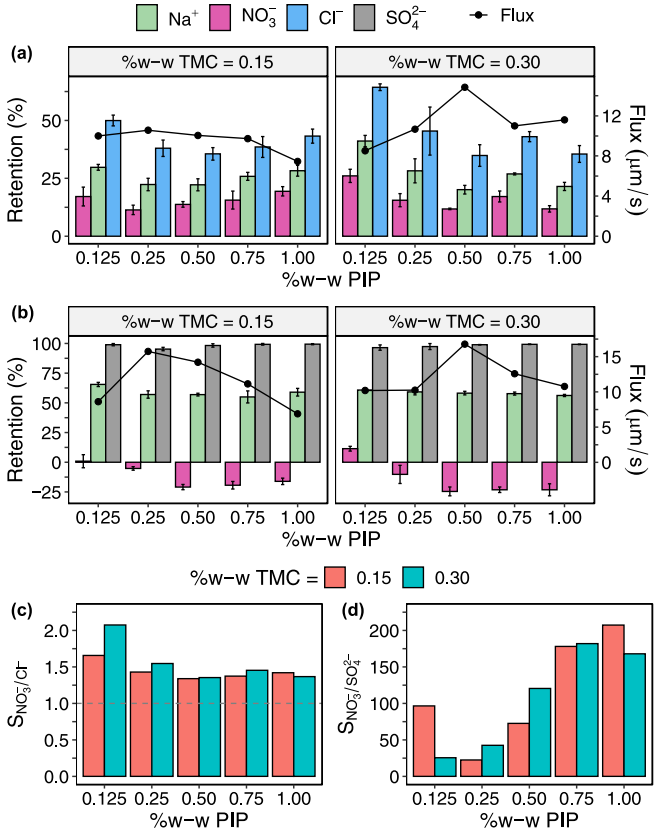



**Fig. 7.** Retentions of ions and permeate fluxes as a function of monomer concentration with feed solution concentration of 200 ppm – (a) $Na^+/NO_3^-/Cl^-$ ternary ion mixtures (*i.e.* mixture of NaCl + $NaNO_3$) (b) $Na^+/NO_3^-/SO_4^{2-}$ ternary ion mixture (*i.e.* mixture of $Na_2SO_4$ + $NaNO_3$). Real selectivity of the ion pairs – (c) $NO_3^-/Cl^-$ (d) $NO_3^-/SO_4^{2-}$.

all ten TFC membranes. In fact, apart from PIP0.125TMC0.15 and PIP0.125TMC0.3, the other membranes show a negative retention of $NO_3^-$ ions. It means for these membranes the permeate solutions have a higher concentration of $NO_3^-$ ions compared to the feed solutions. A careful comparison of Fig. 6 and Fig. 7a shows that the retentions of $NO_3^-$ & $Cl^-$ are larger when the feed solution contains a mixture of NaCl & $NaNO_3$ compared to those for the feed solutions containing the corresponding single salts. The $S_{NO_3^-/Cl^-}$ are slightly higher than the $S^*_{NO_3^-/Cl^-}$ for all the prepared membranes because of the effect of $Na^+$ as a common cation. As $Na^+$ permeates through the negatively charged membranes, it also attracts the anions to permeate through the membranes to maintain electroneutrality. As the permeation of $NO_3^-$ through the membranes is relatively easier through the membranes, $NO_3^-$ permeates through the membrane more than $Cl^-$, driven by $Na^+$ transport to maintain electroneutrality on both sides of the membrane [35,54]. The same phenomenon occurs also in the $Na^+/NO_3^-/SO_4^{2-}$ ternary system. But as $SO_4^{2-}$ is almost completely rejected by the membranes, the electroneutrality is maintained merely owing to the permeation of $NO_3^-$. It forced the filtration system to adopt a negative retention value for all the membranes except PIP0.125TMC0.15 and PIP0.125TMC0.3. These two membranes have larger $r_{pore}$ compared to the other 8 membranes. In general, $S_{NO_3^-/SO_4^{2-}}$ increased with PIP concentration. An interesting observation is PIP0.125TMC0.3 has the lowest $S_{NO_3^-/SO_4^{2-}}$, but the highest $S_{NO_3^-/Cl^-}$ among the ten membranes.

### 4.5. Pore dielectric constant and charge density of the membranes

In 2009 Deon et al. [38] reported the sensibility of $\varepsilon_{pore}$ and $c_x$ to the feed solution composition. They showed that only fitting a mixed salt retention curve allows the unambiguous determination of $\varepsilon_{pore}$ and $c_x$. In contrast, infinite couples of $\varepsilon_{pore}$ and $c_x$ are obtained by fitting single salt retention curves. Because of this, the values of the $\varepsilon_{pore}$ and $c_x$ couple are unique for each mixed salt solution composition. Under this concept, the values of the input parameters are assumed to qualitatively represent the structural parameters of the membrane. They are suitable for comparison among membranes prepared under different conditions to elucidate their effect on selectively removing $NO_3^-$. The impact of the ternary ionic mixtures $Na^+/NO_3^-/Cl^-$ and $Na^+/NO_3^-/SO_4^{2-}$ on $\varepsilon_{pore}$ and $c_x$ of the prepared membranes are depicted in Fig. 8. The following equation is used to determine of $\varepsilon_{pore}$ to take into account its variation with $r_{pore}$.

$$\varepsilon_{pore} = \varepsilon^* + (\varepsilon_{bulk} - \varepsilon^*)\left(1 - \frac{d_{H_2O}}{r_{pore}}\right)^2 \tag{28}$$

As schematically represented in Fig. 8a, it implies that the reduction of $\varepsilon_{pore}$ is caused only by a single molecule of water bound at the pore wall while the dielectric constant at the center of the pore remains unaffected [30]. The dielectric constant of the single layer of water molecules adjacent to the pore wall, $\varepsilon^*$, is determined by the membrane material. In principle, this relationship encapsulates the influence of both membrane material and pore size on the value of $\varepsilon_{pore}$. However, there is no experimental method to determine $\varepsilon^*$. To estimate the $\varepsilon_{pore}$ using this equation, often an arbitrary value is taken for $\varepsilon^*$ [29]. In this work, instead of using an arbitrary value of $\varepsilon^*$, we have used a minimization function to determine $\varepsilon^*$. A series of $\varepsilon^*$ values were tested to find preliminary minimized values of $c_x$ for each PIP concentration. Then, the optimized value was found by minimizing the following objective function.

$$f_{min} = \underset{\varepsilon^*}{\text{argmin}} \sum_{j=1}^{N_{PIP}} \left( \underset{c_x}{\text{argmin}} \sum_{i=1}^{N_{ions}} \frac{\left(R_{i,j}^{mod} - R_{i,j}^{exp}\right)^2}{\sigma_{i,j}^2} \right) \tag{29}$$

For the membranes prepared using a TMC concentration 0.15 and 0.3 w-

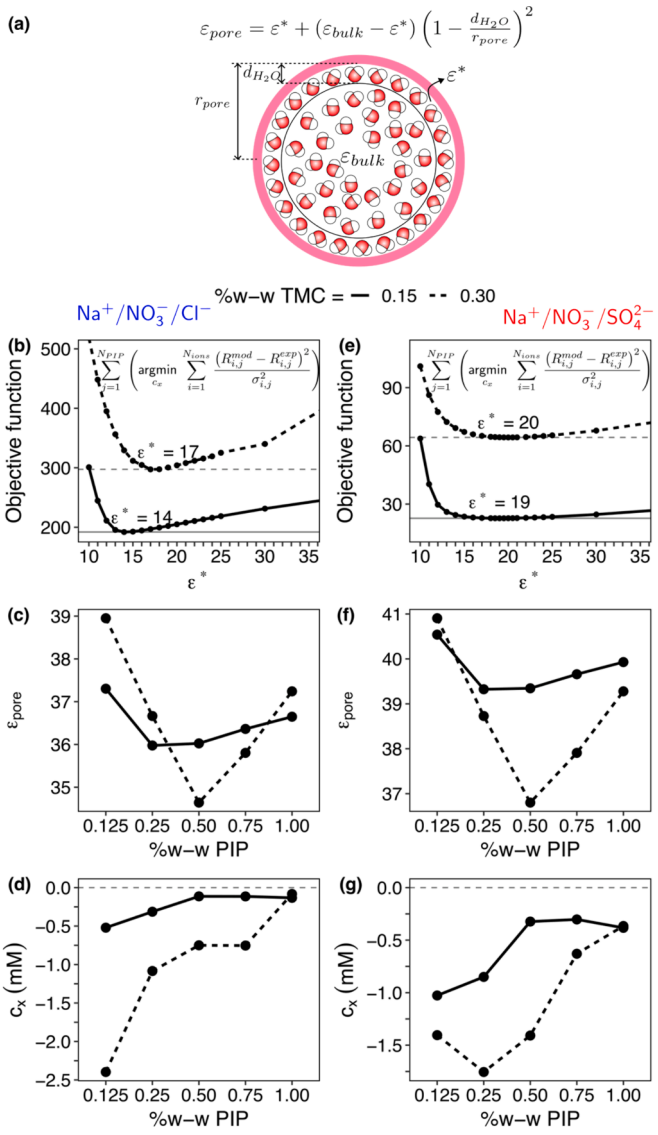



**Fig. 8.** (a) Schematic representation of the single layer of water molecules adjacent to the pore wall with restricted orientation, causing the reduction of dielectric constant of water inside the pore. Minimization function to find the optimized values of $\varepsilon^*$ of the membranes prepared using TMC concentrations of 0.15 and 0.3 w-w% – (b) $Na^+/NO_3^-/Cl^-$ and (c) $Na^+/NO_3^-/SO_4^{2-}$ ternary mixtures. $\varepsilon_{pore}$ of the membranes – (d) $Na^+/NO_3^-/Cl^-$ and (e) $Na^+/NO_3^-/SO_4^{2-}$ ternary mixtures. $c_x$ of the membranes – (d) $Na^+/NO_3^-/Cl^-$ and (e) $Na^+/NO_3^-/SO_4^{2-}$ ternary mixtures.

w%, the optimized values of $\varepsilon^*$ are 14 and 17 for the ternary ionic mixtures $Na^+/NO_3^-/Cl^-$, while $\varepsilon^*$ are 19 and 20 for the ternary ionic mixtures $Na^+/NO_3^-/SO_4^{2-}$, respectively. The corresponding $\varepsilon_{pore}$ values of the membranes for the ternary ionic mixtures $Na^+/NO_3^-/Cl^-$ and $Na^+/NO_3^-/SO_4^{2-}$ are plotted in Fig. 8c and f, respectively. Fig. 8d and g show that, for both ternary ionic mixtures, the membranes prepared using a TMC concentration of 0.3 w-w% show more negative charge compared to those using a TMC concentration of 0.15 w-w%. It implies at a higher TMC concentration, a larger amount of unreacted carboxylic groups are present in the PA layer of the TFC membranes [23,24,55]. With the exception of PIP0.125TMC0.3, the increase of PIP concentration leads to a decrease of negative charge density. This change is stronger for the series of membranes prepared using a TMC concentration of 0.3 w-w% compared to those using a TMC concentration of 0.15 w-w%. This is a result of the expected increase in the number of

unreacted amino groups as the PIP concentration increases during the IP reaction [19]. The difference between the negative charge densities of the two series of membranes decrease with increasing PIP concentration while at PIP concentration 1.0 w-w% the charge density becomes independent of TMC concentration.

### 4.6. Simulation of ion retention of the tertiary mixtures by the DSPM-DE model

The determined $r_{pore}$, $\Delta x_e$, $\varepsilon_{pore}$ and $c_x$ of the membranes were used to simulate the retention behavior of the membranes when the feed solution contained the tertiary ionic mixtures $Na^+/NO_3^-/SO_4^{2-}$ and $Na^+/NO_3^-/Cl^-$ by the DSPM-DE model, respectively. Fig. 9 shows that, while the model successfully simulate the retention behavior of $Na^+/NO_3^-/SO_4^{2-}$ (Fig. 9b), it fails to simulate the retention behavior of the membranes for the feed solution containing $Na^+/NO_3^-/Cl^-$ mixture.

A careful inspection of Fig. 9 shows that the model successfully simulates the retention of $Na^+$ from the feed solution containing $Na^+/NO_3^-/Cl^-$ mixture for all the membranes prepared using the TMC concentration of 0.15 w-w%. For membranes prepared using the TMC concentration of 0.3 w-w%, the model also describes the trend of $Na^+$ retention change with the change of PIP concentration, although there are some deviations between the experimental and simulated $Na^+$ retentions. The model slightly overestimates the $Na^+$ retention of PIP0.125TMC0.3 while it slightly underestimates the $Na^+$ retentions of PIP0.25TMC0.3 and PIP0.5TMC0.3. However, the model cannot describe the anion retention behavior when the feed solution contains a $Na^+/NO_3^-/Cl^-$ mixture. The model underestimates the $Cl^-$ retentions and overestimates the $NO_3^-$ retentions of the membranes. According to the model, the retentions of $Cl^-$ and $NO_3^-$ should be almost equal and there should be no selectivity for this ion pair. Therefore, it is evident that the failure to describe the anion retention behavior of the membranes for the mixture $Na^+/NO_3^-/Cl^-$ is not related to the determination of $r_{pore}$, $\Delta x_e$, $\varepsilon_{pore}$ and $c_x$. The DSPM-DE model simply considers $NO_3^-$ and $Cl^-$ as two monovalent ions of similar size and charge and fails to take into account the underlying physical property of the ions which leads to higher permeation of $NO_3^-$ through the membranes compared to that of $Cl^-$. As already mentioned in section 4.3, the selective permeation of $NO_3^-$ over $Cl^-$ originates from the difference in energy barrier of dehydration and ionic charge density of the two ions [10].

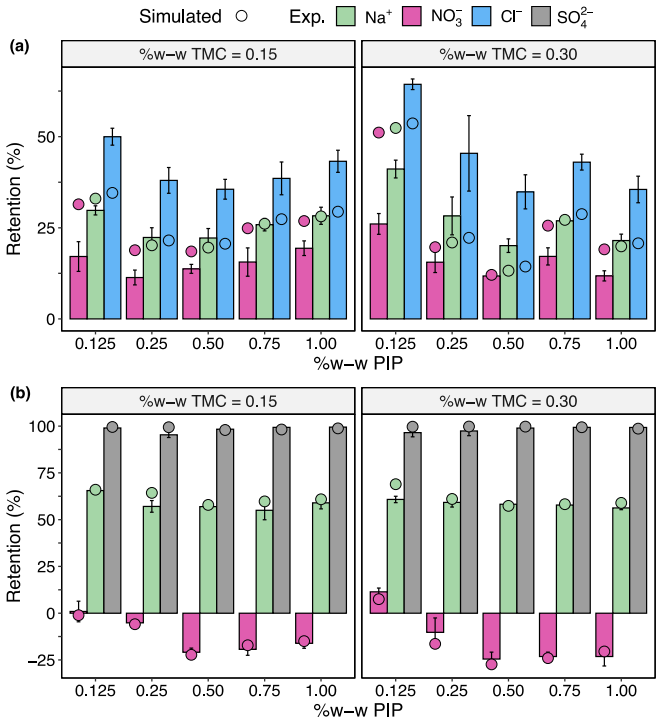



**Fig. 9.** Description of ion retention behavior of the membranes by the DSPM-DE model (simulated and experimental retention values). (a) The model fails to describe the ion retention behavior of the $Na^+/NO_3^-/Cl^-$ ternary ion mixtures. (b)The model successfully describes the ion retention behavior of the $Na^+/NO_3^-/SO_4^{2-}$ ternary ion mixture.

#### 4.6.1. Ion exclusion mechanism: Steric, dielectric and Donnan exclusion coefficients

The three exclusion or partition coefficients of the ions of $Na^+/NO_3^-/SO_4^{2-}$ at the pore entrance are presented in Fig. 10 and Fig. 11a. In order to visualize their importance in the total partition or exclusion, their product is also presented and is referred to as the overall exclusion coefficient (Fig. 11b). It is important to note that the closer to 1 the exclusion coefficient is, the less impact it has on the exclusion. Steric exclusion is directly related to the size of ions and $r_{pore}$. It is more significant (*i.e.* has smaller values) for larger ions and smaller pore sizes. Fig. 10a shows that the values of the steric exclusion coefficients for the same ion vary in the same fashion as the $r_{pore}$ with varying PIP and TMC concentrations. The values of the steric exclusion coefficients scales linearly with $r_{pore}$ (supporting information). From the values of the steric exclusion coefficients, we can infer the order of the sizes of ions, without any previous knowledge *i.e.* the size of $NO_3^- < Na^+ < SO_4^{2-}$.

Fig. 10b shows with the change of the monomer concentration, the values of the dielectric exclusion coefficients also follow the same trend as $r_{pore}$. Indeed, a smaller pore size is associated with a smaller pore dielectric constant [29,56]. Consequently, ions experience larger solvation energy barriers within membranes with smaller pore sizes, thereby increasing the dielectric exclusion (*i.e.* decreasing the dielectric exclusion coefficient). Unlike steric exclusion coefficients, when plotted against $r_{pore}$ the values of dielectric exclusion coefficients of the membranes prepared at different TMC concentration appear parallel to each other (supporting information). This means that two membranes prepared at different TMC concentrations with the same pore size will have different values of $\varepsilon_{pore}$, with the smaller corresponding to the smaller TMC concentration during the IP reaction. This is due to the different

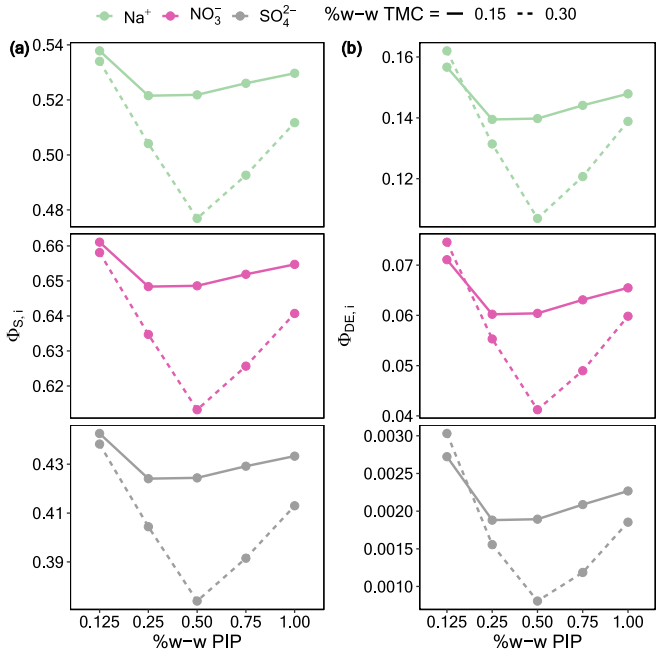



**Fig. 10.** Individual exclusion or partition coefficients of the ternary ionic mixture $Na^+/NO_3^-/SO_4^{2-}$: (a) steric and (b) dielectric at pore entrance.

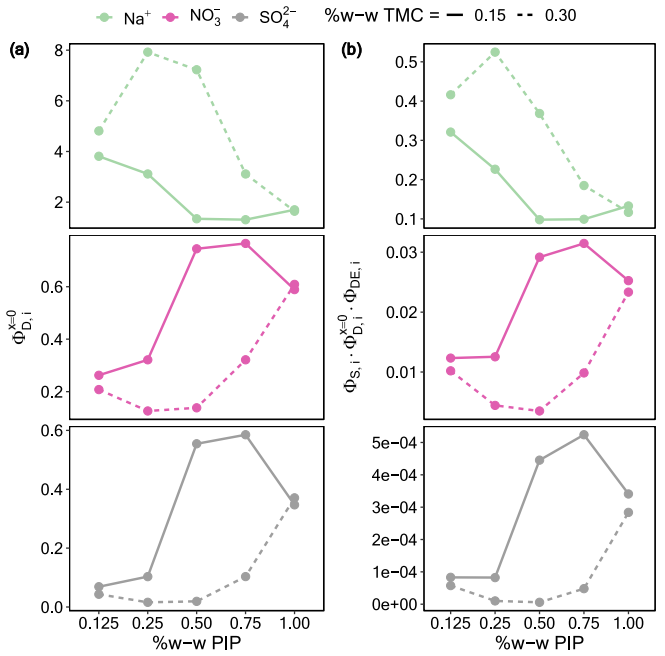



**Fig. 11.** Individual exclusion or partition coefficients of the ternary ionic mixture $Na^+/NO_3^-/SO_4^{2-}$: (a) Donnan and (b) overall exclusion coefficient. The overall exclusion coefficient is computed as the product of the three individual coefficients.

values of $\varepsilon^*$ for membranes prepared at different TMC concentrations.

When comparing different ions for the same membrane, dielectric exclusion is stronger for $SO_4^{2-} > NO_3^- > Na^+$. This is related to the solvation energy barrier. In fact, $Na^+$ and $NO_3^-$ have the same valence, but $NO_3^-$ experiences a larger energy barrier due to its smaller size, causing a stronger dielectric exclusion. $SO_4^{2-}$ is larger than $NO_3^-$, and because of its higher valence, it experiences a much stronger dielectric exclusion. Actually, this exclusion coefficient holds the biggest difference between these anions. Importantly, the dielectric exclusion coefficient is the smallest. This means that dielectric is the principal exclusion mechanism in the separation of $NO_3^-$ and $SO_4^{2-}$ for all the prepared membranes [32].

The Donnan exclusion effect, which arises from the non-uniform distribution of ions on both sides of the membranes, influences the interaction of ions in the presence of the membrane. Under this effect, counter-ions such as $Na^+$ are attracted towards the pore openings due to electrostatic interactions, while co-ions like $SO_4^{2-}$ and $NO_3^-$ experience electrostatic repulsion. Therefore, in the case of $Na^+$, the Donnan exclusion coefficients are greater than 1 (more attracted) and the values become larger with increasing negative charge density of the membranes. Fig. 11a shows that $Na^+$ is more electrostatically attracted towards the pore openings of the membranes prepared using TMC concentration 0.3 w-w% compared to those using TMC concentration 0.15 w-w% during IP. Similarly, for $SO_4^{2-}$ and $NO_3^-$ smaller values (below 1) are representative of the stronger electrostatic repulsion of the membranes prepared using TMC concentration 0.3 w-w%. For the range of PIP concentrations tested, the Donnan exclusion coefficient varies to a greater extent. Accordingly, the effects of PIP and TMC concentration on the overall exclusion coefficients (Fig. 11b) for all the ions are observed through the Donnan exclusion coefficient values. However, the dielectric exclusion is the primary exclusion mechanism which strongly contributes to the selective entrance of $NO_3^-$ at the pores of the membrane compared to that of $SO_4^{2-}$.

#### 4.6.2. Ion permeation mechanism: Advection, electromigration and diffusion

In Fig. 12 and Fig. 13a, the different contributions to and the transmembrane total molar flux of each species of the ternary ionic mixture $Na^+/NO_3^-/SO_4^{2-}$ are presented for the fabricated membranes. The difference in advective fluxes for membranes prepared at different TMC concentrations (Fig. 12) are directly related to the overall exclusion coefficients (Fig. 11b). The advective flux is associated with the concentration of a species inside the membrane's active layer. A stronger exclusion (smaller exclusion coefficient) means a smaller concentration of an ion and thereby a smaller advective flux. Therefore, the membranes prepared using a TMC concentration of 0.15 w-w% display larger advective fluxes for anions and smaller for cations compared to those prepared using a TMC concentration of 0.3 w-w%.

In general, membranes prepared at a higher PIP concentration display smaller advective fluxes for $Na^+$. The advective fluxes of $NO_3^-$ and $SO_4^{2-}$ in the membranes PIP0.5TMC0.15, PIP0.75TMC0.15 and PIP1TMC0.15 do not follow the trend of the overall exclusion coefficient. Their advective fluxes decrease with increasing PIP concentration. This is because the permeate flux inside the membrane's active layer also determines the advective flux of ions (Eq. (23)). As a result, the advective fluxes decrease with increasing PIP concentration, like the trend of the permeate flux (Fig. 7b). For the same reason, the advective fluxes of $Na^+$ for PIP0.25TMC0.15 and PIP0.5TMC0.30 membranes are the largest among the membranes prepared using TMC concentrations of 0.15 and 0.3 w-w%, respectively.

The effect of PIP and TMC concentration in the IP reaction on the electromigrative fluxes of ions is observed in Fig. 12b. The trend of electromigrative fluxes depends on the charge of the ion. The electromigrative fluxes of $Na^+$ are negative while those of $NO_3^-$ and $SO_4^{2-}$ are positive. Hence, while the overall transport of the $Na^+$ ions is from the feed to permeate side of the membranes, the contribution of electromigrative flux acts in the opposite direction. In the case of $Na^+$, the trend of advective and electromigrative fluxes with varying monomer concentrations appear as mirror image of each other. The largest negative $Na^+$ electromigrative fluxes are attained by the PIP0.25TMC0.15 and PIP0.5TMC0.30 among the membranes prepared using TMC concentration 0.15 and 0.3 w-w%, respectively.

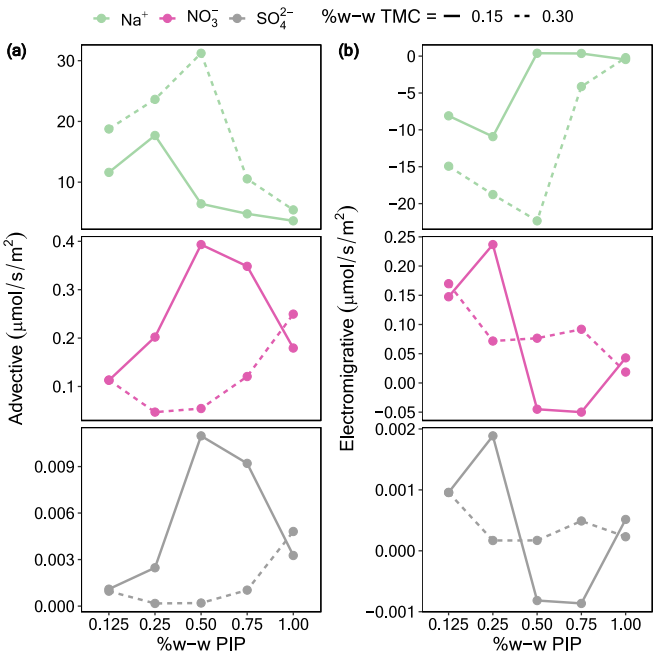



**Fig. 12.** Transmembrane fluxes of the ternary ionic mixture $Na^+/NO_3^-/SO_4^{2-}$ for the fabricated membranes: (a) advective and (b) electromigrative.

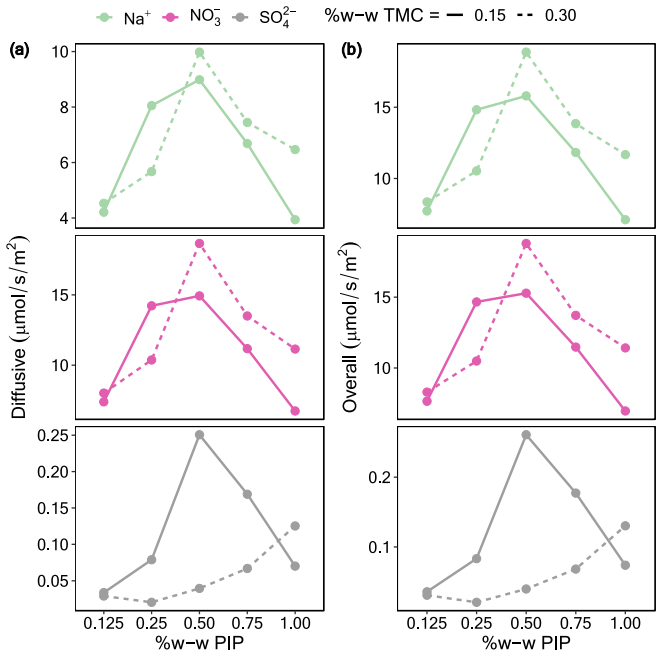



**Fig. 13.** Transmembrane fluxes of the ternary ionic mixture $Na^+/NO_3^-/SO_4^{2-}$ for the fabricated membranes: (a) diffusive, and (b) total molar flux. Total molar flux is computed as the sum of the others.

These large negative electromigrative fluxes counterbalance their advective counterparts to not break the electroneutrality condition on the permeate side [54]. In the case of $NO_3^-$ and $SO_4^{2-}$, the trends of their electromigrative fluxes with varying PIP and TMC concentrations are the same. Because of their lower concentration in the active layer, compared to $Na^+$, the pattern of their electromigrative fluxes is determined by an interaction between the electrical potential gradient and their concentration in the active layer of the membrane. Actually, inside the active layer of the membrane, an electrical potential profile is developed because of the transport of ionic species through the charged PA matrix. The electrical potential gradient is proportional to $c_x$ [57]. Therefore, $c_x$ determines the electromigrative fluxes by its effect on both the electrical potential and the exclusion mechanisms. In this respect, the $NO_3^-$ and $SO_4^{2-}$ electromigrative fluxes act in the direction opposite to that of $Na^+$. Although $SO_4^{2-}$ is bivalent, its electromigrative flux is smaller than that of monovalent $NO_3^-$. This is due to the fact that the concentration of $SO_4^{2-}$ in the active layer of the membranes is smaller than that of $NO_3^-$ due to its stronger exclusion.

The effect of PIP concentration on the values of diffusive flux (Fig. 13a) is similar to that on $\Delta x_e$ (Fig. 5b), *i.e.* in general, larger fluxes are attained within thinner active layers. In particular, the $SO_4^{2-}$ diffusive flux pattern is similar to its advective flux.

Interestingly, this does not hold for $Na^+$ and $NO_3^-$. The diffusive fluxes of $Na^+$ and $NO_3^-$ are similar in magnitude and display the same effect of the PIP and TMC concentrations. Diffusive fluxes are driven by the concentration gradients inside the membrane's selective layer and also depend on their mobility, reflected in their diffusion coefficients. The concentration of $SO_4^{2-}$ inside the active layer is very low compared to that of $NO_3^-$, as $SO_4^{2-}$ is strongly excluded at the interphase between the selective layer of the membrane and feed solution. For this reason, to maintain electroneutrality conditions inside the membrane's active layer, the $NO_3^-$ concentration profile must be similar to that of $Na^+$. Indeed, the offset between these two profiles is similar to the $c_x$ values. This leads to similar diffusive fluxes of $NO_3^-$ and $Na^+$, in spite of their different mobilities ($D_{NO_3^-,\infty} = 1.90$ vs. $D_{Na^+,\infty} = 1.33 m^2/s$ [41]). Both $Na^+$ and $NO_3^-$ diffusive fluxes are governed by electroneutrality. In consequence, when considering the diffusive fluxes of $NO_3^-$ and $Na^+$, the impact of TMC remains inconclusive due to the opposing effects of TMC concentration on $NO_3^-$ and $Na^+$ exclusion. On the other hand, the influence of PIP on these fluxes becomes evident based on the $\Delta x_e$ values.

The total molar fluxes of the three ions are in line with their diffusive fluxes (Fig. 14). The diffusive flux is the largest contribution to total molar flux, as shown in Fig. 13a. In the case of $Na^+$, diffusion accounts for approximately 55 % of the total flux, while for the anions, this contribution exceeds 90 %. Consequently, the impact of PIP and TMC concentration on the total molar flux mirrors their effects on the diffusive fluxes.

## 5. Conclusions

The mass transport mechanism responsible for the $NO_3^-$ selectivity of NF membranes having a PA selective layer is thoroughly investigated on the basis of the DSPM-DE model. The difference of ideal selectivities and real selectivities revealed that $Na^+$ promotes the permeation of $NO_3^-$ for feed solutions containing the tertiary ionic mixtures $Na^+/NO_3^-/SO_4^{2-}$ and $Na^+/NO_3^-/Cl^-$, respectively. The DSPM-DE model could not simulate the retention results of the $Na^+/Cl^-/NO_3^-$ system, but it successfully simulated the experimental results of $Na^+/NO_3^-/SO_4^{2-}$. In this work, for the first time, we have demonstrated how the exclusion coefficients (*i.e.* Donnan, steric and dielectric) and modes of transport (*i.e.* advection, electromigration and diffusion) contributing to total transmembrane molar flux of ions vary with the change of PIP and TMC concentration used to prepare the membrane. At the initial stage of IP polymerization, both TMC and PIP concentration dictate the structural parameters of the PA. At a later stage, the growth of the PA layer is limited by the diffusion of PIP through the incipient layer. Hence, the overall thickness (observed by SEM) of the PA layer did not change significantly due to the change of TMC. However, a higher TMC concentration resulted in membranes with smaller $\Delta x_e$ and $r_{pore}$ values. Consequently, for PIP concentrations of 0.25 – 1 %w-w the steric and dielectric exclusion play a less significant role to determine ion partitioning at the interface of the membrane for the membranes prepared using TMC concentration of 0.15 %w-w compared to those prepared using TMC concentration of 0.3 %w-w. Indeed, the $r_{pore}$ influenced the dielectric exclusion, which is the main exclusion mechanism responsible for $NO_3^-/SO_4^{2-}$ separation. We used a new minimization scheme to obtain $\varepsilon_{pore}$ and $c_x$ values of the fabricated membranes to elucidate the experimental mixed salt retention results with the DSPM-DE model. $c_x$ determines the Donnan exclusion. For PIP concentration of 0.25 – 0.75 %w-w, the Donnan exclusion of $NO_3^-$ and $SO_4^{2-}$ at the surface of the membranes prepared using a TMC concentration of 0.3 %w-w is stronger compared to those prepared using a TMC concentration of 0.15 %w-w. The change of the overall exclusion coefficient with the monomer concentration follows

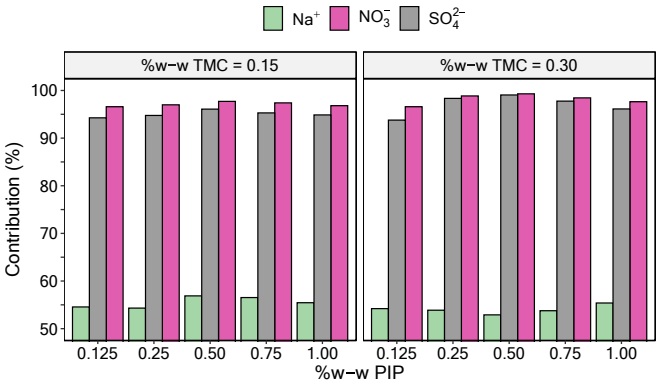



**Fig. 14.** Diffusion contribution to overall molar flux for the fabricated membranes.

the same trend as the Donnan exclusion coefficient. However, the mass transport resistance of the membrane, imparted by the $\Delta x_e$ values, affected the diffusive flux. This, in turn, governed the total molar flux of ions across the membrane's active layer. Hence, the coupled diffusion of $Na^+$ and $NO_3^-$ was responsible for the negative retention values of $NO_3^-$. The results of this study indicate that the fabrication of thinner and/or less porous, negatively charged PA active layers should be targeted for $NO_3^-$ selective separation. Although these results shed some light on the $NO_3^-$ separation capabilities of NF membranes having a PA selective layer, future studies should aim at new systematic studies involving other IP reaction conditions and different operating parameters. Thus, the transport and exclusion mechanisms can be systematically correlated with the IP reaction and the filtration conditions. This will help to further the understanding of the PA layer features to better design NF membranes with high $NO_3^-$ separation efficiencies.

## Funding

This work was funded by the Hereon-I$^2$B-Project NanoMem.

## CRediT authorship contribution statement

**Nicolás Cevallos-Cueva:** Writing – review & editing, Writing – original draft, Software, Methodology, Investigation, Formal analysis, Data curation, Conceptualization. **Md. Mushfequr Rahman:** Writing – review & editing, Writing – original draft, Visualization, Supervision, Resources, Project administration, Conceptualization. **Hluf Hailu Kinfu:** Writing – review & editing, Methodology. **Volker Abetz:** Writing – review & editing, Supervision.

## Declaration of competing interest

The authors declare that they have no known competing financial interests or personal relationships that could have appeared to influence the work reported in this paper.

## Data availability

Data will be made available on request.

## Acknowledgments

The authors would like to acknowledge Maren Brinkmann for the PEG analysis in GPC, Juliana Clodt and Barbara Bajer for fabricating the polyacrylonitrile support, Erik Schneider for the SEM analysis, Evgeni Sperling for the AFM analysis, Anke-Lisa Höhme and Martin Held for the TEM analysis, and Jan Pohlmann for setting up the flux and retention measurement facilities.

## Appendix A. Supplementary data

Supplementary data to this article can be found online at https://doi.org/10.1016/j.cej.2024.152775.

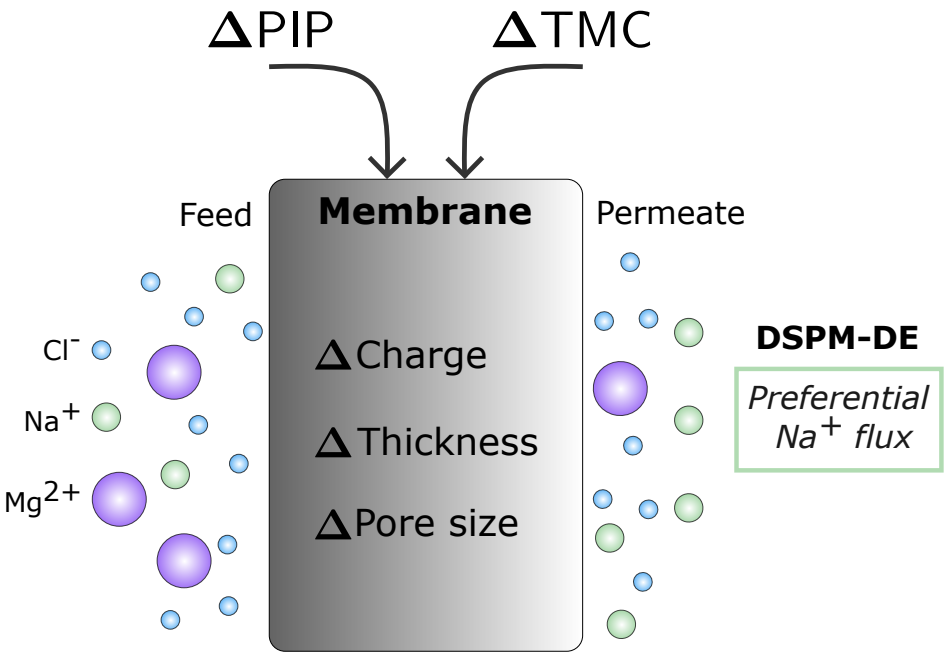
## References

[1] D.M. Manassaram, L.C. Backer, D.M. Moll, A review of nitrates in drinking water: Maternal exposure and adverse reproductive and developmental outcomes, Environ. Health Perspect. (2006) 320–327.
[2] M. Lunau, M. Voss, M. Erickson, C. Dziallas, K. Casciotti, H. Ducklow, Excess nitrate loads to coastal waters reduces nitrate removal efficiency: mechanism and implications for coastal eutrophication, Environ. Microbiol. 15 (2013) 1492–1504, https://doi.org/10.1111/j.1462-2920.2012.02773.x.
[3] E. Abascal, L. Gómez-Coma, I. Ortiz, A. Ortiz, Global diagnosis of nitrate pollution in groundwater and review of removal technologies, Sci. Total Environ. 810 (2022) 152233, https://doi.org/10.1016/j.scitotenv.2021.152233.
[4] Bmel, Bmu, Nitratbericht 2020. Gemeinsamer Bericht der Bundesministerien für Umwelt, Naturschutz und nukleare Sicherheit (BMU) sowie für Ernährung und Landwirtschaft (BMEL), Bonn, Deutschland, 2020.
[5] F. Wendland, S. Bergmann, M. Eisele, H. Gömann, F. Herrmann, P. Kreins, R. Kunkel, Model-based analysis of nitrate concentration in the leachate-the north rhine-westfalia case study, Germany, Water (switzerland) 12 (2020) 550, https://doi.org/10.3390/w12020550.
[6] Y. Zhao, T. Tong, X. Wang, S. Lin, E.M. Reid, Y. Chen, Differentiating solutes with precise nanofiltration for next generation environmental separations: a review, Environ. Sci. Tech. 55 (2021) 1359–1376, https://doi.org/10.1021/acs.est.0c04593.
[7] A. Popova, R. Rattanakom, Z.Q. Yu, Z. Li, K. Nakagawa, T. Fujioka, Evaluating the potential of nanofiltration membranes for removing ammonium, nitrate, and nitrite in drinking water sources, Water Res. 244 (2023) 120484, https://doi.org/10.1016/j.watres.2023.120484.
[8] A. Santafé-Moros, J.M. Gozálvez-Zafrilla, J. Lora-García, Performance of commercial nanofiltration membranes in the removal of nitrate ions, Desalination 185 (2005) 281–287, https://doi.org/10.1016/J.DESAL.2005.02.080.
[9] F. Garcia, D. Ciceron, A. Saboni, S. Alexandrova, Nitrate ions elimination from drinking water by nanofiltration: Membrane choice, Sep. Purif. Technol. 52 (2006) 196–200, https://doi.org/10.1016/j.seppur.2006.03.023.
[10] R. Epsztein, W. Cheng, E. Shaulsky, N. Dizge, M. Elimelech, Elucidating the mechanisms underlying the difference between chloride and nitrate rejection in nanofiltration, J Membrane Sci 548 (2018) 694–701, https://doi.org/10.1016/j.memsci.2017.10.049.
[11] D.X. Wang, M. Su, Z.Y. Yu, X.L. Wang, M. Ando, T. Shintani, Separation performance of a nanofiltration membrane influenced by species and concentration of ions, Desalination 175 (2005) 219–225, https://doi.org/10.1016/j.desal.2004.10.009.
[12] S.S. Wadekar, R.D. Vidic, Influence of active layer on separation potentials of nanofiltration membranes for inorganic ions, Environ. Sci. Tech. 51 (2017) 5658–5665, https://doi.org/10.1021/acs.est.6b05973.
[13] L. Zou, S. Zhang, J. Liu, Y. Cao, G. Qian, Y.Y. Li, Z.P. Xu, Nitrate removal from groundwater using negatively charged nanofiltration membrane, Environ. Sci. Pollut. Res. 26 (2019) 34197–34204, https://doi.org/10.1007/s11356-018-3829-6.
[14] K. Wang, X. Wang, B. Januszewski, Y. Liu, D. Li, R. Fu, M. Elimelech, X. Huang, Tailored design of nanofiltration membranes for water treatment based on synthesis–property–performance relationships, Chem. Soc. Rev. 51 (2022) 672–719, https://doi.org/10.1039/D0CS01599G.
[15] Yang, Zhou, Feng, Rui, Zhang, Zhang, A Review on Reverse Osmosis and Nanofiltration Membranes for Water Purification, Polymers 11 (2019) 1252. https://doi.org/10.3390/polym11081252.
[16] A.L. Ahmad, B.S. Ooi, A.W. Mohammad, J.P. Choudhury, Composite nanofiltration polyamide membrane: A study on the diamine ratio and its performance evaluation, Ind. Eng. Chem. Res. 43 (2004) 8074–8082, https://doi.org/10.1021/IE0497994/ASSET/IMAGES/LARGE/IE0497994F00012.JPEG.
[17] S.H. Huang, C.J. Hsu, D.J. Liaw, C.C. Hu, K.R. Lee, J.Y. Lai, Effect of chemical structures of amines on physicochemical properties of active layers and dehydration of isopropanol through interfacially polymerized thin-film composite membranes, J Membrane Sci 307 (2008) 73–81, https://doi.org/10.1016/J.MEMSCI.2007.09.014.
[18] A.L. Ahmad, B.S. Ooi, Properties–performance of thin film composites membrane: study on trimesoyl chloride content and polymerization time, J Membrane Sci 255 (2005) 67–77, https://doi.org/10.1016/J.MEMSCI.2005.01.021.
[19] Y.l. Liu, Y.y. Zhao, X.m. Wang, X.h. Wen, X. Huang, Y.F. Xie, Effect of varying piperazine concentration and post-modification on prepared nanofiltration membranes in selectively rejecting organic micropollutants and salts, J Membrane Sci 582 (2019) 274–283, https://doi.org/10.1016/j.memsci.2019.04.018.
[20] N.K. Saha, S.V. Joshi, Performance evaluation of thin film composite polyamide nanofiltration membrane with variation in monomer type, J Membrane Sci 342 (2009) 60–69, https://doi.org/10.1016/j.memsci.2009.06.025.
[21] T. Zhang, R.Y. Fu, K.P. Wang, Y.W. Gao, H.R. Li, X.M. Wang, Y.F. Xie, L.a. Hou, Effect of synthesis conditions on the non-uniformity of nanofiltration membrane pore size distribution, J Membrane Sci 647 (2022) 120304, https://doi.org/10.1016/j.memsci.2022.120304.
[22] R. Nadler, S. Srebnik, Molecular simulation of polyamide synthesis by interfacial polymerization, J Membrane Sci 315 (2008) 100–105, https://doi.org/10.1016/j.memsci.2008.02.023.
[23] J. Tian, H. Chang, S. Gao, R. Zhang, How to fabricate a negatively charged NF membrane for heavy metal removal via the interfacial polymerization between PIP and TMC? Desalination 491 (2020) 114499 https://doi.org/10.1016/j.desal.2020.114499.
[24] R. Zhang, S. Yu, W. Shi, J. Zhu, B. Van der Bruggen, Support membrane pore blockage (SMPB): An important phenomenon during the fabrication of thin film composite membrane via interfacial polymerization, Sep. Purif. Technol. 215 (2019) 670–680, https://doi.org/10.1016/J.SEPPUR.2019.01.045.
[25] Q.Y. Zhu, L.K. Wu, L.Q. Li, L.W. Zhuang, S.M. Xue, Z.L. Xu, Y.J. Tang, Novel insight on the effect of the monomer concentration on the polypiperazine-amide nanofiltration membrane, Ind. Eng. Chem. Res. 61 (2022) 5843–5852, https://doi.org/10.1021/ACS.IECR.2C00478/ASSET/IMAGES/LARGE/IE2C00478_0013.JPEG.
[26] K.S. Spiegler, O. Kedem, Thermodynamics of hyperfiltration (reverse osmosis): criteria for efficient membranes, Desalination 1 (1966) 311–326, https://doi.org/10.1016/S0011-9164(00)80018-1.
[27] X.L. Wang, T. Tsuru, S.i. Nakao, S. Kimura, Electrolyte transport through nanofiltration membranes by the space-charge model and the comparison with Teorell-Meyer-Sievers model, J Membrane Sci 103 (1995) 117–133, https://doi.org/10.1016/0376-7388(94)00317-R.

[28] T. Tsuru, S.i. Nakao, S. Kimura, Calculation of ion rejection by extended nernst-planck Equation with charged reverse osmosis membranes for single and mixed electrolyte solutions, J. Chem. Eng. Jpn 24 (1991) 511–517, https://doi.org/10.1252/jcej.24.511.
[29] W.R. Bowen, J.S. Welfoot, Modelling the performance of membrane nanofiltration-critical assessment and model development, Chem. Eng. Sci. 57 (2002) 1121–1137, https://doi.org/10.1016/S0009-2509(01)00413-4.
[30] R. Wang, S. Lin, Pore model for nanofiltration: History, theoretical framework, key predictions, limitations, and prospects, J Membrane Sci 620 (2021) 118809, https://doi.org/10.1016/j.memsci.2020.118809.
[31] S. Bandini, Modelling the mechanism of charge formation in NF membranes: Theory and application, J Membrane Sci 264 (2005) 75–86, https://doi.org/10.1016/j.memsci.2005.03.055.
[32] A. Santafé-Moros, J.M. Gozálvez-Zafrilla, J. Lora-García, Applicability of the DSPM with dielectric exclusion to a high rejection nanofiltration membrane in the separation of nitrate solutions, Desalination 221 (2008) 268–276, https://doi.org/10.1016/J.DESAL.2007.01.083.
[33] M. Micari, D. Diamantidou, B. Heijman, M. Moser, A. Haidari, H. Spanjers, V. Bertsch, Experimental and theoretical characterization of commercial nanofiltration membranes for the treatment of ion exchange spent regenerant, J Membrane Sci 606 (2020) 118117, https://doi.org/10.1016/j.memsci.2020.118117.
[34] A. Escoda, S. Déon, P. Fievet, Assessment of dielectric contribution in the modeling of multi-ionic transport through nanofiltration membranes, J Membrane Sci 378 (2011) 214–223, https://doi.org/10.1016/J.MEMSCI.2011.05.004.
[35] O. Labban, C. Liu, T.H. Chong, J.H. Lienhard V,, Fundamentals of low-pressure nanofiltration: Membrane characterization, modeling, and understanding the multi-ionic interactions in water softening, J Membrane Sci 521 (2017) 18–32, https://doi.org/10.1016/j.memsci.2016.08.062.
[36] S. Castaño Osorio, P.M. Biesheuvel, J.E. Dykstra, E. Virga, Nanofiltration of complex mixtures: The effect of the adsorption of divalent ions on membrane retention, Desalination 527 (2022) 115552, https://doi.org/10.1016/j.desal.2022.115552.
[37] C.L. Ritt, J.R. Werber, M. Wang, Z. Yang, Y. Zhao, H.J. Kulik, M. Elimelech, Ionization behavior of nanoporous polyamide membranes, in: Proceedings of the National Academy of Sciences of the United States of America 117, 2020, pp. 30191–30200, https://doi.org/10.1073/PNAS.2008421117/SUPPL_FILE/PNAS.2008421117.SAPP.PDF.
[38] S. Déon, P. Dutournié, L. Limousy, P. Bourseau, Transport of salt mixtures through nanofiltration membranes: Numerical identification of electric and dielectric contributions, Sep. Purif. Technol. 69 (2009) 225–233, https://doi.org/10.1016/J.SEPPUR.2009.07.022.
[39] D.L. Oatley, L. Llenas, R. Pérez, P.M. Williams, X. Martínez-Lladó, M. Rovira, Review of the dielectric properties of nanofiltration membranes and verification of the single oriented layer approximation, Advances in Colloid and Interface Science, Elsevier (2012) 1–11.
[40] V. Geraldes, M.D. Afonso, Prediction of the concentration polarization in the nanofiltration/reverse osmosis of dilute multi-ionic solutions, J Membrane Sci 300 (2007) 20–27, https://doi.org/10.1016/J.MEMSCI.2007.04.025.
[41] V. Geraldes, A.M. Brites Alves, Computer program for simulation of mass transport in nanofiltration membranes, J Membrane Sci 321 (2008) 172–182, https://doi.org/10.1016/j.memsci.2008.04.054.
[42] P.M. Biesheuvel, J.E. Dykstra, Physics of Electrochemical Processes (2020).
[43] A. Szymczyk, M. Sbaï, P. Fievet, Analysis of the pressure-induced potential arising through composite membranes with selective surface layers, Langmuir 21 (2005) 1818–1826, https://doi.org/10.1021/la048399i.
[44] X.L. Wang, Y.Y. Fang, C.H. Tu, B. van der Bruggen, Modelling of the separation performance and electrokinetic properties of nanofiltration membranes, Int. Rev. Phys. Chem. 31 (2012) 111–130, https://doi.org/10.1080/0144235X.2012.659049.
[45] D. Rehman, J.H. Lienhard, Global optimization for accurate and efficient parameter estimation in nanofiltration, Journal of Membrane Science Letters 2 (2022) 100034, https://doi.org/10.1016/J.MEMLET.2022.100034.
[46] Z. Tan, S. Chen, X. Peng, L. Zhang, C. Gao, Polyamide membranes with nanoscale Turing structures for water purification, Science 360 (2018) 518–521, https://doi.org/10.1126/science.aar6308.
[47] V. Freger, S. Srebnik, Mathematical model of charge and density distributions in interfacial polymerization of thin films, J. Appl. Polym. Sci. 88 (2003) 1162–1169, https://doi.org/10.1002/app.11716.
[48] S.A. Sundet, Morphology of the rejecting surface of aromatic polyamide membranes for desalination, J. Membr. Sci. 76 (1993) 175–183, https://doi.org/10.1016/0376-7388(93)85215-I.
[49] V. Freger, Kinetics of film formation by interfacial polycondensation, Langmuir 21 (2005) 1884–1894, https://doi.org/10.1021/la048085v.
[50] X. Yang, Monitoring the Interfacial Polymerization of Piperazine and Trimesoyl Chloride with Hydrophilic Interlayer or Macromolecular Additive by In Situ FT-IR Spectroscopy, Membranes 10 (2020) 12.
[51] L.E. Peng, Z. Yang, L. Long, S. Zhou, H. Guo, C.Y. Tang, A critical review on porous substrates of TFC polyamide membranes: Mechanisms, membrane performances, and future perspectives, J. Membr. Sci. 641 (2022) 119871, https://doi.org/10.1016/j.memsci.2021.119871.
[52] Q. Gan, C. Wu, L. Long, L.E. Peng, Z. Yang, H. Guo, C.Y. Tang, Does Surface Roughness Necessarily Increase the Fouling Propensity of Polyamide Reverse Osmosis Membranes by Humic Acid? Environ. Sci. Tech. 57 (2023) 2548–2556, https://doi.org/10.1021/acs.est.2c07872.
[53] C. Tang, M.L. Bruening, Ion separations with membranes, J. Polym. Sci. 58 (2020) 2831–2856, https://doi.org/10.1002/pol.20200500.
[54] A. Yaroshchuk, M.L. Bruening, E. Zholkovskiy, Modelling nano filtration of electrolyte solutions, Adv. Colloid Interface Sci. 268 (2019) 39–63.
[55] C. Klaysom, S. Hermans, A. Gahlaut, S. Van Craenenbroeck, I.F.J. Vankelecom, Polyamide/Polyacrylonitrile (PA/PAN) thin film composite osmosis membranes: Film optimization, characterization and performance evaluation, J Membrane Sci 445 (2013) 25–33, https://doi.org/10.1016/J.MEMSCI.2013.05.037.
[56] D. Lu, Z. Yao, L. Jiao, M. Waheed, Z. Sun, L. Zhang, Separation mechanism, selectivity enhancement strategies and advanced materials for mono-/multivalent ion-selective nanofiltration membrane, Advanced Membranes 2 (2022) 100032, https://doi.org/10.1016/j.advmem.2022.100032.
[57] B. Su, X. Duan, M. Dou, X. Gao, C. Gao, Charge characteristics of nanofiltration membrane by streaming potential method, Adv. Mat. Res. 396–398 (2012) 547–551, https://doi.org/10.4028/www.scientific.net/AMR.396-398.547.

## 3.2. Publication II: Mass transport mechanisms insights of selective sodium/magnesium separation through nanofiltration membranes

Building on Publication I, this section extends the concentration-based fabrication approach to $Na^+/Mg^{2+}$ separation and examines how monomer concentration-driven descriptor shifts translate into selectivity changes when interpreted through the same effective descriptor set. The mechanistic interpretation remains formulated in terms of coupled interfacial partitioning and in-pore transport, so that these changes are interpreted as coupled descriptor shifts rather than as isolated performance trends. This section prepares the transition to the subsequent sections by shifting the fabrication focus from monomer concentration to aqueous-phase monomer chemistry.



Journal of Membrane Science 721 (2025) 123808

Contents lists available at ScienceDirect

Journal of Membrane Science

journal homepage: www.elsevier.com/locate/memsci

# Mass transport mechanisms insights of selective sodium/magnesium separation through nanofiltration membranes

Nicolás Cevallos-Cueva [a], Md. Mushfequr Rahman [a,*], Hluf Hailu Kinfu [a], Volker Abetz [a,b]

[a] Helmholtz-Zentrum Hereon, Institute of Membrane Research, Max-Planck-Straße 1, 21502, Geesthacht, Germany
[b] University of Hamburg, Institute of Physical Chemistry, Martin-Luther-King-Platz 6, 20146, Hamburg, Germany

ARTICLE INFO

*Keywords:*
Interfacial polymerization
Nanofiltration membranes
Thin film composite membranes
Sodium/magnesium separation
DSPM-DE model

ABSTRACT

This study investigates the selective ion separation capabilities of interfacially polymerized nanofiltration (NF) membranes, focusing on the effect of piperazine (PIP) and trimesoyl chloride (TMC) concentrations on $Na^+/Mg^{2+}$ selectivity. By varying the concentrations of PIP and TMC during interfacial polymerization (IP), we altered the membranes' physicochemical characteristics and assessed their performance. The Donnan Steric Pore Model with Dielectric Exclusion (DSPM-DE) was used to explore the correlations between the DSPM-DE input parameters and the partitioning mechanisms and transmembrane fluxes of $Na^+$ and $Mg^{2+}$ in terms of the monomer concentrations. Our findings reveal that variations in the thickness-to-porosity ratio and the effective membrane charge density, influenced by higher PIP and lower TMC concentrations, enhance the $Na^+/Mg^{2+}$ separation capabilities of the membranes. This study provides a mechanistic understanding of selective $Na^+/Mg^{2+}$ separation in terms of PIP and TMC concentrations, elucidating the underlying transport and exclusion mechanisms. These insights are important for optimizing membrane fabrication by IP and designing NF membranes for efficient $Na^+/Mg^{2+}$ separation, which is essential due to the importance of magnesium as a critical raw material.

## 1. Introduction

Nanofiltration (NF) is a pressure-driven membrane process that can be used to selectively retain multivalent ions while allowing monovalent ions to permeate. NF membranes achieve the selective separation of ions based on their size, charge, diffusivity, and solubility [1]. To fully exploit the separation capabilities of NF membranes and minimize energy consumption, it is essential to select membranes with tailored properties [2]. Due to the similar hydrated ionic radii of $Mg^{2+}$ and $Na^+$, separation based solely on sieving or steric effects might be insufficient. Therefore, non-sieving mechanisms, such as Donnan or charge effects, become more significant, with a positively charged membrane surface being particularly effective in enhancing divalent/monovalent cation selectivity [1–4]. This underscores the importance of elucidating the role of the membrane's characteristics and underlying ion permeation mechanisms that influence cation selectivity, particularly in the context of $Na^+/Mg^{2+}$ separation. In our previous study [5], we demonstrated the effectiveness of NF membranes in selectively separating $NO_3^-$/ $SO_4^{2-}$ ions, where dielectric exclusion and diffusion were identified as the dominant exclusion and transport mechanisms, respectively.

Despite advancements in NF membrane fabrication, a research gap remains regarding the systematic influence of monomer concentrations in interfacial polymerization (IP) on $Na^+$ and $Mg^{2+}$ separation in terms of mass transport modeling. The Donnan Steric Pore Model with Dielectric Exclusion (DSPM-DE) is a state-of-the-art model that characterizes the membranes based on their physicochemical features, namely the pore radius ($r_{pore}$), the thickness-to-porosity ratio of the active layer ($\Delta x_e$), the charge density ($c_x$), and the pore dielectric constant ($\varepsilon_{pore}$) [6]. These membrane characteristics serve as the input parameters of the model, determining the extent of the exclusion mechanisms and the magnitude of the transmembrane ionic fluxes, which ultimately drive the ion selectivity [6–10].

Previous studies on cation selectivity modeling have primarily focused on the effects of NF membrane operating parameters and synthesis conditions [8,9,11–22]. In the context of the DSPM-DE model, variations in the intrinsic characteristics of the membranes, resulting from changes in operating parameters and synthesis conditions, are reflected as changes in the input parameters of the model. The influence of the operating parameters, including temperature, pH, and feed solution concentration on cation separation has been extensively investigated [8,

* Corresponding author.
*E-mail address:* mushfequr.rahman@hereon.de (Md.M. Rahman).

https://doi.org/10.1016/j.memsci.2025.123808
Received 17 October 2024; Received in revised form 17 January 2025; Accepted 1 February 2025
Available online 4 February 2025
0376-7388/© 2025 The Authors. Published by Elsevier B.V. This is an open access article under the CC BY license (http://creativecommons.org/licenses/by/4.0/).

11,13,15–20]. However, these studies typically focus on variations in only two input parameters of the model. Conversely, only a few studies have focused on coupling the fabrication conditions of NF membranes with the DSPM-DE model [21–23]. These studies generally performed sensitivity analyses by varying one or two DSPM-DE input parameters at a time. For example, Labban et al. [23] fabricated membranes using layer-by-layer deposition and performed a sensitivity analysis to optimize a membrane for a desalination pretreatment. Furthermore, Léniz-Pizarro et al. [22] synthesized NF membranes using interfacial polymerization (IP) between piperazine (PIP) and trimesoyl chloride (TMC) with the addition of polyallylamine hydrochloride (PAH) to yield positively charged membranes for the selective separation of multivalent cations. They utilized the DSPM-DE model to better understand the effect of the addition of PAH on the separation focusing mainly on $c_x$ and $\varepsilon_{pore}$. However, these studies reveal a gap in understanding the combined effects of all membrane physicochemical characteristics within the context of NF membrane fabrication. Our study addresses this gap by systematically varying all four DSPM-DE input parameters through changes in the fabrication conditions. Unlike our previous study of anion separation [5], the selective transport mechanisms governing $Na^+$ and $Mg^{2+}$ separation, where Donnan becomes a dominant factor, have remained less explored. By exploring the correlations between the DSPM-DE input parameters, the partitioning mechanisms, and transmembrane molar fluxes of $Na^+$ and $Mg^{2+}$, we provide a comprehensive assessment of the impact of intrinsic membrane characteristics on cation selectivity.

Most commercial NF membranes are fabricated by IP. They are thin-film composite (TFC) membranes, comprising a thin polyamide (PA) active layer on top of a porous support [24]. Among the different IP reaction conditions, the monomer concentrations play a crucial role in dictating the final characteristics of the membranes, altering the thickness, porosity, surface charge, and roughness of the active layer [2,5,25–36]. Thus, varying the monomer concentrations during IP is expected to affect the four DSPM-DE input parameters of the resulting membranes, considering their concurrent influence [5,35,36]. Following our earlier work on $NO_3^-/SO_4^{2-}$ separation [5], this study extends the investigation to the selective separation of $Na^+$ and $Mg^{2+}$ ions.

In this study, for the first time, we investigated the influence of the concentrations of the monomers PIP and TMC on the $Mg^{2+}/Na^+$ selectivity of the TFC NF membranes using the DSPM-DE model. We systematically varied the concentrations of the monomers to alter the membranes' physicochemical characteristics and evaluated their separation performance with PEG 200, single salt (NaCl, $MgCl_2$, $Na_2SO_4$, and $MgSO_4$), and mixed salt retention tests (NaCl + $MgCl_2$ and $Na_2SO_4$ + $MgSO_4$). For the first time, we provide a mechanistic understanding of the phenomena underlying $Mg^{2+}$ and $Na^+$ separation in terms of PIP and TMC concentration by correlating the membranes' physicochemical features with the DSPM-DE input parameters. These correlations elucidated the role of the membranes' characteristics in their performance, offering new insights into the partitioning and transmembrane ion fluxes. Unlike our earlier work focusing on $NO_3^-/SO_4^{2-}$ separation [5], this study provides novel insights into how PIP and TMC concentrations affect $Na^+/Mg^{2+}$ separation in TFC NF membranes. This knowledge is crucial for optimizing membrane fabrication conditions and designing NF membranes specifically targeted for efficient $Na^+/Mg^{2+}$ separation. Efficient separation of $Mg^{2+}$ from $Na^+$ is vital, as magnesium is considered a "critical raw material" by the European Commission due to its essential and sustainable supply [37].

## 2. Materials & methods

### 2.1. Materials

All chemicals were used as received. Piperazine anhydrous (PIP) (>99 %), trimesoyl chloride (TMC), and *n*-heptane were purchased from Sigma-Aldrich Chemie GmbH (Germany). Ultrafiltration polyacrylonitrile (PAN) membrane support was prepared at and supplied by Helmholtz-Zentrum Hereon. Poly (ethylene glycol) (PEG) of average molecular weight 200 Da was purchased from VWR International GmbH (Germany). NaCl (>99.5 %) and $Na_2SO_4$ (>99 %) were purchased from Merck KGaA (Germany) and Carl Roth Gmbh (Germany), respectively. $MgCl.6H_2O$ (>99 %) and $MgSO_4$ (>99.5 %) were purchased from Sigma-Aldrich Chemie GmbH (Germany).

### 2.2. Methods

#### 2.2.1. Fabrication of PA membranes

TFC membranes consisting of a PA active layer on top of a porous PAN support were fabricated by IP with aqueous PIP and organic TMC solutions of varying concentrations. A minimum of three membranes was fabricated under each of the conditions presented in Table 1, which summarizes the monomer concentrations we used.

One day before the synthesis of the TFC membranes, the PAN support was immersed in ultrapure DI water; PIP and TMC were dissolved in ultrapure DI water and HPLC-grade n-heptane, respectively. One-minute rubber rolling and dust-free Kim wipes were used to remove any droplets from the surface of the PAN supports. Then, a 6-min immersion of the support in 350 ml PIP solution was carried out. Next, any remaining droplets on top of the PAN support were removed by the previously mentioned procedure.

The supports were clamped onto a 5.1 cm × 15.9 cm glass plate, with a frame consisting of one layer of nitrile rubber and one PTFE frame. Then, the TMC solutions were poured on top of the soaked PAN supports to start the 90-s IP reactions. The IP reaction was stopped by pouring 150 ml of pure *n*-heptane. Then, the TFC membranes were air-dried for 30 min at room temperature, cured for 30 min at 60 °C under vacuum, and finally stored in ultrapure DI water.

#### 2.2.2. Characterization

The membrane morphology was analyzed with scanning electron microscopy (SEM). SEM images were captured with a Merlin SEM (Zeiss, Jena, Germany) at accelerating voltages between 1.5 and 3 kV using an InLens secondary electron detector. Before imaging, the samples were dried under vacuum at 60 °C for at least 72 h and coated with 1–1.5 nm platinum using a CCU-010 coating device (Safematic, Zizers, Switzerland). The cross-fractured specimens were prepared in liquid nitrogen.

The topography data of the membrane surfaces were obtained by an Atomic Force Microscopy MultiMode 8 instrument from Bruker, USA, in Tapping mode. Typical scan areas were 3 μm × 3 μm. RTESPA-150 probes (tip radius ≈ 8 nm, spring constant ≈ 5 N/m) were applied for these measurements. Roughness values Rq and Ra were calculated with the program NanoScope Analysis 1.9. Rq, also called RMS roughness, is the root mean square average of height deviations taken from the mean image data plane.

**Table 1**
PIP and TMC concentrations used during IP to fabricate TFC PA membranes.

| PIP (%w-w) | TMC (%w-w) | Label |
|---|---|---|
| 0.125 | 0.15 | PIP0.125TMC0.15 |
| 0.25 | 0.15 | PIP0.25TMC0.15 |
| 0.50 | 0.15 | PIP0.5TMC0.15 |
| 0.75 | 0.15 | PIP0.75TMC0.15 |
| 1.00 | 0.15 | PIP1TMC0.15 |
| 0.125 | 0.30 | PIP0.125TMC0.3 |
| 0.25 | 0.30 | PIP0.25TMC0.3 |
| 0.50 | 0.30 | PIP0.5TMC0.3 |
| 0.75 | 0.30 | PIP0.75TMC0.3 |
| 1.00 | 0.30 | PIP1TMC0.3 |

#### 2.2.3. Performance evaluation

Each fabricated membrane was evaluated according to this section.

A stirrer cell (EMD Millipore XFUF07601) with a 3-cm long stirrer was used for the retention and pure water permeance evaluation experiments in dead-end filtration mode. The effective area was reduced to 2.14 $cm^2$.

The pure water permeance (PWP) was calculated with the data recorded during the water compaction step, which comprised ultrapure DI water permeation for at least 2 h at 4 bar and room temperature:

$$PWP = \frac{\Delta m}{\delta_{H_2O} A_{mb} \Delta t \Delta P} \quad (1)$$

where $\Delta m$ is the change of mass, $\delta_{H_2O}$ density of liquid water at room temperature, $A_{mb}$ effective membrane area, $\Delta t$ the elapsed time, and $\Delta P$ the transmembrane pressure.

*2.2.3.1. Ion retention.* Following the water compaction step, salt solutions were added to the stirring cell. Single salt experiments were carried out using 200 ppm solutions of NaCl, $MgCl_2$, $Na_2SO_4$, and $MgSO_4$. Mixed salt experiments were performed using 200 ppm of $Na^+/Mg^{2+}$ equimolar mixtures of NaCl + $MgCl_2$ and $Na_2SO_4$+$MgSO_4$. The transmembrane pressure was set to 3 bars. Permeate samples collected during the first 2 h were discarded. Then, 1 ml retentate and permeate samples were collected to ensure that a steady state had been reached. As the retentate concentration varies with time in dead-end mode, the retention, $R_{i,obs}$, was computed using the average concentration of the feed and retentate solution:

$$R_{i,obs} = 1 - \frac{2c_{i,p}}{c_{i,f} + c_{i,r}} \quad (2)$$

where $c_{i,p}$, $c_{i,f}$, $c_{i,r}$ are the concentrations of species $i$ in the permeate, feed, and retentate solutions, respectively.

The concentration of each ionic species was quantified with an Ion Chromatograph (Dionex ICS600, Thermosicher Scientific Inc., USA).

The ideal selectivity, $S^*_{a/b}$, from single salt retention tests and the real selectivity, $S_{a/b}$, from mixed salt retention test were computed with the following equation:

$$S^*_{a/b} \text{ or } S_{a/b} = \frac{1 - R_{a,obs}}{1 - R_{b,obs}} \quad (3)$$

*2.2.3.2. PEG retention.* PEG retention tests were performed similarly to ion retention tests. A 500 ppm PEG 200 solution was used for each test, after the water compaction step. The retention tests were carried out at transmembrane pressure values of 0.5, 1.0, 1.5, 2.0, 2.5, 3.0, 3.5, and 4.0 bars to determine the PEG 200 retention at different solution velocities. The solution or solvent velocities were computed with:

$$J_v = \frac{\Delta m}{\delta_{H_2O} A_{mb} \Delta t} \quad (4)$$

The PEG concentration was measured with Gel Permeation Chromatography (GPC) (VWR-Hitachi 2130 pump, Hitachi, Darmstadt, Germany).

*2.2.3.3. Fitting.* To fully solve the DSPM-DE model, the membrane-related input parameters, namely $r_{pore}$, $\Delta x_e$, $\varepsilon_{pore}$, and $c_x$, need to be determined. They were determined by fitting retention test data. We used data from PEG 200 retention experiments for determining $r_{pore}$ and $\Delta x_e$ (supporting information), while data from mixed salt retention tests were used for determination of $\varepsilon_{pore}$ and $c_x$. The details of the fitting procedure and the set of equations used to solve the model are described in the supporting information.

## 3. Results and discussion

### 3.1. Membrane morphology and water permeance

Cross-sections of the TFC membranes were investigated with SEM to determine the thickness of the PA layer (Figs. 1 and 2). The thickness of the PA layer increased with PIP concentration. The top surface of the prepared membranes was investigated both with SEM and AFM. The SEM micrographs demonstrate heterogeneous granular features, which are typical for PA layers [38]. The formation of such rough heterogeneous surface is associated with the complex reaction kinetics of IP, monomer partitioning, and diffusion of monomers in the two-phase system. The surface roughness of the PA layer has long been correlated with the permeance of the membrane. A general intuition has been that the higher the surface roughness, the higher the permeance. By now, it is well established that although it is logical to claim that an increased interfacial area between the feed solution and membrane active layer can lead to high permeance, the irregular morphology of the PA layer has additional features that influence the permeance. The thickness of PA layers in TFC membranes varies significantly due to their inherent heterogeneity, which directly impacts local mass transport. This variation in thickness creates regions where the resistance to mass transport differs, leading to an uneven distribution of permeance across the membrane. One key factor influencing this resistance is the "funnel effect", as schematically represented in Fig. 3a. This phenomenon occurs because permeating substances can more easily reach the pores of the substrate through areas of the PA layer directly above these pores. In

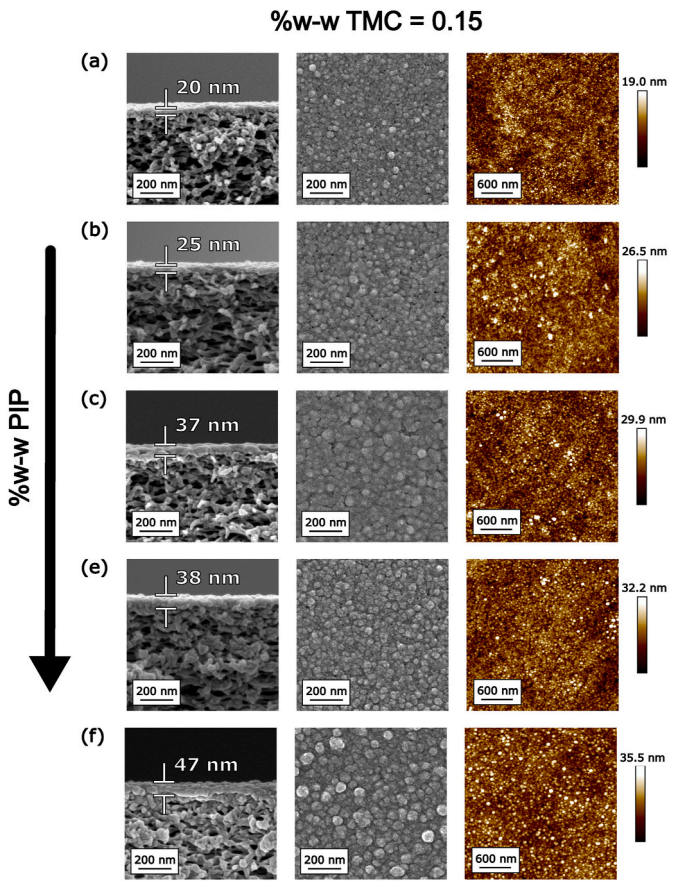



**Fig. 1.** Morphologies of the fabricated membranes at %w-w TMC = 0.15. (a) %w-w PIP = 0.125 (b) %w-w PIP = 0.25 (c) %w-w PIP = 0.50 (d) %w-w PIP = 0.75 and (e) %w-w PIP = 1.0. The left micrographs are SEM cross-sectional images, the centered micrographs SEM top surface images, and the right images AFM surface images. The average observed thickness of the PA layer is indicated in each cross-sectional image.

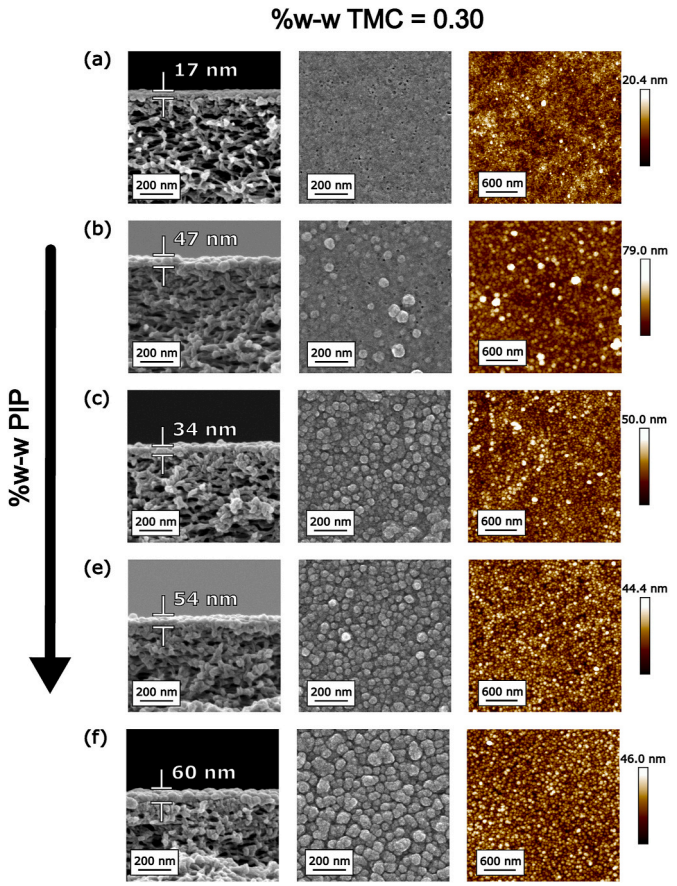



**Fig. 2.** Morphologies of the fabricated membranes at %w-w TMC = 0.30. (a) %w-w PIP = 0.125 (b) %w-w PIP = 0.25 (c) %w-w PIP = 0.50 (d) %w-w PIP = 0.75 and (e) %w-w PIP = 1.0. The left micrographs are SEM cross-sectional images, the centered micrographs SEM top surface images, and the right images AFM surface images. The average observed thickness of the PA layer is indicated in each cross-sectional image.

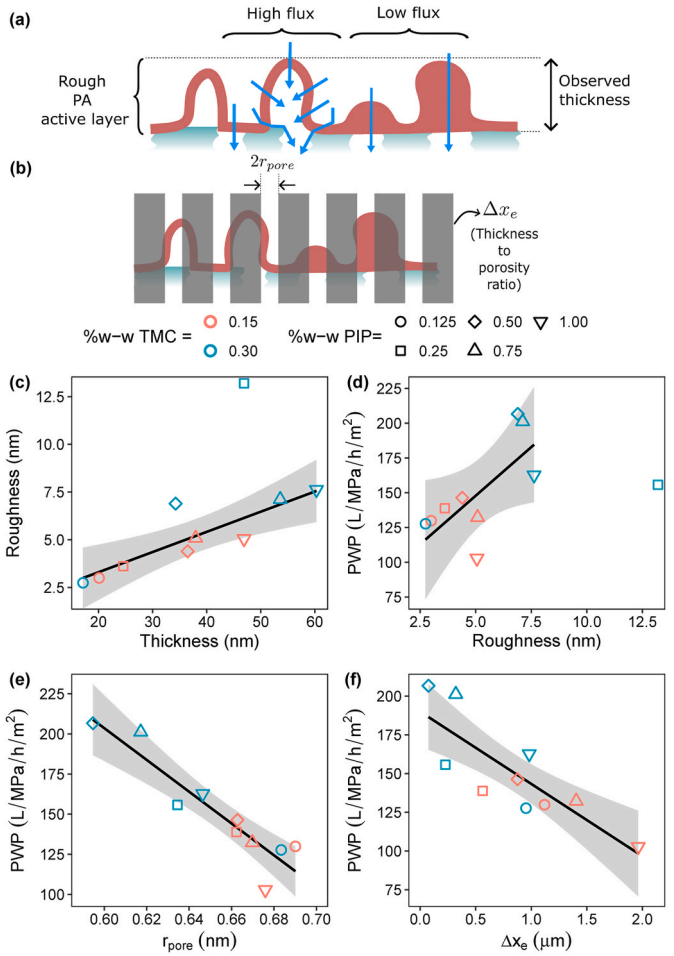



**Fig. 3.** Schematic representation and plots: (a) The heterogeneous morphology of the PA layer. (b) The DSPM-DE model assumes the PA layer is composed of equally spaced, perpendicularly aligned cylinders with radius $r_{pore}$ and thickness-to-porosity ratio $\Delta x_e$. (c) RMS roughness versus thickness (obtained from SEM). (d) Pure water permeance (PWP) vs. RMS roughness. (e) PWP vs. $r_{pore}$ (obtained from PEG retention tests). (f) PWP vs. $\Delta x_e$ (obtained from PEG 200 retention tests).

contrast, regions of the PA layer that are farther from the substrate pores require a much longer path length for permeation, increasing resistance in these areas. Beneath the surface of the heterogeneous PA layers, there are regions with nanovoids. These nanovoids help mitigate the "funnel effect" by providing easier passage for permeating substances, enabling them to reach the substrate pores more efficiently. As a result, TFC membranes with PA layers exhibit localized regions of significantly higher permeance compared to neighboring areas. The DSPM-DE model considers that the selective layer of the nanofiltration membrane is composed of equally spaced perpendicularly aligned cylinders (Fig. 3b). Under this assumption, the influence of surface roughness on the permeance is averaged out by the input parameter $\Delta x_e$ which represents the effective thickness-to-porosity ratio. We have explored the covariance and correlation of the variables RMS surface roughness (obtained from AFM), average observed thickness (obtained from SEM), $r_{pore}$ (obtained from PEG retention), $\Delta x_e$ (obtained from PEG retention) and pure water permeance (PWP). Both roughness and thickness of the PA layer increased with PIP concentration for the membranes prepared using TMC concentration 0.15 w-w% (Figs. 1) and 0.3 w-w% (Fig. 2). Consequently, a positive covariance is observed between the roughness and the thickness of the membranes (Fig. 3c). In other words, the higher roughness of the membranes comes at the expense of a greater overall thickness of the PA layer. The PWP increases with the roughness as expected. Additionally, a positive covariance is observed between PWP and roughness (Fig. 3d). This suggests that the roughness of the PA layers plays a more dominant role in determining the resistance of the membranes to water permeation compared to overall thickness of the PA layer. This conclusion is supported by the fact that an increase in overall thickness might also imply an increase in resistance to water transport, which would typically lead to a decrease in PWP. Therefore, the observed increase in PWP with roughness indicates that roughness is the more influential factor in dictating PWP. It is also observed that PWP decreases with increasing $r_{pore}$ which is counterintuitive. It suggests while $r_{pore}$ is representative of the size sieving feature of the membranes, it does not dictate the resistance against mass transport through the membranes. The $r_{pore}$ values of all the membranes range between 0.6 and 0.7 nm. In other words, the obtained $r_{pore}$ values are rather similar to each other and $r_{pore}$ cannot explain the resistance of the membranes against permeation of water. The input parameter $\Delta x_e$ is also a measure of the resistance of the membrane to mass transport. As expected, there is a negative covariance between PWP and $\Delta x_e$, i.e., PWP decreases with the increase of $\Delta x_e$. In what follows we have demonstrated $\Delta x_e$ is also a very important parameter to determine the ion permeation through the membrane.

### 3.2. Ion retention and selectivity

We have thoroughly investigated the retention and $Na^+/Mg^{2+}$ ion selectivity of the prepared membranes. Often the $Na^+/Mg^{2+}$ selectivity of the membranes is evaluated from the retention of single salts from

their respective aqueous solution. In this work, we have thoroughly investigated both single and mixed salt retention behavior to understand the role of co-ions and counterions on the ideal and real selectivity of the membranes. The influence of $Cl^-$ as counterion on the $Na^+/Mg^{2+}$ ideal and real selectivities of the membranes is depicted in Fig. 4. Single salt retention tests results show that the $Mg^{2+}$ rejection is larger than the $Na^+$ rejection for all the membranes fabricated at a PIP concentration larger than 0.5% w-w regardless of the TMC concentration. The rejection of $Na^+$ is higher than that of $Mg^{2+}$ for PIP0.125TMC0.15, PIP0.125 TMC0.3 and PIP0.25TMC0.3 membranes. This is also observed in the values of the ideal selectivity being smaller than 1 (Fig. 4c). Therefore, it was expected that PIP0.125TMC0.15, PIP0.125 TMC0.3, and PIP0.25TMC0.3 membranes would allow faster permeation of $Mg^{2+}$ compared to $Na^+$ when the feed solution contains a mixture of NaCl and $MgCl_2$, i.e., a ternary ion mixture of $Na^+$, $Mg^{2+}$ and $Cl^-$. However, that was not the case. The rejection of $Mg^{2+}$ is larger than that of $Na^+$ for all the membranes, highlighting the selective separation of the membranes. The rejection of $Na^+$ even reaches negative values, which generally become more negative as PIP concentration increases.

$Na^+$ and $Mg^{2+}$ ions were almost completely retained (i.e., 100% retention) by the membranes when the feed solutions contained $Na_2SO_4$ and $MgSO_4$ single salts, respectively (Fig. 5a). In most cases, it was observed that $Na^+$ was retained more than $Mg^{2+}$ which is reflected in the $Na^+/Mg^{2+}$ ideal selectivities being smaller than 1. But when the feed solution contained $Na^+/Mg^{2+}/SO_4^{2-}$ ternary ion mixtures, $Mg^{2+}$ was retained more than $Na^+$ and the $Na^+/Mg^{2+}$ real selectivities were larger than 1. From our detailed investigation of retention and selectivities of the membranes using feed solutions containing binary and ternary ion systems, it is evident that the ideal and real $Na^+/Mg^{2+}$ selectivities are substantially different from each other. Contrary to chloride salts, there is not a clear tendency of the effect of PIP and TMC concentrations. Similar to the $Na_2SO_4$ and $MgSO_4$ single salt retention tests, the trend of retention of $Na^+/Mg^{2+}/SO_4^{2-}$ does not exhibit a clear pattern with PIP concentration. Almost all of $Mg^{2+}$ is retained, resulting in nearly 100 % retention. This leads to S values reaching approximately 726 (Fig. 5d). S values increase with PIP concentration and with lower TMC concentration. This trend is similar to the $Na^+/Mg^{2+}/Cl^-$ system. However, the S values (and the ions' retention) for the $Na^+/Mg^{2+}/SO_4^{2-}$ are larger. This is similar to the difference in $Na^+$ and $Mg^{2+}$ retentions between

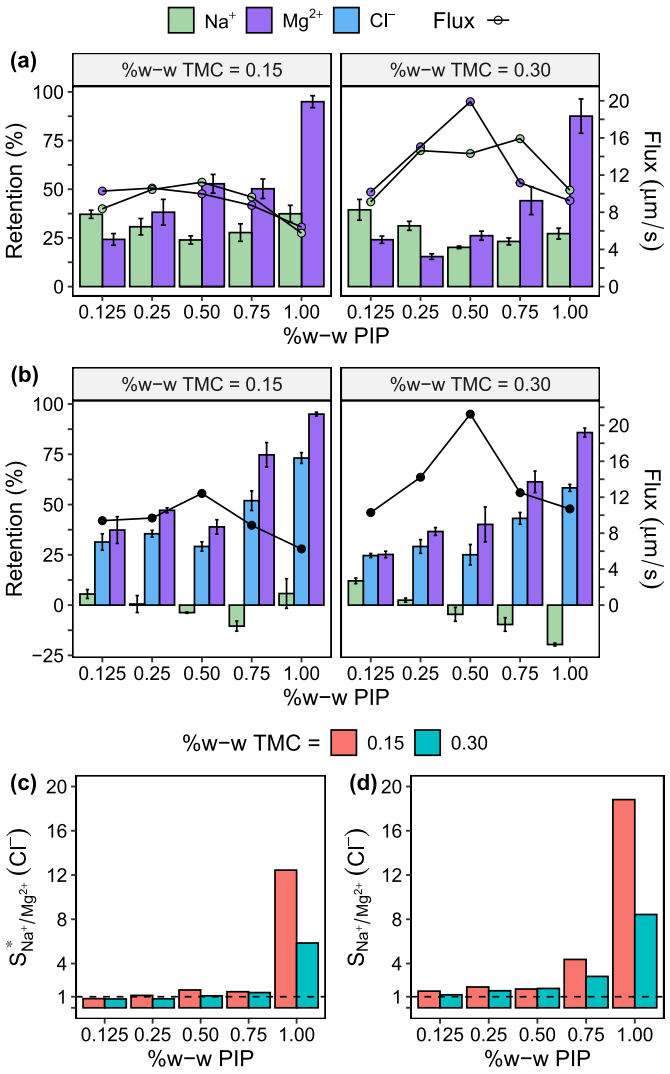



**Fig. 4.** (a) Retentions of $Na^+$ and $Mg^{2+}$ by the fabricated membranes with feed solutions containing single salts, i.e., NaCl and $MgCl_2$, respectively. (b) Retentions of ions from the feed solution containing a mixture of NaCl and $MgCl_2$, i.e., a ternary ion mixture of $Na^+$, $Mg^{2+}$ and $Cl^-$. (c) Ideal selectivities of $Na^+$ over $Mg^{2+}$ (obtained from single salt retention). (d) real selectivity (obtained from mixed salt retention).

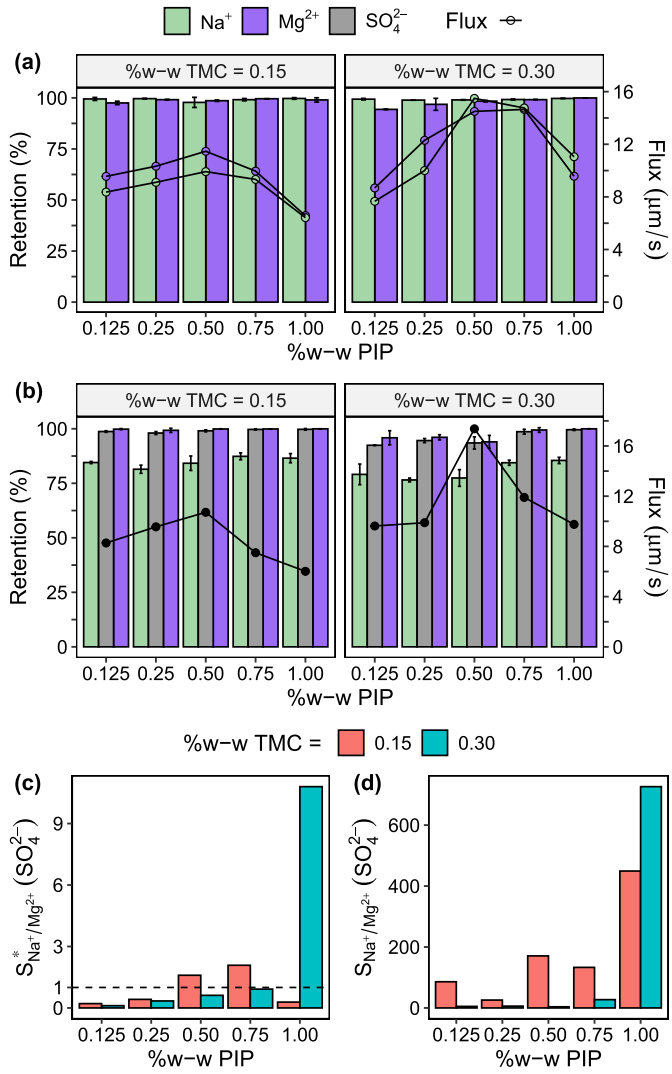



**Fig. 5.** (a) Retentions of $Na^+$ and $Mg^{2+}$ by the membranes from feed solutions containing single salts, i.e., $Na_2SO_4$ and $MgSO_4$, respectively. (b) Retentions of ions from the feed solution containing a mixture of $Na_2SO_4$ and $MgSO_4$, i.e., a ternary ion mixture of $Na^+$, $Mg^{2+}$ and $SO_4^{2-}$. (c) Ideal selectivities of $Na^+$ over $Mg^{2+}$ (obtained from single salt retention). (d) real selectivity (obtained from mixed salt retention).

chloride and sulfate systems in single salt retention tests. Therefore, it is important to investigate the effect of the common anion on ion retention and selectivity values. This is done through the DSPM-DE model, presented in the following section. Moreover, from Figs. 4d and 5d it is evident that the real selectivities of PIP1TMC0.15 and PIP1 TMC0.3 are substantially larger than other membranes for both the $Na^+$/ $Mg^{2+}$/ $Cl^-$ and $Na^+/Mg^{2+}/SO_4^{2-}$ ternary ion systems. From the mass transport modeling, it will also be clear how these two membranes differ from the others.

### 3.3. Mass transport modelling

The retention behavior of the prepared membranes for the feed solution containing the ternary ion mixture $Na^+/Mg^{2+}/Cl^-$ was successfully modelled on the basis of the DSPM-DE model (supporting information). The concentration and electrical potential profiles inside the membranes' active layers were obtained (Fig. 6a). These profiles were discretized (Fig. 6b) and linearized to solve the model (supporting information). However, it was not possible to model the retention behavior of the membranes for the feed solutions containing the ternary ion mixture $Na^+/Mg^{2+}/SO_4^{2-}$(details provided in supporting information). The retention of the ions by membranes is pictured as a combination of three steps: (i) partitioning of the ions at the interface between feed solution and membrane, (ii) ion transport through the membrane, and (iii) partitioning of the ions at the interface between membrane and permeate solution. According to the DSPM-DE model, the ion partitioning at the interfaces occurs as a result of three exclusion mechanisms: (i) steric, (ii) dielectric, and (iii) Donnan (Fig. 6a). The partitioning of ions at the interface between feed solution and the membrane is expressed as [6]:

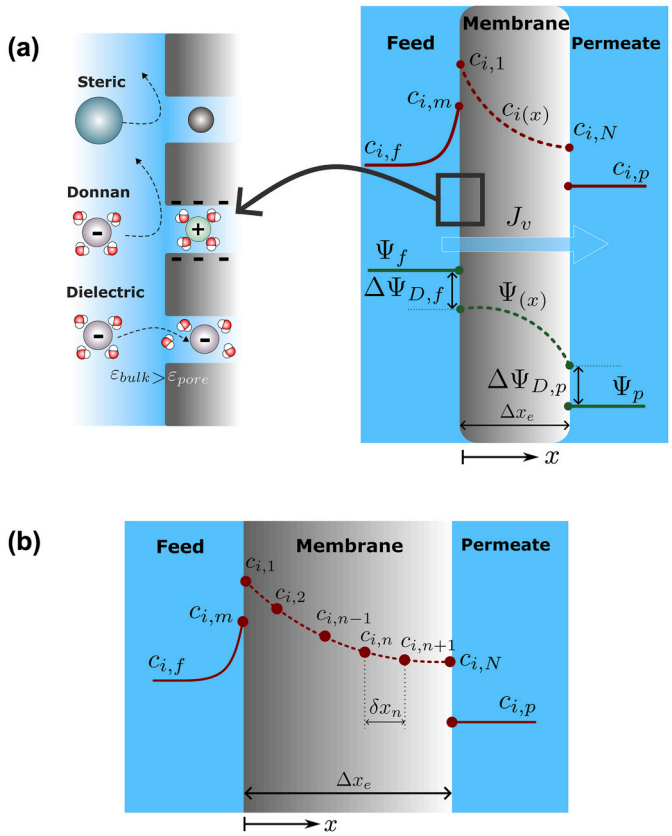



**Fig. 6.** Schematic representations of: (a) the exclusion mechanisms at the pore openings and the theoretical concentration and electrical potential profiles developed across the membrane's active layer during NF operation, and (b) the discretized scheme of such concentration profile.

$$c_{i,1}\gamma_{i,1} = c_{i,m}\gamma_{i,m}\Phi_{S,i}\Phi_{D,i}^{x=0}\Phi_{DE,i} \quad (5)$$

where $c_{i,1}$ is the concentration of ion $i$ at the pore entrance on the feed side; $\gamma_{i,1}$ and $\gamma_{i,m}$ are the activity coefficients of ion $i$ at the pore entrance on the feed side and in the feed-solution/membrane interface, respectively. $\Phi_{S,i}$ is the steric exclusion coefficient, $\Phi_{DE,i}$ is the dielectric exclusion coefficient and $\Phi_{D,i}^{x=0}$ is the Donnan exclusion coefficient. The product of these terms (i.e., $\Phi_{S,i}\Phi_{D,i}^{x=0}\Phi_{DE,i}$) is termed as the overall exclusion coefficient. Similarly, the equilibrium correlation at the interface between the membrane's active layer and the permeate side is given by:

$$c_{i,N}\gamma_{i,N} = c_{i,p}\gamma_{i,p}\Phi_{S,i}\Phi_{D,i}^{x=\Delta x_e}\Phi_{DE,i} \quad (6)$$

$\gamma_i$ are computed with Davies equation (supporting information)

In what follows, we thoroughly discuss the individual contributions of steric, dielectric and Donnan exclusion or partitioning of $Na^+$, $Mg^{2+}$ and $Cl^-$ at the feed-solution/membrane interface in the ten membranes prepared in this work.

The steric exclusion coefficient, $\Phi_{S,i}$, represents the probability of an ion entering the pore of the membrane based on its size.

$$\Phi_{S,i} = (1-\lambda_i)^2 \quad (7)$$

$$\lambda_i = \frac{r_i}{r_{pore}} \quad (8)$$

where $r_{pore}$ is the effective radius of the pores of the membrane and $r_i$ is the ionic radius.

The bare ionic radius (also termed as crystal ionic radius) of $Cl^-$ (1.81 Å) > $Na^+$ (0.95 Å) > $Mg^{2+}$ (0.65 Å) [39,40]. Owing to the ion-water affinity, it is essential to take into account the radii of the hydrated ions rather than the bare ions to interpret the mass transport phenomenon. In general, ions with smaller bare ionic radius and higher charge have larger hydrated ionic radius compared to those having larger crystal ionic radius and smaller charge. By convention, Stokes radii are used as input parameters in DSPM-DE models as a measure of the size of the hydrated ions. The Stokes radius of $Mg^{2+}$ (3.47 Å) > $Na^+$ (1.84 Å) > $Cl^-$ (1.21 Å) [39,40]. The Stokes ionic radii are calculated from the limiting ionic equivalent conductance. It essentially means that the mobility of an ion together with its neighboring water molecules (which have the same mobility as the ion) is translated into the size of the hydrated ion. The Stokes ionic radii are often referred to as the radius of a hard sphere where the ion and the neighboring water molecules are considered as a part of the same entity. Therefore, $Mg^{2+}$, $Na^+$, and $Cl^-$ are schematically represented as a purple, green, and blue sphere in Fig. 7, respectively. All of the prepared membranes have $r_{pore}$ larger than the Stokes radius of the 3 ions. Therefore, $\Phi_{S,i}$ of the 3 ions are smaller than 1. In other words, the pore size of the membrane is not small enough to completely exclude the ions as a result of steric hindrance. $Mg^{2+}$ has the lowest value of the steric exclusion coefficient due to its largest Stokes radius among the 3 ions. The $\Phi_{S,i}$ of the 3 ions increase linearly with the increase of pore size as result of the change of PIP and TMC concentration during IP. The slope of the trend line of $\Phi_{S,i}$ vs. $r_{pore}$ plot is the largest for $Mg^{2+}$ followed by $Na^+$ and $Cl^-$ (supporting information Figure SI4). Hence, for the given membranes having $r_{pore}$ in the range of approximately 0.6–0.7 nm the increase in the steric exclusion coefficient of $Mg^{2+}$ (owing to change of pore size) is larger than $Na^+$ and $Cl^-$. $\Phi_{S,i}$ just quantifies how difficult it is for the ions to enter the pores of the membranes owing to the size of the hydrated ions (i.e., solvated ions).

The solvation of an ion in water can be visualized as follows. Water molecules acquire random orientation as a result of thermal motion in bulk water. When an ion is introduced to the bulk water, it exerts an electric field around itself. Water molecules, having permanent dipole

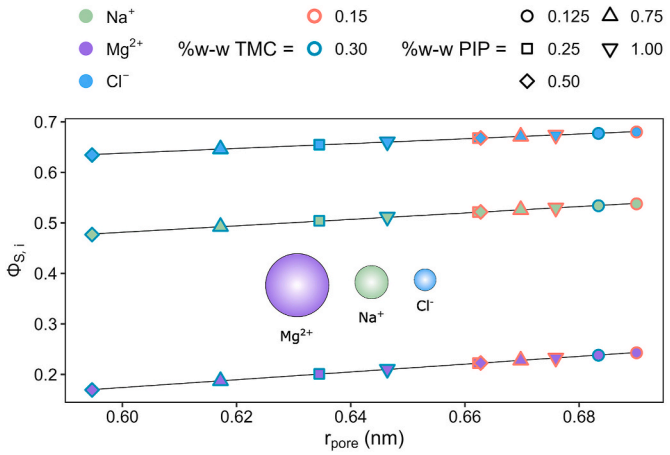



**Fig. 7.** Steric exclusion or partitioning coefficients of $Mg^{2+}$, $Na^{+}$, and $Cl^{-}$ as a function of the effective pore radius, $r_{pore}$, of the fabricated membranes. Each shape of the data points corresponds to a different PIP concentration, and the border color of the data points indicates the TMC concentration (cyan for 0.30 w-w% and orange for 0.15 w-w%).

moments, reorient surrounding the ion in response to the electric field. Consequently, the electrostatic forces between two neighboring ions are largely reduced in an aqueous medium. In other words, water is a strong dielectric medium. The dielectric constant of bulk water (i.e., the relative permittivity) is approximately 80 [6]. The dielectric constant of the water is largely reduced inside the pores of a NF membrane, i.e., the reorientation of water molecules is limited due to spatial confinement. It is difficult for the water molecules inside the pores to solvate an ion compared to the molecules of bulk water. Thus, it is energetically favorable for the ions to stay in the bulk feed solution, which is a region of larger dielectric constant, than the narrow pores. In order to enter the confined region having a lower dielectric constant (i.e., the pores of the membrane), the ions have to overcome a solvation energy barrier. The DSPM-DE model takes into account the exclusion of ions at the membrane feed solution interfase, originating from this phenomenon, using the dielectric exclusion coefficient $\Phi_{DE,i}$.

$$\Phi_{DE,i} = exp\left(\frac{-\Delta W_i}{k_B T}\right) \tag{9}$$

where $\Delta W_i$ is the solvation energy barrier, $k_B$ the Boltzmann constant, and $T$ the temperature. $\Delta W_i$ is computed through the Born formula with the values of the dielectric constant inside the pores, $\varepsilon_{pore}$, and in the bulk solution, $\varepsilon_{bulk}$:

$$\Delta W_i = \frac{z_i^2 e_0^2}{8\pi\varepsilon_0 r_i}\left(\frac{1}{\varepsilon_{pore}} - \frac{1}{\varepsilon_{bulk}}\right) \tag{10}$$

where $z_i$ is the ion valence, $e_0$ is the electronic charge, and $\varepsilon_0$ the permittivity of vacuum.

The water molecules have reduced freedom inside the pores compared to the bulk, leading to smaller value of $\varepsilon_{pore}$ compared to $\varepsilon_{bulk}$. There is ongoing debate regarding the underlying physical mechanism responsible for the reduced dielectric constant of water in confinement. Varghese et al. [41] found that the water molecules in the immediate vicinity of the solid surface (i.e., pore walls) have significantly low rotational diffusion which leads to a low dielectric constant. It is obvious that for very small $r_{pore}$ the dielectric constant of the water molecules near the pore walls will dictate the overall value of $\varepsilon_{pore}$. In this work, we assume that the reduction in dielectric constant of water in the pore (compared to bulk water) is caused by a single layer of water molecules next to the pore wall (schematically represented in Fig. 8a) [6]. The thickness of this layer is equal to the diameter of a single water molecule, i.e., $d_{H_2O} = 0.28$ nm [42]. The dielectric constant of water of this layer is

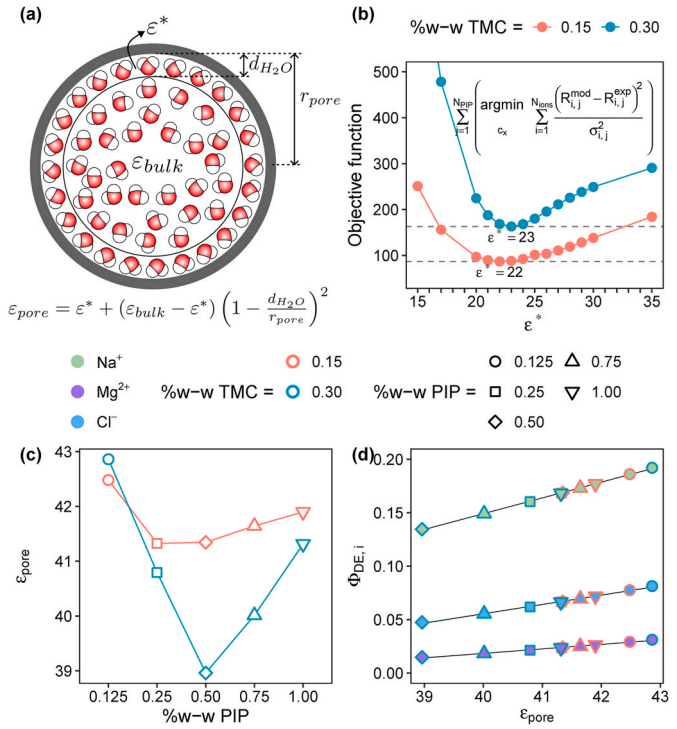



**Fig. 8.** (a) Schematic representation of water molecules in confined pores of the membrane. (b) Determination of $\varepsilon^*$ for the membranes prepared using TMC concentration 0.15 and 0.3 w-w%, respectively. (c) Variation of $\varepsilon_{pore}$ with monomer concentration. (d) Variation of $\Phi_{DE,i}$ of $Na^{+}$, $Mg^{2+}$, and $Cl^{-}$ with $\varepsilon_{pore}$. For (c) and (d), each shape of the data points corresponds to a different PIP concentration, and the border color of the data points indicates the TMC concentration (cyan for 0.30 w-w% and orange for 0.15 w-w%).

$\varepsilon^*$. The $\varepsilon_{pore}$ is computed using a radial geometry-based formula [6].

$$\varepsilon_{pore} = \varepsilon^* + (\varepsilon_{bulk} - \varepsilon^*)\left(1 - \frac{d_{H_2O}}{r_{pore}}\right)^2 \tag{11}$$

It is a prerequisite to determine $r_{pore}$ and $\varepsilon^*$ in order to use this relation to compute $\varepsilon_{pore}$. While $r_{pore}$ is determined from retention of PEG 200, there is no empirical method to determine $\varepsilon^*$. Bowen et al. [42] assumed that $\varepsilon^*$ may reach the high-frequency limit of the dielectric constant of water. Therefore, they used $\varepsilon^* = 6$ to calculate $\varepsilon_{pore}$ of the Desal-DK membrane. Hussain et al. [43] determined the experimental rejection of NaCl at the isoelectric point and determined $\varepsilon^*$ by fitting the experimental rejection data with modelled rejection data where steric and dielectric exclusion was considered to be the only exclusion parameters. They reported for Desal-HL membrane $\varepsilon^* = 34$ (when Stokes radius is used). The value of $\varepsilon^*$ originates from the affinity of water molecules with the pore walls [6]. Hence, the nature and content of the functional groups at the pore walls are likely to play a dictating role for the $\varepsilon^*$ of a given membrane. Similar to our previous work [5], we assumed the value of $\varepsilon^*$ changes only with the TMC concentration. Double minimization with the following objective function was used to determine $\varepsilon^*$ and $c_x$ simultaneously.

$$f_{min} = \underset{\varepsilon^*}{\text{argmin}} \sum_{j=1}^{N_{PIP}} \left( \underset{c_x}{\text{argmin}} \sum_{i=1}^{N_{ions}} \frac{\left(R_{i,j}^{mod} - R_{i,j}^{exp}\right)^2}{\sigma_{i,j}^2} \right) \tag{12}$$

The subscript $i$ cycles through all ionic species and $j$ through all PIP concentrations for the same TMC concentration. $R_{i,j}^{mod}$ is the simulated retention and $R_{i,j}^{exp}$ is the average experimental rejection value of at least 3 replications for the membranes fabricated at every PIP concentration. To bias the minimizations towards more experimentally confident

values, $\sigma_{i,j}^2$ was computed with the unbiased variance equation [44]. A series of $\varepsilon^*$ values were tested to find preliminary minima of $c_x$ for each PIP concentration. Then, the optimized $\varepsilon^*$ value was found by minimizing the sum of the previously minimized differences across all membranes prepared at the same TMC concentration. The optimized values of $\varepsilon^*$ for the membranes prepared using TMC concentrations 0.15 and 0.3 w-w% are 22 and 23, respectively (Fig. 8b). As the obtained $\varepsilon^*$ values are rather close to each other and $\varepsilon_{bulk}$ is constant (i.e., $\varepsilon_{bulk} = 80$), the variation of $\varepsilon_{pore}$ due to the change of monomer concentration originates mostly from the variation of $r_{pore}$ (equation (11)). The change in PIP concentration between 0.125 and 1.0 w-w% brought about a larger variation of $\varepsilon_{pore}$ for the membranes prepared using a TMC concentration of 0.3 w-w% compared to 0.15 w-w%. $Mg^{2+}$ has smaller $\Phi_{DE,i}$ compared to $Na^+$. Owing to the higher valency, $Mg^{2+}$ experiences a larger solvation energy barrier to enter the pores of the membrane compared to $Na^+$. Fig. 8d shows $\Phi_{DE,i}$ of $Na^+$, $Mg^{2+}$ and $Cl^-$ scale linearly with $\varepsilon_{pore}$. A rather perfect linear relationship is observed between $\Phi_{DE,i}$ and $\varepsilon_{pore}$ for the values of $\varepsilon_{pore}$ in the range 39–43 having $R^2$ values between 0.99 and 1.00 (supporting information Figure SI5). However, equations (9) and (10) imply that $\Phi_{DE,i}$ increases exponentially with $\varepsilon_{pore}$. Thus, the linear relationships (i.e., the equations of the trend lines presented in Fig. 8d and Figure SI5) would not be valid for all values of $\varepsilon_{pore}$. PIP0.5TMC0.3 has the smallest $\varepsilon_{pore}$ value (≈39) while PIP.125TMC0.3 has the highest $\varepsilon_{pore}$ value (≈43) among the prepared membranes. The difference in $\Phi_{DE,i}$ for $Na^+$ and $Mg^{2+}$ is the lowest for PIP0.5TMC0.3, having $\varepsilon_{pore}$ value of 39, and the highest for PIP.125TMC0.3, having $\varepsilon_{pore}$ value of 43 (Fig. 8d). Although the increase of $\varepsilon_{pore}$ leads to a weaker dielectric exclusion (larger $\Phi_{DE,i}$ values), the selective dielectric partitioning between $Na^+$ and $Mg^{2+}$ (i.e., higher tendency of $Na^+$ to enter the pore of the membrane compared to $Mg^{2+}$) linearly increases with $\varepsilon_{pore}$ in the range of 39–43, which corresponds to an increase of $r_{pore}$ from 0.7 to 0.8 nm. That is the main implication of Fig. 8d which, to the best of our knowledge, has never been reported before.

Fig. 9 shows the change in the effective charge density, $c_x$, of the membranes with the concentration of the monomers. For both TMC concentrations of 0.15 and 0.30 w-w%, the membranes prepared using 0.125 w-w% PIP displayed the most negative $c_x$. The negative $c_x$ decreased gradually with the increase in PIP concentration. The membranes prepared using 1 w-w% PIP concentration showed positive $c_x$. The DSPM-DE model ensures that the electroneutrality condition is fulfilled in the feed solution, permeate solution, and membrane, respectively. In the fluid phases, i.e., the feed and the permeate solution, the summation of the products of valences and the concentrations of all the ions is zero.

$$0 = \sum_{i=1}^{N_c} z_i c_{i,m} \tag{13}$$

$$0 = \sum_{i=1}^{N_c} z_i c_{i,p} \tag{14}$$

However, inside the membrane's active layer, the electroneutrality condition will only be fulfilled if the sum of charge of the permeating ions is equal and opposite to $c_x$ of the membrane.

$$-c_x = \sum_{i=1}^{N_c} z_i c_i \tag{15}$$

It essentially means that an unequal distribution of ions will occur at the interface between the feed solution and the membrane due to the interaction of the ions with the fixed charge of the membrane. The resulting potential from this unequal distribution of ions is termed as the Donnan potential ($\Delta\Psi_D$), which attracts the counterions (with respect to the fixed charge of the membrane) towards the membrane and repels the coions. The Donnan exclusion coefficient $\Phi_{D,i}^{x=0}$ at the feed-solution/membrane interface is expressed as:

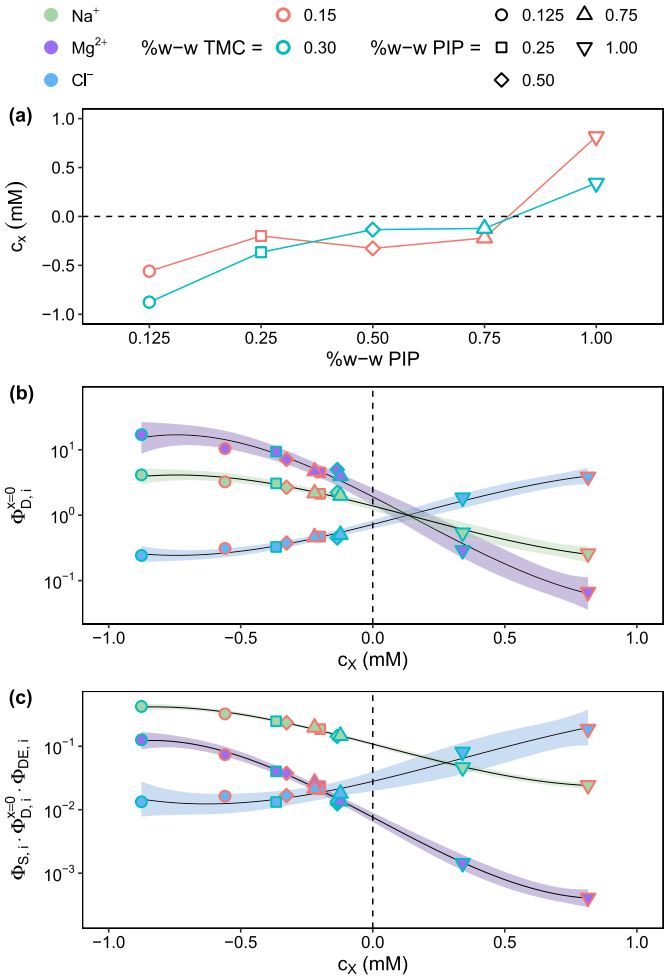



**Fig. 9.** For the ternary ion mixture of $Na^+$, $Mg^{2+}$, and $Cl^-$, (a) $c_x$ as a function of the PIP and TMC concentrations during IP, individual exclusion or partitioning coefficients as a function of $c_x$: (b) Donnan, and (c) overall. The trend lines are third-order polynomials (details in supporting information). Each shape of the data points corresponds to a different PIP concentration, and the border color of the data points indicates the TMC concentration (cyan for 0.30 w-w% and orange for 0.15 w-w%).

$$\Phi_{D,i}^{x=0} = exp\left(\frac{-z_i F}{RT}\Delta\Psi_{D,f}\right) \tag{16}$$

where $\Delta\Psi_{D,f}$ is the Donnan potential at the feed-solution/membrane interface, $R$ is the ideal gas constant, and $T$ the temperature.

As $c_x$ ranges from approximately −0.9 to +0.8 mM, we could examine the influence of a gradual change of $c_x$ on $\Phi_{D,i}^{x=0}$. A detailed investigation revealed that for $Na^+$, $Mg^{2+}$ and $Cl^-$ the $log\left(\Phi_{D,i}^{x=0}\right)$ is a cubic function of $c_x$ (supporting information Figure SI6). To the best of our knowledge, this relationship has never been reported before. $\Phi_{D,i}^{x=0}$ of $Cl^-$ increases gradually as the value of $c_x$ changes from −0.9 to +0.8. A wonderful demonstration of the change of $\Phi_{D,i}^{x=0}$ for monovalent and divalent cation (i.e., $Na^+$ and $Mg^{2+}$) owing to the change of $c_x$ between −0.9 and + 0.8 mM is depicted in Fig. 9b. The $\Phi_{D,i}^{x=0}$ value of $Mg^{2+}$ is larger than that of $Na^+$ in case of PIP0.125TMC0.3 with $c_x = -0.9$ mM, that is, the exclusion of $Mg^{2+}$ owing to the Donnan potential is lower than that of $Na^+$. As $c_x$ become less negative, the difference between the $\Phi_{D,i}^{x=0}$ values of $Mg^{2+}$ and $Na^+$ also decreases. Eventually, the $\Phi_{D,i}^{x=0}$ values of $Mg^{2+}$ and $Na^+$ reverses, i.e., the exclusion of $Mg^{2+}$ due to

Donnan potential becomes higher than that of $Na^+$ for PIP1TMC0.15 and PIP1TMC0.3 which have positive $c_x$.

The overall exclusion coefficients of $Na^+$, $Mg^{2+}$, and $Cl^-$ are largely dictated by $\Phi_{D,i}^{x=0}$ (Fig. 9c). The overall exclusion coefficient is a cubic function of $c_x$ as well (supporting information Figure SI7). An overall higher exclusion of $Mg^{2+}$ compared to $Na^+$ is observed for all the prepared membranes at the feed-solution/membrane interface. However, it is evident that, as the value of $c_x$ gradually changes from −0.9 to 0.8 mM (i.e., the overall negative charge decreases and eventually the charge becomes positive), the selective partitioning between $Na^+$ and $Mg^{2+}$ at the interface between the feed solution and membrane increases. PIP1TMC0.15 displays the highest selective partitioning of $Mg^{2+}$ over $Na^+$ at the interface. It is noteworthy that PIP1TMC0.15 not only has the most positive $c_x$, but also the highest real selectivity of $Na^+$ over $Mg^{2+}$ among the membranes for the ternary ion mixture of $Na^+$, $Mg^{2+}$, and $Cl^-$ (Fig. 4d).

In a dead-end filtration mode, the molar flux of an ion through the membrane in steady state is the product of the concentration of the ion in the permeate side, $c_{i,p}$ , and the solution flux, $J_v$. The DSPM-DE model allows us to gain insight into the mechanism of mass transport by individually examining the advective, diffusive and electromigrative contributions to the molar flux of every ion of the feed solution.

$$J_i = J_v c_{i,p} = J_{i,adv} + J_{i,diff} + J_{i,elec} \tag{17}$$

While $J_i$ is a result of the applied pressure gradient (i.e., transmembrane pressure), $J_{i,adv}$ , $J_{i,diff}$, and $J_{i,elec}$ show us the contributions driven by the solvent flow, the ion concentration gradient, and electric potential gradient across the membrane, respectively.

$$J_{i,adv} = K_{i,a} c_i J_v \tag{18}$$

$$J_{i,diff} = -K_{i,d} D_{i,\infty} \frac{dc_i}{dx} \tag{19}$$

$$J_{i,elec} = -\frac{z_i F c_i K_{i,d} D_{i,\infty}}{RT} \frac{d\Psi}{dx} \tag{20}$$

where $K_{i,a}$ and $K_{i,d}$ are the hindrance factors of advection and diffusion, respectively. $D_{i,\infty}$ is the diffusion coefficient in the bulk, $c_i$ is the concentration of ion $i$ inside the membrane's active layer. Details of the computation of the contributions to molar flux are described in the supporting information.

As equation (18) shows, the advective flux $(J_{i,adv})$ is a function of concentration of each species in the membrane $(c_i)$ and the solution flux $(J_v)$. It is clear from the discussion in the previous section that the overall exclusion coefficient at the feed-solution/membrane interface determines the concentration of each ion entering the membrane. Figs. 9c and 10a show, when plotted against $c_x$, the trend of $J_{i,adv}$ of the three ions through the prepared membranes has some similarity to the trend of overall exclusion coefficients (i.e., $\Phi_{S,i}\Phi_{D,i}^{x=0}\Phi_{DE,i}$). As the value of $c_x$ changes from −0.9 to 0.8, $J_{i,adv}$ of $Cl^-$ increases while those of $Na^+$ and $Mg^{2+}$ decrease as a result of the overall exclusion coefficients. However, $J_v$ is not a function of $c_x$ rather it is a function of $\Delta x_e$ (supporting information Figure SI8). $J_{i,adv}$ of $Mg^{2+}$ and $Cl^-$ follows a cubic function of $c_x$ with $R^2$ values of 0.98 and 0.96, respectively (supporting information Figure SI9). In the case of $Na^+$, the cubic function trendline is not such a good fit with an $R^2$ value of 0.89. It is noteworthy that for all the negative membranes (i.e., for 8 of the 10 prepared membranes) $Na^+$ is less excluded at the feed-solution/membrane interface compared to $Mg^{2+}$ and $Cl^-$(Fig. 9c). Since higher amounts of $Na^+$ enter the negative membranes, $J_v$ has a stronger influence on determining $J_{i,adv}$ of $Na^+$ compared to $Mg^{2+}$ and $Cl^-$ in these membranes. As the solution flux is not a function of $c_x$, $J_{i,adv}$ tends to deviate from the cubic relationship with $c_x$.

The electromigrative $(J_{i,elec})$ and diffusive fluxes $(J_{i,diff})$ for the three ions are plotted in Fig. 10b and c, respectively. $J_{i,adv}$, $J_{i,diff}$ and $J_{i,elec}$ of

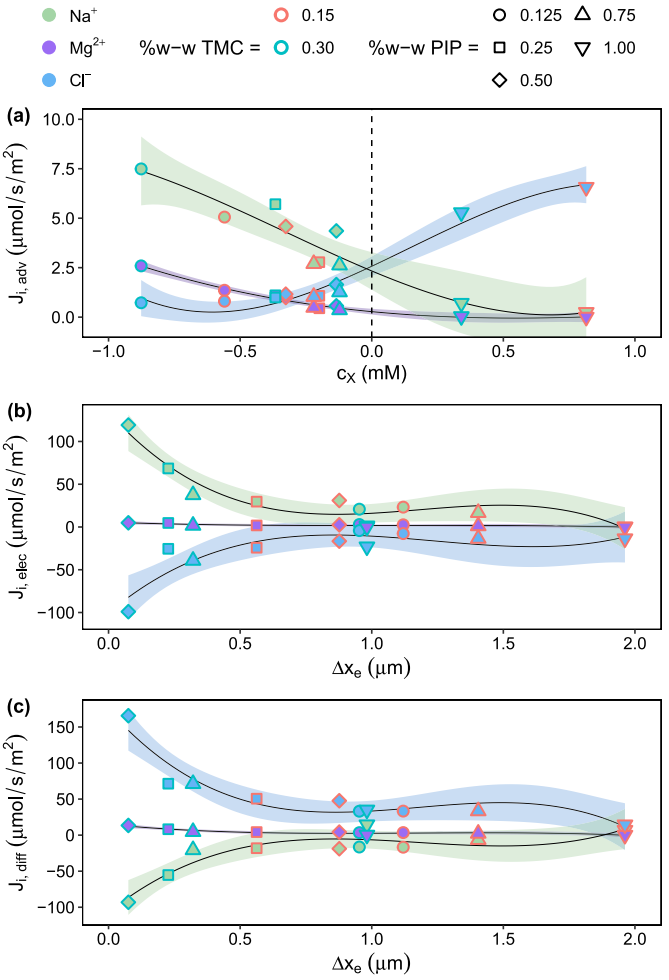



**Fig. 10.** Transmembrane fluxes of the ternary ion mixture of $Na^+$, $Mg^{2+}$, and $Cl^-$ for the fabricated membranes: (a) advective as a function of $c_x$, (b) electromigrative, and (c) diffusive as a function of $\Delta x_e$. The trend lines are third-order polynomials (details in supporting information). Each shape of the data points corresponds to a different PIP concentration, and the border color of the data points indicates the TMC concentration (cyan for 0.30 w-w% and orange for 0.15 w-w%).

$Mg^{2+}$ are positive for all the prepared membranes. It implies that the advective, diffusive, and electromigrative contributions to molar flux of $Mg^{2+}$ act always from the feed toward the permeate side. In the case of $Cl^-$, $J_{i,diff}$ is positive while $J_{i,elec}$ is negative for all the membranes. On the other hand, for $Na^+$, $J_{i,diff}$ is negative for 8 of the 10 prepared membranes and $J_{i,elec}$ is always positive. $Na^+$ has positive $J_{i,diff}$ only in the case of PIP1TMC0.15 and PIP1TMC0.3.

The concentration gradient is the driving force of the diffusive flux. Thus, $J_{i,diff}$ being larger in absolute value for thinner membranes stems from the correlation between the concentration gradients with $\Delta x_e$ (supporting information Figure SI15). It is evident from Fig. 10b and c that the trend of $J_{i,elec}$ and $J_{i,diff}$ as a function of $\Delta x_e$ (i.e., the thickness-to-porosity ratio) are mirror images of each other in case of $Na^+$ and $Cl^-$. These observations provide unprecedented insight into the mechanisms of ion transport from the feed to the permeate side of the membranes.

Among the three ions, $Cl^-$ has the highest mobility (i.e., largest infinite dilution diffusion coefficient, $D_{i,\infty}$, and smallest Stokes radius) which is the main factor responsible for $Cl^-$ having larger absolute values of diffusive flux $(J_{i,diff})$, compared to $Na^+$ and $Mg^{2+}$. For $Cl^-$, large positive $J_{i,diff}$ is counterbalanced by negative electromigrative flux $(J_{i,elec})$ as shown in Fig. 10b and c. It means that the spontaneously arising electric fields develop to hinder $Cl^-$ diffusive transport to reach

electroneutrality condition on the permeate side. This condition is also translated into the zero-current condition within the membrane's active layer ($\Sigma z_i J_i = 0$). Diffusion, undoubtedly, originates from concentration gradients, which are bound by electroneutrality condition within the membrane's active layer (supporting information). But these observations intrigued us to investigate the covariance of $J_{i,diff}$ and the spontaneous electric fields that arise in the membranes $\left(-\frac{d\Psi}{dx}\right)$ (supporting information Figure SI13). A positive covariance was observed between $J_{i,diff}$ and $-\frac{d\Psi}{dx}$ in case of $Mg^{2+}$ and $Cl^-$. However, in the case of $Na^+$, the covariance is negative. Simultaneously, these electric fields drive positive electromigrative transport of cations in all the membranes. The difference between the electromigrative fluxes of $Na^+$ and $Mg^{2+}$ results mainly from their mobility and concentration inside the membrane's active layer. Both are smaller for $Mg^{2+}$ because of the smaller diffusion coefficient and its stronger overall partitioning compared to those of $Na^+$ (Fig. 9c)

Fig. 11 presents how these contributions affect the total molar transport ($J_i$) of ions from the feed to the permeate solutions. For the three ions, $J_i$ follows a cubic relationship with $\Delta x_e$ similar to the diffusive $(J_{i,diff})$ and electromigrative $(J_{i,elec})$ contributions (supporting information Figures SI10-SI12). This is a result of $J_{i,diff}$ and $J_{i,elec}$ being the largest contributions to $J_i$ as observed in Fig. 11c–e. The absolute values of the relative contributions of $J_{i,diff}$ and $J_{i,elec}$, presented in Fig. 11c and d, are larger than 1 for $Cl^-$ and $Na^+$. For $Cl^-$, $J_i$ is smaller than $J_{i,diff}$, due to the negative $J_{i,elec}$ acting in the opposite direction (from the permeate to the feed side). As a result, $J_{Cl^-,diff}/J_{Cl^-}$ and $J_{Cl^-,elec}/J_{Cl^-}$ values are larger than 1 and negative, respectively. In the case of $Mg^{2+}$, $J_{Mg^{2+},diff}/J_{Mg^{2+}}$ is smaller than 1 for all the membranes. The largest $J_{Mg^{2+},diff}/J_{Mg^{2+}}$ value corresponds to the positively-charged membranes PIP1TMC0.15 and PIP1TMC0.3 owing to the stronger overall exclusion experienced by $Mg^{2+}$, i.e., smaller overall exclusion coefficient (Fig. 9c). In other words, compared to the negatively-charged membranes, the concentration of $Mg^{2+}$ within the positively-charged membranes' active layers is largely decreased, resulting in smaller $J_{i,adv}$ and $J_{i,elec}$. Concerning $Na^+$, $J_{Na^+,elec}/J_{Na^+}$ is larger than 1 for all the negatively-charged membranes. It means that $J_{Na^+,elec}$ is larger than $J_{Na^+}$ because of the

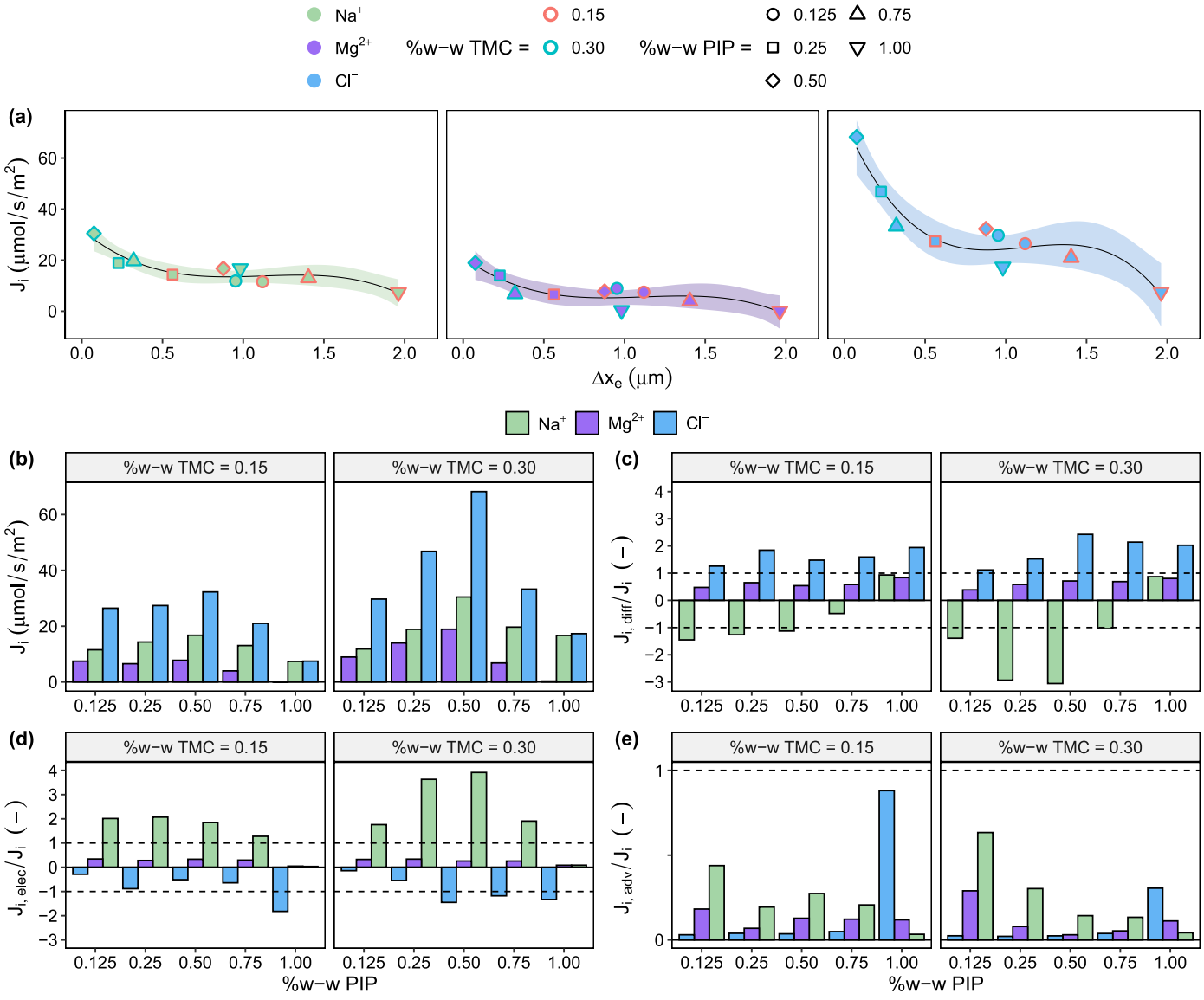



**Fig. 11.** Total transmembrane molar fluxes of the ternary ion mixture of $Na^+$, $Mg^{2+}$, and $Cl^-$ for the fabricated membranes as a function of (a) $\Delta x_e$ and (b) monomer concentrations. Ratios of the (c) diffusive, (c) electromigrative, and (d) advective contributions to the total transmembrane molar fluxes. The trend lines in (a) are third-order polynomials (details in supporting information). For (a), each shape of the data points corresponds to a different PIP concentration, and the border color of the data points indicates the TMC concentration (cyan for 0.30 w-w% and orange for 0.15 w-w%).

negative $J_{Na^+,diff}$. This did not hold for the positively charged PIP1TMC0.15 and PIP1TMC0.3 membranes, which render positive $J_{Na^+,diff}$. For this reason, $J_{Na^+}$ behaves differently between the negatively- and positively-charged membranes.

For the negatively-charged membranes, positive electromigrative flux of $Na^+$ $\left(J_{Na^+,elec}\right)$ accelerates its transport across the active layer from the feed side to the permeate side. The large total flux of $Na^+$ $(J_{Na^+})$, resulting from its electromigrative contribution, is the reason for its retention reaching negative values (Fig. 4b). As mentioned before, the spontaneously-arising electric field resulted from the large diffusive fluxes of $Cl^-$ which varies according to $\Delta x_e$. Interestingly, the highest selectivity of $Na^+/Mg^{2+}$ is not achieved by the membranes exhibiting the smallest values of $\Delta x_e$ which is PIP0.5TMC0.3. This is a result of the effect PIP and TMC concentrations have on $c_x$ and $\Delta x_e$. As the PIP concentration increases (from PIP0.25 for TMC0.15 and from PIP0.5 for the TMC0.3 membranes) and the TMC concentration decreases, $J_{Na^+,diff}$ and $J_{Mg^{2+},diff}$ decrease in absolute value due to the increase in $\Delta x_e$. Similarly, $c_x$ becomes less negative, increasing the difference in overall exclusion of $Na^+$ and $Mg^{2+}$ (Fig. 9c). This hinders less the Na $^+$ concentration than $Mg^{2+}$ inside the membrane's active layer as PIP concentration increases. Consequently, the positive $J_{Na^+,elec}$ decreases less than $J_{Mg^{2+},elec}$ with increasing PIP concentration. These result in a higher decrease in $J_{Mg^{2+}}$ than in $J_{Na^+}$. Accordingly, the highest selectivity values are achieved by PIP0.75TMC0.15 and PIP0.75TMC0.3 among the negatively-charged membranes.

Similarly, the positively-charged membranes PIP1TMC0.15 and PIP1TMC0.3 achieve the highest $Na^+/Mg^{2+}$ selectivity among all the prepared membranes (Fig. 4d). $Na^+$ and $Mg^{2+}$ concentration inside their active layers are smaller compared to the negatively-charged membranes as a result of Donnan exclusion. In consequence, their electromigrative and advective fluxes ($J_{i,elec}$ and $J_{i,adv}$) drop, as expressed in Equations (18) and (20). However, their diffusive fluxes $\left(J_{i,diff}\right)$ take over their overall transmembrane transport from the feed to the permeate side. This is observed through the values of $J_{Na^+,diff}/\ J_{Na^+}$ and $J_{Mg^{2+},diff}/J_{Mg^{2+}}$ being close to 1 for both PIP1TMC0.15 and PIP1TMC0.3 membranes. A careful inspection of Fig. 11b shows that their total transmembrane fluxes of $Na^+$ and $Cl^-$ ($J_{Na^+}$ and $J_{Cl^-}$) are similar for both PIP1TMC0.15 and PIP1TMC0.3 membranes. This similarity is necessary to attain zero-current conditions $(\Sigma z_i J_i = 0)$ because $J_{Mg^{2+}}$ is almost negligible. Since $Mg^{2+}$ is excluded the most by these two membranes (Fig. 9c), the concentration profiles of $Cl^-$ and $Na^+$ are parallel (supporting information Figure SI14) to reach electroneutrality conditions within the membranes' active layers. This indicates that their concentration gradients are coupled, suggesting that $J_{Na^+}$ is determined by $J_{Cl^-,diff}$. Consequently, membranes PIP1TMC0.15 and PIP1TMC0.30 attain the largest values of $Na^+/Mg^{2+}$ selectivity among all the fabricated membranes. Considering all these factors, between the two positively-charged membranes, PIP1TMC0.15 achieves the largest selectivity due to its stronger Donnan exclusion owing to its largest positive $c_x$ value (Fig. 9a).

## 4. Conclusions

In this study, we assessed the effect of the concentrations of PIP and TMC during IP on the $Na^+/Mg^{2+}$ selective separation performance of TFC membranes having a PA selective layer, based on the DSPM-DE model. The effect of PIP and TMC concentrations on the $Na^+/\ Mg^{2+}$ separation capabilities of the membranes was particularly dictated by $\Delta x_e$ and $c_x$.

Our findings corroborate that $\Delta x_e$, comprising the porosity, tortuosity, actual thickness (observed by SEM), and roughness of the PA layer (obtained from AFM), is a measure of the mass transport resistance of the membranes. PWP tests revealed that the roughness of the PA layer plays a dominant role in determining the PWP values of the fabricated membranes. Although the actual thickness of the PA layer contributes to the overall resistance, it is less significant than the roughness. Additionally, $\Delta x_e$ was found to correspond with the magnitude of the diffusive fluxes. Interestingly, the diffusion of the most mobile and smallest ion, $Cl^-$, dictated the magnitude of the spontaneously generated electric field. To attain zero current conditions, the generated electric field impaired $Cl^-$ transport as the primary effect and accelerated $Na^+$ and $Mg^{2+}$ transport through their electromigrative fluxes. As a result, $\Delta x_e$ played a key role in determining the transmembrane ionic fluxes.

The difference in the transmembrane fluxes between $Na^+$ and $Mg^{2+}$ primarily arose from the different impact of PIP and TMC concentrations on both diffusive and electromigrative fluxes. The separation between $Na^+$ and $Mg^{2+}$ was mainly impacted by $c_x$, which governs the Donnan exclusion coefficients at the pore entrance. In general, the $c_x$ values became more positive or less negative with higher PIP and lower TMC concentrations. Specifically, the positively charged membranes achieved the highest $Na^+/Mg^{2+}$ selectivity among all the prepared membranes. The concentrations of $Na^+$ and $Mg^{2+}$ inside the active layers of the positively charged membranes were lower compared to the negatively charged membranes. Consequently, their electromigrative and advective fluxes decreased, but their diffusive fluxes dominated the overall transmembrane transport from the feed to the permeate side. The coupling of $Cl^-$ and $Na^+$ diffusion was necessary to attain zero current conditions. The experimental retention results confirmed that higher PIP and lower TMC concentrations resulted in larger ideal and real $Na^+/Mg^{2+}$ selectivity. Accordingly, the most positively-charged membrane, PIP1TM0.15, demonstrated the highest $Na^+/Mg^{2+}$ real selectivity.

## CRediT authorship contribution statement

**Nicolás Cevallos-Cueva:** Writing – review & editing, Writing – original draft, Validation, Software, Methodology, Investigation, Formal analysis, Data curation, Conceptualization. **Md. Mushfequr Rahman:** Writing – review & editing, Writing – original draft, Visualization, Supervision, Resources, Funding acquisition, Formal analysis, Conceptualization. **Hluf Hailu Kinfu:** Writing – review & editing, Methodology. **Volker Abetz:** Writing – review & editing, Supervision.

## Funding

This work was funded by the Hereon-I$^2$B-Project NanoMem.

## Declaration of competing interest

The authors declare that they have no known competing financial interests or personal relationships that could have appeared to influence the work reported in this paper.

## Acknowledgments

The authors would like to acknowledge Maren Brinkmann for the PEG analysis in GPC, Juliana Clodt and Barbara Bajer for fabricating the polyacrylonitrile support, Erik Schneider for the SEM analysis, Evgeni Sperling for the AFM analysis, and Jan Pohlmann for setting up the flux and retention measurement facilities.

## Nomenclature

| Variable | Description | Units |
|---|---|---|
| $A$ | temperature dependent correction factor for the activity coefficient | (−) |
| $A_{mb}$ | effective membrane area for filtration experiments | $m^2$ |
| $c_{i,1}$ | concentration of ion $i$ at the pore entrance on the feed side | $mol/m^3$ |
| $c_{i,f}$ | concentration of ion $i$ in the feed solution | $mol/m^3$ |
| $c_{i,N}$ | concentration of ion $i$ at the pore entrance on the permeate side | $mol/m^3$ |
| $c_{i,p}$ | concentration of ion $i$ in the permeate | $mol/m^3$ |
| $c_{i,m}$ | concentration of ion $i$ in the feed-solution/membrane interface | $mol/m^3$ |
| $c_{i,n}$ | concentration of ion $i$ in node $n$ | $mol/m^3$ |
| $c_{i,r}$ | concentration of ion $i$ in the retentate | $mol/m^3$ |
| $c_i$ | concentration of ion $i$ in the membrane active layer | $mol/m^3$ |
| $c_x$ | volumetric membrane charge density | $mol/m^3$ |
| $d_{H_2O}$ | thickness of a single layer of water molecules | m |
| $D_{i,\infty}$ | diffusion coefficient of species $i$ in the bulk | $m^2/s$ |
| $e_0$ | electronic charge | 1.602E-09 C/J |
| $F$ | Faraday constant | 96500 C/mol |
| $J_{i,adv}$ | advective flux of species $i$ | $mol/m^2/s$ |
| $J_{i,diff}$ | diffusive flux of species $i$ | $mol/m^2/s$ |
| $J_{i,elect}$ | electromigrative flux of species $i$ | $mol/m^2/s$ |
| $J_i$ | molar flux of species $i$ | $mol/m^2/s$ |
| $J_v$ | solution flux | m/s |
| $k_{c,i}$ | mass transfer coefficient of species $i$ in the bulk | m/s |
| $k^*_{c,i}$ | corrected mass transfer coefficient | m/s |
| $K_{i,a}$ | hindrance factor of advection | (−) |
| $K_{i,d}$ | hindrance factor of diffusion | (−) |
| $k_B$ | Boltzmann constant | 1.38066E-23 J/K |
| $L$ | characteristic length of the stirrer | 0.03 m |
| $N_A$ | Avogadro number | 6.023E23 |
| $N_c$ | number of ions in the system | (−) |
| NF | nanofiltration | (−) |
| PA | polyamide | (−) |
| PAN | polyacrylonitrile | (−) |
| $Pe_m$ | Peclet number | (−) |
| PIP | piperazine | (−) |
| PWP | pure water permeance | $L/MPa/h/m^2$ |
| RMS | root mean square | (−) |
| $R$ | ideal gas constant | 8.314 J/K/mol |
| $R_{i,real}^{model}$ | theoretical retention of species $i$ at infinite stirring velocity | (−) |
| $R_{i,j}^{exp}$ | experimental retention of ion $i$ | (−) |
| $R_{i,j}^{mod}$ | modelled retention of ion $i$ | (−) |
| $R_{i,obs}$ | observed or experimental retention of species $i$ | (−) |
| $R_{i,real}$ | retention of species $i$ at infinite stirring velocity | (−) |
| $r_{pore}$ | effective pore radius | m |
| $r_i$ | stokes radius of species $i$ | m |
| $Re$ | Reynolds number | (−) |
| $S_{a/b}$ | selectivity (real) from mixed salt retention tests | (−) |
| $S^*_{a/b}$ | selectivity (ideal) from single salt retention tests | (−) |
| $Sc$ | Schmidt number | (−) |
| $Sh$ | Sherwood number | (−) |
| $T$ | temperature | K |
| TFC | Thin film composite membrane | (−) |
| TMC | Trimesoyl Chloride | (−) |
| $x$ | direction across the membrane active layer from the feed towards the permeate side | m |
| $z_i$ | valence of ion $i$ | (−) |
| **Greek** | | |
| $\Delta\Psi_{D,f}$ | Donnan potential at the feed-solution/membrane interface | V |
| $\Delta\Psi_{D,p}$ | Donnan potential at the permeate-solution/membrane interface | V |
| $\Delta m$ | change of mass | g |
| $\Delta t$ | elapsed time | s |
| $\Delta W_i$ | Born solvation energy barrier of ion $i$ | J |
| $\Delta x_e$ | thickness-to-porosity ratio (effective membrane active layer thickness) | m |
| $\delta x_n$ | distance between two consecutive nodes | m |
| $\delta_{H_2O}$ | density of liquid water at room temperature | $g/m^3$ |
| $\gamma_{i,1}$ | activity coefficient of ion $i$ at the pore entrance on the feed side | (−) |
| $\gamma_{i,m}$ | activity coefficient of ion $i$ in the feed-solution/membrane interface | (−) |
| $\gamma_{i,N}$ | activity coefficient of ion $i$ at the pore entrance on the permeate side | (−) |
| $\gamma_{i,p}$ | activity coefficient of ion $i$ in the permeate | (−) |
| $\lambda_i$ | ratio of solute to pore radius | (−) |
| $\omega$ | stirring speed | $s^{-1}$ |
| $\Phi_{D,i}^{x=0}$ | Donnan exclusion coefficient of ion $i$ at the pore entrance on the feed side | (−) |
| $\Phi_{D,i}^{x=\Delta x_e}$ | Donnan exclusion coefficient of ion $i$ at the pore entrance on the permeate side | (−) |
| $\Phi_{DE,i}$ | dielectric exclusion coefficients of ion $i$ | (−) |
| $\Phi_{S,i}$ | steric exclusion coefficient of ion $i$ | (−) |
| $\Psi$ | electrical potential inside the membrane active layer | V |
| $\Psi_n$ | electrical potential in node $n$ | V |

(*continued on next page*)

(*continued*)

| Variable | Description | Units |
|---|---|---|
| $\Psi_f$ | electrical potential in feed solution | V |
| $\Psi_p$ | electrical potential in permeate solution | V |
| $\sigma^2_{i,j}$ | variance | (−) |
| $\varepsilon_{bulk}$ | dielectric constant of water in the bulk | (−) |
| $\varepsilon_{pore}$ | dielectric constant of water inside the pores | (−) |
| $\varepsilon_0$ | permittivity of vacuum | 8.854E-12 F/m |
| $\varepsilon_r$ | dielectric constant of the medium | (−) |
| $\varepsilon^*$ | dielectric constant of a single layer of water molecules next to the pore walls | (−) |
| $\xi$ | electrical potential gradient at the feed-solution/membrane interface | V/m |

## Appendix A. Supplementary data

Supplementary data to this article can be found online at https://doi.org/10.1016/j.memsci.2025.123808.

## Data availability

Data will be made available on request.

## References


[1] Y. Zhao, T. Tong, X. Wang, S. Lin, E.M. Reid, Y. Chen, Differentiating solutes with precise nanofiltration for next generation environmental separations: a review, Environ. Sci. Technol. 55 (2021) 1359–1376, https://doi.org/10.1021/acs.est.0c04593.

[2] K. Wang, X. Wang, B. Januszewski, Y. Liu, D. Li, R. Fu, M. Elimelech, X. Huang, Tailored design of nanofiltration membranes for water treatment based on synthesis–property–performance relationships, Chem. Soc. Rev. 51 (2) (2022) 672–719, https://doi.org/10.1039/D0CS01599G.

[3] L. Zhang, M. Hu, H. Matsuyama, X. Li, Preparation strategies of the positively charged nanofiltration membrane: a comprehensive review, Separ. Purif. Technol. 334 (2024), https://doi.org/10.1016/j.seppur.2023.126011, 126011-126011.

[4] D. Lu, Z. Yao, L. Jiao, M. Waheed, Z. Sun, L. Zhang, Separation mechanism, selectivity enhancement strategies and advanced materials for mono-/multivalent ion-selective nanofiltration membrane, Adv. Membr. 2 (2022) 100032, https://doi.org/10.1016/j.advmem.2022.100032.

[5] N. Cevallos-Cueva, M.M. Rahman, H.H. Kinfu, V. Abetz, Mass transport mechanism of nitrate selective nanofiltration membranes on the basis of the Donnan steric pore model with dielectric exclusion (DSPM-DE), Chem. Eng. J. 493 (2024), https://doi.org/10.1016/j.cej.2024.152775.

[6] R. Wang, S. Lin, Pore model for nanofiltration: history, theoretical framework, key predictions, limitations, and prospects, J. Membr. Sci. 620 (2021) 118809, https://doi.org/10.1016/j.memsci.2020.118809.

[7] A. Szymczyk, C. Labbez, P. Fievet, A. Vidonne, A. Foissy, J. Pagetti, Contribution of convection, diffusion and migration to electrolyte transport through nanofiltration membranes, Adv. Colloid Interface Sci. 103 (2003) 77–94, https://doi.org/10.1016/S0001-8686(02)00094-5.

[8] Z.H. Foo, D. Rehman, A.T. Bouma, S. Monsalvo, J.H. Lienhard, Lithium concentration from salt-lake brine by donnan-enhanced nanofiltration, Environ. Sci. Technol. 57 (15) (2023) 6320–6330, https://doi.org/10.1021/acs.est.2c08584.

[9] Y. Roy, D.M. Warsinger, J.H. Lienhard, Effect of temperature on ion transport in nanofiltration membranes: diffusion, convection and electromigration, Desalination 420 (2017) 241–257, https://doi.org/10.1016/j.desal.2017.07.020.

[10] A. Pérez-González, R. Ibáñez, P. Gómez, A.M. Urtiaga, I. Ortiz, J.A. Irabien, Nanofiltration separation of polyvalent and monovalent anions in desalination brines, J. Membr. Sci. 473 (2015) 16–27, https://doi.org/10.1016/j.memsci.2014.08.045.

[11] M. Micari, D. Diamantidou, B. Heijman, M. Moser, A. Haidari, H. Spanjers, V. Bertsch, Experimental and theoretical characterization of commercial nanofiltration membranes for the treatment of ion exchange spent regenerant, J. Membr. Sci. 606 (2020) 118117, https://doi.org/10.1016/j.memsci.2020.118117.

[12] N. Li, C. Guo, H. Shi, Z. Xu, P. Xu, K. Teng, M. Shan, X. Qian, Analysis of Mg2+/Li+ separation mechanism by charged nanofiltration membranes: visual simulation, Nanotechnology 32 (2021), https://doi.org/10.1088/1361-6528/abc98b.

[13] O. Labban, C. Liu, T.H. Chong, J.H. Lienhard V, Fundamentals of low-pressure nanofiltration: membrane characterization, modeling, and understanding the multi-ionic interactions in water softening, J. Membr. Sci. 521 (2017) 18–32, https://doi.org/10.1016/j.memsci.2016.08.062.

[14] S.B. Rutten, M.A. Junker, L.H. Leal, W.M. de Vos, R.G.H. Lammertink, J. de Grooth, Influence of dominant salts on the removal of trace micropollutants by hollow fiber nanofiltration membranes, J. Membr. Sci. 678 (2023), https://doi.org/10.1016/j.memsci.2023.121625.

[15] S. Bandini, Modelling the mechanism of charge formation in NF membranes: theory and application, J. Membr. Sci. 264 (2005) 75–86, https://doi.org/10.1016/j.memsci.2005.03.055.

[16] S. Déon, P. Dutournié, L. Limousy, P. Bourseau, Transport of salt mixtures through nanofiltration membranes: numerical identification of electric and dielectric contributions, Separ. Purif. Technol. 69 (2009) 225–233, https://doi.org/10.1016/J.SEPPUR.2009.07.022.

[17] S. Déon, A. Escoda, P. Fievet, P. Dutournié, P. Bourseau, How to use a multi-ionic transport model to fully predict rejection of mineral salts by nanofiltration membranes, Chem. Eng. J. 189–190 (2012) 24–31, https://doi.org/10.1016/j.cej.2012.02.014.

[18] A. Escoda, S. Déon, P. Fievet, Assessment of dielectric contribution in the modeling of multi-ionic transport through nanofiltration membranes, J. Membr. Sci. 378 (2011) 214–223, https://doi.org/10.1016/J.MEMSCI.2011.05.004.

[19] S. Castaño Osorio, P.M. Biesheuvel, J.E. Dykstra, E. Virga, Nanofiltration of complex mixtures: the effect of the adsorption of divalent ions on membrane retention, Desalination 527 (2022) 115552, https://doi.org/10.1016/j.desal.2022.115552.

[20] S.S. Wadekar, R.D. Vidic, Influence of active layer on separation potentials of nanofiltration membranes for inorganic ions, Environ. Sci. Technol. 51 (10) (2017) 5658–5665, https://doi.org/10.1021/acs.est.6b05973.

[21] M.A. Junker, E. te Brinke, C.M. Vall Compte, R.G.H. Lammertink, J. de Grooth, W. M. de Vos, Asymmetric polyelectrolyte multilayer nanofiltration membranes: structural characterisation via transport phenomena, J. Membr. Sci. 681 (2023), https://doi.org/10.1016/j.memsci.2023.121718, 121718-121718.

[22] F. Léniz-Pizarro, C. Liu, A. Colburn, I.C. Escobar, D. Bhattacharyya, Positively charged nanofiltration membrane synthesis, transport models, and lanthanides separation, J. Membr. Sci. 620 (2021), https://doi.org/10.1016/j.memsci.2020.118973.

[23] O. Labban, C. Liu, T.H. Chong, J.H. Lienhard, Relating transport modeling to nanofiltration membrane fabrication: navigating the permeability-selectivity trade-off in desalination pretreatment, J. Membr. Sci. 554 (2018) 26–38, https://doi.org/10.1016/j.memsci.2018.02.053.

[24] Zhou Yang, Rui Feng, Zhang Zhang, A review on reverse osmosis and nanofiltration membranes for water purification, Polymers 11 (2019) 1252, https://doi.org/10.3390/polym11081252.

[25] A.L. Ahmad, B.S. Ooi, A.W. Mohammad, J.P. Choudhury, Composite nanofiltration polyamide membrane: a study on the diamine ratio and its performance evaluation, Ind. Eng. Chem. Res. 43 (25) (2004) 8074–8082, https://doi.org/10.1021/ie0497994.

[26] S.H. Huang, C.J. Hsu, D.J. Liaw, C.C. Hu, K.R. Lee, J.Y. Lai, Effect of chemical structures of amines on physicochemical properties of active layers and dehydration of isopropanol through interfacially polymerized thin-film composite membranes, J. Membr. Sci. 307 (2008) 73–81, https://doi.org/10.1016/J.MEMSCI.2007.09.014.

[27] A.L. Ahmad, B.S. Ooi, Properties–performance of thin film composites membrane: study on trimesoyl chloride content and polymerization time, J. Membr. Sci. 255 (2005) 67–77, https://doi.org/10.1016/J.MEMSCI.2005.01.021.

[28] Y.l. Liu, Y.y. Zhao, X.m. Wang, X.h. Wen, X. Huang, Y.F. Xie, Effect of varying piperazine concentration and post-modification on prepared nanofiltration membranes in selectively rejecting organic micropollutants and salts, J. Membr. Sci. 582 (2019) 274–283, https://doi.org/10.1016/j.memsci.2019.04.018.

[29] N.K. Saha, S.V. Joshi, Performance evaluation of thin film composite polyamide nanofiltration membrane with variation in monomer type, J. Membr. Sci. 342 (1–2) (2009) 60–69, https://doi.org/10.1016/j.memsci.2009.06.025.

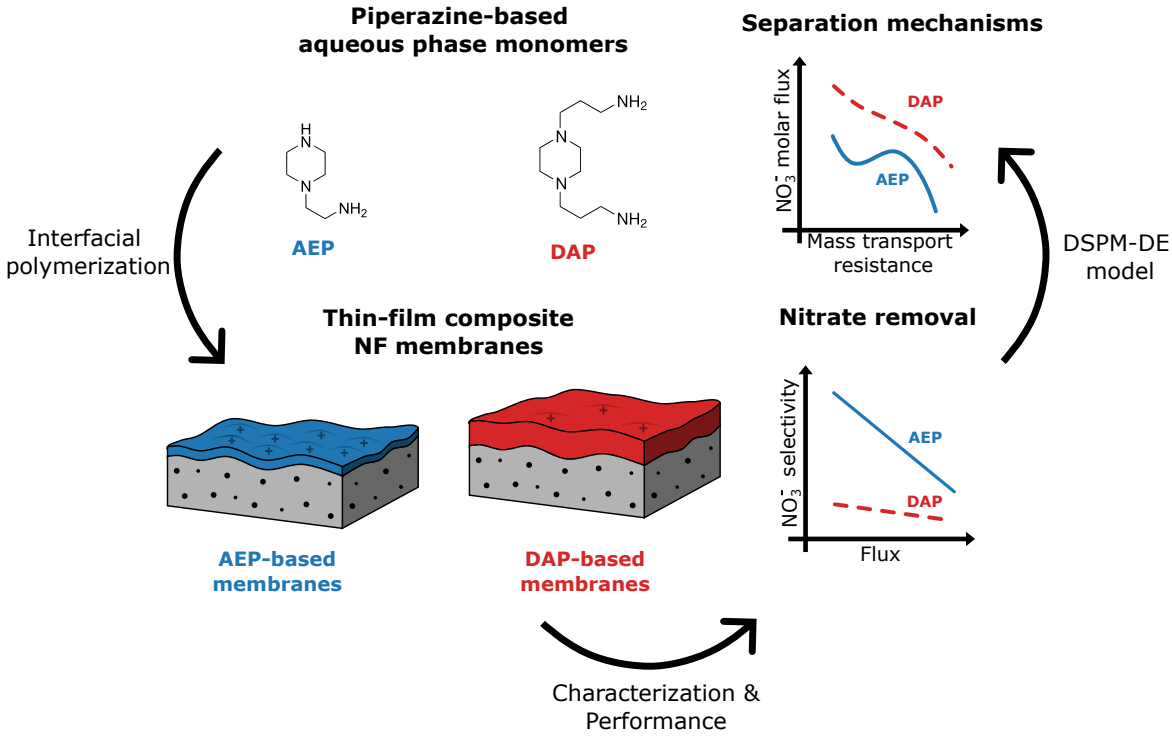
[30] T. Zhang, R.Y. Fu, K.P. Wang, Y.W. Gao, H.R. Li, X.M. Wang, Y.F. Xie, L.a. Hou, Effect of synthesis conditions on the non-uniformity of nanofiltration membrane pore size distribution, J. Membr. Sci. 647 (2022) 120304, https://doi.org/10.1016/j.memsci.2022.120304.

[31] R. Nadler, S. Srebnik, Molecular simulation of polyamide synthesis by interfacial polymerization, J. Membr. Sci. 315 (1–2) (2008) 100–105, https://doi.org/10.1016/j.memsci.2008.02.023.

[32] J. Tian, H. Chang, S. Gao, R. Zhang, How to fabricate a negatively charged NF membrane for heavy metal removal via the interfacial polymerization between PIP and TMC? Desalination 491 (2020) 114499 https://doi.org/10.1016/j.desal.2020.114499.
[33] R. Zhang, S. Yu, W. Shi, J. Zhu, B. Van der Bruggen, Support membrane pore blockage (SMPB): an important phenomenon during the fabrication of thin film composite membrane via interfacial polymerization, Separ. Purif. Technol. 215 (2019) 670–680, https://doi.org/10.1016/J.SEPPUR.2019.01.045.
[34] Q.Y. Zhu, L.K. Wu, L.Q. Li, L.W. Zhuang, S.M. Xue, Z.L. Xu, Y.J. Tang, Novel insight on the effect of the monomer concentration on the polypiperazine-amide nanofiltration membrane, Ind. Eng. Chem. Res. 61 (2022) 5843–5852, https://doi.org/10.1021/acs.iecr.2c00478.
[35] Y. Zhao, X. Tong, Y. Chen, Fit-for-purpose design of nanofiltration membranes for simultaneous nutrient recovery and micropollutant removal, Environ. Sci. Technol. 55 (5) (2021) 3352–3361, https://doi.org/10.1021/acs.est.0c08101.
[36] R.y. Fu, T. Zhang, X.m. Wang, Rigorous determination of pore size non-uniformity for nanofiltration membranes by incorporating the effects on mass transport, Desalination 549 (2023), https://doi.org/10.1016/j.desal.2022.116318, 116318-116318.
[37] EuropeanCommission, Critical Raw Materials Resilience: Charting a Path towards Greater Security and Sustainability, 2020.
[38] Z. Tan, S. Chen, X. Peng, L. Zhang, C. Gao, Polyamide membranes with nanoscale Turing structures for water purification, Science 360 (6388) (2018) 518–521, https://doi.org/10.1126/science.aar6308.
[39] C. Tang, M.L. Bruening, Ion separations with membranes, J. Polym. Sci. 58 (20) (2020) 2831–2856, https://doi.org/10.1002/pol.20200500.
[40] E.R. Nightingale Jr., Phenomenological theory of ion solvation. Effective radii of hydrated ions, J. Phys. Chem. 63 (9) (1959) 1381–1387, https://doi.org/10.1021/j150579a011.
[41] S. Varghese, S.K. Kannam, J.S. Hansen, S.P. Sathian, Effect of hydrogen bonds on the dielectric properties of interfacial water, Langmuir 35 (24) (2019) 8159–8166, https://doi.org/10.1021/acs.langmuir.9b00543.
[42] W.R. Bowen, J.S. Welfoot, Modelling the performance of membrane nanofiltration-critical assessment and model development, Chem. Eng. Sci. 57 (2002) 1121–1137, https://doi.org/10.1016/S0009-2509(01)00413-4.
[43] A.A. Hussain, S.K. Nataraj, M.E.E. Abashar, I.S. Al-Mutaz, T.M. Aminabhavi, Prediction of physical properties of nanofiltration membranes using experiment and theoretical models, J. Membr. Sci. 310 (1) (2008) 321–336, https://doi.org/10.1016/j.memsci.2007.11.005.
[44] D. Rehman, J.H. Lienhard, Global optimization for accurate and efficient parameter estimation in nanofiltration, J. Membr. Sci. Lett. 2 (2022) 100034, https://doi.org/10.1016/J.MEMLET.2022.100034.

## 3.3. Publication III: Effect of piperazine-based monomer structure on nanofiltration membrane selectivity: A DSPM-DE analysis of nitrate transport

This section shifts the fabrication focus from monomer concentration to monomer identity by comparing PIP-derived chemistries (AEP vs. DAP) for nitrate-selective NF under single- and mixed-electrolyte conditions. The analysis remains expressed through the same effective descriptor set within the DSPM-DE interpretation, so that selectivity shifts driven by monomer chemistry are interpreted in the same mechanistic framework used throughout this dissertation. In this framing, these shifts are also interpreted in terms of how the permeance–selectivity trade-off is expressed within the same mass transport framework. This provides the bridge to Publication IV, where the same variation in monomer chemistry is extended to $Na^+/Mg^{2+}$ selectivity under explicit common-anion variation.



Journal of Membrane Science 736 (2025) 124642



Contents lists available at ScienceDirect

Journal of Membrane Science

journal homepage: www.elsevier.com/locate/memsci





# Effect of piperazine-based monomer structure on nanofiltration membrane selectivity: A DSPM-DE analysis of nitrate transport

Nicolás Cevallos-Cueva [a], Md. Mushfequr Rahman [a,*], Hluf Hailu Kinfu [a], Volker Abetz [a,b]

[a] Helmholtz-Zentrum Hereon, Institute of Membrane Research, Max-Planck-Straße 1, 21502, Geesthacht, Germany
[b] University of Hamburg, Institute of Physical Chemistry, Martin-Luther-King-Platz 6, 20146, Hamburg, Germany

ARTICLE INFO

*Keywords:*
Interfacial polymerization
Nanofiltration membranes
Piperazine-based monomers
Thin film composite membranes
Nitrate removal
Ion selectivity
DSPM-DE model

ABSTRACT

Nitrate contamination in water supplies poses significant environmental and public health risks, necessitating the development of efficient nanofiltration (NF) membranes. We investigate the impact of two structurally distinct piperazine-based monomers (aminoethylpiperazine (AEP) and 1,4-bis(3-aminopropyl)piperazine (DAP)) on the morphology and nitrate separation performance of thin-film composite (TFC) NF membranes. We fabricated ten membranes via interfacial polymerization by systematically varying the concentrations of AEP or DAP to achieve distinct physicochemical characteristics. Their separation performance was evaluated through water permeance, poly(ethylene glycol) (PEG 200) rejection, and salt retention tests. The Donnan Steric Pore Model with Dielectric Exclusion (DSPM–DE) was employed to understand the underlying ion rejection and transport mechanisms. Compared to AEP-based membranes, DAP-based membranes within the tested concentration range yielded thicker and more open structures with lower net charge density, leading to higher flux but lower nitrate selectivity. In contrast, AEP-based membranes often yielded thinner layers and stronger positive charge densities, enhancing anion partitioning. Negative nitrate retention was observed for some membranes when the net membrane charge density was close to zero. These findings underscore the crucial role of monomer structure and concentration in controlling effective pore size, charge density, and ion transport. This study provides mechanistic insights into the flux–selectivity trade-off, guiding the design of NF membranes through structurally distinct piperazine-based monomers for selective nitrate removal.

## 1. Introduction

Global nitrate contamination in water supplies has emerged as a significant environmental and public health concern due to its association with conditions such as methemoglobinemia in infants and its contribution to eutrophication [1,2]. Intensive agricultural practices have resulted in elevated nitrate concentrations in both surface and groundwater in certain regions of Germany, exceeding the permissible limits of 50 ppm [3–5]. In this context, nanofiltration (NF) membranes present a promising solution for selective ion separation owing to their tunable performance, ability to handle complex water streams, and low operational costs compared to other nitrate removal methods such as reverse osmosis or ion exchange [6–11]. However, NF membranes frequently encounter the trade-off between selectivity and permeability, which may limit their practical implementation.

Recent studies indicate that controlling membrane fabrication conditions can further refine this trade-off [12–16]. Thin-film composite (TFC) membranes fabricated by interfacial polymerization (IP) are highly sensitive to the characteristics of the monomers, including functional groups, spatial configuration, size, and reactivity. These factors significantly influence both the membrane formation and its ultimate performance [6,8]. For instance, aqueous-phase monomers with slower diffusion rates and lower reactivity, like polyphenols, tend to produce thicker polyester selective layers with increased porosity and reduced crosslinking [17]. In contrast, more reactive monomers, like piperazine (PIP), typically result in denser and thinner polyamide selective layers [18]. Additionally, the membrane's net charge is determined by the ionizable moieties in the selective layer [19], which originate from the monomers and their concentrations during IP. For example, replacing PIP with polyethylenimine as the aqueous-phase monomer can lead to a membrane with a higher positive charge owing to the protonation of multiple amine groups [20]. Furthermore, increasing the PIP concentration can decrease a membrane's negative charge, thereby enhancing cation selectivity [21,22]. Even subtle

* Corresponding author.
*E-mail address:* mushfequr.rahman@hereon.de (Md.M. Rahman).

https://doi.org/10.1016/j.memsci.2025.124642
Received 1 May 2025; Received in revised form 29 August 2025; Accepted 1 September 2025
Available online 3 September 2025
0376-7388/© 2025 The Author(s). Published by Elsevier B.V. This is an open access article under the CC BY license (http://creativecommons.org/licenses/by/4.0/).

changes in monomer structure can significantly influence membrane performance [23]. Since membrane performance is governed by its physicochemical properties, variations in membrane morphology and charge density can affect how specific ions, such as nitrate, permeate through the membrane [24]. Of all aqueous-phase monomers, PIP is the most successful and widely utilized for TFC NF membrane fabrication. The PIP-derived monomers, aminoethylpiperazine (AEP) and 1,4-bis (3-aminopropyl)piperazine (DAP) were chosen in this study owing to their distinct chemical structures. AEP contains both a primary amine on its side chain and a secondary amine in the PIP ring, while DAP has two primary amines on alkyl chains. These structural differences influence the balance between diffusion and crosslinking during IP, resulting in polyamide (PA) selective layers with distinct thicknesses, pore sizes, and charge densities [8,23,25–28]. For instance, the presence of these additional amines allows AEP and DAP to generate PA layers with tunable, often positive, surface charge compared to conventional PIP-based membranes. However, although the structure of the monomer provides the basis for certain membrane properties, the resulting thickness, pore size, and charge density are also dependent on the interplay of IP reaction conditions and support properties [6]. Understanding how monomer structure, along with IP reaction conditions, affects the membrane properties that govern ion transport is important for optimizing both permeance and selectivity.

To shed light on these phenomena, we use the Donnan-Steric Pore Model with Dielectric Exclusion (DSPM–DE) [14]. This model provides a mechanistic understanding of ion transport, by accounting for the exclusion mechanisms at the bulk-solutions/membrane interfaces while breaking down total transmembrane ion flux into advective, electromigrative, and diffusive contributions [14,22,24,29–32]. This approach can elucidate the influence of physicochemical characteristics of the membranes on selective nitrate transport. Our previous work on PIP-based membranes [24] was focused on the impact of monomer concentration on nitrate removal, emphasizing the role of dielectric exclusion and diffusion. Although PIP membranes exhibited relatively high nitrate selectivity, the influence of the aqueous-phase monomer's molecular structure on nitrate separation performance remains to be explored. More importantly, no studies have ever reported the influence of monomer structure on the underlying mass transport mechanisms responsible for the separation of nitrate or any other ions by NF membranes. Although previous studies on AEP or DAP-based membranes have established how monomer selection and IP reaction conditions alter membrane charge and permeability, they relied exclusively on experimental observations and did not systematically examine the fundamental transport mechanism governing ion separation [8,23,25–28]. This study addresses that gap by focusing on AEP and DAP monomers, investigating their impact on the trade-off between permeability and selectivity and providing insights into mass transport mechanisms responsible for selective transport of nitrate.

In this study, we systematically examined the role of the aqueous-phase monomer in determining NF membrane performance, emphasizing the interplay between membrane physicochemical characteristics and nitrate-selective transport. Unlike our previous study on PIP-based membranes, which focused on the effect of monomer concentration, this work explored how structural differences between AEP and DAP affect nitrate separation using the DSPM-DE model. We fabricated five membranes at varying concentrations of each monomer, resulting in a total of ten membranes. The morphological properties of these membranes were characterized through scanning electron microscopy (SEM) and atomic force microscopy (AFM) analyses, and their separation performance was evaluated through water permeance, PEG 200, and both single- and mixed-salts retention tests targeting nitrate-selective separation. The DSPM-DE model was subsequently applied to elucidate the mechanisms governing ion transport. Finally, we analyzed how these variations shape the trade-off between flux and selectivity. Overall, this study broadens our mechanistic understanding of selective nitrate transport in NF membranes and contributes to the development of advanced membrane materials tailored for targeted water treatment applications.

## 2. Materials and methods

### 2.1. Materials

All chemicals were used as received without additional modification. 1-(2-aminoethyl)piperazine (AEP, >99 %), 1,4-bis(3-aminopropyl) piperazine (DAP, >99 %), trimesoyl chloride (TMC), and *n*-heptane were purchased from Sigma-Aldrich Chemie GmbH (Germany). Microporous polyacrylonitrile (PAN) membrane, produced via nonsolvent induced phase separation at Helmholtz-Zentrum Hereon, served as the support. Poly(ethylene glycol) (PEG, average molecular weight 200 Da) was obtained from VWR International GmbH, while the salts NaCl (>99.5 %), $Na_2SO_4$ (>99 %), and $NaNO_3$ were purchased from Merck KGaA, Carl Roth GmbH, and Honeywell Specialty Chemicals Seelze GmbH, respectively.

### 2.2. Methods

#### 2.2.1. Fabrication of TFC NF membranes

TFC membranes were prepared by interfacial polymerization (IP) on PAN supports. The aqueous (AEP or DAP) and organic phase monomers (TMC) were dissolved in ultrapure DI water and HPLC-grade *n*-heptane, respectively. ThePAN supports were first soaked in ultrapure deionized (DI) water for 24 h before membrane synthesis. Excess water was gently removed from the surface of the soaked PAN supports by a 1-min rubber rolling followed by dust-free Kim wipes to avoid any droplets on the surface of the support. The PAN support was then immersed in a 350-mL aqueous solution of either DAP or AEP at one of five concentrations for 6 min. Next, the same rolling and wiping procedure was applied again to remove any residual aqueous solution from the surface of the soaked support.

The soaked PAN supports were fixed onto a 5.1 cm × 15.9 cm glass plate comprising a nitrile rubber layer and a PTFE frame. A 0.30 %w-w TMC solution was then poured over the surface of the AEP- or DAP-soaked supports to start the IP reaction for 90 s. To stop the reaction, 150 mL of pure *n*-heptane was poured over the membrane surface. The resulting TFC membranes were then air-dried at room temperature for 30 min, heat-treated at 60 °C under vacuum for 30 min, and finally stored in ultrapure DI water at room temperature. At least three membranes were fabricated under each IP condition.

To systematically assess the effect of monomer concentration on membrane performance, a ten-fold range of concentration for each monomer was explored. Preliminary tests showed that, when using identical concentration values, DAP-based membranes exhibited excessively low permeance, whereas AEP-based membranes were too thin to form a defect-free selective layer. Accordingly, we selected three overlapping concentrations (0.10, 0.30, and 0.50 % w-w) to enable direct comparison, with two additional lower concentrations for DAP (0.05 and 0.075 % w-w) and two higher concentrations for AEP (0.70 and 1.00 % w-w). In total, five well-spaced concentrations were evaluated for each monomer, yielding membranes with adequate flux and reproducible morphology across the entire series, as shown in Table 1.

#### 2.2.2. Morphology characterization

The surface and cross-sectional morphologies of the membranes were analyzed using scanning electron microscopy (SEM). Samples were first dried under vacuum at 60 °C for at least 72 h, sputter-coated with a 1.0–1.5 nm platinum layer, and imaged using a Zeiss Merlin SEM operating at 1.5–3 kV. Atomic force microscopy (AFM) was used to analyze the topography of the membrane surfaces. AFM measurements were carried out in tapping mode on a Bruker MultiMode 8 instrument over scan areas of 3 μm × 3 μm using RTESPA-150 probes (tip radius ≈ 8 nm); roughness parameters (Rq and Ra) were computed with NanoScope

**Table 1**
Aqueous-phase monomers and concentrations used during IP at a fixed TMC concentration (0.30 % w–w) to fabricate TFC NF membranes. Full IP conditions are described in the membrane fabrication methodology preceding this table.

| Aqueous-phase monomer | Concentration (%w-w) | Label |
|---|---|---|
| AEP | 0.10 | AEP0.1 |
| AEP | 0.30 | AEP0.3 |
| AEP | 0.50 | AEP0.5 |
| AEP | 0.70 | AEP0.7 |
| AEP | 1.00 | AEP1 |
| DAP | 0.05 | DAP0.05 |
| DAP | 0.075 | DAP0.075 |
| DAP | 0.10 | DAP0.1 |
| DAP | 0.30 | DAP0.3 |
| DAP | 0.50 | DAP0.5 |

Analysis software. Rq, also called RMS roughness, is the root mean square average of height deviations taken from the mean image data plane.

### 2.2.3. Performance evaluation

Membrane performance was assessed via pure water permeance and retention experiments using a stirred dead-end filtration cell (effective area = 2.14 $cm^2$) supplied by Millipore. The pure water permeance (PWP) was calculated with the data recorded during the water compaction step, which comprised ultrapure DI water permeation for at least 2 h at 4 bar and room temperature, using the following equation:

$$PWP = \frac{\Delta m}{\delta_{H_2O} A_{mb} \Delta t \Delta P} \quad (1)$$

where $\Delta m$ is the change of mass, $\delta_{H_2O}$ is the density of liquid water at room temperature, $A_{mb}$ is the effective membrane area, $\Delta t$ is the elapsed time, and $\Delta P$ is the transmembrane pressure.

### 2.2.4. Ion retention

After the water compaction procedure, the membranes were evaluated via ion retention tests using both single and mixed salt solutions. To minimize concentration polarization, the cell was stirred at 300 rpm, and all experiments were repeated at least three times. Salt solutions were added into the stirred dead-end filtration cell. Single salt retention tests were performed with 200 ppm aqueous solutions of NaCl, $NaNO_3$, and $Na_2SO_4$. For mixed salt experiments, equimolar mixtures containing 200 ppm of $NO_3^-$ and $SO_4^{2-}$ or $NO_3^-$ and $Cl^-$ were prepared using combinations of NaCl + $NaNO_3$ and $NaNO_3$ + $Na_2SO_4$. The transmembrane pressure was consistently maintained at 3 bar. To ensure steady state had been reached, permeate samples collected during the first 2 h were discarded. Then, 1 mL retentate and permeate samples were collected. As the retentate concentration varies with time in dead-end mode, the retention ($R_{i,obs}$) was computed using the average concentration of the feed and retentate solution:

$$R_{i,obs} = 1 - \frac{2c_{i,p}}{c_{i,f} + c_{i,r}} \quad (2)$$

where $c_{i,p}$, $c_{i,f}$, $c_{i,r}$ are the concentrations of species $i$ in the permeate, feed, and retentate solutions, respectively. These concentrations were quantified with an Ion Chromatograph (Dionex ICS600, Thermo Fisher Scientific Inc., USA).

The ideal selectivity, $S^*_{a/b}$, from single salt retention tests and the real selectivity, $S_{a/b}$, from mixed salt retention tests were computed with the following equation:

$$S^*_{a/b} \text{ or } S_{a/b} = \frac{1 - R_{a,obs}}{1 - R_{b,obs}} \quad (3)$$

### 2.2.5. PEG retention

PEG 200 retention experiments were performed under different transmembrane pressures (0.5, 1.0, 1.5, 2.0, 2.5, 3.0, 3.5, and 4.0 bar) to determine the retention at different flow rates. The flow rates were computed with:

$$J_v = \frac{\Delta m}{\delta_{H_2O} A_{mb} \Delta t} \quad (4)$$

The PEG concentration was measured with Gel Permeation Chromatography (GPC) (VWR-Hitachi 2130 pump, Hitachi, Darmstadt, Germany).

### 2.2.6. DSPM-DE model

To simulate ion transport through the membranes via the DSPM-DE model, the model's input parameters, namely thickness-to-porosity ratio ($\Delta x_e$), pore radius ($r_{pore}$), pore dielectric constant ($\varepsilon_{pore}$), and membrane charge density ($c_x$), were calculated by fitting experimental retention data. Retention tests with PEG 200 were used to determine $r_{pore}$ and $\Delta x_e$, while mixed salt experiments for estimating $\varepsilon_{pore}$ and $c_x$. A dual annealing optimization algorithm, implemented in Python using the SciPy library with the Nelder-Mead method as local optimizer (with a convergence tolerance of $10^{-6}$), was used to perform the parameter fitting. Details of the fitting are described elsewhere [24].

## 3. Results and discussion

### 3.1. Morphology and baseline properties

The structural differences between AEP and DAP significantly impact the IP process with TMC [23]. In addition to influencing the diffusion rates of aqueous-phase monomers, these differences lead to distinct interface reactivities with TMC and differences in incipient PA layer densities. When the two phases come into contact in the IP process, a fast polycondensation reaction occurs at the interface, forming a polymer barrier that restricts the further diffusion of aqueous-phase monomers into the organic phase. It is well established that the IP reaction primarily takes place in the organic phase (in close vicinity to the interphase) due to the higher partition coefficient of the amine monomers in the organic phase [33]. Consequently, from this point onward, the polymerization reaction depends on a continuous supply of monomers, coupling the kinetics of the chemical reaction with the diffusion of the aqueous-phase monomer through the incipient PA layer [33]. To capture this complex interdependence, the Eyring activation state theory is used, which integrates diffusion rates with reaction kinetics by considering the energy required for reactants to pass through a high-energy transition state (TS) to transform into products [34]:

$$\mathrm{k} = \frac{k_B T}{h} e^{-\frac{\Delta G^{\ddagger}}{RT}} \quad (5)$$

where the activation free energy is:

$$\Delta G^{\ddagger} = \Delta H^{\ddagger} - \mathrm{T}\Delta S^{\ddagger} \quad (6)$$

In practical terms, a lower $\Delta G^{\ddagger}$ indicates a faster IP process due to either lower energy barriers or more favorable molecular configurations. $\Delta H^{\ddagger}$ represents the energy required to reach the TS and $\Delta S^{\ddagger}$ represents the change in degrees of freedom of the TS (i.e., change of molecular order during this transition) [34,35]. AEP bears one primary amine on its side chain and a secondary amine in the piperazine ring, which provides a higher electron density for nucleophilic attack on TMC and can also adopt ring conformations that favorably influence $\Delta S^{\ddagger}$. This combination effectively lowers $\Delta H^{\ddagger}$ and helps stabilize the TS, thereby resulting in a reduced $\Delta G^{\ddagger}$ and faster IP reaction (i.e., increased rate of both molecular diffusion and chemical reaction). Conversely, DAP's primary amines, located on longer propyl side chains, exhibit lower nucleophilicity, which increases $\Delta H^{\ddagger}$ and potentially limits entropic freedom at the TS. This leads to a higher $\Delta G^{\ddagger}$ and slower IP process. Consequently,

AEP rapidly forms a dense, incipient layer that limits further monomer penetration, thereby "locking in" a comparatively denser crosslinked network. On the other hand, DAP forms a less dense, more open incipient PA layer that allows further monomer diffusion into the organic phase [36,37], as schematically represented in Fig. 1A. Therefore, the chemical structure of the monomer alters TS stabilization, directly influencing the overall surface morphology and thickness of the resulting PA layer (Fig. 1B–C) [8].

SEM analysis confirms these trends. In the case of DAP-based membranes, SEM top-surface micrographs of DAP0.05, DAP0.075, and DAP0.1 reveal an uneven and incomplete coverage of the PA layer on top of the PAN support (Fig. 1B–top row). At higher DAP concentrations, membranes DAP0.3 and DAP0.5 display a more uniform, fully developed and smoother PA layer. In contrast, AEP membranes consistently yield a rough PA layer across all investigated concentrations (Fig. 1C–top row).

PA layer thickness generally increases with higher aqueous-phase monomer concentrations due to self-limited diffusion growth [24,33]. As shown in Fig. 1B (bottom row) and D, DAP membranes indeed show a continuous increase in PA thickness with increasing DAP concentration. This trend is attributed to the more open incipient PA layer formed by DAP, which facilitates further monomer diffusion into the organic phase and continued layer growth. In contrast, AEP membranes exhibit a similar thickness increase at lower concentrations but reach a plateau beyond 0.3 % w-w (Fig. 1C, bottom row, and D). This occurs as the dense, rapidly formed PA layer limits additional monomer penetration, thereby limiting additional PA layer growth. Under comparable concentration conditions, AEP membranes exhibit slightly thicker selective layers than DAP membranes at 0.1 and 0.3 % w-w. However, when the DAP concentration increases from 0.3 to 0.5 % w-w (Fig. 1D), the membrane thickness increases almost four-fold. Notably, despite AEP's smaller molecular size, DAP demonstrates greater sensitivity to monomer concentration variations, influencing PA layer growth more significantly. We attribute the abrupt thickness increase observed for DAP between 0.3 and 0.5 % w-w (Fig. 1D) to a concentration-triggered transition in the IP growth regime. Because DAP forms a more open, less crosslinked incipient PA layer, increasing the DAP concentration promotes (i) coalescence from patchy to fully continuous coverage together with a smoother topography (Fig. 1B–E) and (ii) a transient stage in which the nascent film remains sufficiently permeable to sustain enhanced DAP diffusion through the layer. The resulting non-linear increase in monomer supply to the organic phase enables the reaction front to penetrate deeper before densification stabilizes the structure, thereby producing the step-change in thickness at 0.5 % w-w. Surface roughness measurements analyses further evidence the influence of DAP concentration. Fig. 1E shows the correlation between surface RMS roughness and monomer concentration. Membranes fabricated at lower DAP concentrations (0.05–0.1 % w-w) exhibit increasing RMS roughness with increasing monomer concentration, like AEP membranes. However, at higher DAP concentrations (0.3–0.5 % w-w), these nodular features coalesce into a much smoother surface. This smoother topography is evidence of DAP's lower reactivity. As DAP concentration increases, the extended diffusion allowed by its less dense incipient layer enables these segments to coalesce into a uniform, smooth surface. In contrast, AEP membranes develop rough, nodular surfaces due to rapid, diffusion-limited PA layer formation, a characteristic typically observed in PA layers formed by highly reactive monomers, such as PIP [8,14,23]. These results demonstrate the significant role of monomer structure in dictating PA layer morphology and thickness. Tailoring the molecular structure of monomers, such as switching from a single ethyl side group (AEP) to double propyl side groups (DAP), can influence the balance between diffusion-limited growth and interface-localized reaction, ultimately determining the performance of the membrane.

### 3.2. Membrane performance characteristics

The surface morphology of the PA membranes significantly influences their water transport properties. In Fig. 2A, a pronounced drop in pure water permeance (PWP) is observed as DAP concentration increases from 0.05 to 0.5 % w-w. This trend aligns with the increase in PA layer thickness, as evidenced by SEM micrographs (Fig. 2B), highlighting the direct impact of layer thickness on PWP. In contrast, AEP membranes show a more intricate response: as AEP concentration increases from 0.1 to 0.3 % w-w, PWP initially increases before decreasing again at 1.0 % w-w. Unlike DAP membranes, the thickness of AEP membranes does not directly correlate with PWP (Fig. 2B). This non-monotonic trend suggests that factors beyond thickness influence PWP [22]. Notably, at comparable concentrations (0.1, 0.3, and 0.5 % w-w), AEP membranes exhibit higher PWP than their DAP counterparts (Fig. 2A) even though AEP membranes also appear thicker. To better understand these apparently contradictory results, we calculated the thickness-to-porosity ratio, $\Delta x_e$, through PEG 200 retention tests. This ratio serves as an average metric of the morphological features that collectively govern mass transport resistance (i.e., larger $\Delta x_e$ values indicate higher resistance) [22,24]. Fig. 2C illustrates that, across all membranes, PWP and $\Delta x_e$ display a negative covariance. For DAP membranes, $\Delta x_e$ consistently decreases with increasing DAP concentration (similar to thickness of the PA layer), indicating that the large increase in thickness dominates the overall resistance. In contrast, the relationship between AEP concentration and mass transport resistance is less straightforward, suggesting that multiple morphological features, such as the roughness of the PA active layer, play a significant role. This is consistent with our previous findings for PIP-based membranes [22]. Furthermore, at the same concentrations (0.1, 0.3, and 0.5 % w-w), DAP membranes exhibit larger $\Delta x_e$ values than AEP membranes. Notably, although no monotonic trend between RMS roughness and PWP is observed across all fabricated membranes, direct comparisons of AEP and DAP membranes prepared at the same concentrations (0.3 % and 0.5 % w-w) show that the rougher PA layers render higher PWP, an effect attributed to the increased interfacial area facilitating water transport (Fig. S1A).This suggests that the lower reactivity of DAP (owing to its two 3-aminopropyl groups) results in thicker, smoother, and less permeable PA layers relative to AEP, even at equivalent monomer concentrations.

Building on the previous analysis of membrane morphology and PWP, we next examine the single-salt ion retention behavior to further elucidate how differences in AEP and DAP structures influence membrane performance, as shown in Fig. 3. As expected, anion retention typically decreases with increasing solution flux, indicative of either thinner or less crosslinked PA layers resulting from lower monomer concentrations. As presented in Fig. 3B, the $NO_3^-/Cl^-$ ideal selectivity decreases with increasing flux, consistent with a typical permeability-selectivity trade-off. For negatively charged nanofiltration (NF) membranes, electrostatic and steric effects typically lead to stronger retention of sulfate ($SO_4^{2-}$) compared to nitrate ($NO_3^-$) or chloride ($Cl^-$). Yet DAP0.1, DAP0.3, and DAP0.5 membranes show lower $SO_4^{2-}$ than $NO_3^-$ retention, resulting in an ideal selectivity below unity (Fig. 3C). This selectivity increases at higher DAP concentrations, suggesting that the thicker, more uniform layers observed in those membranes render a stronger size and charge-based exclusion effect. In contrast, AEP membranes consistently exhibit higher $SO_4^{2-}$ retention across all tested AEP concentrations, implying that electrostatic and steric effects are more pronounced in these highly crosslinked PA layers. An unexpected trend emerges with increasing flux: the $NO_3^-/SO_4^{2-}$ ideal selectivity tends to increase, suggesting that reduced mass-transfer resistance at high flux may increase the influence of electrostatic repulsion at the feed-solution/membrane interface. From a practical point of view, neither AEP nor DAP membranes go beyond rather small selectivity values in the range 0.4–1.6 for $NO_3^-/SO_4^{2-}$ or $NO_3^-/Cl^-$, suggesting only modest ion separation under the tested conditions. As shown in Fig. S2, the $NO_3^-$

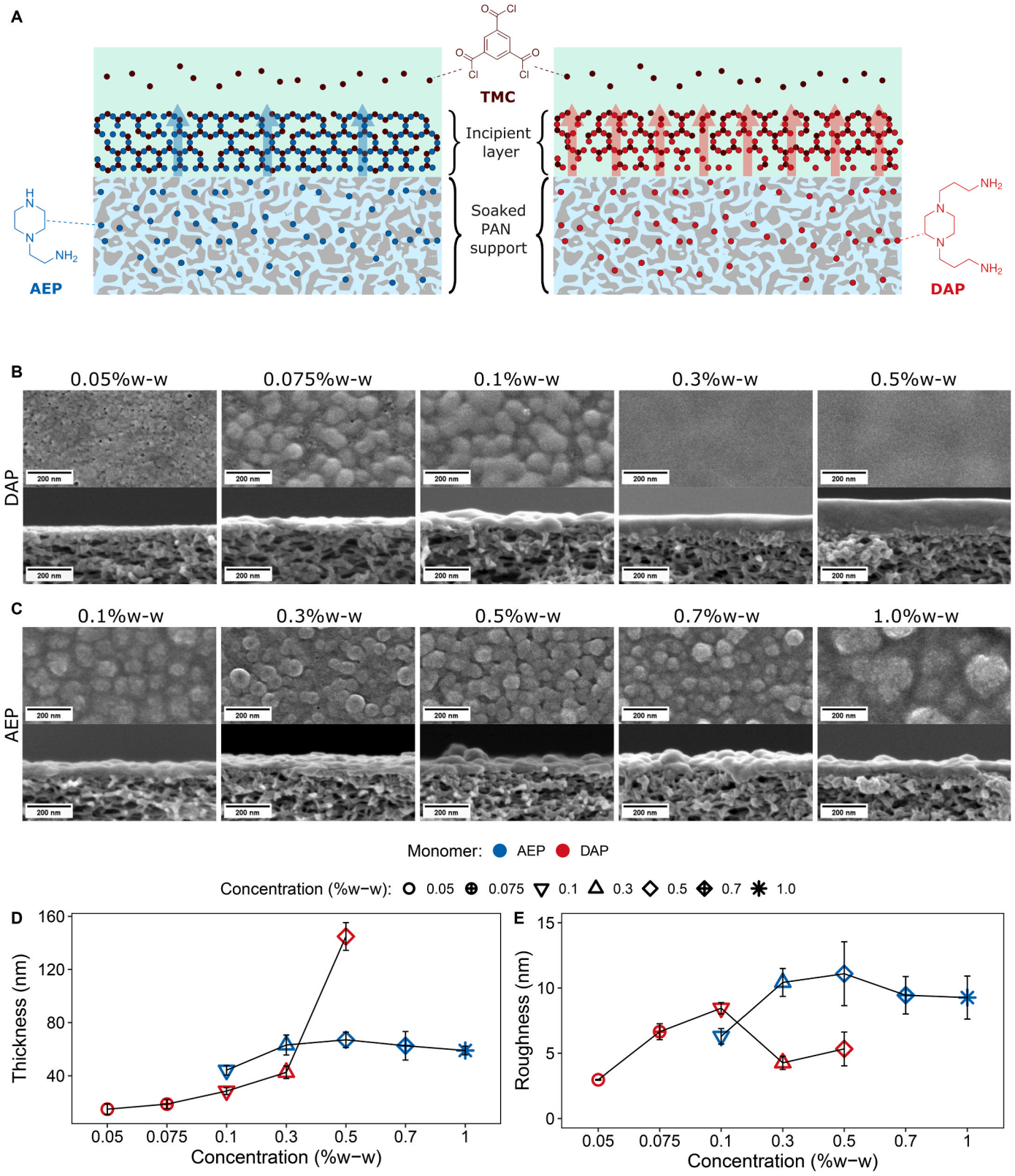



**Fig. 1.** Impact of AEP and DAP monomer structure on PA membrane morphology. (A) Schematic representation of PA formation for AEP and DAP monomers. AEP rapidly forms a dense, crosslinked incipient PA layer that restricts further monomer diffusion, leading to a compact structure. In contrast, DAP forms a more open and less crosslinked incipient PA layer, allowing deeper monomer penetration and continued reaction within the organic phase. (B) SEM micrographs of DAP membranes (top: surface view, bottom: cross-section). (C) SEM micrographs of AEP membranes (top: surface view, bottom: cross-section). (D) Average PA layer thickness on the PAN support as a function of aqueous-phase monomer concentration; error bars represent the standard deviation of thickness measured at different positions along the length of a single membrane. (E) RMS roughness of the PA layers as a function of aqueous-phase monomer concentration.

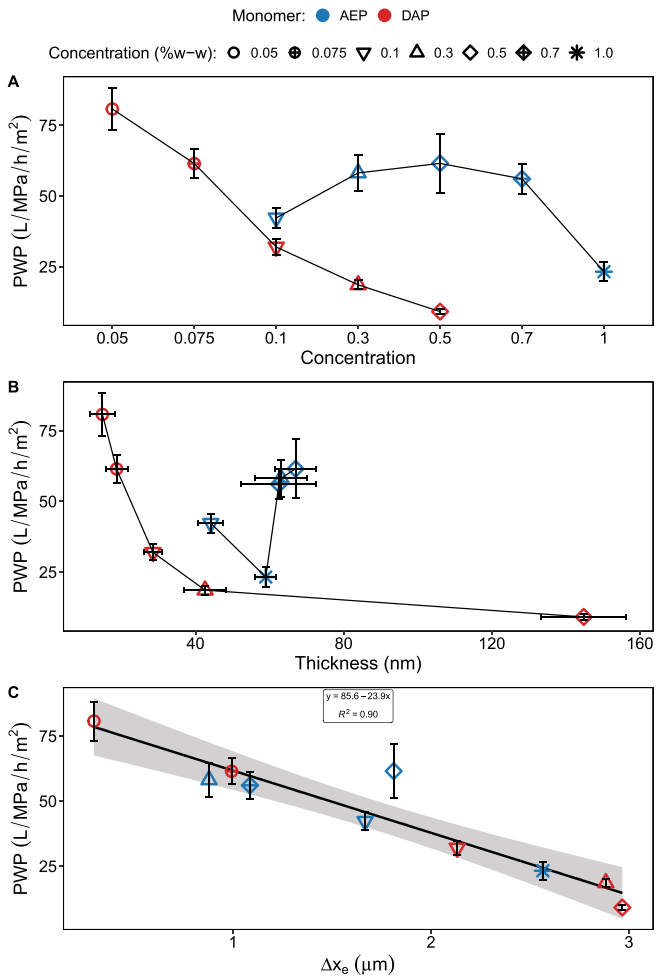



**Fig. 2.** Pure water permeance (PWP) of the fabricated membranes as a function of: (A) aqueous-phase monomer concentration, (B) observed PA thickness (obtained from SEM, with horizontal error bars representing the standard deviation of thickness measured at multiple positions along the length of a single membrane), (C) $\Delta x_e$ (obtained from PEG 200 retention tests); the gray shaded region denotes the 95 % pointwise confidence interval for the fitted regression, indicating the range within which the true mean PWP is expected to lie with 95 % probability.

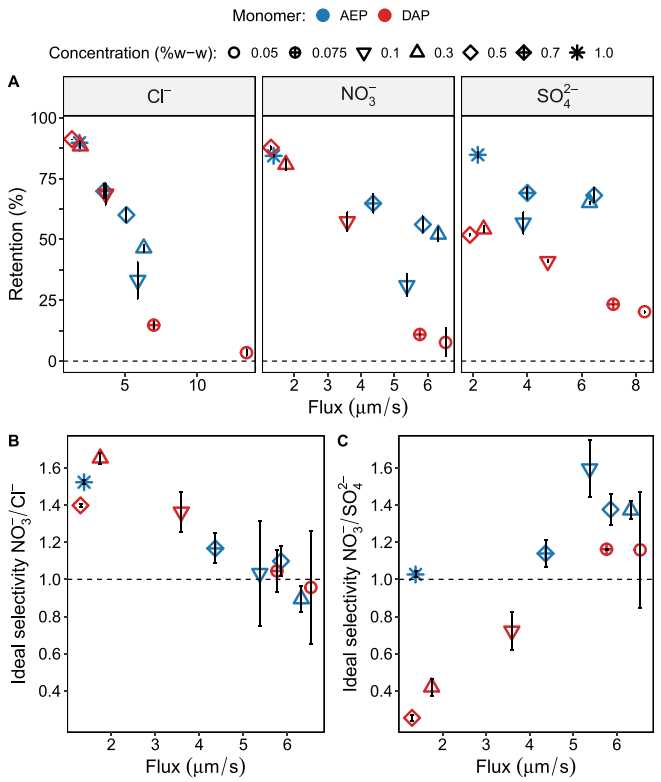



**Fig. 3.** Single-salt retention performance of the fabricated membranes: (A) Retention of $Cl^-$, $NO_3^-$, and $SO_4^{2-}$ as a function of flux. (B) Ideal selectivity of $NO_3^-/Cl^-$ versus flux. (C) Ideal selectivity of $NO_3^-/SO_4^{2-}$ versus flux.

retention performance of the fabricated AEP and DAP membranes does not surpass that of commercially available membranes. Nevertheless, AEP membranes consistently attain $NO_3^-/SO_4^{2-}$ selectivity larger than 1 and frequently outperform their DAP counterparts at similar monomer concentrations. No clear dependence of $NO_3^-/Cl^-$ or $NO_3^-/SO_4^{2-}$ ideal selectivity on PA layer roughness was observed (Fig. S1B and C), indicating that ion selectivity remains governed by steric and charge effects rather than by topographical features. These findings highlight the significant impact of amine monomer structure on the interplay of membrane permeability and charge interactions governing ion-specific transport.

We further investigated two multi-ion systems: $Na^+/Cl^-/NO_3^-$ and $Na^+/NO_3^-/SO_4^{2-}$ to understand how AEP and DAP membranes respond under more complex filtration conditions. As shown in Fig. 4A and B, retention of all ions decreases with flux in both systems, which is consistent with the hypothesis that less crosslinked PA layers facilitate higher permeation rates. From a practical standpoint, these trends imply that IP conditions can be tuned to favor either higher throughput by forming less crosslinked, more open PA layers, or enhanced nitrate removal by generating more crosslinked PA layers. In the $Na^+/Cl^-/NO_3^-$ system, no separation between $Cl^-$ and $NO_3^-$ is observed, as their selectivity values range around 1 (Fig. 4C). For the $Na^+/NO_3^-/SO_4^{2-}$ system, $SO_4^{2-}$ retention consistently exceeds that of $NO_3^-$ across all the membranes, indicating a preferential transport of $NO_3^-$ into the permeate. Some membranes (AEP0.1, DAP0.05, DAP0.075) even show negative rejections of $NO_3^-$ (Fig. 4B). Negative $NO_3^-$ retention indicates a larger $NO_3^-$ concentration on the permeate than the feed side. This phenomenon, observed in membranes fabricated at low monomer concentrations, suggests a coupled transmembrane ion transport [24]. In general, AEP membranes exhibit a higher ion retention than DAP membranes, likely due to smaller pore size or higher charge density. As shown in Fig. 4D, the resulting $NO_3^-/SO_4^{2-}$ selectivity follows a typical permeability-selectivity trade-off, i.e., less permeable membranes achieve higher selectivity. This implies a correlation between preferential transport of $NO_3^-$ over $SO_4^{2-}$ with the mass transport resistance of the membranes.

Consistent with our previous study on PIP-based TFC membranes [24], these observations indicate that diffusion appears to govern $NO_3^-$ transport, though the extent of this mechanism differs between AEP and DAP membranes. Specifically, AEP membranes exhibit higher $NO_3^-/SO_4^{2-}$ real selectivity but experience a steeper decline with increasing flux, while DAP membranes maintain a more stable selectivity trend despite exhibiting larger changes in mass transport resistance as quantified by $\Delta x_e$ (Fig. 2C). These observations suggest that applying the DSPM-DE model could provide further insights into the interplay between membrane properties and mass transport in these ion systems. Additionally, data from our previous study on PIP-based membranes display a higher $NO_3^-/SO_4^{2-}$ selectivity compared to both AEP and DAP membranes (Fig. S3), thereby further illustrating the significant impact of monomer structure on ion-selective membrane performance.

We employed equimolar 200 ppm feeds of $NO_3^-$, $Cl^-$, and $SO_4^{2-}$ to maintain equal concentration and ionic strength for all anions. This

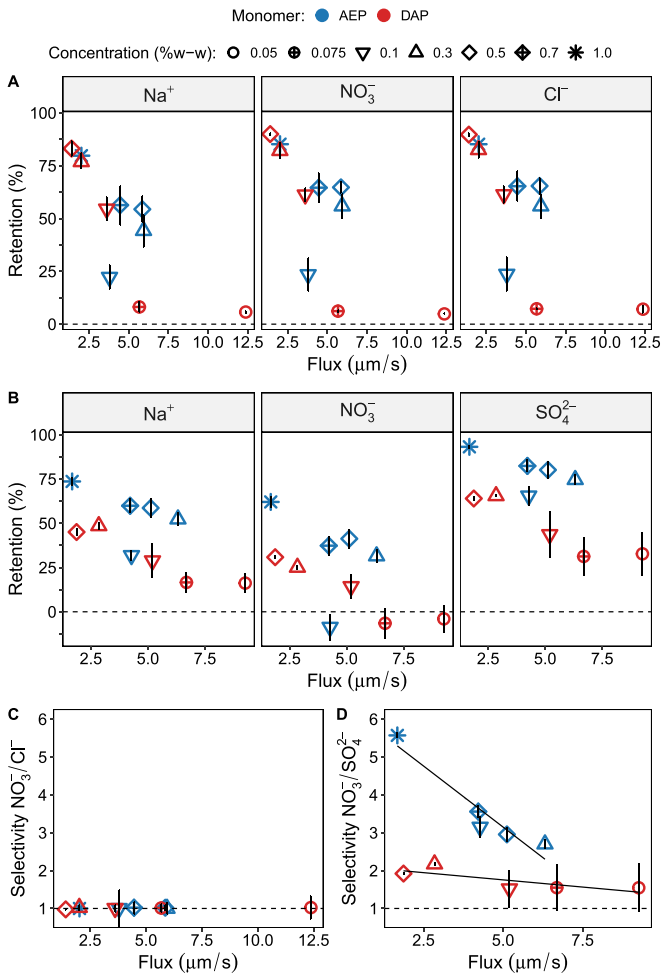



**Fig. 4.** Mixed-salt retention performance of the fabricated membranes. Ion retention as a function of solution flux: (A) $Na^+/Cl^-/NO_3^-$ system, (B) $Na^+/NO_3^-/SO_4^{2-}$ system. (C) $NO_3^-/Cl^-$ selectivity versus solution flux. (D) $NO_3^-/SO_4^{2-}$ selectivity versus solution flux.

provided a consistent benchmark to compare their partitioning and transport behavior within each membrane and across the AEP-DAP series. These conditions also represent the upper range of nitrate levels typically reported in impacted water supplies [3–5]. Accordingly, the trends discussed above are interpreted as responses to membrane morphology and charge rather than differences in feed composition.

Although absolute retentions will vary with composition, the qualitative trends identified here are expected to persist. At higher ionic strengths, electrostatic attraction of anions to the positively charged membrane interface decreases, diminishing its relative contribution. Simultaneously, dielectric exclusion becomes more significant, enhancing overall anion exclusion. We hypothesize that this would increase the $NO_3^-/SO_4^{2-}$ selectivity with increasing $SO_4^{2-}$ feed concentration, since $SO_4^{2-}$ experiences stronger solvation-related barriers. In the case of $Cl^-$, further increase of $Cl^-$ concentration may even lead to membrane charge reversal [38]. A net negatively charged membrane would electrostatically repel $Cl^-$ more strongly than $NO_3^-$. Coupled with $Cl^-$'s smaller hydrated volume, this leads to larger exclusion of $Cl^-$, thereby increasing the $NO_3^-/Cl^-$ selectivity. The comparative differences between AEP- and DAP-based membranes remain governed by their distinct $r_{pore}$, $\Delta x_e$, and $c_x$ values, which are analyzed next.

### 3.3. Mechanistic insights

The DSPM-DE model was used to simulate $Na^+/NO_3^-/SO_4^{2-}$ mixed-salt retention tests, providing a mechanistic comparison between AEP and DAP membranes. The model's input parameters, thickness-to-porosity ratio ($\Delta x_e$), pore radius ($r_{pore}$), pore dielectric constant ($\varepsilon_{pore}$), and membrane charge density ($c_x$), as well as the method for obtaining them, have been thoroughly described in our previous publication [24]. Specifically, $\Delta x_e$ quantifies the mass transport resistance of the membrane, $r_{pore}$ determines steric exclusion. $\varepsilon_{pore}$ governs ion solvation energy barriers due to pore confinement, and $c_x$ affects electrostatic interactions with ions. Consistent with our earlier work [24], we assumed that $\varepsilon_{pore}$ varies only with $r_{pore}$, while its reduction, compared to the dielectric constant of water in the bulk solution ($\varepsilon_{bulk}$), stems from a single layer of water molecules next to the pore walls, whose thickness is $d_{H_2O}$. This layer is characterized by a distinct dielectric constant ($\varepsilon^*$), which arises from the interaction of water molecules with the pore wall's functional groups [14]. This assumption is based on dielectric exclusion being described as a difference in solvation energy barriers between the bulk and inside the pores of the membrane due to confinement of water molecules. As there are no experimental methods to determine $\varepsilon^*$, previous studies have relied on arbitrary values [39]. Consequently, in this study, $\varepsilon^*$ was assumed to depend only on the aqueous-phase monomer (AEP or DAP) (details in Supporting Information).

$$\varepsilon_{pore} = \varepsilon^* + (\varepsilon_{bulk} - \varepsilon^*)\left(1 - \frac{d_{H_2O}}{r_{pore}}\right)^2 \tag{7}$$

The slight overprediction of $Na^+$ and $NO_3^-$ and the corresponding underprediction of $SO_4^{2-}$ (Fig. S6) arise from adopting a single "effective" pore radius in the DSPM-DE framework. This simplifying assumption does not capture the full pore-size distribution inherent to interfacially polymerized PA layers. In the present membranes, these deviations are small and do not affect the mechanistic trends discussed. However, they should be considered a limitation when applying the model to other membranes or conditions.

#### 3.3.1. Exclusion phenomena

The exclusion phenomenon at the feed-solution/membrane interface is described by the exclusion or partitioning coefficients, which depend on the physicochemical characteristics of the membranes, represented by the model's input parameters. These coefficients quantify individual contributions of steric, dielectric, and electrostatic effects, enabling us to interpret the experimental differences in $NO_3^-$ and $SO_4^{2-}$ selectivity observed between AEP and DAP membranes.

$$\Phi_{S,i} = \left(1 - \frac{r_i}{r_{pore}}\right)^2 \tag{8}$$

$$\Phi_{DE,i} = exp\left(\frac{z_i^2 e_0^2}{8\pi\varepsilon_0 r_i k_B T}\left(\frac{1}{\varepsilon_{bulk}} - \frac{1}{\varepsilon_{pore}}\right)\right) \tag{9}$$

$$\Phi_{D,i}^{x=0} = exp\left(\frac{-z_i F}{RT}\Delta\Psi_{D,f}\right) \tag{10}$$

where $\Phi_{S,i}$, $\Phi_{DE,i}$, and $\Phi_{D,i}^{x=0}$ are the steric, dielectric, and Donnan exclusion coefficients, respectively. $r_i$ is the Stokes radius, $z_i$ the ion valence, $e_0$ the electronic charge, $\varepsilon_0$ the permittivity of vacuum, and $T$ the temperature. $R$ is the ideal gas constant, $F$ the Faraday constant, and $\Delta\Psi_{D,f}$ the Donnan potential.

$\Phi_{S,i}$ represents the size-based barrier to ions entering the pore; $\Phi_{DE,i}$ quantifies the effect of pore confinement on ion solvation energies, and $\Phi_{D,i}^{x=0}$ captures the impact of electrostatic interactions.

Fig. 5 illustrates the variation of steric and dielectric exclusion coefficients, derived by the DSPM-DE model, as a function of pore size,

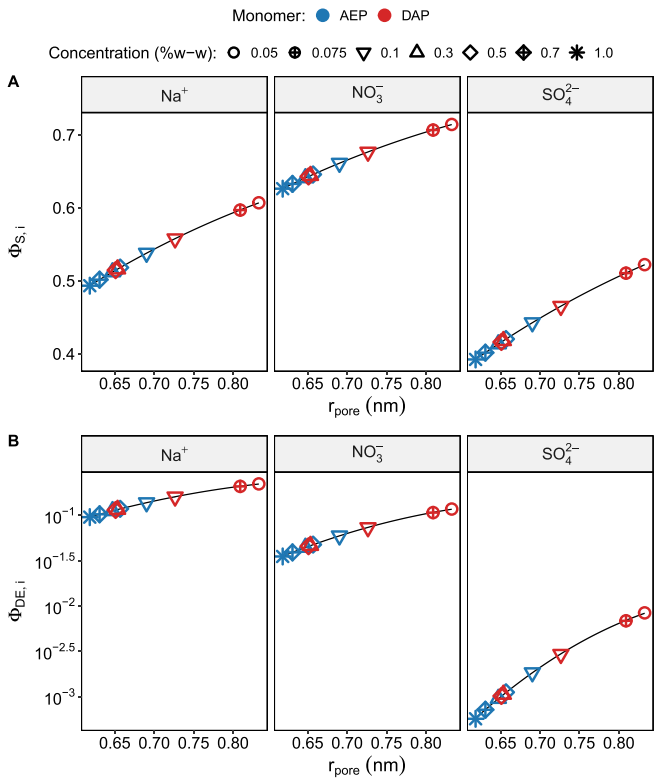



**Fig. 5.** (A) Steric and (B) dielectric exclusion (partitioning) coefficients of $Na^+$, $NO_3^-$, and $SO_4^{2-}$ as a function of the effective pore radius, $r_{pore}$, for the fabricated membranes.

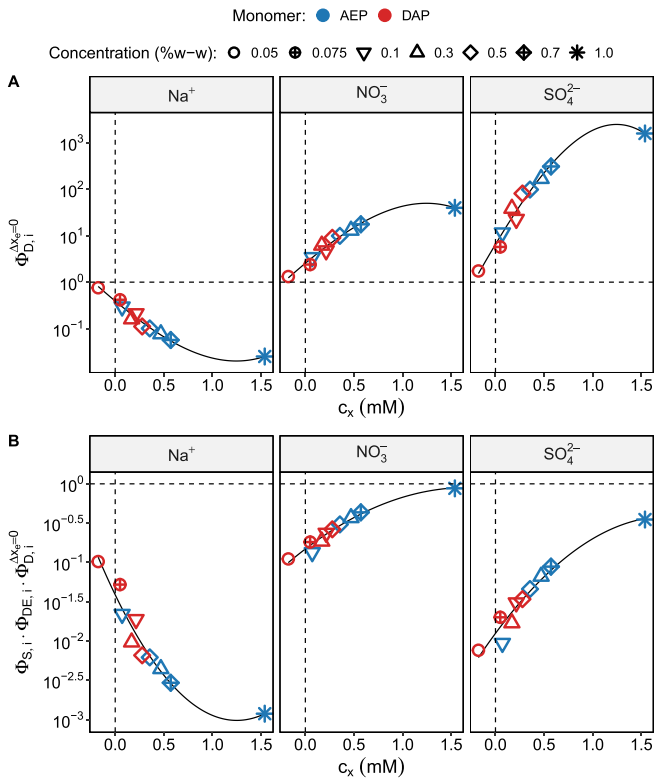



**Fig. 6.** (A) Donnan and (B) overall exclusion (partitioning) coefficients of $Na^+$, $NO_3^-$, and $SO_4^{2-}$ as a function of the effective membrane charge density, $c_x$, for the fabricated membranes.

$r_{pore}$, for the fabricated membranes. In general, DAP membranes achieve larger $r_{pore}$ values under similar fabrication conditions, consistent with the less dense PA layer fabricated with DAP. Notably, increasing the monomer concentration tenfold reduces $r_{pore}$ from 0.69 nm to 0.62 nm in AEP membranes (~11.6 % decrease), whereas DAP membranes experience a more pronounced ~27.3 % reduction (from 0.83 nm to 0.65 nm). AEP membranes show slightly stronger steric and dielectric exclusions, aligned with their generally smaller $r_{pore}$ values (details in Supporting Information).

As expected, the steric exclusion coefficients of $Na^+$, $NO_3^-$, and $SO_4^{2-}$ follow the anticipated trend based on ion size, with $SO_4^{2-}$ exhibiting the highest exclusion (i.e. the smallest coefficient) (Fig. 5A). Meanwhile, the dielectric exclusion coefficients decrease with decreasing pore dimensions, reflecting the smaller $\varepsilon_{pore}$ values and larger solvation energy barrier within confined pores (Fig. 5B). The decline is most pronounced for $SO_4^{2-}$ due to its divalent charge and ion size. Therefore, the difference between the dielectric exclusion coefficient of $NO_3^-$ and $SO_4^{2-}$ widens with decreasing $r_{pore}$. For instance, there is a difference of approximately two orders of magnitude for AEP1 membrane, which attains the smallest $r_{pore}$. Although the magnitude of $r_{pore}$ differs between AEP and DAP membranes, both sets of data follow the same trend in dielectric exclusion owing to the same $\varepsilon^*$ for both membrane types (Supporting Information). Thus, differences in dielectric exclusion between AEP and DAP membranes are driven only by $r_{pore}$ rather than monomer chemical structure.

The electrostatic interactions between membranes and ions exhibit distinct differences between AEP and DAP membranes. Fig. 6A presents the Donnan exclusion coefficients for $Na^+$, $NO_3^-$, and $SO_4^{2-}$ as functions of the membrane charge density ($c_x$) derived from the DSPM-DE model. Consistent with our previous study [24], increasing the amine concentration (AEP or DAP) increases $c_x$, thereby intensifying electrostatic interactions. However, AEP and DAP membranes respond differently: a tenfold rise in AEP concentration results in over a 2000 % increase in $c_x$ (from +0.07 mM to +1.54 mM), whereas similar increase in DAP yields only ~258 % growth in $c_x$ (from −0.18 mM to +0.17 mM). This disparity arises from DAP's lower reactivity, which promotes a more voluminous network formation and yields thicker but less charged membranes, whereas AEP forms comparatively thinner, highly charged PA layers. As the membrane's positive $c_x$ increases, $Na^+$ experiences stronger electrostatic repulsion (Donnan coefficient <1), while anions ($NO_3^-$ and $SO_4^{2-}$) are increasingly attracted (Donnan coefficient >1). Among the anions, $SO_4^{2-}$ shows the steepest response to increasing $c_x$ owing to its divalent negative charge, with the difference in Donnan exclusion between $NO_3^-$ and $SO_4^{2-}$ growing nearly an order of magnitude under the most highly charged conditions (AEP1 membrane). These findings reveal how variations in membrane $c_x$, driven by monomer chemistry and concentration, control the electrostatic partitioning of ions, a key factor in the selective transport behavior of charged NF membranes.

The overall exclusion (or partitioning) coefficients, which integrate steric, dielectric, and Donnan contributions, are functions of $c_x$ for both AEP and DAP membranes, as shown in Fig. 6B. This confirms that the main driver of overall ion partitioning is $c_x$ at the feed-solution/membrane interface. Therefore, AEP membranes display more extreme changes in overall exclusion than DAP membranes, reflecting their larger $c_x$. As $c_x$ increases with higher AEP or DAP concentrations, the electrostatic repulsion of $Na^+$ intensifies, while anions ($NO_3^-$ and $SO_4^{2-}$) experience weaker exclusion. In particular, the steep variation of Donnan exclusion with $c_x$ largely dictates the total exclusion trend, overshadowing dielectric effects. This behavior contrasts with our earlier findings using PIP monomer, where dielectric effects had a more pronounced impact [24]. This interplay yields interesting results for $NO_3^-$ and $SO_4^{2-}$ separation. While increasing amine monomer concentration does increase $SO_4^{2-}$ dielectric exclusion (due to smaller pore

sizes), it also increases positive $c_x$ values, enhancing the electrostatic attraction of $SO_4^{2-}$ even more. Consequently, membranes fabricated at higher AEP or DAP concentrations exhibit smaller differences in $NO_3^-$ and $SO_4^{2-}$ overall exclusion, despite increased differences in dielectric exclusion coefficient. In contrast, membranes prepared with lower concentrations, having weaker positive $c_x$, display larger $NO_3^-/SO_4^{2-}$ exclusion differences because Donnan interactions do not compete as strongly with dielectric exclusion. These observations demonstrate that membrane chemistry and morphology (AEP vs. DAP) fundamentally tune the balance of steric, dielectric, and electrostatic interactions. Modulating membrane charge through monomer concentration and chemical structure is the dominant factor for tuning ion partitioning, with dielectric exclusion playing a secondary, but significant role in $NO_3^-$ and $SO_4^{2-}$ separation.

### 3.3.2. *Transmembrane molar fluxes*

In steady state, the extended Nernst-Planck equation describes the transport of each ion, *i*, through the membrane's active layer by considering its contributions, i.e., advection, electromigration, and diffusion:

$$J_i = J_v c_{i,p} = J_{i,adv} + J_{i,elec} + J_{i,diff} \tag{11}$$

$$J_{i,adv} = K_{i,a} c_i J_v \tag{12}$$

$$J_{i,elec} = -\frac{z_i F c_i K_{i,d} D_{i,\infty}}{RT} \frac{d\Psi}{dx} \tag{13}$$

$$J_{i,diff} = -K_{i,d} D_{i,\infty} \frac{dc_i}{dx} \tag{14}$$

where $J_i$ is the total molar flux, $J_v$ is the solution flux, $c_{i,p}$ is the permeate concentration. $J_{i,adv}$ is the advective contribution (driven by solvent flow), $K_{i,a}$ is the hindrance factor of advection, and $c_i$ is the concentration inside the membrane's active layer. $J_{i,elec}$ is the electromigrative contribution (driven by the electrical potential gradient), $K_{i,d}$ is the hindrance factor of diffusion, $D_{i,\infty}$ is the diffusion coefficient in the bulk solution, and $\Psi$ is the electrical potential. $J_{i,diff}$ is the diffusive contribution (driven by the concentration gradient), and $x$ is the direction across the membrane active layer from the feed towards the permeate side.

We now examine the contribution of each transport mechanism to the total transmembrane molar fluxes. Fig. 7 presents the advective and electromigrative flux contributions for $Na^+$, $NO_3^-$, and $SO_4^{2-}$ as functions of $c_x$. In Fig. 7 we have also included our previously published results on PIP membranes [24]. In the current study, we used varying concentrations of DAP and AEP monomers (at constant TMC concentration) to fabricate a total of ten membranes, nine of which carry a positive charge. In contrast, in our previously published work, we prepared five membranes using varying PIP concentration, but the same TMC concentration as in this study. All five membranes were negatively charged. By incorporating these previously published results alongside the data from the current study, we can draw meaningful comparisons between membranes with positive and negative charges. This combined dataset provides valuable insights into how membrane charge density influences ion transport under the DSPM–DE model. As expected, the advective flux is closely related to the overall exclusion, which is governed by $c_x$ (Fig. 6B). This relationship stems from ion concentration inside the membrane's active layer, where a higher concentration (i.e., larger overall exclusion coefficient) leads to a larger advective flux. Consequently, strongly negative charged membranes (e.g., PIP-based membranes) favor $Na^+$ partitioning and advective transport, whereas strongly positive AEP- or DAP-based membranes promote greater anion advective flux. Notably, AEP membranes show steeper variations in advective flux with changing $c_x$, as they generally attain higher positive charges. In contrast, DAP membranes, being closer to neutral, display more moderate changes in advective flux, even when the solution flux

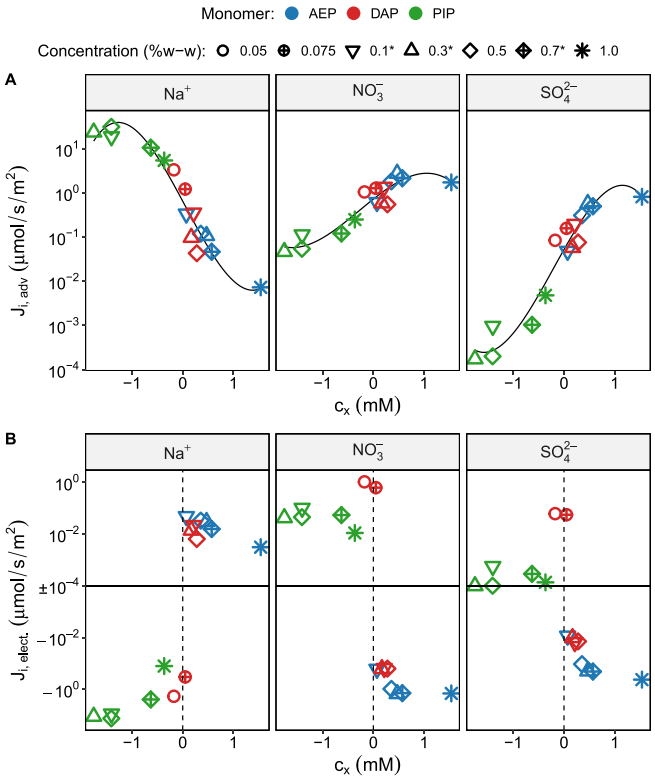



**Fig. 7.** Transmembrane molar fluxes of $Na^+$, $NO_3^-$, and $SO_4^{2-}$ as a function of the effective membrane charge density ($c_x$) for the fabricated membranes: (A) Advective flux and (B) Electromigrative flux for the fabricated membranes. For clarity, symbols marked with an asterisk (*) in the legend correspond to previously reported PIP-based membranes [24] at concentrations: 0.1* = 0.125 % w-w, 0.3* = 0.25 % w-w, and 0.7* = 0.75 % w-w.

varies more steeply, aligning with larger variation of $\Delta x_e$. This underscores the critical role of $c_x$ in determining the advective flux, exceeding the influence of the solution flux through the membrane's active layer.

Fig. 7b shows the electromigrative flux of each ion, plotted on a mixed-sign log axis so that both positive and negative values appear on a logarithmic scale. This approach effectively shows differences spanning multiple orders of magnitude while retaining the sign of the flux, which reflects the direction of ion transport. Positive flux indicates ion transport toward the permeate side, while negative flux indicates ion transport toward the feed side. Unlike the advective flux, the electromigrative flux does not follow a uniform monotonic trend across all membranes; its direction and magnitude are strongly dependent on whether an ion acts as a coion or a counterion, which in turn is governed by the sign and magnitude of $c_x$. Counterions exhibit negative electromigrative fluxes that counterbalance their large advective fluxes, thereby preventing excessive accumulation in the permeate (i.e., breaking electroneutrality condition). Hence, in negatively charged PIP membranes, $Na^+$ has a larger negative electromigrative component, while in positively charged AEP or DAP membranes, the anions $NO_3^-$ and $SO_4^{2-}$ assume that role. Across all monomer types, increased $|c_x|$ intensifies these electromigrative effects, as stronger membrane charges enhance coions exclusion more effectively while driving larger counterion fluxes through stronger electric fields. In other words, coion electromigrative fluxes remain less sensitive to $c_x$, as their concentrations in the membrane's active layer are already low. Overall, these results demonstrate that $c_x$ remains the primary factor regulating the advective-electromigrative interplay in $Na^+/NO_3^-/SO_4^{2-}$ transport, with the specific sign and magnitude of $c_x$ dictating which ions experience the most significant effects.

Fig. 8 presents the diffusive fluxes and total transmembrane molar fluxes of $Na^+$, $NO_3^-$ and $SO_4^{2-}$ as functions of $\Delta x_e$ for the fabricated membranes. Diffusion is driven by the concentration gradient across the membrane's active layer but modulated by hindrance effects that limit ion transport through the membrane pores. Although increasing $\Delta x_e$ values reduce diffusion [22], the extent of this decline is strongly influenced by the physicochemical properties of each membrane. Compared to AEP membranes, DAP membranes tend to yield more open porous structures, i.e., larger $r_{pore}$ and less hindrance [40,41]. Consequently, the DAP membranes exhibit larger diffusive fluxes at comparable $\Delta x_e$ values. This behavior is consistent with their lower overall retention of $NO_3^-$ and $SO_4^{2-}$ (Fig. 4B). For instance, DAP0.05 membrane combines the smallest $\Delta x_e$ and largest $r_{pore}$, allowing both anions to diffusive similarly and yielding the second lowest $NO_3^-/SO_4^{2-}$ selectivity among the tested membranes. Moreover, DAP0.05 membrane, displaying a slightly negative $c_x$, can exhibit negative retention. This result agrees with our previous observations in negatively charged PIP membranes [24], where $Na^+$ diffusion drives a large concurrent $NO_3^-$ diffusive flux to maintain electroneutrality [42]. Because $SO_4^{2-}$ is more strongly excluded at the feed-solution/membrane interface in a negatively charged membrane, $NO_3^-$ and $Na^+$ must diffuse together through similar concentration gradients, making diffusion the dominant mechanism for $NO_3^-$ transport. Consequently, $NO_3^-$ concentration in the permeate exceeds that in the feed, thereby yielding negative retention (Supporting Information). On the other hand, AEP membranes are generally denser (i.e., smaller $r_{pore}$ [40,41] and diffusive fluxes) but can develop stronger positive $c_x$, reducing anion exclusion and enhancing attraction at the feed-solution/membrane interface. For instance, the AEP1 membrane shows the highest $NO_3^-/SO_4^{2-}$ selectivity, consistent with the large difference in the diffusive (and total) fluxes of these anions at larger $\Delta x_e$ values (Fig. 8A and B). Similarly, the AEP0.1

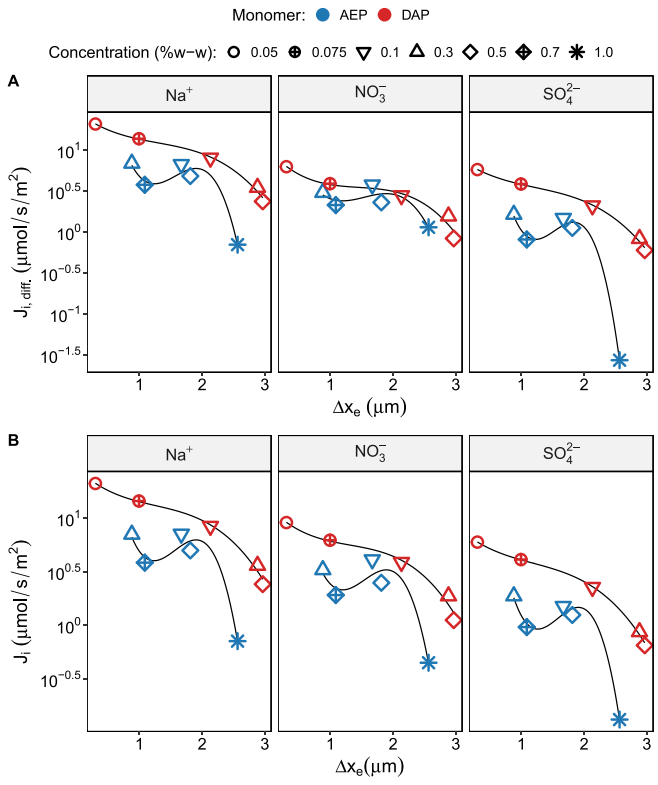



**Fig. 8.** Transmembrane molar fluxes of $Na^+$, $NO_3^-$, and $SO_4^{2-}$ as a function of $\Delta x_e$: (A) Diffusive flux and (B) Total transmembrane flux for the fabricated membranes. The lines connecting the data points are included only to guide the eye and do not correspond to any fitted function or additional interpolation.

membrane has a negative $NO_3^-$ retention (Fig. 4B), reflecting its large $NO_3^-$ total flux (including a significant diffusive contribution) but weakest overall $NO_3^-$ exclusion at the feed-solution/membrane interface (i.e., smallest net $c_x$ of AEP membranes). These examples demonstrate that the interplay of smaller $r_{pore}$ and greater positive $c_x$ values within AEP membranes, as a function of monomer concentration, can alter the diffusive and total fluxes of specific ions. As a result, $NO_3^-$ and $SO_4^{2-}$ exhibit larger differences in fluxes, leading to the higher $NO_3^-/SO_4^{2-}$ selectivity observed for AEP membranes. When examining the total flux (the sum of advective, electromigrative, and diffusive contributions), the structural and charge-driven differences between AEP and DAP become more evident. For DAP membranes, smaller changes in $c_x$ keep advective and electromigrative contributions relatively stable as $\Delta x_e$ varies with changing DAP concentration. Thus, decreasing diffusive flux with increasing $\Delta x_e$ dominates the overall transport. Nonetheless, it is important to note that AEP membranes also exhibit diffusive-driven trends: as $\Delta x_e$ increases, their total flux decreases similar to their diffusive flux. However, AEP membranes' broad variation in $c_x$ might intensify or mitigate these $\Delta x_e$-based diffusion effects, leading to a stronger or weaker overall exclusion of $NO_3^-$ and $SO_4^{2-}$. In other words, AEP membranes' total flux trends are still driven mainly by diffusion, but may deviate from a simple correlation with $\Delta x_e$, particularly when electrostatic interactions intensify, resulting in increased $NO_3^-/SO_4^{2-}$ selectivity at specific AEP concentrations. Owing to relatively stable $c_x$ values, $NO_3^-$ and $SO_4^{2-}$ remain relatively close in total flux values, explaining the lower $NO_3^-/SO_4^{2-}$ selectivity observed for DAP membranes. In contrast, AEP membranes yield broader variations in $c_x$, increasing the differences between $NO_3^-$ and $SO_4^{2-}$ fluxes, as illustrated by the large $NO_3^-$ total flux of AEP0.1 and the strong $NO_3^-/SO_4^{2-}$ separation in AEP1. These observations align with the observed trade-off between flux and selectivity (Fig. 4D). On one hand, larger, more open pores (DAP membranes) render higher overall transmembrane fluxes but weaker $NO_3^-/SO_4^{2-}$ separation. On the other hand, smaller, more highly charged pores (AEP membranes) can attain higher $NO_3^-/SO_4^{2-}$ selectivity, particularly at extreme monomer concentrations, at the expense of total flux. This interplay of pore hindrance, $c_x$, and ion-specific exclusion explains why some AEP membranes (e.g., AEP1) achieve high selectivity, while others (e.g., AEP0.1) demonstrate negative $NO_3^-$ retention.

## 4. Conclusion

This study explored the impact of two structurally distinct piperazine-based monomers, AEP (aminoethylpiperazine) and DAP (1,4-bis(3-aminopropyl)piperazine), on the morphology and performance of TFC membranes for $NO_3^-$ and $SO_4^{2-}$ separation. By systematically varying the aqueous-phase monomer concentrations and employing experimental characterization with DSPM-DE modeling, we elucidated how membrane properties – pore size ($r_{pore}$), thickness to porosity ratio ($\Delta x_e$), and charge density ($c_x$) – determine its ability to reject these anions.

Our results indicate that the structural differences between AEP and DAP significantly impact the IP process with TMC. AEP, which bears a primary amine on its side chain and a secondary amine within the ring, exhibited greater reactivity and generally produced thinner active layers with smaller pores. It also displayed broader changes in net positive charge, creating large shifts in electrostatic interactions. By comparison, DAP produced thicker active layers with more open pores, resulting in higher diffusive fluxes and smaller changes in $c_x$. In terms of water flux, AEP membranes did not always exhibit a direct correlation between PA layer thickness and permeance, thereby highlighting the influence of additional morphological factors. Meanwhile, DAP's reduced overall reactivity (owing to its two 3-aminopropyl groups) produced thicker, smoother, and less permeable layers at equivalent concentrations.

Applying the DSPM–DE model enabled us to break down the transmembrane fluxes into advective, electromigrative, and diffusive contributions, elucidating how thickness, pore size, and membrane charge

each contribute to $NO_3^-/SO_4^{2-}$ separation. For DAP membranes, smaller changes in $c_x$ keep advective and electromigrative contributions relatively stable across changes in $\Delta x_e$; therefore, diffusion becomes the dominant factor in total transmembrane molar fluxes. This led to $NO_3^-$ and $SO_4^{2-}$ exhibiting similar total transmembrane molar fluxes, resulting in lower selectivity. In contrast, AEP membranes develop larger positive $c_x$ values, which can intensify or mitigate $\Delta x_e$-based diffusion effects through increased ion partitioning at the feed-solution/membrane interface. This mechanistic difference accounts for phenomena such as negative $NO_3^-$ retention (when $c_x$ approaches zero or is slightly negative) and improved selectivity in highly charged AEP membranes (e.g., AEP1) at the expense of reduced solution flux.

By comparing diffusive and total transmembrane molar fluxes, we explained why DAP's larger pores and smaller charge changes exhibit larger fluxes and reduced anion separation. On the other hand, AEP membranes yield generally smaller pores (i.e., stronger steric hindrance) and stronger electrostatic effects. This significantly alters the fluxes of individual ions, causing larger differences between $NO_3^-$ and $SO_4^{2-}$, as observed for AEP1 membrane. Although the resulting selective transport often reduces the overall flux, it improves $NO_3^-/SO_4^{2-}$ separation. These findings confirm the typical trade-off between flux and selectivity and demonstrate how targeted monomer design can modulate membrane morphology and charge characteristics to meet specific separation objectives. Although these findings provide a mechanistic framework for tuning flux and $NO_3^-/SO_4^{2-}$ selectivity through monomer structure, they are specific to AEP and DAP monomers. Owing to the rapid and highly sensitive nature of the IP process, any attempt to generalize these results to other types of monomer chemistries is not straightforward. Each monomer system brings its own reactivity and diffusion characteristics, which can affect membrane formation and, ultimately, its mass transport features. Practically, these results suggest that lower monomer reactivity or conditions favoring less dense PA layers will increase ion flux at the expense of selectivity, while higher monomer reactivity - yielding denser, more highly charged films - will favor $NO_3^-/SO_4^{2-}$ selective separation but reduce permeance. Accordingly, extending these design principles to new membrane chemistries will require careful, system-specific validation.

In conclusion, even subtle modifications in monomer chemistry and concentration can profoundly impact PA layer formation and ion transport. Utilizing DSPM–DE modeling to elucidate flux contributions and partitioning, we clarified why certain membranes achieve high $NO_3^-$ selectivity (AEP 1), negative $NO_3^-$ retention (DAP 0.05, DAP0.075, and AEP 0.1), or intermediate behavior.

In addition to elucidating the interplay between pore size, charge density, and flux-selectivity trade-offs, this work uniquely demonstrates that the chemical structure of the aqueous-phase monomer, beyond its concentration, serves as an important variable for tuning NF membrane performance. By comparing two structurally distinct piperazine derivatives (AEP and DAP) within the same DSPM-DE model, we show for the first time that aqueous-phase monomer identity controls the balance of dielectric and Donnan exclusion, enabling systematic decoupling of solvation and electrostatic effects. This mechanistic understanding departs from our previous PIP-only studies, where dielectric exclusion dominated. These insights provide a framework for the rational design of next generation charged TFC membranes tailored for specific $NO_3^-$ separation. While this study exclusively focuses on the effect of the aqueous-phase monomer, we note that systematic variation of the organic-phase monomer chemistry could likewise influence PA layer formation and membrane performance and thus presents an important direction for future research.

## CRediT authorship contribution statement

**Nicolás Cevallos-Cueva:** Writing – review & editing, Writing – original draft, Software, Methodology, Investigation, Formal analysis, Data curation, Conceptualization. **Md. Mushfequr Rahman:** Writing – review & editing, Visualization, Supervision, Resources, Project administration, Conceptualization. **Hluf Hailu Kinfu:** Writing – review & editing, Methodology. **Volker Abetz:** Writing – review & editing, Supervision.

## Funding

This work was funded by the Hereon-I$^2$B-Project NanoMem.

## Declaration of competing interest

The authors declare that they have no known competing financial interests or personal relationships that could have appeared to influence the work reported in this paper.

## Acknowledgments

The authors would like to acknowledge Maren Brinkmann for the PEG analysis in GPC, Juliana Clodt and Barbara Bajer for fabricating the polyacrylonitrile support, Erik Schneider for the SEM analysis, Evgeni Sperling for the AFM analysis, and Jan Pohlmann for setting up the flux and retention measurement facilities.

## Appendix A. Supplementary data

Supplementary data to this article can be found online at https://doi.org/10.1016/j.memsci.2025.124642.

## Data availability

Data will be made available on request.

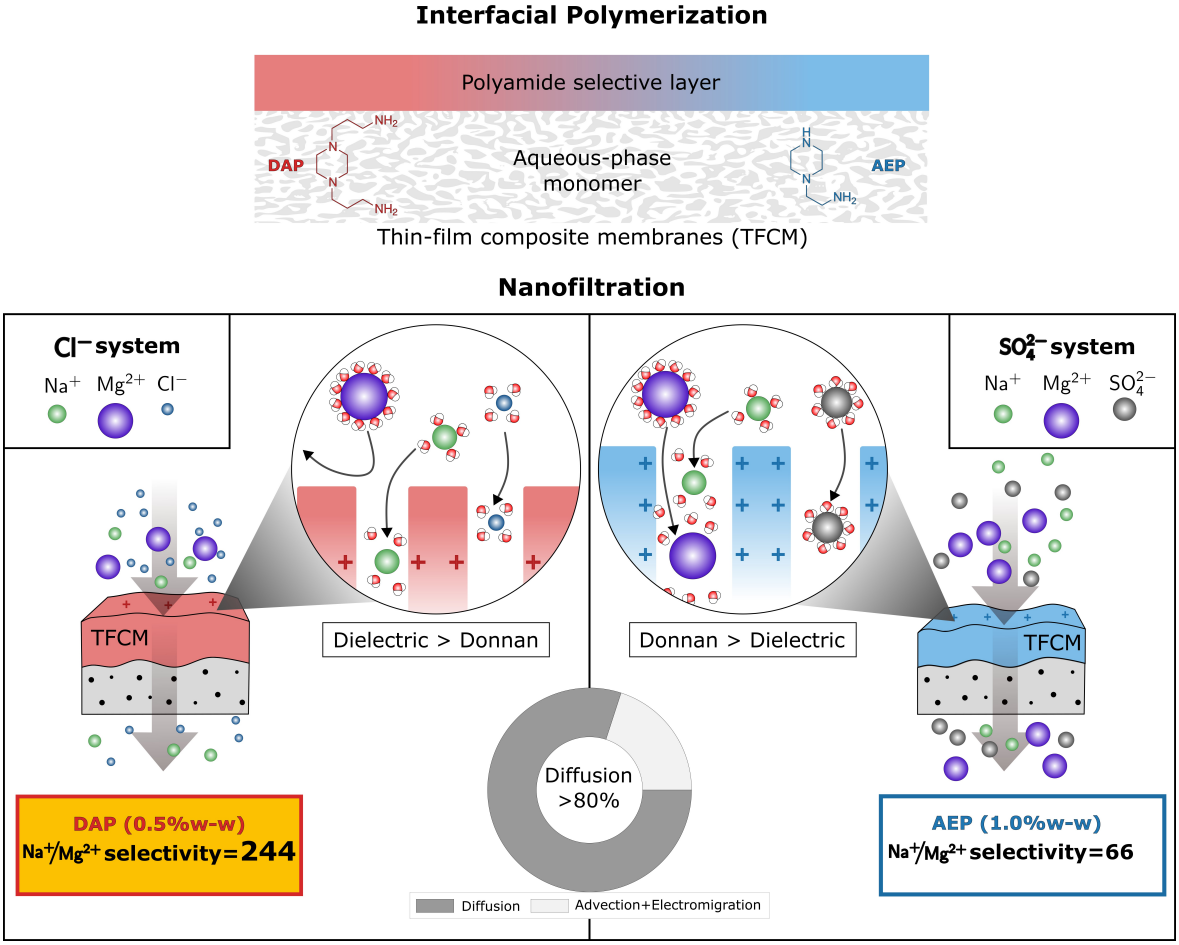
## References

[1] D.M. Manassaram, L.C. Backer, D.M. Moll, A review of nitrates in drinking water: maternal exposure and adverse reproductive and developmental outcomes, Environ. Health Perspect. 114 (2006) 320–327, https://doi.org/10.1289/ehp.8407.
[2] M. Lunau, M. Voss, M. Erickson, C. Dziallas, K. Casciotti, H. Ducklow, Excess nitrate loads to coastal waters reduces nitrate removal efficiency: mechanism and implications for coastal eutrophication, Environ. Microbiol. 15 (2013) 1492–1504, https://doi.org/10.1111/j.1462-2920.2012.02773.x.
[3] Bmu Bmel, Nitratbericht, Gemeinsamer Bericht Der Bundesministerien Für Umwelt, Naturschutz Und Nukleare Sicherheit (BMU) Sowie Für Ernährung Und Landwirtschaft (BMEL), 2020. Bonn, Deutschland, 2020.
[4] E. Abascal, L. Gómez-Coma, I. Ortiz, A. Ortiz, Global diagnosis of nitrate pollution in groundwater and review of removal technologies, Sci. Total Environ. 810 (2022) 152233, https://doi.org/10.1016/j.scitotenv.2021.152233, 152233.
[5] DVWG, Too many animals - too little land. https://www.dvgw.de/english-pages/topics/water/nitrates-and-drinking-water, 2023 accessed 19.02.2025 2025.
[6] K. Wang, X. Wang, B. Januszewski, Y. Liu, D. Li, R. Fu, M. Elimelech, X. Huang, Tailored design of nanofiltration membranes for water treatment based on synthesis–property–performance relationships, Chem. Soc. Rev. 51 (2) (2022) 672–719, https://doi.org/10.1039/D0CS01599G.
[7] M. Paul, S.D. Jons, Chemistry and fabrication of polymeric nanofiltration membranes: a review, Polymer 103 (2016) 417–456, https://doi.org/10.1016/j.polymer.2016.07.085.
[8] Y. Liu, L.L. Liu, B. Narendra, X.R. Chen, S.C. Feng, Y.H. Wan, J.Q. Luo, Advancing high-performance nanofiltration membranes: tailoring monomer molecular design to enhance diffusion-reaction synergy in interfacial polymerization, Desalination 598 (2025), https://doi.org/10.1016/j.desal.2024.118415.
[9] R. Epsztein, R.M. DuChanois, C.L. Ritt, A. Noy, M. Elimelech, Towards single-species selectivity of membranes with subnanometre pores, Nat. Nanotechnol. 15 (2020) 426–436, https://doi.org/10.1038/s41565-020-0713-6.
[10] Zhou Yang, Rui Feng, Zhang Zhang, A review on reverse osmosis and nanofiltration membranes for water purification, Polymers 11 (2019) 1252, https://doi.org/10.3390/polym11081252.
[11] C. Tang, M.L. Bruening, Ion separations with membranes, J. Polym. Sci. 58 (2020) 2831–2856, https://doi.org/10.1002/pol.20200500.
[12] X.H. Zhai, J.Y. Hu, Z. Chu, J.H. Zou, X.S. Li, Z.W. Wang, Rethinking nanofiltration membrane design for breaking the trade-off in Li/Mg separation: a comprehensive analysis based on the separation factor-lithium flux (S-JLi) framework, J. Membr. Sci. 717 (2025), https://doi.org/10.1016/j.memsci.2024.123558.
[13] O. Labban, C. Liu, T.H. Chong, J.H. Lienhard, Relating transport modeling to nanofiltration membrane fabrication: navigating the permeability-selectivity trade-

off in desalination pretreatment, J. Membr. Sci. 554 (2018) 26–38, https://doi.org/10.1016/j.memsci.2018.02.053.
[14] R. Wang, S. Lin, Pore model for nanofiltration: history, theoretical framework, key predictions, limitations, and prospects, J. Membr. Sci. 620 (2021) 118809, https://doi.org/10.1016/j.memsci.2020.118809.
[15] R.J. Zhang, J.Y. Tian, S.S. Gao, B. van der Bruggen, How to coordinate the trade-off between water permeability and salt rejection in nanofiltration? J. Mater. Chem. A 8 (18) (2020) 8831–8847, https://doi.org/10.1039/d0ta02510k.
[16] Y.L. Liu, K.P. Wang, Z.X. Zhou, X.X. Wei, S.J. Xia, X.M. Wang, Y.F. Xie, X. Huang, Boosting the performance of nanofiltration membranes in removing organic micropollutants: trade-off effect, strategy evaluation, and prospective development, Environ. Sci. Technol. (2022), https://doi.org/10.1021/acs.est.2c06579.
[17] P.R. Jin, J.Y. Zhu, S.S. Yuan, G. Zhang, A. Volodine, M.M. Tian, J.X. Wang, P. Luis, B. Van der Bruggen, Erythritol-based polyester loose nanofiltration membrane with fast water transport for efficient dye/salt separation, Chem. Eng. J. 406 (2021), https://doi.org/10.1016/j.cej.2020.126796.
[18] V. Freger, Swelling and morphology of the skin layer of polyamide composite membranes: an atomic force microscopy study, Environ. Sci. Technol. 38 (11) (2004) 3168–3175, https://doi.org/10.1021/es034815u.
[19] C.L. Ritt, J.R. Werber, M. Wang, Z. Yang, Y. Zhao, H.J. Kulik, M. Elimelech, Ionization behavior of nanoporous polyamide membranes, Proc. Natl. Acad. Sci. U. S. A 117 (2020) 30191–30200, https://doi.org/10.1073/pnas.2008421117.
[20] Y.M. Shi, H. Wen, D.P. Hu, J. Wang, Z.W. Dai, Z. Yang, W.B. Yu, S. Liang, J. K. Yang, S.S. Yuan, B. van der Bruggen, Polyamide nanofiltration membranes with enhanced surface charge difference via large aqueous monomer, J. Membr. Sci. 713 (2025), https://doi.org/10.1016/j.memsci.2024.123284.
[21] Y.l. Liu, Y.y. Zhao, X.m. Wang, X.h. Wen, X. Huang, Y.F. Xie, Effect of varying piperazine concentration and post-modification on prepared nanofiltration membranes in selectively rejecting organic micropollutants and salts, J. Membr. Sci. 582 (2019) 274–283, https://doi.org/10.1016/j.memsci.2019.04.018.
[22] N. Cevallos-Cueva, M.M. Rahman, H.H. Kinfu, V. Abetz, Mass transport mechanisms insights of selective sodium/magnesium separation through nanofiltration membranes, J. Membr. Sci. 721 (2025) 123808, https://doi.org/10.1016/J.MEMSCI.2025.123808, 123808.
[23] S. Veríssimo, K.V. Peinemann, J. Bordado, Influence of the diamine structure on the nanofiltration performance, surface morphology and surface charge of the composite polyamide membranes, J. Membr. Sci. 279 (2006) 266–275, https://doi.org/10.1016/j.memsci.2005.12.014.
[24] N. Cevallos-Cueva, M.M. Rahman, H.H. Kinfu, V. Abetz, Mass transport mechanism of nitrate selective nanofiltration membranes on the basis of the Donnan steric pore model with dielectric exclusion (DSPM-DE), Chem. Eng. J. 493 (2024), https://doi.org/10.1016/j.cej.2024.152775.
[25] L. Wang, Y.K. Lin, Y.H. Tang, D. Ren, X.L. Wang, Fabrication of oppositely charged thin-film composite polyamide membranes with tunable nanofiltration performance by using a piperazine derivative, J. Membr. Sci. 634 (2021), https://doi.org/10.1016/j.memsci.2021.119405.
[26] N.K. Saha, S.V. Joshi, Performance evaluation of thin film composite polyamide nanofiltration membrane with variation in monomer type, J. Membr. Sci. 342 (1–2) (2009) 60–69, https://doi.org/10.1016/j.memsci.2009.06.025.
[27] X. Li, C. Zhang, S. Zhang, J. Li, B. He, Z. Cui, Preparation and characterization of positively charged polyamide composite nanofiltration hollow fiber membrane for lithium and magnesium separation, Desalination 369 (2015) 26–36, https://doi.org/10.1016/J.DESAL.2015.04.027.
[28] Y.F. Yan, J. Wang, W.B. Wang, C. Han, Fine-tuning polyamide membrane pores and charge for enhanced Li+/Mg2+separation, J. Membr. Sci. 721 (2025), https://doi.org/10.1016/j.memsci.2025.123812.
[29] A. Szymczyk, C. Labbez, P. Fievet, A. Vidonne, A. Foissy, J. Pagetti, Contribution of convection, diffusion and migration to electrolyte transport through nanofiltration membranes, Adv. Colloid Interface Sci. 103 (2003) 77–94, https://doi.org/10.1016/S0001-8686(02)00094-5.
[30] Z.H. Foo, D. Rehman, A.T. Bouma, S. Monsalvo, J.H. Lienhard, Lithium concentration from salt-lake brine by donnan-enhanced nanofiltration, Environ. Sci. Technol. 57 (15) (2023) 6320–6330, https://doi.org/10.1021/acs.est.2c08584.
[31] Y. Roy, D.M. Warsinger, J.H. Lienhard, Effect of temperature on ion transport in nanofiltration membranes: diffusion, convection and electromigration, Desalination 420 (2017) 241–257, https://doi.org/10.1016/j.desal.2017.07.020.
[32] A. Pérez-González, R. Ibáñez, P. Gómez, A.M. Urtiaga, I. Ortiz, J.A. Irabien, Nanofiltration separation of polyvalent and monovalent anions in desalination brines, J. Membr. Sci. 473 (2015) 16–27, https://doi.org/10.1016/j.memsci.2014.08.045.
[33] V. Freger, G.Z. Ramon, Polyamide desalination membranes: formation, structure, and properties, Prog. Polym. Sci. 122 (2021) 101451, https://doi.org/10.1016/j.progpolymsci.2021.101451, 101451.
[34] K.J. Laidler, M.C. King, The development of transition-state theory, J Phys Chem-Us 87 (15) (1983) 2657–2664, https://doi.org/10.1021/j100238a002.
[35] M.I. Page, W.P. Jencks, Entropic contributions to rate accelerations in enzymic and intramolecular reactions and chelate effect, Proc. Natl. Acad. Sci. U. S. A 68 (8) (1971) 1678, https://doi.org/10.1073/pnas.68.8.1678.
[36] Z. Hao, X.X. Tian, V. Mankol, Q.H. Li, J.X. Wang, Z. Wang, S. Zhao, Polyamide nanofiltration membrane fabricated with ultra-low concentration triaminoguanidine showing efficient desalination performance, J. Membr. Sci. 672 (2023), https://doi.org/10.1016/j.memsci.2023.121449.
[37] K.M. Fan, Z.H. Mai, Y.L. Liu, X.P. Wang, Y.D. Huang, P. Cheng, S.J. Xia, H. Matsuyama, Fabrication of dense polyester nanofiltration membranes with superior fouling and chlorine resistance: effect of polyol monomer properties and underlying mechanisms, Acs Est Eng 3 (11) (2023) 1738–1747, https://doi.org/10.1021/acsestengg.3c00203.
[38] L. Bruni, S. Bandini, The role of the electrolyte on the mechanism of charge formation in polyamide nanofiltration membranes, J. Membr. Sci. 308 (1–2) (2008) 136–151, https://doi.org/10.1016/j.memsci.2007.09.061.
[39] W.R. Bowen, J.S. Welfoot, Modelling the performance of membrane nanofiltration-critical assessment and model development, Chem. Eng. Sci. 57 (2002) 1121–1137, https://doi.org/10.1016/S0009-2509(01)00413-4.
[40] P. Dechadilok, W.M. Deen, Hindrance factors for diffusion and convection in pores, Ind. Eng. Chem. Res. 45 (21) (2006) 6953–6959, https://doi.org/10.1021/ie051387n.
[41] G.M. Mavrovouniotis, H. Brenner, Hindered sedimentation, diffusion, and dispersion coefficients for brownian spheres in circular cylindrical pores, J. Colloid Interface Sci. 124 (1) (1988) 269–283, https://doi.org/10.1016/0021-9797(88)90348-7.
[42] A. Yaroshchuk, M.L. Bruening, E. Zholkovskiy, Modelling nano filtration of electrolyte solutions, Adv. Colloid Interface Sci. 268 (2019) 39–63, https://doi.org/10.1016/j.cis.2019.03.004.

## 3.4. Publication IV: Common anion and piperazine-based monomer chemistry tune $Na^+/Mg^{2+}$ selectivity in nanofiltration: A mechanistic mass-transport analysis

The final section combines aqueous-phase monomer chemistry with electrolyte identity to clarify how the common anion reshapes $Na^+/Mg^{2+}$ selectivity within a single descriptor-based interpretation. By maintaining the same mechanistic framework and treating $Cl^-$ and $SO_4^{2-}$ as a solution variable, this study completes the cumulative sequence. It also provides the immediate basis for connecting how fabrication and electrolyte environment together shape selectivity under mixed-salt conditions.



Desalination 622 (2026) 119765

Contents lists available at ScienceDirect

Desalination

journal homepage: www.elsevier.com/locate/desal

# Common anion and piperazine-based monomer chemistry tune $Na^+/Mg^{2+}$ selectivity in nanofiltration: A mechanistic mass-transport analysis

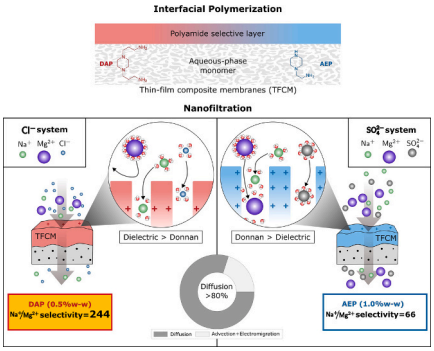
Nicolás Cevallos-Cueva [a], Md. Mushfequr Rahman [a,*], Hluf Hailu Kinfu [a], Volker Abetz [a,b]

[a] Helmholtz-Zentrum Hereon, Institute of Membrane Research, Max-Planck-Straße 1, 21502, Geesthacht, Germany
[b] University of Hamburg, Institute of Physical Chemistry, Martin-Luther-King-Platz 6, 20146, Hamburg, Germany

## HIGHLIGHTS

- DAP0.5 in $Cl^-$: Na/Mg selectivity 244 at practical permeance
- AEP1.0 in $SO_4^{2-}$ attains selectivity 66.
- Monomer and common anion tunes $\varepsilon_{pore}$, charge density, and selectivity
- $Cl^-$ system dielectric-dominated; $SO_4^{2-}$ system Donnan-dominated
- Cation transport diffusion-dominated; anion fluxes counterbalance charge

## GRAPHICAL ABSTRACT




## ARTICLE INFO

*Keywords:*
Interfacial polymerization
Nanofiltration membranes
Piperazine-based monomers
Thin film composite membranes
Na/Mg separation
Ion selectivity
DSPM-DE model

## ABSTRACT

Selective separation of $Na^+$ and $Mg^{2+}$ is fundamental to softening and brine valorization, yet the joint roles of monomer chemistry and electrolyte environment in nanofiltration (NF) remain incompletely resolved. In this work, we report an exceptionally high $Na^+/Mg^{2+}$ selectivity of 244, achieved using a thin-film composite membrane with a polyamide selective layer formed via interfacial polymerization. Systematic studies were conducted on membranes prepared with controlled variations in the aqueous-phase monomers, 1,4-bis(3-aminopropyl)piperazine (DAP) and 2-aminoethylpiperazine (AEP). The highest $Na^+/Mg^{2+}$ selectivity was obtained for the membrane synthesized with 0.5 % w-w DAP in the aqueous phase. The variation of aqueous-phase monomer concentration allowed us to tune the polyamide layer structure and charge, which altered ion transport resistance. Ion separation performance was evaluated using single- and mixed-salt systems (NaCl + $MgCl_2$, $Na_2SO_4$ + $MgSO_4$), supported by Donnan Steric Pore Model with Dielectric Exclusion (DSPM-DE) analysis to quantify steric, Donnan, and dielectric partitioning and their coupling to advective, diffusive, and electromigrative fluxes. The common anion ($Cl^-$ vs $SO_4^{2-}$) critically governed $Na^+/Mg^{2+}$ selectivity by shifting the balance between Donnan and dielectric exclusion. In $Cl^-$ feeds, tighter pores and smaller fitted dielectric constants strengthened dielectric exclusion of $Mg^{2+}$, driving a steeper suppression of $Mg^{2+}$ transport and yielding the highest $Na^+/Mg^{2+}$ selectivity of 244 for DAP (0.5 % w-w). In the $SO_4^{2-}$ system, higher fitted dielectric constants favored Donnan partitioning, with selectivity peaking at 66 for AEP at the highest concentration tested (1.0 %w-w). In positively-charged membranes, cation transport was diffusion-dominated (>80 % of flux), while anion fluxes show strong

* Corresponding author.
*E-mail address:* mushfequr.rahman@hereon.de (Md.M. Rahman).

https://doi.org/10.1016/j.desal.2025.119765
Received 23 October 2025; Received in revised form 9 December 2025; Accepted 14 December 2025
Available online 15 December 2025
0011-9164/© 2025 The Authors. Published by Elsevier B.V. This is an open access article under the CC BY license (http://creativecommons.org/licenses/by/4.0/).

advection or diffusion–electromigration cancelation. These results establish a mechanistic basis linking monomer chemistry, common anion identity, and coupled ion transport, guiding system-specific NF membrane design for selective $Na^+/Mg^{2+}$ separation.

## 1. Introduction

Selective separation of sodium ($Na^+$) and magnesium ($Mg^{2+}$) ions is a persistent challenge in water treatment, desalination, and resource recovery from natural and industrial brines. Efficient removal or recovery of $Mg^{2+}$ is particularly important given its designation as a critical raw material [1], emphasizing the need for separation processes with high $Na^+/Mg^{2+}$ selectivity and practical throughput. Nanofiltration (NF) membranes are attractive for such separations because their pore, surface charge, and chemical structure can be tuned, enabling control of both partitioning and transport [2–5]. Beyond size-based sieving, Donnan (electrostatic) and dielectric effects are increasingly recognized as key contributors to ion selectivity in NF [6–10].

Membrane charge alone, however, does not control selectivity in NF membranes. The electrolyte environment in the feed solution can significantly modulate the separation behavior of the membrane. Both simulations and experiments have shown higher $Na^+/Mg^{2+}$ selectivity when $SO_4^{2-}$ is the co-ion compared with $Cl^-$, with mechanisms that depend on membrane charge. Donnan exclusion dominates in negatively charged membranes, whereas dielectric effects have a stronger influence in neutral membranes [11–13]. Moreover, co-ion partitioning and transport [14], along with ion-specific adsorption and screening, have impact in the pore dielectric constant and shape salt rejection and selectivity [6,8,15–18]. Despite these advances, a comprehensive, mechanistic understanding that integrates membrane structure and charge with electrolyte identity remains underexplored.

Thin-film composite (TFC) NF membranes fabricated by interfacial polymerization (IP) enable tunable control over their physicochemical features such as active layer thickness, roughness, pore size, and charge density [19]. Importantly, both the chemical structure and concentration of the aqueous-phase monomers determine not only the resultant membrane charge but also the active layer morphology and transport behavior [12,20,21]. Since these factors are closely coupled and often interdependent, mechanistic models are required to understand how membrane structure, charge, and solution composition together determine ion transport and selectivity [22]. The Donnan Steric Pore Model with Dielectric Exclusion (DSPM-DE) provides such a framework by linking membrane properties (e.g., pore size, thickness-to-porosity ratio, charge density, and pore dielectric constant) to ion partitioning and fluxes governed by advection, diffusion and electromigration [9,11,23–26]. In our earlier work [12], we systematically explored piperazine (PIP)-based membranes and showed that shifting the membrane from negative to positive charge by varying monomer concentration enhanced $Na^+/Mg^{2+}$ selectivity. DSPM-DE model analysis indicated that the resulting electrical potential gradient across the active layer suppressed $Cl^-$ diffusion and secondarily accelerated cation transport, underscoring the role of the common anion in this separation [12]. However, that mechanistic picture was largely limited to negatively charged or weakly positive membranes. The effects of increasing positive charge density, particularly its interplay with anion identity, have not been systematically studied. More broadly, simultaneous variation of aqueous-phase monomer structure and concentration, together with control over the common anion, has not been comprehensively evaluated with a unified mechanistic treatment.

Here we address this gap by employing two structurally distinct piperazine-based monomers 2-aminoethyl piperazine (AEP) and 1,4-bis (3-aminopropyl) piperazine (DAP) as aqueous-phase monomers. Both retain the rigid six-membered piperazine ring but introduce additional primary amines on short aliphatic side chains (one in AEP; two in DAP). These extra amines increase the amine-to-acyl-chloride stoichiometric ratio during IP, decreasing the residual acyl chlorides that hydrolyze to carboxylates and increasing the density of protonatable groups within the PA layer. Consequently, AEP- and DAP-based membranes can exhibit less negative or even positive surface charge compared to PIP-based analogues [27–29]. Consistent with this expectation, our previous nitrate study measured positive apparent charge densities for AEP- and DAP-based membranes [21]. According to our earlier work on PIP-based membranes [12], a more positive charge enhances $Na^+/Mg^{2+}$ selectivity, typically at the cost of permeance; the ethyl group in AEP and the dual propyl groups in DAP are expected to temper excessive crosslinking without sacrificing permeance, as observed for other positively charged NF membranes [30–33]. Beyond charge, these structural differences produce PA layers with distinct morphologies and transport properties [27–29,34–37]. Therefore, AEP and DAP as aqueous-phase monomers provide access to tunable positive charge and morphology, which, together with electrolyte environment, enable mechanistic analysis of $Na^+/Mg^{2+}$ selectivity.

This study not only focuses on $Na^+/Mg^{2+}$ separations but also systematically clarifies the role of the common anion ($Cl^-$ vs. $SO_4^{2-}$) together with AEP/DAP chemistry, closing the mechanistic gap identified above. In this work, the membrane fabrication conditions are used to systematically tune the PA structure, charge, and dielectric environment to develop a mechanistic description of $Na^+/Mg^{2+}$ separation, rather than to optimize a specific fabrication protocol. Therefore, our focus is on how aqueous-phase monomer structure and concentration, together with the common anion, control ion partitioning and transport in AEP- and DAP-based NF membranes.

Therefore, in this work, we systematically varied the concentration of both AEP and DAP as aqueous-phase monomers to fabricate a series of TFC NF membranes and evaluated single- and mixed-salt retentions (NaCl, $MgCl_2$, $Na_2SO_4$, $MgSO_4$). We then applied the DSPM-DE model to mechanistically link measured performance to membrane structure and charge, quantifying the contributions of steric, Donnan, and dielectric partitioning and their coupling to advective, diffusive, and electromigrative transport. This approach elucidates how monomer chemistry and concentration, together with the common anion, govern $Na^+/Mg^{2+}$ selectivity and provides practical guidance for designing cation-selective NF membranes with tunable performance. Collectively, these insights expand our understanding of ion separation in NF membranes and guide the development of materials with efficient, tunable cation selectivity, while clarifying the mechanistic origins of $Na^+/Mg^{2+}$ selectivity.

## 2. Methodology

### 2.1. Materials

All chemicals were used as received without additional modification. For membrane fabrication, 1-(2-aminoethyl)piperazine (AEP, >99 %), 1,4-bis(3-aminopropyl)piperazine (DAP, >99 %), trimesoyl chloride (TMC), and *n*-heptane were purchased from Sigma-Aldrich Chemie GmbH (Germany). The support was a microporous polyacrylonitrile (PAN) membrane, produced via nonsolvent induced phase separation at Helmholtz-Zentrum Hereon. Poly(ethylene glycol) (PEG, average molecular weight 200 Da) was obtained from VWR International GmbH, while the salts NaCl (>99.5 %) and $Na_2SO_4$ (>99 %) were purchased from Merck KGaA and Carl Roth GmbH, respectively. $MgCl_2.6H_2O$ (>99 %) and $MgSO_4$ (>99.5 %) were purchased from Sigma-Aldrich Chemie GmbH (Germany).

### 2.2. Methods

Thin-film composite (TFC) membranes were fabricated via interfacial polymerization (IP) on polyacrylonitrile (PAN) supports. The PAN supports were first immersed in ultrapure deionized water for 24 h. Excess water was then gently removed by rolling a rubber roller over the wetted support for one minute and wiping with dust-free Kimwipes to eliminate any visible droplets. Each support was subsequently submerged in 350 mL of an aqueous solution of either 2-aminoethylpiperazine (AEP) or 1,4-bis(3-aminopropyl)piperazine (DAP) for 6 min.

Preliminary experiments indicated that DAP-based membranes prepared at identical concentrations displayed very low permeance, while AEP-based membranes yielded overly thin defective layers. Therefore, three overlapping concentrations (0.10, 0.30, and 0.50 %w-w) were chosen for direct comparison; in addition, two lower concentrations for DAP (0.05 and 0.075 %w-w) and two higher concentrations for AEP (0.70 and 1.00 %w-w) were included. This resulted in five well-spaced monomer concentrations per monomer.

The soaked supports were mounted onto a 5.1 × 15.9 cm glass plate fitted with a nitrile rubber gasket and PTFE frame. IP was initiated by pouring a 0.30 %w-w solution of trimesoyl chloride (TMC) in HPLC-grade *n*-heptane over soaked support and allowing the reaction to proceed for 90 s. To quench the IP reaction, 150 mL of pure *n*-heptane was applied to the membrane surface. The freshly formed TFC membranes were air-dried at room temperature for 30 min, then heat-treated under vacuum at 60 °C for an additional 30 min. Finally, membranes were stored in ultrapure deionized water at ambient conditions until use. At least three replicate membranes were produced for each set of IP conditions. The membranes are labeled AEPx or DAPx, where x is the %w-w concentration of the respective aqueous-phase monomer during the IP reaction.

#### 2.2.1. Morphology characterization

Surface and cross-sectional features of the membranes were examined by scanning electron microscopy (SEM). Prior to imaging, samples were desiccated in a vacuum oven at 60 °C for no less than 72 h, then coated with a ≈ 1.0–1.5 nm layer of platinum via sputtering. Imaging was performed on a Zeiss Merlin SEM under an accelerating voltage of 1.5–3 kV.

The topographical characteristics of the membrane surfaces were characterized by atomic force microscopy in tapping mode using a Bruker MultiMode 8 instrument. Measurements were acquired over 3 μm × 3 μm scans with RTESPA-150 probes (nominal tip radius ~ 8 nm). Surface roughness parameters (Rq and Ra) were extracted from the height data using NanoScope Analysis software. Here, Rq (also termed the root-mean-square roughness) is defined as the square root of the mean of the squared deviations of surface heights from the mean plane.

#### 2.2.2. Separation performance evaluation

Membrane performance was characterized by measuring water permeance and solute rejection in a stirred dead-end filtration cell (Millipore) equipped with a 2.14 $cm^2$ effective membrane area. Prior to any retention tests, each membrane was compacted by filtering ultrapure deionized water at 4 bar and room temperature for at least 2 h, until a steady permeate flux was reached. The pure water permeance (PWP) was then calculated from the steady-state compaction data according to:

$$PWP = \frac{\Delta m}{\delta_{H_2O} A_{mb} \Delta t \Delta P} \tag{1}$$

where $\Delta m$ is the change of mass, $\delta_{H_2O}$ is the density of liquid water at room temperature, $A_{mb}$ is the effective membrane area (2.14 $cm^2$), $\Delta t$ is the elapsed time, and $\Delta P$ is the transmembrane pressure.

*2.2.2.1. PEG retention.* To characterize the structure of the interfacially polymerized membranes, retention measurements were carried out with poly(ethylene glycol) 200 (PEG 200) at transmembrane pressures of 0.5, 1.0, 1.5, 2.0, 2.5, 3.0, 3.5, and 4.0 bar. At each pressure, permeate was collected over a defined time interval ($\Delta t$), and the volume flux ($J_v$) was determined by:

$$J_v = \frac{\Delta m}{\delta_{H_2O} A_{mb} \Delta t} \tag{2}$$

The PEG concentration was measured with gel permeation chromatography (GPC) (VWR-Hitachi 2130 pump, Hitachi, Darmstadt, Germany).

*2.2.2.2. Ion retention.* Membrane performance was characterized by measuring ion rejection under both single-salt and mixed-salt conditions. All tests were conducted in a stirred dead-end filtration cell (300 rpm) to suppress concentration polarization, and each run was repeated at least three times. For single-salt experiments, 200 mg/L solutions of NaCl, $MgCl_2$, $Na_2SO_4$, and $MgSO_4$ were prepared and introduced into the cell. Mixed-salt feeds were prepared by combining NaCl + $MgCl_2$ or $Na_2SO_4$ + $MgSO_4$ to yield equimolar concentrations of $Na^+/Mg^{2+}$, at a total ion concentration of 200 mg/L. These solutions were selected as idealized chloride- and sulfate-dominated model electrolytes that capture the major ions present in natural and industrial brines, while allowing us to isolate the effect of the common anion on $Na^+/Mg^{2+}$ separation. The transmembrane pressure was kept constant at 3 bar. To ensure steady-state conditions, permeate collected during the initial two hours was discarded; then, 1 mL samples of feed, retentate, and permeate were collected for analysis. Because retentate concentration changes over time in dead-end mode, the observed retention for species *i* ($R_{i,obs}$) was calculated using an average of feed and retentate concentrations:

$$R_{i,obs} = 1 - \frac{2c_{i,p}}{c_{i,f} + c_{i,r}} \tag{3}$$

where $c_{i,p}$, $c_{i,f}$, $c_{i,r}$ are the concentrations of species *i* in the permeate, feed, and retentate solutions, respectively. These concentrations were quantified with an ion chromatograph (Dionex ICS600, Thermo Fisher Scientific Inc., USA).

From these retention data, both the ideal selectivity, $S^*_{a/b}$, calculated from single salt retention tests and the real selectivity, $S_{a/b}$, from mixed salt retention tests were determined using:

$$S^*_{a/b} \text{ or } S_{a/b} = \frac{1 - R_{a,obs}}{1 - R_{b,obs}} \tag{4}$$

#### 2.2.3. DSPM-DE model

The membranes' input parameters required by the DSPM-DE model are the thickness-to-porosity ratio ($\Delta x_e$), pore radius ($r_{pore}$), pore dielectric constant ($\varepsilon_{pore}$), and membrane charge density ($c_X$). For the DSPM-DE analysis, we did not aim to determine a full pore size distribution, because only an effective pore radius is needed as the pore-size descriptor in the model. This effective $r_{pore}$ and $\Delta x_e$ were obtained from PEG 200 retention measured at different transmembrane pressures [38–41], as described in Section 2.2.2.1. $\varepsilon_{pore}$ and $c_X$ were determined by fitting mixed-salt rejection measurements. Parameter estimation was performed in Python using SciPy's dual-annealing global optimizer coupled with a Nelder-Mead local search (convergence tolerance $10^{-6}$). Further details of the DSPM-DE model equations and the fitting procedure are provided in the Supporting Information.

## 3. Results and discussion

### 3.1. Membrane fabrication and structural characterization

Interfacial polymerization (IP) with AEP and DAP yields polyamide

(PA) layers with distinct growth modes, as evidenced by representative SEM cross-sections and surface topographies of the PA active layers (Fig. 1A and B). AEP, whose secondary amine in the ring accelerates interfacial polycondensation, produces a compact, nodular PA layer within the first few seconds of reaction. In contrast, the lower reactivity of DAP leads to formation of a more open incipient network that enables continued monomer diffusion and deeper polymerization into the organic phase [21]. These qualitative differences during early-stage growth are consistent with the observed morphologies.

These kinetic differences manifest in different thickness and roughness characteristics (Fig. 1C and D). For DAP-based membranes, the observed PA layer thickness increases continuously from ≈15 nm at 0.05 % w-w to 145 nm at 0.5 % w-w, accompanied by a progressive smoothing of the surface as nodular features coalesce. In contrast, AEP-based membranes undergo self-limited diffusion growth, thickening only up to ≈63 nm by 0.30 % w-w before plateauing [42]; their RMS roughness remains high across most of the concentration range (0.3–1.0 % w-w).

While microscopy provides valuable insight into surface and cross-sectional morphology, it does not directly allow to predict mass transport resistance. To capture the mass transport resistance of the polyamide selective layer, mass transport descriptors are derived from PEG 200 retention tests. These descriptors reinforce the qualitative morphological observations. The rougher PA layer in the AEP-based membranes increases the surface area available for transport, which partially counterbalances the larger hydraulic resistance expected from thicker active layers. $\Delta x_e$ is an average metric of transport resistance. $\Delta x_e$ is generally smaller for AEP-based membranes even for membranes displaying thicker active layers (Fig. 1E). $r_{pore}$ tightens with monomer concentration for both membranes but remains consistently larger for DAP (0.83 to 0.65 nm) than for AEP-based membranes (0.69 to 0.62 nm) over a ten-fold increase (Fig. 1F), indicating a looser PA network.

These observations highlight that aqueous-phase monomer selection provides a practical approach to tailoring pore size and transport resistance. These structural differences foreshadow systematic changes in ion separation performance that we examine in the next sections.

### 3.2. Single salt retention and influence of common anion

Building on the previous analysis where increasing aqueous-phase monomer concentration produced a tighter active layer and increased mass-transport resistance, we now assess how the electrolyte environment influences ion-selective separation. We first evaluated single-salt retentions (NaCl, $MgCl_2$, $Na_2SO_4$, and $MgSO_4$) to evaluate the role of common anion in $Na^+/Mg^{2+}$ separation (Fig. 2).

At the low monomer concentrations, retentions of sulfate salts exceed those of the corresponding chlorides (e.g., AEP0.1: $Na_2SO_4$ ≈ 50 % and $MgSO_4$ ≈ 80 % vs. NaCl ≈ 30 % and $MgCl_2$ ≈ 50 %; Fig. 2A). Increasing AEP or DAP concentration reverses the trend, and chloride salts exhibit higher retention (e.g., AEP1.0: NaCl ≈ 80 % vs. $Na_2SO_4$ ≈ 70 %). In most cases, $Mg^{2+}$ is retained more strongly than $Na^+$, with a notable exception at very low DAP concentration (DAP0.05), where $Na^+$ retention surpasses $Mg^{2+}$. Comparing AEP- and DAP-based membranes at equal monomer concentrations (i.e., 0.1, 0.3, and 0.5 %w-w), the AEP-based membranes attain higher retention of $Na_2SO_4$ and $MgSO_4$, whereas smaller NaCl and $MgCl_2$ relative to the DAP-based.

The ideal $Na^+/Mg^{2+}$ selectivity (S*, Eq. 4) increases markedly with monomer concentration and increases more strongly when $Cl^-$ is the common anion (Fig. 2B). For AEP-based membranes, S* increases from ≈ 1.4 to 79.6 in $Cl^-$ (~57-fold) and from ≈ 2.3 to 33.9 in $SO_4^{2-}$ (~15-fold); DAP-based membranes show analogous increases (≈ 1 to 19 in $Cl^-$; ≈ 0.9 to 6.3 in $SO_4^{2-}$). These selectivity gains are accompanied with reduced water permeance due to thicker/tighter active layers (Section 3.1).

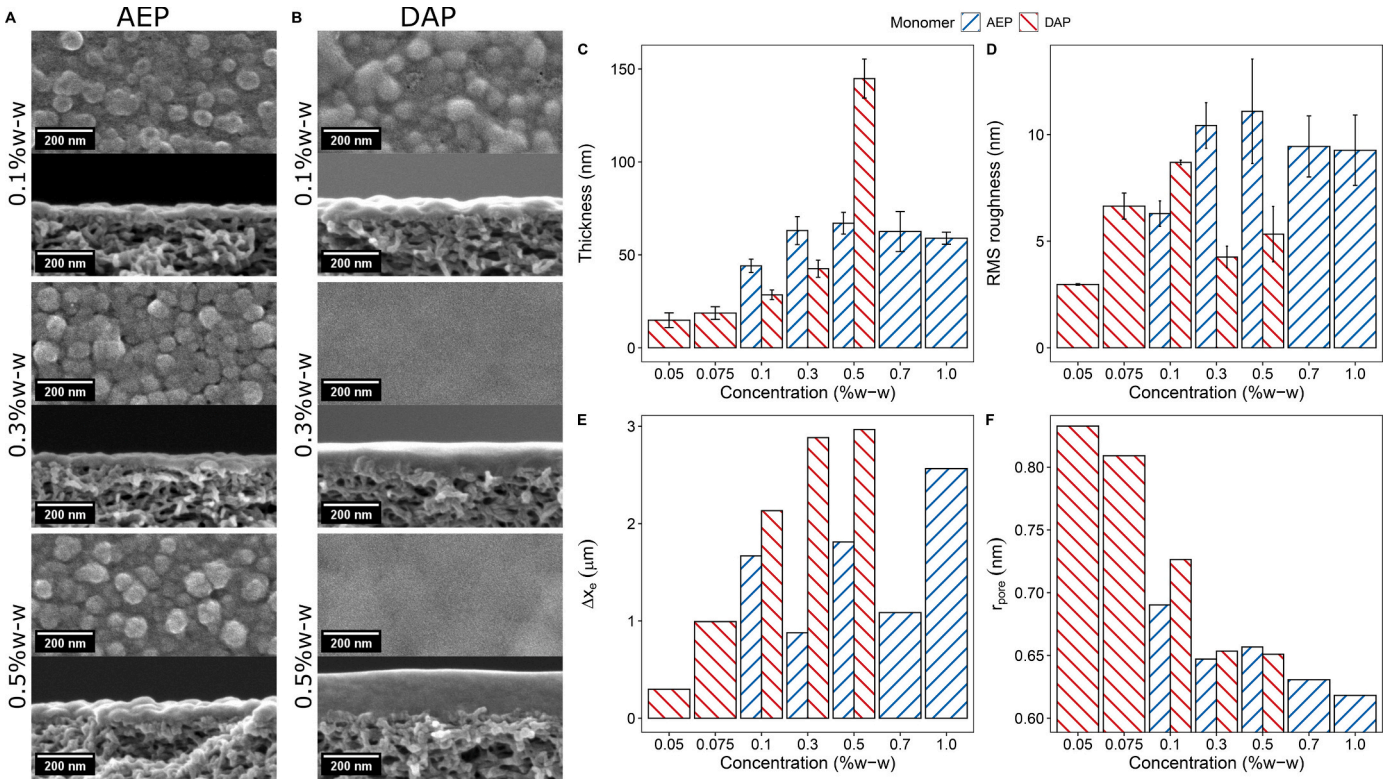



**Fig. 1.** Representative SEM cross-sections and surface topographies of the polyamide (PA) active layers fabricated with (A) AEP and (B) DAP. (C) Average PA layer thickness on the PAN support (error bars represent the standard deviation of thickness measured at different positions along the length of a single membrane), (D) RMS roughness of the PA layer, (E) thickness-to-porosity ratio, $\Delta x_e$, and (F) effective pore radius, $r_{pore}$, as functions of aqueous-phase monomer concentration. The complete set of SEM micrographs for all fabrication conditions is provided in the Supporting Information.

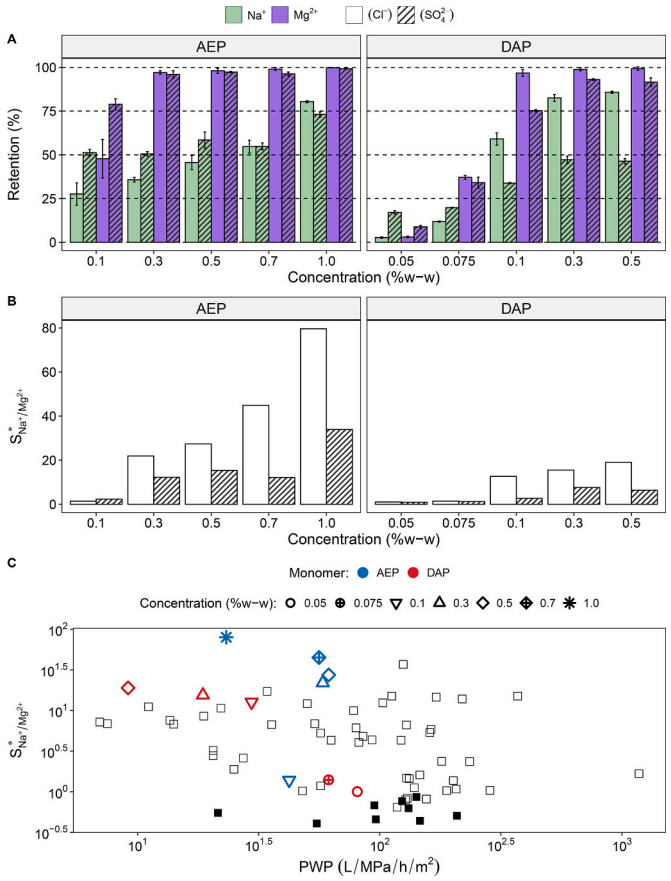



**Fig. 2.** Single-salt retention performance of the fabricated membranes. (A) Cation retention and (B) Ideal $Na^+/Mg^{2+}$ selectivity ($S^*_{Na^+/Mg^{2+}}$) as functions of the aqueous-phase monomer concentration for single salts. The anion in parentheses is the corresponding anion of the single salt, e.g., $Na^+(SO_4^{2-})$ represents $Na^+$ retention from $Na_2SO_4$ retention tests. (C) Comparison of $S^*_{Na^+/Mg^{2+}}$ (from NaCl and $MgCl_2$ single-salt retention tests) and pure water permeance (PWP) of the fabricated membranes (colored symbols) with commercially available NF membranes (black filled squares) and lab-made NF membranes (black open squares). Literature data were adapted from [19,30,31,34–37,45–64], with corresponding values summarized in Table S2. Although the data in (C) were obtained under different testing conditions, this comparison highlights the range of $Na^+/Mg^{2+}$ selectivities achievable by NF membranes and underscores the competitive performance of the fabricated membranes relative to both commercial and lab-made benchmarks.

The anion-dependent trends in retention and selectivity are consistent with classical electrostatic and dielectric effects. At low charge, stronger co-ion exclusion for $SO_4^{2-}$, coupled via electroneutrality to cation partitioning, correlates with higher sulfate-salt retentions. As monomer concentration increases and the PA becomes net-positive [43], Donnan partitioning reverses, leading to higher chloride-salt retention.

Fig. 2C benchmarks the membranes developed in this work against both commercial NF membranes and other lab-fabricated membranes reported in literature by plotting the $Na^+/Mg^{2+}$ ideal selectivity S* (from NaCl and $MgCl_2$ single-salt tests) against pure water permeance (PWP). The comparison clearly demonstrates that seven of the ten membranes prepared here achieve higher selectivity than most reported membranes, highlighting the effectiveness of tailoring the aqueous-phase monomer chemistry. Among them, three DAP-based and four AEP-based membranes show particularly strong performance. The AEP1.0 stands out with a S* ≈ 80, that surpasses all other membranes in the dataset, while maintaining a permeance within typical commercial NF membrane permeance values. DAP-based membranes achieve slightly lower S* in $Cl^-$ yet remain competitive in this comparison. This unique combination of very high $Na^+/Mg^{2+}$ selectivity with practical permeance underscores the potential of tuning aqueous-phase monomer structure and exploiting anion identity to drive cation-selective NF toward benchmark performance.

In summary, the single-salt results suggest that membrane charge and dielectric confinement, both tunable via the aqueous-phase monomer, work with the electrolyte environment to control $Na^+/Mg^{2+}$ separation. Next, we test whether these trends persist under mixed-salt conditions, where ion competition and coupling become relevant [44].

### 3.3. Mixed salt retention and influence of common anion

Mixed-salt tests (equimolar $Na^+/Mg^{2+}$ with $Cl^-$ or $SO_4^{2-}$) underscore the strong role of the common anion in $Na^+/Mg^{2+}$ separation (Fig. 3). For both AEP- and DAP-based membranes, increasing aqueous-phase monomer concentration leads to higher retentions of all ions, with $Mg^{2+}$ rejected more strongly than $Na^+$. As expected, gains in retention are accompanied by some loss in flux (Supporting Information).

The anion dependence is pronounced and monomer specific. For AEP-based membranes, $Na^+$ retention is higher in the $SO_4^{2-}$ mixture at low monomer concentrations (AEP0.1-AEP0.5), whereas at higher concentrations the $Cl^-$ mixture yields larger $Na^+$ and $Mg^{2+}$ retentions (Fig. 3A-B). In contrast, DAP-based membranes show higher retentions in the $Cl^-$ system at all but the lowest concentrations (DAP0.05 and DAP0.075). These mixed-salt behaviors mirror the single-salt baseline trends (Fig. 2), indicating that the underlying separation mechanisms persist under competitive ion transport and rejection conditions.

Selectivity trends reflect these patterns. $Na^+/Mg^{2+}$ selectivity increases with monomer concentration for both ionic systems and is consistently higher in the $Cl^-$ system. At equal monomer concentrations (0.1, 0.3, 0.5 % w-w), DAP-based membranes deliver higher selectivity in $Cl^-$, with DAP0.5 reaching S ≈ 244. In contrast, AEP-based membranes exhibit higher selectivity in the $SO_4^{2-}$ system, with AEP1.0 reaching S ≈ 66. These outcomes underscore the combined roles of membrane structure and charge together with electrolyte environment in shaping $Na^+/Mg^{2+}$ separation performance.

Fig. 3D benchmarks the $Na^+/Mg^{2+}$ selectivity of the fabricated membranes under mixed-salt conditions against both commercial NF membranes and representative lab-made membranes reported in the literature, plotted as a function of solution flux. Consistent with the single-salt results (Fig. 2C), seven of the ten membranes fabricated in this work maintain superior performance, achieving higher selectivity than most reported membranes while operating within the typical permeance window of commercial NF membranes. Remarkably, in the mixed-salt system, the DAP0.5 membrane exhibited the highest $Na^+/Mg^{2+}$ selectivity, surpassing all other membranes included in the benchmark comparison. The AEP1.0 membrane, while no longer the top performer, still ranked second overall and clearly outperformed both commercial benchmarks and the majority of reported lab membranes. Together, these results demonstrate that the design strategy yields membranes with exceptional ion selectivity in both single- and mixed-salt environments, and further highlight that the balance of monomer chemistry and electrolyte conditions can shift which formulations achieve peak performance.

In summary, the common anion controls not only absolute ion retention but also the $Na^+/Mg^{2+}$ selectivity across AEP- and DAP-based membranes. This indicates that the relative contributions of Donnan and dielectric interactions depend on the electrolyte environment (common anion) as well as monomer chemistry and concentration. To quantify these mechanisms and their implications for interfacial partitioning, transport, and selectivity, we next apply the DSPM-DE model.

### 3.4. DSPM-DE model

To mechanistically interpret the observed $Na^+/Mg^{2+}$ separation trends, we fitted the mixed-salt retention data to the DSPM-DE model

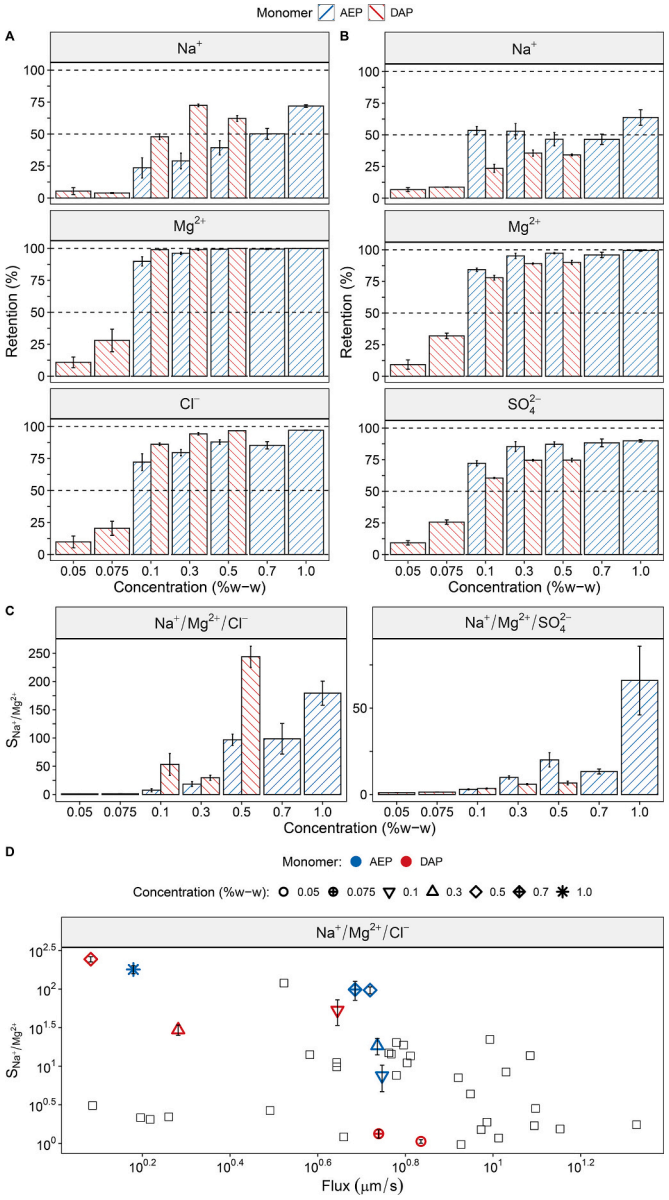



**Fig. 3.** Mixed-salt retention performance of the fabricated membranes. Ion retention as a function of the aqueous-phase monomer concentration for (A) NaCl + $MgCl_2$ and (B) $Na_2SO_4$ + $MgSO_4$ mixed salts. (C) Real $Na^+/Mg^{2+}$ selectivity ($S_{Na^+/Mg^{2+}}$) as a function of aqueous-phase monomer concentration for each ionic system. (D) Comparison of $S_{Na^+/Mg^{2+}}$ (from NaCl + $MgCl_2$ mixed-salts tests) and solution flux of the fabricated membranes (colored symbols) with lab-made NF membranes (black open squares). Literature data were adapted from [12,13,65–69], with corresponding values summarized in Table S3. Although the data in (D) were obtained under different testing conditions, this comparison highlights the range of $Na^+/Mg^{2+}$ selectivities achievable by NF membranes and underscores the competitive performance of the fabricated membranes relative to reported lab-made benchmarks.

and obtained the fitted pore dielectric constant ($\varepsilon_{pore}$) and membrane charge density ($c_X$) as a function of the aqueous-phase monomer concentration and common anion. In parallel, the effective pore radius ($r_{pore}$) and thickness-to-porosity ratio ($\Delta x_e$) were determined independently from PEG 200 retention tests (Fig. 1E-F). The fitted parameters are summarized in Fig. 4A-B ($\varepsilon_{pore}$) and Fig. 4C-D ($c_X$). These fitted parameters provide a consistent framework to link experimental rejection data with fundamental membrane properties, thereby enabling a deeper understanding of ion-specific separation mechanisms.

In this framework, dielectric confinement is captured by $\varepsilon_{pore}$, which

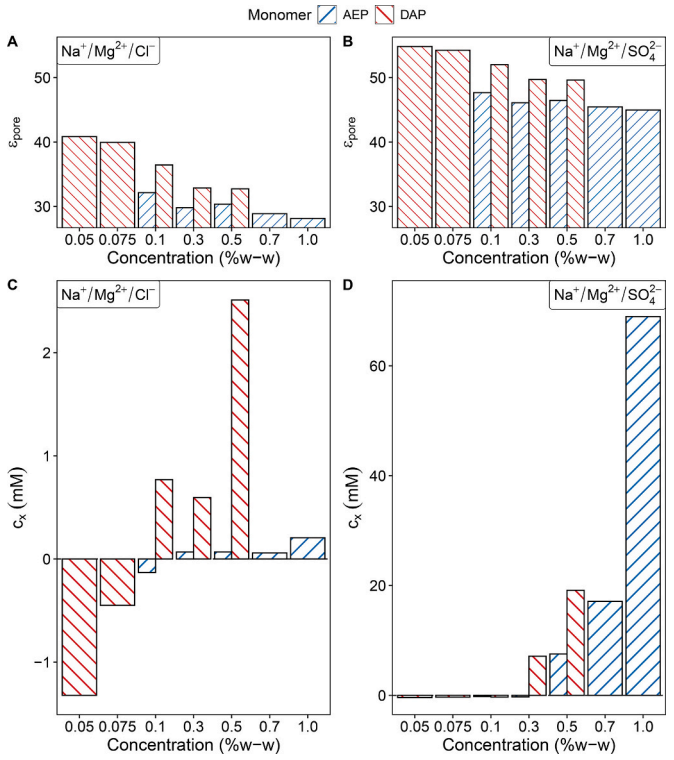



**Fig. 4.** Fitted input parameters obtained from mixed ion retention tests as a function of the aqueous-phase monomer concentration. $Na^+/Mg^{2+}/Cl^-$: (A) $\varepsilon_{pore}$ and (C) $c_x$. $Na^+/Mg^{2+}/ SO_4^{2-}$: (B) $\varepsilon_{pore}$ and (D) $c_x$.

takes into account the phenomenon that inside the nanometer-scale pores the water molecules experience restricted mobility compared to the bulk water. In extremely narrow pores, the dielectric response of the water molecules near the pore walls dominates the overall $\varepsilon_{pore}$. Eq. 5 represents a simple model in which the reduction of water's dielectric constant within the pore arises primarily from a single interfacial layer of water molecules having thickness $d_{H_2O}$ with dielectric constant $\varepsilon^*$ surrounding a bulk-like core with dielectric constant $\varepsilon_{bulk}$. Here, $\varepsilon^*$ varies with the ionic system ($Na^+/Mg^{2+}/Cl^-$ or $Na^+/Mg^{2+}/ SO_4^{2-}$) and the aqueous-phase monomer (AEP vs. DAP), so that $\varepsilon_{pore}$ captures systematic dependencies on both membrane structure and electrolyte environment (details in Supporting Information). Throughout, $\varepsilon_{pore}$ and $c_X$ should be interpreted as fitted (apparent) parameters that represent the combined effects required to reproduce the measured retentions.

$$\varepsilon_{pore} = \varepsilon^* + (\varepsilon_{bulk} - \varepsilon^*)\left(1 - \frac{d_{H_2O}}{r_{pore}}\right)^2 \quad (5)$$

We first report the trends in $\varepsilon_{pore}$ and $c_X$ (Fig. 4), then quantify interfacial partitioning at the feed-solution/membrane interface using steric, dielectric, and Donnan coefficients, and finally analyze how these partitioning effects combine with advection, diffusion, and electromigration to produce total transmembrane fluxes and selectivity.

As defined in Eq. (5), $\varepsilon_{pore}$ reflects dielectric confinement within the pore. Thus, pore tightening (smaller $r_{pore}$) lowers $\varepsilon_{pore}$. Fig. 4A-B shows that $\varepsilon_{pore}$ decreases with increasing monomer concentration for both membrane chemistries, but with a pronounced anion dependence. In the $Cl^-$ system, $\varepsilon_{pore}$ drops by ~12 % for AEP (32 to 28) and ~ 20 % for DAP (41 to 33) over a ten-fold concentration increase. In the $SO_4^{2-}$ system, the decreases are smaller: ~6 % for AEP (48 to 45) and ~ 10 % for DAP (55 to 50). These changes indicate that the dielectric response of the pore environment is not fixed but strongly influenced by external solution conditions and membrane chemistry. Consistent with these trends, the fitted $\varepsilon^*$ values are consistently higher in the $SO_4^{2-}$ system (i.e., AEP:

30; DAP: 35) than in $Cl^-$ (AEP: 6; DAP: 10) (Supporting Information), yielding higher $\varepsilon_{pore}$ in the $SO_4^{2-}$ system. These results indicate that both pore confinement (via $r_{pore}$) and the pore-wall/water interaction (via $\varepsilon^*$) determine $\varepsilon_{pore}$.

Physically, the higher $\varepsilon^*$ (and thus higher $\varepsilon_{pore}$) in the $SO_4^{2-}$ system is consistent with anion-specific hydration that increases water uptake in the polyamide network [70]. The strongly hydrated $SO_4^{2-}$ ion, together with associated fixed charges, draws additional water into the PA network, promoting pore hydration/swelling, thereby elevating $\varepsilon^*$. By Eq. (5), this yields higher $\varepsilon_{pore}$ in the $SO_4^{2-}$ system. In contrast, the $Cl^-$ system exhibits lower $\varepsilon^*$ and a stronger sensitivity of water polarization to confinement, producing lower $\varepsilon_{pore}$ and a steeper decline as pores tighten. Overall, these findings highlight that $\varepsilon_{pore}$ is a dynamic descriptor of pore environments, reflecting both structural confinement and specific ion-polymer interactions. We discuss the consequences of these dielectric environments for interfacial partitioning in Section 3.4.1.

Within the DSPM-DE framework, $c_X$ is obtained by fitting mixed-salt rejection data and should be regarded as the apparent effective charge that enables consistent, relative comparison across membranes and conditions. Ion-dependent variations in fitted $c_X$ have been reported previously for ion-selective NF membranes, originating from interfacial phenomena such as anion adsorption, electrostatic screening, and binding-association effects that are not explicitly represented in the model [18,23,67,71,72]. Accordingly, the fitted $c_X$ adjusts to capture the observed ion retentions. Hence, $c_X$ is a practical descriptor representing the real charge density of the membrane in a particular feed solution environment. We also measured the streaming zeta potential of all membranes. The corresponding values are reported in the Supporting Information (Table S1). Fig. 4C-D presents the fitted $c_X$ values for all membranes in both ionic systems.

Across both chemistries, $c_X$ increases with aqueous-phase monomer concentration, reflecting greater protonation of amine sites [43]. At the lowest concentrations some membranes remain near-neutral or slightly negative. At equal monomer concentrations (0.1–0.5 % w-w), DAP-based membranes exhibit larger $|c_X|$ than AEP-based membranes, and across all membranes, $c_X$ is generally more positive in the $SO_4^{2-}$ system than in $Cl^-$ (Fig. 4C-D). These anion-specific differences are consistent with competitive interfacial interactions: the smaller, less strongly hydrated $Cl^-$ ion (3.32 Å) can more effectively screen positive sites than $SO_4^{2-}$ (3.79 Å), resulting in a lower apparent $c_X$ in the $Cl^-$ system [73,74].

Membranes with the highest positive $c_X$ also achieve the largest $Na^+/Mg^{2+}$ selectivities in their respective systems (e.g., DAP0.5 in $Cl^-$: $S \approx 244$; AEP1.0 in $SO_4^{2-}$: $S \approx 66$), underscoring the role of charge in driving $Na^+/Mg^{2+}$ separation. However, the $SO_4^{2-}$ system, despite larger $c_X$, does not always yield the highest selectivity because its higher $\varepsilon_{pore}$ weakens dielectric exclusion. Thus, $c_X$ and the dielectric environment act together to determine separation performance (see Section 3.3 and Fig. 4C-D for $\varepsilon_{pore}$).

### 3.4.1. Exclusion phenomena at the feed-solution/membrane interface

With the fitted pore dielectric constant ($\varepsilon_{pore}$) and membrane charge density ($c_X$) quantitatively determined for each fabricated membrane and ionic system, along with the effective pore radius ($r_{pore}$) and thickness-to-porosity ratio ($\Delta x_e$), we can now evaluate interfacial partitioning at the feed-solution/membrane interface. Specifically, we evaluate the three DSPM-DE partitioning or exclusion coefficients as functions of aqueous-phase monomer concentration and chemistry (AEP vs. DAP): the steric coefficient ($\Phi_{S,i}$), the dielectric coefficient ($\Phi_{DE,i}$), and the Donnan ($\Phi_{D,i}^{x=0}$) coefficient. For all three, values below unity indicate net exclusion of species $i$ at the interface, while values above unity indicate enrichment (e.g., counter-ion uptake).

Results for $\Phi_{S,i}$, $\Phi_{DE,i}$, and $\Phi_{D,i}^{x=0}$ are presented in Fig. 5-Fig. 7, respectively, followed by the combined overall exclusion $\Phi_{overall,i} = \Phi_{S,i} \cdot \Phi_{DE,i} \cdot \Phi_{D,i}^{x=0}$ in Fig. 8. We report empirical trends in each subsection and then integrate these results to discuss their joint implications for selectivity in Section 3.4.2 on transmembrane transport. By analyzing these three mechanisms separately and then together, we establish a structured pathway linking intrinsic membrane/electrolyte parameters (Fig. 4) to interfacial partitioning (Fig. 5-Fig. 8) and, ultimately to fluxes and selectivity, i.e., separation performance of the membranes.

*3.4.1.1. Steric exclusion.* Steric partitioning quantifies size-based entry of ions into the pore. For cylindrical pores, the steric exclusion coefficient is given by

$$\Phi_{S,i} = \left(1 - \frac{r_i}{r_{pore}}\right)^2 \tag{6}$$

where $\Phi_{S,i} < 1$ denotes exclusion at the feed-solution/membrane interface. Because $\Phi_{S,i}$ depends only on the size ratio $r_i/r_{pore}$, ions of the same hydrated size experience identical steric partitioning. As the aqueous-phase monomer increases, $r_{pore}$ decreases and $\Phi_{S,i}$ declines for all species (Fig. 5).

At the same monomer concentrations, AEP-based membranes generally exhibit smaller $r_{pore}$ than DAP-based (≈ 0.62–0.69 nm vs. 0.65–0.83 nm; Fig. 1E), yielding stronger steric exclusion (i.e., smaller

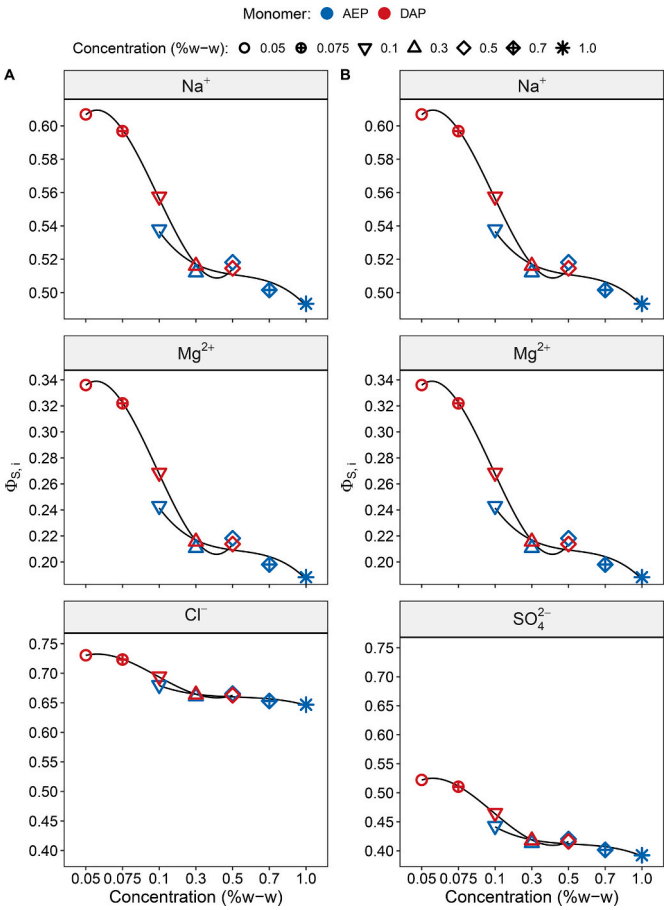



**Fig. 5.** Steric exclusion or partitioning coefficients ($\Phi_{S,i}$)) vs. aqueous-phase monomer concentration of the ternary ionic mixtures: (A) $Na^+/Mg^{2+}/Cl^-$; (B) $Na^+/Mg^{2+}/SO_4^{2-}$. Each shape of the data points corresponds to a different aqueous-phase monomer concentration, and the color of the data points indicates the aqueous-phase monomer (blue for AEP and red for DAP). (For interpretation of the references to color in this figure legend, the reader is referred to the web version of this article.)

$\Phi_{S,i}$) in AEP-based. A notable exception occurs at 0.5 %w-w monomer concentration. DAP0.5 shows a slightly smaller $r_{pore}$ than AEP0.5 (Fig. 3F), which is reflected by a correspondingly smaller $\Phi_{S,i}$ in Fig. 5. In both anion systems, $Na^+$ and $Mg^{2+}$ share the same $\Phi_{S,i}$ (identical $r_i$ dependence), whereas $Cl^-$, with a smaller hydrated radius than $SO_4^{2-}$, exhibits a larger $\Phi_{S,i}$ (i.e., weaker steric exclusion) than $SO_4^{2-}$ under otherwise identical conditions.

These observations confirm that steric exclusion decreases monotonically with pore tightening. $\Phi_{S,i}$ depends only on ion size and thus does not distinguish between the monovalent $Na^+$ and divalent $Mg^{2+}$. Sterics alone cannot account for the experimentally observed $Na^+/Mg^{2+}$ selectivity.

*3.4.1.2. Dielectric exclusion.* Dielectric partitioning or exclusion quantifies the Born-solvation penalty [75] that arises when ions transfer from bulk water ($\varepsilon_{bulk}$) into a pore with lower effective dielectric constant ($\varepsilon_{pore}$). The dielectric constant exclusion coefficient for species $i$ is

$$\Phi_{DE,i} = exp\left( -\frac{z_i^2 e_0^2}{8\pi\varepsilon_0 r_i k_B T}\left(\frac{1}{\varepsilon_{bulk}} - \frac{1}{\varepsilon_{pore}}\right)\right) \quad (7)$$

where $r_i$ is the Stokes radius, $z_i$ the ion valence, $e_0$ the electronic charge, $\varepsilon_0$ the permittivity of vacuum, $k_B$ the Boltzmann constant, $T$ temperature. Thus, $\Phi_{DE,i}$ decreases (i.e. dielectric exclusion strengthens) as $\varepsilon_{pore}$ decreases (Supporting Information), and scales with $z_i^2$, making divalent ions to experience a stronger exclusion than monovalent ions. In the DSPM-DE model, dielectric exclusion is a coarse-grained representation of the ion self-energy difference between bulk and pore environments. This self-energy contains contributions from both local Born solvation and interfacial image-charge effects. While the model does not resolve image charge effects explicitly through position-dependent boundary terms, their influence is included implicitly in the dielectric exclusion parameter [10,75].

Fig. 6 plots $\Phi_{DE,i}$ as a function of the aqueous-phase monomer concentrations for both ionic systems. Increasing monomer concentration decreases $\varepsilon_{pore}$ (via stronger nanoconfinement), leading to a monotonic decline in $\Phi_{DE,i}$ for all ions. This decline is markedly steeper in the $Cl^-$ system because fitted $\varepsilon^*$ values are lower than in the $SO_4^{2-}$ system, yielding smaller $\varepsilon_{pore}$ and higher solvation-energy barriers at comparable conditions.

Comparing AEP- and DAP-based membranes at equal monomer concentration, AEP-based membranes exhibit stronger dielectric exclusion (smaller $\Phi_{DE,i}$) than DAP-based membranes, consistent with their generally smaller $r_{pore}$ and lower $\varepsilon^*$ values. Because of the $z_i^2$ dependence, $\Phi_{DE,Mg^{2+}}$ is smaller than $\Phi_{DE,Na^+}$ in both systems. The ratio $\Phi_{DE,Na^+} : \Phi_{DE,Mg^{2+}}$ is most pronounced in the $Cl^-$ system (Supporting Information), where $\varepsilon_{pore}$ is lower. These trends are summarized in Fig. 6 and provide the basis for the $Na^+/Mg^{2+}$ selectivity differences developed in the following subsections.

*3.4.1.3. Donnan exclusion.* Donnan exclusion or partitioning arises from the interfacial potential difference ($\Delta\Psi_{D,f}$) generated by fixed membrane charges [11]. The Donnan exclusion coefficient ($\Phi_{D,i}^{x=0}$) at the feed-solution/membrane interface is defined as:

$$\Phi_{D,i}^{x=0} = exp\left(\frac{-z_i F}{RT}\Delta\Psi_{D,f}\right) \quad (8)$$

such that $\Phi_{D,i}^{x=0} < 1$ indicates co-ion repulsion and $\Phi_{D,i}^{x=0} > 1$ indicates counter-ion enrichment (feed toward membrane). Trends in $\Phi_{D,i}^{x=0}$ versus aqueous-phase monomer concentration are shown in Fig. 7 for the $Na^+/Mg^{2+}/Cl^-$ and $Na^+/Mg^{2+}/SO_4^{2-}$ ternary mixtures.

In both membrane series, increasing monomer concentration increases the density of protonated amines and thereby $c_X$, intensifying co-ion ($Na^+$ and $Mg^{2+}$) repulsion and counter-ion ($Cl^-$ and $SO_4^{2-}$) uptake.

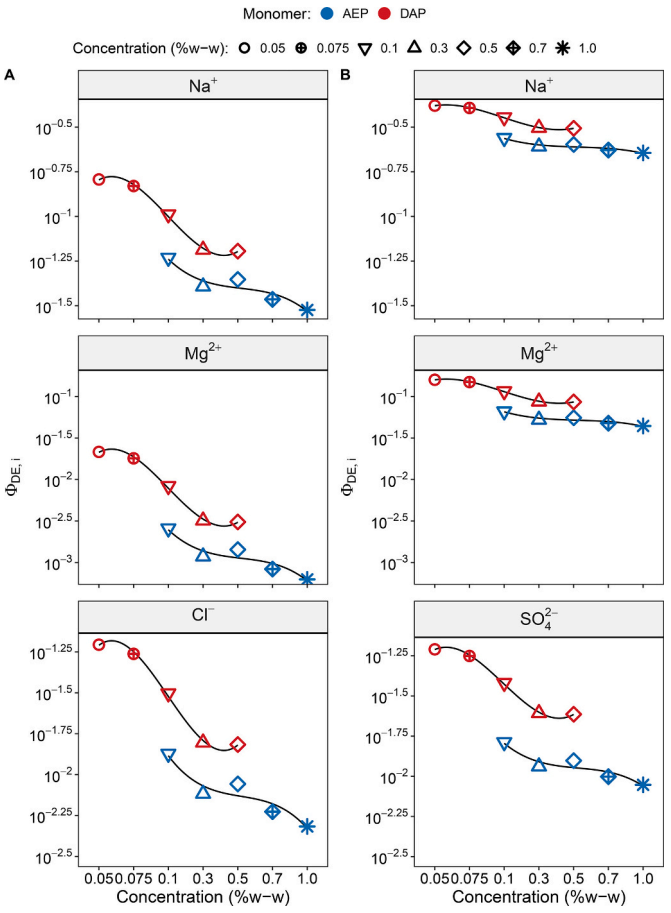



**Fig. 6.** Dielectric exclusion or partitioning coefficients $(\Phi_{DE,i})$ vs. aqueous-phase monomer concentration of the ternary ionic mixtures: (A) $Na^+/Mg^{2+}/Cl^-$; (B) $Na^+/Mg^{2+}/SO_4^{2-}$. Each shape of the data points corresponds to a different aqueous-phase monomer concentration, and the color of the data points indicates the aqueous-phase monomer (blue for AEP and red for DAP). (For interpretation of the references to color in this figure legend, the reader is referred to the web version of this article.)

At equivalent monomer concentration, DAP-based membranes exhibit larger $|c_X|$than AEP-based membranes; accordingly, DAP-based membranes show smaller $\Phi_{D,i}^{x=0}$ for cations, and larger $\Phi_{D,i}^{x=0}$ for anions.

Despite the steeper $c_X$ increase in the $SO_4^{2-}$ system (e.g., AEP:-0.22 to 69 mM; DAP:-0.41 to 19.13 mM), the decline in $\Phi_{D,i}^{x=0}$ for $Na^+$ and $Mg^{2+}$ with increasing monomer concentration is less pronounced than in the $Cl^-$ system, especially for DAP. This behavior reflects modulation by the pore dielectric constant. $\varepsilon_{pore}$ is consistently higher in the $SO_4^{2-}$ system, which partially offsets the impact of increased $c_X$ on Donnan exclusion. Consequently, the minima in $\Phi_{D,i}^{x=0}$ values for $Na^+$ and $Mg^{2+}$ occur in the highest-charge membranes (i.e., DAP0.5 in the $Cl^-$ system and AEP1.0 in the $SO_4^{2-}$ system) which also correspond to the membranes exhibiting the highest $Na^+/Mg^{2+}$ selectivity (Fig. 3C).

In summary, Donnan exclusion strengthens with increasing $c_X$, but its apparent magnitude depends on the common anion through $\varepsilon_{pore}$. The interplay between $c_X$ and $\varepsilon_{pore}$ explains the stronger Donnan exclusion observed in DAP-based membranes (at equal monomer concentration) and the less pronounced $\Phi_{D,i}^{x=0}$ decline in the $SO_4^{2-}$ system relative to $Cl^-$, as shown in Fig. 7.

*3.4.1.4. Overall exclusion.* To quantify the combined impact of steric, Donnan, and dielectric partitioning at the feed-solution/membrane interface, we define the overall exclusion coefficient as the product of

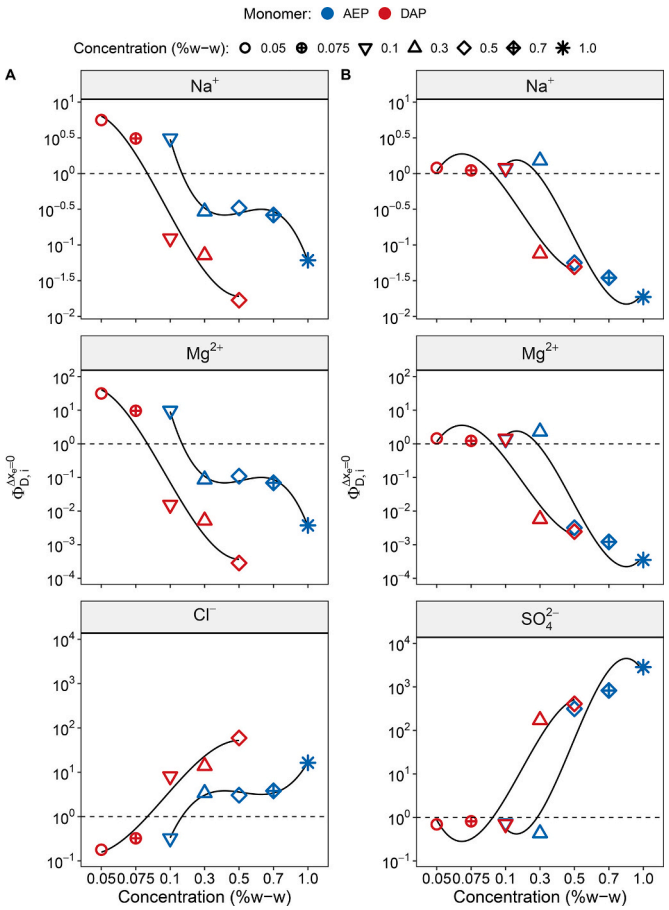



**Fig. 7.** Donnan exclusion or partitioning coefficients $\left(\Phi_{D,i}^{\Delta x_e=0}\right)$ vs. aqueous-phase monomer concentration of the ternary ionic mixtures: (A) $Na^+/Mg^{2+}/Cl^-$; (B) $Na^+/Mg^{2+}/SO_4^{2-}$. Each shape of the data points corresponds to a different aqueous-phase monomer concentration, and the color of the data points indicates the aqueous-phase monomer (blue for AEP and red for DAP). (For interpretation of the references to color in this figure legend, the reader is referred to the web version of this article.)

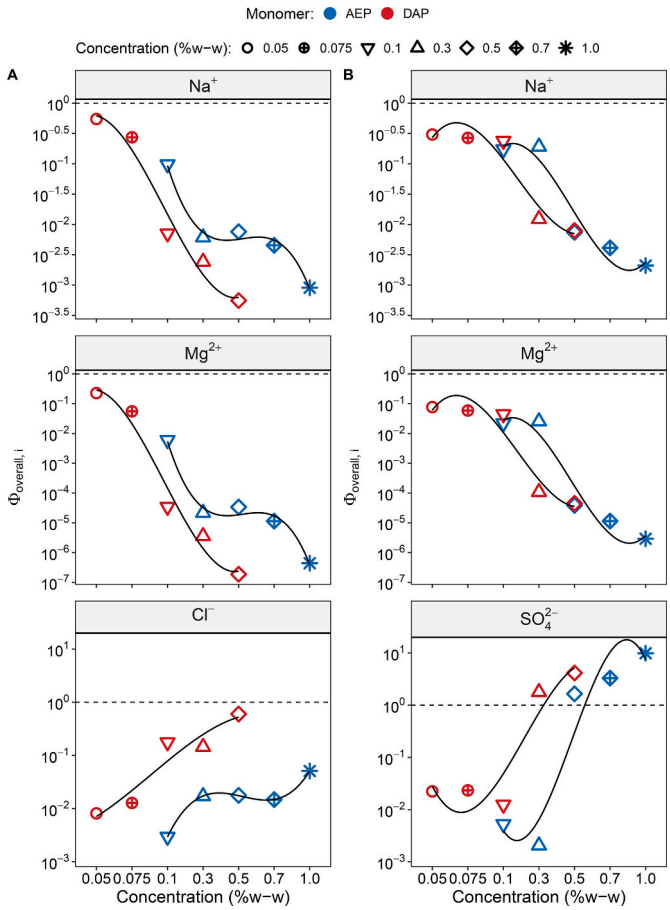



**Fig. 8.** Overall exclusion or partitioning coefficients $\left(\Phi_{overall,i}\right)$ vs. aqueous-phase monomer concentration of the ternary ionic mixtures: (A) $Na^+/Mg^{2+}/Cl^-$; (B) $Na^+/Mg^{2+}/SO_4^{2-}$. Each shape of the data points corresponds to a different aqueous-phase monomer concentration, and the color of the data points indicates the aqueous-phase monomer (blue for AEP and red for DAP). (For interpretation of the references to color in this figure legend, the reader is referred to the web version of this article.)

the three contributions, $\Phi_{overall,i} = \Phi_{S,i} \cdot \Phi_{DE,i} \cdot \Phi_{D,i}^{x=0}$.

Fig. 8 reports $\Phi_{overall,i}$ as a function of aqueous-phase monomer concentration for the $Na^+/Mg^{2+}/Cl^-$ and $Na^+/Mg^{2+}/SO_4^{2-}$ ionic systems. The global trends closely follow those of Donnan exclusion, underscoring the significant influence of $c_X$ in modulating interfacial partitioning.

For $Na^+$, $Mg^{2+}$, and $Cl^-$, $\Phi_{overall,i} < 1$ across all concentrations, indicating net exclusion at the feed-solution/membrane interface. In contrast, $SO_4^{2-}$ attains $\Phi_{overall,i} > 1$ in positively charged membranes (DAP0.3–0.5; AEP0.5, AEP0.7, AEP1.0) consistent with counterion enrichment within the membrane driven by electrostatic attraction.

Comparison between AEP- and DAP-based membranes at the same monomer concentrations reveals anion specific differences. In the $Cl^-$ system (Fig. 8A), AEP-based membranes exhibit larger overall cation $\Phi_{overall,i}$ than DAP-based, mirroring the Donnan trend and contrasting with the stronger dielectric exclusion observed in AEP-based membranes. In the $SO_4^{2-}$ system (Fig. 8B), $Na^+$ and $Mg^{2+}$ $\Phi_{overall,i}$ values do not differ significantly between AEP- and DAP-based membranes, with AEP- exceeding DAP-based primarily at 0.3 %w-w monomer concentration. These observations highlight how the balance of Donnan and dielectric contributions determines $\Phi_{overall,i}$ in a monomer and anion-specific manner [9,10].

The $Na^+ - Mg^{2+}$ difference in $\Phi_{overall,i}$ increases with increasing monomer concentration, reflecting the combined effects of higher $c_X$ (stronger electrostatic repulsion) and narrower, more confining pores (smaller $r_{pore}$ and lower $\varepsilon_{pore}$), which amplify $Mg^{2+}$ exclusion more than $Na^+$. This widening is more pronounced in the $Cl^-$ system, where smaller $\varepsilon_{pore}$ elevate solvation-energy barriers, leading to a steeper decrease in $\Phi_{overall,i}$ for $Mg^{2+}$ compared with the $SO_4^{2-}$ system. Therefore, dielectric exclusion dominates the preferential $Mg^{2+}$ over $Na^+$ exclusion in the $Cl^-$ system (owing to lower $\varepsilon_{pore}$ values), whereas Donnan exclusion is the primary mechanism in the $SO_4^{2-}$ system, where higher $\varepsilon_{pore}$ partially offsets the effect of increased $c_X$.

These results establish $\Phi_{overall,i}$ as a concise but powerful descriptor of ion partitioning that integrates membrane structure and charge with the electrolyte environment. They also demonstrate how tuning monomer concentration and aqueous-phase monomer during IP can be targeted to tune the $Na^+/Mg^{2+}$ partitioning ahead of the transmembrane transport analysis presented next.

### 3.4.2. *Transmembrane molar fluxes*

In the DSPM-DE model, ion transport across the active layer is quantified using the extended Nernst–Planck (ENP) equation, in which the total molar flux of species $i$ is expressed as the sum of diffusive, advective, and electromigrative contributions:

$$J_i = J_v c_{i,p} = J_{i,adv} + J_{i,diff} + J_{i,elec} \tag{9}$$

where $J_i$ is the total molar flux, $J_v$ is the volumetric solution flux, $c_{i,p}$ is

the permeate concentration, $J_{i,adv}$ the advective contribution, $J_{i,elec}$ the electromigrative contribution, and $J_{i,diff}$ the diffusive contribution.

The spatial coordinate $x$ is defined to increase from the feed side to the permeate side of the membrane, with positive flux directed toward the permeate. The ion concentrations within the membrane active layer $c_i(x)$ are set by the interfacial partitioning coefficients described in Section 3.4.1.

Fig. 9-Fig. 11 summarize the empirical trends for each flux contribution (i.e., advection, diffusion, and electromigration). Fig. 12 depicts how these terms combine to yield the total transmembrane molar flux, along with Table 1-Table 2, to compare magnitudes, contributions, and couplings across ionic systems ($Cl^-$ vs. $SO_4^{2-}$) and membranes (AEP- vs. DAP-based). This organization links the fitted membrane/electrolyte parameters (Fig. 4) and interfacial partitioning (Fig. 5-Fig. 8) to transport (Fig. 9-Fig. 12) and, ultimately, to selectivity (Fig. 3C-D).

*3.4.2.1. Advective flux.* Advection represents the transport of species with the permeating solvent and is hindered by nanometer-scale pore confinement [76]. Accordingly, the advective flux ($J_{i,adv}$) of species $i$ is:

$$J_{i,adv} = K_{i,a} c_i J_v \tag{10}$$

where $K_{i,a}$ is the hindrance factor of advection and $c_i$ the ion concentration inside the membrane's active layer.

Fig. 9 compares $J_{i,adv}$ of $Na^+$, $Mg^{2+}$, $Cl^-$, and $SO_4^{2-}$ across aqueous-phase monomer concentration for both the $Cl^-$ and $SO_4^{2-}$ systems. For cations, $J_{Na^+,adv}$ decreases by several orders of magnitude with increasing monomer concentration, with a steeper decline in the $Cl^-$ system. At matched conditions, AEP-based membranes exhibit larger $J_{Na^+,adv}$ and $J_{Mg^{2+},adv}$ than DAP-based membranes, reflecting higher cation concentration within the active layer ($c_i$). For anions, $J_{SO_4^{2-},adv}$ increases sharply with monomer concentration (up to 3 orders of magnitude for AEP-based membranes), whereas $J_{Cl^-,adv}$ shows a much weaker increase. Consequently, the gap between $J_{Na^+,adv}$ and $J_{Mg^{2+},adv}$ is most pronounced in the $Cl^-$ system, consistent with the trends in overall ion-exclusion trends (Fig. 8). These empirical differences are shown in Fig. 9.

*3.4.2.2. Diffusive flux.* Diffusive flux transport stems from concentration gradients within the membrane's active layer and is attenuated by nanoscale pore confinement [76]. The diffusive molar flux of species $i$ ($J_{i,diff}$) is described by:

$$J_{i,diff} = -K_{i,d} D_{i,\infty} \frac{dc_i}{dx} \tag{11}$$

where $K_{i,d}$ is the hindrance factor of diffusion, $D_{i,\infty}$ the diffusion coefficient in the bulk solution, $c_i$ the ion concentration inside the membrane's active layer, and $x$ is the direction across the membrane's active layer from the feed toward the permeate side.

Fig. 10 plots the diffusive flux of $Na^+$, $Mg^{2+}$, $Cl^-$, and $SO_4^{2-}$ as a function of the aqueous-phase monomer concentration for both $Cl^-$ and $SO_4^{2-}$ systems. Logarithmic scale is used to capture both positive (toward permeate) and negative (toward feed) fluxes over multiple orders of magnitude.

In the $Cl^-$ system, $J_{Na^+,diff}$ is negative for the negatively charged membranes (DAP0.05, DAP0.075, and AEP0.1), and becomes positive as $c_X$ increases with monomer concentration; its magnitude then declines at the highest concentrations. In the $SO_4^{2-}$ system, negative $J_{Na^+,diff}$ occurs only for DAP0.05 and DAP0.075, reflecting their weaker cation exclusion at negative charge density. Across both anion systems, $J_{Mg^{2+},diff}$ decreases monotonically with monomer concentration, reflecting the combined Donnan and dielectric exclusions that flatten the $Mg^{2+}$ concentration profile and reduce $dc_{Mg^{2+}}/dx$. Under these conditions, electroneutrality couples $Na^+$ and anion gradients, yielding parallel trends in their diffusive fluxes at higher monomer concentration (Supporting Information).

The diffusive fluxes of $Cl^-$ and $SO_4^{2-}$ generally decrease with increasing monomer concentration, influenced by $\Delta x_e$ (Supporting Information), hindrance, and ion mobility. Owing to its smaller Stokes radius (3.32 Å), $Cl^-$ typically exhibits larger $J_{i,diff}$ than $SO_4^{2-}$ across comparable conditions. An exception occurs for DAP0.5 in the $Cl^-$ system, where the strong cation exclusion flattens both $Na^+$ and $Cl^-$ concentration profiles (Supporting Information), lowering $J_{Cl^-,diff}$ below that of $SO_4^{2-}$. Consistent with their generally larger $r_{pore}$, DAP-based membranes show reduced diffusive hindrance and thus higher anion diffusive fluxes than AEP-based membranes at similar $\Delta x_e$ (e.g., DAP0.075 vs. AEP0.3).

These results show that diffusive transport through AEP- and DAP-based NF membranes is governed by the same Donnan/dielectric interplay that dictates ion exclusion at the feed-solution/membrane interface. The magnitude and even the direction of diffusive fluxes can be tuned by the combined choice of monomer chemistry, monomer concentration, and the identity of the common anion.

*3.4.2.3. Electromigrative flux.* The electromigrative transport arises from the electrical potential gradient across the active layer, which develops in response to both pressure and concentration-driven ion transport. This contribution, $J_{i,elec}$, is described by:

$$J_{i,elec} = -\frac{z_i F c_i K_{i,d} D_{i,\infty}}{RT} \frac{d\Psi}{dx} \tag{12}$$

where $z_i$ is the ion valence, $F$ the Faraday constant, $c_i$ the ion concentration within the membrane's active layer, $K_{i,d}$ the hindrance factor of diffusion, $R$ the universal gas constant, $T$ temperature, and $\frac{d\Psi}{dx}$ the electrical potential gradient across the membrane's active layer from the feed toward the permeate side.

Fig. 11 plots $J_{i,elec}$ versus aqueous-phase monomer concentration on a mixed-sign logarithmic axis. In the $Cl^-$ system (Fig. 11A), $J_{Na^+,elec}$ and

**Table 1**
Relative contributions of diffusion, advection, and electromigration to the total molar flux for each ion in the $Na^+/Mg^{2+}/Cl^-$ mixture, as computed for all fabricated membranes. Each contribution is expressed as the ratio of the respective transport mode to the total transmembrane molar flux.

| Membrane | $c_X$ (mM) | Diffusive contribution | | | Advective contribution | | | Electromigrative contribution | | |
|---|---|---|---|---|---|---|---|---|---|---|
| | | $Na^+$ | $Mg^{2+}$ | $Cl^-$ | $Na^+$ | $Mg^{2+}$ | $Cl^-$ | $Na^+$ | $Mg^{2+}$ | $Cl^-$ |
| AEP0.1 | −0.13 | −0.15 | 0.70 | 1.14 | 0.17 | 0.09 | 0.01 | 0.98 | 0.21 | −0.15 |
| AEP0.3 | 0.07 | 0.94 | 0.86 | 1.91 | 0.01 | 0.05 | 0.11 | 0.05 | 0.09 | −1.02 |
| AEP0.5 | 0.07 | 0.91 | 0.79 | 1.86 | 0.02 | 0.10 | 0.16 | 0.06 | 0.11 | −1.02 |
| AEP0.7 | 0.06 | 0.94 | 0.85 | 1.93 | 0.01 | 0.06 | 0.13 | 0.05 | 0.08 | −1.06 |
| AEP1.0 | 0.21 | 0.98 | 0.94 | 2.03 | 0.01 | 0.05 | 1.49 | 0.01 | 0.01 | −2.52 |
| DAP0.05 | −1.32 | −0.86 | 0.35 | 1.02 | 0.75 | 0.37 | 0.01 | 1.11 | 0.28 | −0.03 |
| DAP0.075 | −0.45 | −1.54 | 0.56 | 1.22 | 0.36 | 0.11 | 0.02 | 2.18 | 0.33 | −0.24 |
| DAP0.1 | 0.77 | 0.97 | 0.89 | 1.90 | 0.02 | 0.08 | 1.53 | 0.02 | 0.03 | −2.43 |
| DAP0.3 | 0.59 | 0.98 | 0.92 | 1.99 | 0.01 | 0.06 | 2.16 | 0.01 | 0.02 | −3.15 |
| DAP0.5 | 2.51 | 0.99 | 0.95 | 2.00 | 0.01 | 0.04 | 24.84 | 0.00 | 0.01 | −25.84 |

**Table 2**
Relative contributions of diffusion, advection, and electromigration to the total molar flux for each ion in the $Na^+/Mg^{2+}/SO_4^{2-}$ mixture, as computed for all fabricated membranes. Each contribution is expressed as the ratio of the respective transport mode to the total transmembrane molar flux.

| Membrane | $c_X$ (mM) | Diffusive contribution | | | Advective contribution | | | Electromigrative contribution | | |
|---|---|---|---|---|---|---|---|---|---|---|
| | | $Na^+$ | $Mg^{2+}$ | $SO_4^{2-}$ | $Na^+$ | $Mg^{2+}$ | $SO_4^{2-}$ | $Na^+$ | $Mg^{2+}$ | $SO_4^{2-}$ |
| AEP0.1 | −0.22 | 0.22 | 0.75 | 0.99 | 0.50 | 0.20 | 0.03 | 0.28 | 0.05 | −0.02 |
| AEP0.3 | −0.28 | 0.60 | 0.62 | 0.97 | 0.90 | 0.48 | 0.02 | −0.50 | −0.10 | 0.01 |
| AEP0.5 | 7.53 | 0.96 | 0.87 | 0.61 | 0.02 | 0.10 | 20.51 | 0.02 | 0.03 | −20.12 |
| AEP0.7 | 17.09 | 0.98 | 0.93 | 0.61 | 0.01 | 0.05 | 43.51 | 0.01 | 0.02 | −43.12 |
| AEP1.0 | 68.97 | 0.98 | 0.93 | 0.60 | 0.01 | 0.06 | 281.98 | 0.01 | 0.02 | −281.58 |
| DAP0.05 | −0.41 | −0.33 | 0.73 | 1.07 | 0.40 | 0.13 | 0.03 | 0.92 | 0.15 | −0.10 |
| DAP0.075 | −0.33 | −0.14 | 0.74 | 1.07 | 0.37 | 0.13 | 0.04 | 0.77 | 0.13 | −0.11 |
| DAP0.1 | −0.32 | 0.18 | 0.70 | 0.99 | 0.51 | 0.24 | 0.04 | 0.32 | 0.06 | −0.03 |
| DAP0.3 | 7.12 | 0.96 | 0.90 | 0.62 | 0.02 | 0.08 | 12.55 | 0.02 | 0.02 | −12.16 |
| DAP0.5 | 19.13 | 0.97 | 0.92 | 0.62 | 0.02 | 0.06 | 36.95 | 0.01 | 0.02 | −36.57 |

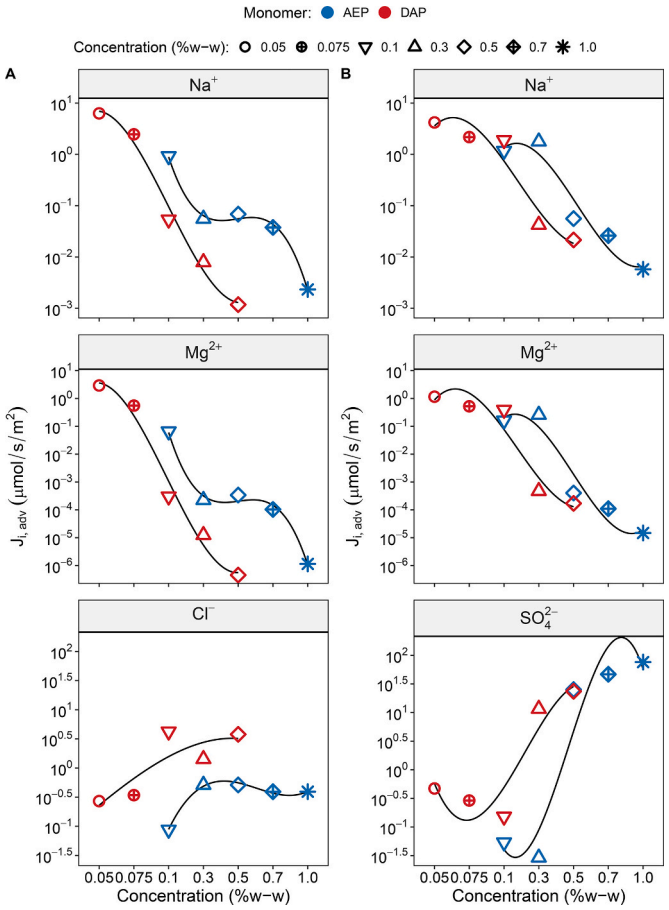



**Fig. 9.** Advective molar flux ($J_{i,adv}$) vs. aqueous-phase monomer concentration of the ternary ionic mixtures: (A) $Na^+/Mg^{2+}/Cl^-$; (B) $Na^+/Mg^{2+}/SO_4^{2-}$. Each shape of the data points corresponds to a different aqueous-phase monomer concentration, and the color of the data points indicates the aqueous-phase monomer (blue for AEP and red for DAP). (For interpretation of the references to color in this figure legend, the reader is referred to the web version of this article.)

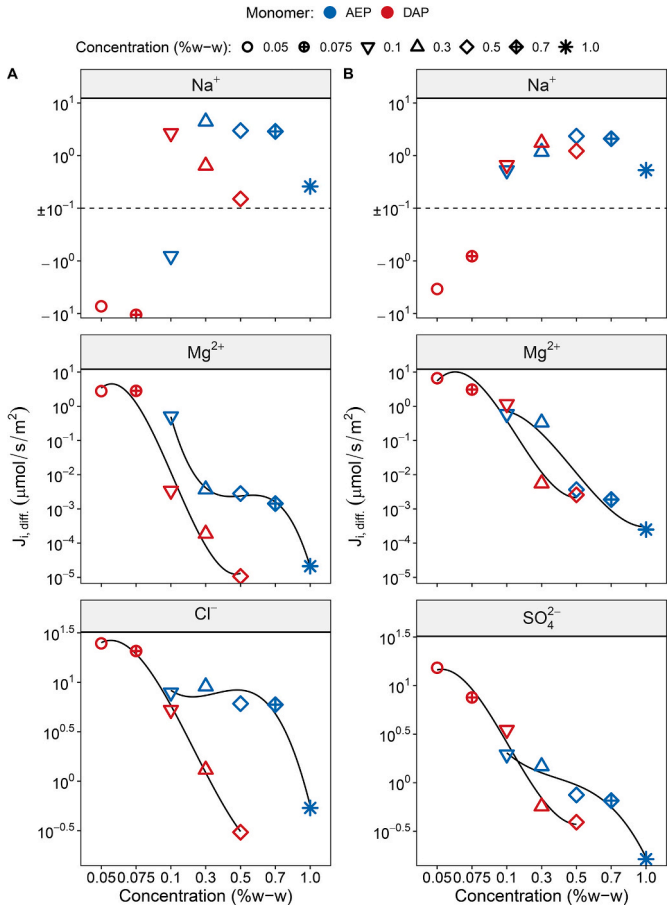



**Fig. 10.** Diffusive molar flux ($J_{i,diff}$) vs. aqueous-phase monomer concentration of the ternary ionic mixtures: (A) $Na^+/Mg^{2+}/Cl^-$; (B) $Na^+/Mg^{2+}/SO_4^{2-}$. Each shape of the data points corresponds to a different aqueous-phase monomer concentration, and the color of the data points indicates the aqueous-phase monomer (blue for AEP and red for DAP). (For interpretation of the references to color in this figure legend, the reader is referred to the web version of this article.)

$J_{Mg^{2+},elec}$ are positive (toward the permeate side) for all membranes and decrease monotonically as the aqueous-phase monomer concentration increases. AEP-based membranes exhibit larger cation electromigrative fluxes than DAP-based membranes, consistent with their higher cation concentration within the membrane (weaker overall exclusion), which magnify $c_i$ in Eq. 12. In the $SO_4^{2-}$ system (Fig. 11B), the same trend holds except for AEP0.3, where $J_{Na^+,elec}$ and $J_{Mg^{2+},elec}$ become negative, reflecting a unique electrical potential profile under weak overall exclusion.

For anions, $J_{Cl^-,elec}$ and $J_{SO_4^{2-},elec}$ are generally negative (toward the feed side) across both membrane series, again with AEP0.3 as the exception. The magnitude of $J_{SO_4^{2-},elec}$ grows by roughly two to three orders of magnitude as monomer concentration increases ten-fold (AEP0.1 to AEP1.0; DAP0.05 to DAP0.5), whereas $J_{Cl^-,elec}$ shows much weaker sensitivity to monomer type or concentration.

A detailed decomposition of the interplay between electromigration,

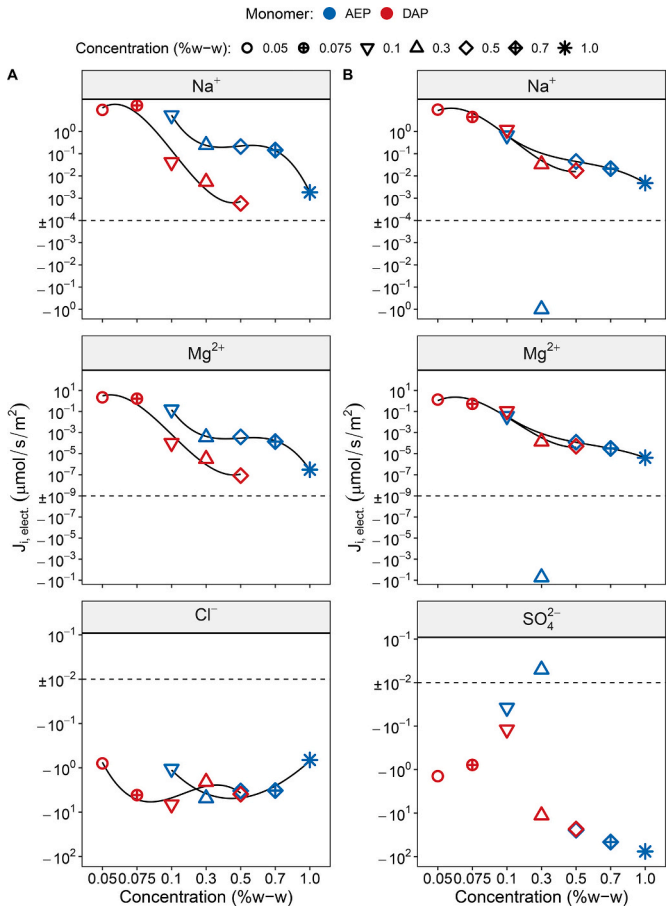



**Fig. 11.** Electromigrative molar flux ($J_{i,elect.}$) vs. aqueous-phase monomer concentration of the ternary ionic mixtures: (A) $Na^+/Mg^{2+}/Cl^-$; (B) $Na^+/Mg^{2+}/SO_4^{2-}$. Each shape of the data points corresponds to a different aqueous-phase monomer concentration, and the color of the data points indicates the aqueous-phase monomer (blue for AEP and red for DAP). (For interpretation of the references to color in this figure legend, the reader is referred to the web version of this article.)

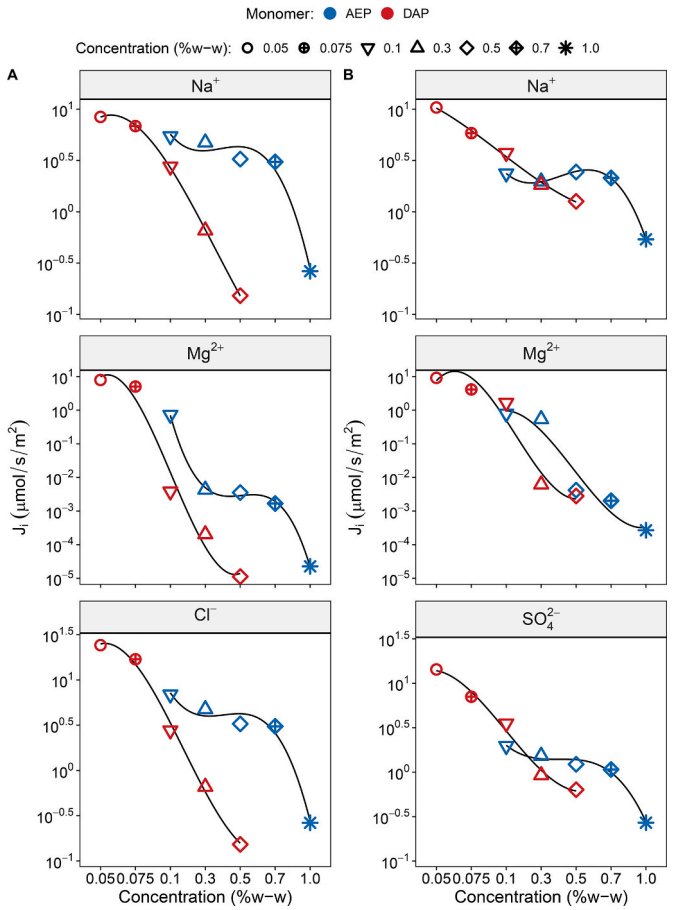



**Fig. 12.** Total molar flux ($J_i$) vs. aqueous-phase monomer concentration of the ternary ionic mixtures: (A) $Na^+/Mg^{2+}/Cl^-$; (B) $Na^+/Mg^{2+}/SO_4^{2-}$. Each shape of the data points corresponds to a different aqueous-phase monomer concentration, and the color of the data points indicates the aqueous-phase monomer (blue for AEP and red for DAP). (For interpretation of the references to color in this figure legend, the reader is referred to the web version of this article.)

diffusion and advection in determining the total ion flux is presented next, with quantitative comparisons provided in Table 1 and Table 2 and Fig. 12.

*3.4.2.4. Total transmembrane molar flux.* Having quantified the individual contributions of advection, diffusion, and electromigration, we now examine how these combine to yield the total transmembrane molar flux for each ion, $J_i$, (Fig. 12). According to the extended Nernst-Planck equation Eq. 9, $J_i$ directly determines the permeate concentrations and, consequently, the $Na^+/Mg^{2+}$ selectivity, making it the central output of the DSPM-DE model.

Across both membrane chemistries, increasing aqueous-phase monomer concentration reduces $J_i$ for both $Na^+$ and $Mg^{2+}$, with $Mg^{2+}$ decreasing more steeply, particularly in the $Cl^-$ system. This differential decrease underlines the experimentally observed increase in $Na^+/Mg^{2+}$ selectivity from ~1.4 to 244 as membranes become more positively charged and pores tighten (Fig. 3C). The trend reflects preferential strengthening of $Mg^{2+}$ exclusion by combined Donnan and dielectric effects.

Analysis of the flux components (Table 1 and Table 2) reveals that diffusion is the dominant cation transport mode in positively charged membranes. The diffusion term contributes >80 % of total $Na^+$ and $Mg^{2+}$ flux, and $J_{i,diff}$ is linearly correlated with $J_i$ ($R^2 \approx 1$) (Supporting Information), while advective and electromigrative terms contribute <20 %. Mechanistically, increasing $c_X$ (more positive fixed charge) and decreasing $r_{pore}$ (increasing dielectric confinement) flatten the $Mg^{2+}$ concentration profile in the active layer, reducing its gradient and suppressing $J_{Mg^{2+},diff}$ more than $J_{Na^+,diff}$.

In contrast, anion transport is characterized by a near cancelation between advection and electromigration in positively charged membranes. For $SO_4^{2-}$, the advective and electromigrative contributions are large and opposite in sign. For example, in AEP1.0 the $SO_4^{2-}$ terms are +281.9 (advection) and − 281.6 (electromigrative), reflecting the role of electromigration in preventing counter-ion accumulation in the permeate (Table 2). For $Cl^-$, the compensating electromigrative term has similar magnitude across AEP- and DAP-based membranes, but it counterbalances diffusion in AEP-based membranes and advection in DAP-based membranes, consistent with their distinct balances of exclusion and hydrodynamic hindrance (Table 1). These behaviors highlight the role of spontaneously arising electric fields as a dynamic response that enforces electroneutrality while modulating anion transport.

Electroneutrality further couples cation and anion fluxes. In the $Cl^-$ system, total $J_{Na^+}$ and $J_{Cl^-}$ remain closely correlated (Supporting Information). In the $SO_4^{2-}$ system, the total fluxes satisfy the 2:1 stoichiometric ratio $J_{Na^+} : J_{SO_4^{2-}} = 2:1$, reflecting charge balance over the active layer (Supporting Information). Together with the dominance of cation diffusion, these constraints explain why $Na^+/Mg^{2+}$ selectivity increases with monomer concentration: dielectric exclusion and Donnan repulsion

attenuate $Mg^{2+}$ diffusion more strongly than $Na^{+}$, whereas anion electromigration adjusts to maintain neutrality without increasing divalent cation transport.

The interplay between ion transport and hydraulic resistance explains apparent discrepancies between modeled fluxes and experimental retention. In the $SO_4^{2-}$ system, DAP-based membranes can exhibit larger $J_i$ but also larger $\Delta x_e$ (greater mass-transport resistance), which lowers solution flux and yields higher permeate concentrations than AEP-based membranes. Thus, differences in $J_i$ do not necessarily translate into higher retention for DAP (Fig. 12B vs. Fig. 3B). Conversely, in the $Cl^-$ system the combination of tighter pores and lower fitted $\varepsilon^*$ strengthens dielectric exclusion of $Mg^{2+}$; together with charge effects, this favors $Na^+$ transport over $Mg^{2+}$ and leads to the highest $Na^+/Mg^{2+}$ selectivity in the most positively charged DAP-based membrane (DAP0.5, $S_{Na^+/Mg^{2+}} = 244$), while AEP-based membranes achieve lower selectivity despite smaller $\Delta x_e$ (Fig. 12A, Fig. 3A).

In summary, diffusion governs cation transport, particularly in positively charged membranes, whereas anion fluxes emerge from a compensating balance of advection and electromigration set by membrane charge and common-anion identity. The pronounced $Mg^{2+}$ flux decrease in the $Cl^-$ system originates from stronger dielectric confinement (smaller $\varepsilon_{pore}$), while in the $SO_4^{2-}$ system, higher $\varepsilon_{pore}$ reduces dielectric exclusion and shifts selectivity control toward Donnan partitioning. These insights elucidate the observed selectivity trends and provide guidance on how monomer chemistry and concentration during IP tune $c_X$, $r_{pore}$, $\varepsilon_{pore}$ and $\Delta x_e$ for targeted $Na^+/Mg^{2+}$ separation.

## 4. Conclusions

The main contribution of this study is to establish a mechanistic framework that links interfacial-polymerization conditions, the resulting membrane structure and charge, and the electrolyte environment to $Na^+/Mg^{2+}$ separation. The specific AEP/DAP-based fabrication method serves as a controlled example of how such mechanistic principles can be applied.

We demonstrated that aqueous-phase monomer (AEP vs. DAP) and common anion identity ($Cl^-$ vs. $SO_4^{2-}$) jointly modulate $Na^+/Mg^{2+}$ separation in interfacially polymerized NF membranes. By combining structural characterization with single- and mixed-salt tests and fitting the DSPM-DE model, we linked membrane structure and apparent charge/dielectric environment to the observed selectivity trends.

Structurally, AEP forms more compact and rougher PA layers with smaller effective pore radius ($r_{pore}$) and lower overall transport resistance than DAP at equal concentration. These differences translate into distinct balances of Donnan and dielectric effects. In the $Cl^-$ system, tighter pores and lower fitted pore dielectric constant ($\varepsilon_{pore}$) strengthen dielectric exclusion of $Mg^{2+}$, while in $SO_4^{2-}$ feeds, higher fitted $\varepsilon_{pore}$ partially offsets dielectric effects and shifts control toward Donnan partitioning.

Real $Na^+/Mg^{2+}$ selectivity (S) increases with monomer concentration for both AEP- and DAP-based membranes, reaching $S \approx 244$ for DAP0.5 in the $Cl^-$ system. In $SO_4^{2-}$, AEP1.0 attains $S \approx 66$, consistent with stronger apparent positive charge but weaker dielectric exclusion. Notably, very high selectivity is achieved at permeances within the range of commercial and lab-made reported NF membranes, highlighting practical relevance even though the intrinsic flux–selectivity trade-off is not being surpassed. Overall, these results highlight that the common anion identity dictates how charge and dielectric confinement translate into separation performance.

In positively charged membranes, cation transport is dominated by diffusion (>80 % of total), with combined Donnan and dielectric exclusion preferentially suppressing $Mg^{2+}$ transport relative to $Na^+$ as pores tighten and $c_X$ increases with increasing monomer concentration. This preferential $Mg^{2+}$ suppression couples $Na^+$ and anion transport via electroneutrality. In the $Cl^-$ system, total flux of $Na^+$ and $Cl^-$ remain closely correlated, whereas in the $SO_4^{2-}$ system the total fluxes satisfy the 2:1 $Na^+$:$SO_4^{2-}$ stoichiometry ratio, both trends arising from charge balance across the active layer. Moreover, in the $Cl^-$ system, the compensating electromigrative $Cl^-$ flux is of similar magnitude across AEP- and DAP-based, but it counterbalances diffusion in AEP- and advection in DAP-based membranes, consistent with their distinct balances of exclusion and hydrodynamic hindrance. These behaviors highlight that spontaneously arising internal fields act as dynamic responses that enforce electroneutrality while modulating anion transport.

Although these trends describe a mechanistic route to tune $Na^+/Mg^{2+}$ selectivity through aqueous-phase monomer chemistry and the common anion, they are specific to the AEP- and DAP-based series and to the $Cl^-$ and $SO_4^{2-}$ systems evaluated here. Because interfacial polymerization is rapid and sensitive to monomer reactivity and diffusion, extending these relationships to other monomer chemistries is not straightforward: changes in reaction-diffusion balance will reshape the PA network and its mass transport characteristics. Importantly, preferential suppression of $Mg^{2+}$ transport couples $Na^+$ and counter-ion transport through electroneutrality; the advection-electromigration compensation that enforces charge balance is electrolyte dependent and should be established for each system rather than assumed from the present cases. Accordingly, applying these principles to new monomers or ionic systems will require system-specific validation using the same DSPM-DE framework.

In conclusion, this work shows that targeted design of membrane chemistry and structure, together with selection of the electrolyte environment, enables tuning of selective $Na^+/Mg^{2+}$ separation in NF. Within the AEP-/DAP-based series examined here, the identity of the common anion ($Cl^-$ vs. $SO_4^{2-}$) not only modulates the balance between Donnan and dielectric exclusion but also governs the advection-electromigration balance that enforces electroneutrality, thereby enhancing or diminishing the separation performance. By linking these effects to the DSPM-DE model, this study provides a mechanistic basis for fabricating NF membranes tailored for $Na^+/Mg^{2+}$ separation and for system-specific optimization in resource recovery applications.

## CRediT authorship contribution statement

**Nicolás Cevallos-Cueva:** Writing – review & editing, Writing – original draft, Software, Methodology, Investigation, Formal analysis, Data curation, Conceptualization. **Md. Mushfequr Rahman:** Writing – review & editing, Visualization, Supervision, Resources, Project administration, Conceptualization. **Hluf Hailu Kinfu:** Writing – review & editing, Methodology. **Volker Abetz:** Writing – review & editing, Supervision.

## Funding

This work was funded by the Hereon-I$^2$B-Project NanoMem.

## Declaration of competing interest

The authors declare that they have no known competing financial interests or personal relationships that could have appeared to influence the work reported in this paper.

## Acknowledgments

The authors would like to acknowledge Maren Brinkmann for the PEG analysis in GPC, Juliana Clodt and Barbara Bajer for fabricating the polyacrylonitrile support, Erik Schneider for the SEM analysis, Evgeni Sperling for the AFM analysis, and Jan Pohlmann for setting up the flux and retention measurement facilities.

## Appendix A. Supplementary data

Supplementary data to this article can be found online at https://doi.org/10.1016/j.desal.2025.119765.

## Data availability

Data will be made available on request.

## References


[1] EuropeanCommission, Critical Raw Materials Resilience: Charting a Path towards Greater Security and Sustainability, 2020.

[2] Y. Zhao, T. Tong, X. Wang, S. Lin, E.M. Reid, Y. Chen, Differentiating solutes with precise nanofiltration for next generation environmental separations: a review, Environ. Sci. Technol. 55 (2021) 1359–1376, https://doi.org/10.1021/acs.est.0c04593.

[3] R. Epsztein, R.M. DuChanois, C.L. Ritt, A. Noy, M. Elimelech, Towards single-species selectivity of membranes with subnanometre pores, Nat. Nanotechnol. 15 (2020) 426–436, https://doi.org/10.1038/s41565-020-0713-6.

[4] M. Figueira, D. Rodriguez-Jim, J. Lopez, M. Reig, J.L. Cortina, C. Valderrama, Experimental and economic evaluation of nanofiltration as a pre-treatment for added-value elements recovery from seawater desalination brines, Desalination 549 (2023), https://doi.org/10.1016/j.desal.2022.116321.

[5] M. Figueira, D. Rodríguez-Jiménez, J. López, M. Reiga, J.L. Cortina, C. Valderrama, Evaluation of the nanofiltration of brines from seawater desalination plants as pre-treatment in a multimineral brine extraction process, Sep. Purif. Technol. 322 (2023), https://doi.org/10.1016/j.seppur.2023.124232.

[6] X.H. Zhai, S.H. Lin, X.S. Li, Z.W. Wang, The hidden role of the dielectric effect in nanofiltration: a novel perspective to unravel new ion separation mechanisms, Environ. Sci. Technol. 58 (35) (2024) 15874–15884, https://doi.org/10.1021/acs.est.4c07510.

[7] X.H. Zhai, Y.L. Wang, R.B. Dai, X.S. Li, Z.W. Wang, Roles of anion-cation coupling transport and dehydration-induced ion-membrane interaction in precise separation of ions by nanofiltration membranes, Environ. Sci. Technol. (2022), https://doi.org/10.1021/acs.est.2c04772.

[8] T.Y. Tsou, J.P. Hsu, H.Y. Yu, Unraveling the impact of ion adsorption and dielectric exclusion on nanofiltration through pH-regulated cylindrical nanopores, J. Membr. Sci. 714 (2025), https://doi.org/10.1016/j.memsci.2024.123399.

[9] A. Saavedra, H. Valdés, J. Velásquez, S. Hernández, Comparative analysis of donnan steric partitioning pore model and dielectric exclusion applied to the fractionation of aqueous saline solutions through nanofiltration, Chemengineering 8 (2) (2024), https://doi.org/10.3390/chemengineering8020039.

[10] Y.Y. Liu, J.F. Ran, Q. Guo, L.L. Gao, L.B. Zhang, S.H. Yin, S.W. Li, Contribution of dielectric exclusion to mass transfer in nanofiltration membrane: charge volume density and dielectric constant, Sep. Purif. Technol. 356 (2025), https://doi.org/10.1016/j.seppur.2024.129995.

[11] R. Wang, S. Lin, Pore model for nanofiltration: history, theoretical framework, key predictions, limitations, and prospects, J. Membr. Sci. 620 (2021) 118809, https://doi.org/10.1016/j.memsci.2020.118809.

[12] N. Cevallos-Cueva, M.M. Rahman, H.H. Kinfu, V. Abetz, Mass transport mechanisms insights of selective sodium/magnesium separation through nanofiltration membranes, J. Membr. Sci. 721 (2025) 123808, https://doi.org/10.1016/J.MEMSCI.2025.123808.

[13] H.H. Kinfu, M.M. Rahman, N. Cevallos-Cueva, V. Abetz, Ion selective metal-phenolic network nanofiltration membranes: the role of counterions and predictive modeling, J. Membr. Sci. 733 (2025), https://doi.org/10.1016/j.memsci.2025.124320.

[14] Y. Guo, J.L. He, J.W. Zhang, M. Sheng, Z.W. Wang, M. Elimelech, L. Wang, Deciphering co-ion and counterion transport in polyamide desalination membranes reveals ion selectivity mechanisms, Sci. Adv. 11 (23) (2025), https://doi.org/10.1126/sciadv.adu8302.

[15] J.Q. Luo, Y.H. Wan, Effects of pH and salt on nanofiltration-a critical review, J. Membr. Sci. 438 (2013) 18–28, https://doi.org/10.1016/j.memsci.2013.03.029.

[16] R.S. Roth, L. Birnhack, M. Avidar, E.A. Hjelvik, A.P. Straub, R. Epsztein, Effect of solution ions on the charge and performance of nanofiltration membranes, NPJ Clean Water 7 (1) (2024), https://doi.org/10.1038/s41545-024-00322-9.

[17] H.Y. Guo, X.Q. Gao, K.C. Yu, X.M. Wang, S.M. Liu, Ion adsorption on nanofiltration membrane surface and its effect on rejection of charged solutes: a zeta potential approach, Sep. Purif. Technol. 326 (2023), https://doi.org/10.1016/j.seppur.2023.124830.

[18] S. Castaño Osorio, P.M. Biesheuvel, J.E. Dykstra, E. Virga, Nanofiltration of complex mixtures: the effect of the adsorption of divalent ions on membrane retention, Desalination 527 (2022) 115552, https://doi.org/10.1016/j.desal.2022.115552.

[19] K. Wang, X. Wang, B. Januszewski, Y. Liu, D. Li, R. Fu, M. Elimelech, X. Huang, Tailored design of nanofiltration membranes for water treatment based on synthesis–property–performance relationships, Chem. Soc. Rev. 51 (2) (2022) 672–719, https://doi.org/10.1039/D0CS01599G.

[20] Y. Liu, L.L. Liu, B. Narendra, X.R. Chen, S.C. Feng, Y.H. Wan, J.Q. Luo, Advancing high-performance nanofiltration membranes: tailoring monomer molecular design to enhance diffusion-reaction synergy in interfacial polymerization, Desalination 598 (2025), https://doi.org/10.1016/j.desal.2024.118415.

[21] N. Cevallos-Cueva, M.M. Rahman, H.H. Kinfu, V. Abetz, Effect of piperazine-based monomer structure on nanofiltration membrane selectivity: a DSPM-DE analysis of nitrate transport, J. Membr. Sci. 736 (2025), https://doi.org/10.1016/j.memsci.2025.124642.

[22] O. Labban, C. Liu, T.H. Chong, J.H. Lienhard, Relating transport modeling to nanofiltration membrane fabrication: navigating the permeability-selectivity trade-off in desalination pretreatment, J. Membr. Sci. 554 (2018) 26–38, https://doi.org/10.1016/j.memsci.2018.02.053.

[23] M. Micari, D. Diamantidou, B. Heijman, M. Moser, A. Haidari, H. Spanjers, V. Bertsch, Experimental and theoretical characterization of commercial nanofiltration membranes for the treatment of ion exchange spent regenerant, J. Membr. Sci. 606 (2020) 118117, https://doi.org/10.1016/j.memsci.2020.118117.

[24] A. Szymczyk, C. Labbez, P. Fievet, A. Vidonne, A. Foissy, J. Pagetti, Contribution of convection, diffusion and migration to electrolyte transport through nanofiltration membranes, Adv. Colloid Interf. Sci. 103 (2003) 77–94, https://doi.org/10.1016/S0001-8686(02)00094-5.

[25] Z.H. Foo, D. Rehman, A.T. Bouma, S. Monsalvo, J.H. Lienhard, Lithium concentration from salt-lake brine by donnan-enhanced nanofiltration, Environ. Sci. Technol. 57 (15) (2023) 6320–6330, https://doi.org/10.1021/acs.est.2c08584.

[26] Y. Roy, D.M. Warsinger, J.H. Lienhard, Effect of temperature on ion transport in nanofiltration membranes: diffusion, convection and electromigration, Desalination 420 (2017) 241–257, https://doi.org/10.1016/j.desal.2017.07.020.

[27] S. Veríssimo, K.V. Peinemann, J. Bordado, Influence of the diamine structure on the nanofiltration performance, surface morphology and surface charge of the composite polyamide membranes, J. Membr. Sci. 279 (2006) 266–275, https://doi.org/10.1016/j.memsci.2005.12.014.

[28] N.K. Saha, S.V. Joshi, Performance evaluation of thin film composite polyamide nanofiltration membrane with variation in monomer type, J. Membr. Sci. 342 (1–2) (2009) 60–69, https://doi.org/10.1016/j.memsci.2009.06.025.

[29] X.D. Weng, Y.L. Ji, F.Y. Zhao, Q.F. An, C.J. Gao, Tailoring the structure of polyamide thin film composite membrane with zwitterions to achieve high water permeability and antifouling property, RSC Adv. 5 (120) (2015) 98730–98739, https://doi.org/10.1039/c5ra18640d.

[30] P. Zhao, F. Guo, L.F. Wang, H.E. Zhen, N. Zhang, S.H. Yin, G.L. Zhou, X.H. Ruan, G. H. He, X.B. Jiang, Nanofiltration membrane with modified nano-gradient structure and positive charge for Li separation from high Mg/Li ratio brine, Desalination 577 (2024), https://doi.org/10.1016/j.desal.2024.117394.

[31] P. Xu, W. Wang, X.M. Qian, H.B. Wang, C.S. Guo, N. Li, Z.W. Xu, K.Y. Teng, Z. Wang, Positive charged PEI-TMC composite nanofiltration membrane for separation of Li and Mg from brine with high Mg/Li ratio, Desalination 449 (2019) 57–68, https://doi.org/10.1016/j.desal.2018.10.019.

[32] K. Sharma, N. Akther, Y. Choo, P.F. Zhang, H. Matsuyama, H.K. Shon, G. Naidu, Positively charged nanofiltration membranes for enhancing magnesium separation from seawater, Desalination 568 (2023), https://doi.org/10.1016/j.desal.2023.117026.

[33] X.Y. Zeng, C.C. Meng, Z.H. Xu, X.W. Li, H.C. Zhu, G.M. Li, Recent advances on the positively-charged nanofiltration membranes for Mg/Li separation through interfacial polymerization, Nanomaterials-Basel 15 (13) (2025), https://doi.org/10.3390/nano15130967.

[34] P.P. Su, M. Xu, C.W. Wang, Y.B. Li, Poly-(aminoethyl piperazine) membranes with ultra-thin selective layers prepared via a rate-retarded interfacial polymerization method, J. Membr. Sci. 714 (2025), https://doi.org/10.1016/j.memsci.2024.123415.

[35] L. Wang, Y.K. Lin, Y.H. Tang, D. Ren, X.L. Wang, Fabrication of oppositely charged thin-film composite polyamide membranes with tunable nanofiltration performance by using a piperazine derivative, J. Membr. Sci. 634 (2021), https://doi.org/10.1016/j.memsci.2021.119405.

[36] X. Li, C. Zhang, S. Zhang, J. Li, B. He, Z. Cui, Preparation and characterization of positively charged polyamide composite nanofiltration hollow fiber membrane for lithium and magnesium separation, Desalination 369 (2015) 26–36, https://doi.org/10.1016/J.DESAL.2015.04.027.

[37] Y.F. Yan, J. Wang, W.B. Wang, C. Han, Fine-tuning polyamide membrane pores and charge for enhanced Li+/ Mg2+separation, J. Membr. Sci. 721 (2025), https://doi.org/10.1016/j.memsci.2025.123812.

[38] A.L. Ahmad, B.S. Ooi, Properties–performance of thin film composites membrane: study on trimesoyl chloride content and polymerization time, J. Membr. Sci. 255 (2005) 67–77, https://doi.org/10.1016/J.MEMSCI.2005.01.021.

[39] A.L. Ahmad, B.S. Ooi, A.W. Mohammad, J.P. Choudhury, Effect of constricted polymerization time on nanofiltration membrane characteristic and performance: a study using the donnan steric pore flow model, J. Appl. Polym. Sci. 94 (1) (2004) 394–399, https://doi.org/10.1002/app.20904.

[40] F. Léniz-Pizarro, C. Liu, A. Colburn, I.C. Escobar, D. Bhattacharyya, Positively charged nanofiltration membrane synthesis, transport models, and lanthanides separation, J. Membr. Sci. 620 (2021), https://doi.org/10.1016/j.memsci.2020.118973.

[41] A. Santafé-Moros, J.M. Gozálvez-Zafrilla, J. Lora-García, Applicability of the DSPM with dielectric exclusion to a high rejection nanofiltration membrane in the separation of nitrate solutions, Desalination 221 (2008) 268–276, https://doi.org/10.1016/J.DESAL.2007.01.083.

[42] V. Freger, G.Z. Ramon, Polyamide desalination membranes: formation, structure, and properties, Prog. Polym. Sci. 122 (2021) 101451, https://doi.org/10.1016/j.progpolymsci.2021.101451.

[43] C.L. Ritt, J.R. Werber, M. Wang, Z. Yang, Y. Zhao, H.J. Kulik, M. Elimelech, Ionization behavior of nanoporous polyamide membranes, Proc. Natl. Acad. Sci. USA 117 (2020) 30191–30200, https://doi.org/10.1073/pnas.2008421117.
[44] L.L. Liu, S.H. Lin, X.Y. Xu, Y.H. Wan, W.J. Song, J.Q. Luo, Preference of negatively charged membranes in magnesium and lithium separation by nanofiltration, nature communications 16 (1) (2025), https://doi.org/10.1038/s41467-025-61336-6.
[45] M. Alsuhybani, A. Alshahrani, A.S. Haidyrah, Synthesis, characterization, and evaluation of evaporated casting MWCNT/chitosan composite membranes for water desalination, J. Chem. 2020 (2020), https://doi.org/10.1155/2020/5207680.
[46] R.H. Du, J.S. Zhao, Properties of poly (N,N-dimethylaminoethyl methacrylate)/polysulfone positively charged composite nanofiltration membrane, J. Membr. Sci. 239 (2) (2004) 183–188, https://doi.org/10.1016/j.memsci.2004.03.029.
[47] L.F. Fang, M.Y. Zhou, L. Cheng, B.K. Zhu, H. Matsuyama, S.F. Zhao, Positively charged nanofiltration membrane based on cross-linked polyvinyl chloride copolymer, J. Membr. Sci. 572 (2019) 28–37, https://doi.org/10.1016/j.memsci.2018.10.054.
[48] Y.X. Feng, H.W. Peng, Q. Zhao, Fabrication of high performance Mg2+/Li+ nanofiltration membranes by surface grafting of quaternized bipyridine, Sep. Purif. Technol. 280 (2022), https://doi.org/10.1016/j.seppur.2021.119848.
[49] B.Y. He, H.W. Peng, Y. Chen, Q. Zhao, High performance polyamide nanofiltration membranes enabled by surface modification of imidazolium ionic liquid, J. Membr. Sci. 608 (2020), https://doi.org/10.1016/j.memsci.2020.118202.
[50] R.H. Huang, G.H. Chen, M.K. Sun, C.J. Gao, Preparation and characterization of quaterinized chitosan/poly(acrylonitrile) composite nanofiltration membrane from anhydride mixture cross-linking, Sep. Purif. Technol. 58 (3) (2008) 393–399, https://doi.org/10.1016/j.seppur.2007.05.013.
[51] R.H. Huang, G.H. Chen, M.K. Sun, C.J. Gao, Preparation and characterization of composite NF membrane from a graft copolymer of trimethylallyl ammonium chloride onto chitosan by toluene diisocyanate cross-linking, Desalination 239 (1–3) (2009) 38–45, https://doi.org/10.1016/j.desal.2008.02.023.
[52] Y.L. Ji, Q.F. An, F.Y. Zaho, C.J. Gao, Fabrication of chitosan/PDMCHEA blend positively charged membranes with improved mechanical properties and high nanofiltration performances, Desalination 357 (2015) 8–15, https://doi.org/10.1016/j.desal.2014.11.005.
[53] Y. Liang, Y. Zhu, C. Liu, K.R. Lee, W.S. Hung, Z. Wang, Y. Li, M. Elimelech, J. Jin, S. Lin, Polyamide nanofiltration membrane with highly uniform sub-nanometre pores for sub-1 Å precision separation, Nat. Commun. 11 (2020) 1–9, https://doi.org/10.1038/s41467-020-15771-2.
[54] C. Liu, L. Shi, R. Wang, Crosslinked layer-by-layer polyelectrolyte nanofiltration hollow fiber membrane for low-pressure water softening with the presence of SO42− in feed water, J. Membr. Sci. 486 (2015) 169–176, https://doi.org/10.1016/j.memsci.2015.03.050.
[55] F.G. Meng, F. Song, Y.X. Yao, G.M. Liu, S.S. Zhao, Ultrastable nanofiltration membranes engineered by polydopamine-assisted polyelectrolyte layer-by-layer assembly for water reclamation, ACS Sustain. Chem. Eng. 8 (29) (2020) 10928–10938, https://doi.org/10.1021/acssuschemeng.0c03318.
[56] T. Mu, H.Z. Zhang, J.Y. Sun, Z.L. Xu, Three-channel capillary nanofiltration membrane with quaternary ammonium incorporated for efficient heavy metals removal, Sep. Purif. Technol. 248 (2020), https://doi.org/10.1016/j.seppur.2020.117133.
[57] F. Soyekwo, H. Wen, D. Liao, C.K. Liu, Nanofiltration membranes modified with a clustered multiquaternary ammonium-based ionic liquid for improved magnesium/lithium separation, ACS Appl. Mater. Interfaces 14 (28) (2022) 32420–32432, https://doi.org/10.1021/acsami.2c03650.
[58] X.Z. Wei, Z.Q. Gana, Y.J. Shen, Z.L. Qiu, L.F. Fang, B.K. Zhu, Negatively-charged nanofiltration membrane and its hexavalent chromium removal performance, J. Colloid Interface Sci. 553 (2019) 475–483, https://doi.org/10.1016/j.jcis.2019.06.051.
[59] H.H. Wu, Y.K. Lin, W.Y. Feng, T.Y. Liu, L. Wang, H. Yao, X.L. Wang, A novel nanofiltration membrane with [MimAP][Tf 2 N] ionic liquid for utilization of lithium from brines with high Mg/Li ratio, J. Membr. Sci. 603 (2020), https://doi.org/10.1016/j.memsci.2020.117997.
[60] T.W. Xu, W.H. Yang, A novel positively charged composite membranes for nanofiltration prepared from poly(2,6-dimethyl-1,4-phenylene oxide) by in situ amines crosslinking, J. Membr. Sci. 215 (1–2) (2003) 25–32, https://doi.org/10.1016/S0376-7388(02)00599-9.
[61] C. Yan, S.H. Zhang, D.L. Yang, X.G. Jian, Preparation and characterization of chloromethylated/quaternized poly(phthalazinone ether sulfone ketone) for positively charged nanofiltration membranes, J. Appl. Polym. Sci. 107 (3) (2008) 1809–1816, https://doi.org/10.1002/app.27226.
[62] B.B. Yang, K.F. Gu, S.H. Wang, Z. Yi, Y. Zhou, C.J. Gao, Chitosan nanofiltration membranes with gradient cross-linking and improved mechanical performance for the removal of divalent salts and heavy metal ions, Desalination 516 (2021), https://doi.org/10.1016/j.desal.2021.115200.
[63] Y. Yang, Y. Li, K.L. Goh, C.H. Tan, R. Wang, Dopamine-intercalated polyelectrolyte multilayered nanofiltration membranes: toward high permselectivity and ion-ion selectivity, J. Membr. Sci. 648 (2022), https://doi.org/10.1016/j.memsci.2022.120337.
[64] Z.Z. Zhang, M.M. Rahman, I. Ternes, B. Bajer, V. Abetz, Engineering soft nanochannels in isoporous block copolymer nanofiltration membranes for ion separation, J. Membr. Sci. 691 (2024), https://doi.org/10.1016/j.memsci.2023.122270.
[65] S. Déon, Z. Koubaa, E. Korzhova, A. Airoudj, P. Fievet, V. Roucoules, Understanding the impact of poly(allylamine) plasma grafting on the filtration performances of a commercial polymeric membrane, Sep. Purif. Technol. 212 (2019) 30–39, https://doi.org/10.1016/j.seppur.2018.11.004.
[66] W.X. Fang, L. Shi, R. Wang, Interfacially polymerized composite nanofiltration hollow fiber membranes for low-pressure water softening, J. Membr. Sci. 430 (2013) 129–139, https://doi.org/10.1016/j.memsci.2012.12.011.
[67] O. Labban, C. Liu, T.H. Chong, J.H. Lienhard V, Fundamentals of low-pressure nanofiltration: membrane characterization, modeling, and understanding the multi-ionic interactions in water softening, J. Membr. Sci. 521 (2017) 18–32, https://doi.org/10.1016/j.memsci.2016.08.062.
[68] Y.T. Liu, J.M. Sipe, W.H. Xu, X.W. Zhu, L.M. Bai, D.L. Xu, G.B. Li, H. Liang, M. R. Wiesner, Study on the mechanisms for the influence of nanomaterials on the separation performance of nanocomposite membrane from a modeling perspective, Desalination 532 (2022), https://doi.org/10.1016/j.desal.2022.115740.
[69] O.Y. Lu, R. Malaisamy, M.L. Bruening, Multilayer polyelectrolyte films as nanofiltration membranes for separating monovalent and divalent cations, J. Membr. Sci. 310 (1–2) (2008) 76–84, https://doi.org/10.1016/j.memsci.2007.10.031.
[70] V. Freger, Dielectric exclusion, an eminence grise, Adv. Colloid Interf. Sci. 319 (2023), https://doi.org/10.1016/j.cis.2023.102972.
[71] S.S. Wadekar, R.D. Vidic, Influence of active layer on separation potentials of nanofiltration membranes for inorganic ions, Environ. Sci. Technol. 51 (10) (2017) 5658–5665, https://doi.org/10.1021/acs.est.6b05973.
[72] S. Déon, A. Escoda, P. Fievet, A transport model considering charge adsorption inside pores to describe salts rejection by nanofiltration membranes, Chem. Eng. Sci. 66 (12) (2011) 2823–2832, https://doi.org/10.1016/j.ces.2011.03.043.
[73] L. Bruni, S. Bandini, The role of the electrolyte on the mechanism of charge formation in polyamide nanofiltration membranes, J. Membr. Sci. 308 (1–2) (2008) 136–151, https://doi.org/10.1016/j.memsci.2007.09.061.
[74] A.E. Childress, M. Elimelech, Effect of solution chemistry on the surface charge of polymeric reverse osmosis and nanofiltration membranes, J. Membr. Sci. 119 (2) (1996) 253–268, https://doi.org/10.1016/0376-7388(96)00127-5.
[75] D.L. Oatley, L. Llenas, R. Pérez, P.M. Williams, X. Martínez-Lladó, M. Rovira, Review of the dielectric properties of nanofiltration membranes and verification of the single oriented layer approximation, Adv. Colloid Interf. Sci. 173 (2012) 1–11, https://doi.org/10.1016/j.cis.2012.02.001.
[76] W.M. Deen, Hindered transport of large molecules in liquid-filled pores, AICHE J. 33 (9) (1987) 1409–1425, https://doi.org/10.1002/aic.690330902.

# 4

# Comprehensive Discussion

This cumulative dissertation set out to strengthen the mechanistic link between IP design variables and selective ion transport in PA TFC NF membranes. The guiding premise, established in the preceding chapters, is that selective performance cannot be interpreted reliably from rejection trends alone. Instead, it must be expressed through coupled interfacial partitioning and in-pore transport, formulated in terms of an effective descriptor set ($r_{\mathrm{pore}}, \Delta x_e, c_{\mathrm{X}}, \varepsilon_{\mathrm{pore}}$). The discussion below synthesizes that evidence across the four publications and defines the limits within which the resulting descriptors remain mechanistically interpretable.

The discussion is organized around three main questions. First, how do IP variables, namely monomer concentration and aqueous-phase monomer identity, position membranes within a coupled descriptor space rather than shifting a single dominant property? Second, how does electrolyte identity, particularly common-anion effects, reshape the same descriptor set and the relative contributions of Donnan and dielectric effects under mixed-salt conditions? Third, what interpretability constraints follow when fitted parameters represent effective quantities that may be non-unique and condition-dependent, and how can robust fitting strategies still support physically based conclusions?

Sections 4.1–4.5 develop these questions by synthesizing the results of Publications I–IV across changes in fabrication conditions, aqueous-phase monomer chemistry, and electrolyte identity. Section 4.6 then reflects on the limitations and outlook of this interpretation, and Section 4.7 consolidates the findings into an outcome statement.

## 4.1. From IP Variables to Effective Descriptors

A key knowledge gap identified in Section 1.5 was the lack of systematic evidence that connects IP conditions to *coupled* shifts in ($r_{\mathrm{pore}}, \Delta x_e, c_{\mathrm{X}}, \varepsilon_{\mathrm{pore}}$), particularly under mixed-electrolyte environments where selectivity can change qualitatively. Publications I–II address this knowledge gap by using a single fabrication family (PIP/TMC) while varying monomer concentrations in a defined concentration space and interpreting the resulting membranes under different ionic systems using the same DSPM-DE framework.

Across the PIP/TMC series, the PA layer thickness increases consistently with increasing aqueous-phase monomer concentration. Even allowing for the uncertainty inherent to SEM-based thickness quantification, the thickness shift is unambiguous in direction and magnitude. In particular, PA thickness increases two-fold when PIP increases from 0.125 to

1.0%w-w, whereas increasing TMC from 0.15 to 0.30%w-w does not produce a significant thickness increase. In contrast, the organic-phase monomer concentration influences the effective transport descriptors more strongly than it alters the observed thickness. This distinction is important mechanistically: it emphasizes that measured PA layer thickness alone is insufficient to predict separation performance, because $\Delta x_e$ is an effective thickness-to-porosity ratio inferred from transport. Therefore, it effectively captures multiple sources of resistance (i.e., structural heterogeneity, roughness contributions, connected pore volume and pathway tortuosity), which cannot be inferred from thickness measurements alone.

Two inferences emerge when Publications I and II are considered together. First, monomer concentrations do not tune solely one descriptor; rather, they shift a *descriptor set*. In the PIP-based membranes, increases in PIP concentration drive systematic changes in $\Delta x_e$ and in apparent charge $c_X$, while changes in TMC concentration can tighten $r_{\mathrm{pore}}$ and reduce $\Delta x_e$ without producing a comparably clear effect in the SEM thickness. To illustrate this, in Publication I at a TMC concentration of 0.15%w-w $r_{\mathrm{pore}}$ spans from 0.65 to 0.70 nm, whereas at 0.30%w-w $r_{\mathrm{pore}}$ varies from 0.60 to 0.70 nm, and both $r_{\mathrm{pore}}$ and $\Delta x_e$ are lower at 0.30%w-w. Second, the same fabrication shift can appear differently depending on the ionic system used to evaluate it. This is not a contradiction; it is a direct consequence of the descriptors being *effective*, i.e., inferred from transport under a given electrolyte environment.

Publication III extends the same logic beyond concentration effects by introducing aqueous-phase monomer identity (AEP vs. DAP). Importantly, comparing monomer identity does not simply shift performance; it alters the formation pathway and thereby the coupled descriptors. The AEP system is associated with faster early-stage network formation that can restrict monomer penetration, thereby locking in a denser incipient layer. In contrast, the DAP system forms a comparatively more open incipient PA network that continues to grow differently as diffusion proceeds (Fig. 1 in Publication III). At the descriptor level, this appears as a systematic contrast: At comparable $\Delta x_e$, DAP-based membranes tend toward larger $r_{\mathrm{pore}}$ and higher diffusive fluxes, whereas AEP-based membranes more readily develop smaller $r_{\mathrm{pore}}$ with stronger shifts in $c_X$.

Taken together, the four-publication set closes the fabrication–descriptor knowledge gap in a specific sense relevant to membrane design. Rather than inferring mechanisms from selectivity trends alone, the dissertation establishes how IP fabrication conditions move membranes through a coupled descriptor space. This space can be compared across different separation problems, while preserving a common mechanistic interpretation of exclusion and transport contributions.

## 4.2. When Mechanisms Control Selectivity

A second theme of Section 1.5 is that selective $Na^+/Mg^{2+}$ separation and $NO_3^-$ removal are not governed by a single exclusion mechanism; they arise from coupled partitioning and coupled transport, whose relative balance shifts with changes in $c_X$ and electrolyte environment. The collective evidence across Publications I–IV shows that the relevant question is rarely which mechanism dominates in NF, but instead: *under which descriptor combination and electrolyte environment does a given contribution become decisive for the targeted separation?*

### 4.2.1. $NO_3^-/SO_4^{2-}$: when dielectric exclusion controls separation

Within the PIP/TMC series (Publication I), $NO_3^-/SO_4^{2-}$ separation is most consistently accounted for by dielectric exclusion as the primary discriminator between the two anions. $r_{pore}$ serves as a key controlling descriptor because it co-varies with the dielectric barrier experienced inside confined pores. This descriptor-based view clarifies why changes in monomer concentrations can sharpen nitrate selectivity even when pore-size shifts appear modest: a small tightening of $r_{pore}$ can translate into a disproportionately larger solvation-energy penalty under lower $\varepsilon_{pore}$. In the same dataset, flux decomposition further indicates that diffusion contributes the majority of the anion total flux. As a result, descriptor changes affecting concentration gradients and partitioning are directly reflected in the observed retention.

At the same time, Publication I highlights an interpretive limitation that is important for this dissertation: nitrate behavior in mixed electrolytes cannot be treated as a purely anion-specific interpretation. Under certain ternary mixtures, coupling through the counter-ion can promote nitrate permeation to the extent that negative retention is observed. Importantly, this counterintuitive outcome is reproduced and elucidated within the coupled partitioning–transport framework rather than being an anomaly. At the same time, not all ionic systems are captured equally well by the mechanistic model without additional refinement. Publication I reproduced $Na^+/NO_3^-/SO_4^{2-}$ trends, whereas $Na^+/NO_3^-/Cl^-$ could not be simulated within the same DSPM-DE framework and would require additional refinement. Importantly, this discrepancy is not attributable to the fitted membrane descriptor set ($r_{pore}$, $\Delta x_e$, $\varepsilon_{pore}$, $c_X$), but to a missing ion-specific contribution in the model physics. Within the DSPM-DE model, $NO_3^-$ and $Cl^-$ are represented as two monovalent ions of comparable size and charge. Indeed, the framework does not account for differences in dehydration energy and ionic charge density that promote preferential $NO_3^-$ permeation. Accordingly, reproducing $Na^+/NO_3^-/Cl^-$ behavior would require model refinement that introduces such ion-specific effects beyond the current monovalent-ion representation.

Publication III demonstrates that changing aqueous-phase monomer identity shifts the mechanistic balance. In the AEP/DAP series, overall partitioning differences between $NO_3^-$ and $SO_4^{2-}$ are governed primarily by $c_X$ through Donnan exclusion trends (Fig. 6 of Publication III). Here, dielectric exclusion remains relevant but no longer the main discriminator across the tested concentration range. A key implication is that a membrane can exhibit increasing dielectric discrimination while simultaneously showing reduced *overall* separation between $NO_3^-$ and $SO_4^{2-}$. This occurs if charge-driven partitioning shifts become sufficiently strong to counterbalance the dielectric contrast, directly resolving the monomer-chemistry knowledge gap identified in Section 1.5.2. Monomer identity is not an empirical parameter, but a variable that changes the coupled descriptor set. Therefore, it shifts which mechanisms matter most for the targeted selectivity.

### 4.2.2. $Na^+/Mg^{2+}$: preferential $Mg^{2+}$ diffusion suppression

For $Na^+/Mg^{2+}$ separation (Publications II and IV), the most robust conclusion across publications is that selectivity increases when $Mg^{2+}$ transport is attenuated more strongly than $Na^+$ transport as membranes become more charge-selective and more confining. This can be stated within DSPM-DE as follows: cation transport is dominated by diffusion. Descriptor changes

(more positive $c_X$, smaller $r_{pore}$ and lower $\varepsilon_{pore}$) reduce the $Mg^{2+}$ concentration gradient in the active layer more strongly than the $Na^+$ gradient. Therefore, $J_{Mg^{2+},diff}$ is suppressed more strongly.

Publication II establishes, within a single membrane series (PIP/TMC), why $\Delta x_e$ and $c_X$ are the most decisive synthesis-linked descriptors for $Na^+/Mg^{2+}$ separation outcomes. $\Delta x_e$ links directly to the magnitude of diffusive fluxes, and the diffusion of the most mobile ion can set the magnitude of the internally generated electrical field required to satisfy the zero-current condition. In parallel, $c_X$ governs Donnan partitioning at the pore entrance, thereby setting the internal ion concentrations affecting both diffusion and electromigration terms. As a result, the mechanistic conclusion is not if charge dominates or if resistance dominates. Instead, the mechanistic message is that IP conditions co-tune charge and resistance, and the observed selectivity reflects how that co-tuning shifts the coupled flux contributions under electroneutrality constraints.

Publication IV extends this conclusion beyond a single monomer family. It shows that the same mechanistic logic holds across AEP- and DAP-based chemistries, while the *electrolyte environment* shifts which exclusion contribution dominates. In $Cl^-$-containing systems, stronger dielectric confinement (lower $\varepsilon_{pore}$) amplifies the preferential exclusion of $Mg^{2+}$. In $SO_4^{2-}$-containing systems, higher $\varepsilon_{pore}$ weakens dielectric penalties and shifts the selectivity control toward Donnan exclusion. Accordingly, this addresses the common-ion knowledge gap identified in Section 1.5.2: the common anion does not simply rescale observed retentions, but instead changes how the descriptor set translates into exclusion and flux coupling.

## 4.3. Electrolyte Identity Reshapes Effective Descriptors

A recurring limitation in the literature (Section 1.5.2) is the implicit treatment of the membrane as fixed while the electrolyte environment is varied. This assumption persists despite clear indications that electrolyte identity can reshape effective membrane descriptors. Publication IV provides the clearest evidence within this dissertation that this concern is justified for PA TFC NF. The fitted dielectric environment is not a fixed property of the polymer network, but a dynamic descriptor of the pore dielectric environment that responds to the electrolyte identity.

Two results are important here. First, the fitted single-layer dielectric constant $\varepsilon^*$ (and thus $\varepsilon_{pore}$) is different between $Cl^-$ and $SO_4^{2-}$ systems for the same membrane chemistry, yielding higher $\varepsilon_{pore}$ in $SO_4^{2-}$ systems ($\varepsilon^*$ is $Cl^-$: AEP 6, DAP 10 vs. $SO_4^{2-}$: AEP 30, DAP 35 ). Second, $c_X$ is also electrolyte-dependent, with the $SO_4^{2-}$ system tending to exhibit more positive values than the $Cl^-$ system, consistent with ion-specific screening differences at charged sites (Fig. 4C–D in Publication IV). Accordingly, a descriptor set inferred under one common-ion identity should not be applied to another unless the electrolyte dependence of $\varepsilon_{pore}$ and $c_X$ has been established.

This electrolyte dependence also clarifies why more charge does not automatically translate into higher selectivity. In the $SO_4^{2-}$ system, higher $c_X$ can strengthen Donnan exclusion, but higher $\varepsilon_{pore}$ simultaneously reduces dielectric penalties. Thus, the net selectivity outcome reflects the balance of these two shifts rather than a single monotonic trend with charge. Accordingly, the dissertation reframes electrolyte identity from an external operating variable into a modifier of the effective descriptor combination that governs both partitioning and

transport.

## 4.4. Robust Fitting and Interpretability Constraints

Section 1.5 emphasizes that mechanistic NF models are powerful because they impose a physically structured framework for describing partitioning and transport, yet they also come with a constraint: fitted parameters are effective and may be non-unique, particularly under mixed-salt conditions where compensating descriptor changes can reproduce similar outcomes. The dissertation addresses this interpretability knowledge gap through consistency and systematic variation, but it also exposes where identifiability limits remain.

Across the four publications, the same fitting framework is applied to obtain $\varepsilon_{\mathrm{pore}}$ through a minimization strategy rather than adopting an arbitrary dielectric constant. Comparability across Publications I–IV was maintained by holding the modeling scheme fixed and by applying the same minimization-based strategy to estimate $\varepsilon^*$ as the intermediate quantity from which $\varepsilon_{\mathrm{pore}}$ was calculated. While the assumed grouping of $\varepsilon^*$ was defined study-wise (e.g. by TMC concentration, by monomer chemistry, and in Publication IV additionally by common anion), the numerical estimation procedure itself remained consistent across the dissertation. Importantly, parameter trends were constrained by design through datasets spanning multiple ion systems, including mixed-electrolyte environments, to increase information content and reduce the likelihood that similar fits arise from compensating descriptor changes. However, convergence limitations were observed when attempting to fit dielectric and charge descriptors simultaneously for some systems. This indicates that meaningful parameter identification requires sufficient contrast among membranes and sufficiently informative datasets to separate the roles of $c_X$ and $\varepsilon_{\mathrm{pore}}$. This manifested as system-dependent representation limits. For example, within the PIP/TMC series it was possible to reproduce $Na^+/Mg^{2+}/Cl^-$ behavior but not $Na^+/Mg^{2+}/SO_4^{2-}$ under the same fitting strategy (Publication II). Therefore, these cases are treated here as boundaries of model applicability under the studied conditions, not as a basis for assigning absolute parameter values. This practical observation is not simply methodological. It corroborates the conceptual idea that effective descriptors "absorb" multiple forms of heterogeneity, thereby requiring robust study designs to remain interpretable.

Two statements remain useful for design despite these constraints. First, *relative* parameter trends across a systematically varied membrane series are more reliable than standalone absolute parameter values. Accordingly, the dissertation is organized to prioritize interpretability alongside thematic progression. It progresses from fabrication-driven mapping (Publications I–II) to monomer-identity effects (Publication III) and finally to electrolyte-identity integration (Publication IV). Second, mechanistic interpretation should be treated as condition-specific: the descriptors and their derived exclusion/flux contributions represent the membrane *as determined* under a defined electrolyte environment and set of operating conditions, rather than as universal material constants.

Within this framing, several reported relationships are mechanistically informative, including the strong nonlinearity of Donnan exclusion with $c_X$ and the sensitivity of dielectric exclusion to changes in $\varepsilon_{\mathrm{pore}}$ coupled to $r_{\mathrm{pore}}$. Specifically, they clarify how small descriptor shifts can amplify partitioning differences and internal electric field responses under electroneutrality conditions. Consequently, this dissertation uses the effective parameters to

develop mechanistic interpretations that remain consistent with the observed trends and flux decompositions.

## 4.5. Design Implications

A practical motivation behind the dissertation is that intuitive design rules often fail for mixed-electrolyte separations. Here, the same structural change can increase or decrease selectivity depending on how it reshapes Donnan and dielectric contributions and the internal potential gradient. Taken together, the combined results support three design implications that are more specific than generic recommendations to fabricate denser membranes.

A common trade-off is that selectivity increases are often accompanied by lower permeance, particularly when selectivity relies on tuning electrostatic effects that also influence water and ion transport. Within the present descriptor set, this coupling emerges most directly through $\Delta x_e$: fabrication routes that increase charge-based selectivity often increase $\Delta x_e$, thereby reducing solvent permeance and weakening diffusion-driven ion fluxes. At the same time, this trade-off is not universal. In some cases, selectivity improves primarily through partitioning shifts while $\Delta x_e$ remains nearly constant. This can occur, for example, when electrolyte- and monomer-chemistry-driven changes in $\varepsilon_{\text{pore}}$ strengthen dielectric exclusion or when $c_X$-driven Donnan partitioning preferentially reduces the in-pore concentration of the preferentially rejected ion. Under such conditions, the same selectivity gain can be achieved with smaller increases in transport resistance. Therefore, the design question is not whether selectivity and permeance necessarily trade off, but whether a given fabrication variable or electrolyte condition shifts performance mainly through $\Delta x_e$ (resistance) changes or mainly through partitioning changes within the coupled descriptor framework.

### 4.5.1. Nitrate removal design: manage coupled transport

For $NO_3^-$ under mixed electrolytes, the dissertation indicates that $NO_3^-$ selectivity increases most reliably when the membrane is positioned in a region of descriptor space where dielectric penalties discriminate strongly against the competing anion (i.e., $SO_4^{2-}$). In practice, this points toward fabrication routes that reduce $r_{\text{pore}}$ and lower $\varepsilon_{\text{pore}}$, thereby amplifying dielectric discrimination. At the same time, multicomponent coupling can, under certain electrolyte environments and descriptor combinations, promote preferential $NO_3^-$ permeation and thus negative $NO_3^-$ retention. For nitrate removal, such behavior is not an anomaly. Rather, it implies a process inversion: the retentate constitutes the nitrate-depleted product stream, whereas the permeate represents a smaller nitrate-enriched stream that requires appropriate handling.

Publication III further indicates that monomer identity can tune charge-driven partitioning strongly, but this tuning must be treated as a trade-off. Specifically, increasing positive $c_X$ can weaken anion exclusion. Accordingly, it must be counterbalanced by steric and dielectric confinement to maintain $NO_3^-/SO_4^{2-}$ separation.

### 4.5.2. $Na^+/Mg^{2+}$ design: preferential $Mg^{2+}$ suppression

For $Na^+/Mg^{2+}$, the clearest design strategy is to maximize the differential suppression of $Mg^{2+}$ diffusion relative to $Na^+$. This can be pursued by co-tuning $c_X$ (Donnan repulsion) and the dielectric confinement set by $r_{pore}$ and $\varepsilon^*$. As cation diffusion dominates total cation fluxes under positively charged conditions, strategies that increase $c_X$ and tighten pores will primarily act by flattening $Mg^{2+}$ concentration gradients inside the active layer. Importantly, the dissertation clarifies that anion fluxes also play an important role. Specifically, in positively charged membranes, advection and electromigration can counterbalance strongly, and this balance depends on electrolyte identity. Therefore, performance optimization for $Na^+/Mg^{2+}$ separation cannot neglect the counter-ion, because electroneutrality forces coupled responses that can reshape the internal electric field and, thereby, the cation flux contributions.

### 4.5.3. Electrolyte-specific design rules

The common-anion comparison yields a design principle that is straightforward, yet often not implemented in practice. In particular, the target separation must be specified together with a representative electrolyte environment, because $\varepsilon_{pore}$ and $c_X$ can vary with ion identity, thereby shifting which mechanism governs selectivity. Publication IV shows that in $Cl^-$ systems, tighter confinement together with lower $\varepsilon_{pore}$ strengthens dielectric exclusion of $Mg^{2+}$ and can yield very high $Na^+/Mg^{2+}$ selectivity ($\approx$ 244 for DAP0.5 in $Cl^-$ vs. $\approx$ 66 for AEP1 in $SO_4^{2-}$ feeds). In contrast, in $SO_4^{2-}$ systems higher $\varepsilon_{pore}$ attenuates dielectric penalties and shifts the design focus toward charge-controlled partitioning. Thus, the same membrane is not expected to occupy the same descriptor combination across $Cl^-$- and $SO_4^{2-}$-dominated feeds. Design choices should be evaluated within the intended ionic context rather than extrapolated.

## 4.6. Limitations and Outlook

Several limitations follow directly from the dissertation's scope and, importantly, they point to clear next steps rather than weakening the mechanistic conclusions. First, the IP variables explored here are intentionally limited to monomer concentration and aqueous-phase monomer identity, with a fixed organic-phase monomer chemistry. Because IP is strongly sensitive to the reaction–diffusion balance, extending the descriptor-mapping framework to other organic-phase chemistries is a clear next step. The same applies to broader process parameters (e.g. solvent choice, additives, reaction time, post-treatments). However, such extensions should be established through system-specific validation.

Second, the model-based descriptor set is transport-relevant and mechanistically structured, yet it remains effective. Therefore, future work should pair systematic descriptor fitting with independent experimental constraints that narrow the range of consistent descriptor combinations (e.g. complementary measurements sensitive to charge distribution and dielectric effects). In addition, it should broaden validation across additional electrolyte families where ion-specific interactions may further reshape $\varepsilon_{pore}$ and $c_X$.

Third, the dissertation shows that mixed-salt transport can yield counterintuitive, yet mechanistically consistent, behavior such as negative $NO_3^-$ retention under specific electrolyte

environments. This reflects coupled transport and ion–ion interactions rather than an experimental anomaly. At the same time, model fidelity can depend on the particular ionic system used to evaluate the membrane when ion-specific effects beyond the DSPM-DE framework become significant. Accordingly, future mechanistic studies should treat the selection of probing electrolytes as part of the experimental design, not as an interchangeable screening matrix. Also, they should expand the joint variation of operating conditions and fabrication conditions in a way that preserves mechanistic interpretability.

## 4.7. Outcome

Taken together, the dissertation shows that selective ion transport in PA TFC NF membranes is best understood not as the consequence of tuning one dominant membrane property, but as movement through a coupled effective descriptor space. This space is defined by $r_{\mathrm{pore}}$, $\Delta x_e$, $c_X$, and $\varepsilon_{\mathrm{pore}}$. Across Publications I–IV, both monomer concentration and aqueous-phase monomer identity shift this descriptor set in a systematic but coupled manner. Accordingly, fabrication variables do not act through isolated changes in pore size, charge, or thickness alone. Rather, they reposition the membrane within a transport-relevant descriptor combination that governs both interfacial partitioning and in-pore flux coupling under mixed-electrolyte conditions.

Within the PIP/TMC series, the combined results further show that measured PA thickness trends alone are insufficient to explain separation performance. The transport-relevant resistance is more consistently captured by $\Delta x_e$, which consolidates thickness-to-porosity effects together with structural heterogeneity into an effective transport descriptor. In this sense, increasing aqueous-phase monomer concentration most clearly shifts $\Delta x_e$ and $c_X$. By contrast, increasing the organic-phase monomer concentration can reduce $r_{\mathrm{pore}}$ and $\Delta x_e$ without necessarily producing a correspondingly clear change in the measured PA thickness. This directly addresses the fabrication–descriptor knowledge gap identified in Section 1.5.2: IP variables position membranes within a coupled descriptor space rather than tuning a single dominant structural feature.

The same descriptor-based interpretation clarifies why the governing mechanism depends on both membrane chemistry and electrolyte environment. For nitrate-selective NF, Publication I shows that within the PIP/TMC concentration series, $NO_3^-/SO_4^{2-}$ separation is most consistently explained by dielectric exclusion. Here, modest changes in $r_{\mathrm{pore}}$ become mechanistically amplified through the associated dielectric barrier inside confined pores. At the same time, Publication III shows that monomer-chemistry-driven shifts in $c_X$ can reorganize the mechanistic balance such that Donnan exclusion becomes the main discriminator across the AEP/DAP series. Dielectric exclusion remains relevant but secondary. Thus, the dissertation resolves the monomer-chemistry effect knowledge gap not by assigning aqueous-phase monomer identity an empirical role. Rather, it shows how monomer identity reshapes the coupled descriptor set and, through it, the balance of exclusion mechanisms.

For $Na^+/Mg^{2+}$ separation, the most robust mechanistic conclusion across Publications II and IV is that selectivity increases when $Mg^{2+}$ transport is suppressed more strongly than $Na^+$ transport. This occurs as membranes become more charge-selective and more confining. Within the present descriptor-based interpretation, this occurs because increases in positive $c_X$, together with reductions in $r_{\mathrm{pore}}$ and changes in $\varepsilon_{\mathrm{pore}}$, reduce the $Mg^{2+}$ concentration gradient

inside the active layer more strongly than that of $Na^+$. This preferentially attenuates $Mg^{2+}$ diffusion under electroneutrality-constrained flux coupling. In this way, the dissertation shows that $Na^+/Mg^{2+}$ selectivity cannot be interpreted from cation behavior alone. Counter-ion transport also reshapes the internal electric field and redistributes the relative contributions of diffusion, electromigration, and advection.

A further outcome is that electrolyte identity must not be treated solely as an external operating condition applied to a fixed membrane. The electrolyte environment itself reshapes the effective descriptor combination through which partitioning and transport are interpreted. Publication IV demonstrates that the effective dielectric environment and apparent fixed charge are themselves electrolyte-dependent, with systematic differences between $Cl^-$- and $SO_4^{2-}$-containing systems. As a result, descriptor values inferred under one common-anion environment cannot be transferred directly to another without validation. This finding closes the common-ion knowledge gap identified in Section 1.5.2. It shows that electrolyte identity reshapes the effective descriptor combination and thus shifts whether selectivity is governed more strongly by Donnan or dielectric exclusion.

Taken together, these findings must be interpreted within the established limits of the modeling framework. The fitted descriptors are effective quantities and are therefore not guaranteed to be unique or directly equivalent to independently measurable structural properties. Their values can absorb heterogeneity in charge distribution, pore structure, dielectric environment, and ion-specific interactions not included in the model. Accordingly, the main conclusions are not based on absolute parameter values in isolation. Instead, they rely on relative trends across controlled membrane series analyzed within a consistent fitting framework and under clearly defined electrolyte environments.

Within those interpretive boundaries, the dissertation provides a physically based interpretation of how IP variables, aqueous-phase monomer identity, and electrolyte identity jointly shape selective ion transport in PA TFC NF membranes, with implications for membrane design. For nitrate removal, the results show that selectivity must be designed by considering multicomponent coupling and the balance between charge-driven partitioning and dielectric discrimination. For $Na^+/Mg^{2+}$ separation, they show that the key design objective is the preferential suppression of $Mg^{2+}$ transport through coupled tuning of charge selectivity and confinement. More broadly, the work establishes that rational positioning of NF membranes for magnesium-focused separations and nitrate removal requires descriptor-based, condition-specific mechanistic interpretation under defined electrolyte environments. It cannot rely on extrapolation from nominal membrane structure or from single-salt performance alone.

# References


[1] B. Van der Bruggen, C. Vandecasteele, T. V. Gestel, W. Doyen, R. Leysen, *Environmental Progress* **2003**, *22*, 46–56, DOI 10.1002/ep.670220116.

[2] R. W. Baker, *Membrane Technology and Applications*, 3rd, John Wiley & Sons Ltd., **2012**, DOI 10.1002/9781118359686.

[3] W. J. Koros, Y. H. Ma, T. Shimidzu, *Pure and Applied Chemistry* **1996**, *68*, 1479–1489, DOI 10.1351/pac199668071479.

[4] M. Heiranian, H. Fan, L. Wang, X. Lu, M. Elimelech, *Chemical Society Reviews* **2023**, *52*, 8455–8480, DOI 10.1039/d3cs00395g.

[5] M. Qasim, M. Badrelzaman, N. N. Darwish, N. A. Darwish, N. Hilal, *Desalination* **2019**, *459*, 59–104, DOI 10.1016/J.DESAL.2019.02.008.

[6] B. Van der Bruggen, C. Vandecasteele, *Environmental Pollution* **2003**, *122*, 435–445, DOI 10.1016/S0269-7491(02)00308-1.

[7] R. Wang, S. Lin, *Journal of Membrane Science* **2021**, *620*, 118809, DOI 10.1016/j.memsci.2020.118809.

[8] Y. Guo, J. He, J. Zhang, M. Sheng, Z. Wang, M. Elimelech, L. Wang, *Science Advances* **2025**, *11*, 8302, DOI 10.1126/sciadv.adu8302.

[9] A. W. Mohammad, Y. H. Teow, W. L. Ang, Y. T. Chung, D. L. Oatley-Radcliffe, N. Hilal, *Desalination* **2015**, *356*, 226–254, DOI 10.1016/j.desal.2014.10.043.

[10] C. Tang, M. L. Bruening, *Journal of Polymer Science* **2020**, *58*, 2831–2856, DOI 10.1002/pol.20200500.

[11] D. L. Oatley-Radcliffe, S. R. Williams, M. S. Barrow, P. M. Williams, *Desalination* **2014**, *343*, 154–161, DOI 10.1016/j.desal.2013.10.001.

[12] A. Yaroshchuk, M. L. Bruening, E. Zholkovskiy, *Advances in Colloid and Interface Science* **2019**, *268*, 39–63, DOI 10.1016/j.cis.2019.03.004.

[13] A. Szymczyk, P. Fievet, *Journal of Membrane Science* **2005**, *252*, 77–88, DOI 10.1016/J.MEMSCI.2004.12.002.

[14] V. Freger, *Advances in Colloid and Interface Science* **2023**, *319*, 102972, DOI 10.1016/j.cis.2023.102972.

[15] A. Szymczyk, C. Labbez, P. Fievet, A. Vidonne, A. Foissy, J. Pagetti, *Advances in Colloid and Interface Science* **2003**, *103*, 77–94, DOI 10.1016/S0001-8686(02)00094-5.

[16] H. Guo, X. Li, W. Yang, Z. Yao, Y. Mei, L. E. Peng, Z. Yang, S. Shao, C. Y. Tang, *Frontiers of Chemical Science and Engineering* **2022**, *16*, 681–698, DOI 10.1007/S11705-021-2103-5.

[17] European Commission, Critical Raw Materials Resilience: Charting a Path towards greater Security and Sustainability, Report, **2020**, https://eur-lex.europa.eu/legal-content/EN/TXT/?uri=CELEX:52020DC0474.

[18] D. Fontana, F. Forte, M. Pietrantonio, S. Pucciarmati, C. Marcoaldi, *Environment, Development and Sustainability* **2023**, *25*, 13733–13754, DOI 10.1007/s10668-022-02663-2.

[19] A. Panagopoulos, K. J. Haralambous, M. Loizidou, *Science of The Total Environment* **2019**, *693*, 133545, DOI 10.1016/J.SCITOTENV.2019.07.351.

[20] M. Figueira, D. Rodríguez-Jiménez, J. López, M. Reig, J. L. Cortina, C. Valderrama, *Desalination* **2023**, *549*, 116321, DOI 10.1016/J.DESAL.2022.116321.

[21] C. Morgante, X. Ma, X. Chen, D. Wang, V. Boffa, V. Stathopoulos, J. Lopez, J. L. Cortina, A. Cipollina, A. Tamburini, G. Micale, *Journal of Membrane Science* **2023**, *685*, 121941, DOI 10.1016/J.MEMSCI.2023.121941.

[22] C. Morgante, T. Moghadamfar, J. Lopez, J. L. Cortina, A. Tamburini, *Journal of Environmental Management* **2024**, *360*, 121192, DOI 10.1016/J.JENVMAN.2024.121192.

[23] E. Abascal, L. Gómez-Coma, I. Ortiz, A. Ortiz, *Science of the Total Environment* **2022**, *810*, 152233, DOI 10.1016/j.scitotenv.2021.152233.

[24] D. M. Manassaram, L. C. Backer, D. M. Moll, *Environmental Health Perspectives* **2006**, *114*, 320–327, DOI 10.1289/ehp.8407.

[25] M. Lunau, M. Voss, M. Erickson, C. Dziallas, K. Casciotti, H. Ducklow, *Environmental Microbiology* **2013**, *15*, 1492–1504, DOI 10.1111/J.1462-2920.2012.02773.x.

[26] A. Popova, R. Rattanakom, Z. Q. Yu, Z. Li, K. Nakagawa, T. Fujioka, *Water Research* **2023**, *244*, 120484, DOI 10.1016/j.watres.2023.120484.

[27] A. Santafé-Moros, J. M. Gozálvez-Zafrilla, J. Lora-García, *Desalination* **2005**, *185*, 281–287, DOI 10.1016/j.desal.2005.02.080.

[28] F. Garcia, D. Ciceron, A. Saboni, S. Alexandrova, *Separation and Purification Technology* **2006**, *52*, 196–200, DOI 10.1016/j.seppur.2006.03.023.

[29] R. Epsztein, W. Cheng, E. Shaulsky, N. Dizge, M. Elimelech, *Journal of Membrane Science* **2018**, *548*, 694–701, DOI 10.1016/j.memsci.2017.10.049.

[30] D. X. Wang, M. Su, Z. Y. Yu, X. L. Wang, M. Ando, T. Shintani, *Desalination* **2005**, *175*, 219–225, DOI 10.1016/j.desal.2004.10.009.

[31] S. S. Wadekar, R. D. Vidic, *Environmental Science and Technology* **2017**, *51*, 5658–5665, DOI 10.1021/acs.est.6b05973.

[32] L. Zou, S. Zhang, J. Liu, Y. Cao, G. Qian, Y. Y. Li, Z. P. Xu, *Environmental Science and Pollution Research* **2019**, *26*, 34197–34204, DOI 10.1007/s11356-018-3829-6.

[33] W. J. Lau, A. F. Ismail, N. Misdan, M. A. Kassim, *Desalination* **2012**, *287*, 190–199, DOI 10.1016/J.DESAL.2011.04.004.

[34] R. J. Petersen, *Journal of Membrane Science* **1993**, *83*, 81–150, DOI 10.1016/0376-7388(93)80014-O.

[35] L. Y. Ng, A. W. Mohammad, C. Y. Ng, *Advances in Colloid and Interface Science* **2013**, *197-198*, 85–107, DOI 10.1016/J.CIS.2013.04.004.

[36] S. Karan, Z. Jiang, A. G. Livingston, *Science* **2015**, *348*, 1347–1351, DOI 10.1126/science.aaa5058.

[37] J. M. Gohil, P. Ray, *Separation and Purification Technology* **2017**, *181*, 159–182, DOI 10.1016/j.seppur.2017.03.020.

[38] K. Wang, X. Wang, B. Januszewski, Y. Liu, D. Li, R. Fu, M. Elimelech, X. Huang, *Chemical Society Reviews* **2022**, *51*, 672–719, DOI 10.1039/d0cs01599g.

[39] M. J. Raaijmakers, N. E. Benes, *Progress in Polymer Science* **2016**, *63*, 86–142, DOI 10.1016/J.PROGPOLYMSCI.2016.06.004.

[40] X. Lu, M. Elimelech, *Chemical Society Reviews* **2021**, *50*, 6290–6307, DOI 10.1039/D0CS00502A.

[41] J. Di, H. Wang, L. Zhang, Z. Chen, Y. Zhang, B. B. Mamba, M. Qiu, J. Guo, L. Shao, *Desalination* **2024**, *592*, 118167, DOI 10.1016/J.DESAL.2024.118167.

[42] Y. Song, J. B. Fan, S. Wang, *Materials Chemistry Frontiers* **2017**, *1*, 1028–1040, DOI 10.1039/C6QM00325G.

[43] K. Bean, C. F. Black, N. Govan, P. Reynolds, M. R. Sambrook, *Journal of Colloid and Interface Science* **2012**, *366*, 16–22, DOI 10.1016/J.JCIS.2011.09.054.

[44] J. Huang, R. B. Kaner, *Journal of the American Chemical Society* **2003**, *126*, 851–855, DOI 10.1021/JA0371754.

[45] S. Guo, B. Yuan, J. Wu, H. Wang, J. Luo, C. Yuan, *Desalination* **2024**, *571*, 117112, DOI 10.1016/J.DESAL.2023.117112.

[46] P. W. Morgan, *Condensation Polymers: By Interfacial and Solution Methods*, John Wiley & Sons, Inc., **1965**, DOI 10.1002/ange.19660781632.

[47] J. E. Cadotte, *U.S. Patent*, 4,277,344, **1979**.

[48] P. Vandezande, L. E. Gevers, I. F. Vankelecom, *Chemical Society Reviews* **2008**, *37*, 365–405, DOI 10.1039/B610848M.

[49] V. Freger, *Langmuir* **2003**, *19*, 4791–4797, DOI 10.1021/la020920q.

[50] V. Freger, *Langmuir* **2005**, *21*, 1884–1894, DOI 10.1021/LA048085V.

[51] V. Freger, G. Z. Ramon, *Progress in Polymer Science* **2021**, *122*, 101451, DOI 10.1016/j.progpolymsci.2021.101451.

[52] A. L. Ahmad, B. S. Ooi, A. W. Mohammad, J. P. Choudhury, *Journal of Applied Polymer Science* **2004**, *94*, 394–399, DOI 10.1002/app.20904.

[53] A. L. Ahmad, B. S. Ooi, *Journal of Membrane Science* **2005**, *255*, 67–77, DOI 10.1016/J.MEMSCI.2005.01.021.

[54] N. Misdan, W. J. Lau, A. F. Ismail, *Journal of Polymer Engineering* **2015**, *35*, 71–78, DOI 10.1515/POLYENG-2014-0146.

[55] C. L. Ritt, J. R. Werber, M. Wang, Z. Yang, Y. Zhao, H. J. Kulik, M. Elimelech, *Proceedings of the National Academy of Sciences of the United States of America* **2020**, *117*, 30191–30200, DOI 10.1073/pnas.2008421117.

[56] E. Maaskant, PhD thesis, University of Twente, Netherlands, **2018**, DOI 10.3990/1.9789036545167.

[57] Y.-L. Liu, Y.-Y. Zhao, X.-M. Wang, X.-H. Wen, X. Huang, Y. F. Xie, *Journal of Membrane Science* **2019**, *582*, 274–283, DOI 10.1016/j.memsci.2019.04.018.

[58] J. Xue, Z. Jiao, R. Bi, R. Zhang, X. You, F. Wang, L. Zhou, Y. Su, Z. Jiang, *Journal of Membrane Science* **2019**, *584*, 282–289, DOI 10.1016/J.MEMSCI.2019.04.077.

[59] M. M. Jayarani, P. R. Rajmohanan, S. S. Kulkarni, U. K. Kharul, *Desalination* **2000**, *130*, 1–16, DOI 10.1016/S0011-9164(00)00070-9.

[60] Y. Yao, P. Zhang, C. Jiang, R. M. DuChanois, X. Zhang, M. Elimelech, *Nature Sustainability* **2021**, *4*, 138–146, DOI 10.1038/s41893-020-00619-w.

[61] M. Hirose, Y. Minamizaki, Y. Kamiyama, *Journal of Membrane Science* **1997**, *123*, 151–156, DOI 10.1016/S0376-7388(96)00180-9.

[62] C. Y. Tang, Y. N. Kwon, J. O. Leckie, *Desalination* **2009**, *242*, 168–182, DOI 10.1016/J.DESAL.2008.04.004.

[63] C. Jiang, L. Zhang, P. Li, H. Sun, Y. Hou, Q. J. Niu, *ACS Applied Materials and Interfaces* **2020**, *12*, 25304–25315, DOI 10.1021/acsami.0c05166.

[64] Y. Liu, L. Liu, B. Narendra, X. Chen, S. Feng, Y. Wan, J. Luo, *Desalination* **2025**, *598*, 118415, DOI 10.1016/J.DESAL.2024.118415.

[65] E. Maaskant, W. Vogel, T. J. Dingemans, N. E. Benes, *Journal of Membrane Science* **2018**, *567*, 321–328, DOI 10.1016/J.MEMSCI.2018.09.032.

[66] V. Z. Nikonov, L. B. Sokolov, *Polymer Science U.S.S.R.* **1966**, *8*, 1684–1690, DOI 10.1016/0032-3950(66)90009-8.

[67] A. Deshmukh, M. Elimelech, J. H. Lienhard, *Chemical Engineering Journal* **2025**, *524*, 169670, DOI 10.1016/J.CEJ.2025.169670.

[68] S. Zhou, W. Xu, Z. Wang, K. Yao, C. Ji, T. Hou, Y. He, H. Guo, *Nano Letters* **2025**, *25*, 8287–8293, DOI 10.1021/ACS.NANOLETT.5C01408.

[69] C. Liu, C. Y. Zhu, C. Zhang, H. C. Yang, Z. K. Xu, *Progress in Polymer Science* **2024**, *152*, 101815, DOI 10.1016/J.PROGPOLYMSCI.2024.101815.

[70] I. Nulens, A. B. Zvi, I. F. Vankelecom, G. Z. Ramon, *Journal of Membrane Science* **2022**, *656*, 120593, DOI 10.1016/J.MEMSCI.2022.120593.

[71] I. Nulens, R. Peters, R. Verbeke, D. M. Davenport, C. V. Goethem, B. D. Ketelaere, P. Goos, K. V. Agrawal, I. F. Vankelecom, *Journal of Membrane Science* **2023**, *667*, 121155, DOI 10.1016/J.MEMSCI.2022.121155.

[72] T. D. Matthews, H. Yan, D. G. Cahill, O. Coronell, B. J. Mariñas, *Journal of Membrane Science* **2013**, *429*, 71–80, DOI 10.1016/J.MEMSCI.2012.11.040.

[73] A. Nowbahar, V. Mansard, J. M. Mecca, M. Paul, T. Arrowood, T. M. Squires, *Journal of the American Chemical Society* **2018**, *140*, 3173–3176, DOI 10.1021/jacs.7b12121.

[74] N. K. Saha, S. V. Joshi, *Journal of Membrane Science* **2009**, *342*, 60–69, DOI 10.1016/j.memsci.2009.06.025.

[75] Q. Y. Zhu, L. K. Wu, L. Q. Li, L. W. Zhuang, S. M. Xue, Z. L. Xu, Y. J. Tang, *Industrial and Engineering Chemistry Research* **2022**, *61*, 5843–5852, DOI 10.1021/acs.iecr.2c00478.

[76] R. Zhang, S. Yu, W. Shi, J. Zhu, B. Van der Bruggen, *Separation and Purification Technology* **2019**, *215*, 670–680, DOI 10.1016/J.SEPPUR.2019.01.045.

[77] J. Tian, H. Chang, S. Gao, R. Zhang, *Desalination* **2020**, *491*, 114499, DOI 10.1016/j.desal.2020.114499.

[78] X. Zhu, X. Cheng, X. Luo, Y. Liu, D. Xu, X. Tang, Z. Gan, L. Yang, G. Li, H. Liang, *Environmental Science & Technology* **2020**, *54*, 6365–6374, DOI 10.1021/ACS.EST.9B06779.

[79] W. Zhao, H. Liu, N. Meng, M. Jian, H. Wang, X. Zhang, *Journal of Membrane Science* **2018**, *565*, 380–389, DOI 10.1016/J.MEMSCI.2018.08.047.

[80] S. Behera, A. K. Suresh, *Chemical Engineering Research and Design* **2019**, *146*, 154–161, DOI 10.1016/J.CHERD.2019.03.030.

[81] C. Liu, J. Yang, B. B. Guo, S. Agarwal, A. Greiner, Z. K. Xu, *Angewandte Chemie International Edition* **2021**, *60*, 14636–14643, DOI 10.1002/anie.202103555.

[82] S. Bason, Y. Kaufman, V. Freger, *Journal of Physical Chemistry B* **2010**, *114*, 3510–3517, DOI 10.1021/JP911615N.

[83] X. H. Ma, Z. K. Yao, Z. Yang, H. Guo, Z. L. Xu, C. Y. Tang, M. Elimelech, *Environmental Science and Technology Letters* **2018**, *5*, 123–130, DOI 10.1021/ACS.ESTLETT.8B00016.

[84] L. Lin, R. Lopez, G. Z. Ramon, O. Coronell, *Journal of Membrane Science* **2016**, *497*, 365–376, DOI 10.1016/J.MEMSCI.2015.09.020.

[85] C. Y. Tang, Y. N. Kwon, J. O. Leckie, *Journal of Membrane Science* **2007**, *287*, 146–156, DOI 10.1016/J.MEMSCI.2006.10.038.

[86] F. A. Pacheco, I. Pinnau, M. Reinhard, J. O. Leckie, *Journal of Membrane Science* **2010**, *358*, 51–59, DOI 10.1016/J.MEMSCI.2010.04.032.

[87] V. Freger, *Environmental Science and Technology* **2004**, *38*, 3168–3175, DOI 10.1021/ES034815U.

[88] E. Dražević, K. Košutić, V. Freger, *Water Research* **2014**, *49*, 444–452, DOI 10.1016/J.WATRES.2013.10.029.

[89] I. J. Roh, *Journal of Membrane Science* **2002**, *198*, 63–74, DOI 10.1016/S0376-7388(01)00630-5.

[90] A. Ben-David, S. Bason, J. Jopp, Y. Oren, V. Freger, *Journal of Membrane Science* **2006**, *281*, 480–490, DOI 10.1016/J.MEMSCI.2006.04.017.

[91] O. Coronell, B. J. Mariñas, X. Zhang, D. G. Cahill, *Environmental Science and Technology* **2008**, *42*, 5260–5266, DOI 10.1021/ES8002712.

[92] B. Mi, O. Coronell, B. J. Mariñas, F. Watanabe, D. G. Cahill, I. Petrov, *Journal of Membrane Science* **2006**, *282*, 71–81, DOI 10.1016/J.MEMSCI.2006.05.015.

[93] O. Coronell, B. J. Mariñas, D. G. Cahill, *Environmental Science and Technology* **2011**, *45*, 4513–4520, DOI 10.1021/ES200007H.

[94] M. Bass, V. Freger, *Journal of Membrane Science* **2015**, *492*, 348–354, DOI 10.1016/J.MEMSCI.2015.05.059.

[95] K. Baransi-Karkaby, M. Bass, S. Levchenko, S. Eitan, V. Freger, *Environmental Science and Technology* **2017**, *51*, 2347–2354, DOI 10.1021/ACS.EST.6B05260.

[96] X. Ma, Z. Yang, Z. Yao, H. Guo, Z. Xu, C. Y. Tang, *Journal of Colloid and Interface Science* **2019**, *540*, 382–388, DOI 10.1016/J.JCIS.2019.01.033.

[97] Z. Tan, S. Chen, X. Peng, L. Zhang, C. Gao, *Science* **2018**, *360*, 518–521, DOI 10.1126/SCIENCE.AAR6308.

[98] X. Song, B. Gan, S. Qi, H. Guo, C. Y. Tang, Y. Zhou, C. Gao, *Environmental Science & Technology* **2020**, *54*, 3559–3569, DOI 10.1021/ACS.EST.9B05892.

[99] T. E. Culp, Y. X. Shen, M. Geitner, M. Paul, A. Roy, M. J. Behr, S. Rosenberg, J. Gu, M. Kumar, E. D. Gomez, *Proceedings of the National Academy of Sciences* **2018**, *115*, 8694–8699, DOI 10.1073/PNAS.1804708115.

[100] M. C. Wong, L. Lin, O. Coronell, E. M. Hoek, G. Z. Ramon, *Journal of Membrane Science* **2016**, *500*, 124–135, DOI 10.1016/J.MEMSCI.2015.11.033.

[101] C. Shang, D. Pranantyo, S. Zhang, *Environmental Science & Technology* **2020**, *54*, 5288–5296, DOI 10.1021/ACS.EST.0C00535.

[102] B. Liu, S. Wang, P. Zhao, H. Liang, W. Zhang, J. Crittenden, *Applied Surface Science* **2018**, *435*, 415–423, DOI 10.1016/J.APSUSC.2017.11.126.

[103] Y. Kobayashi, A. Kinomura, S. Kazama, K. Inoue, T. Toyama, Y. Nagai, K. Haraya, H. F. Mohamed, B. E. O'Rourke, N. Oshima, R. Suzuki, *Journal of Physics: Conference Series* **2016**, *674*, 012017, DOI 10.1088/1742-6596/674/1/012017.

[104] J. Stawikowska, A. G. Livingston, *Journal of Membrane Science* **2012**, *413-414*, 1–16, DOI 10.1016/J.MEMSCI.2012.02.033.

[105] S. J. Kim, S. Kook, B. E. O'Rourke, J. Lee, M. Hwang, Y. Kobayashi, R. Suzuki, I. S. Kim, *Journal of Membrane Science* **2017**, *527*, 143–151, DOI 10.1016/J.MEMSCI.2016.12.064.

[106] S. Bason, O. Kedem, V. Freger, *Journal of Membrane Science* **2009**, *326*, 197–204, DOI 10.1016/J.MEMSCI.2008.09.054.

[107] K. Košutić, D. Dolar, B. Kunst, *Journal of Membrane Science* **2006**, *282*, 109–114, DOI 10.1016/J.MEMSCI.2006.05.010.

[108] S. Déon, P. Dutournlé, P. Bourseau, *AIChE Journal* **2007**, *53*, 1952–1969, DOI 10.1002/aic.11207.

[109] S. H. Kim, S. Y. Kwak, T. Suzuki, *Environmental Science and Technology* **2005**, *39*, 1764–1770, DOI 10.1021/ES049453K.

[110] D. G. Cahill, V. Freger, S. Y. Kwak, *MRS Bulletin* **2008**, *33*, 27–32, DOI 10.1557/mrs2008.11.

[111] R. Zhang, J. Tian, S. Gao, B. Van der Bruggen, *Journal of Materials Chemistry A* **2020**, *8*, 8831–8847, DOI 10.1039/D0TA02510K.

[112] Y. Liang, Y. Zhu, C. Liu, K. R. Lee, W. S. Hung, Z. Wang, Y. Li, M. Elimelech, J. Jin, S. Lin, *Nature Communications* **2020**, *11*, 1–9, DOI 10.1038/s41467-020-15771-2.

[113] S. Liu, S. Ganti-Agrawal, S. Keten, R. M. Lueptow, *Journal of Membrane Science* **2022**, *644*, 120057, DOI 10.1016/j.memsci.2021.120057.

[114] E. P. Chan, A. P. Young, J. H. Lee, J. Y. Chung, C. M. Stafford, *Journal of Polymer Science Part B: Polymer Physics* **2013**, *51*, 385–391, DOI 10.1002/POLB.23235.

[115] J. Schaep, C. Vandecasteele, *Journal of Membrane Science* **2001**, *188*, 129–136, DOI 10.1016/S0376-7388(01)00368-4.

[116] M. Nyström, M. Lindström, E. Matthiasson, *Colloids and Surfaces* **1989**, *36*, 297–312, DOI 10.1016/0166-6622(89)80245-8.

[117] S. Veríssimo, K. V. Peinemann, J. Bordado, *Journal of Membrane Science* **2006**, *279*, 266–275, DOI 10.1016/j.memsci.2005.12.014.

[118] X. Li, C. Zhang, S. Zhang, J. Li, B. He, Z. Cui, *Desalination* **2015**, *369*, 26–36, DOI 10.1016/J.DESAL.2015.04.027.

[119] Y. Yan, J. Wang, W. Wang, C. Han, *Journal of Membrane Science* **2025**, *721*, 123812, DOI 10.1016/J.MEMSCI.2025.123812.

[120] X. Song, B. Gan, Z. Yang, C. Y. Tang, C. Gao, *Journal of Membrane Science* **2019**, *582*, 342–349, DOI 10.1016/J.MEMSCI.2019.04.027.

[121] M. B. Wu, Y. Lv, H. C. Yang, L. F. Liu, X. Zhang, Z. K. Xu, *Journal of Membrane Science* **2016**, *515*, 238–244, DOI 10.1016/J.MEMSCI.2016.05.056.

[122] Z. Jiang, S. Karan, A. G. Livingston, *Advanced Materials* **2018**, *30*, DOI 10.1002/ADMA.201705973.

[123] J. Zhu, J. Hou, R. Zhang, S. Yuan, J. Li, M. Tian, P. Wang, Y. Zhang, A. Volodin, B. Van der Bruggen, *Journal of Materials Chemistry A* **2018**, *6*, 15701–15709, DOI 10.1039/C8TA05687K.

[124] M. Kim, S. J. Park, J. H. Lee, *Journal of Membrane Science* **2024**, *700*, 122728, DOI 10.1016/J.MEMSCI.2024.122728.

[125] Y. Zhao, T. Tong, X. Wang, S. Lin, E. M. Reid, Y. Chen, *Environmental Science and Technology* **2021**, *55*, 1359–1376, DOI 10.1021/acs.est.0c04593.

[126] L. Zhang, M. Hu, H. Matsuyama, X. Li, *Separation and Purification Technology* **2024**, *334*, 126011, DOI 10.1016/J.SEPPUR.2023.126011.

[127] D. Lu, Z. Yao, L. Jiao, M. Waheed, Z. Sun, L. Zhang, *Advanced Membranes* **2022**, *2*, 100032, DOI 10.1016/j.advmem.2022.100032.

[128] E. R. Nightingale, *Journal of Physical Chemistry* **1959**, *63*, 1381–1387, DOI 10.1021/J150579A011.

[129] T. Zhang, R. Y. Fu, K. P. Wang, Y. W. Gao, H. R. Li, X. M. Wang, Y. F. Xie, L. Hou, *Journal of Membrane Science* **2022**, *647*, 120304, DOI 10.1016/j.memsci.2022.120304.

[130] M. A. Junker, E. te Brinke, C. M. Vall Compte, R. G. Lammertink, J. de Grooth, W. M. de Vos, *Journal of Membrane Science* **2023**, *681*, 121718, DOI 10.1016/j.memsci.2023.121718.

[131] J. Luo, Y. Wan, *Journal of Membrane Science* **2013**, *438*, 18–28, DOI 10.1016/J.MEMSCI.2013.03.029.

[132] G. Hurwitz, G. R. Guillen, E. M. Hoek, *Journal of Membrane Science* **2010**, *349*, 349–357, DOI 10.1016/J.MEMSCI.2009.11.063.

[133] E. I. Mouhoumed, A. Szymczyk, A. Schäfer, L. Paugam, Y. H. La, *Journal of Membrane Science* **2014**, *461*, 130–138, DOI 10.1016/J.MEMSCI.2014.03.025.

[134] R. S. Roth, L. Birnhack, M. Avidar, E. A. Hjelvik, A. P. Straub, R. Epsztein, *npj Clean Water* **2024**, *7*, 1–9, DOI 10.1038/s41545-024-00322-9.

[135] D. Rehman, F. Sheriff, J. H. Lienhard, *Water Research* **2023**, *243*, 120325, DOI 10.1016/J.WATRES.2023.120325.

[136] T. Y. Tsou, J. P. Hsu, H. Y. Yu, *Journal of Membrane Science* **2025**, *714*, 123399, DOI 10.1016/J.MEMSCI.2024.123399.

[137] D. L. Oatley, L. Llenas, R. Pérez, P. M. Williams, X. Martínez-Lladó, M. Rovira, *Advances in Colloid and Interface Science* **2012**, *173*, 1–11, DOI 10.1016/j.cis.2012.02.001.

[138] A. E. Yaroshchuk, *Advances in Colloid and Interface Science* **2000**, *85*, 193–230, DOI 10.1016/S0001-8686(99)00021-4.

[139] X. Zhai, S. Lin, X. Li, Z. Wang, *Environmental Science & Technology* **2024**, *58*, 15874–15884, DOI 10.1021/ACS.EST.4C07510.

[140] R. Epsztein, R. M. DuChanois, C. L. Ritt, A. Noy, M. Elimelech, *Nature Nanotechnology* **2020**, *15*, 426–436, DOI 10.1038/s41565-020-0713-6.

[141] S. Bandini, D. Vezzani, *Chemical Engineering Science* **2003**, *58*, 3303–3326, DOI 10.1016/S0009-2509(03)00212-4.

[142] O. Agboola, J. Maree, A. Kolesnikov, R. Mbaya, R. Sadiku, *Environmental Chemistry Letters* **2014**, *13*, 37–47, DOI 10.1007/S10311-014-0486-Y.

[143] R. Schlögl, *Berichte der Bunsengesellschaft für physikalische Chemie* **1966**, *70*, 400–414, DOI 10.1002/BBPC.19660700403.

[144] L. Dresner, *Desalination* **1972**, *10*, 27–46, DOI 10.1016/S0011-9164(00)80245-3.

[145] W. R. Bowen, H. Mukhtar, *Journal of Membrane Science* **1996**, *112*, 263–274, DOI 10.1016/0376-7388(95)00302-9.

[146] P. M. Biesheuvel, J. E. Dykstra, *Physics of Electrochemical Processes*, **2020**.

[147] T. Roy, J. Andrej, V. A. Beck, *Journal of Computational Physics* **2023**, *475*, 111859, DOI 10.1016/J.JCP.2022.111859.

[148] Z. Song, X. Cao, H. Huang, *Physical Review E* **2018**, *98*, 032404, DOI 10.1103/PhysRevE.98.032404.

[149] B. Li, B. Lu, Z. Wang, J. A. McCammon, *Physica A: Statistical Mechanics and its Applications* **2010**, *389*, 1329–1345, DOI 10.1016/J.PHYSA.2009.12.024.

[150] W. R. Bowen, J. S. Welfoot, *Chemical Engineering Science* **2002**, *57*, 1121–1137, DOI 10.1016/S0009-2509(01)00413-4.

[151] K. Krabbenhøft, J. Krabbenhøft, *Cement and Concrete Research* **2008**, *38*, 77–88, DOI 10.1016/J.CEMCONRES.2007.08.006.

[152] A. Szymczyk, M. Sbaï, P. Fievet, *Langmuir* **2005**, *21*, 1818–1826, DOI 10.1021/la048399i.

[153] K. S. Spiegler, O. Kedem, *Desalination* **1966**, *1*, 311–326, DOI 10.1016/S0011-9164(00)80018-1.

[154] W. R. Bowen, A. W. Mohammad, N. Hilal, *Journal of Membrane Science* **1997**, *126*, 91–105, DOI 10.1016/S0376-7388(96)00276-1.

[155] V. Geraldes, A. M. Brites Alves, *Journal of Membrane Science* **2008**, *321*, 172–182, DOI 10.1016/j.memsci.2008.04.054.

[156] V. Geraldes, M. D. Afonso, *Journal of Membrane Science* **2007**, *300*, 20–27, DOI 10.1016/J.MEMSCI.2007.04.025.

[157] S. Bandini, *Journal of Membrane Science* **2005**, *264*, 75–86, DOI 10.1016/j.memsci.2005.03.055.

[158] A. Santafé-Moros, J. M. Gozálvez-Zafrilla, J. Lora-García, *Desalination* **2008**, *221*, 268–276, DOI 10.1016/J.DESAL.2007.01.083.

[159] M. Micari, D. Diamantidou, B. Heijman, M. Moser, A. Haidari, H. Spanjers, V. Bertsch, *Journal of Membrane Science* **2020**, *606*, 118117, DOI 10.1016/j.memsci.2020.118117.

[160] A. Escoda, S. Déon, P. Fievet, *Journal of Membrane Science* **2011**, *378*, 214–223, DOI 10.1016/j.memsci.2011.05.004.

[161] O. Labban, C. Liu, T. H. Chong, J. H. Lienhard V, *Journal of Membrane Science* **2017**, *521*, 18–32, DOI 10.1016/j.memsci.2016.08.062.

[162] S. Castaño Osorio, P. Biesheuvel, J. Dykstra, E. Virga, *Desalination* **2022**, *527*, 115552, DOI 10.1016/j.desal.2022.115552.

[163] S. Déon, A. Escoda, P. Fievet, *Chemical Engineering Science* **2011**, *66*, 2823–2832, DOI 10.1016/J.CES.2011.03.043.

[164] H.-y. Guo, X.-q. Gao, K.-c. Yu, X.-m. Wang, S.-m. Liu, *Separation and Purification Technology* **2023**, *326*, 124830, DOI 10.1016/J.SEPPUR.2023.124830.

[165] S. Déon, P. Dutournié, L. Limousy, P. Bourseau, *Separation and Purification Technology* **2009**, *69*, 225–233, DOI 10.1016/j.seppur.2009.07.022.

[166] A. A. Hussain, S. K. Nataraj, M. E. Abashar, I. S. Al-Mutaz, T. M. Aminabhavi, *Journal of Membrane Science* **2008**, *310*, 321–336, DOI 10.1016/j.memsci.2007.11.005.

[167] D. Rehman, J. H. Lienhard, *Journal of Membrane Science Letters* **2022**, *2*, 100034, DOI 10.1016/J.MEMLET.2022.100034.

[168] X. Zhai, J. Hu, Z. Chu, J. Zou, X. Li, Z. Wang, *Journal of Membrane Science* **2025**, *717*, 123558, DOI 10.1016/j.memsci.2024.123558.

[169] O. Labban, C. Liu, T. H. Chong, J. H. Lienhard, *Journal of Membrane Science* **2018**, *554*, 26–38, DOI 10.1016/j.memsci.2018.02.053.

[170] Y. Liu, J. Ran, Q. Guo, L. Gao, L. Zhang, S. Yin, S. Li, *Separation and Purification Technology* **2025**, *356*, 129995, DOI 10.1016/J.SEPPUR.2024.129995.

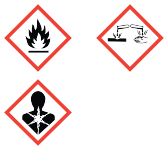
[171] F. Léniz-Pizarro, C. Liu, A. Colburn, I. C. Escobar, D. Bhattacharyya, *Journal of Membrane Science* **2021**, *620*, DOI 10.1016/j.memsci.2020.118973.

[172] Z. H. Foo, D. Rehman, A. T. Bouma, S. Monsalvo, J. H. Lienhard, *Environmental Science and Technology* **2023**, *57*, 6320–6330, DOI 10.1021/acs.est.2c08584.

# Appendix

## List of hazardous substances used in the study according to GHS

**Table A.1:** List of hazardous substances used in the study according to GHS/CLP.

| Substance | GHS Symbol | Hazard-Statement | Precautionary statement |
|---|---|---|---|
| Piperazine anhydrous (PIP) |  | H314; H317; H334; H361fd | P201; P260; P280; P303+P361+P353; P304+P340+P310; P305+P351+P338 |
| Trimesoyl chloride (TMC) |  | H314 | P260; P280; P301+P330+P331; P303+P361+P353; P304+P340+P310; P305+P351+P338 |
| *n*-Heptane |  | H225; H304; H315; H336; H410 | P210; P233; P273; P301+P310; P303+P361+P353; P331 |
| 1-(2-Aminoethyl)piperazine (AEP) |  | H302; H311; H314; H317; H412 | P273; P280; P301+P312+P330; P303+P361+P353; P305+P351+P338 |
| 1,4-Bis(3-aminopropyl)piperazine (DAP) |  | H314 | P280; P305+P351+P338; P310 |
| Sodium nitrate ($NaNO_3$) |  | H272; H319 | P210; P220; P264; P280; P305+P351+P338; P337+P313 |

| Substance | GHS Symbol | Hazard-Statement | Precautionary statement |
|---|---|---|---|
| Liquid nitrogen |  | H281 | P282; P336+P315; P403 |

# Online accessible Supporting Information

## Supporting Information Publication I

This section contains the Supporting Information of Publication I, available online with DOI: 10.1016/j.cej.2024.152775

# Supporting Information

## Mass transport mechanism of nitrate selective nanofiltration membranes on the basis of the Donnan Steric Pore Model with Dielectric Exclusion (DSPM-DE) model

Nicolás Cevallos-Cueva, Md. Mushfequr Rahman*,
Hluf Hailu Kinfu, and Volker Abetz

## Contents

**1 Membrane fabrication** **SI2**

**2 Retention experiments** **SI3**

**3 Determination of the input parameters of the DSPM-DE model** **SI3**
3.1 $\mathbf{r_{pore}}$ and $\Delta\mathbf{x_e}$ . . . . . SI3
3.2 $\varepsilon_{\mathbf{pore}}$ and $\mathbf{c_x}$ . . . . . SI4

**4 Linearized equations from the DSPM-DE model** **SI5**
4.1 Feed solution domain . . . . . SI6
4.2 Membrane active layer . . . . . SI7
4.3 Permeate domain . . . . . SI8

**5 Contributions to molar flux** **SI8**
5.1 Advection . . . . . SI8
5.2 Electromigration . . . . . SI8
5.3 Diffusion . . . . . SI8

**6 Characterization** **SI9**
6.1 FTIR . . . . . SI9
6.2 Zeta potential . . . . . SI9

**7 Steric and Dielectric exclusion coefficients vs. $\mathbf{r_{pore}}$** **SI10**

**References** **SI11**

# 1 Membrane fabrication

Aqueous and organic solutions of PIP and TMC with defined concentrations were prepared in ultrapure DI water and HPLC grade *n*-heptane, respectively. Both aqueous and organic solutions were prepared the day before to stir them overnight, so that both monomers were completely dissolved. Firstly, PAN supports were immersed in ultra-pure DI water overnight. Then, they were rubber-rolled for 1 min, followed by gently removing any remaining droplets with dust-free Kim wipes on top of the PAN supports. The support was then immersed for 6 min in 350 ml of an aqueous solution containing PIP. Right after, the process of rolling rubber and Kim wipes was repeated. The PAN support was then clamped onto a 5.1 cm × 15.9 cm glass plate, along with a frame consisting of one layer of nitrile rubber and one of PTFE frame, to finally pour the organic solution. This set up was used to assure the IP reaction takes place only on top of the PAN support. The IP reaction was carried out for 90 s (contact time). To stop the reaction, 150 ml of pure *n*-heptane was poured thoroughly. Afterwards, the membrane was exposed to air under a fume hood at room temperature for 30 min. Finally, a heat treatment was performed at 60 °C for 30 min inside a vacuum oven. The membranes were stored in ultra-pure DI water until characterization. A schematic representation of the membrane fabrication process is depicted in Figure SI1.

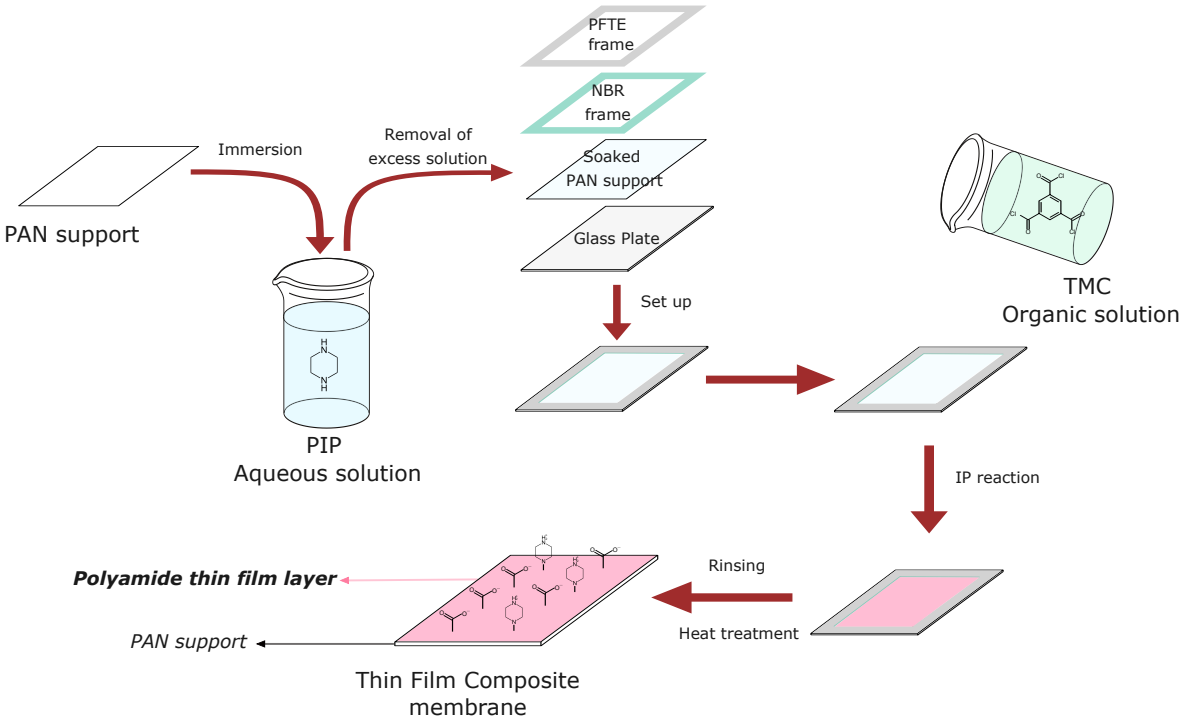



**Figure SI1:** Schematic representation of fabrication method of TFC membranes consisting of a thin selective polyamide layer on top of PAN porous support.

# 2 Retention experiments

Before every retention experiment, ultrapure DI water was permeated through the membrane samples at 4 bars for at least 2 h as a compaction step. NaCl, $NaNO_3$, and $Na_2SO_4$ were used as test salts for single salt experiments, while $NaNO_3$+$Na_2SO_4$ and NaCl + $NaNO_3$ were used for mixed salt experiments. After the water compaction step, a feed salt solution of 200 ppm was added to the cell. For mixed salt experiments, the salt solutions comprised an equimolar mixture of anions and the corresponding concentration of cation ($Na^+$) so that the total concentration of the solution was 200 ppm. Samples from the first 2 h of permeation were discarded. Then, three permeate and retentate samples (approximately 1 ml of each)were collected. This was done to ensure that the system had reached a steady state. All tests were performed at 3 bars of transmembrane pressure. In dead-end filtration mode, retentate concentration changes as the retention test proceeds. Therefore, to take into account that phenomenon, the retention of each ionic species was computed by considering the average concentration of feed solution and retentate solution with the formula:

$$R_{i,obs} = 1 - \frac{2c_{i,p}}{c_{i,f} + c_{i,r}} \tag{SI1}$$

Concentration was quantified in an Ion Chromatograph (Dionex ICS600, Thermofisher Scientific Inc., USA).

Following the water compaction step, a 500 ppm PEG 200 solution was permeated through the membrane samples. After discarding the first 2 h of permeation, three permeate samples and retentate samples were collected (approx. 1ml). The transmembrane pressure applied to the system was varied to obtain a plot of retention as a function of the solution velocity. The transmembrane pressure values used in this experiment were: 0.5, 1, 1.5, 2, 2.5, 3, 3.5, 4 bars. Samples from PEG 200 solution retention measurements, performed in the same setup, were analyzed using gel permeation chromatography (GPC) (VWR-Hitachi 2130 pump, Hitachi, Darmstadt, Germany).

# 3 Determination of the input parameters of the DSPM-DE model

## 3.1 $r_{pore}$ and $\Delta x_e$

From the PEG 200 retention tests, different rejection values were obtained for different transmembrane pressure values for each membrane. As a result, a plot of the rejection vs. solvent flux or velocity was generated. By considering the effect of concentration polarization, which depends on the solvent velocity, $J_v$, and the mass transfer coefficient, $k_{c,i}$, the real rejection was obtained, $R_{i,real}$, (retention at infinite stirring velocity[1] from the experimental or observed

rejection, $R_{i,obs}$):

$$\ln\left(\frac{1-R_{i,real}}{R_{i,real}}\right) = \ln\left(\frac{1-R_{i,obs}}{R_{i,obs}}\right) - \frac{J_v}{k_{c,i}} \tag{SI2}$$

Solvent flux or velocity was obtained with:

$$J_v = \frac{\Delta m}{\delta_{H_2O} A_{mb} \Delta t} \tag{SI3}$$

$k_{c,i}$ is a function of the stirring speed, $\omega$. It is obtained with:

$$k_{c,i} = 0.23 Re^{0.567} Sc^{0.33} \omega^{0.567} \tag{SI4}$$

To compute $Re$, the characteristic length needed is the radius of the stirrer (3 cm) and the velocity is the stirring speed, $\omega$. Then, $R_{i,real}$ was fitted to the following equation that considers the flux of PEG 200 across the membrane is due to only diffusion and advection and the exclusion at the pore openings is due to steric effects[2]:

$$R_{i,real}^{model} = 1 - \frac{K_{i,a}\Phi_{S,i}}{1 - e^{-Pe_m} \cdot (1 - K_{i,a}\Phi_{S,i})} \tag{SI5}$$

The Peclet number is given by:

$$Pe_m = \frac{K_{i,a} J_v \Delta x_e}{K_{i,d} D_{i,\infty}} \tag{SI6}$$

Therefore, for each membrane $r_{pore}$and $\Delta x_e$ were fitted simultaneously to minimize the following objective function:

$$\underset{r_{pore},\, \Delta x_e}{\text{argmin}} \sum_{k=1}^{N_{J_v}} \left(R_{i,real}^{model} - R_{i,real}\right)^2 \tag{SI7}$$

### 3.2 $\varepsilon_{pore}$ and $c_x$

The results of mixed ionic retention tests were used to fit the DSPM-DE model to determine $\varepsilon_{pore}$ and $c_x$. Usually, a large number of experiments are required to determine the input parameters of the DSPM-DE model[3].

To account for the effect of $r_{pore}$ on the dielectric exclusion, the reduction of $\varepsilon_{pore}$ is assumed to be caused only by a single molecule of water bound at the pore wall[2]. This single layer of water strongly interacts with the pore wall, restricting its orientation. Accordingly, the dielectric constant of this layer of water, $\varepsilon^*$, is much lower than that of the bulk solution. In addition, the dielectric constant in the center of the pore is considered to be unaffected; it

has the same value as the bulk. The overall dielectric constant inside the pore is assumed to be a volume-weight average of the dielectric constants of water molecules at the pore wall and the center of the pore, corresponding to the bulk value:

$$\varepsilon_{pore} = \varepsilon^* + (\varepsilon_{bulk} - \varepsilon^*)\left(1 - \frac{d_{H_2O}}{r_{pore}}\right)^2 \tag{SI8}$$

According to Bowen et al. 1997[1], $d_{H_2O}$= 0.28 nm. Therefore, according to this equation $\varepsilon_{pore} = f(\varepsilon^*, r_{pore})$. In the present study, $\varepsilon^*$ is assumed to be constant for each value of TMC concentration. So $\varepsilon_{pore}$ is considered to vary only because of the variation of $r_{pore}$ for membranes prepared at the same TMC concentration. Consequently, fitting was carried out separately for each series of membranes prepared at the same TMC concentration.

Double minimization was carried out. Firstly, preliminary $c_x$ values were calculated for every PIP concentration at each $\varepsilon^*$ value tested by minimizing the sum of the differences between experimental, $R_{i,j}^{exp}$, and calculated rejection, $R_{i,j}^{mod}$, of each ion. With each value of $\varepsilon^*$ tested, $\varepsilon_{pore}$ was computed with fitted $r_{pore}$ from the previous section. Secondly, the determination of $\varepsilon^*$ involved minimizing the sum of the previously minimized differences across all membranes prepared at different PIP concentrations (same TMC concentration), as described by the following objective function:

$$\underset{\varepsilon^*}{\text{argmin}} \sum_{j=1}^{N_{PIP}} \left( \underset{c_x}{\text{argmin}} \sum_{i=1}^{N_{ions}} \frac{\left(R_{i,j}^{mod} - R_{i,j}^{exp}\right)^2}{\sigma_{i,j}^2} \right) \tag{SI9}$$

The subscript $i$ cycles through all ionic species and $j$ through all PIP concentrations for the same TMC concentration. $R_{i,j}^{exp}$ is the average experimental rejection value of at least 3 replications for the membranes fabricated at every PIP concentration. To bias the minimizations towards more experimentally confident values, $\sigma_{i,j}^2$ was computed with the unbiased variance equation[3] .

Finally, the method was repeated for the next TMC concentration. As a result, while each series of membranes prepared at the same TMC concentration resulted in one value of $\varepsilon^*$, each IP reaction condition (with varying PIP and TMC concentrations) resulted in a distinct $c_x$ value. This $\varepsilon^*$ value, along with fitted $r_{pore}$, determined a unique $\varepsilon_{pore}$ value using Equation (SI8) for every membrane fabricated under the same reaction parameters.

## 4 Linearized equations from the DSPM-DE model

The set of linear and discretized equations obtained to solve the system of equations are presented in this section. Figure SI2 shows the discretization scheme of the membrane's active layer. The linear coefficients of each equation are inside square brackets. Superscript

* denotes variables calculated in the previous iteration. In the first iteration, the superscripted variables correspond to the initial guess. The set of equations is solved to calculate at each node the electrical potential and concentration of each ion[4].

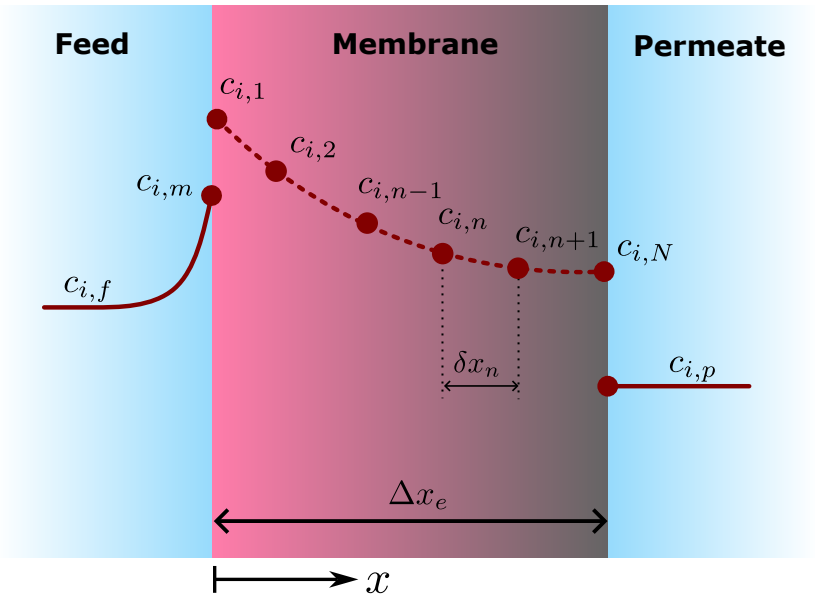



**Figure SI2:** Schematic representation of the concentration profile during NF experiments with the discretization scheme inside the active layer of the membrane.

## 4.1 Feed solution domain

Mass transfer equation through the boundary layer:

$$[k_{c,i}^{\cdot} - J_v]c_{i,m} + [J_v]c_{i,p} + [z_i c_{i,m} D_{i,\infty} \frac{F}{RT}]\xi = [c_{i,f} k_{c,i}^{\cdot}] \tag{SI10}$$

Electroneutrality condition:

$$\sum_{i=1}^{N_c} [z_i] c_{i,m} = 0 \tag{SI11}$$

Partitioning equation between the feed solution and the membrane active layer:

$$\begin{aligned} &[\gamma_{i,1}^*]c_{i,1} + [\gamma_{i,m}^* c_{i,m}^* z_i D_{i,\infty} \frac{F}{RT} \Phi_{S,i} \Phi_{DE,i} \exp\left(-z_i \frac{F}{RT} \Psi_1^*\right)]\Psi_1 \\ &= \left[\gamma_{i,m}^* c_{i,m} \Phi_{S,i} \Phi_{DE,i} \exp\left(-z_i \frac{F}{RT} \Psi_1^*\right)\left(1 + z_i \frac{F}{RT} \Psi_1^*\right)\right] \end{aligned} \tag{SI12}$$

## 4.2 Membrane active layer

The linearized and discretized Extended Nernst-Planck Equation for each component, $i$, is given by Equation (SI13):

$$[A_{i,n}]c_{i,n} + [B_{i,n}]c_{i,n+1} + [C_{i,n}]\Psi_n + [D_{i,n}]\Psi_{n+1} + [E_{i,n}]c_{i,p} = F_{i,n} \tag{SI13}$$

$$[A_{i,n}] = \frac{K_{i,d}D_{i,\infty}}{\delta x_n} + \frac{z_i F K_{i,d} D_{i,\infty}}{RT}\frac{\Psi^*_{n+1} - \Psi^*_n}{2\delta x_n} + \frac{K_{i,a}J_v}{2} \tag{SI14}$$

$$[B_{i,n}] = -\frac{K_{i,d}D_{i,\infty}}{\delta x_n} + \frac{z_i F K_{i,d} D_{i,\infty}}{RT}\frac{\Psi^*_{n+1} - \Psi^*_n}{2\delta x_n} + \frac{K_{i,a}J_v}{2} \tag{SI15}$$

$$[C_{i,n}] = \frac{z_i F K_{i,d} D_{i,\infty}}{RT}\frac{c^*_{i,n+1} + c^*_{i,n}}{2\delta x_n} \tag{SI16}$$

$$[D_{i,n}] = -\frac{z_i F K_{i,d} D_{i,\infty}}{RT}\frac{c^*_{i,n+1} + c^*_{i,n}}{2\delta x_n} \tag{SI17}$$

$$[E_{i,n}] = -J_v \tag{SI18}$$

$$[F_{i,n}] = -\frac{z_i F K_{i,d} D_{i,\infty}}{RT}\frac{c^*_{i,n+1} + c^*_{i,n}}{2}\frac{\Psi^*_{n+1} - \Psi^*_n}{\delta x_n} \tag{SI19}$$

The electroneutrality condition for each node $n$ is:

$$\sum_{i=1}^{N_c}[z_i]c_{i,n} = [-c_x] \tag{SI20}$$

### 4.3 Permeate domain

Similar to the feed solution/membrane interface, the linearized partitioning correlation is given by:

$$\begin{aligned}
&[\gamma_{i,N}^*]c_{i,N} - [\gamma_{i,p}^*\Phi_{S,i}\Phi_{DE,i}\exp\left(z_i\frac{F}{RT}\left(\Psi_p^* - \Psi_N^*\right)\right)]c_{i,p} \\
&+[\gamma_{i,p}^* c_{i,p}^* z_i\frac{F}{RT}\Phi_{S,i}\Phi_{DE,i}\exp\left(z_i\frac{F}{RT}\left(\Psi_p^* - \Psi_N^*\right)\right)]\Psi_N \\
&-[\gamma_{i,p}^* c_{i,p}^* z_i\frac{F}{RT}\Phi_{S,i}\Phi_{DE,i}\exp\left(z_i\frac{F}{RT}\left(\Psi_p^* - \Psi_N^*\right)\right)]\Psi_p \\
=-&\left[\gamma_{i,p}^* c_{i,p}^* z_i\frac{F}{RT}\Phi_{S,i}\Phi_{DE,i}\exp\left(z_i\frac{F}{RT}\left(\Psi_p^* - \Psi_N^*\right)\right)\left(z_i\frac{F}{RT}\left(\Psi_p^* - \Psi_N^*\right)\right)\right]
\end{aligned} \tag{SI21}$$

The electroneutrality condition in the permeate side:

$$\sum_{i=1}^{N_c}[z_i]c_{i,p} = 0 \tag{SI22}$$

## 5 Contributions to molar flux

The contributions of advection, diffusion and electromigration to molar flux across the membrane active layer were determined with the discretized forms of the ENP (Equation (SI23)). The concentration and potential profiles were considered linear for qualitative comparison and analysis.

$$J_i = -K_{i,d}D_{i,\infty}\frac{dc_i}{dx} - \frac{z_i F c_i K_{i,d}D_{i,\infty}}{RT}\frac{d\Psi}{dx} + K_{i,a}c_i J_v \tag{SI23}$$

### 5.1 Advection

$$J_{i,adv} = \frac{K_{i,c}(c_{i,n+1} + c_{i,n})J_v}{2} \tag{SI24}$$

### 5.2 Electromigration

$$J_{i,elec} = -\frac{z_i F(c_{i,n+1} + c_{i,n})K_{i,d}D_{i,\infty}}{2RT}\frac{\Psi_n - \Psi_{n-1}}{\delta x_n} \tag{SI25}$$

### 5.3 Diffusion

$$J_{i,diff} = -K_{i,d}D_{i,\infty}\frac{c_{i,n+1} - c_{i,n}}{\delta x_n} \tag{SI26}$$

# 6 Characterization

## 6.1 FTIR

ATR-FTIR spectra were measured using a Bruker Alpha (diamond-ATR unit) (Bruker, Karlsruhe, Germany) in the region of 100 - 2000 $cm^{-1}$ with a resolution of 4 cm-1 for 32 scans.

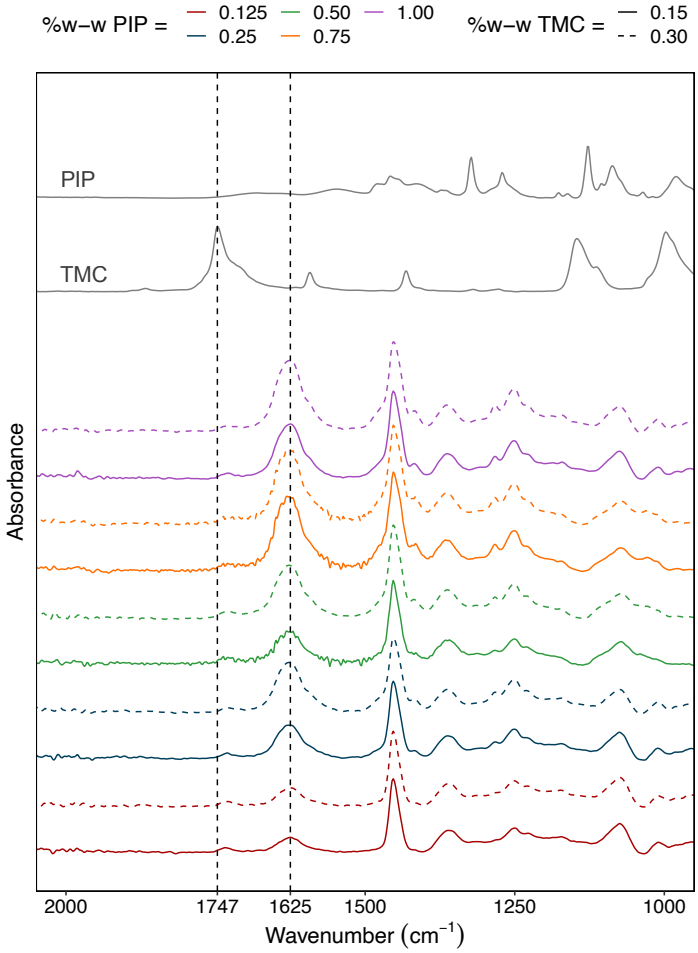



**Figure SI3:** ATR-FTIR spectra for PIP and TMC monomers, and the fabricated membranes at different PIP and TMC concentrations. The band observed at 1747 $cm^{-1}$ in the TMC spectrum corresponds to the stretching vibration of the carbonyl group from the acid chloride functional groups in TMC. This carbonyl band is shifted to 1625 $cm^{-1}$ in the membranes' spectra because of the replacement of chloride by nitrogen in the PA layers synthetized on top of the PAN supports[5].

## 6.2 Zeta potential

The zeta potential was measured using 1 mM NaCl with a SurPASS 3 electrokinetic analyzer (Anton Paar, Austria). The Helmholtz-Smoluchowski equation was used to correlate the

streaming potential with the zeta potential[6]:

$$Zeta\,Potential = \frac{dU}{d\Delta P} \cdot \frac{\eta}{\varepsilon_0 \varepsilon_r} \cdot \frac{L}{A} \cdot \frac{1}{R} \tag{SI27}$$

where $U$ is the streaming potential and $\Delta P$ the pressure difference. $\eta$ and $\varepsilon_0$ $\varepsilon_r$ are the viscosity and the dielectric constant of the electrolyte solution. $L$ is the length of the rectangular slit channel formed between two planar surfaces and $A$ is its cross-section. $R$ is the electrical resistance inside the streaming channel.

**Table SI1:** Mean ± standard deviation zeta potential values obtained at a pH≈6.5 for the fabricated membranes at different monomers' concentration

| PIP (%w-w) | TMC (%w-w) | Zeta Potential (mV) |
|---|---|---|
| 0.125 | 0.15 | -17.69±0.31 |
| 0.25 | 0.15 | -25.11±0.55 |
| 0.50 | 0.15 | -22.71±0.98 |
| 0.75 | 0.15 | -19.15±0.56 |
| 1.00 | 0.15 | -26.58±0.47 |
| 0.125 | 0.30 | -29.37±0.80 |
| 0.25 | 0.30 | -21.85±0.38 |
| 0.50 | 0.30 | -27.02±0.46 |
| 0.75 | 0.30 | -12.80±1.42 |
| 1.00 | 0.30 | -32.78±0.82 |

## 7 Steric and Dielectric exclusion coefficients vs. $r_{pore}$

Figure SI4 presents the correlation of steric exclusion coefficients, $\phi_{S,i}$, with $r_{pore}$, as well as the parallel trends observed for dielectric exclusion coefficients, $\phi_{DE,i}$, of membranes prepared at different TMC concentrations when plotted against $r_{pore}$.

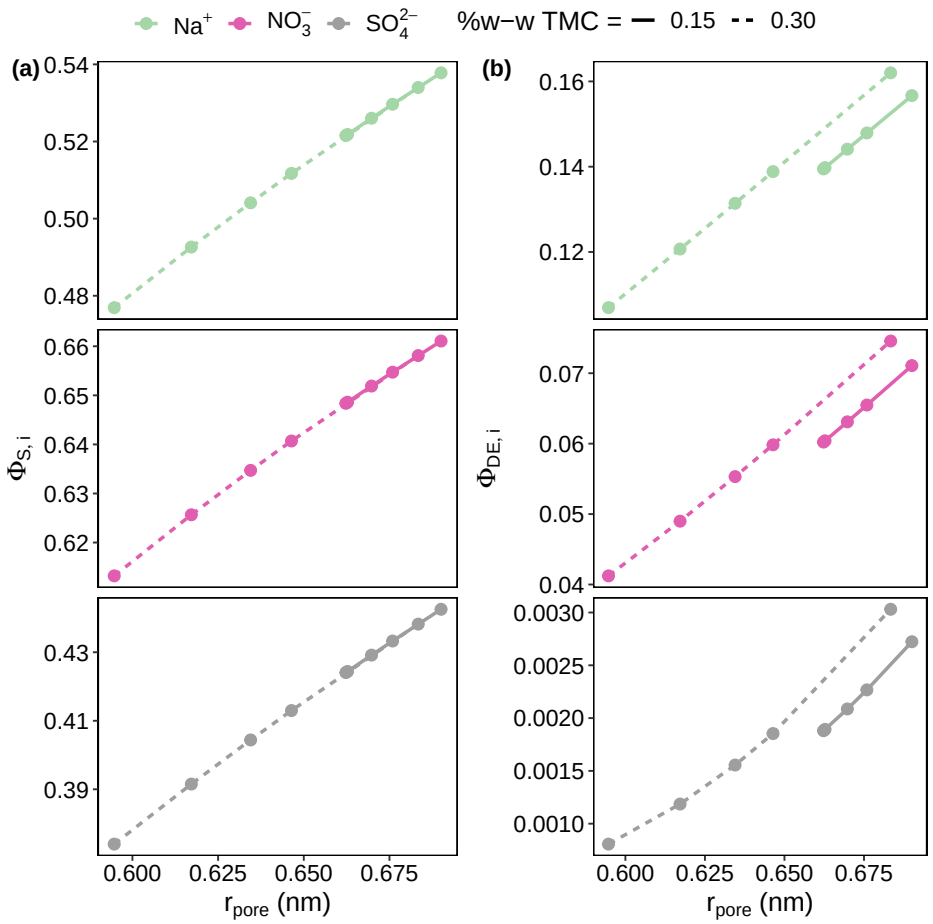



**Figure SI4:** (a) Steric and (b) dielectric exclusion coefficients as a function of $r_{pore}$.

## References


[1] W. R. Bowen, A. W. Mohammad, N. Hilal, Characterisation of nanofiltration membranes for predictive purposes - Use of salts, uncharged solutes and atomic force microscopy, Journal of Membrane Science 126 (1) (1997) 91–105. https://doi.org/10.1016/S0376-7388(96)00276-1.

[2] R. Wang, S. Lin, Pore model for nanofiltration: History, theoretical framework, key predictions, limitations, and prospects, Journal of Membrane Science 620 (July 2020) (2021) 118809. https://doi.org/10.1016/j.memsci.2020.118809.

[3] D. Rehman, J. H. Lienhard, Global optimization for accurate and efficient parameter estimation in nanofiltration, Journal of Membrane Science Letters 2 (2) (2022) 100034. https://doi.org/10.1016/J.MEMLET.2022.100034.

[4] V. Geraldes, M. D. Afonso, Prediction of the concentration polarization in the nanofiltration/reverse osmosis of dilute multi-ionic solutions, Journal of Membrane Science 300 (1-2) (2007) 20–27. https://doi.org/10.1016/J.MEMSCI.2007.04.025.

[5] J. Coates, Interpretation of Infrared Spectra, A Practical Approach, Encyclopedia of Analytical Chemistry (2006) 1–23. https://doi.org/10.1002/9780470027318.a5606.

[6] F. Léniz-Pizarro, C. Liu, A. Colburn, I. C. Escobar, D. Bhattacharyya, Positively charged nanofiltration membrane synthesis, transport models, and lanthanides separation, Journal of Membrane Science 620 (September 2020) (2021). https://doi.org/10.1016/j.memsci.2020.118973.

## Supporting Information Publication II

This section contains the Supporting Information of Publication II, available online with DOI: 10.1016/j.memsci.2025.123808

# Supporting Information

# Mass transport mechanisms insights of selective sodium/magnesium separation through nanofiltration membranes

Nicolás Cevallos-Cueva[a], Md. Mushfequr Rahman[a,*], Hluf Hailu Kinfu[a], and Volker Abetz[a,b]

[a] *Helmholtz-Zentrum Hereon, Institute of Membrane Research, Max-Planck-Straße 1, 21502 Geesthacht, Germany*

[b] *University of Hamburg, Institute of Physical Chemistry, Martin-Luther-King-Platz 6, 20146 Hamburg, Germany*

[*] *Corresponding author: mushfequr.rahman@hereon.de*

## Contents

**1 DSPM-DE model** **SI2**
- 1.1 Linearized equations . . . SI2
- 1.2 Contributions to molar flux . . . SI4

**2 Fitting** **SI4**
- 2.1 $\mathbf{r_{pore}}$ and $\Delta\mathbf{x_e}$ . . . SI5
- 2.2 $\varepsilon^*$ and $\mathbf{c_x}$ . . . SI5
  - $Na^+/Mg^{2+}/SO_4^{2-}$ . . . SI5
  - $Na^+/Mg^{2+}/Cl^-$ . . . SI7

**3 Mass transport modelling $Na^+/Mg^{2+}/Cl^-$** **SI8**
- 3.1 Exclusion coefficients . . . SI8
- 3.2 Solution flux . . . SI9
- 3.3 Contributions to molar flux . . . SI10
- 3.4 Concentration profiles . . . SI12

**References** **SI15**

# 1 DSPM-DE model

This section presents the linear and discretized equations derived to solve the system of equations [1]. The set of linear equations was solved iteratively in Python via Linear Algebra Package (LAPACK) from the NumPy library. The linear coefficients for each equation are enclosed in brackets. In each iteration, the linear coefficients are updated and the system of linear equations is solved again until the residuals are smaller than $10^{-4}$. Variables with a superscript $*$ indicate values calculated in the previous iteration. During the first iteration, these superscripted variables represent the initial guess. The equations are solved to determine the electrical potential and ion concentrations at each node, i.e. concentration and electrical potential profiles. Additionally, we provided the equations used to compute the constant values or physical constants, which were not solved iteratively.

## 1.1 Linearized equations from the DSPM-DE model

**Feed solution domain**

$$[k_{c,i}^{\bullet} - J_v]c_{i,m} + [J_v]c_{i,p} + [z_i c_{i,m} D_{i,\infty}\frac{F}{RT}]\xi = [c_{i,f}k_{c,i}^{\bullet}] \tag{SI1}$$

$$\sum_{i=1}^{N_{ions}} [z_i]c_{i,m} = 0 \tag{SI2}$$

$$\begin{aligned}[\gamma_{i,1}^{*}]c_{i,1} + [\gamma_{i,m}^{*}c_{i,m}^{*}z_i D_{i,\infty}\frac{F}{RT}\Phi_{S,i}\Phi_{DE,i}\,\mathsf{exp}\left(-z_i\frac{F}{RT}\Psi_1^{*}\right)]\Psi_1 \\ = \left[\gamma_{i,m}^{*}c_{i,m}\Phi_{S,i}\Phi_{DE,i}\,\mathsf{exp}\left(-z_i\frac{F}{RT}\Psi_1^{*}\right)\left(1 + z_i\frac{F}{RT}\Psi_1^{*}\right)\right]\end{aligned} \tag{SI3}$$

**Membrane active layer**

$$[A_{i,n}]c_{i,n} + [B_{i,n}]c_{i,n+1} + [C_{i,n}]\Psi_n + [D_{i,n}]\Psi_{n+1} + [E_{i,n}]c_{i,p} = F_{i,n} \tag{SI4}$$

$$[A_{i,n}] = \frac{K_{i,d}D_{i,\infty}}{\delta x_n} + \frac{z_i F K_{i,d}D_{i,\infty}}{RT}\frac{\Psi_{n+1}^{*} - \Psi_n^{*}}{2\delta x_n} + \frac{K_{i,a}J_v}{2} \tag{SI5}$$

$$[B_{i,n}] = -\frac{K_{i,d}D_{i,\infty}}{\delta x_n} + \frac{z_i F K_{i,d}D_{i,\infty}}{RT}\frac{\Psi_{n+1}^{*} - \Psi_n^{*}}{2\delta x_n} + \frac{K_{i,a}J_v}{2} \tag{SI6}$$

$$[C_{i,n}] = \frac{z_i F K_{i,d}D_{i,\infty}}{RT}\frac{c_{i,n+1}^{*} + c_{i,n}^{*}}{2\delta x_n} \tag{SI7}$$

$$[D_{i,n}] = -\frac{z_i F K_{i,d}D_{i,\infty}}{RT}\frac{c_{i,n+1}^{*} + c_{i,n}^{*}}{2\delta x_n} \tag{SI8}$$

$$[E_{i,n}] = -J_v \tag{SI9}$$

$$[F_{i,n}] = -\frac{z_i F K_{i,d} D_{i,\infty}}{RT} \frac{c^*_{i,n+1} + c^*_{i,n}}{2} \frac{\Psi^*_{n+1} - \Psi^*_n}{\delta x_n} \tag{SI10}$$

$$\sum_{i=1}^{N_{ions}} [z_i] c_{i,n} = [-c_x] \tag{SI11}$$

**Permeate solution domain**

$$\begin{aligned} &[\gamma^*_{i,N}] c_{i,N} - [\gamma^*_{i,p} \Phi_{S,i} \Phi_{DE,i} \exp\left(z_i \frac{F}{RT}\left(\Psi^*_p - \Psi^*_N\right)\right)] c_{i,p} \\ &+[\gamma^*_{i,p} c^*_{i,p} z_i \frac{F}{RT} \Phi_{S,i} \Phi_{DE,i} \exp\left(z_i \frac{F}{RT}\left(\Psi^*_p - \Psi^*_N\right)\right)] \Psi_N \\ &-[\gamma^*_{i,p} c^*_{i,p} z_i \frac{F}{RT} \Phi_{S,i} \Phi_{DE,i} \exp\left(z_i \frac{F}{RT}\left(\Psi^*_p - \Psi^*_N\right)\right)] \Psi_p \\ = &-\left[\gamma^*_{i,p} c^*_{i,p} z_i \frac{F}{RT} \Phi_{S,i} \Phi_{DE,i} \exp\left(z_i \frac{F}{RT}\left(\Psi^*_p - \Psi^*_N\right)\right)\left(z_i \frac{F}{RT}\left(\Psi^*_p - \Psi^*_N\right)\right)\right] \end{aligned} \tag{SI12}$$

$$\sum_{i=1}^{N_{ions}} [z_i] c_{i,p} = 0 \tag{SI13}$$

**Constant values and physical constants**

$$\delta x_n = \frac{\Delta x_e}{n} \tag{SI14}$$

$$\ln(\gamma_i) = -A z_i \left(\frac{\sqrt{I}}{1+\sqrt{I}} - 0.3I\right) \tag{SI15}$$

$$A = \frac{e_0^3 \sqrt{N_A}}{\ln(10) 4\pi \sqrt{2\varepsilon_0^3 \varepsilon_r^3 k_B^3 T^3}} \tag{SI16}$$

$$k^{\bullet}_{c,i} = k_{c,i} \left(\frac{J_v}{k_{c,i}} + \left(1 + 0.26\left(\frac{J_v}{k_{c,i}}\right)^{1.4}\right)^{-1.7}\right) \tag{SI17}$$

$$k_{c,i} = \frac{Sh \cdot D_{i,\infty}}{L} \tag{SI18}$$

$$Sh = 0.23 Re^{0.567} Sc^{0.33} \tag{SI19}$$

$$K_{i,a} = \frac{1 + 3.867\lambda_i - 1.907\lambda_i^2 - 0.834\lambda_i^3}{1 + 1.867\lambda_i - 0.741\lambda_i^2} \tag{SI20}$$

$$K_{i,d} = \begin{cases} \dfrac{\left[\begin{array}{c} 1 + \frac{9}{8}\lambda_i \ln(\lambda_i) - 1.56034\lambda_i \\ +0.528155\lambda_i^2 + 1.91521\lambda_i^3 - 2.81903\lambda_i^4 \\ +0.270788\lambda_i^5 + 1.10115\lambda_i^6 - 0.435933\lambda_i^7 \end{array}\right]}{(1-\lambda_i)^2}, & \text{if } \lambda_i \leq 0.95. \\ 0.984\left(\frac{1-\lambda_i}{\lambda_i}\right)^{2.5}, & \text{if } \lambda_i > 0.95. \end{cases} \tag{SI21}$$

$$\Phi_{S,i} \;=\; (1-\lambda_i)^2 \tag{SI22}$$

$$\Phi_{DE,i} = exp\left(\frac{-\Delta W_i}{k_B T}\right) \tag{SI23}$$

$$\Delta W_i = \frac{z_i^2 e_0^2}{8\pi\varepsilon_0 r_i}\left(\frac{1}{\varepsilon_{pore}} - \frac{1}{\varepsilon_{bulk}}\right) \tag{SI24}$$

### 1.2 Contributions to molar flux

The contributions of advection, diffusion and electromigration to molar flux across the membrane active layer were determined with the discretized forms of the Extended Nernst Planck Equation (Eq. (SI25)). The concentration and potential profiles were considered linear for qualitative comparison and analysis.

$$J_i = -K_{i,d}D_{i,\infty}\frac{dc_i}{dx} - \frac{z_i F c_i K_{i,d} D_{i,\infty}}{RT}\frac{d\Psi}{dx} + K_{i,a}c_i J_v \tag{SI25}$$

**Advection**

$$J_{i,adv} = \frac{K_{i,c}(c_{i,n+1} + c_{i,n})J_v}{2} \tag{SI26}$$

**Electromigration**

$$J_{i,elec} = -\frac{z_i F(c_{i,n+1} + c_{i,n})K_{i,d}D_{i,\infty}}{2RT}\frac{\Psi_n - \Psi_{n-1}}{\delta x_n} \tag{SI27}$$

**Diffusion**

$$J_{i,diff} = -K_{i,d}D_{i,\infty}\frac{c_{i,n+1} - c_{i,n}}{\delta x_n} \tag{SI28}$$

## 2 Fitting

Fitting was performed by minimizing an objective function with a dual annealing algorithm in Python, from the SciPy library [2]. We used Nelder-Meald as the local optimizer, with a tolerance of $10^{-6}$ set as the convergence criterion.

## 2.1 $r_{pore}$ and $\Delta x_e$

The PEG retention at an infinite stirring velocity ($R_{i,real}$) was computed with the PEG 200 experimental retention values ($R_{i,obs}$) at different solvent velocities [3]:

$$\ln\left(\frac{1-R_{i,real}}{R_{i,real}}\right) = \ln\left(\frac{1-R_{i,obs}}{R_{i,obs}}\right) - \frac{J_v}{k_{c,i}} \tag{SI29}$$

The mass transfer coefficient was computed with the following equations. The characteristic length and the velocity values of the Reynolds number are half the length of the stirrer (3 cm) and the stirring velocity, respectively.

$$k_{c,i} = 0.23 Re^{0.567} Sc^{0.33} \tag{SI30}$$

Then, the following objective function was minimized by fitting $r_{pore}$ and $\Delta x_e$ for each membrane:

$$\underset{r_{pore},\,\Delta x_e}{\operatorname{argmin}} \sum_{k=1}^{N_{J_v}} \left(R_{i,real}^{model} - R_{i,real}\right)^2 \tag{SI31}$$

The formula to compute $R_{i,real}^{model}$ considers that there is only steric effect determining the exclusion of PEG 200 and its flux across the membranes' active layer comprises diffusion and advection only [4]:

$$R_{i,real}^{model} = 1 - \frac{K_{i,a}\Phi_{S,i}}{1 - e^{-Pe_m}\cdot(1 - K_{i,a}\Phi_{S,i})} \tag{SI32}$$

$$Pe_m = \frac{K_{i,a} J_v \Delta x_e}{K_{i,d} D_{i,\infty}} \tag{SI33}$$

The results of fitting PEG 200 are presented in Figure SI1.

## 2.2 $\varepsilon^*$ and $c_x$

### $Na^+/Mg^{2+}/SO_4^{2-}$

The mixed salt retention tests of feed solutions containing $Na^+/Mg^{2+}/SO_4^{2-}$ could not be fitted to the DSPM-DE model due to the retention values of $Mg^{2+}$and $SO_4^{2-}$ which are close to 100%. This case is similar to fitting single salt retention test results, which is not applicable to get $c_x$ and the $\varepsilon_{pore}$. These two input parameters cannot be unambiguously determined

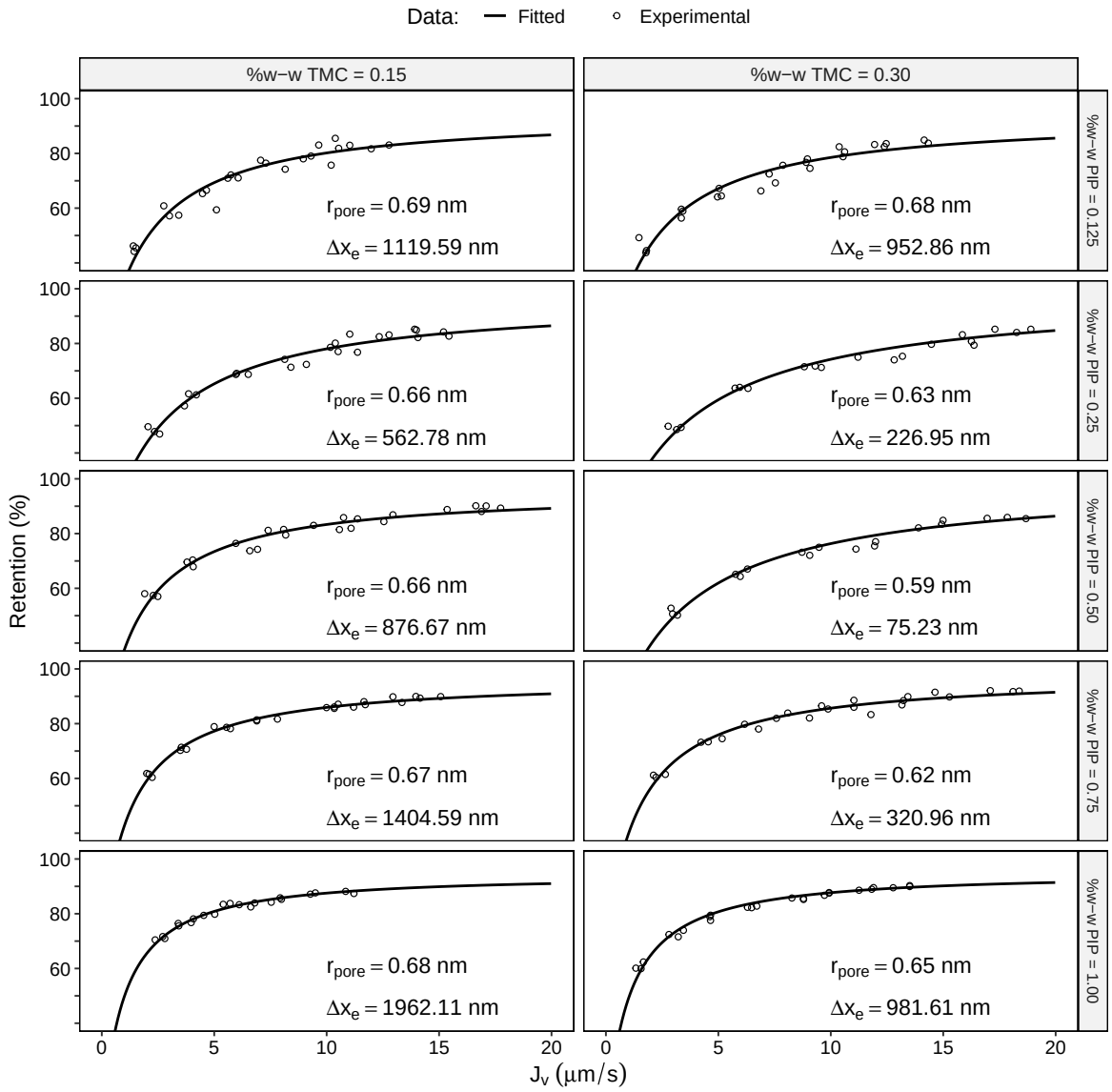



**Figure SI1:** Fitted vs. Experimental PEG 200 retention tests results for the fabricated membranes with the optimized values of $r_{pore}$ and $\Delta x_e$.

due to the coupling of ion fluxes and the counterbalancing effect they have on each other [5], [6]. As shown in Figure SI2, the objective function (Eq. (SI34) ) does not have a clear minimum; it continues to decrease for $\varepsilon^*$ values smaller than the high-frequency limit of the dielectric constant of water ($\varepsilon^* = 6$).

$$f_{min} = \sum_{j=1}^{N_{PIP}} \left( \underset{c_x}{\text{argmin}} \sum_{i=1}^{N_{ions}} \frac{\left(R_{i,j}^{mod} - R_{i,j}^{exp}\right)^2}{\sigma_{i,j}^2} \right) \tag{SI34}$$

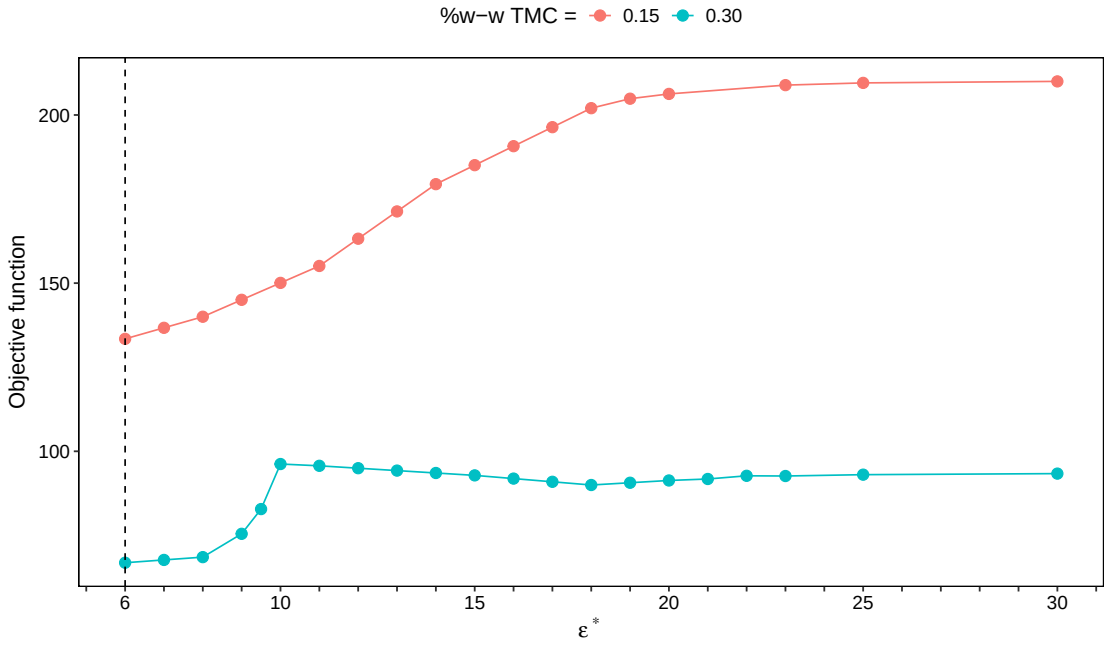



**Figure SI2:** Minimization function to determine the optimized values of $\varepsilon^*$ of the membranes prepared using different TMC concentrations for the ternary ionic mixture $Na^+/Mg^{2+}/SO_4^{2-}$.

## $Na^+/Mg^{2+}/Cl^-$

The retention performance of the prepared membranes for the feed solution containing the $Na^+/Mg^{2+}/Cl^-$ ternary ion mixture was accurately modeled using the DSPM-DE framework as shown in Figure SI3.

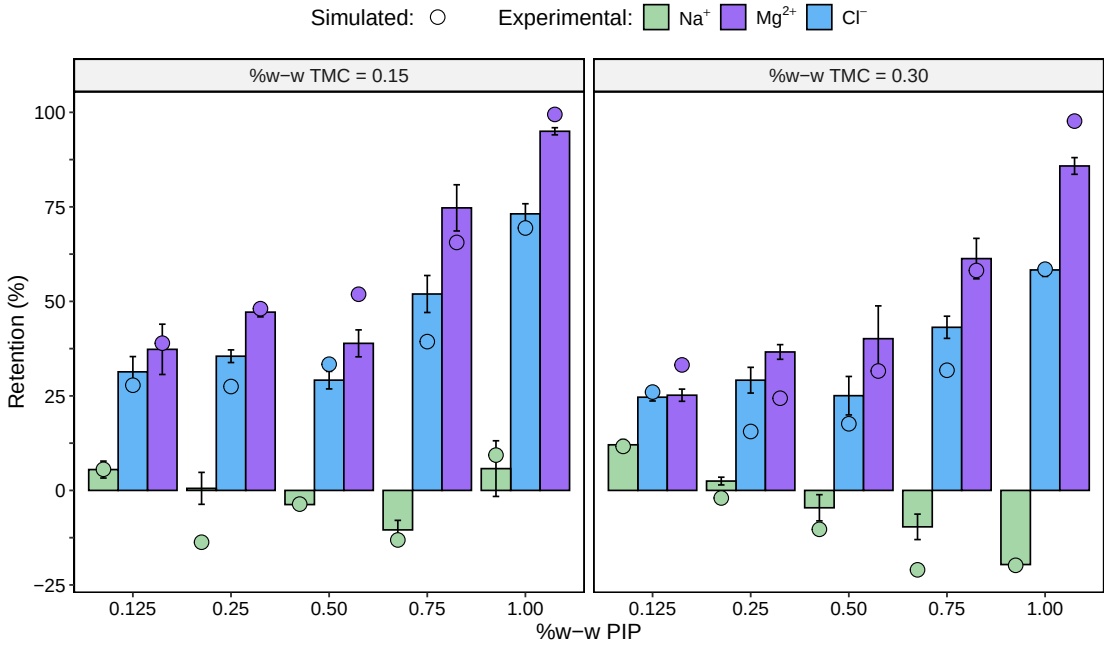



**Figure SI3:** Simulated and experimental mixed salt retention results for the fabricated membranes with $Na^+/Mg^{2+}/Cl^-$ ternary ion mixture.

# 3 Mass transport modelling $Na^+/Mg^{2+}/Cl^-$

## 3.1 Exclusion coefficients

The equations of the trend lines of the individual exclusion or partitioning coefficients are shown in Figures SI4-SI7.

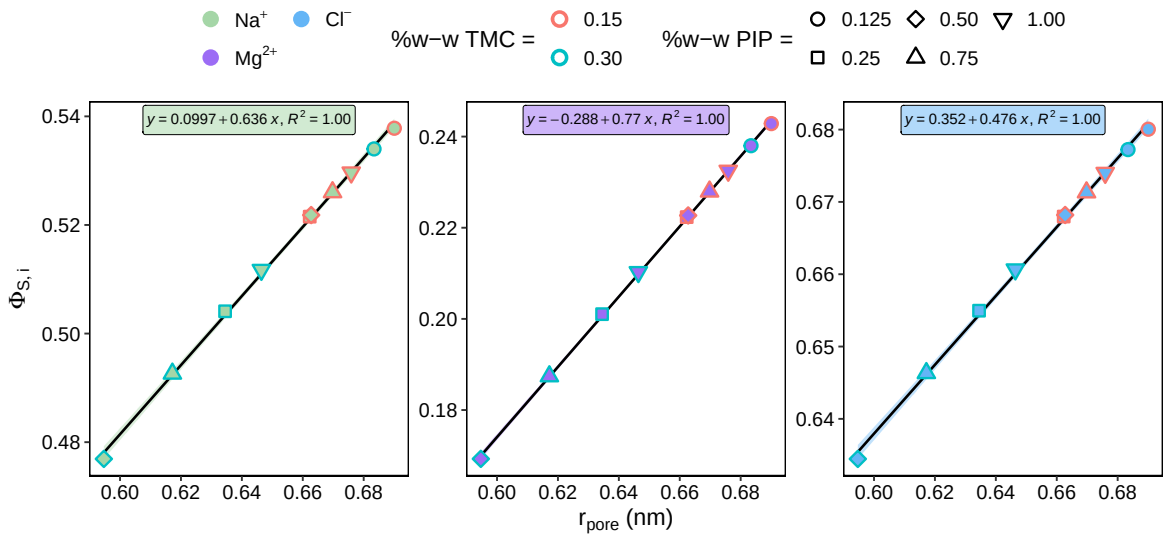



**Figure SI4:** Steric exclusion or partitioning coefficients of the ternary ion mixture $Na^+/Mg^{2+}/Cl^-$ for the fabricated membranes as a function of $r_{pore}$.

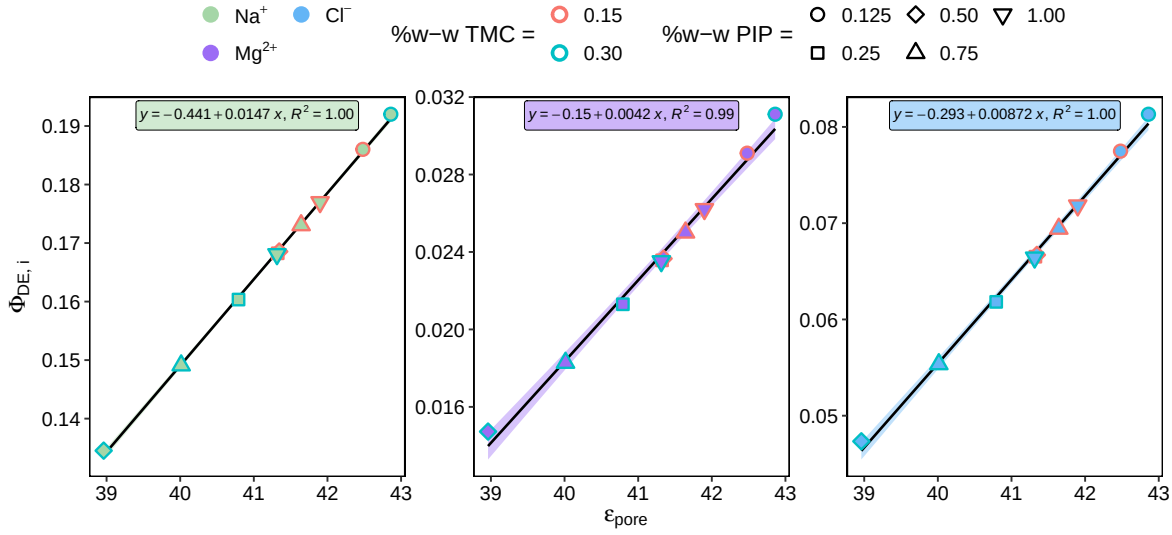



**Figure SI5:** Dielectric exclusion or partitioning coefficients of the ternary ion mixture $Na^+/Mg^{2+}/Cl^-$ for the fabricated membranes as a function of $\varepsilon_{pore}$.

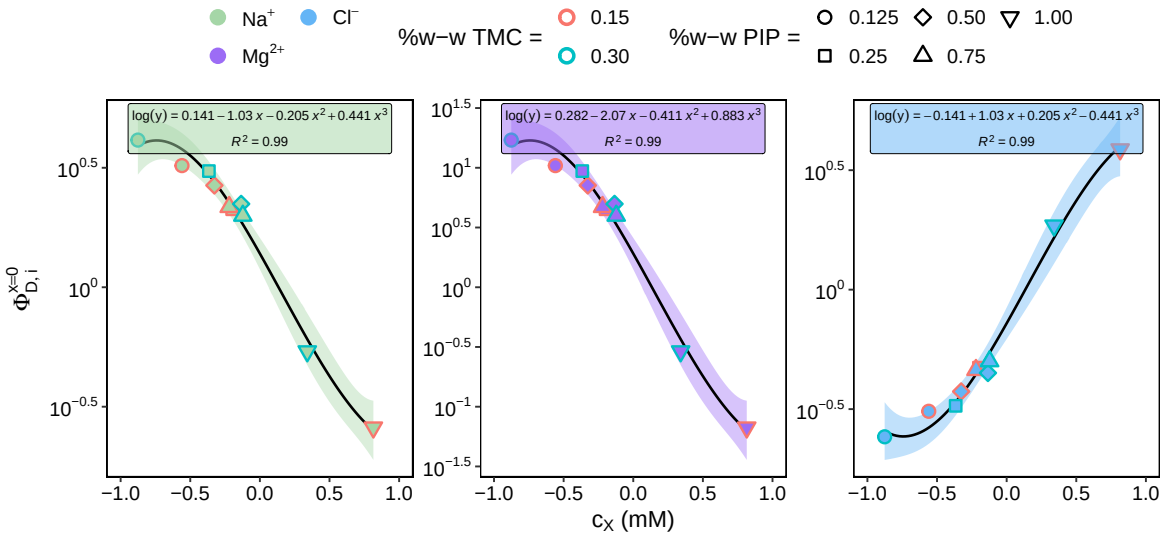



**Figure SI6:** Donnan exclusion or partitioning coefficients of the ternary ion mixture $Na^+/Mg^{2+}/Cl^-$ for the fabricated membranes as a function of $c_x$.

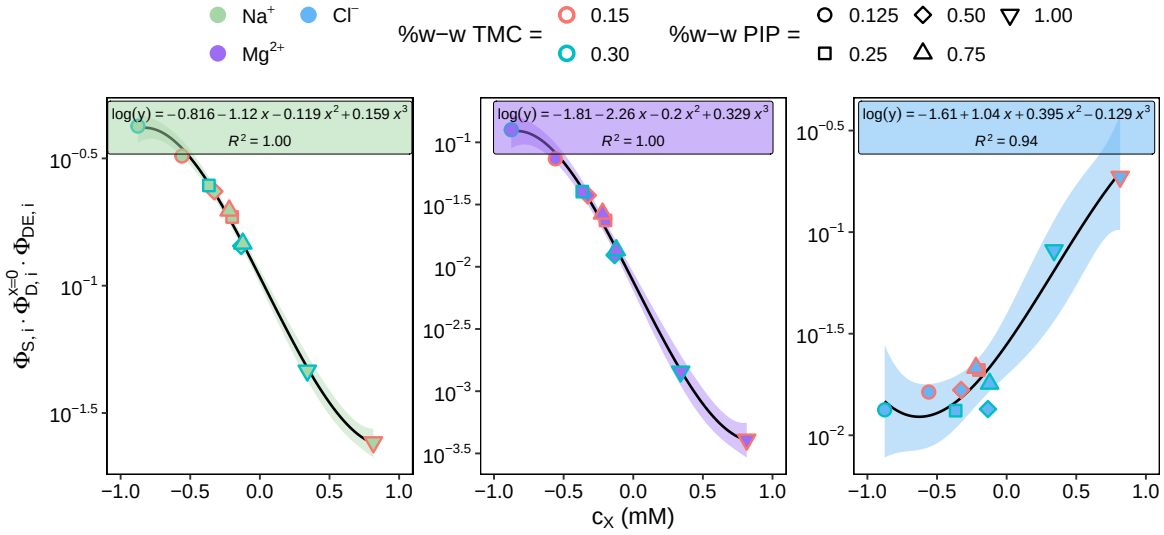



**Figure SI7:** Overall exclusion or partitioning coefficients of the ternary ion mixture $Na^+/Mg^{2+}/Cl^-$ for the fabricated membranes as a function of $c_x$.

## 3.2 Solution flux

Figure SI8 shows the trend of the solution flux, $J_v$, of the ternary ion mixture $Na^+/Mg^{2+}/Cl^-$ is not a function of $c_x$ but $\Delta x_e$. This is because $\Delta x_e$ is a measure of the mass transport resistance of the membranes. Thus, the trend line of Figure SI8a is represented by $y = f(1/x)$.

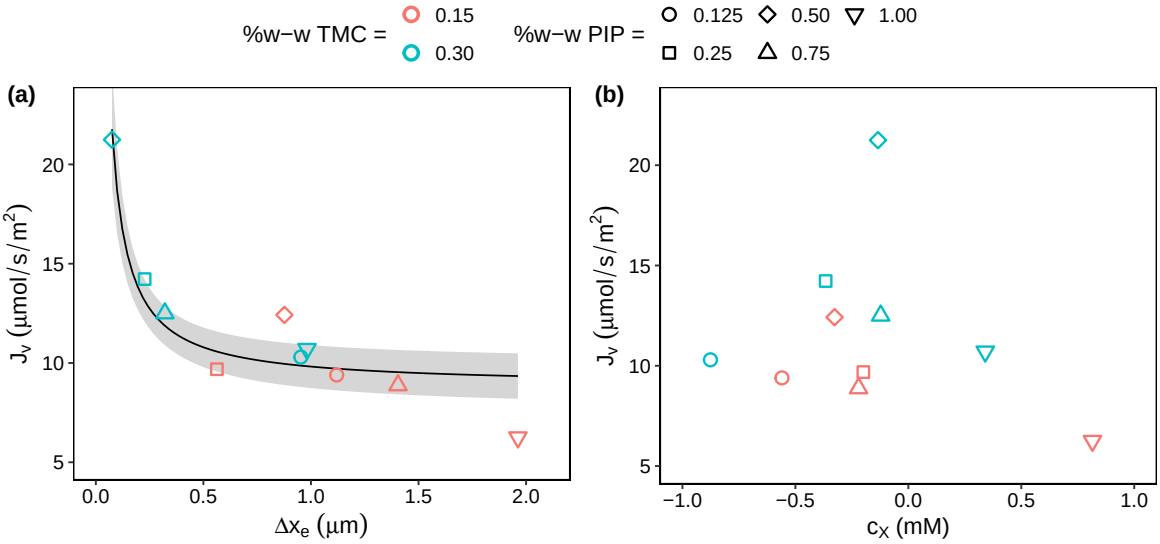



**Figure SI8:** Solution flux of the ternary ion mixture $Na^+/Mg^{2+}/Cl^-$ for the fabricated membranes as a function of (a) $\Delta x_e$ and (b) $c_x$.

## 3.3 Contributions to molar flux

The equations of the trend lines for the contributions and the transmembrane molar fluxes are shown in Figures SI9-SI11 and SI12, respectively.

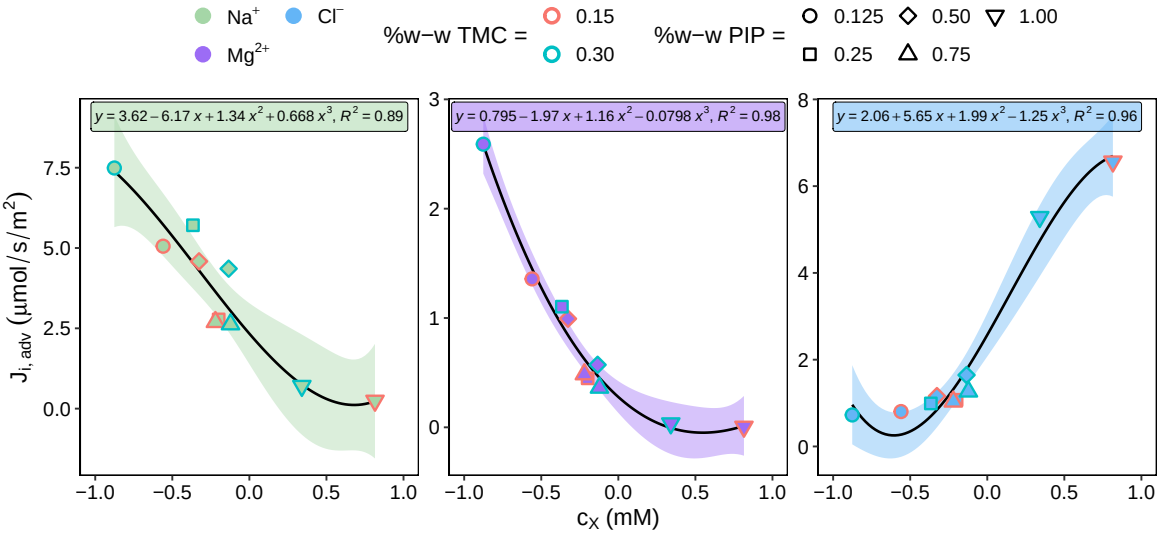



**Figure SI9:** Advective fluxes of the ternary ion mixture $Na^+/Mg^{2+}/Cl^-$ for the fabricated membranes as a function of $c_x$.

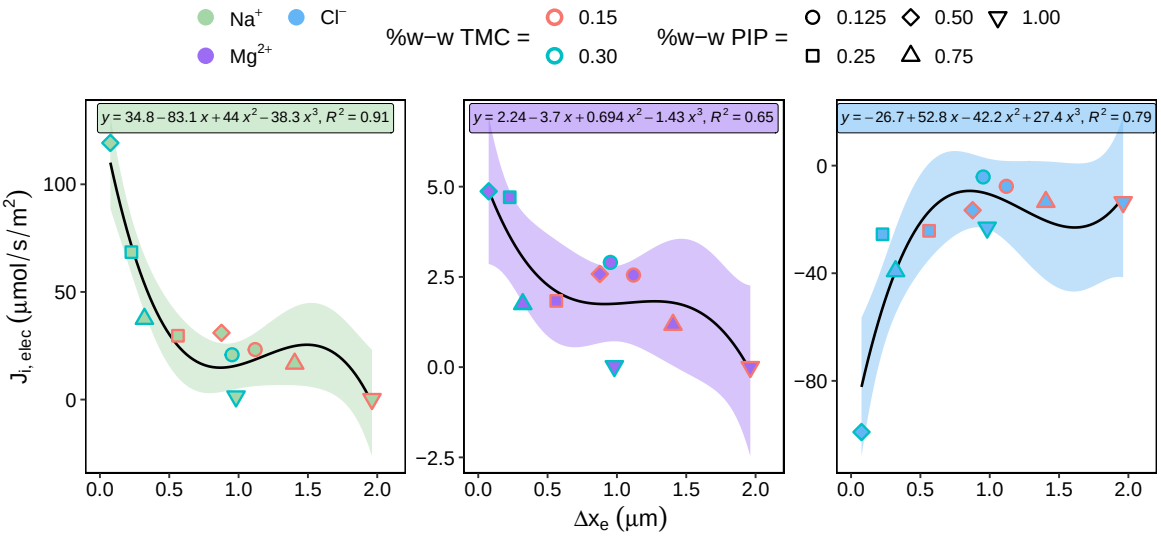



**Figure SI10:** Electromigrative fluxes of the ternary ion mixture $Na^+/Mg^{2+}/Cl^-$ for the fabricated membranes as a function of $\Delta x_e$.

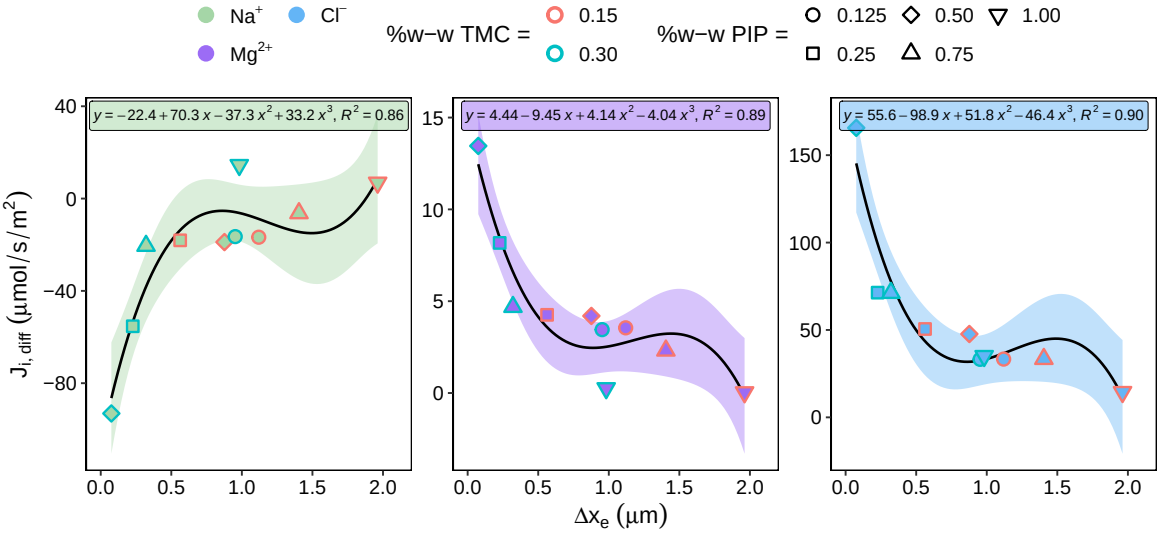



**Figure SI11:** Diffusive fluxes of the ternary ion mixture $Na^+/Mg^{2+}/Cl^-$ for the fabricated membranes as a function of $\Delta x_e$.

Figure SI13 shows the linear trend lines of the simulated diffusive fluxes of the three ions as a function of the electric fields. Based on the $R^2$ values, the strongest correlation between the diffusive fluxes and the electric fields corresponds to $Cl^-$. In other words, the large positive diffusive fluxes of $Cl^-$ are counterbalanced by negative electromigrative fluxes through spontaneously-arising electric fields.

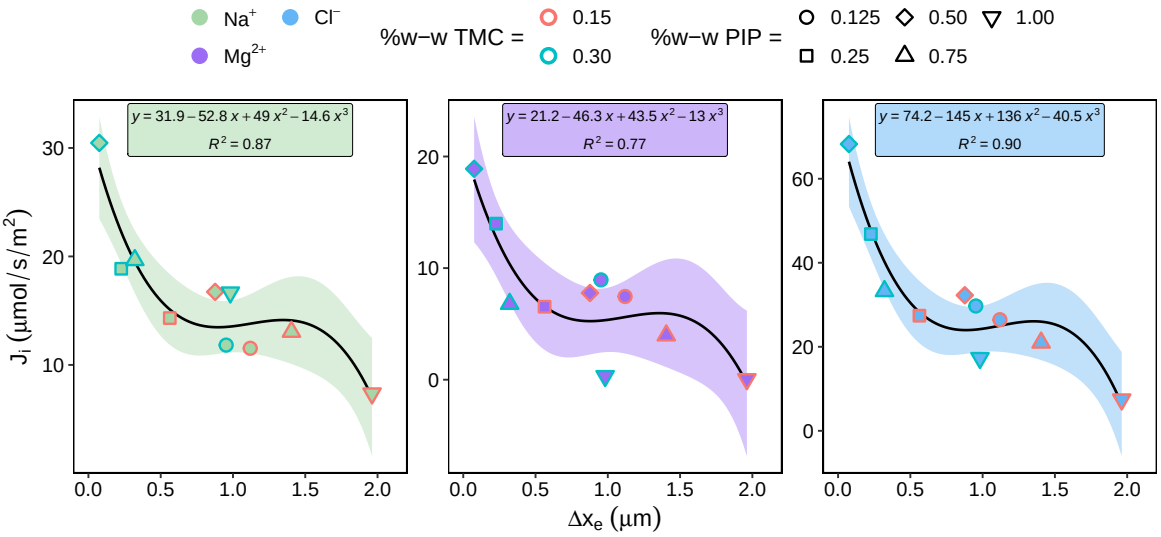



**Figure SI12:** Total transmembrane molar fluxes of the ternary ion mixture $Na^+/Mg^{2+}/Cl^-$ for the fabricated membranes as a function of $\Delta x_e$.

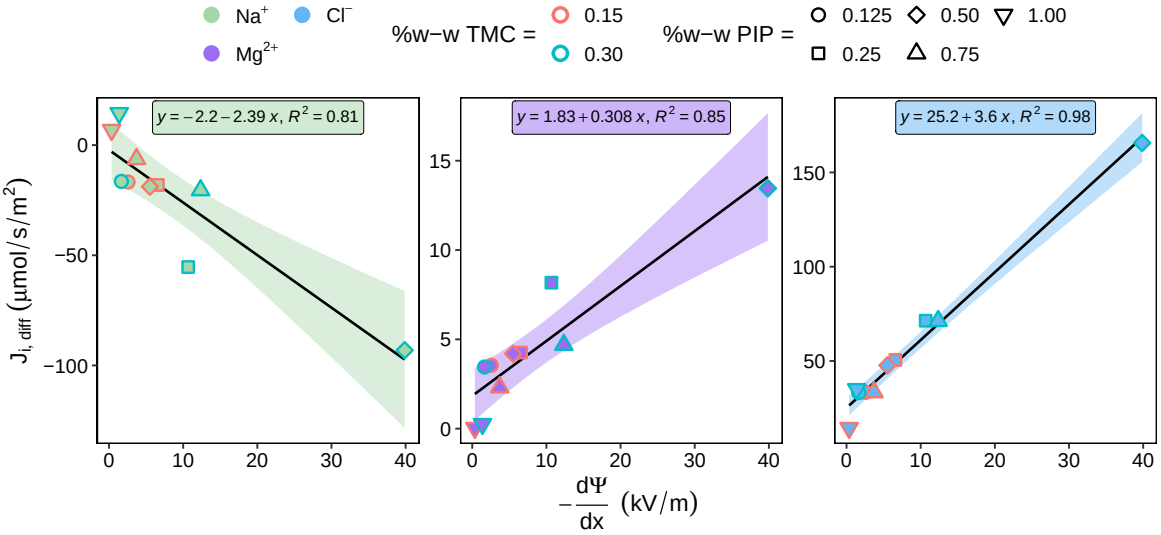



**Figure SI13:** Simulated ion diffusive fluxes as a function of the electrical potential gradient across the fabricated membranes' active layers of the ternary ion mixture $Na^+/Mg^{2+}/Cl^-$.

## 3.4 Concentration profiles

Figure SI14 presents the concentration profiles of $Na^+$, $Mg^{2+}$ and $Cl^-$ within the membranes' active layers. The x-axis represents the $x$ coordinate across the active layer, normalized by $\Delta x_e$ to allow for comparison of concentration profiles among the fabricated membranes with different $\Delta x_e$ values. Here, $x = 0.0$ corresponds to the pore entrance from the feed side, while $x = \Delta x_e$ corresponds to the pore exit on the permeate side.

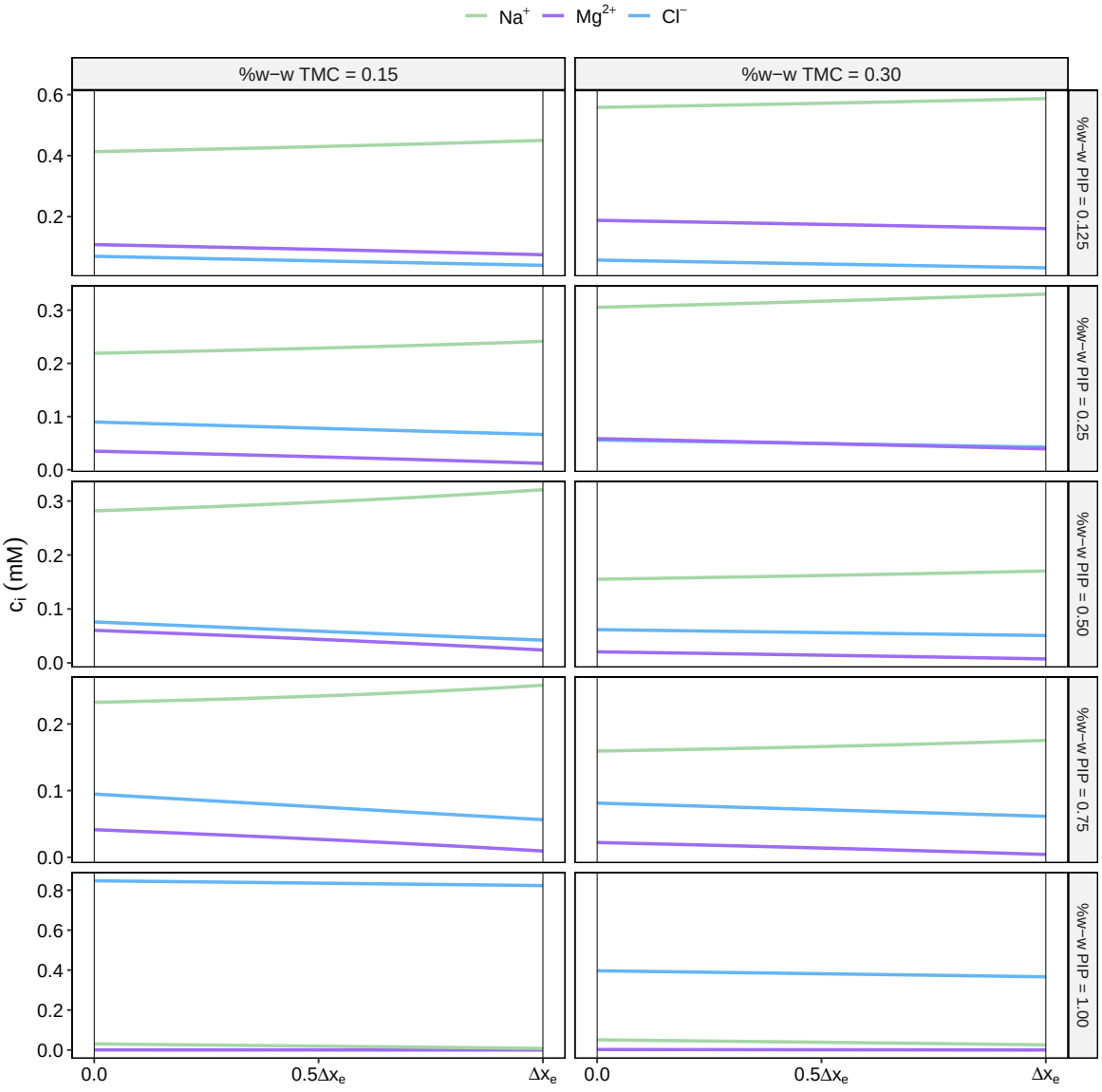



**Figure SI14:** Simulated concentration profiles across the fabricated membranes' active layers of the ternary ion mixture $Na^+/Mg^{2+}/Cl^-$ during NaCl and $MgCl_2$ mixed salt retention tests as a function of $\Delta x_e$.

### Concentration gradients

At every $x$ position inside the membrane's active layer, the relationship among the concentration gradients is derived from the electroneutrality condition (Eq. (SI35)), assuming that $c_x$ is constant in the $x$ direction.

$$-c_x = \sum_{i=1}^{N_{ions}} z_i c_i \tag{SI35}$$

$$0 = \sum_{i=1}^{N_{ions}} z_i \frac{dc_i}{dx} \tag{SI36}$$

$$\frac{dc_{Na^+}}{dx} + 2\frac{dc_{Mg^{2+}}}{dx} - \frac{dc_{Cl^-}}{dx} = 0 \tag{SI37}$$

In Figure SI15, we illustrate the decreasing trend in absolute value of the simulated concentration gradients of the ternary ion mixture $Na^+/Mg^{2+}/Cl^-$ inside the membranes' active layer as a function of $\Delta x_e$. The trend lines are represented by $y = f(1/x)$.

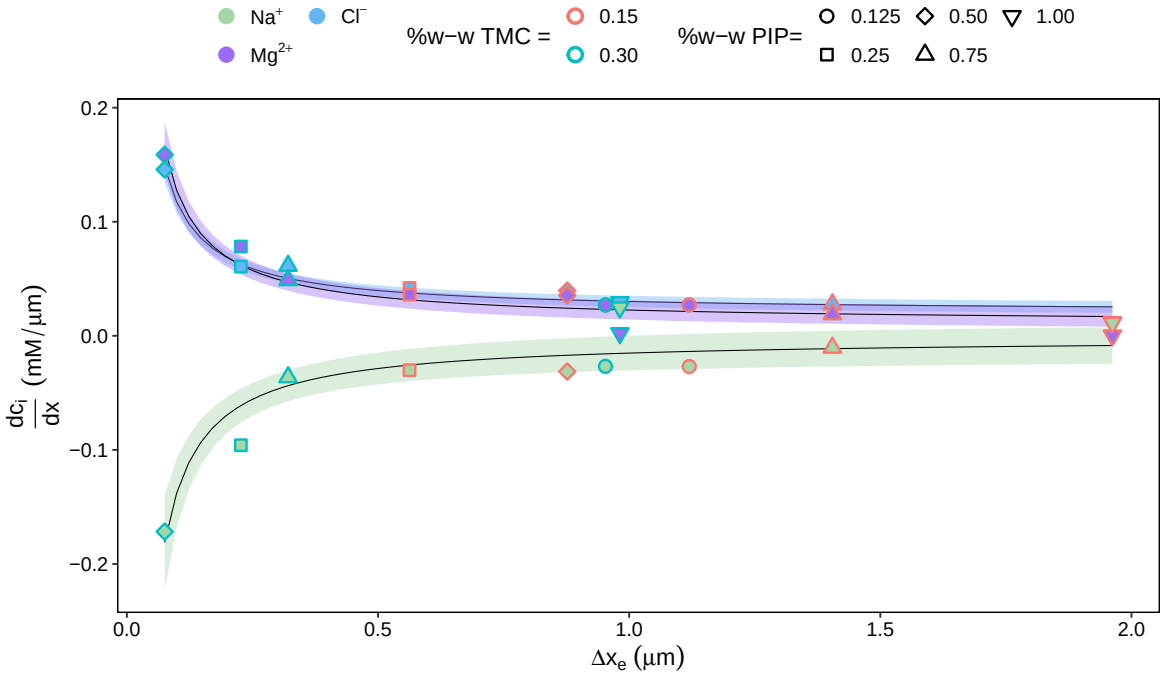



**Figure SI15:** Simulated concentration gradients across the fabricated membranes' active layers of the ternary ion mixture $Na^+/Mg^{2+}/Cl^-$ as a function of $\Delta x_e$.

## References


[1] V. Geraldes, M. D. Afonso, Prediction of the concentration polarization in the nanofiltration/reverse osmosis of dilute multi-ionic solutions, Journal of Membrane Science 300 (1-2) (2007) 20–27. https://doi.org/10.1016/J.MEMSCI.2007.04.025.

[2] D. Rehman, J. H. Lienhard, Global optimization for accurate and efficient parameter estimation in nanofiltration, Journal of Membrane Science Letters 2 (2) (2022) 100034. https://doi.org/10.1016/J.MEMLET.2022.100034.

[3] W. R. Bowen, A. W. Mohammad, N. Hilal, Characterisation of nanofiltration membranes for predictive purposes - Use of salts, uncharged solutes and atomic force microscopy, Journal of Membrane Science 126 (1) (1997) 91–105. https://doi.org/10.1016/S0376-7388(96)00276-1.

[4] R. Wang, S. Lin, Pore model for nanofiltration: History, theoretical framework, key predictions, limitations, and prospects, Journal of Membrane Science 620 (July 2020) (2021) 118809. https://doi.org/10.1016/j.memsci.2020.118809.

[5] S. Déon, P. Dutournié, L. Limousy, P. Bourseau, Transport of salt mixtures through nanofiltration membranes: Numerical identification of electric and dielectric contributions, Separation and Purification Technology 69 (3) (2009) 225–233. https://doi.org/10.1016/j.seppur.2009.07.022.

[6] S. B. Rutten, M. A. Junker, L. H. Leal, W. M. de Vos, R. G. Lammertink, J. de Grooth, Influence of dominant salts on the removal of trace micropollutants by hollow fiber nanofiltration membranes, Journal of Membrane Science 678 (2023) 121625. https://doi.org/10.1016/j.memsci.2023.121625.

## Supporting Information Publication III

This section contains the Supporting Information of Publication III, available online with DOI: 10.1016/j.memsci.2025.124642

# Supporting Information

## Effect of piperazine-based monomer structure on nanofiltration membrane selectivity: a DSPM-DE analysis of nitrate transport

Nicolás Cevallos-Cueva[a], Md. Mushfequr Rahman[a,*], Hluf Hailu Kinfu[a], and Volker Abetz[a,b]

[a] *Helmholtz-Zentrum Hereon, Institute of Membrane Research, Max-Planck-Straße 1, 21502 Geesthacht, Germany*

[b] *University of Hamburg, Institute of Physical Chemistry, Martin-Luther-King-Platz 6, 20146 Hamburg, Germany*

[*] *Corresponding author: mushfequr.rahman@hereon.de*

---

## Contents

**1 Membranes morphology & performance** **S2**

1.1 Roughness effect . . . . . S2

1.2 $NO_3^-$ separation performance comparison . . . . . S3

**2 Fitting DSPM-DE model** **S4**

2.1 $r_{pore}$ and $\Delta x_e$ . . . . . S4

2.2 $\varepsilon^*$ and $c_x$ . . . . . S5

2.3 Summary . . . . . S7

**3 Mass transport modeling** **S8**

**References** **S9**

# 1 Membranes morphology & performance

## 1.1 Roughness effect

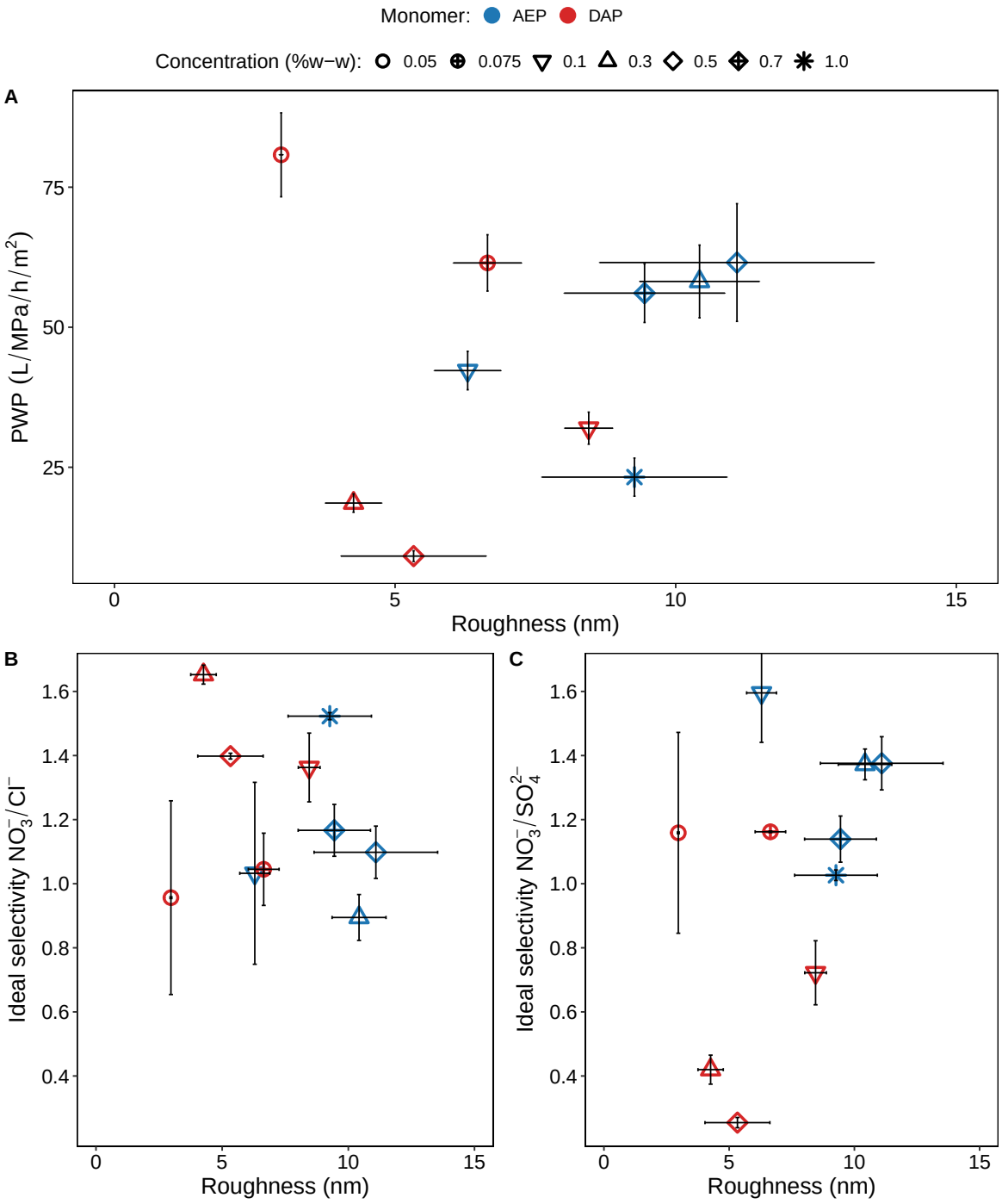



**Fig. S1:** Effect of RMS roughness of the PA layer on: (A) Pure water permeance (PWP), (B) ideal selectivity of $NO_3^-/Cl^-$, and (C) ideal selectivity of $NO_3^-/SO_4^{2-}$.

## 1.2 $NO_3^-$ separation performance comparison

The $NO_3^-$ retention performance of the fabricated AEP and DAP membranes is compared against commercial membranes (Fig. S2) and against PIP-based membranes (Fig. S3).

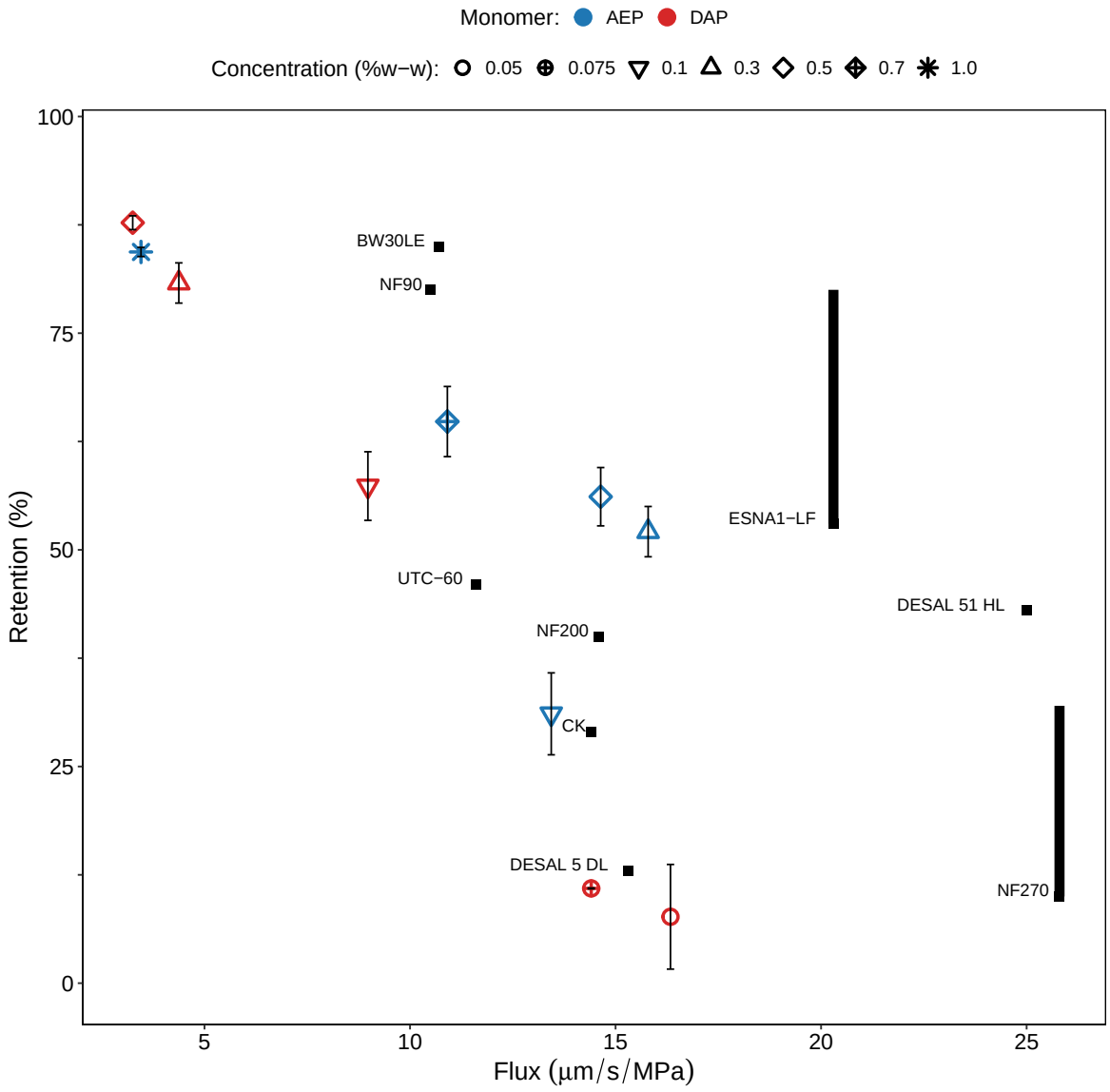



**Fig. S2:** Comparison of the $NO_3^-$ retention performance of the fabricated membranes (colored data points) against commercial membranes from the literature (black squares and bars). Data was taken and adapted from references [1]–[4].

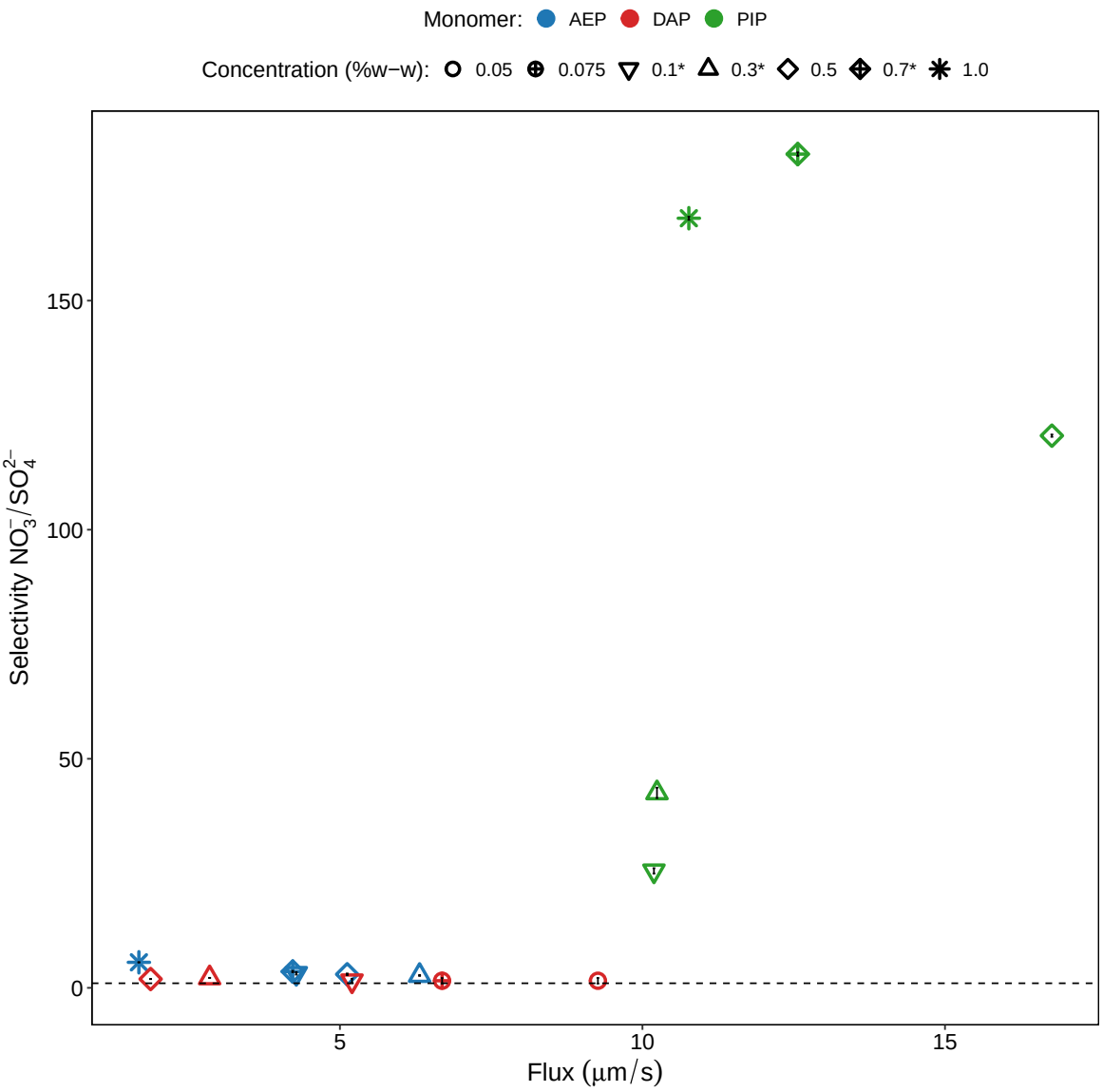



**Fig. S3:** $NO_3^-/SO_4^{2-}$ selectivity as a function of solution flux. For clarity, symbols marked with an asterisk (*) in the legend correspond to previously reported PIP-based membranes [5] at concentrations: 0.1* = 0.125 % w-w, 0.3* = 0.25 % w-w, and 0.7* = 0.75 % w-w.

# 2 Fitting DSPM-DE model

## 2.1 $r_{pore}$ and $\Delta x_e$

The procedure to determine $r_{pore}$ and $\Delta x_e$ relies on fitting PEG 200 retention tests carried out at different solvent velocities. Determining $r_{pore}$ and $\Delta x_e$ is important because these parameters define size-related phenomena (e.g., partitioning, hindrance, confinement, etc.) and the mass transport resistance of the membranes under the DSPM-DE model, enabling accurate description of membrane transport phenomena. The detailed procedure is described in our previous publications [5] [6]. The results are presented in Fig. S4:

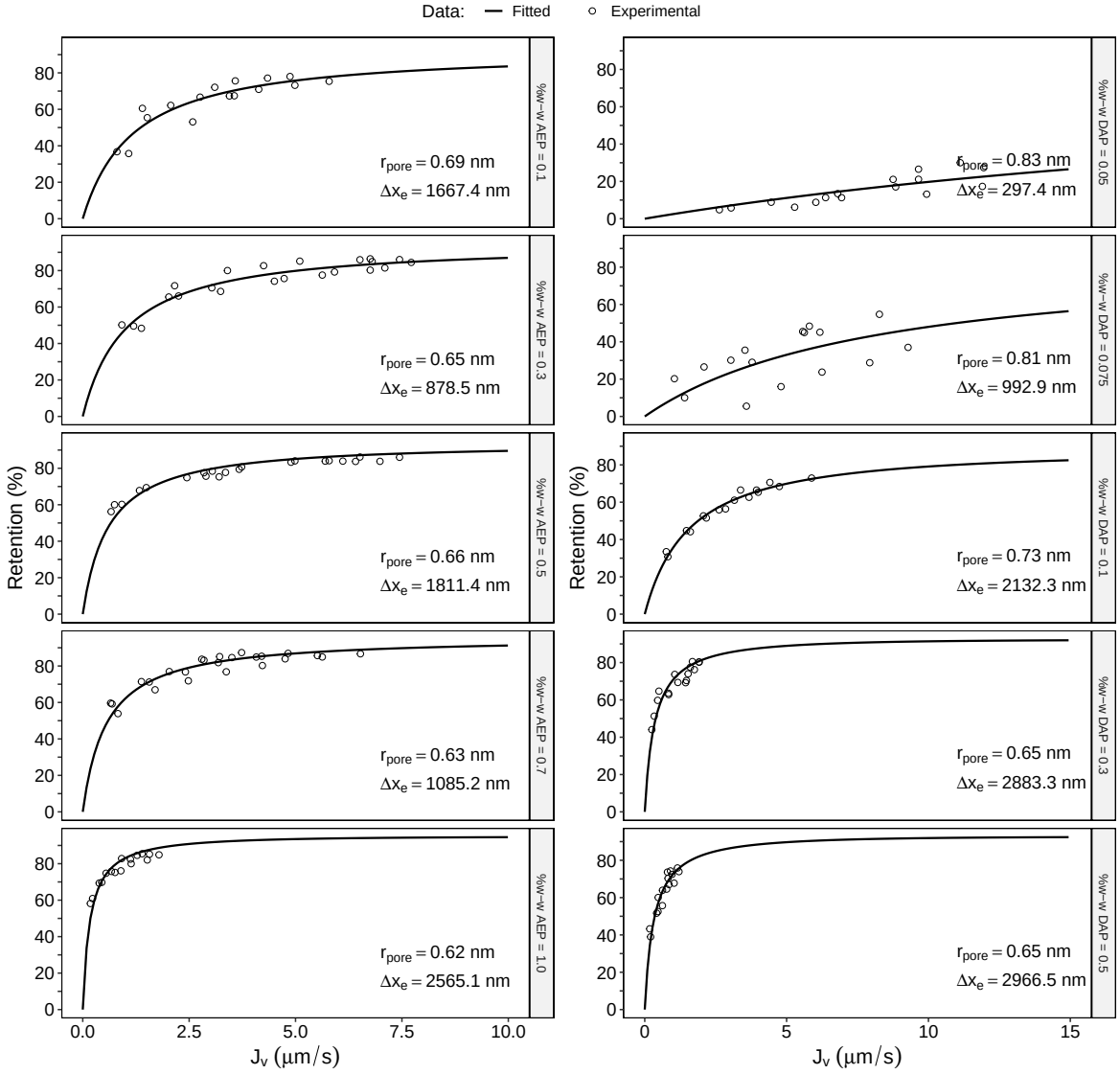



**Fig. S4:** Fitted vs. Experimental PEG 200 retention tests results for the fabricated membranes with the optimized values of $r_{pore}$ and $\Delta x_e$.

## 2.2 $\varepsilon^*$ and $c_x$

We assume that $\varepsilon^*$ is constant for membranes prepared with each aqueous-phase monomer (AEP and DAP). Accordingly, we conducted two separate fitting procedures (i.e., one for each series of membrane fabricated with either AEP or DAP). First, we tested different values of $\varepsilon^*$ to find preliminary values of $c_x$ for each membrane by minimizing the squared difference between the experimental ($R_{i,j}^{exp}$) and the calculated retention of each ion ($R_{i,j}^{mod}$). Next, we determined $\varepsilon^*$ by minimizing the sum of the previously minimized differences across all membranes prepared with the same aqueous-phase monomer:

$$f_{min} = \underset{\varepsilon^*}{\text{argmin}} \sum_{j=1}^{N_{AEP/DAP}} \left( \underset{c_x}{\text{argmin}} \sum_{i=1}^{N_{ions}} \frac{\left(R_{i,j}^{mod} - R_{i,j}^{exp}\right)^2}{\sigma_{i,j}^2} \right) \tag{S1}$$

The subscript $i$ cycles through all ionic species and $j$ through all aqueous-phase monomer concentrations used to fabricate membranes with the same monomer (AEP or DAP). $R_{i,j}^{mod}$ is the simulated retention and $R_{i,j}^{exp}$ is the average experimental rejection value of at least 3 replications for each fabricated membrane. To bias the minimizations towards more experimentally confident values, $\sigma_{i,j}^2$, was computed with the unbiased variance equation.

As shown in Fig. S5, the optimized values of $\varepsilon^*$ for AEP and DAP membranes were both determined to be 17.

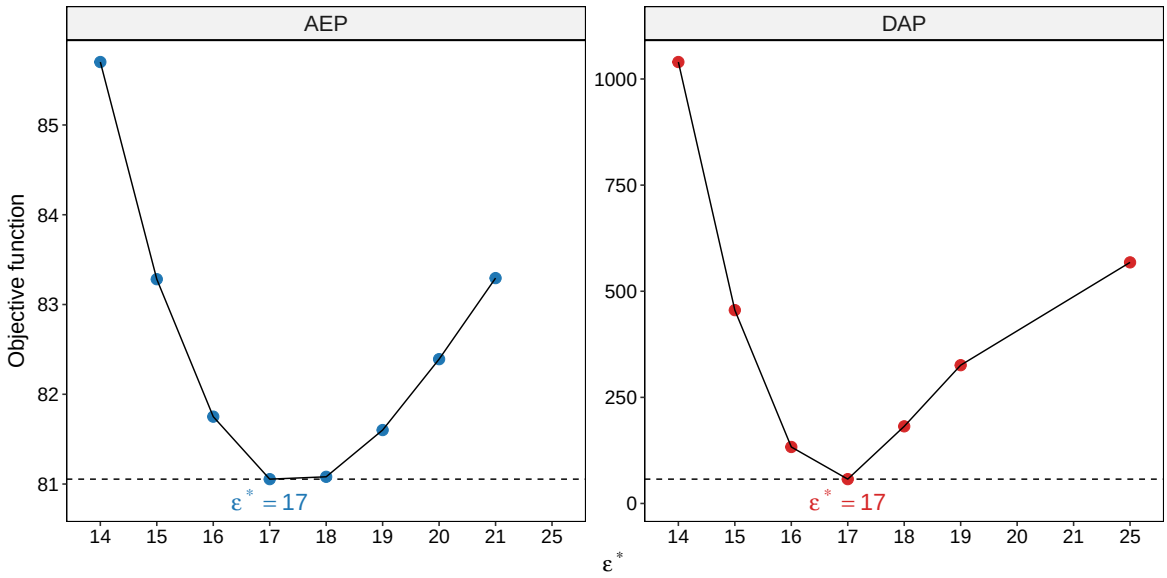



**Fig. S5:** Minimization function to determine $\varepsilon^*$ for the fabricated membranes using AEP and DAP monomers.

Using the described fitting procedure, we determined a unique set of DSPM-DE input parameters for each IP reaction condition, which allowed us to simulate the retention performance of the fabricated membranes. The accurate simulation shown in Fig. S6 indicates that the fitted DSPM-DE input parameters effectively capture the physicochemical features of the membranes determining ion transport, thereby supporting reliability of our mechanistic analysis.

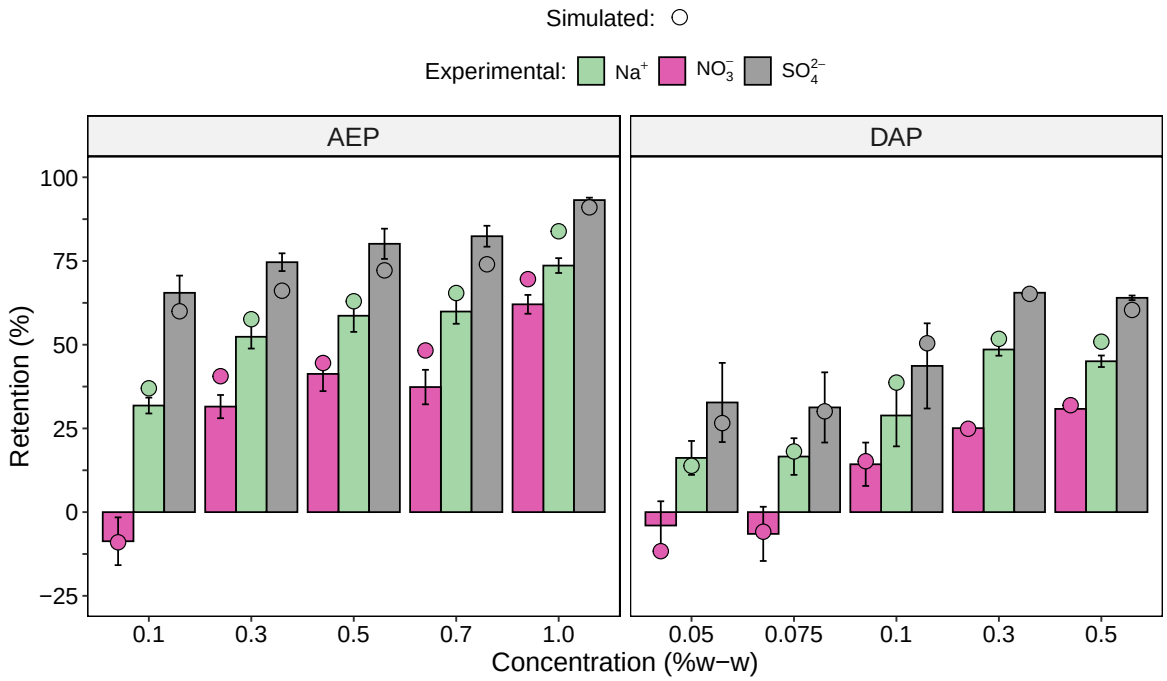



**Fig. S6:** Simulated and experimental retention tests of the ternary ion mixture $Na^+/NO_3^-/SO_4^{2-}$ for the fabricated membranes.

## 2.3 Summary

The input parameters used in the DSPM–DE model of the fabricated membranes are summarized in Table S1.

**Table S1:** Input parameters for the DSPM-DE model used to simulate membranes prepared with varying AEP and DAP monomer concentrations.

| Monomer | Concentration (% w-w) | $r_{pore}$ (nm) | $\Delta x_e$ ($\mu$m) | $c_x$ (mM) | $\varepsilon_{pore}$ (-) |
|---|---|---|---|---|---|
| AEP | 0.1 | 0.690 | 1.667 | 0.071 | 39.256 |
| AEP | 0.3 | 0.647 | 0.879 | 0.469 | 37.275 |
| AEP | 0.5 | 0.657 | 1.811 | 0.355 | 37.735 |
| AEP | 0.7 | 0.631 | 1.085 | 0.571 | 36.477 |
| AEP | 1.0 | 0.618 | 2.565 | 1.537 | 35.856 |
| DAP | 0.05 | 0.833 | 0.297 | -0.175 | 44.757 |
| DAP | 0.075 | 0.809 | 0.993 | 0.049 | 43.941 |
| DAP | 0.1 | 0.726 | 2.132 | 0.214 | 40.795 |
| DAP | 0.3 | 0.653 | 2.883 | 0.169 | 37.577 |
| DAP | 0.5 | 0.651 | 2.967 | 0.277 | 37.460 |

## 3 Mass transport modeling

The concentration profiles of $Na^+$,$NO_3^-$, and $SO_4^{2-}$ within the active layers of the fabricated membranes are presented in Fig. S7. The $x$-axis represents the spatial coordinate across the membrane's selective layer. To facilitate direct comparison among membranes with different $\Delta x_e$, the $x$-axis values were normalized by $\Delta x_e$. In this normalized framework:

- $x = 0$ represents the pore entrance at the feed-solution/membrane interface
- $x = \Delta x_e$ represents the pore exit at the permeate-solution/membrane interface.

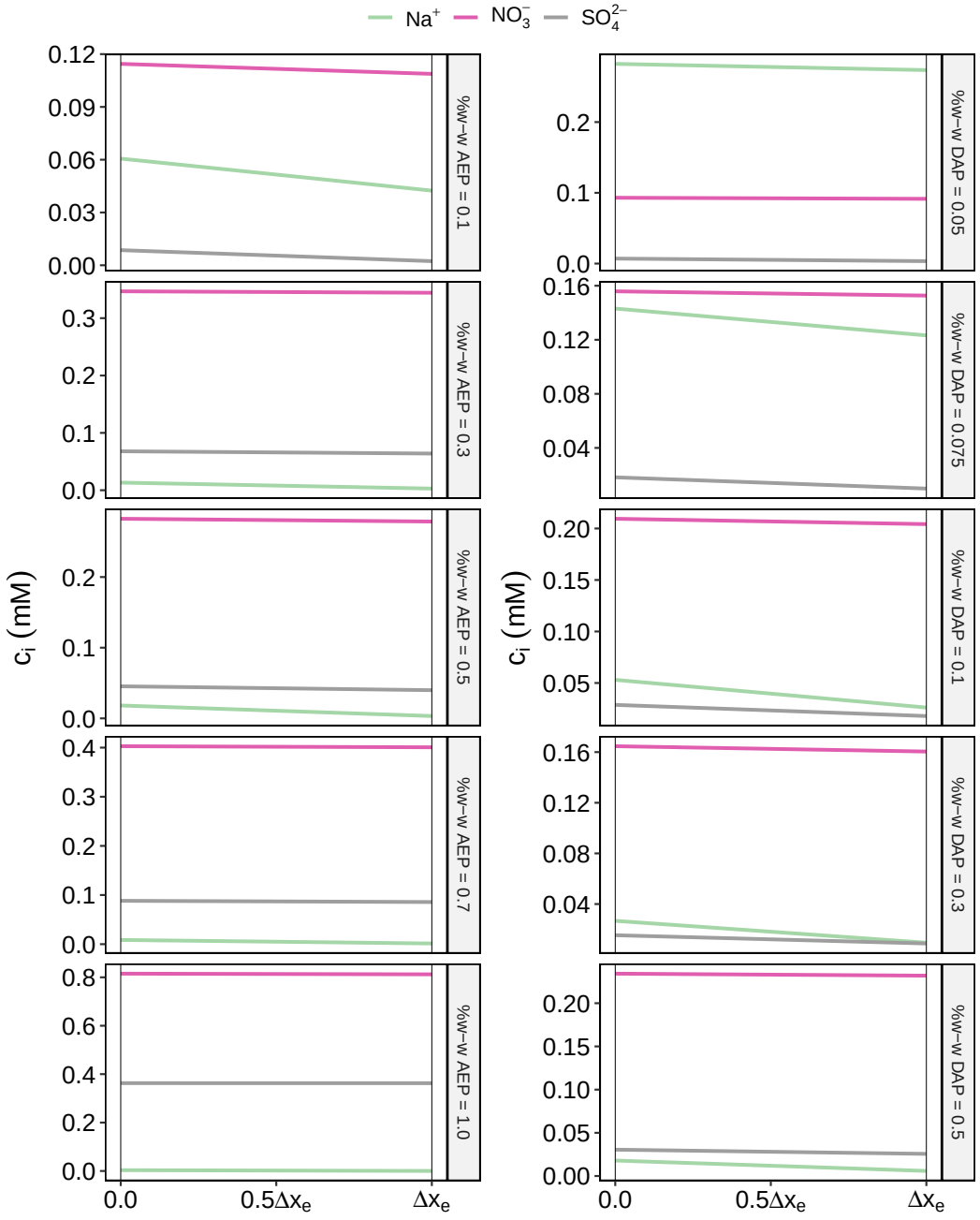



**Fig. S7:** Simulated concentration profiles across the active layers of the fabricated membranes of the ternary ion mixture $Na^+/NO_3^-/SO_4^{2-}$ during mixed salt retention tests as a function of $\Delta x_e$.

## References


[1] A. Popova, R. Rattanakom, Z.-Q. Yu, Z. Li, K. Nakagawa, T. Fujioka, Evaluating the potential of nanofiltration membranes for removing ammonium, nitrate, and nitrite in drinking water sources, Water Research 244 (2023) 120484. https://doi.org/https://doi.org/10.1016/j.watres.2023.120484.

[2] J. Joseph, Y.-A. Boussouga, M. Di Vincenzo, M. Barboiu, A. I. Schäfer, Selectivity of artificial water channel-polyamide composite membranes towards inorganic contaminants, Journal of Membrane Science 664 (2022) 121019. https://doi.org/https://doi.org/10.1016/j.memsci.2022.121019.

[3] R. Epsztein, W. Cheng, E. Shaulsky, N. Dizge, M. Elimelech, Elucidating the mechanisms underlying the difference between chloride and nitrate rejection in nanofiltration, Journal of Membrane Science 548 (2018) 694–701. https://doi.org/https://doi.org/10.1016/j.memsci.2017.10.049.

[4] L. Zou, S. Zhang, J. Liu, Y. Cao, G. Qian, Y. Y. Li, Z. P. Xu, Nitrate removal from groundwater using negatively charged nanofiltration membrane, Environmental Science and Pollution Research 26 (33) (2019) 34197–34204. https://doi.org/10.1007/s11356-018-3829-6.

[5] N. Cevallos-Cueva, M. M. Rahman, H. H. Kinfu, V. Abetz, Mass transport mechanism of nitrate selective nanofiltration membranes on the basis of the donnan steric pore model with dielectric exclusion (dspm-de), Chemical Engineering Journal 493 (2024). https://doi.org/10.1016/j.cej.2024.152775.

[6] N. Cevallos-Cueva, M. M. Rahman, H. H. Kinfu, V. Abetz, Mass transport mechanisms insights of selective sodium/magnesium separation through nanofiltration membranes, Journal of Membrane Science 721 (2025) 123808–123808. https://doi.org/10.1016/J.MEMSCI.2025.123808.

## Supporting Information Publication IV

This section contains the Supporting Information of Publication IV, available online with DOI: 10.1016/j.desal.2025.119765

# Supporting Information

## Common anion and piperazine-based monomer chemistry tune $Na^+/Mg^{2+}$ selectivity in nanofiltration: a mechanistic mass-transport analysis

Nicolás Cevallos-Cueva[a], Md. Mushfequr Rahman[a,*], Hluf Hailu Kinfu[a], and Volker Abetz[a,b]

[a] *Helmholtz-Zentrum Hereon, Institute of Membrane Research, Max-Planck-Straße 1, 21502 Geesthacht, Germany*

[b] *University of Hamburg, Institute of Physical Chemistry, Martin-Luther-King-Platz 6, 20146 Hamburg, Germany*

[*] *Corresponding author: mushfequr.rahman@hereon.de*

## Contents

**1 Characterization** **S2**
- 1.1 SEM analysis . . . S2
- 1.2 Zeta potential . . . S2

**2 Retention tests** **S3**
- 2.1 Single salts . . . S3
- 2.2 Mixed salts . . . S6

**3 DSPM-DE model** **S8**
- 3.1 Equations . . . S8
- 3.2 Linearized and discretized equations . . . S11
- 3.3 Fitting . . . S12
  - $r_{pore}$ and $\Delta x_e$ . . . S12
  - $\varepsilon^*$ and $c_x$ . . . S13

**4 Mass transport modelling** **S16**
- 4.1 Exclusion phenomena . . . S16
- 4.2 Transmembrane molar transport . . . S18

**References** **S24**

# 1 Characterization

## 1.1 SEM analysis

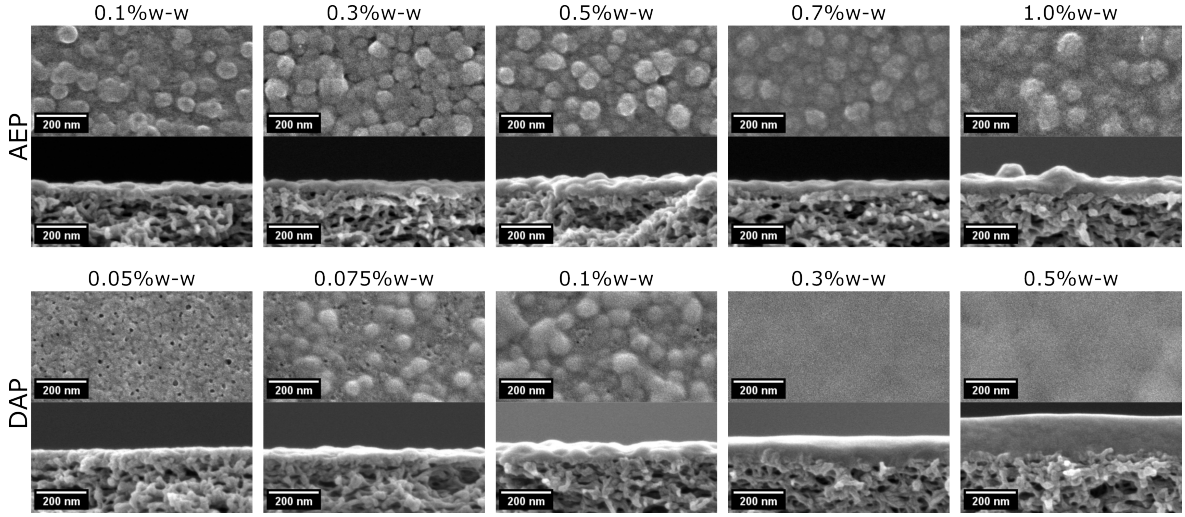



**Fig. S1:** SEM micrographs of the polyamide (PA) active layers fabricated with AEP and DAP membranes (top: surface view, bottom: cross-section).

## 1.2 Zeta potential

The streaming zeta potential of the membranes was determined in 1 mM NaCl using a SurPASS 3 electrokinetic analyser (Anton Paar, Austria). The streaming potential was converted to zeta potential using the Helmholtz–Smoluchowski relation:

$$Zeta\ Potential = \frac{dU}{d\Delta P} \cdot \frac{\eta}{\varepsilon_0 \varepsilon_r} \cdot \frac{L}{A} \cdot \frac{1}{R} \tag{S1}$$

where $U$ corresponds to the measured streaming potential generated across the channel, while $\Delta P$ is the applied pressure difference driving the flow. The term $\eta$ denotes the electrolyte viscosity, and $\varepsilon_0 \varepsilon_r$ reflects its permittivity. The geometry of the streaming channel is described by its length $L$ and cross-sectional area $A$, and $R$ represents the electrical resistance of the channel during the measurement.

**Table S1:** Mean ± standard deviation zeta-potential values measured at pH ≈ 6.5 for membranes prepared with AEP or DAP at different monomer concentrations.

| Membrane | Zeta Potential (mV) | Membrane | Zeta Potential (mV) |
|---|---|---|---|
| DAP0.05 | -26.3 ± 1.0 | AEP0.1 | -28.4 ± 0.3 |
| DAP0.075 | -27.6 ± 0.9 | AEP0.3 | -20.4 ± 1.6 |
| DAP0.1 | -19.3 ± 0.6 | AEP0.5 | -14.3 ± 2.2 |
| DAP0.3 | -30.7 ± 0.9 | AEP0.7 | -15.7 ± 1.3 |
| DAP0.5 | -7.2 ± 0.5 | AEP1.0 | -14.0 ± 1.2 |

# 2 Retention tests

## 2.1 Single salts

**Table S2:** Comparison of performance of reported nanofiltration membranes for $Na^+/Mg^{2+}$ separation in single-salt systems.

| Membrane | $R_{NaCl}$ (%) | $R_{MgCl_2}$ (%) | Ideal selectivity $Na^+/Mg^{2+}$ | Permeance $(L/MPa/h/m^2)$ | Reference |
|---|---|---|---|---|---|
| PEI-TMC | 34.0 | 90.4 | 6.9 | 53.9[1] | [1] |
| DABIL-5 | 19.0 | 94.6 | 15.0 | 371.2[1] | [1] |
| LBL*1.5C | 33.5 | 98.2 | 36.9 | 125.0 | [2] |
| SARIP TFC NF | 27.0 | 95.0 | 14.6 | 171.0[1] | [3] |
| [PAH/DA/PSS]4 | 27.9 | 94.8 | 13.9 | 219.0[1] | [4] |
| NF-PD | 40.0 | 7.0 | 0.6 | 117.9[1] | [5] |
| PES-50-3L | 32.0 | 53.9 | 1.5 | 129.0[1] | [6] |
| QAPPESK NF | 31.0 | 84.0 | 4.3 | 122.5[1] | [7] |
| PPO AM10 | 36.0 | 73.0 | 2.4 | 180.0[1] | [8] |
| QBPD | 52.9 | 91.2 | 5.4 | 161.0[1] | [9] |
| MPQ | 22.0 | 88.2 | 6.6 | 128.9[1] | [10] |
| CTS/TGIC/PESU | 51.0 | 92.0 | 6.1 | 79.8[1] | [11] |
| PVC-g-PDMA | 70.0 | 93.1 | 4.3 | 93.0[1] | [12] |
| MWCNT/chitosan | 45.0 | 92.0 | 6.9 | 7.5[1] | [13] |
| CTS/PDMCHEA | 57.1 | 97.5 | 17.2 | 34.3[1] | [14] |
| HACC/PAN NF-1 | 60.6 | 94.8 | 7.6 | 13.6[1] | [15] |
| HACC/PAN NF-2 | 69.7 | 95.8 | 7.2 | 7.0[1] | [15] |
| GCTACC/PAN | 62.6 | 94.5 | 6.8 | 14.1[1] | [16] |
| PDMAEMA/PSF | 77.8 | 98.0 | 11.1 | 11.1[1] | [17] |
| NF-IL-2.0% | 30.1 | 83.8 | 4.3 | 63.0[1] | [18] |
| PIP-TMC-AMIB | 20.8 | 58.0 | 1.9 | 25.0[1] | [19] |
| B0M72 | 39.7 | 91.0 | 6.7 | 35.8[1] | [20] |
| B5M72 | 60.0 | 91.7 | 4.8 | 85.3[1] | [20] |
| B7M72 | 40.7 | 74.8 | 2.4 | 235.0[1] | [20] |
| B10M72 | 31.9 | 59.2 | 1.7 | 1176.2[1] | [20] |
| PEI-TMC-M1 | 60.2 | 85.7 | 2.8 | 20.5[1] | [21] |

*Continued on next page*

[1] from pure water flux

*Table S2 – continued from previous page*

| Membrane | $R_{NaCl}$ (%) | $R_{MgCl_2}$ (%) | Ideal selectivity $Na^+/Mg^{2+}$ | Permeance $(L/MPa/h/m^2)$ | Reference |
|---|---|---|---|---|---|
| PEI-TMC-M2 | 63.2 | 88.6 | 3.2 | 20.5[1] | [21] |
| PEI-TMC-M3 | 71.3 | 96.6 | 8.5 | 18.8[1] | [21] |
| PEI-TMC-M4 | 65.9 | 96.8 | 10.7 | 22.1[1] | [21] |
| PEI-TMC | 36.9 | 94.8 | 12.1 | 50.2[1] | [21] |
| AEP-I | 17.4 | 20.5 | 1.0 | 285.0[2] | [22] |
| AEP-H | 19.5 | 22.0 | 1.0 | 189.0[2] | [22] |
| AEP-O | 16.9 | 29.7 | 1.2 | 57.0[2] | [22] |
| AEP/TMC=240 | 35.2 | 93.5 | 10.0 | 78.0[1] | [23] |
| AEP/TMC=15 | 34.1 | 83.7 | 4.0 | 82.0[1] | [23] |
| DAPP-TMC | 23.0 | 70.4 | 2.6 | 27.3[2] | [24] |
| PEI/AEP-TMC | 36.9 | 95.8 | 15.0 | 112.0[1] | [25] |
| AEP-TMC | 32.7 | 34.4 | 1.0 | 48.0[1] | [25] |
| PEI-TMC | 30.8 | 86.9 | 5.3 | 57.0[1] | [25] |
| PIP0.125TMC0.15 | 37.1 | 24.2 | 0.8 | 129.9[1] | [26] |
| PIP0.125TMC0.30 | 39.4 | 24.1 | 0.8 | 127.7[1] | [26] |
| PIP0.25TMC0.15 | 30.7 | 38.2 | 1.1 | 138.9[1] | [26] |
| PIP0.25TMC0.30 | 31.2 | 15.4 | 0.8 | 155.8[1] | [26] |
| PIP0.5TMC0.15 | 24.0 | 52.8 | 1.6 | 146.4[1] | [26] |
| PIP0.5TMC0.30 | 20.2 | 26.2 | 1.1 | 206.7[1] | [26] |
| PIP0.75TMC0.15 | 27.8 | 50.3 | 1.5 | 132.3[1] | [26] |
| PIP0.75TMC0.30 | 23.2 | 44.1 | 1.4 | 201.2[1] | [26] |
| PIP1TMC0.15 | 37.4 | 95.0 | 12.4 | 102.8[1] | [26] |
| PIP1TMC0.30 | 27.2 | 87.6 | 5.9 | 162.7[1] | [26] |
| Commercial | - | - | 0.9 | 14.2[1] | [26] |
| Commercial | - | - | 0.8 | 12.4[1] | [26] |
| Commercial | - | - | 0.6 | 13.2[1] | [26] |
| Commercial | - | - | 0.4 | 14.7[1] | [26] |
| Commercial | - | - | 0.5 | 20.8[1] | [26] |
| Commercial | - | - | 0.5 | 9.6[1] | [26] |

*Continued on next page*

[2]from NaCl solution flux

*Table S2 – continued from previous page*

| **Membrane** | **$R_{NaCl}$** (%) | **$R_{MgCl_2}$** (%) | **Ideal selectivity $Na^+/Mg^{2+}$** | **Permeance** $(L/MPa/h/m^2)$ | **Reference** |
|---|---|---|---|---|---|
| Commercial | - | - | 0.4 | 5.5[1] | [26] |
| Commercial | - | - | 0.6 | 2.1[1] | [26] |
| Commercial | - | - | 0.7 | 9.5[1] | [26] |
| AEP0.1 | 27.6 | 47.8 | 1.4 | 42.3[1] | This work |
| AEP0.3 | 35.7 | 97.1 | 21.9 | 58.2[1] | This work |
| AEP0.5 | 45.6 | 98.0 | 27.4 | 61.6[1] | This work |
| AEP0.7 | 54.7 | 99.0 | 44.9 | 56.1[1] | This work |
| AEP1.0 | 80.4 | 99.8 | 79.6 | 23.2[1] | This work |
| DAP0.05 | 2.7 | 3.0 | 1.0 | 80.8[1] | This work |
| DAP0.075 | 11.8 | 37.1 | 1.4 | 61.5[1] | This work |
| DAP0.1 | 59.1 | 96.8 | 12.7 | 29.6[1] | This work |
| DAP0.3 | 82.5 | 98.9 | 15.5 | 18.6[1] | This work |
| DAP0.5 | 85.8 | 99.3 | 18.7 | 9.1[1] | This work |

## 2.2 Mixed salts

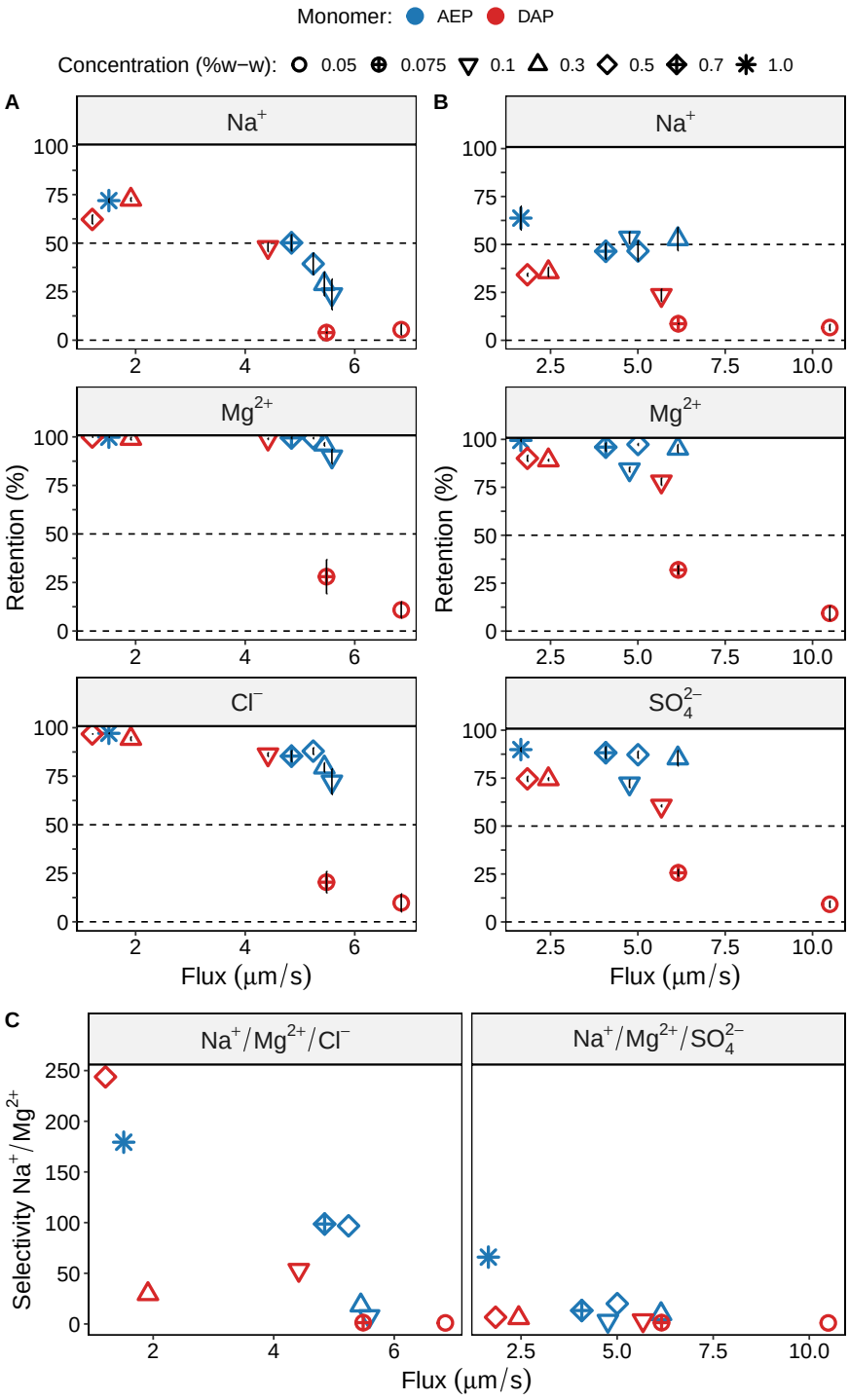



**Fig. S2:** Mixed-salt retention performance of the fabricated membranes. Ion retention as a function of solution flux: (A) $Na^+/Mg^{2+}/Cl^-$ system, (B) $Na^+/Mg^{2+}/SO_4^{2-}$ system. (C) $Na^+/Mg^{2+}$ selectivity vs. solution flux.

**Table S3:** Comparison of performance of reported nanofiltration membranes for $Na^+/Mg^{2+}$ separation in mixed-salt systems.

| **Membrane** | $\mathbf{R_{Na^+}}$ (%) | $\mathbf{R_{Mg^{2+}}}$ (%) | **Real selectivity** $\mathbf{Na^+/Mg^{2+}}$ | **Flux** $(\mu\mathbf{m/s})$ | **Reference** |
|---|---|---|---|---|---|
| A, [PSS/PAH]4PSS | -35.0 | 82.3 | 7.6 | 6.0 | [27] |
| B, [PSS/PAH]4 | -27.0 | 88.6 | 11.1 | 4.4 | [27] |
| C, [PSS/PAH]4 | -20.0 | 87.8 | 9.8 | 4.4 | [27] |
| D, [PSS/PAH]4 | -13.0 | 92.0 | 14.1 | 3.8 | [27] |
| E, [PSS/PAH]4 | -9.0 | 92.0 | 13.6 | 6.5 | [27] |
| F, [PSS/PAH]4 | -20.0 | 94.1 | 20.3 | 6.0 | [27] |
| G, [PSS/PAH]4 | -13.0 | 92.4 | 14.9 | 5.8 | [27] |
| H, [PSS/PAH]4 | -13.0 | 89.8 | 11.1 | 6.4 | [27] |
| I, [PSS/PAH]3 | -17.0 | 83.5 | 7.1 | 8.3 | [27] |
| J, [PSS/PAH]4 | -3.0 | 92.5 | 13.7 | 12.2 | [27] |
| K, [PSS/PAH]4 | -11.0 | 95.0 | 22.2 | 9.8 | [27] |
| LBL-C | -7.6 | 99.1 | 119.6 | 3.3 | [28] |
| Modified GK membrane | 4.0 | 64.0 | 2.7 | 3.1 | [29] |
| NF-C | 34.2 | 70.3 | 2.2 | 1.8 | [30] |
| NF-0 | 22.2 | 63.9 | 2.2 | 1.6 | [30] |
| Composite NF hollow fiber | 26.6 | 94.9 | 14.4 | 5.9 | [31] |
| 1TA-4.5Fe | 15.6 | 12.8 | 1.0 | 8.5 | [32] |
| 1TA-5Fe | 17.4 | 32.0 | 1.2 | 4.6 | [32] |
| 1TA-6Fe | 30.6 | 66.1 | 2.0 | 1.7 | [32] |
| 1TA-8Fe | 36.9 | 79.6 | 3.1 | 1.2 | [32] |
| PIP0.125TMC0.15 | 5.5 | 37.3 | 1.5 | 9.4 | [26] |
| PIP0.125TMC0.30 | 12.1 | 25.2 | 1.2 | 10.3 | [26] |
| PIP0.25TMC0.15 | 0.5 | 47.2 | 1.9 | 9.7 | [26] |
| PIP0.25TMC0.30 | 2.5 | 36.6 | 1.5 | 14.2 | [26] |
| PIP0.5TMC0.15 | -3.7 | 38.9 | 1.7 | 12.4 | [26] |
| PIP0.5TMC0.30 | -4.6 | 40.1 | 1.7 | 21.2 | [26] |
| PIP0.75TMC0.15 | -10.4 | 74.7 | 4.4 | 8.9 | [26] |
| PIP0.75TMC0.30 | -9.6 | 61.3 | 2.8 | 12.5 | [26] |
| PIP1TMC0.15 | 5.8 | 95.0 | 18.8 | 6.3 | [26] |
| PIP1TMC0.30 | -19.6 | 85.8 | 8.4 | 10.7 | [26] |

*Continued on next page*

*Table S3 – continued from previous page*

| Membrane | $R_{Na^+}$ (%) | $R_{Mg^{2+}}$ (%) | Real selectivity $Na^+/Mg^{2+}$ | Flux $(\mu m/s)$ | Reference |
|---|---|---|---|---|---|
| AEP0.1 | 23.6 | 89.8 | 7.5 | 5.6 | This work |
| AEP0.3 | 29.0 | 96.1 | 18.4 | 5.4 | This work |
| AEP0.5 | 39.3 | 99.4 | 96.8 | 5.2 | This work |
| AEP0.7 | 50.2 | 99.5 | 98.6 | 4.8 | This work |
| AEP1.0 | 71.9 | 99.8 | 179.3 | 1.5 | This work |
| DAP0.05 | 5.4 | 10.9 | 1.1 | 6.8 | This work |
| DAP0.075 | 3.9 | 28.0 | 1.3 | 5.5 | This work |
| DAP0.1 | 47.9 | 99.0 | 53.2 | 4.4 | This work |
| DAP0.3 | 72.5 | 99.1 | 29.6 | 1.9 | This work |
| DAP0.5 | 62.2 | 99.8 | 243.8 | 1.2 | This work |

# 3 DSPM-DE model

## 3.1 Equations

The DSPM-DE model describes the transport of ionic species from the feed towards the permeate side under a series of coupled assumptions. In this section, we outline the governing equations of the model together with their linearized counterparts, which were used to solve the system [33] [34].

### Feed-solution domain

The molar flux of each species $i$ across a boundary layer next to the feed-solution/membrane interface is given by [35]:

$$J_i = -k_{c,i}^{\bullet}\left(c_{i,m} - c_{i,f}\right) + J_v c_{i,m} - z_i c_{i,m} D_{i,\infty}\frac{F}{RT}\xi \tag{S2}$$

where $c_{i,m}$ and $c_{i,f}$ are the concentration of ion $i$ in the feed-solution/membrane interface and concentration of ion i in the feed solution, respectively; $z_i$ is the valence of ion $i$; $\xi$ is the electrical potential gradient at the feed-solution/membrane interface. Other constants or parameters are: the Faraday constant, $F$; the ideal gas constant, $R$; the temperature, $T$; the diffusion coefficient of species $i$ in the bulk, $D_{i,\infty}$. The corrected mass transport coefficient, $k_{c,i}^{\bullet}$, is computed by taking into account the solution flux, $J_v$, as follows:

$$k_{c,i}^{\bullet} = k_{c,i}\left(\frac{J_v}{k_{c,i}} + \left(1 + 0.26\left(\frac{J_v}{k_{c,i}}\right)^{1.4}\right)^{-1.7}\right) \tag{S3}$$

where $k_{c,i}$ is calculated by:

$$k_{c,i} = \frac{0.23 Re^{0.567} Sc^{0.33} D_{i,\infty}}{L} \tag{S4}$$

Electroneutrality condition in the given by:

$$\sum_{i=1}^{N_c} z_i c_{i,m} = 0 \tag{S5}$$

The exclusion or partitioning expression at the feed-solution/membrane interface is:

$$c_{i,1}\gamma_{i,1} = c_{i,m}\gamma_{i,m}\Phi_{S,i}\Phi_{D,i}^{x=0}\Phi_{DE,i} \tag{S6}$$

where $c_{i,1}$ is the concentration of ion i at the pore entrance on the feed side; $\gamma_{i,1}$ and $\gamma_{i,m}$ are the activity coefficients of ion $i$ at the pore entrance on the feed side and in the feed-solution/membrane interface, respectively. For ion $i$, $\Phi_{S,i}$ is the steric exclusion coefficient, $\Phi_{DE,i}$ the dielectric exclusion coefficient, and $\Phi_{D,i}^{x=0}$ the Donnan exclusion coefficient of ion $i$ at the pore entrance on the feed side.

$\gamma_i$ is calculated by:

$$\ln(\gamma_i) = -A \cdot z_i \left( \frac{\sqrt{I}}{1+\sqrt{I}} - 0.3I \right) \tag{S7}$$

The ionic strength, $I$, and the temperature dependent correction factor for the activity coefficient, $A$, are given by:

$$I = 0.5 \sum_{i=1}^{Nc} z_i^2 c_i \tag{S8}$$

$$A = \frac{e_0^3 \sqrt{N_A}}{\ln(10) 4\pi \sqrt{2\varepsilon_0^3 \varepsilon_r^3 k_B^3 T^3}} \tag{S9}$$

The steric partitioning coefficient is:

$$\Phi_{S,i} = (1-\lambda_i)^2 \tag{S10}$$

$$\lambda_i = \frac{r_i}{r_{pore}} \tag{S11}$$

with $r_i$ is the Stokes radius of species $i$.

The Donnan exclusion coefficient is computed with the Donnan potential across the feed-solution/membrane interface, $\Delta\Psi_{D,f}$:

$$\Phi_{D,i}^{x=0} = exp\left( \frac{-z_i F}{RT} \Delta\Psi_{D,f} \right) \tag{S12}$$

Based on the Born model, the dielectric coefficient is computed with the values of the dielectric constant inside the pores, $\varepsilon_{pore}$, and in the bulk solution, $\varepsilon_{bulk}$:

$$\Phi_{DE,i} = exp\left( -\frac{z_i^2 e_0^2}{8\pi\varepsilon_0 r_i k_B T} \left( \frac{1}{\varepsilon_{bulk}} - \frac{1}{\varepsilon_{pore}} \right) \right) \tag{S13}$$

## Membrane active layer

The Extended Nernst-Planck Equation of each component, $i$, is:

$$J_i = J_v c_{i,p} = -K_{i,d} D_{i,\infty} \frac{dc_i}{dx} - \frac{z_i F c_i K_{i,d} D_{i,\infty}}{RT} \frac{d\Psi}{dx} + K_{i,a} c_i J_v \tag{S14}$$

where $K_{i,d}$ is the hindrance factor of diffusion; $c_i$ is the concentration of species $i$ in the membrane active layer; $x$ is the coordinate in the direction across the membrane active layer from the feed towards the permeate side; $\Psi$ is the electrical potential inside the membrane active layer; and $K_{i,a}$ is the hindrance factor of advection.

The hindrance factors of advection and diffusion are given by:

$$K_{i,a} = \frac{1 + 3.867\lambda_i - 1.907\lambda_i^2 - 0.834\lambda_i^3}{1 + 1.867\lambda_i - 0.741\lambda_i^2} \tag{S15}$$

$$K_{i,d} = \begin{cases} \dfrac{\begin{bmatrix} 1 + \frac{9}{8}\lambda_i \ln(\lambda_i) - 1.56034\lambda_i \\ +0.528155\lambda_i^2 + 1.91521\lambda_i^3 - 2.81903\lambda_i^4 \\ +0.270788\lambda_i^5 + 1.10115\lambda_i^6 - 0.435933\lambda_i^7 \end{bmatrix}}{(1-\lambda_i)^2}, & \text{if } \lambda_i \leq 0.95. \\ 0.984 \left(\frac{1-\lambda_i}{\lambda_i}\right)^{2.5}, & \text{if } \lambda_i > 0.95. \end{cases} \tag{S16}$$

Electroneutrality condition is maintained inside the membrane active layer between the membrane charge density, $c_x$, and the ionic species:

$$\sum_{i=1}^{N_c} z_i c_i = -c_x \tag{S17}$$

## Permeate-solution domain

Similar to the feed-solution/membrane interface, the exclusion or partitioning at the membrane/permeate-solution interface is:

$$c_{i,N}\gamma_{i,N} = c_{i,p}\gamma_{i,p}\Phi_{S,i}\Phi_{D,i}^{x=\Delta x_e}\Phi_{DE,i} \tag{S18}$$

where $\Phi_{D,i}^{x=\Delta x_e}$ is the Donnan exclusion coefficient of ion $i$ at the pore exit on the permeate side. $c_{i,N}$ and $c_{i,p}$ are the concentration of species $i$ at the pore exit and the permeate solution with their corresponding activity coefficients $\gamma_{i,N}$ and $\gamma_{i,p}$, respectively.

On the permeate solution electroneutrality condition is expressed:

$$\sum_{i=1}^{N_c} z_i c_{i,p} = 0 \tag{S19}$$

## 3.2 Linearized and discretized equations

To solve the system of equations derived from the DSPM-DE model, linearized and discretized formulations were developed. The resulting system was solved iteratively in Python using the Linear Algebra Package (LAPACK) available in the NumPy library. In each iteration, the linear coefficients (enclosed in brackets) were updated, and the system of linear equations was re-solved until the residuals fell below $10^{-4}$. Variables denoted with a superscript $*$ correspond to values from the previous iteration, which in the first iteration represent the initial guess. The iterative procedure yields the electrical potential and ionic concentration at each discretized node, providing the complete concentration and potential profiles across the membrane's active layer [34].

**Table S4:** Linearized and discretized forms of governing equations grouped by domain.

| Linearized & discretized equation | Original equation |
|---|---|
| **Feed solution domain** | |
| $[k_{c,i}^{\bullet} - J_v]c_{i,m} + [J_v]c_{i,p} + [z_i c_{i,m} D_{i,\infty} \frac{F}{RT}]\xi = [c_{i,f} k_{c,i}^{\bullet}]$ | Eq. (S2) |
| $\sum_{i=1}^{N_{ions}} [z_i]c_{i,m} = 0$ | Eq. (S5) |
| **Membrane active layer** | |
| (a) $[A_{i,n}]c_{i,n} + [B_{i,n}]c_{i,n+1} + [C_{i,n}]\Psi_n + [D_{i,n}]\Psi_{n+1} + [E_{i,n}]c_{i,p} = F_{i,n}$<br>(b) $[A_{i,n}] = \frac{K_{i,d}D_{i,\infty}}{\delta x_n} + \frac{z_i F K_{i,d} D_{i,\infty}}{RT} \frac{\Psi_{n+1}^* - \Psi_n^*}{2\delta x_n} + \frac{K_{i,a}J_v}{2}$<br>(c) $[B_{i,n}] = -\frac{K_{i,d}D_{i,\infty}}{\delta x_n} + \frac{z_i F K_{i,d} D_{i,\infty}}{RT} \frac{\Psi_{n+1}^* - \Psi_n^*}{2\delta x_n} + \frac{K_{i,a}J_v}{2}$<br>(d) $[C_{i,n}] = \frac{z_i F K_{i,d} D_{i,\infty}}{RT} \frac{c_{i,n+1}^* + c_{i,n}^*}{2\delta x_n}$<br>(e) $[D_{i,n}] = -\frac{z_i F K_{i,d} D_{i,\infty}}{RT} \frac{c_{i,n+1}^* + c_{i,n}^*}{2\delta x_n}$<br>(f) $[E_{i,n}] = -J_v$<br>(g) $[F_{i,n}] = -\frac{z_i F K_{i,d} D_{i,\infty}}{RT} \frac{c_{i,n+1}^* + c_{i,n}^*}{2} \frac{\Psi_{n+1}^* - \Psi_n^*}{\delta x_n}$ | Eq. (S14) |
| $\sum_{i=1}^{N_{ions}} [z_i]c_{i,n} = [-c_x]$ | Eq. (S17) |
| **Permeate solution domain** | |
| $[\gamma_{i,N}^*]c_{i,N} - [\gamma_{i,p}^* \Phi_{S,i} \Phi_{DE,i} \exp\left(z_i \frac{F}{RT}\left(\Psi_p^* - \Psi_N^*\right)\right)]c_{i,p} +$<br>$[\gamma_{i,p}^* c_{i,p}^* z_i \frac{F}{RT} \Phi_{S,i} \Phi_{DE,i} \exp\left(z_i \frac{F}{RT}\left(\Psi_p^* - \Psi_N^*\right)\right)]\Psi_N -$<br>$[\gamma_{i,p}^* c_{i,p}^* z_i \frac{F}{RT} \Phi_{S,i} \Phi_{DE,i} \exp\left(z_i \frac{F}{RT}\left(\Psi_p^* - \Psi_N^*\right)\right)]\Psi_p =$<br>$-\left[\gamma_{i,p}^* c_{i,p}^* z_i \frac{F}{RT} \Phi_{S,i} \Phi_{DE,i} \exp\left(z_i \frac{F}{RT}\left(\Psi_p^* - \Psi_N^*\right)\right)\left(z_i \frac{F}{RT}\left(\Psi_p^* - \Psi_N^*\right)\right)\right]$ | Eq. (S18) |
| $\sum_{i=1}^{N_{ions}} [z_i]c_{i,p} = 0$ | Eq. (S19) |

## 3.3 Fitting

### $r_{pore}$ and $\Delta x_e$

The effective pore radius ($r_{\text{pore}}$) and the thickness-to-porosity ratio ($\Delta x_e$) were obtained by fitting retention data from PEG 200 filtration experiments performed over a range of solvent velocities.These two parameters are key descriptors of membrane structure in the DSPM-DE model: $r_{\text{pore}}$ determines steric hindrance and confinement effects that control solute partitioning, while $\Delta x_e$ quantifies the hydraulic resistance of the active layer. Together, they enable a mechanistic description of size-dependent transport and its coupling with electrostatic and dielectric exclusion phenomena. The experimental procedure and data treatment used for their determination follow the methodology described in our earlier works [26], [36]. The fitted values for the membranes investigated in this study are summarized in Fig S3

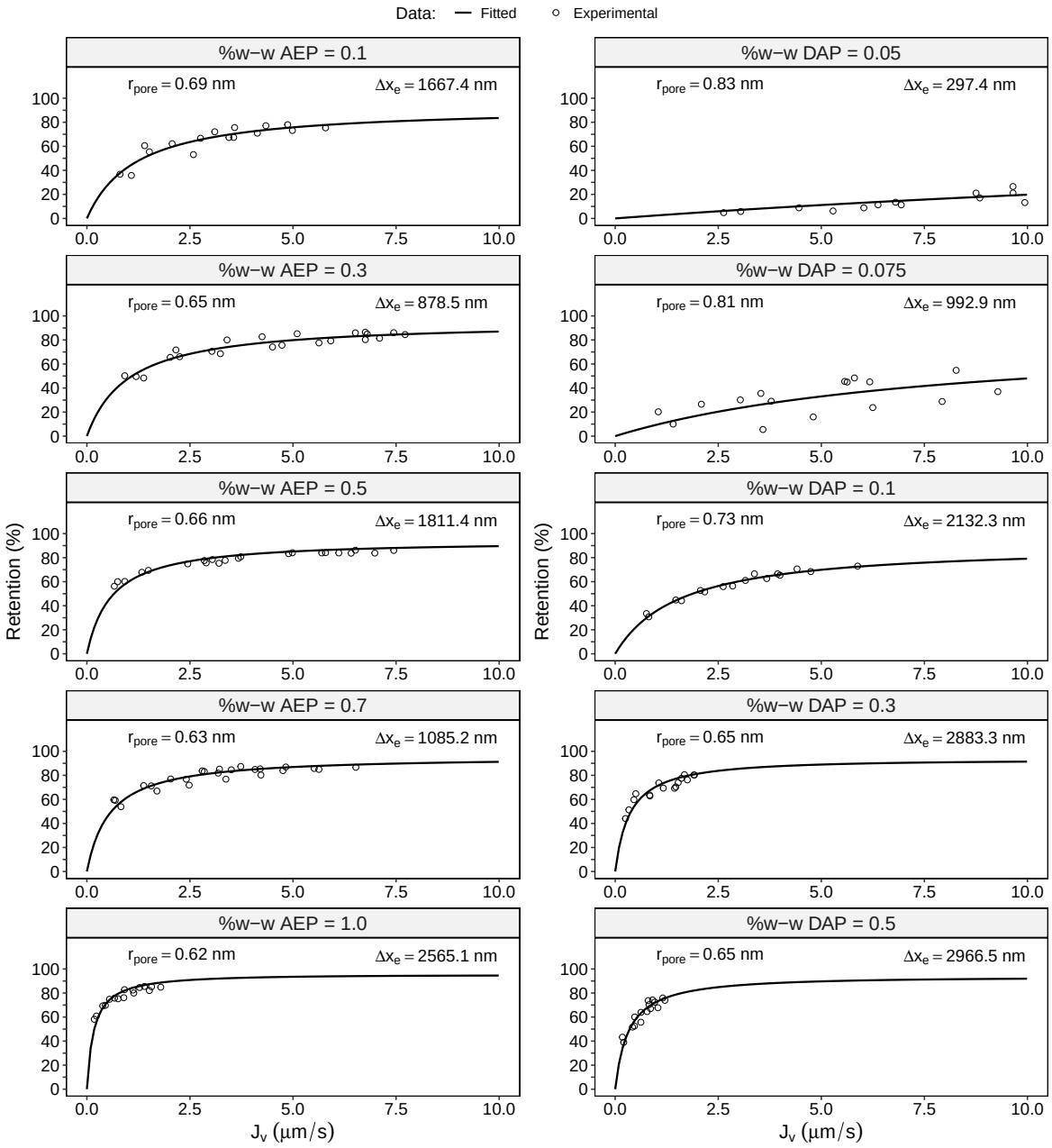



**Fig. S3:** Fitted vs. Experimental PEG 200 retention tests results for the fabricated membranes with the optimized values of $r_{pore}$ and $\Delta x_e$.

### $\varepsilon^*$ and $c_x$

For parameter estimation within the DSPM-DE framework, we assumed that the fitted single-layer dielectric constant ($\varepsilon^*$) was constant for all membranes prepared with a given aqueous-phase monomer (AEP or DAP) and ionic system ($Na^+/Mg^{2+}/Cl^-$ or $Na^+/Mg^{2+}/SO_4^{2-}$). Four independent fitting procedures were therefore conducted: one for each monomer-ionic system combination. In the first step, a range of trial $\varepsilon^*$ values was tested to obtain preliminary estimates of the membrane charge density ($c_x$) for each membrane, by minimizing the squared difference between the experimental ion retentions $\left(R_{i,j}^{exp}\right)$ and those calculated by the model $\left(R_{i,j}^{mod}\right)$. In the second step, $\varepsilon^*$ was determined by minimizing the cumulative squared deviations across all membranes prepared with the same aqueous-phase monomer. For each ionic system, the minimization function is given by:

$$f_{min} = \underset{\varepsilon^*}{\text{argmin}} \sum_{j=1}^{N_{AEP/DAP}} \left( \underset{c_x}{\text{argmin}} \sum_{i=1}^{N_{ions}} \frac{\left(R_{i,j}^{mod} - R_{i,j}^{exp}\right)^2}{\sigma_{i,j}^2} \right) \tag{S20}$$

Here, the subscript $i$ indexes the ionic species, while $j$ denotes the aqueous-phase monomer concentration used to fabricate membranes of the same chemistry (AEP or DAP). Experimental retentions represent the mean of at least three replicate measurements for each membrane. To weight the minimization toward values with higher experimental confidence, the variance $\sigma_{i,j}^2$ was calculated using the unbiased estimator and incorporated into the objective function. In the second step, $\varepsilon^*$ was determined by minimizing the sum of these weighted squared deviations across all membranes prepared with the same aqueous-phase monomer.

Fig. S4A and S5A show the optimized values of $\varepsilon^*$ for AEP and DAP membranes for both ionic systems. Using this procedure, a unique set of DSPM-DE input parameters was obtained for each IP reaction condition and for each ionic system, enabling simulation of the retention performance of the fabricated membranes under two different electrolyte environments. The close agreement between simulated and experimental retentions (Fig. S4B and S5B) confirms that the fitted parameters capture the key physicochemical characteristics governing ion transport, thereby supporting the reliability of our mechanistic analysis.

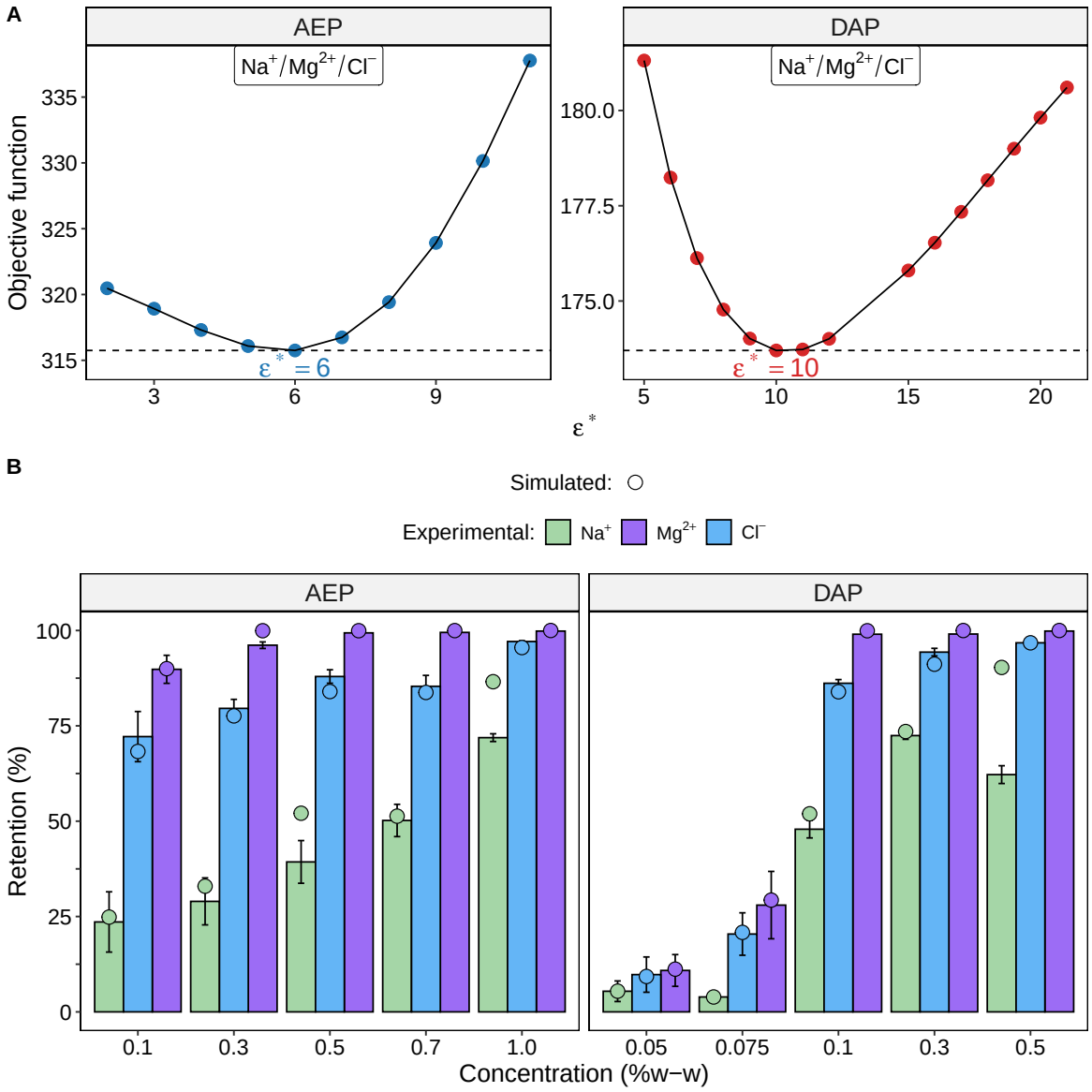



**Fig. S4:** Results of the fitting procedure with the ternary ion mixture $Na^+/Mg^{2+}/Cl^-$ (A) Minimization function to determine $\varepsilon^*$.(B) Simulated and experimental retention tests for the fabricated membranes using AEP and DAP monomers.

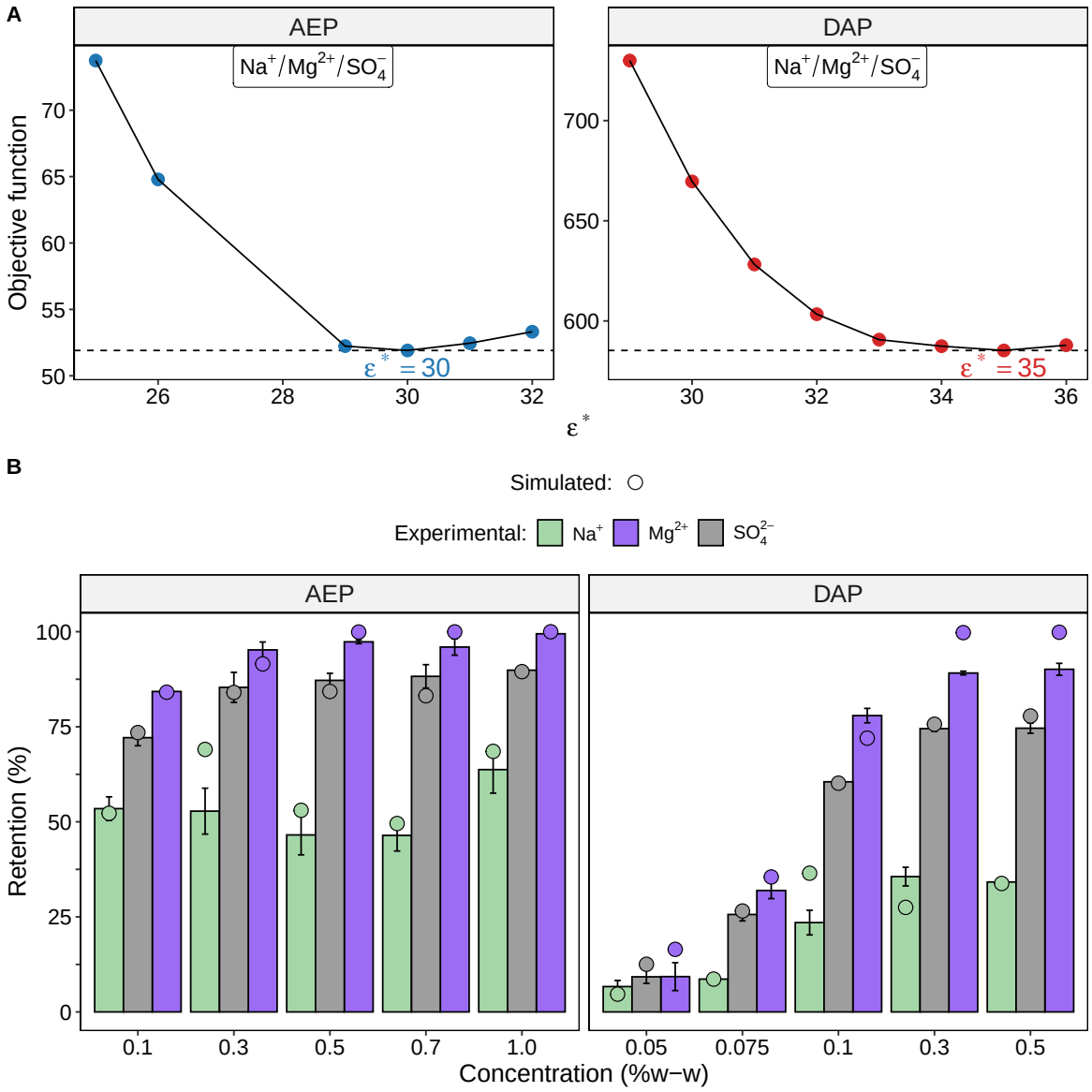



**Fig. S5:** Results of the fitting procedure with the ternary ion mixture $Na^+/Mg^{2+}/SO_4^{2-}$ (A) Minimization function to determine $\varepsilon^*$.(B) Simulated and experimental retention tests for the fabricated membranes using AEP and DAP monomers.

# 4 Mass transport modelling

## 4.1 Exclusion phenomena

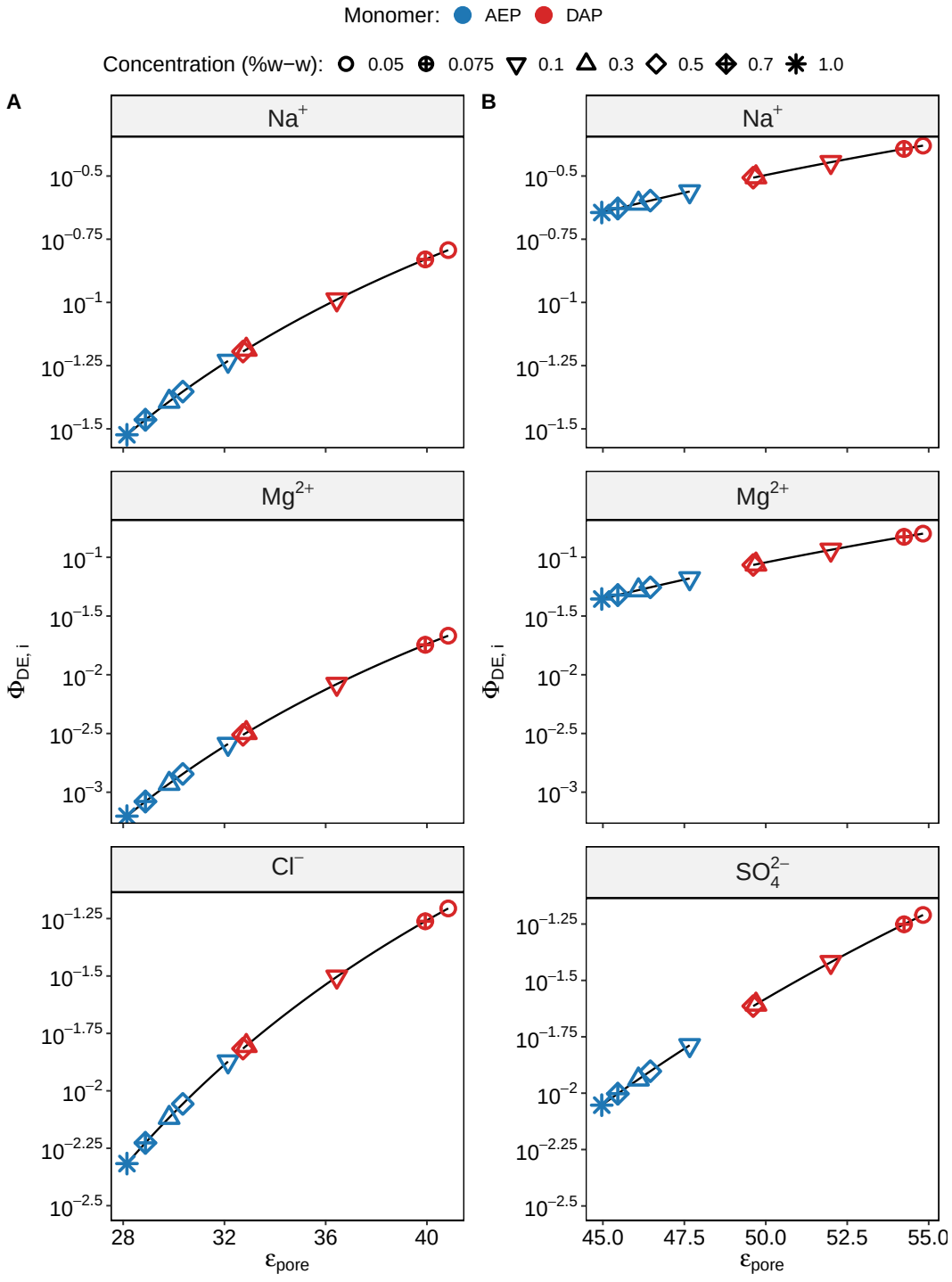



**Fig. S6:** Dielectric exclusion or partitioning coefficients ($\Phi_{DE,i}$) vs. pore dielectric constant ($\varepsilon_{pore}$) of the ternary ionic mixtures: (A) $Na^+/Mg^{2+}/Cl^-$ (B) $Na^+/Mg^{2+}/SO_4^{2-}$. Each shape of the data points corresponds to a different aqueous-phase monomer concentration, and the color of the data points indicates the aqueous-phase monomer (blue for AEP and red for DAP).

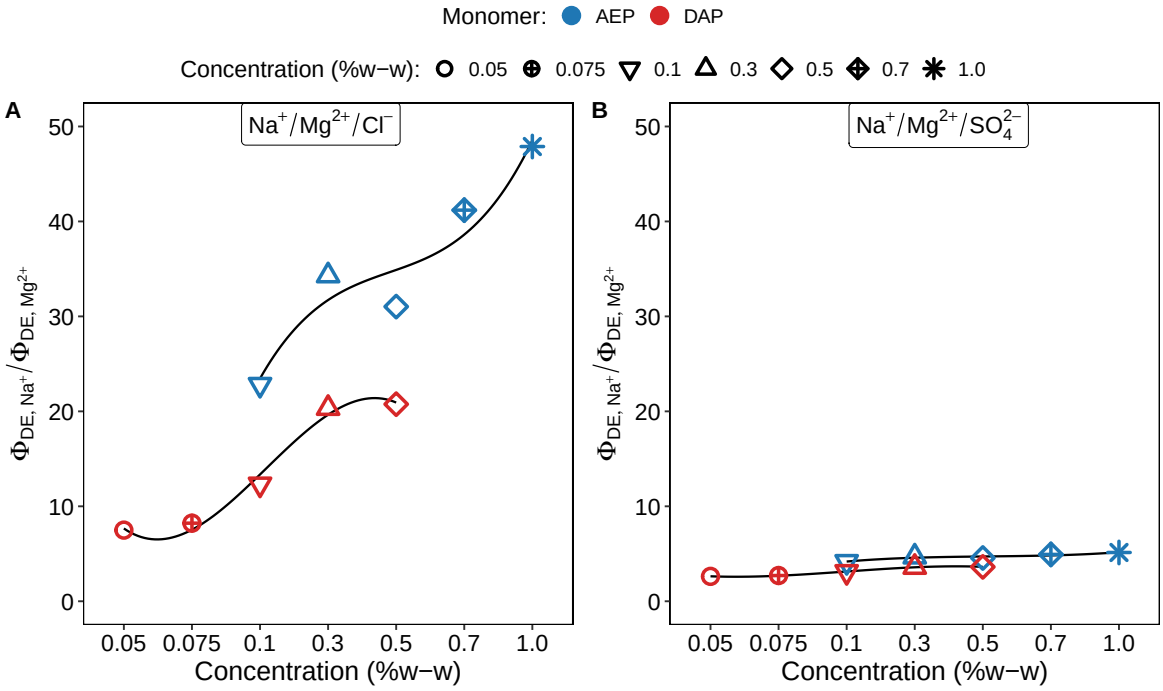



**Fig. S7:** $Na^+/Mg^{2+}$ ratio of dielectric exclusion coefficients ($\Phi_{DE,Na^+}/\Phi_{DE,Mg^{2+}}$) vs. aqueous-phase monomer concentration of the ternary ionic mixtures: (A) $Na^+/Mg^{2+}/Cl^-$ (B) $Na^+/Mg^{2+}/SO_4^{2-}$. Each shape of the data points corresponds to a different aqueous-phase monomer concentration, and the color of the data points indicates the aqueous-phase monomer (blue for AEP and red for DAP).

## 4.2 Transmembrane molar transport

### Diffusive transport

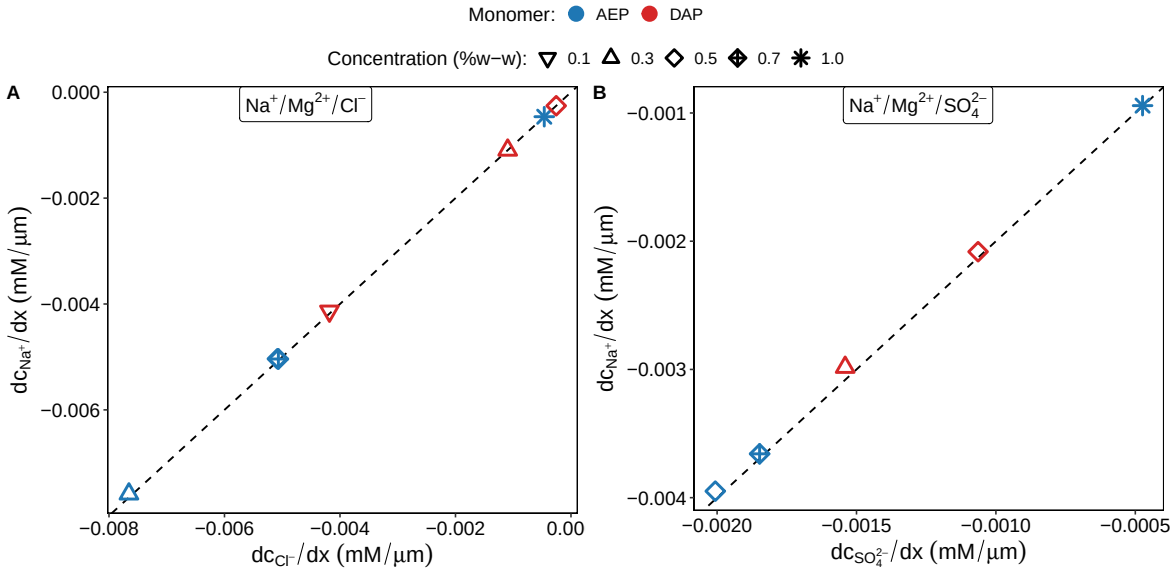



**Fig. S8:** Concentration gradients of $Na^+$ and its corresponding anion within the active layer of positively charged membranes for the ternary ionic mixtures: (A) $Na^+/Mg^{2+}/Cl^-$ and (B) $Na^+/Mg^{2+}/SO_4^{2-}$. Each shape of the data points corresponds to a different aqueous-phase monomer concentration, and the color of the data points indicates the aqueous-phase monomer (blue for AEP and red for DAP). In (A), the dashed line ($y = x$) represents equal concentration gradients for $Na^+$ and the corresponding anion, serving as a reference for assessing gradient coupling. In (B), the dashed line ($y = 2x$) represents the stoichiometric ratio of concentration gradients expected for a divalent counter-anion ($SO_4^{2-}$) relative to $Na^+$ under electroneutrality conditions.

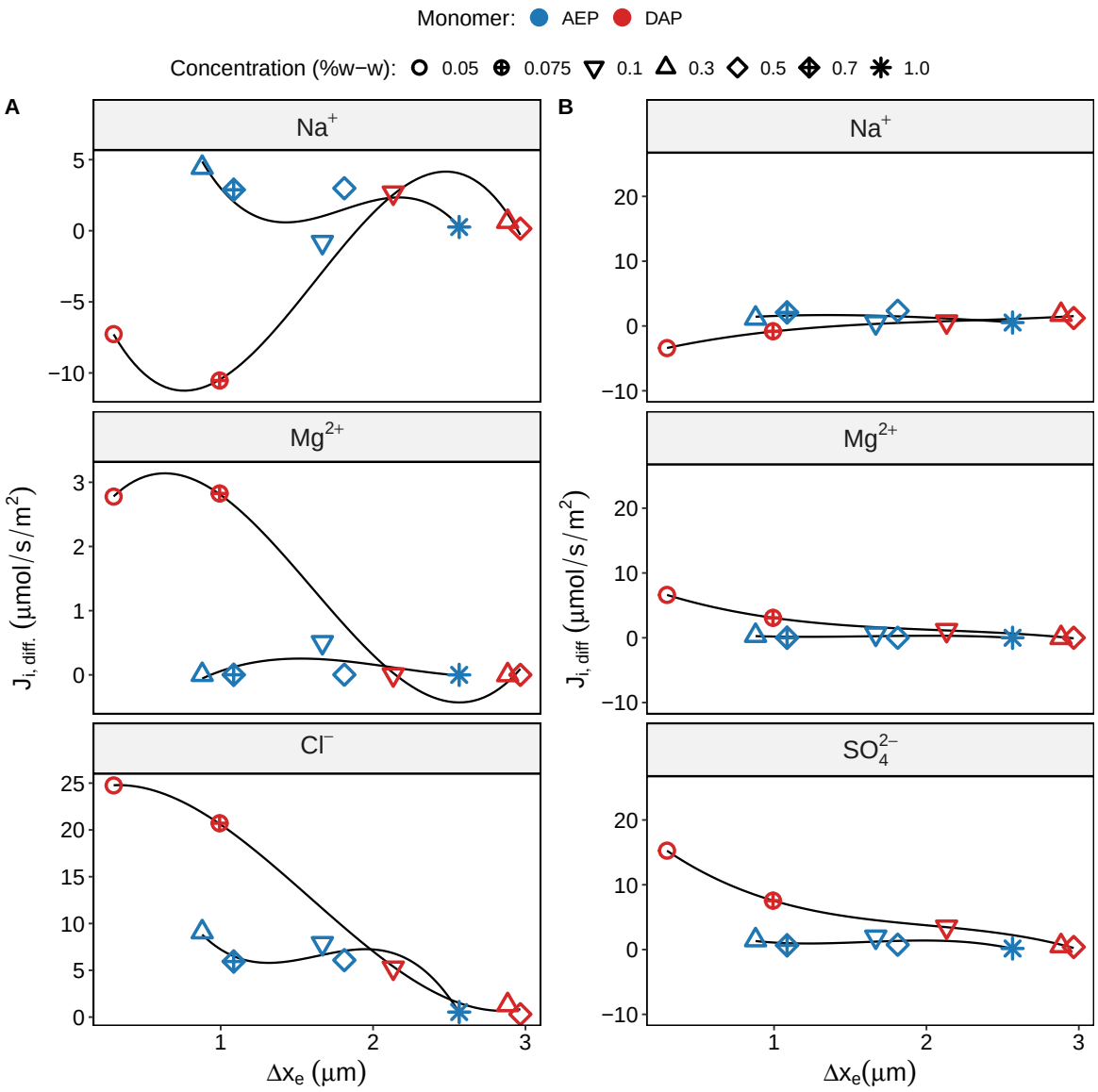



**Fig. S9:** Diffusive molar flux ($J_{i,diff}$) vs. thickness-to-porosity ratio ($\Delta x_e$) of the ternary ionic mixtures: (A) $Na^+/Mg^{2+}/Cl^-$ (B) $Na^+/Mg^{2+}/SO_4^{2-}$. Each shape of the data points corresponds to a different aqueous-phase monomer concentration, and the color of the data points indicates the aqueous-phase monomer (blue for AEP and red for DAP).

The concentration profiles of $Na^+/Mg^{2+}/Cl^-$ and $Na^+/Mg^{2+}/SO_4^{2-}$ within the active layers of the fabricated membranes are presented in Fig. S10 and S11, respectively. The $x$-axis represents the spatial coordinate across the membrane's selective layer. To facilitate direct comparison among membranes with different $\Delta x_e$, the $x$-axis values were normalized by $\Delta x_e$. In this normalized framework:

- $x = 0$ represents the pore entrance at the feed-solution/membrane interface
- $x = \Delta x_e$ represents the pore exit at the permeate-solution/membrane interface.

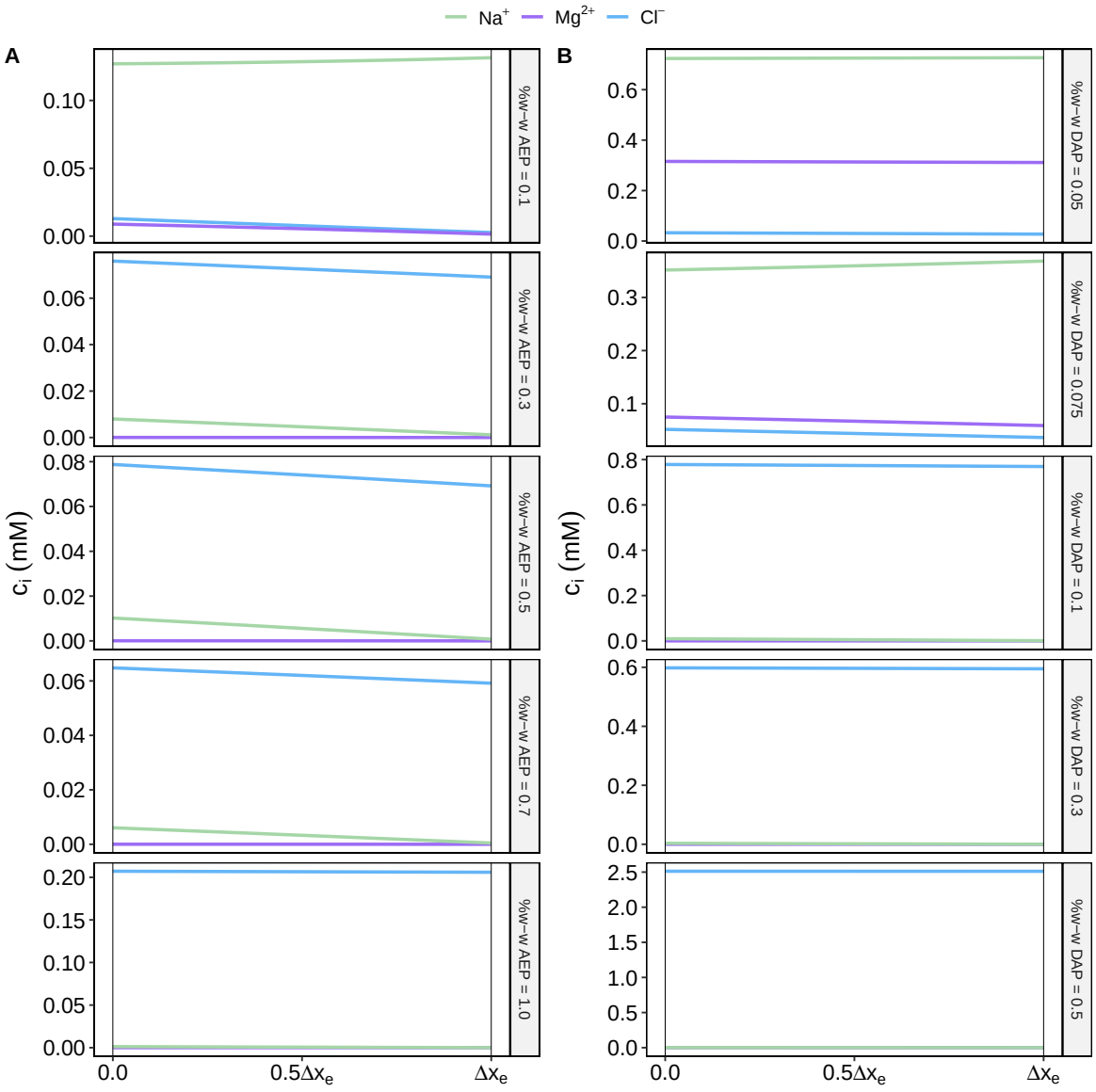



**Fig. S10:** Simulated concentration profiles across the active layers of the fabricated membranes of the ternary ion mixture $Na^+/Mg^{2+}/Cl^-$ during mixed salt retention tests as a function of $\Delta x_e$.

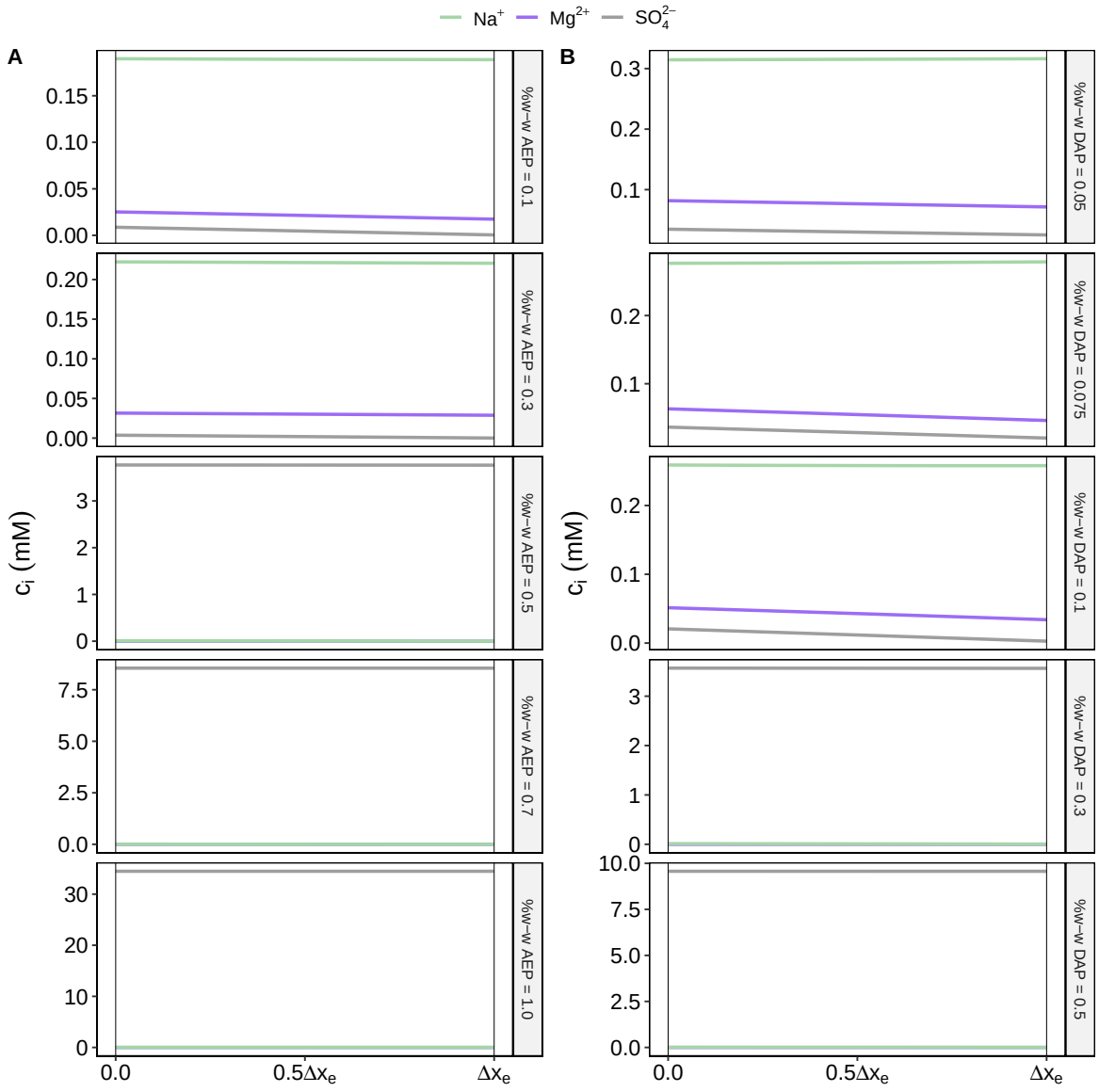



**Fig. S11:** Simulated concentration profiles across the active layers of the fabricated membranes of the ternary ion mixture $Na^+/Mg^{2+}/SO_4^{2-}$ during mixed salt retention tests as a function of $\Delta x_e$.

## Total transmembrane transport

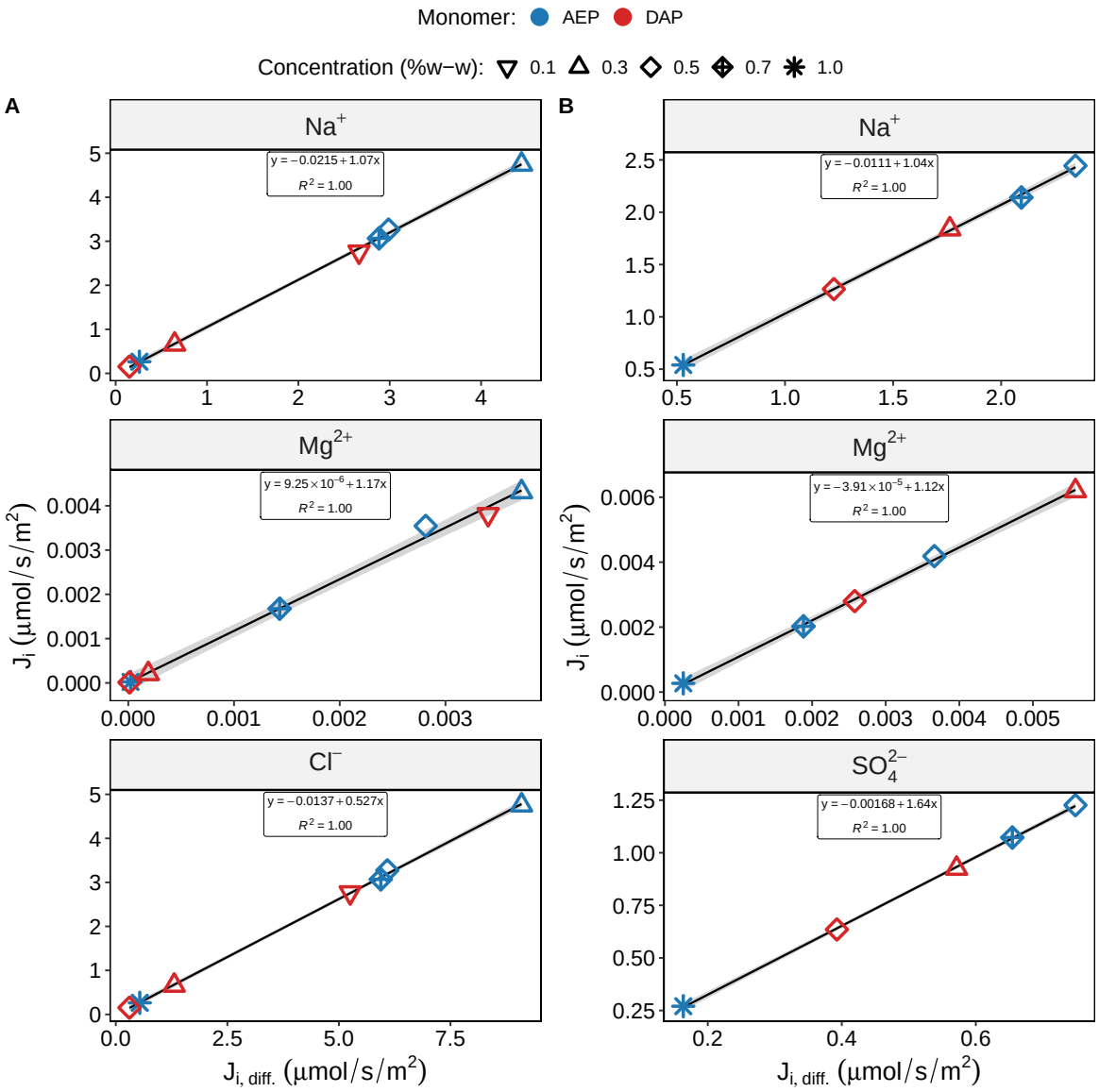



**Fig. S12:** Relationship between total transmembrane molar flux ($J_i$) and diffusive molar flux ($J_{i,diff}$) of the ternary ionic mixtures: (A) $Na^+/Mg^{2+}/Cl^-$ (B) $Na^+/Mg^{2+}/SO_4^{2-}$. Each shape of the data points corresponds to a different aqueous-phase monomer concentration, and the color of the data points indicates the aqueous-phase monomer (blue for AEP and red for DAP). Solid lines show linear fits, with corresponding equations and $R^2$ values provided in the panels.

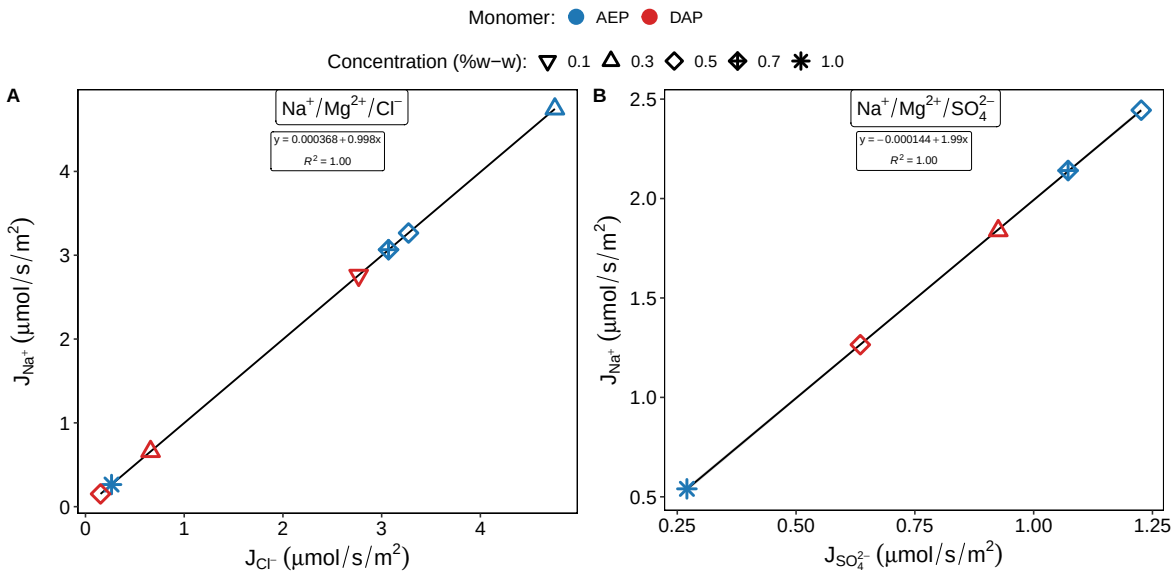



**Fig. S13:** Relationship between total transmembrane molar flux of $Na^+$ ($J_{Na+}$) and corresponding anion of the ternary ionic mixtures: (A) $Na^+/Mg^{2+}/Cl^-$ (B) $Na^+/Mg^{2+}/SO_4^{2-}$. Each shape of the data points corresponds to a different aqueous-phase monomer concentration, and the color of the data points indicates the aqueous-phase monomer (blue for AEP and red for DAP). Solid lines show linear fits, with corresponding equations and $R^2$ values provided in the panels.

# References


[1] F. Soyekwo, H. Wen, D. Liao, C. K. Liu, Nanofiltration membranes modified with a clustered multiquaternary ammonium-based ionic liquid for improved magnesium/lithium separation, Acs Applied Materials Interfaces 14 (28) (2022) 32420–32432. https://doi.org/10.1021/acsami.2c03650.

[2] C. Liu, L. Shi, R. Wang, Crosslinked layer-by-layer polyelectrolyte nanofiltration hollow fiber membrane for low-pressure water softening with the presence of so in feed water, Journal of Membrane Science 486 (2015) 169–176. https://doi.org/10.1016/j.memsci.2015.03.050.

[3] Y. Liang, Y. Zhu, C. Liu, K. R. Lee, W. S. Hung, Z. Wang, Y. Li, M. Elimelech, J. Jin, S. Lin, Polyamide nanofiltration membrane with highly uniform sub-nanometre pores for sub-1 Å precision separation, Nature Communications 11 (2020) 1–9. https://doi.org/10.1038/s41467-020-15771-2.

[4] Y. Yang, Y. Li, K. L. Goh, C. H. Tan, R. Wang, Dopamine-intercalated polyelectrolyte multilayered nanofiltration membranes: Toward high permselectivity and ion-ion selectivity, Journal of Membrane Science 648 (2022). https://doi.org/10.1016/j.memsci.2022.120337.

[5] X. Z. Wei, Z. Q. Gana, Y. J. Shen, Z. L. Qiu, L. F. Fang, B. K. Zhu, Negatively-charged nanofiltration membrane and its hexavalent chromium removal performance, Journal of Colloid and Interface Science 553 (2019) 475–483. https://doi.org/10.1016/j.jcis.2019.06.051.

[6] F. G. Meng, F. Song, Y. X. Yao, G. M. Liu, S. S. Zhao, Ultrastable nanofiltration membranes engineered by polydopamine-assisted polyelectrolyte layer-by-layer assembly for water reclamation, ACS Sustainable Chemistry Engineering 8 (29) (2020) 10928–10938. https://doi.org/10.1021/acssuschemeng.0c03318.

[7] C. Yan, S. H. Zhang, D. L. Yang, X. G. Jian, Preparation and characterization of chloromethylated/quaternized poly(phthalazinone ether sulfone ketone) for positively charged nanofiltration membranes, Journal of Applied Polymer Science 107 (3) (2008) 1809–1816. https://doi.org/10.1002/app.27226.

[8] T. W. Xu, W. H. Yang, A novel positively charged composite membranes for nanofiltration prepared from poly(2,6-dimethyl-1,4-phenylene oxide) by in situ amines crosslinking, Journal of Membrane Science 215 (1-2) (2003) 25–32. https://doi.org/10.1016/S0376-7388(02)00599-9.

[9] Y. X. Feng, H. W. Peng, Q. Zhao, Fabrication of high performance mg/li nanofiltration membranes by surface grafting of quaternized bipyridine, Separation and Purification Technology 280 (2022). https://doi.org/10.1016/j.seppur.2021.119848.

[10] T. Mu, H. Z. Zhang, J. Y. Sun, Z. L. Xu, Three-channel capillary nanofiltration membrane with quaternary ammonium incorporated for efficient heavy metals removal, Separation and Purification Technology 248 (2020). https://doi.org/10.1016/j.seppur.2020.117133.

[11] B. B. Yang, K. F. Gu, S. H. Wang, Z. Yi, Y. Zhou, C. J. Gao, Chitosan nanofiltration membranes with gradient cross-linking and improved mechanical performance for the removal of divalent salts and heavy metal ions, Desalination 516 (2021). https://doi.org/10.1016/j.desal.2021.115200.

[12] L. F. Fang, M. Y. Zhou, L. Cheng, B. K. Zhu, H. Matsuyama, S. F. Zhao, Positively charged nanofiltration membrane based on cross-linked polyvinyl chloride copolymer, Journal of Membrane Science 572 (2019) 28–37. https://doi.org/10.1016/j.memsci.2018.10.054.

[13] M. Alsuhybani, A. Alshahrani, A. S. Haidyrah, Synthesis, characterization, and evaluation of evaporated casting mwcnt/chitosan composite membranes for water desalination, Journal of Chemistry 2020 (2020). https://doi.org/10.1155/2020/5207680.

[14] Y. L. Ji, Q. F. An, F. Y. Zaho, C. J. Gao, Fabrication of chitosan/pdmchea blend positively charged membranes with improved mechanical properties and high nanofiltration performances, Desalination 357 (2015) 8–15. https://doi.org/10.1016/j.desal.2014.11.005.

[15] R. H. Huang, G. H. Chen, M. K. Sun, C. J. Gao, Preparation and characterization of quaterinized chitosan/poly(acrylonitrile) composite nanofiltration membrane from anhydride mixture cross-linking, Separation and Purification Technology 58 (3) (2008) 393–399. https://doi.org/10.1016/j.seppur.2007.05.013.

[16] R. H. Huang, G. H. Chen, M. K. Sun, C. J. Gao, Preparation and characterization of composite nf membrane from a graft copolymer of trimethylallyl ammonium chloride onto chitosan by toluene diisocyanate cross-linking, Desalination 239 (1-3) (2009) 38–45. https://doi.org/10.1016/j.desal.2008.02.023.

[17] R. H. Du, J. S. Zhao, Properties of poly (n,n-dimethylaminoethyl methacrylate)/polysulfone positively charged composite nanofiltration membrane, Journal of Membrane Science 239 (2) (2004) 183–188. https://doi.org/10.1016/j.memsci.2004.03.029.

[18] H. H. Wu, Y. K. Lin, W. Y. Feng, T. Y. Liu, L. Wang, H. Yao, X. L. Wang, A novel nanofiltration membrane with [mimap][tf 2 n] ionic liquid for utilization of lithium from brines with high mg/li ratio, Journal of Membrane Science 603 (2020). https://doi.org/10.1016/j.memsci.2020.117997.

[19] B. Y. He, H. W. Peng, Y. Chen, Q. Zhao, High performance polyamide nanofiltration membranes enabled by surface modification of imidazolium ionic liquid, Journal of Membrane Science 608 (2020). https://doi.org/10.1016/j.memsci.2020.118202.

[20] Z. Z. Zhang, M. M. Rahman, I. Ternes, B. Bajer, V. Abetz, Engineering soft nanochannels in isoporous block copolymer nanofiltration membranes for ion separation, Journal of Membrane Science 691 (2024). https://doi.org/10.1016/j.memsci.2023.122270.

[21] P. Zhao, F. Guo, L. F. Wang, H. E. Zhen, N. Zhang, S. H. Yin, G. L. Zhou, X. H. Ruan, G. H. He, X. B. Jiang, Nanofiltration membrane with modified nano-gradient structure and positive charge for li separation from high mg/li ratio brine, Desalination 577 (2024). https://doi.org/10.1016/j.desal.2024.117394.

[22] P. P. Su, M. Xu, C. W. Wang, Y. B. Li, Poly-(aminoethyl piperazine) membranes with ultra-thin selective layers prepared via a rate-retarded interfacial polymerization method, Journal of Membrane Science 714 (2025). https://doi.org/10.1016/j.memsci.2024.123415.

[23] L. Wang, Y. K. Lin, Y. H. Tang, D. Ren, X. L. Wang, Fabrication of oppositely charged thin-film composite polyamide membranes with tunable nanofiltration performance by using a piperazine derivative, Journal of Membrane Science 634 (2021). https://doi.org/10.1016/j.memsci.2021.119405.

[24] X. Li, C. Zhang, S. Zhang, J. Li, B. He, Z. Cui, Preparation and characterization of positively charged polyamide composite nanofiltration hollow fiber membrane for lithium and magnesium separation, Desalination 369 (2015) 26–36. https://doi.org/10.1016/J.DESAL.2015.04.027.

[25] Y. F. Yan, J. Wang, W. B. Wang, C. Han, Fine-tuning polyamide membrane pores and charge for enhanced li+/ mg2+separation, Journal of Membrane Science 721 (2025). https://doi.org/10.1016/j.memsci.2025.123812.

[26] N. Cevallos-Cueva, M. M. Rahman, H. H. Kinfu, V. Abetz, Mass transport mechanisms insights of selective sodium/magnesium separation through nanofiltration membranes, Journal of Membrane Science 721 (2025) 123808–123808. https://doi.org/10.1016/J.MEMSCI.2025.123808.

[27] O. Y. Lu, R. Malaisamy, M. L. Bruening, Multilayer polyelectrolyte films as nanofiltration membranes for separating monovalent and divalent cations, Journal of Membrane Science 310 (1-2) (2008) 76–84. https://doi.org/10.1016/j.memsci.2007.10.031.

[28] O. Labban, C. Liu, T. H. Chong, J. H. Lienhard V, Fundamentals of low-pressure nanofiltration: Membrane characterization, modeling, and understanding the multi-ionic interactions in water softening, Journal of Membrane Science 521 (2017) 18–32. https://doi.org/10.1016/j.memsci.2016.08.062.

[29] S. Déon, Z. Koubaa, E. Korzhova, A. Airoudj, P. Fievet, V. Roucoules, Understanding the impact of poly(allylamine) plasma grafting on the filtration performances of a commercial polymeric membrane, Separation and Purification Technology 212 (2019) 30–39. https://doi.org/10.1016/j.seppur.2018.11.004.

[30] Y. T. Liu, J. M. Sipe, W. H. Xu, X. W. Zhu, L. M. Bai, D. L. Xu, G. B. Li, H. Liang, M. R. Wiesner, Study on the mechanisms for the influence of nanomaterials on the separation performance of nanocomposite membrane from a modeling perspective, Desalination 532 (2022). https://doi.org/10.1016/j.desal.2022.115740.

[31] W. X. Fang, L. Shi, R. Wang, Interfacially polymerized composite nanofiltration hollow fiber membranes for low-pressure water softening, Journal of Membrane Science 430 (2013) 129–139. https://doi.org/10.1016/j.memsci.2012.12.011.

[32] H. H. Kinfu, M. M. Rahman, N. Cevallos-Cueva, V. Abetz, Ion selective metal-phenolic network nanofiltration membranes: The role of counterions and predictive modeling, Journal of Membrane Science 733 (2025). https://doi.org/10.1016/j.memsci.2025.124320.

[33] R. Wang, S. Lin, Pore model for nanofiltration: History, theoretical framework, key predictions, limitations, and prospects, Journal of Membrane Science 620 (2021) 118809. https://doi.org/10.1016/j.memsci.2020.118809.

[34] V. Geraldes, A. M. Brites Alves, Computer program for simulation of mass transport in nanofiltration membranes, Journal of Membrane Science 321 (2) (2008) 172–182. https://doi.org/10.1016/j.memsci.2008.04.054.

[35] V. Geraldes, M. D. Afonso, Prediction of the concentration polarization in the nanofiltration/reverse osmosis of dilute multi-ionic solutions, Journal of Membrane Science 300 (1-2) (2007) 20–27. https://doi.org/10.1016/J.MEMSCI.2007.04.025.

[36] N. Cevallos-Cueva, M. M. Rahman, H. H. Kinfu, V. Abetz, Mass transport mechanism of nitrate selective nanofiltration membranes on the basis of the donnan steric pore model with dielectric exclusion (dspm-de), Chemical Engineering Journal 493 (2024). https://doi.org/10.1016/j.cej.2024.152775.

# Acknowledgement

Now that this journey has come to an end, I would like to express my sincere gratitude to all the people who made it possible.

First, I would like to thank Prof. Volker Abetz, my doctoral supervisor, for his guidance, support, and trust during these years. His discussions, questions, and insights encouraged me to look beyond the immediate problem, to think more critically, and to develop greater scientific independence.

I am deeply grateful to Md. Mushfequr Rahman. Through his guidance, patience, and example, I learned to think more carefully and work more independently as a researcher. Thank you for believing in me and for always trusting in what I was capable of. Looking back, I can now understand how each piece of advice was part of a bigger picture that was not always obvious to me at the time.

I would also like to thank the Institute of Membrane Research for the support that made the completion of this thesis possible. I am especially grateful to Ivonne and Barbara for their constant help with lab work, and for always taking care of the ion chromatograph, which somehow always found unexpected ways to make things a bit more challenging. I also thank Maren for the GPC analysis and Jan for setting up the retention cells, which became the core of my performance measurements. Finally, I would like to thank Martin, Anke, Erick, and Evgeni, not only for their support with SEM, TEM, and AFM analyses, but also for the discussions that helped me better understand my results.

All my gratitude goes to Hluf, my colleague and friend. I was very lucky to have him by my side during these years. We made it!

Gracias a mi familia y amigos, el alfa y el omega de mi inspiración. Los amo y les dedico este logro.

# Declaration on oath / Affidavit

I hereby declare and affirm that this doctoral dissertation is my own work and that I have not used any aids and sources other than those indicated. If electronic resources based on generative artificial intelligence (gAI) were used in the course of writing this dissertation, I confirm that my own work was the main and value-adding contribution and that complete documentation of all resources used is available in accordance with good scientific practice. I am responsible for any erroneous or distorted content, incorrect references, violations of data protection and copyright law or plagiarism that may have been generated by the gAI.

Hamburg, 13.05.2026 Signature: 